TTI: 0-7013

Performance and Improvement of Texas Poor Boy Continuous Bridge Deck Details: Final Report

Technical Report 0-7013-R1

Cooperative Research Program

TEXAS A&M TRANSPORTATION INSTITUTE

COLLEGE STATION, TEXAS

sponsored by the
Federal Highway Administration and the
Texas Department of Transportation
https://tti.tamu.edu/documents/0-7013-R1.pdf

Technical Report Documentation Page

1. Report No.	2. Government Accession No.	3. Recipient's Catalog No.
FHWA/TX-25/0-7013-R1		

4. Title and Subtitle	5. Report Date
PERFORMANCE AND IMPROVEMENT OF TEXAS POOR BOY CONTINUOUS BRIDGE DECK DETAILS: FINAL REPORT	Published: March 2025
	6. Performing Organization Code
7. Author(s)	8. Performing Organization Report No.
Anna C. Birely, Matthew T. Yarnold, Stefan Hurlebaus, Andrew N. Pearson, Drew D. Krajeck, and Daron Smith	Report 0-7013-R1
9. Performing Organization Name and Address	10. Work Unit No. (TRAIS)
Texas A&M Transportation Institute The Texas A&M University System College Station, Texas 77843-3135	11. Contract or Grant No. Project 0-7013
12. Sponsoring Agency Name and Address	13. Type of Report and Period Covered
Texas Department of Transportation Research and Technology Implementation Office 125 E. 11th Street Austin, Texas 78701-2483	Technical Report: June 2019–August 2023 14. Sponsoring Agency Code

15. Supplementary Notes

Project sponsored by the Texas Department of Transportation and the Federal Highway Administration.
Project Title: Performance and Improvement of Texas Poor Boy Continuous Bridge Deck Details
URL: https://tti.tamu.edu/documents/0-7013-R1.pdf

16. Abstract

The majority of bridges in Texas are constructed with girders as simple spans. A simple-span deck requires expansion joints, which are sources of maintenance and durability issues. To avoid this, continuous decks, known as “poor boy joints” in Texas Department of Transportation (TxDOT) bridges, are an attractive option. These details are commonly known as link slabs. Despite a four-decade history of use, a comprehensive evaluation of the performance of this detailing has not been conducted. In this study, finite element modeling and full-scale experimental tests were used to conduct an evaluation of existing TxDOT continuous deck details and propose design recommendations. Both bonded and debonded link slabs were considered. While both types of link slabs have been investigated in the literature, the investigation presented in this report offers several unique aspects. Consideration of the use of partial-depth precast panels is crucial because the detailing of panels in the link slab region can have a significant influence on cracking in the link slab. Another area impacting the formation of damage is the presence of a crack former on the top and bottom of the deck, a detail commonly used in practice but not investigated via analysis or experimental testing. The experimental tests were full-scale tests and utilized two girder lines, a unique characteristic that allows for documentation of differences in damage in overhangs and between girder lines. Based on the findings of the experimental test program, this report provides design recommendations for limits on which bridges current TxDOT link slab details should be used, as well as recommendations for designs that utilize debonded link slabs, continuous panels, and a haunch gap at the end of the girder.

17. Key Words	18. Distribution Statement
Bridge Deck, Link Slab, Bonded, Debonded, Experimental Tests, Finite Element Modeling, Girder Rotation, Design Recommendations, Poor Boy Joint	No restrictions. This document is available to the public through NTIS: National Technical Information Service Alexandria, Virginia http://www.ntis.gov

19. Security Classif. (of this report)	20. Security Classif. (of this page)	21. No. of Pages	22. Price
Unclassified	Unclassified	494	

Form DOT F 1700.7 (8-72) Reproduction of completed page authorized

PERFORMANCE AND IMPROVEMENT OF TEXAS POOR BOY CONTINUOUS BRIDGE DECK DETAILS: FINAL REPORT

by

Anna C. Birely, PhD
Williams Brothers Associate Professor
Zachry Department of Civil and Environmental Engineering
Texas A&M University
Associate Research Scientist
Texas A&M Transportation Institute

Matthew T. Yarnold, PhD, PE
Former Assistant Professor
Zachry Department of Civil Engineering
Former Assistant Research Engineer
Texas A&M Transportation Institute

Stefan Hurlebaus, PhD, PE
Professor and R.P. Gregory '32 Chair
Zachry Department of Civil and Environmental Engineering
Texas A&M University
Research Engineer
Texas A&M Transportation Institute

and

Andrew N. Pearson, Drew D. Krajeck, and Daron Smith
Graduate Assistant Researcher
Texas A&M Transportation Institute

Report 0-7013-R1
Project 0-7013
Project Title: Performance and Improvement of Texas Poor Boy Continuous Bridge Deck Details

Sponsored by the
Texas Department of Transportation
and the
Federal Highway Administration

Published: March 2025

TEXAS A&M TRANSPORTATION INSTITUTE
College Station, Texas 77843-3135

DISCLAIMER

This research was sponsored by the Texas Department of Transportation (TxDOT) and the Federal Highway Administration (FHWA). The contents of this report reflect the views of the authors, who are responsible for the facts and the accuracy of the data presented herein. The contents do not necessarily reflect the official view or policies of FHWA or TxDOT. This report does not constitute a standard, specification, or regulation.

This report is not intended for construction, bidding, or permit purposes. The researcher in charge of this project was Anna C. Birely.

The United States Government and the State of Texas do not endorse products or manufacturers. Trade or manufacturers' names appear herein solely because they are considered essential to the object of this report.

ACKNOWLEDGMENTS

This project was sponsored by TxDOT and FHWA. The authors thank project directors Chris Glancy and Martin Dassi and members of the Project Monitoring Committee: Michael Hyzak, Taya Retterer, Aaron Garza, and Lianxiang Du. The authors are grateful for the project support provided by Texas A&M University graduate students through various stages of the project, especially Anna Marie Surber for assistance with developing girder design demands; Zhen Zhang for assistance with nondestructive evaluation data; Hyeonki Hong and Amreen Fatima for assistance with the retrofit concrete mix; and numerous other students for assistance in construction and testing of the specimens. Experimental testing would not have been possible without the support of Texas A&M University Center for Infrastructure Renewal High-Bay Lab Director Dr. Pete Keating and lab staff Charlie Droddy and Kirk Martin, as well as Dr. Kinsey Skillen for assistance finishing the decks. Bexar Concrete Works is appreciated for fabricating the prestressed components of the bridge and providing material samples. Concrete mix design for one of the retrofit designs was provided by the research team for TxDOT 0-6982, led by Dr. Mary Beth Hueste. Material for the concrete mix was provided by the TxDOT 0-6982 research project and through a donation by Alamo Cement.

TABLE OF CONTENTS

LIST OF FIGURES

Page

LIST OF TABLES

Page

1. INTRODUCTION

1.1 OVERVIEW

The Texas Department of Transportation (TxDOT) maintains over 55,000 bridges and builds over 500 new bridges every year. With such large inventory to manage, consideration of maintenance and durability issues is critical to providing long-lasting bridges and managing life-cycle costs. A majority of TxDOT bridges have simple-span girders, with a gap between the ends of the girders at the interior supports. At this gap, expansion joints are common sources of maintenance needs and lead to deck durability issues. To reduce the number of expansion joints, link slabs may be used, in which the deck is made continuous between the girder ends. Link slabs may be either bonded link slabs (deck fully composite with the supporting girders) or debonded (portion of the deck at ends is debonded from girder to increase flexibility).

TxDOT has utilized bonded link slabs for approximately four decades. These are commonly referred to as "poor boy" continuous deck details, or poor boy joints (PBJs), because the reinforcement for the link slab region is the same as that used in the remainder of the deck. Figure 1.1 shows the different types of continuous deck details used by TxDOT at the time of this report. Figure 1.1(a) shows the cast-in-place (CIP) details, consisting of #4 reinforcement at a spacing of 9 in. While not shown in the drawing, a ¾-in. chamfer is provided transverse on the bottom of the deck to encourage cracking at the center of the joint.

The majority of new decks in Texas bridges utilize partial-depth precast panels (PCPs) in which the bottom reinforcement is provided by the precast panels and only the top layer of reinforcement is needed in the CIP portion of the deck. Historically, the detailing of the PBJ in partial-depth panels has been to terminate the panels at least 1.5 ft prior to the ends of the girders and to have either a full-depth CIP region or permanent metal deck forms (PMDFs); in this report, such detail is referred to as an offset panel detail. Figure 1.1(b) shows the detail when the full-depth CIP region is used with the offset panel detail. Top reinforcement is simply the top reinforcement in the detail continued through the link slab. Bottom reinforcement is provided spliced with dowel bars extending from the precast panel. More recently, another detailing option, shown in Figure 1.1(c), has been introduced to the TxDOT standards, in which panels are continued the full length of the girders, with panels over the two ends meeting over the gap between the girder ends, and with a ¾-in. timber board separating the panels (board is terminated at the exterior edge of the fascia girders to allow full-depth CIP overhang). The top of the board is chamfered to produce a similar effect to the control location where cracks form. In the flush panel detail, the critical section at the center of the link slab is the depth of only the top CIP portion of the full deck (4.5 in.). Since the slab is thinner here, additional 5-ft long #4 bars are provided between each deck longitudinal bar, effectively providing #4 @ 4.5" instead of # 4 @ 9" as in the other deck designs. The current standards for offset and flush panel details include the use of an intentional crack former above the chamfer/notch. This top surface crack former has not always been used, allowing cracks to occur naturally in some decks.

Although some prior research studies have touched on the performance of PBJs, a comprehensive study has not been conducted. Thus, there is a need to evaluate the performance of bridges using current details and to make recommendations for design alternatives, in particular the performance of the newer flush panel detail. Design alternatives may be driven by constructability and/or performance and may range from minor detailing changes to use of alternative materials. To address these needs, TxDOT initiated Research Project 0-7013. This report documents the results of the project.

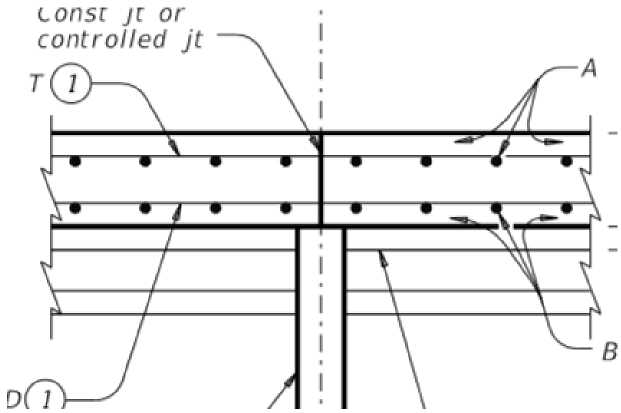

(a) CIP Detail

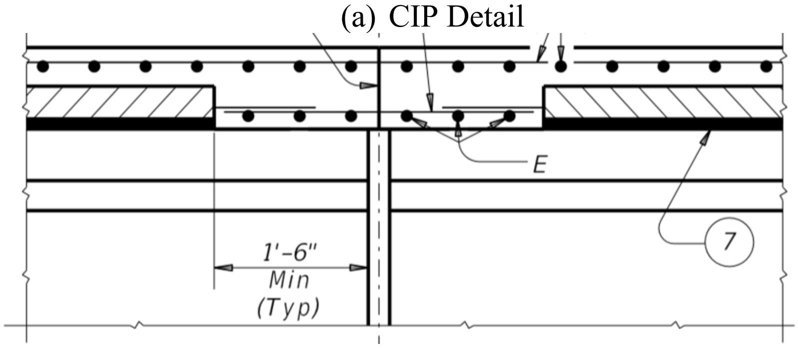

(b) Offset PCP

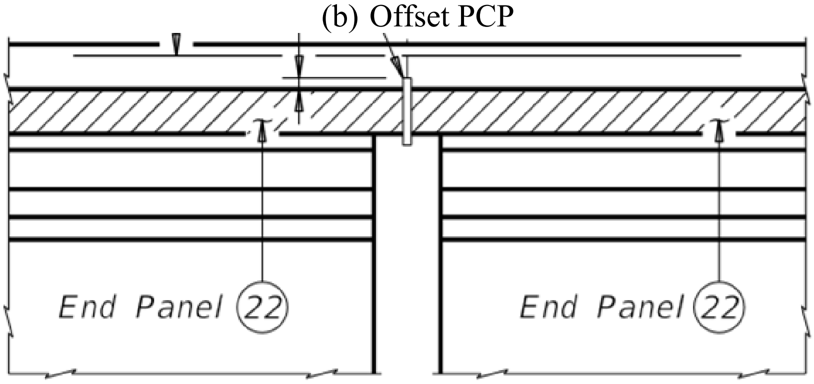

(c) Flush PCP

Figure 1.1. TxDOT poor boy joint continuous deck details (TxDOT bridge standards).

1.2 OBJECTIVES AND SCOPE

The objective of TxDOT Project 0-7013 was to conduct a comprehensive review of PBJ details and to provide recommendations for design and detailing methods to improve or alter the continuous deck details presently used by TxDOT. Specific technical objectives were to understand the performance of existing PBJ details and recommend modified details for new and existing decks.

The investigation of PBJ details was conducted via six tasks (Tasks 2–7) aimed at meeting the technical objectives. Task 1 was dedicated to project management and is not summarized here. Other tasks were as follows:

- Task 2—Literature Review.
- Task 3—Inventory Survey.
- Task 4—Design Considerations.
- Task 5—Finite Element Modeling.
- Task 6—Experimental Testing.
- Task 7—Design Recommendations.

1.3 OVERVIEW OF REPORT

The work in this project was conducted under TxDOT Project 0-7013.

Chapters 2–6 focuses on the evaluation of the literature and evaluation of existing TxDOT bridges containing PBJs. Chapter 2 presents the literature review. Chapter 3 presents the evaluation of bridges based on as-builts and inspection reports. In Chapter 4, the results of the field evaluation of eight bridge decks are presented. Chapter 5 provides a summary of five bridges monitored on the project and the potential implications for design. Chapter 6 presents observations of construction practices.

Chapters 7–11 focuses on the project tasks that advanced the understanding of the performance of TxDOT link slabs and helped form recommendations for developing and evaluating new designs. Chapter 7 presents a summary of design demands and considerations for designs. The individual design details are discussed in Chapter 8, alongside a presentation of finite element model results from investigating each aspect of design. Chapter 9 provides an overview of the full-scale experimental test program that tested six unique link slabs, including two retrofits. The overview includes designs of each specimen, details on construction, discussion of loads applied, and descriptions of the damage observed during each test. Extensive instrumentation was included in each test, with analysis and interpretation of the data provided in Chapter 10. Chapter 11 provides recommendations for the design of link slabs, both standard detailing recommendations for TxDOT I-girder bridges and procedures for unique designs.

Chapter 12 summarizes the project findings and makes recommendations for designs and future research.

2. LITERATURE REVIEW

The objective of TxDOT Project 0-7013 was to conduct a comprehensive review of the poor boy details and to provide recommendations for design and detailing methods to improve or alter the continuous deck details presently used by TxDOT. To support this objective, this chapter provides a summary of related topics found in the literature, including alternative design concepts that have been explored in other research projects.

Section 2.1 provides a summary of terminology used to describe continuous deck detailing. Section 2.2 summarizes the performance of joints. Section 2.3 summarizes the demands continuous decks must be designed for, including findings of previous studies to investigate the most prominent sources of demands and the impact of support conditions. Section 2.4 summarizes research on different types of continuous deck details using conventional and alternative material. Section 2.5 summarizes jointless bridges. Finally, Section 2.6 identifies gaps in the literature that must be addressed in order to meet the research objectives of TxDOT Project 0-7013.

2.1 NOMENCLATURE

The design for bridge deck deformations, forces, and performance should not only consider the deck and connection but also the rest of the superstructure and substructure. Similarities in the terminology used in the literature to describe bridge, deck, and joint characteristics make clarifying these terms an important step in examination of the literature. To support this, Figure 2.1 and Figure 2.2 provide an overview of the bridge characteristics.

Superstructure connectivity describes the connections of the girders and deck between spans (over the bent/pier). A discontinuous superstructure has no structural continuity between girders or in the deck over a support. A discontinuous deck is any deck with a physical discontinuity over the support that results in a gap in the concrete. The gap may be open or closed and is referred to here as an expansion joint. The expansion joint is intended to allow structural movement without transferring forces across the joint. A partially continuous superstructure has simple-span girders, with a continuous deck providing some superstructure connectivity. A superstructure that is continuous for live load is erected with discontinuous girders that are then joined together over the supports to resist live loads as a continuous unit. A continuous superstructure has continuity of both the girders and the deck over the supports. The focus of this study was on the performance of typical Texas bridges, in which the superstructure has partial continuity and girders are simply supported. Thus, the summary of literature provided here focuses on studies with these conditions. Additional studies are included when the findings have relevance to the design of decks for partially continuous superstructures.

In partially continuous superstructures, the gap between the ends of the girders leaves a short span of deck that is unsupported by the girders over the pier. This unsupported portion of the deck, referred to as a continuous slab detail in TxDOT standard drawings, was the focus of this study. Within the literature, the term link slab is often used to describe this portion of the deck. The link slab may or may not include the region of the deck above the ends of the girders. The detailing of the link slab may differ from the rest of the deck to account for the forces and deformations caused by deck continuity and/or to simplify and/or accelerate construction. The detailing may differ in any combination of reinforcement layout, slab thickness, crack-control details, material properties, and bond between the deck and girder ends. In classifying detailing for deck continuity, the primary difference is typically considered to be in the nature of the bond between the deck and girder ends. A debonded link slab is the most common type of continuous deck detailing reported in the literature, and consists of the unsupported portion of the deck and a length of the deck that is debonded from the ends of the girders. Any continuous deck detail that is not debonded from the girders is classified here as a bonded link slab. In some cases, this may include a length of the deck where detailing is modified. In other cases, the bonded link slab may only be referred to as the unsupported length of slab between the girders. The level of difference in detailing between the bonded link slab and the rest of the deck varies, ranging from significant differences to simple changes, such as providing a construction or control joint while keeping the existing deck reinforcement continuous. Texas continuous deck details, informally referred to as Texas poor boy joints, seek to maintain simplicity in design and construction and can be considered one of the simplest implementations of a bonded link slab.

The performance of continuous deck details is impacted by the deformations and forces in the continuous region, which are influenced by interior support conditions abutments, and the interaction of the overall bridge system. A girder support may act like a pin (high shear stiffness), a roller (low shear stiffness), or in between these cases. At an integral abutment, structural continuity is maintained through the approach slab, the bridge deck, the girders, and the abutment itself. In a semi-integral abutment, structural continuity is maintained in the approach slab and bridge deck over the abutment, but the superstructure is disconnected from the abutment. In non-integral abutments, the approach slab, bridge deck, and abutment are all discontinuous at the abutment. At the system level, jointless and seamless bridges are designed with the goal of eliminating joints and improving performance. In jointless bridges, the bridge deck is kept continuous over the whole structure, while deck movement is accounted for with expansion joints in the slabs approaching the bridge. In seamless bridges, the bridge deck and approach slabs are fully continuous. Structural movements accounted for with sufficiently flexible supports and forces caused by deck movement are dissipated gradually by soil interaction in the approach slabs. While jointless and seamless bridges were not the focus of this study, the literature was worth examining because they include a continuous deck component over the interior supports.

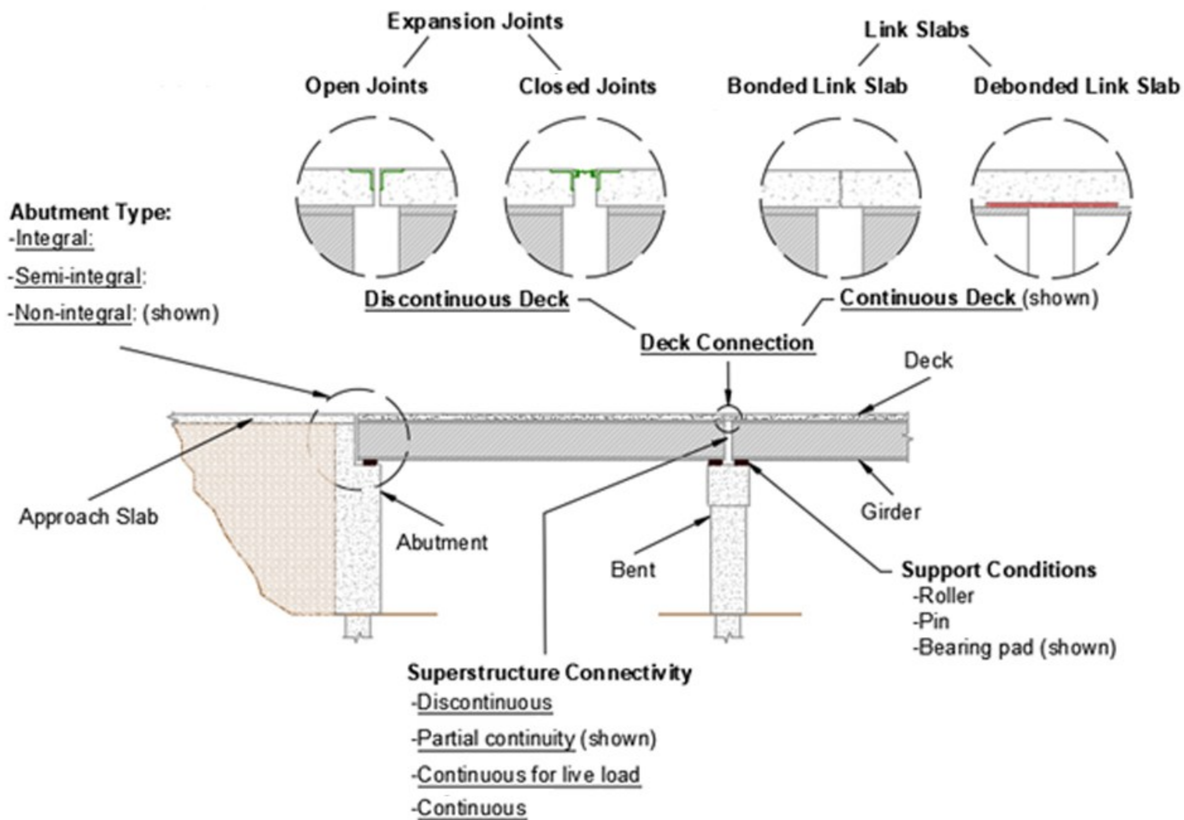

Figure 2.1. Nomenclature diagram for bridge components.

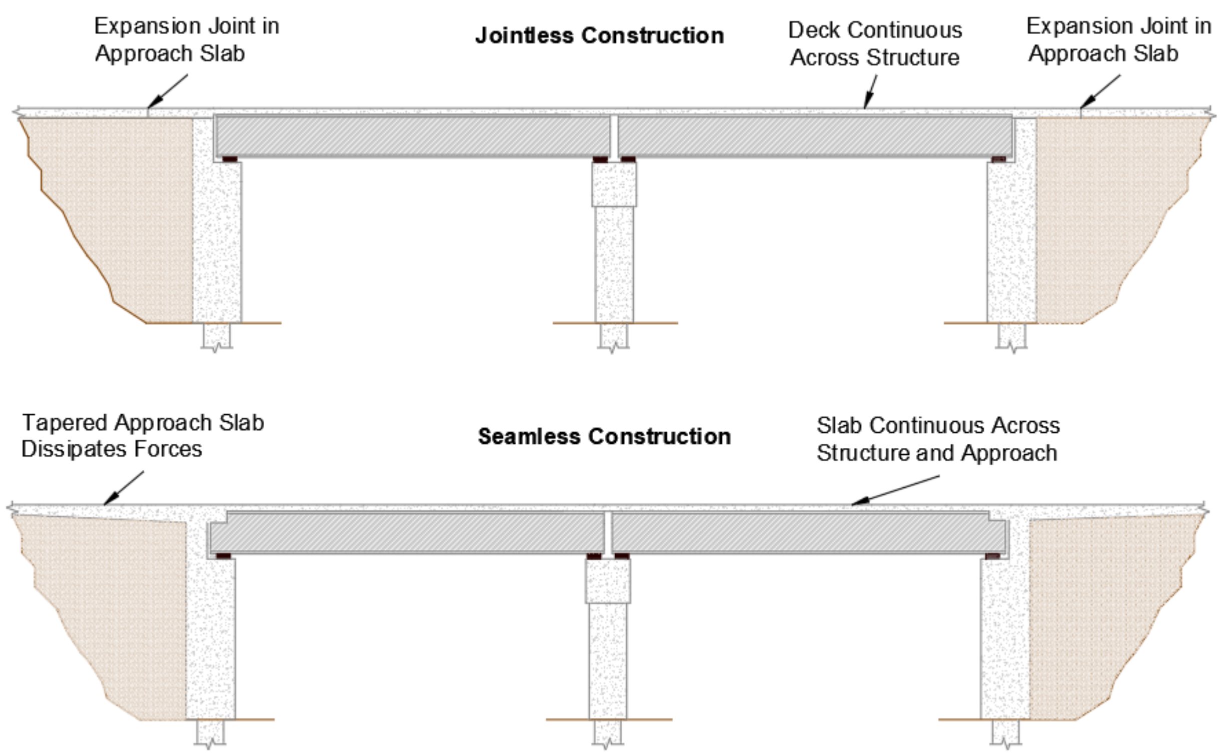

Figure 2.2. Bridge system nomenclature diagram.

2.2 JOINTS IN BRIDGES

Joint design must take into account many sources of movement, including shrinkage, temperature effects, creep, cyclic rotations caused by traffic, bearing deformation, and soil pressure, while maintaining durability and preventing water damage (Burke Jr. 1989). Burke Jr. reviewed the history of bridge deck joint construction and performance and summarized issues engineers faced with expansion joints. In the 1960s and 1970s, the expanded application of deicing chemicals exacerbated issues of bridge deck joint damage. Open or leaking joints led to swift deterioration of bridge substructures. While the use of continuous bridge structures without intermediate joints had been implemented since the 1930s, joint movement at the abutments was still a design issue for such structures.

Joints may be broadly categorized as either open or closed. Open joints include formed joints (see Figure 2.3) and finger-plate joints that allow water and debris to pass through. Closed joints include various types of seals (see Figure 2.3[b–c]) and sliding plates. Poured seals are limited to small deflections. They may include additional elements such as backer rods, bond-breaking material between the sealant and joint filler, or angled steel to reinforce the top edges. Compression seals, which consist of cellular elastomeric structures, may incorporate larger displacements. Cellular seals are a similar concept made of foams. Sliding plate joints (see Figure 2.3[d]) are typically used for displacements up to 4 in. While simple to construct and hardier than elastomeric options, they will allow water to permeate if not sealed and are vulnerable to damage from vertical deflections. Prefabricated elastomeric seals may be sheet or strip style (see Figure 2.3[e]), incorporating deflections up to around 4 in. or more complex plank seals for large deflections up to 13 in. While the performance of deck joints is an area of concern for bridge engineers, the deck itself must also be durable, especially when it comes to controlling cracking that leads to corrosion.

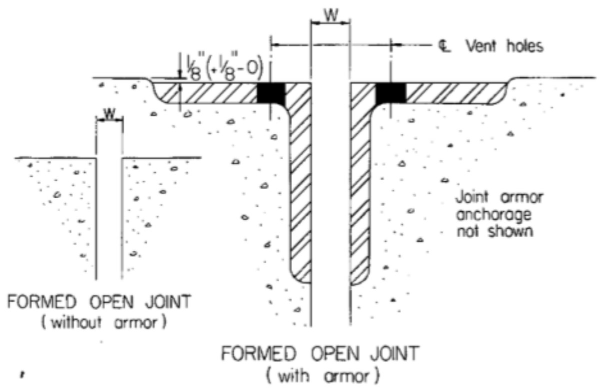

(a) Formed open joints

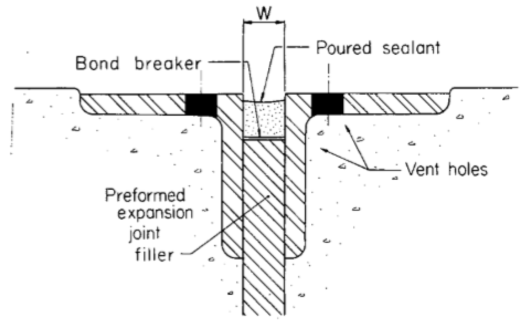

(b) Closed armored joints with a poured seal

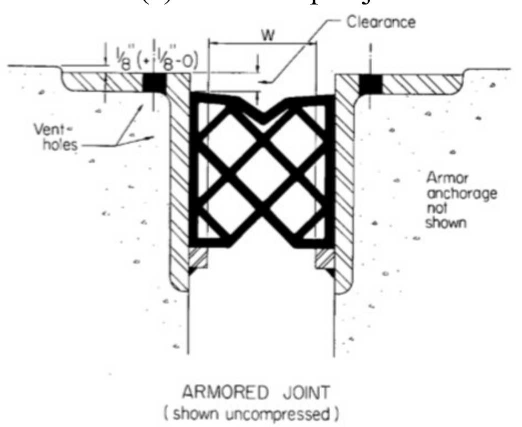

(c) Closed armored joints with a compression seal

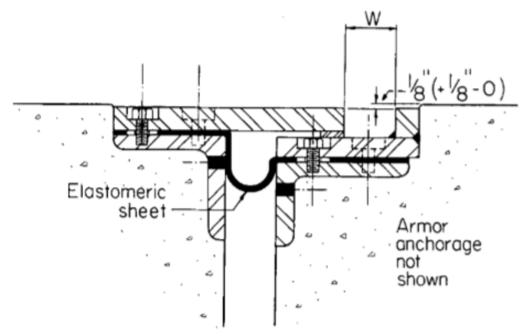

(d) Sealed sliding plate joint

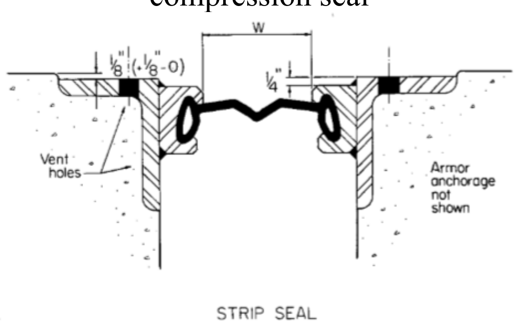

(e) Elastomeric strip seal

Figure 2.3. Examples of joints in discontinuous decks, reprinted from Burke Jr. (1989).

2.3 CONTINUOUS DECK DEMANDS

The eighth edition of the American Association of State Highway and Transportation Officials (AASHTO) Load and Resistance Factor Design (LRFD) Bridge Design Specifications (2017) dictates that forces caused by bridge deformation should be included in design. These deformations arise from uniform temperature changes, temperature gradient, creep, and shrinkage. Shrinkage strains may be calculated with AASHTO Equation 5.4.2.3.3-1 and using factors for volume-to-surface ratio, humidity, concrete strength, and time. The specification provides two procedures for calculating uniform temperature change deformations, using tabular or map-based maximum and minimum temperature values. These values are used in AASHTO Equation 3.12.2.3-1 to find the design range of movement.

Regarding temperature gradient, positive temperature gradient values are chosen with a map and table. Negative gradient values are found similarly and then modified based on deck surface material. These temperatures are applied to a standard thermal gradient (AASHTO Figure 3.12.3-2, shown in Figure 2.4), with dimensions defined by superstructure depth. AASHTO Section 4.6.6 specifies that axial deformation, bending deformation, and associated stresses should be calculated using this temperature gradient. AASHTO Equations C4.6.6.-1 through C4.6.6.-7 may be used to find axial deformation, axial strain, curvature, bending and axial end forces, and internal stresses.

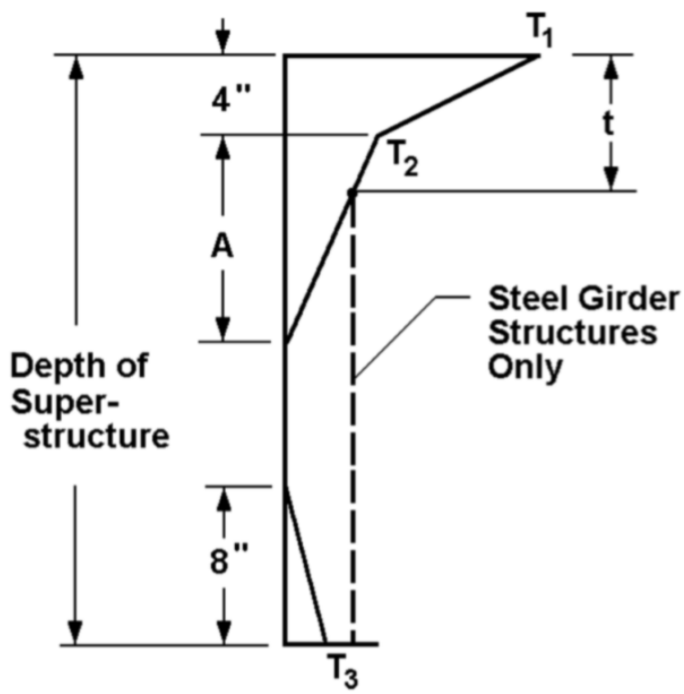

Figure 2.4. Girder temperature gradient, reprinted from AASHTO (2017).

In analyzing the demands in continuous decks, the support conditions can greatly impact the behavior. A number of research studies have focused on this topic and are summarized here to provide background for evaluating the impact of support conditions on TxDOT bridges.

Gastal (1986) developed a nonlinear finite element approximation of a continuous deck bridge structure, incorporating prestressing effects, temperature effects, spring support conditions, and time-dependent load effects. It was observed that the boundary and support conditions greatly affected behavior.

Okeil and ElSafty (2005) developed a method of structural analysis of simply supported bridges with continuous decks, including the effects of slab and beam stiffness and span length. The difficulty in modeling partially continuous bridges arises because of the lack of rotational compatibility across a support at the link slab caused by tensile elongation in the link slab. The rotational behavior also changes with support conditions (see Figure 2.5) because roller supports necessitate the elongation of the girders in tension, while the use of pinned supports causes a reaction at the support to counter the tension in the link slab. The elongation of the girders with roller conditions means a reduced tensile force in the link slab and the prevention of a couple moment between the support and slab (see Figure 2.6). The most common way to capture such behavior in modeling is through the use of finite element methods.

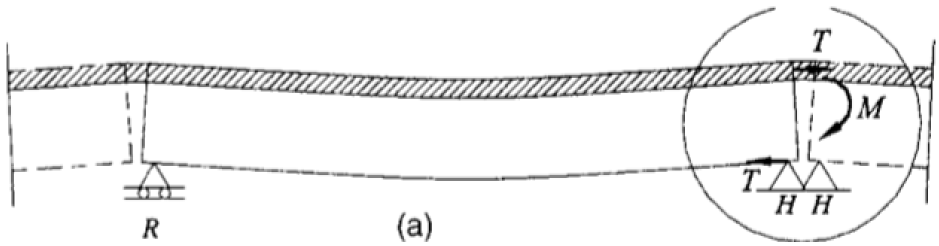

(a)

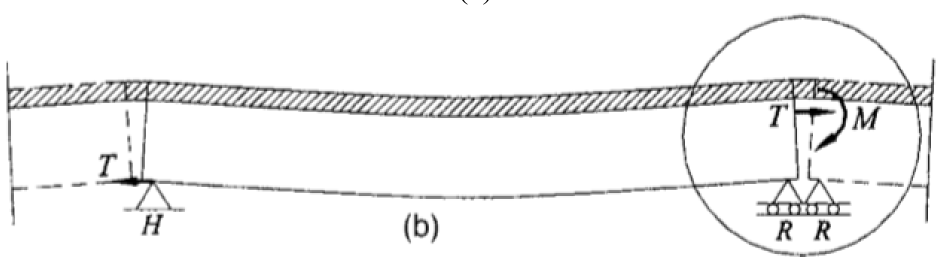

(b)

Figure 2.5. (a) Hinge supports causing a couple moment and tension in the link slab, and (b) roller supports preventing the formation of a couple moment, reducing the tension in the link slab; reprinted from Okeil and ElSafty (2005).

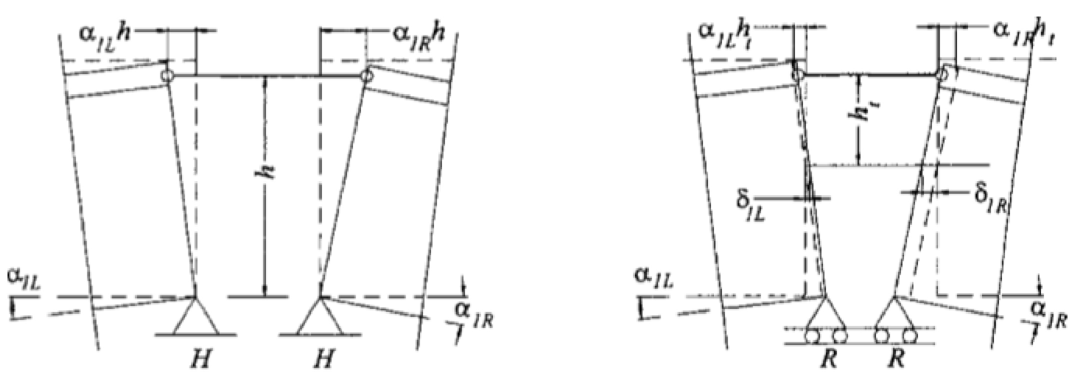

(a) (b)

Figure 2.6. Deformation of the link slab system with (a) pin supports and (b) roller supports; reprinted from Okeil and ElSafty (2005).

Okeil and ElSafty (2005) sought to develop a simpler method for analysis that would still yield reliable solutions. One method that was suggested was a three-moment equation that uses the moment at the supports and the rotations at the link slabs. The equation was developed for both roller and hinged support conditions. The authors also developed influence line equations for the cases and verified their expressions with experimental data from two existing bridges in the literature and with the results of a finite element model. Results showed good agreement to the finite element model and mixed results when compared to the existing bridge data. The major discrepancy between experimental and analytical results was explained by possible longitudinal deformation that was unaccounted for in the simplified experimental structure, which led the analytical result to be overly conservative in its prediction. For realistic designs, it was found that moment continuity in the link slab ranged from 9–22 percent of the moment at the support for an equivalent fully continuous bridge.

Canales and Okeil (2019) examined the behavior of link slabs used with various support conditions. These different conditions included idealized supports with pin and roller configurations, and both fixed and free bearing pad supports. Floating spans are defined as continuous decks above simply supported girders resting on expansion bearing pads, where none of the pads include a detail restraining the girders against longitudinal deformation at the bent. Fixed spans, alternatively, include one or more fixed bearing pad details. Researchers performed a parametric study on this structure type, varying span length and number, as well as girder spacing, span length ratio, support conditions, and temperature.

In the fixed bearing condition, a stiff support connects to a bent that has been designed to resist longitudinal forces, while the remaining expansion bearings allow longitudinal translation of the girder ends and transfer smaller longitudinal forces to the substructure. This structural configuration causes dissimilar longitudinal loads across the supports, affecting the loads through the link slabs.

When compared to idealized hinge-roller-roller-hinge (HRRH) support conditions and roller-hinge-hinge-roller (RHHR) conditions, the above fixed bearing support condition typically results in less longitudinal restraint than both. The RHHR condition causes the highest force through the link slab since the deformation at the girder end beneath the link slab is restricted by the support. Thus, the girder end rotation at the pinned support must be fully borne by the link slab above it, causing a force couple between the link slab and the support. The HRRH condition causes a reduction in the link slab force since the pinned supports lie at the far ends of the spans, causing deflections to be borne along the length of the girder and the link slab together.

The fixed support condition will typically result in further reduced link slab forces since each of the bearing pads provides deformation capacity, even including fixed bearing pad. The floating-support condition provides the largest reduction in link slab forces since longitudinal displacements are distributed across all the low-stiffness supports, resulting in small longitudinal support forces. Temperature effects were included since temperature directly affects the stiffness of bearings, and therefore the forces in the structure.

The bridges studied were designed with reinforced concrete AASHTO girders and a 7.5-in. thick composite slab. The steel-reinforced elastomeric bearings were designed using AASHTO LRFD specifications. It was found that fabricated elastomeric bearings (FEB) pads had six times the shear stiffness of extruded elastomeric bearings (EEB) pads. Live load effects were considered using the HL-93 design truck and lane load. Dead loads were not included in the continuity study due to load sequencing. Creep effects were not considered as part of the scope of the project.

The effect of temperature gradient, which can cause sizeable moments in link slabs, was accounted for using Section 3.12.3 of the 2012 AASHTO specifications (AASHTO 2012). Researchers used expressions to calculate girder end curvature and the corresponding induced moment.

Researchers analyzed 648 line models to incorporate the various parameters, with 324 of those models including link slabs. The line models included five elements for a two-span structure and eight elements for a three-span structure (see Figure 2.7). Notably, the ends of the link slab element were released for moments. Thus, the link slab was only considered to undergo axial force demands. Researchers theorized that the offset of the link slab from the centroid of the section would cause the link slab to contribute an axial force to the system, while the link slab's low moment stiffness would preclude significant development of flexure in the member.

To analyze the parameters, an equivalent stiffness for the structure was defined in terms of each structure parameter (see Figure 2.8). Similarly, an equivalent support stiffness was defined in terms of the support and temperature parameters. F1 is defined as the force at the support, F2 as the force at the centroid, F3 as the link slab force, θ as the girder end rotation, and δ as the girder deformation from axial forces. Using the diagram shown in Figure 2.8, it was possible to solve for the girder end rotation in terms of the stiffness and dimensional parameters. By rearranging terms and substituting, the equivalent stiffness of the whole system, K_{EQ}, is also found. This parameter is used to simply compare the various cases. The model was validated using STAAD software.

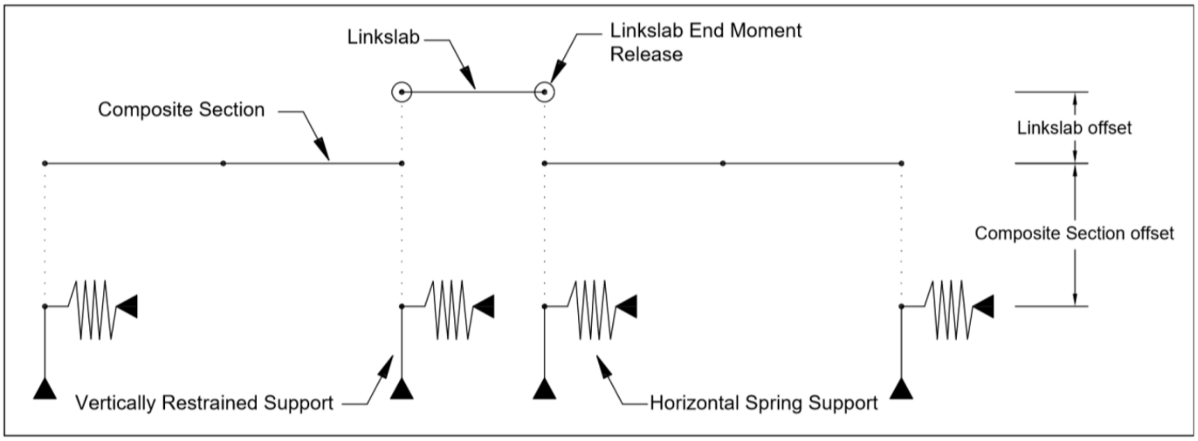

Figure 2.7. Finite element model, reprinted from Canales and Okeil (2019).

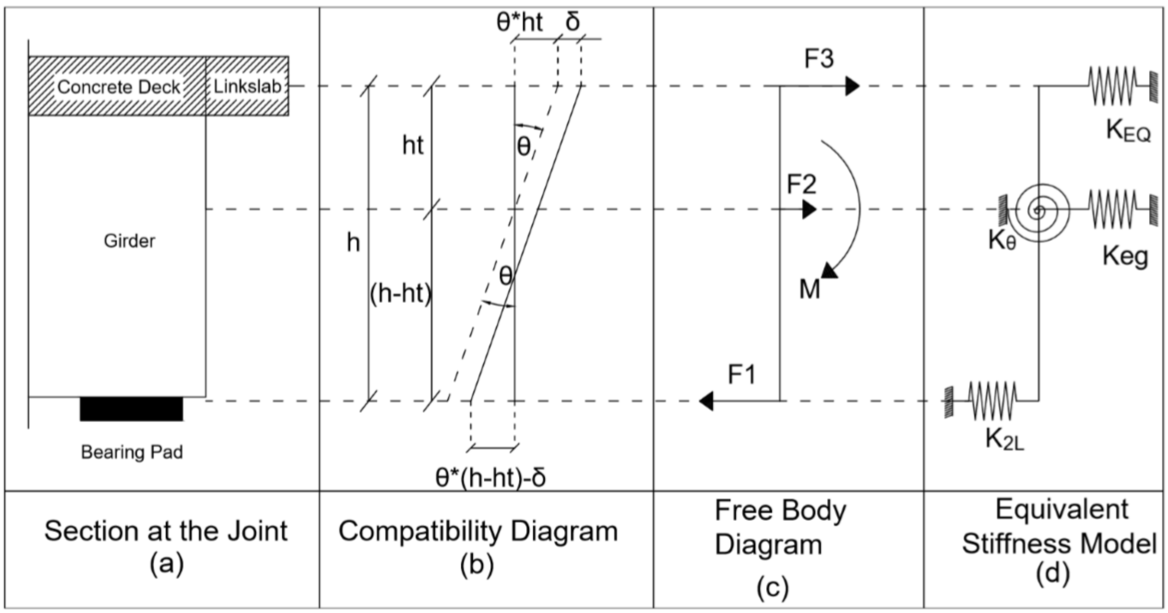

Figure 2.8. Parameter calculation for equivalent stiffness model, reprinted from Canales and Okeil (2019).

For support conditions, the results showed that a pin condition beneath the link slab maximizes tensile demands in the link slab and the continuity of the system. The stiffness of the supports not beneath the link slab have a lesser effect. The relationship between the equivalent system stiffness and the bearing stiffness is proportional. Using EEB supports greatly reduces the link slab force and the girder positive moment when compared to FEB conditions. Still, the reduction in moment was small, under 1 percent, for the conditions studied.

Additionally, decreased temperature causes increased support stiffness and a corresponding increase in link slab force. While live load effects cause a tensile force in the link slab, decreasing temperature causes compressive forces. It was found that the stiffness of the girder did not appreciably affect the tension in the link slab.

Canales Jr. (2019) performed field monitoring of a new 20-span girder bridge with link slabs spanning the Ouachita River in Harrisonburg, Louisiana. One four-span 540-ft segment, three two-span 270-ft segments, and one 135-ft span were all instrumented. In the link slabs, additional No. 6 longitudinal bars were placed in the top and bottom mats at 7-in. spacing. Silicone-sealed crack-control grooves were tested in some link slabs. Internal vibrating wire sensors were placed to record reinforcement forces, and external vibrating wire sensors were placed to record girder end displacements, girder end rotation, and temperature (see Figure 2.9).

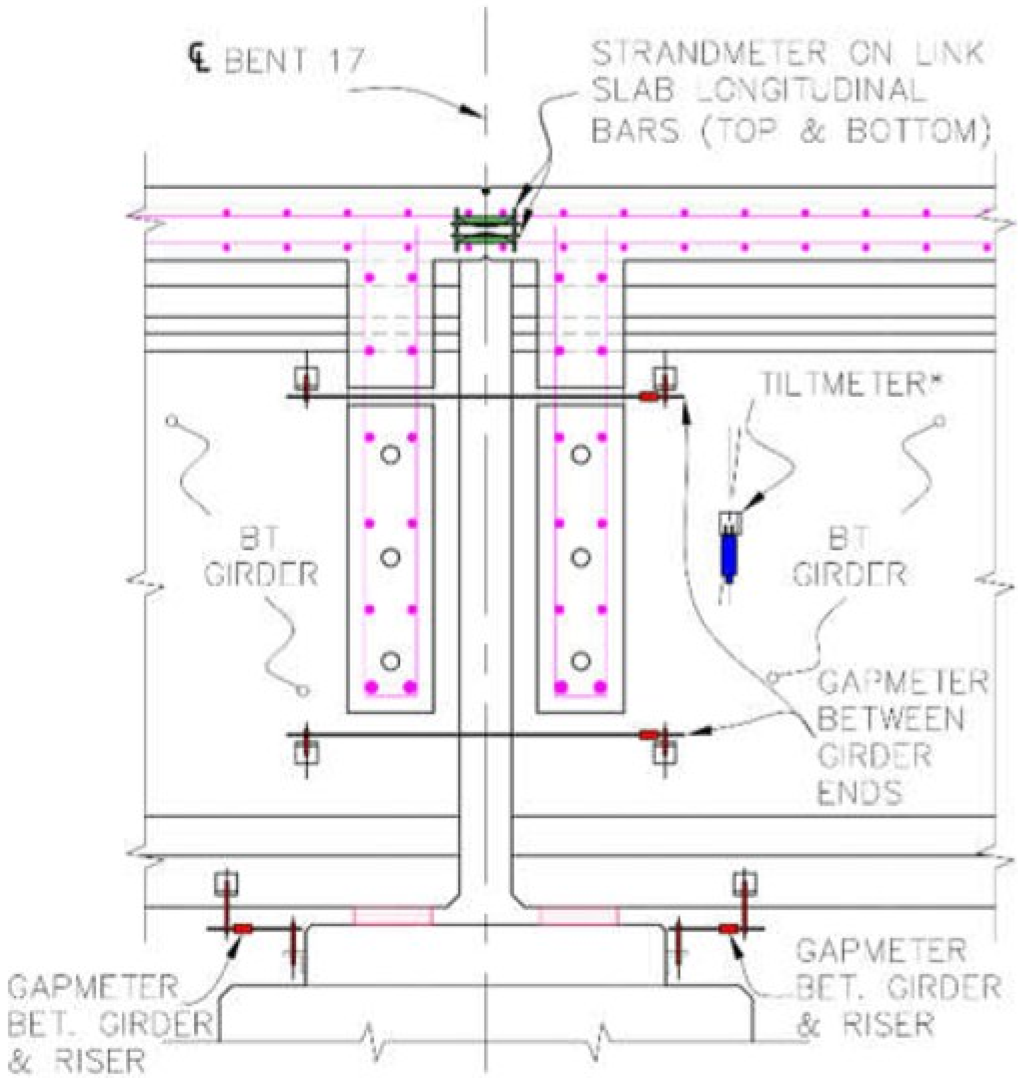

Figure 2.9. Field monitoring instrumentation setup, reprinted from Canales Jr. (2019).

Measurements were taken every three minutes for nearly two years. Researchers conducted visual inspections to monitor cracking and used a live load test to generate data under controlled loading. The displacement values from the link slab reinforcement were used to solve for stress and strain values. Since cracks cause the concrete to have zero stress in tension for the depth of the crack and zero stress in compression wherever cracks remain unclosed, the researchers calculated crack width and location for each loading step. Using an equation for calculating crack width in tensile members made it possible to remove the tensile strength of cracked concrete and establish compressive strength only when concrete surfaces were in contact. This correction for cracking significantly reduced calculated forces in the link slab.

Inspections revealed that transverse cracks formed in all link slabs, including cracks parallel to the silicone-filled crack-control details, which were clearly not effective. When the girder end support had a higher degree of fixity, cracking was found to increase. Girder deflections in the four-span continuous deck unit were smaller than those in the two-span continuous unit, despite having equivalent support conditions and span lengths. The added continuity appears to allow the continuous deck unit to redistribute deformations, and lower crack widths were also found in the four-span unit. Furthermore, the addition of end diaphragms that were secured to their adjacent bent reduced rotations by restraining the girders against deflection. However, units with end diaphragms also had larger crack widths than their floating-support counterparts, indicating that the added restraint caused larger tensile forces in the link slab.

With the pronounced effect that support stiffness has on link slab forces, it is important to be aware of designs that may increase stiffness. For instance, large bearing pads or cold temperatures increase pad stiffness. Additionally, cracking in the link slab has an important effect on the development of bending forces, and sources of deck cracking should be thoroughly analyzed.

In addition to the specific considerations of the demands in the continuous deck over the bent caps, the evaluation of existing detail performance and the development of candidate designs must account for the challenges of cracking that can occur in any part of the bridge deck. Bridge decks must be designed to account for various sources of deformation and stress to prevent deleterious cracking. Pesek et al. (2013) developed an analytical model for cracking in reinforced concrete bridge decks with the goal of understanding and preventing early-age cracking in decks that can cause structural deterioration. The research team's findings were integrated into ConcreteWorks 3.0 software for use by TxDOT engineers. Factors involved in early-age cracking include plastic shrinkage from evaporation, volume change from the cement hydration reaction, long-term drying shrinkage, and temperature deformations. Carbonation shrinkage and moisture gradients may also contribute to cracking behavior. Creep behavior is affected by a wide variety of material, loading, environmental, and geometric conditions, and relaxation in the concrete helps ameliorate generated stresses. Moisture gradients occur when areas of the slab dry at different rates, causing warping of the deck. Carbonation shrinkage is caused by the reaction of cement paste with carbon dioxide, which can lead to corrosion of reinforcing steel in poor quality concrete mixtures. Cracking results when the concrete is restrained against deformation.

Volume change is dependent on concrete mixture ingredients, proportions, and temperature. Particularly in high-performance concrete (HPC), chemical shrinkage can be an issue due to a low water–to–cementitious materials ratio. Chemical shrinkage is caused by air filling pores as the supply of water in the mixture is depleted, leading to a contracting force of surface tension within the pores. Aggregate, which is subject to compressive forces by this cement contraction, helps prevent shrinkage of the system depending on the stiffness and volume fraction of the aggregate. Autogeneous shrinkage, which is related to chemical shrinkage, is defined in terms of the apparent volume change of the system (the total volume of solids, liquid, and air), while total chemical shrinkage is defined in terms of absolute volume change (the volume of the system discounting air). Figure 2.10 shows a representation of chemical changes and shrinkage during the concrete curing process. An analytical model of autogeneous shrinkage by Hedlund (2000) was used for the ConcreteWorks software.

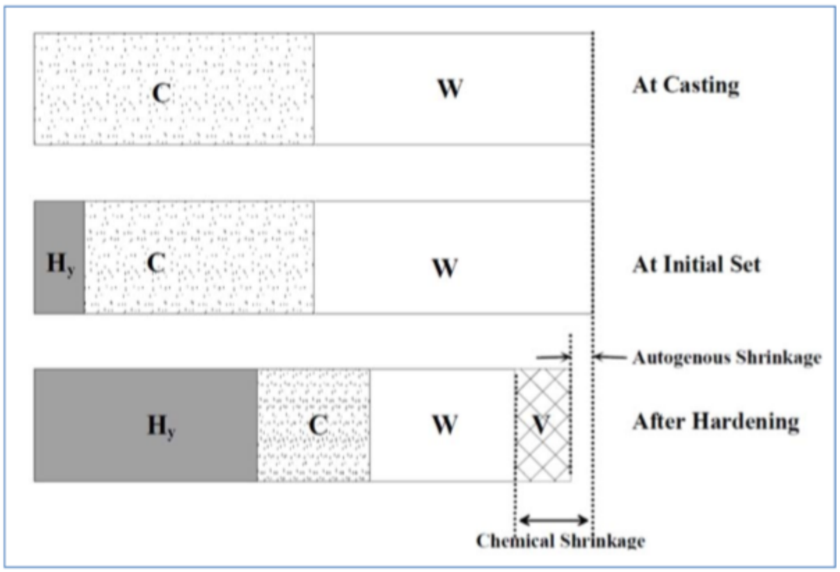

Figure 2.10. Chemical changes and shrinkage during the concrete curing process, reprinted from Holt (2001).

Drying shrinkage is driven by water loss from small pores with a radius less than 50 nm. Stress produced by water loss may be estimated with the Kelvin/Laplace-Gibbs equation, wherein the stress is proportional to surface tension of the pore water and inversely proportional to pore radius. By varying the water–to–cementitious materials ratio, cement characteristics, inclusion of supplemental materials like fly ash or silica fume, admixtures, and aggregates, it is possible to control the size of pores. Some admixtures are also able to lessen surface tension of the pore water in order to control shrinkage. There is a plethora of drying shrinkage models, but the B3 model by Bazant and Murphy (1995) was recognized by Pesek et al. (2013) as a popular choice.

Thermal effects caused by heat of hydration also may contribute to cracking issues when combined with autogenous and drying shrinkage. Temperature from the curing process tends to increase for the first 24 hours, after which the reaction slows to the point where environmental heat loss controls the cracking. Analytical estimates of heat generation have been developed for a wide variety of concrete mixture designs. Finite difference methods have been used to apply heat generation models to structures.

The other dimension of the concrete cracking issue pertains to the concrete's strength development and restraint conditions that allow the deck to resist tensile stress. A primary factor in determining strength is a low water–to–cementitious materials ratio, which corresponds to higher early and long-term strength development. Cement type and fineness have an important influence. Aggregate strength is less of a factor for normal concrete mixtures, but it becomes an important factor for high-strength concrete. The texture, size, and shape of aggregate do have a major effect on concrete tensile capacity. It is important to be mindful of trade-offs in concrete design. For instance, rough aggregate leads to increased tensile strength but also decreased workability. If water is added to restore workability, the advantage of rough aggregate is negated by strength loss. Figure 2.11 shows a diagram of sources of bridge deck cracking.

Methods for estimating concrete maturity include the Nurse-Saul method, which relates concrete temperature at a given time, and the equivalent age method, which relates curing time at a constant temperature to the curing time of a concrete sample. Models for setting time are important to plastic shrinkage and the onset of tensile strength. Models for compressive strength, tensile strength, and elastic modulus must also be considered.

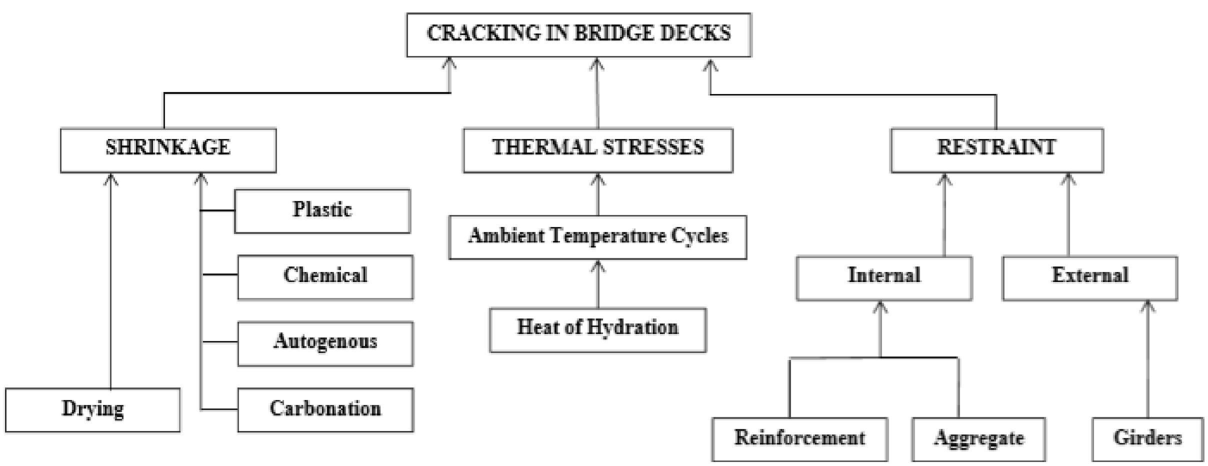

Figure 2.11. Bridge deck cracking sources, reprinted from Pesek et al. (2013).

Pesek et al. (2013) conducted a test program to investigate the early-age cracking behavior of materials commonly used to fabricate TxDOT bridge decks. These constituents included cements, fly ash, blast furnace slag, coarse and fine aggregate, and water reducing and shrinkage reducing admixtures. Materials were used to generate numerous mix designs that were cast into cylinders and prisms for strength, elasticity, and shrinkage testing. Frames were constructed to evaluate restrained cracking behavior and unrestrained shrinkage (see Figure 2.12).

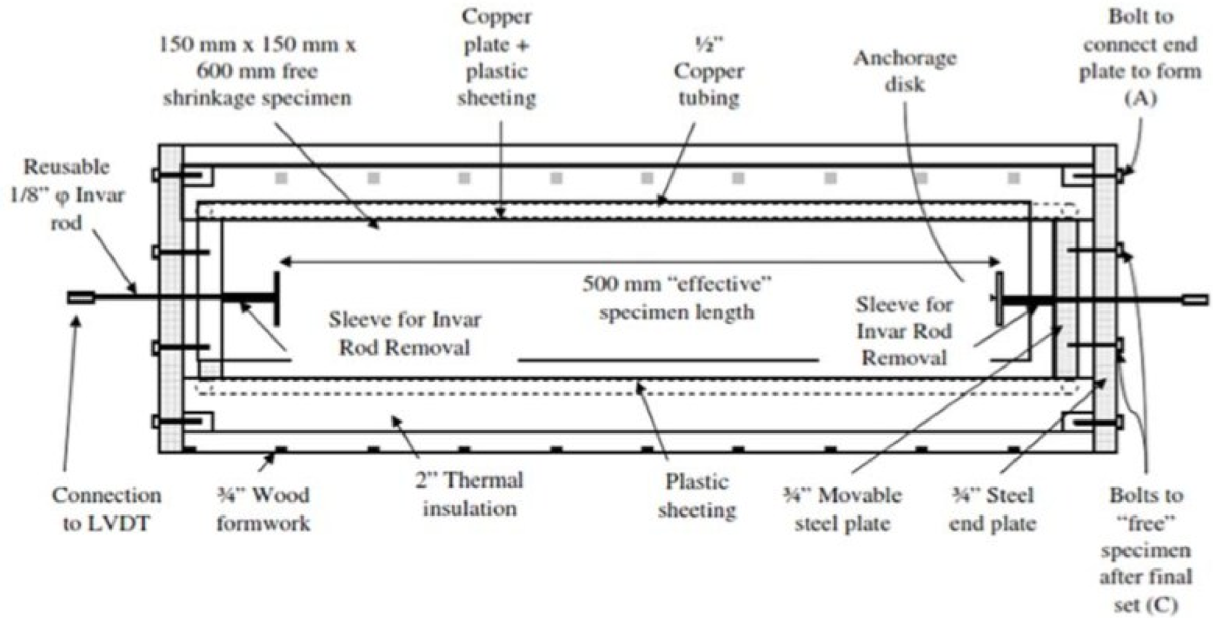

Figure 2.12. Diagram of shrinkage test setup, reprinted from Pesek et al. (2013).

The researchers compared results from their tests with existing analytical models to find inconsistencies in predicted behavior. Six bridge decks were instrumented to record temperature and shrinkage effects, including decks with poor boy details. These controlled cracking joints performed as expected. An updated creep model and plastic shrinkage model were implemented in ConcreteWorks software.

The nonlinear static finite element analysis (FEA) of a concrete girder bridge was conducted by French et al. (1999) with PBEAM software to model cracking behavior. The cracking model included the effects of shrinkage, support conditions, member stiffness, lateral bracing, splices, and elastic modulus of the deck. Moment caused by varying shrinkage between the girders and deck was the most critical source of cracks. A parameter study showed that effective means of reducing cracks included reducing the pace of early-stage shrinkage and reducing concrete modulus. Crack locations depended on support conditions, system stiffness, and lateral brace and splice locations. These findings were supported by surveys of existing bridges. Sections of new concrete deck restrained by mature concrete deck are particularly vulnerable to shrinkage cracking (Frosch et al. 2003). Increased girder spacing, increased deck thickness, and decreased steel reinforcement area all reduced stress from shrinkage.

Concrete deck cracking is an important design concern. For bridge designs that exchange conventional expansion joints for continuous deck details, cracking at the detail location is a special concern.

2.4 CONTINUOUS DECK DETAILS

Previous studies have performed numerical, field, and experimental studies to better understand the behavior and performance of continuous deck details and to validate new design concepts. The findings of these studies can be utilized to better understand the behavior and performance of Texas poor boy details and to develop alternative designs. Herein, details are broadly classified as bonded or debonded. Section 2.4.1 provides a summary of previous research on bonded link slabs, beginning with a detailed discussion of previous work on Texas poor boy details, followed by a discussion of research done on bonded slabs outside of Texas. Section 2.4.2 provides a summary of previous research on unbonded link slabs. Section 2.4.3 summarizes prior and ongoing work related to the use of alternative materials in continuous decks.

2.4.1 Bonded Link Slabs

2.4.1.1 Texas Poor Boy Continuous Deck Detail

In Texas, the poor boy continuous deck detail has been used for decades to continuously join reinforced concrete bridge decks over the supports of simply supported girders. Banks (1984) presented a summary of concrete bridge maintenance and inspection in Texas. At the time, the majority of prestressed concrete bridges incorporated simply supported I-beam superstructures, while box girder systems were gaining popularity. Concrete decks over the simple spans were made continuous for new construction over interior spans. This change in construction practice was made to improve ride quality, reduce the number of deck joints, and prevent the exposure of the substructure to drainage water and deicing salts. Banks noted that foreign material filling expansion joints contributed to concrete spalling on girders in the region of their bearings and to the damage of bents and bent caps due to temperature-induced stresses.

Butler (1988) examined the use of super water reducers in concrete for bridge decks. A three-span test bridge was constructed with a continuous slab over simply supported prestressed concrete girders. After opening to traffic, the only observed cracks on the structure were noticed above the interior bents in the transverse direction.

Burke Jr. (1989) noted that in the 1980s, TxDOT was conducting retrofits of intermediate slab expansion joints with continuous decks (see Figure 2.13). This fully bonded design was different from link slab designs in states such as Utah, which incorporated a polyethylene layer over the beam ends to prevent bonding of the concrete to the top surface of the beam ends. Additionally, the poor boy joint differed from designs in Wisconsin and Ohio, which included concrete cast between the beam ends to make the slab and beams composite.

The horizontal deformability of the bearings was recognized as an important factor in such designs. While cracking in the poor boy slab occurred, the cost savings of avoiding joint construction, maintenance, and repair over the life of the deck were preferable.

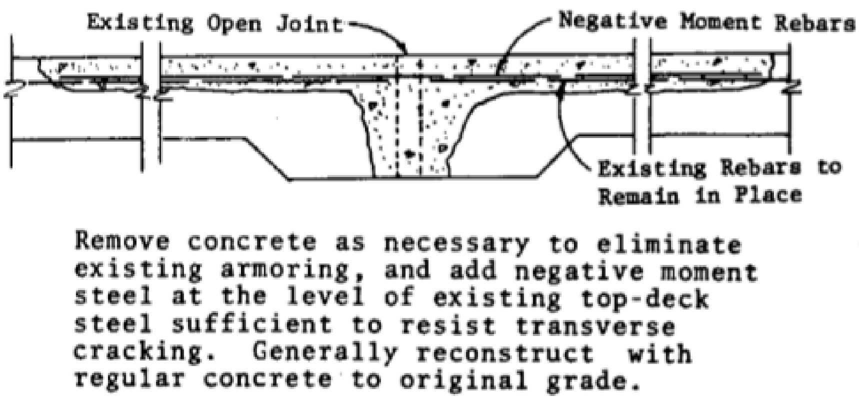

Figure 2.13. 1980s TxDOT expansion joint retrofit to continuous deck, reprinted from Burke Jr. (1989).

Roberts et al. (1993) conducted a field study of the San Antonio "Y" project, which included one highway span joined with poor boy connectivity. The spans consisted of segmental post-tensioned box girders. One two-span segment was left as simply supported over the bent with poor boy continuity in the deck (see Figure 2.14). Such a detail was novel for TxDOT segmental box girder structures. The spans were 75 and 85 ft long and were not connected with continuous tendons. The primary unknowns were whether the joint would cause partially continuous behavior.

The poor boy span was instrumented with grid crack monitors that were read periodically, as well as strain gages to determine deck forces. Data were gathered with a live load truck test (see Figure 2.15). Results showed continuity over the closure slab due to a couple moment between the slab and girder bearing pads (see Figure 2.16). The use of thicker bearing pads with a lower shear modulus to allow less constrained deformation was suggested to reduce this continuity. Even so, cracking of the slab under live load was not observed.

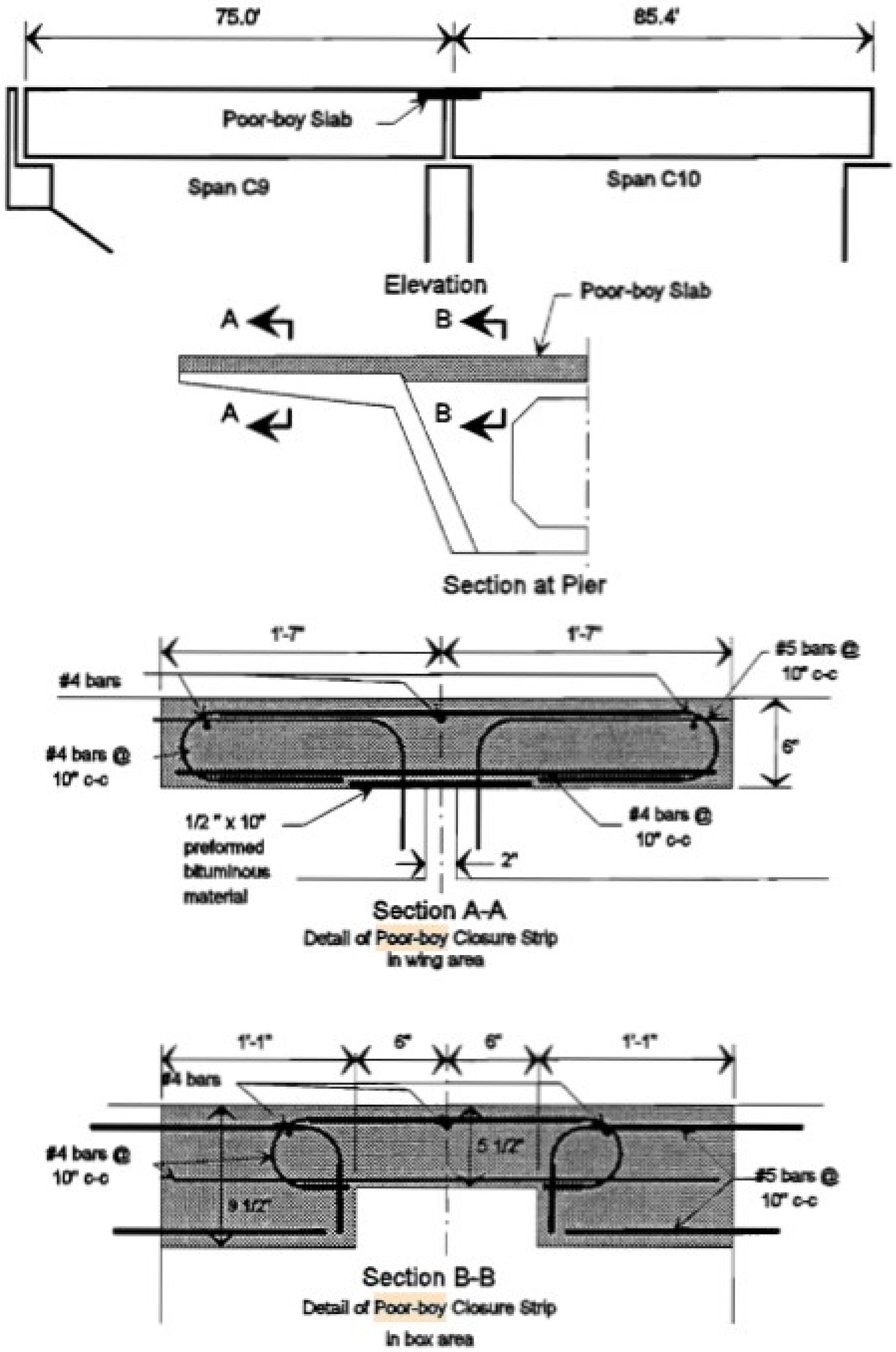

Figure 2.14. Poor boy continuous slab details, reprinted from Roberts et al. (1993).

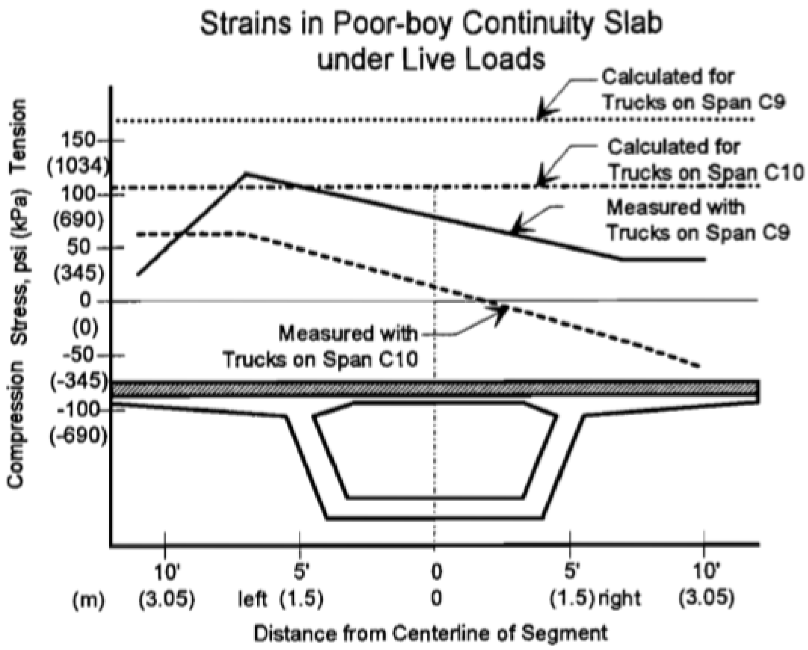

Figure 2.15. Link slab stresses, reprinted from Roberts et al. (1993).

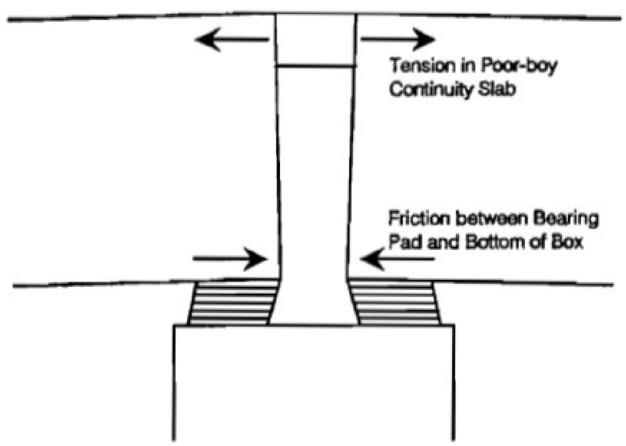

Figure 2.16. Couple moment causing link slab tension, reprinted from Roberts et al. (1993).

English et al. (1994) instrumented and monitored bridges, including ones with poor boy continuity details, in order to investigate the performance of elastomeric bearings. Problem bridges were identified using TxDOT's BRINSAP database. One structure that was investigated was a seven-span bridge over the North Sulphur River near Paris, Texas. This bridge featured only one expansion joint, while the deck was made continuous over the other bents using poor boy deck details. The neoprene bearings on this structure had shifted and torn in many places, causing bent cap damage.

Davis et al. (1999) investigated many aspects of segmental box girder bridge construction on US 183 in Austin, Texas, with the goal of lowering costs and improving performance in both construction and service. Because of complications with designing and constructing the spans as continuous, especially due to difficulty with post-tensioning continuity between spans, much of the structure was designed with simply supported spans. The deck between simple spans was made continuous with poor boy continuity for two to three spans by casting closure decks between the flanges of the box girders (see Figure 2.17). These joint slabs were designed to carry vehicle loads without transferring significant moment between girders. A poor boy continuous slab detail was chosen to reduce the number of expansion joints and because TxDOT has found that “the durability and ride quality of these slabs has proven to be excellent when properly detailed.”

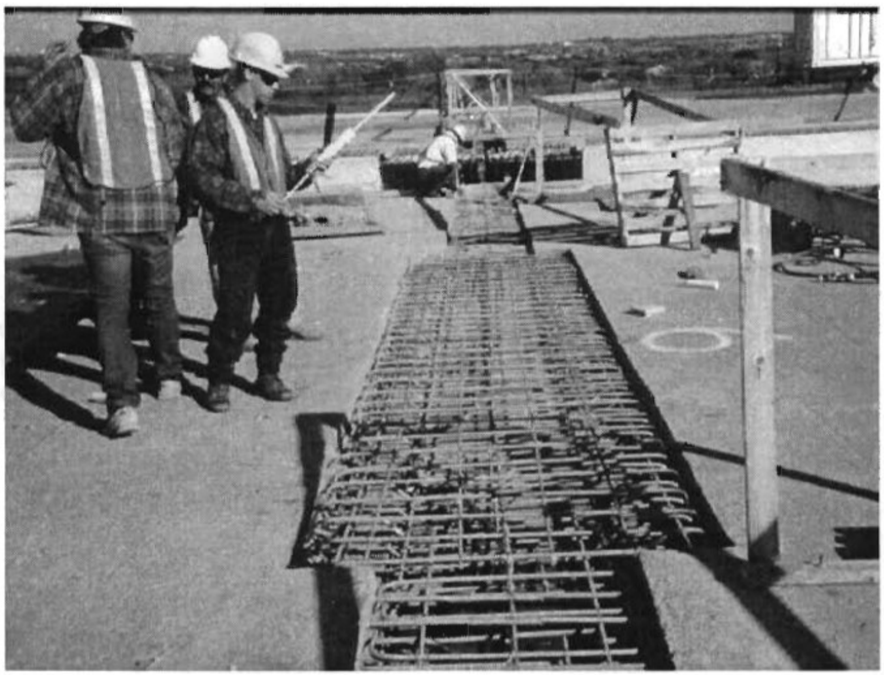

Figure 2.17. Poor boy continuous joint pour, reprinted from Davis et al. (1999).

In addition to wheel loading, the joint slab was designed to withstand tensile, compressive, and bending forces caused by temperature changes. Another load effect that TxDOT engineers wished to avoid was a moment couple caused by tension in the deck and compression at the bearing supports. Bituminous pads were placed across the gap between members at the wings of the section to decrease the bending stiffness of the slab. To ensure that the girders would be able to displace longitudinally from load carried through the poor boy slab detail, low-stiffness elastomeric bearing pads that respond to the longitudinal stress by deforming in shear were installed (see Figure 2.18).

One slab was instrumented with two-layer strain gages prior to the concrete pour in order to evaluate tensile, compressive, and bending strains. The slabs were load tested with trucks to produce a maximum negative couple moment through the force interaction between the poor boy continuous slab details and bearings. Results of the load test showed that the overall axial force in the slab was negligible, but stresses across the slab were nonuniform. Stresses were maximized at the locations where the slab's width varied.

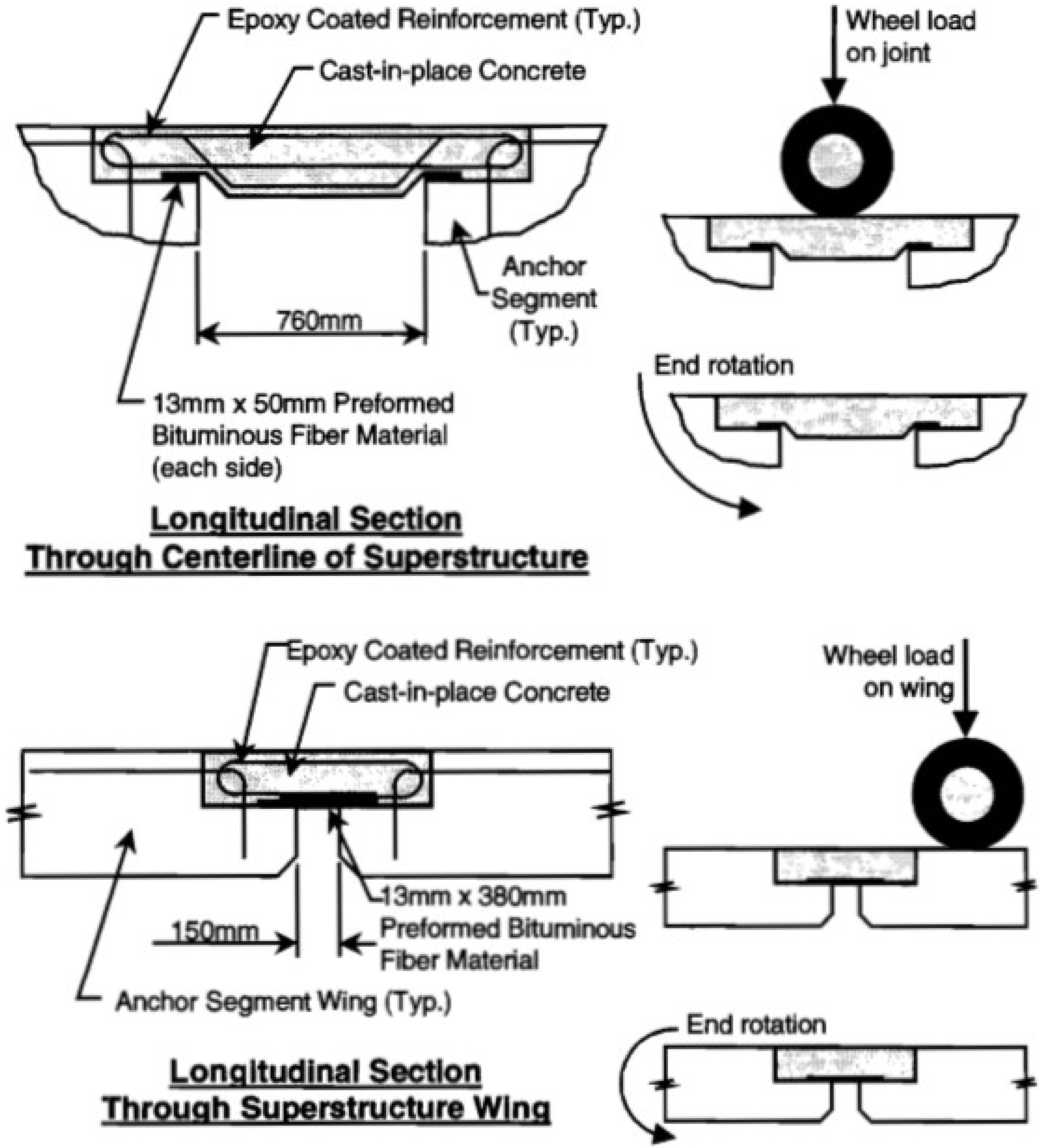

Figure 2.18. Link slab sections, reprinted from Davis et al. (1999).

Researchers determined that the design performed successfully, without significantly changing the behavior of the box girders. Negative moment did develop in some poor boy deck sections due to the design of the fixity block connecting the bottom flange of the girders. After opening to traffic, the poor boy decks were noted for their outstanding ride quality.

Gross and Burns (2000) evaluated two prestressed HPC girder bridges, both with poor boy continuity in their decks. However, the first deck on a bridge in Louetta utilized a continuously cast deck with a construction joint over the bents (see Figure 2.19), while the second deck on a bridge in San Angelo utilized separately poured decks connected by closure pours at each bent. The spans were instrumented with vibrating wire strain gages to determine structural continuity. The San Angelo bridge deck behaved as a simply supported span since negligible strain was recorded in the poor boy link slab. Likewise, minimal strains were recorded in the Louetta deck, indicating simply supported behavior and negligible continuity. Both bridges made use of elastomeric bearing pads, which deform easily in shear, preventing the formation of couple moments at the connection. Given that the connections performed as expected, no design changes were recommended to TxDOT.

Figure 2.19. Louetta bridge, reprinted from Gross and Burns (2000).

The current Texas poor boy detail retains much of the simplicity of older designs. The deck is not debonded from the girders, and no closure pour is provided between the beam ends. With the widespread use of PCPs in Texas bridge construction, researchers have investigated the behavior of such systems in the region of the poor boy joint. Bayrak et al. (2013) investigated the optimization of reinforcement and cracking behavior of bridge decks composed of PCPs and CIP concrete, including those with poor boy continuity. The goals of the project included determining whether a reduced amount of top-mat reinforcement in the CIP slabs was acceptable and managing cracking in the PCPs in order to reduce the cost of damaged materials. Joints between panels and interfaces between PCPs and CIP concrete over supports are vulnerable to cracking due to shrinkage and creep (see Figure 2.20).

A minimum area of reinforcing steel is meant to limit the cracking and prevent damage due to deicing chemical infiltration or freeze-thaw cycles. The poor boy continuous deck detail is used to control cracking over supports while maintaining low-cost maintenance and fabrication. Both long-term concrete shrinkage and negative moment loading cause cracks in the region of poor boy continuity. Researchers sought to determine whether the TxDOT requirement of #4 bars at 9 in. on center longitudinally and #5 bars at 6 in. on center transversely in the top-mat reinforcement could be reduced.

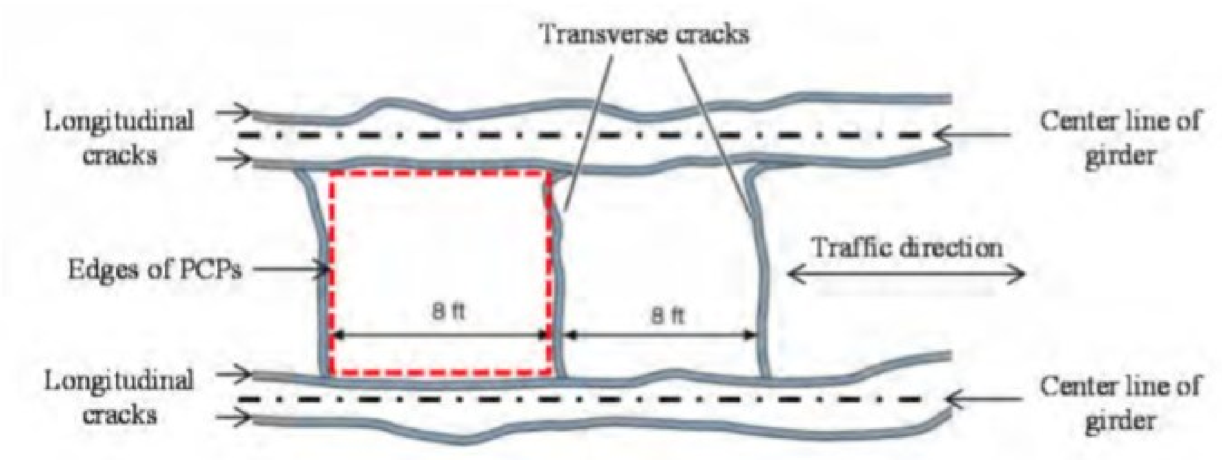

Figure 2.20. Crack pattern for CIP-PCP bridge deck, reprinted from Folliard et al. (2003).

Researchers instrumented poor boy details with gages during construction of two bridge structures with 8-in. deep decks in order to record crack widths. The first structure was the newly constructed Wharton-Weems Overpass, a three-span bridge at the crossing of Choate Road and Shoreacres Boulevard in Houston, Texas. Two exterior spans included standard TxDOT reinforcement, while the third span was designed with reduced transverse reinforcement, #4 bars at 6 in. One of the two poor boy details contained standard reinforcement, while the other contained the reduced reinforcement (see Figure 2.21).

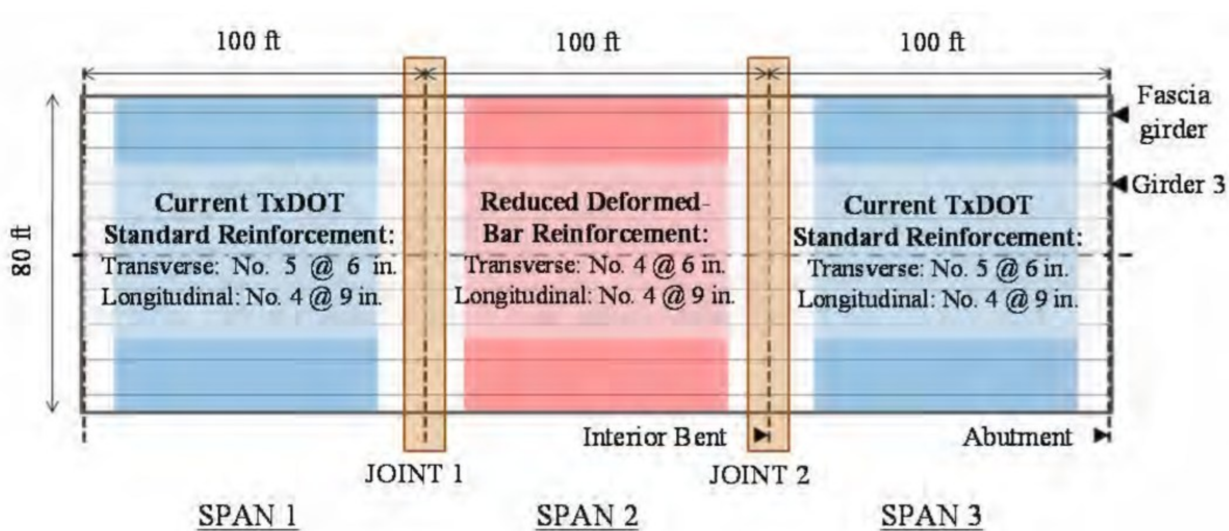

Figure 2.21. Deck reinforcement scheme on Wharton-Weems Overpass, reprinted from Bayrak et al. (2013).

The top-mat reinforcement was instrumented with 16 vibrating wire (VW) strain gages (see Figure 2.22 and Figure 2.23). The gages transmitted data every 30 minutes. The deck was cast in nine hours using concrete with a compressive strength of 4000 psi. Crack formers, known as zip strips, were placed at the poor boy details (see Figure 2.24).

Prior to the application of traffic loads, crack widths were measured two times—once prior to the installation of roadway barriers and once after barrier installation. The transverse cracks at the poor boy slab details in the first inspection measured, on average, 0.013 in. and 0.007 in. wide. These measurements were taken across the entire slab width (see Figure 2.25). The second inspection only considered the half-width of the span that had been instrumented (see Figure 2.26). The average crack width over both bents was found to be 0.010 in. Other transverse cracks were also recorded at PCP joints. The cracking behavior harmonized with a theoretical cracking prediction that used the VW strain gage data to estimate concrete stress. The inspections included applying water on the concrete surface, which reveals cracks after the surface water evaporates.

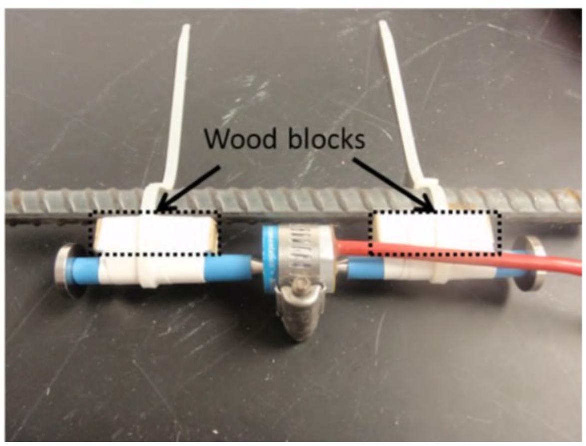

Figure 2.22. Vibrating wire strain gage installation on rebar, reprinted from Bayrak et al. (2013).

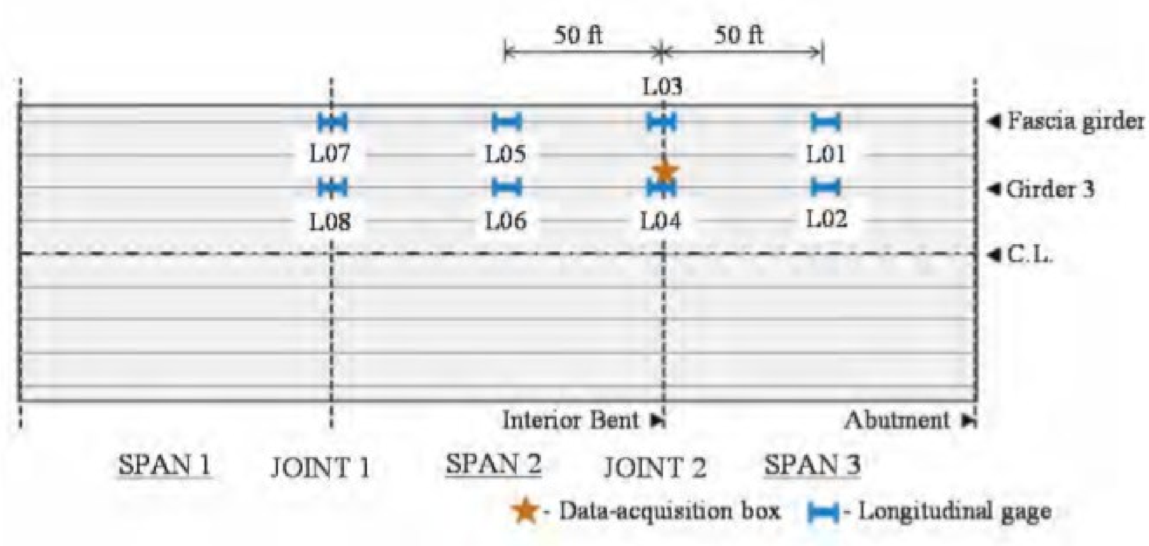

Figure 2.23. Longitudinal bar VW gage layout for the Wharton-Weems Overpass, reprinted from Bayrak et al. (2013).

Figure 2.24. Installation of zip strip crack former, reprinted from Bayrak et al. (2013).

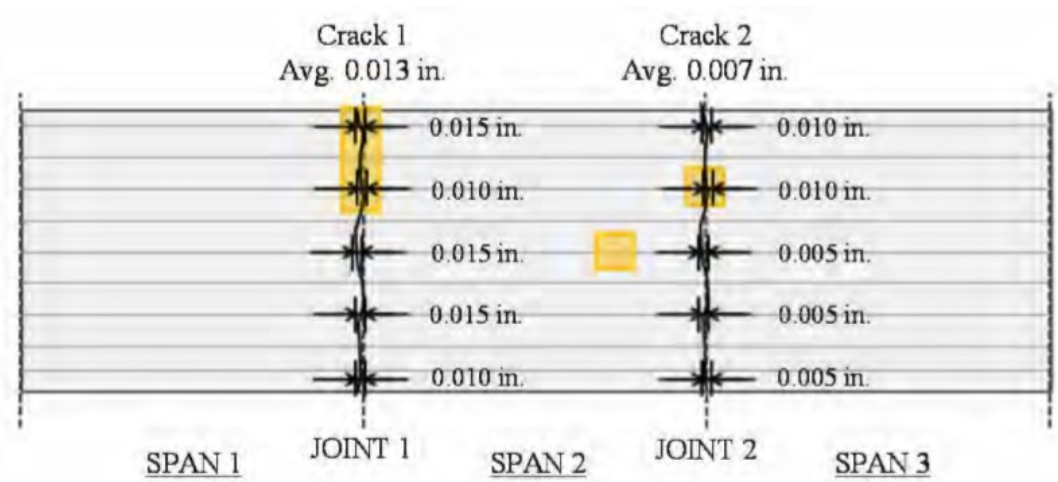

Figure 2.25. Crack widths found in the first inspection of the Wharton-Weems Overpass, reprinted from Bayrak et al. (2013).

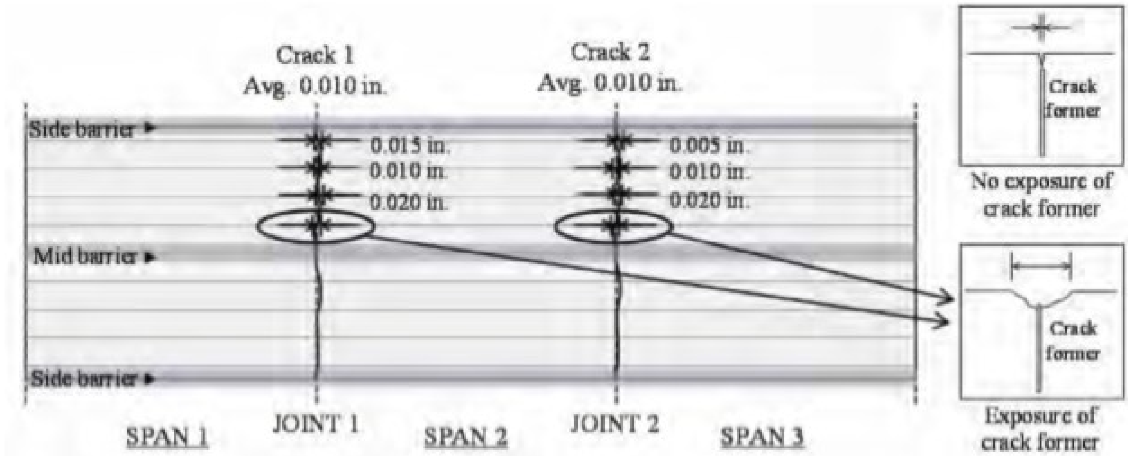

Figure 2.26. Crack widths found in the second inspection of the Wharton-Weems Overpass, reprinted from Bayrak et al. (2013).

The cracks were monitored for months before and after traffic was introduced. Temperature variations produced lower tensile strains in hot weather because expansion of the deck was constrained by the surrounding structure, resulting in added compression forces.

Researchers used an analytical method of predicting cracks in CIP-PCP bridge decks developed by Peterman and Rammirez (1998) and known as the P-method. This method calculates the restraint moment at a deck section, accounting for reduced stiffness from cracking in negative moment regions, differences in creep between PCPs and CIP sections, and shrinkage restraint from PCPs and top-mat reinforcement. If the restraint moment becomes greater than the cracking moment of the CIP section, the deck will crack. Analytical results showed that cracking could be expected as soon as one day after the concrete pour, while strain results showed that cracking occurred around two to three days after the concrete pour.

The second bridge structure was the Lampasas River Bridge on the south frontage road of IH 35 near Belton, Texas. The structure has five spans with varying span lengths and numbers of girders. Like the Wharton-Weems Overpass, the structure utilizes prestressed concrete girders and a PCP with CIP topping deck. The poor boy details connecting Spans 1 to 2 and 4 to 5 were instrumented. Reinforcement included the standard and reduced rebar variations used in the Wharton-Weems Overpass and an additional region with welded-wire reinforcement (see Figure 2.27 and Figure 2.28). The structure was also instrumented with VW strain gages as before (see Figure 2.29). The average crack width at 75 days after pouring of the slab in Joint 4, the location of a poor boy detail, was 0.008 in. Long-term crack development followed a similar pattern to that of the Wharton-Weems Overpass.

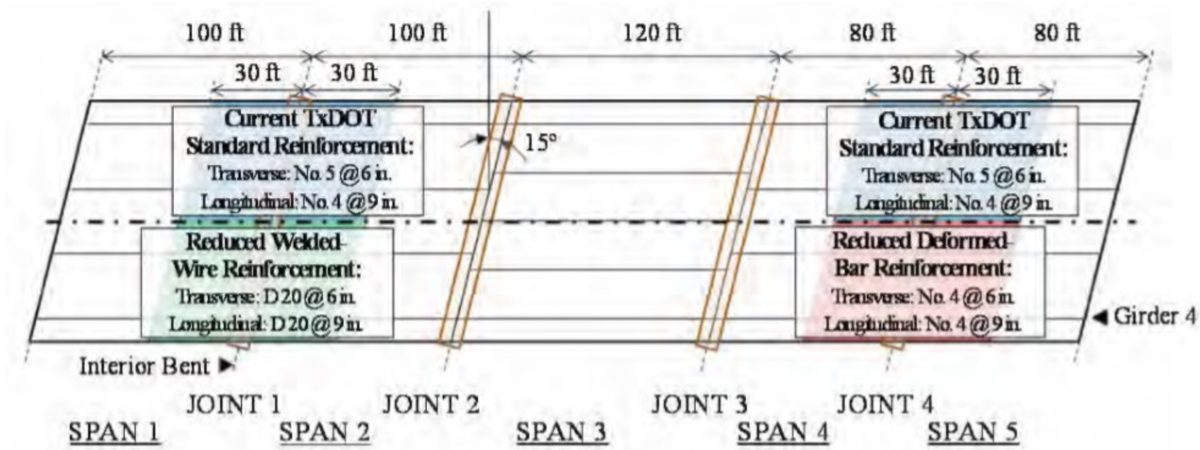

Figure 2.27. Deck reinforcement scheme on Lampasas River Bridge, reprinted from Bayrak et al. (2013).

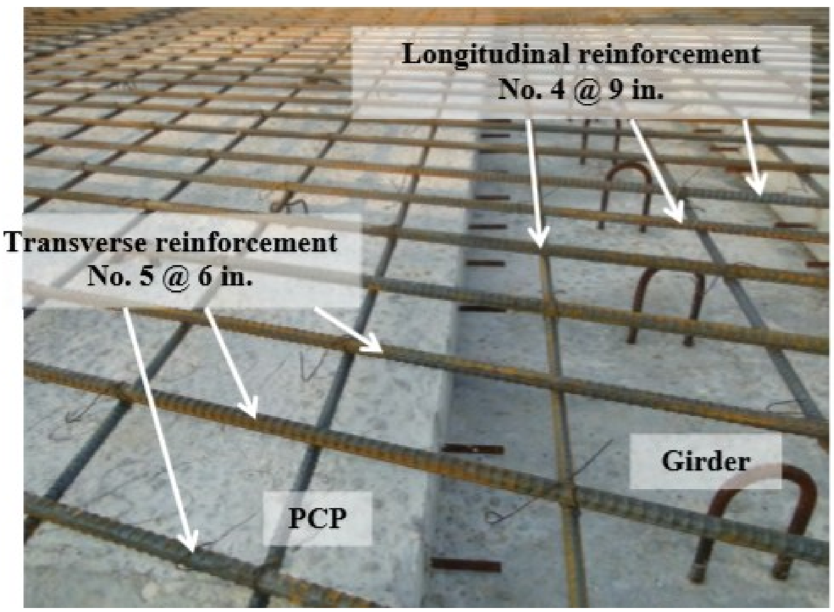

Figure 2.28. Deck reinforcement placement on Lampasas River Bridge, reprinted from Bayrak et al. (2013).

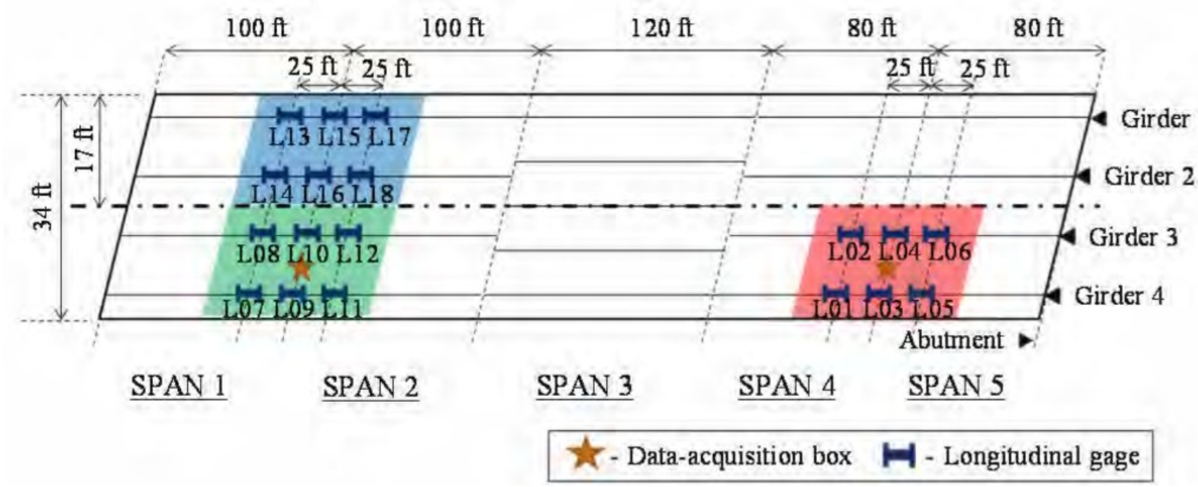

Figure 2.29. Longitudinal bar VW gage layout for the Lampasas River Bridge, reprinted from Bayrak et al. (2013).

Results of the cracking study determined that standard longitudinal reinforcement successfully kept crack widths low over the supports but that the reinforcement nearly reached its yield strain. Therefore, the longitudinal reinforcement should not be reduced in the poor boy details. However, the stress in transverse reinforcement remained well below yield despite the reduced bar area of the alternative reinforcement pattern, indicating that a reduction in transverse reinforcement was appropriate. Researchers concluded that using the reduced rebar layout could reduce material costs by 25 percent, while the welded-wire reinforcement layout could reduce material cost by 5 percent with additional savings in labor.

Munsterman (2017) investigated the use of top-layer steel reinforcement in the negative moment regions of bridge decks made with PCPs beneath a CIP topping slab. The work was part of TxDOT Project 0-6909 (Ge et al. 2021), which examined the behavior of such decks over continuous girders. The use of AASHTO's empirical design method requires decks to be entirely CIP, without the use of PCPs. AASHTO's traditional design method allows the use of PCPs. In Texas, standard details for deck reinforcement were altered in 2014 to reduce the amount of transverse reinforcement while still retaining a greater area of reinforcement than the minimum steel in the empirical design method (see Figure 2.30). Newly constructed bridges with simply supported girders and poor boy continuity in their PCP decks were instrumented to capture the effects of changes in concrete volume and live loading from trucks.

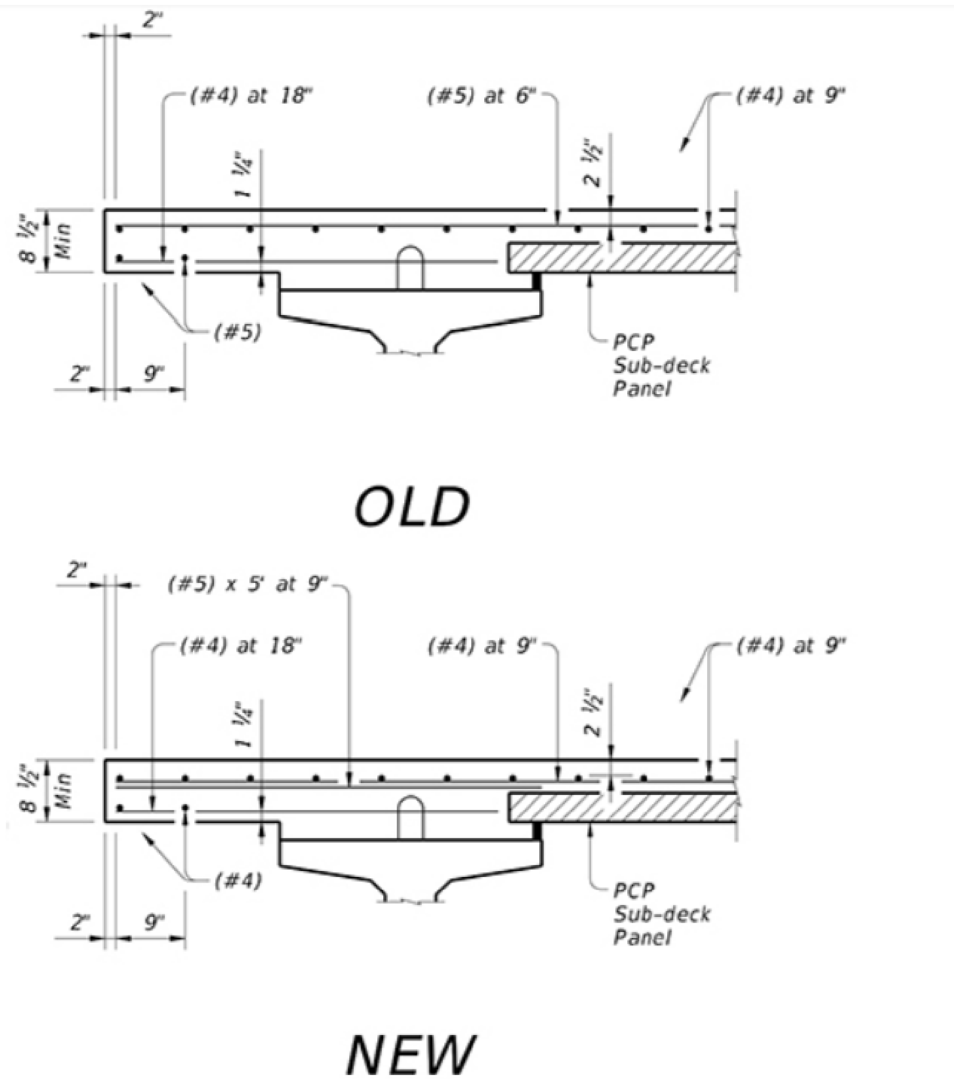

Figure 2.30. Old and new deck reinforcement detail with precast panels, reprinted from Holt and Smith (2014).

PCPs were first used in Texas bridges in 1963, and have been studied to determine deck cracking behavior, shear connector requirements, and interface bond behavior. Using PCPs accelerates the construction process and lessens the required amount of CIP concrete. Full-depth PCPs have also been tested but are limited in their applicability due to the variety of structure geometries used in bridges. Thus, the use of partial-depth PCPs is expected to remain TxDOT's more common construction method for the foreseeable future.

PCPs are reinforced with prestressing strands in the bridge's transverse direction and with mild steel parallel to traffic. They are placed on the girders with an amendable foam bedding strip in between, typically filling gaps of around 0.5 in. to 4 in., which ensures an even placement on the structure (see Figure 2.31). PMDFs are often used in places on the structure not covered by PCPs, such as near the supports in skewed bridges. In the past, a fully CIP deck over plywood forms was another option used near expansion joints. Current details allow PCPs to be placed flush with one another at joint locations, eliminating the need for additional forms. PCPs may be regarded as fully composite with the CIP overlay. American Concrete Institute (ACI) 224-01 recommends in-service crack widths for various conditions, including a 0.007-in. limit for deicing chemical protection.

Figure 2.31. Precast panel size and placement, reprinted from Munsterman (2017).

Three bridges of different geometry but similar sensor layout were instrumented with VW strain gages, which include thermistors to monitor temperature change. At the time of writing, two of the three bridges had been constructed, while the third was incomplete. Each of the bridges utilized simply supported girders beneath a reinforced concrete deck with PCP forms, made continuous with poor boy joints.

TxDOT deck reinforcement, consisting of #4 bars at 9 in. in both the longitudinal and transverse directions, was instrumented over a bent to provide a comparison to alternate reinforcement details. Two alternative reinforcement schemes were installed by tying additional bars to the standard reinforcement. The length of added bars was calculated using development length of a #6 bar. Gages were placed on top-mat reinforcement over the bent with an additional gage placed over the girder in order to define the deck's strain profile, as shown in Figure 2.32. The VW gages were attached to bars with zip ties, with additional instruments attached to the gage with clamps (see Figure 2.33).

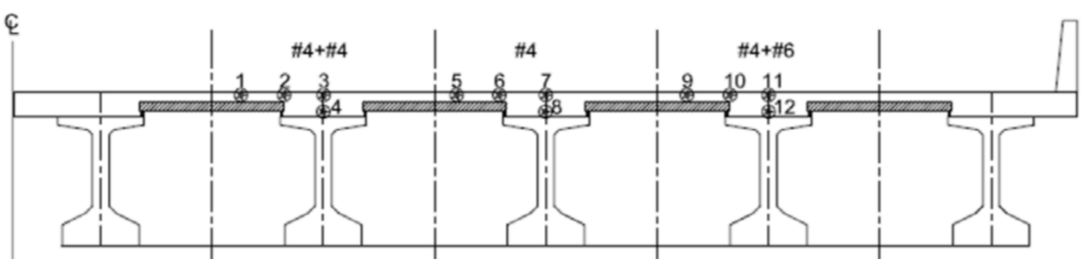

Figure 2.32. Gage placement diagram, reprinted from Munsterman (2017).

Figure 2.33. Gage attachment on reinforcement, reprinted from Munsterman (2017).

The bridge deck was cast during the night for logistical reasons and to avoid excessive heat. A burlap covering was used on top of the slab for moisture control during curing. Measurements were recorded continuously as the decks cured, with strain values zeroed at the point when casting was completed. Researchers considered that 80–90 percent of shrinkage occurred during the first month after casting.

Static live load testing was conducted using two tandem-axle trucks of known weight loaded with sand. Three truck locations were used to maximize negative moment over the bent for each beam line, while two other configurations were used to maximize positive moment in each span. Cracks were recorded and marked during live load tests, as were girder deflections.

The first bridge, located in San Marcos, Texas, on SH 123, was a three-span structure. Three interior girders on one bent on the east span of the bridge were instrumented. The bridge was heavily skewed, leading to the use of PMDF over the bents where PCPs were not continuous (see Figure 2.34).

 

Figure 2.34. PMDF construction due to skew at supports, reprinted from Munsterman (2017).

Across the three girders, one had additional #4 bars attached to the longitudinal steel, a second had existing reinforcement only, and the third had additional #6 bars attached to the longitudinal steel. Each girder was instrumented with four gages, with Gages 1 through 4 on G1, and so forth. The crack in the poor boy was formed using a steel angle along the bottom of the slab at the centerline of the bent. The structure was monitored for 155 days.

A second structure, in Bastrop, Texas, consisted of a highway entrance ramp onto SH 71 with four girder lines and five total spans. The top-mat deck reinforcement consisted of #4 bars at 6 in. in the transverse direction above #4 bars at 9 in. in the longitudinal direction. The span chosen for instrumentation included a thicker, fully CIP deck section over one exterior girder. The difference in construction was considered negligible, and the three interior girders with a PCP formed deck were instrumented. The deck included standard steel reinforcement at one girder line, with 5-ft lengths of #4 bars included in the longitudinal direction, spaced at 4.5 in. in the gaps between existing bars at the second girder line. The gap reinforcement was added in the third girder line, along with #4 longitudinal bars attached to the standard reinforcing bars (see Figure 2.35).

The crack-forming mechanism in this structure consisted of a ¾-in. wooden board, affixed in the gap between abutting PCPs over the bent (see Figure 2.36). Gages were installed above the crack former. The deck was cast and live load tests were conducted in a similar manner to the structure in San Marcos.

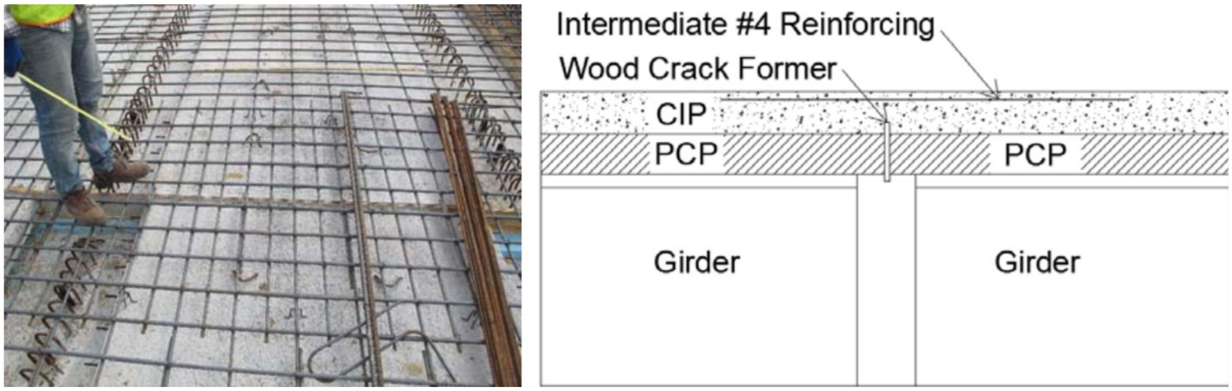

Figure 2.35. Added reinforcement over supports and crack-forming detail, reprinted from Munsterman (2017).

Figure 2.36. Construction of crack-forming wood detail, reprinted from Munsterman (2017).

A third location consisting of two bridges was located in Round Rock, Texas, and is documented by Ge et al. (2021). It consists of two ramps of IH 35 at the junction of SH 45 in Austin, Texas. The girders in these structures are continuously spliced prestressed concrete sections. Reinforcement in the topping slab over the bents include #6 bars at 4.5 in. in the longitudinal direction above #5 bars at 5.5 in. in the transverse direction.

Once the data were gathered, researchers set out to isolate the strain contributions from various sources, including shrinkage, creep, temperature changes, and live load. Thermal strain may be induced due to ambient temperature and direct sunlight. The differential shrinkage between the CIP deck and PCPs can cause cracking as the mature PCPs restrain the topping layer, causing tension in the deck. To account for temperature effects, researchers took measurements at nearly constant temperatures and at 4 a.m. when the temperature gradient had equalized. It was theorized that shear lag was responsible for the different strain values across the slab width.

During live load testing, initial cracking was found to propagate from the location of zip strips in the poor boy joint (see Figure 2.37). The researchers theorized that the high skew of the bridge triggered such a cracking pattern. Crack widths were small enough that attempts to determine their size with a crack gage were unsuccessful, and the cracks closed after the trucks left the structure. Live load tests showed that increasing steel area led to a decrease in strain at the gage locations, with the addition of the #4 and #6 bars leading to 18.6 percent and 50.3 percent reductions, respectively. Compression strains were recorded in the lower gages, demonstrating flexural forces in the poor boy slab.

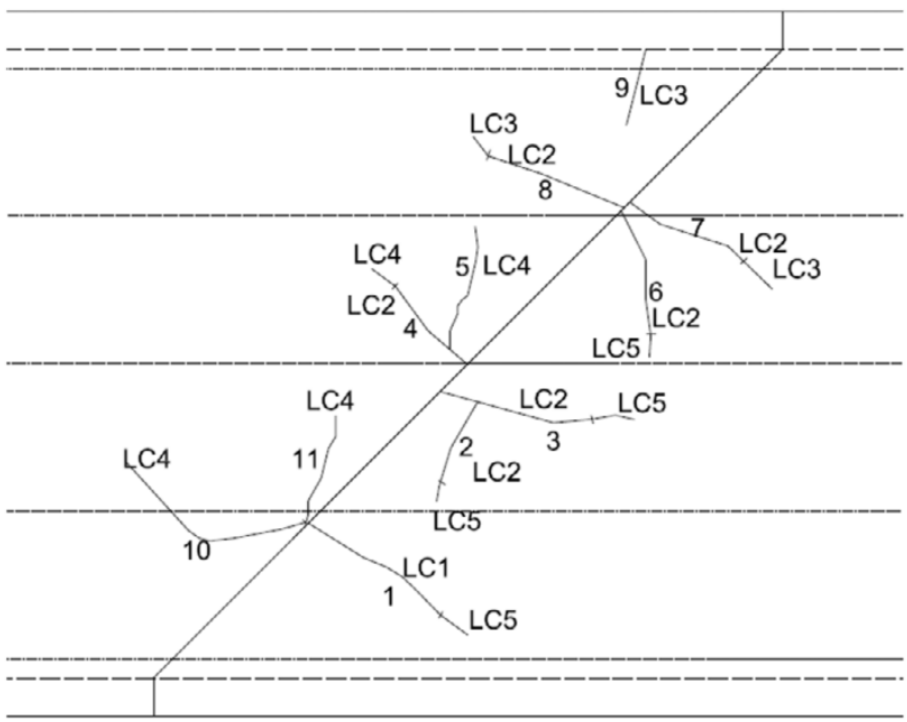

Figure 2.37. Crack propagation from crack former, reprinted from Munsterman (2017).

For the bridge in Bastrop, Texas, VW gages were able to be installed through the wooden crack former, allowing the sensors to capture the full cracking strain. The installation of a guardrail caused a hike in strain for most exterior of the instrumented girders. Similar to the San Marcos structure, increasing longitudinal steel led to a decrease in deck strain, and the strain profile indicated that the slab was in flexure. Without the high degree of skew in the San Marcos structure, the Bastrop bridge displayed a single transverse crack at the control joint location. Researchers theorized that the additional bar placed halfway between the standard reinforcement was the most efficient of the details tested in limiting crack size.

Ge et al. (2021) concluded that crack formers resulted in minor benefits of including additional steel to reduce the strain in poor boy joints.

2.4.1.2 Bonded Continuous Deck Details outside Texas

Charuchaimontri et al. (2008) used finite element models to investigate the effect of different lap reinforcement details within link slabs, with the results verified by three full-scale tests of link slabs. The researchers categorized their link slabs as either long span or short span (see Figure 2.38). While long-span link slabs have enough length to facilitate low flexural stiffness without debonding, short-span link slabs are often debonded from girders to reduce flexural stiffness. Researchers aimed to develop a model for long-span link slabs that takes the nonlinear behavior due to distributed cracking into account, rather than using elastic beam theory and considering a cracked section at midspan. An effective moment of inertia, cracking behavior, and failure mode were predicted. Researchers analyzed long-span link slabs for axial deformations, translation and rotation of the ends of the link slab, and direct loading. Three full-scale, long-span link slab specimens were tested to evaluate the performance of three corresponding reinforcement details under midspan loading (see Figure 2.39).

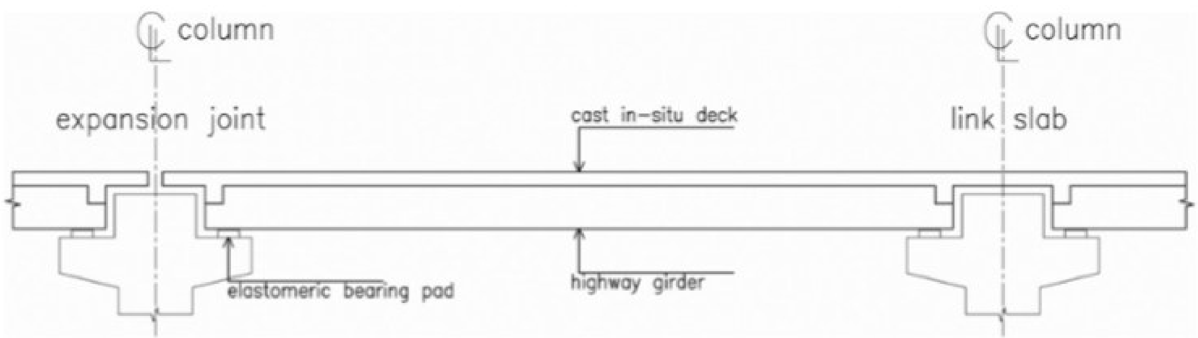

(a) Long span link slab

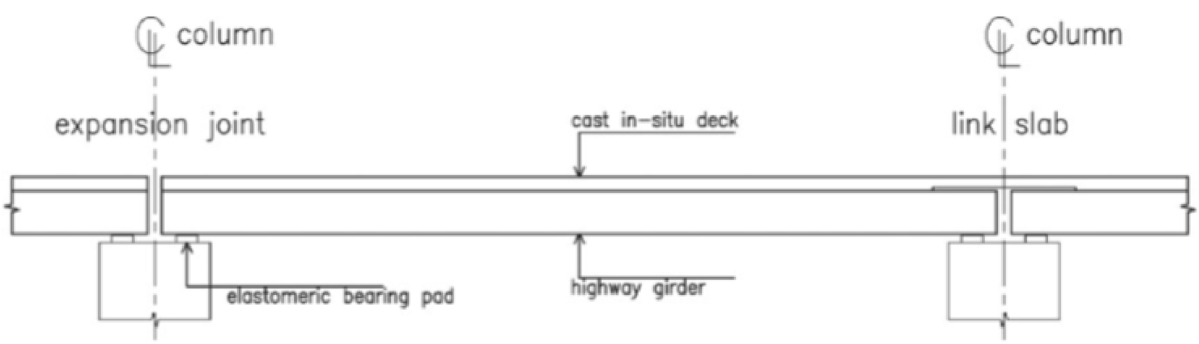

(b) Short span link slab

Figure 2.38. Short- and long-span link slabs, reprinted from Charuchaimontri et al. (2008).

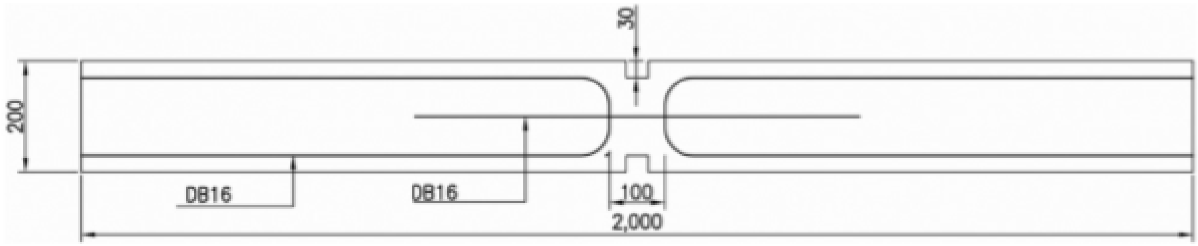

(a) Mid-span hinge (LS_000)

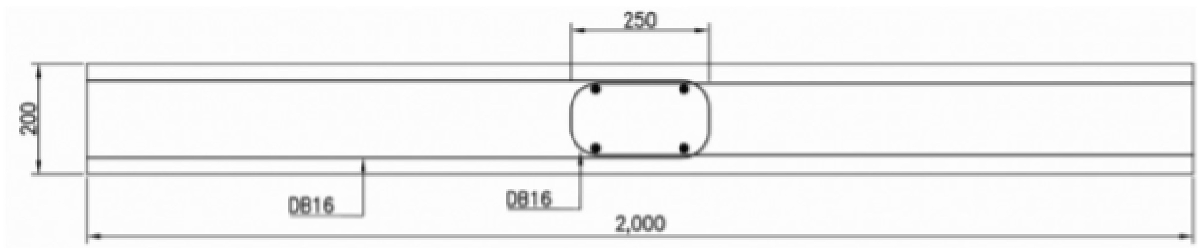

(b) Semi continous (LS_025)

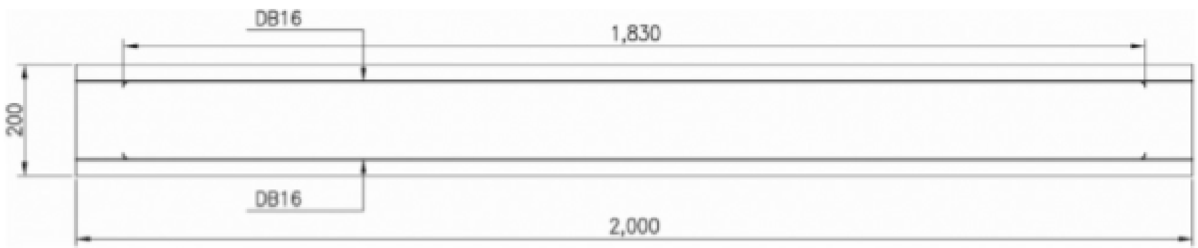

(c) Fully continous (LS_183)

Figure 2.39. Tested reinforcement details, reprinted from Charuchaimontri et al. (2008).

FEA was conducted using a microplane constitutive model for concrete and smeared crack fracture theory, using the constant stiffness method or secant stiffness method to solve the system. Branson's formula was used to estimate the effective moment of inertia in the section. Crack propagation independent of element size and position was made possible by using crack band theory. A bilinear constitutive model was used for reinforcing steel.

Boundary conditions were taken as fixed for in-span loading since the girder stiffness is much higher than link slab stiffness. Results showed that crack distribution was similar across the three designs for end translation since the critical moment is located at the slab ends where the three reinforcement designs are equivalent. While the cracking behavior for midspan loading near the supports was similar among the designs, at midspan, the cracking behavior was different. The fully continuous lap reinforcement detail exhibited the lowest crack widths.

The midspan case was physically modeled and tested to confirm the FEA results. Three specimens (Figure 2.40), 200 mm (7.87 in.) thick by 2,000 mm (78.74 in.) long by 1,000 mm (39.37 in.) wide, were loaded by an actuator and steel loading plate that simulated an AASHTO wheel load. The slab was instrumented, top and bottom, with strain gages, while LVDTs were added to gather out-of-plane displacement. After repeated loading to service levels, followed by loading to failure, the fully continuous lap detail was shown to have the lowest crack widths at a given loading level. The specimens failed in shear prior to reinforcement yielding.

Figure 2.40. Test setup, reprinted from Charuchaimontri et al. (2008).

While top reinforcement behavior was similar in FEA and experimental testing, the bottom reinforcement strains were dissimilar. Researchers theorized that the discrepancies arose from issues with strain gage and crack positions, as well as local deformation under the loading block. Using the ACI building code, estimated crack widths were found to be similar to experimental crack widths for the midspan hinge and semicontinuous reinforcement cases.

Lam et al. (2008) detailed the efforts of the Ministry of Transportation of Ontario (MTO) to retrofit simply supported, multi-span bridges with joints by the addition of link slabs to form a continuous deck over simply supported girders. The Trent Canal Bridge is a four-span structure that was rehabilitated in 1995 with 1.2-m (3.9-ft) wide haunched link slabs (see Figure 2.41). The haunched deck was 315 mm (12.4 in.) deep, beneath a topping pout 60 mm (2.36 in.) thick. The link slab was reinforced top and bottom with steel layers and connected to diaphragms with shear studs. After 13 years, the structure was in good condition, showing no issues.

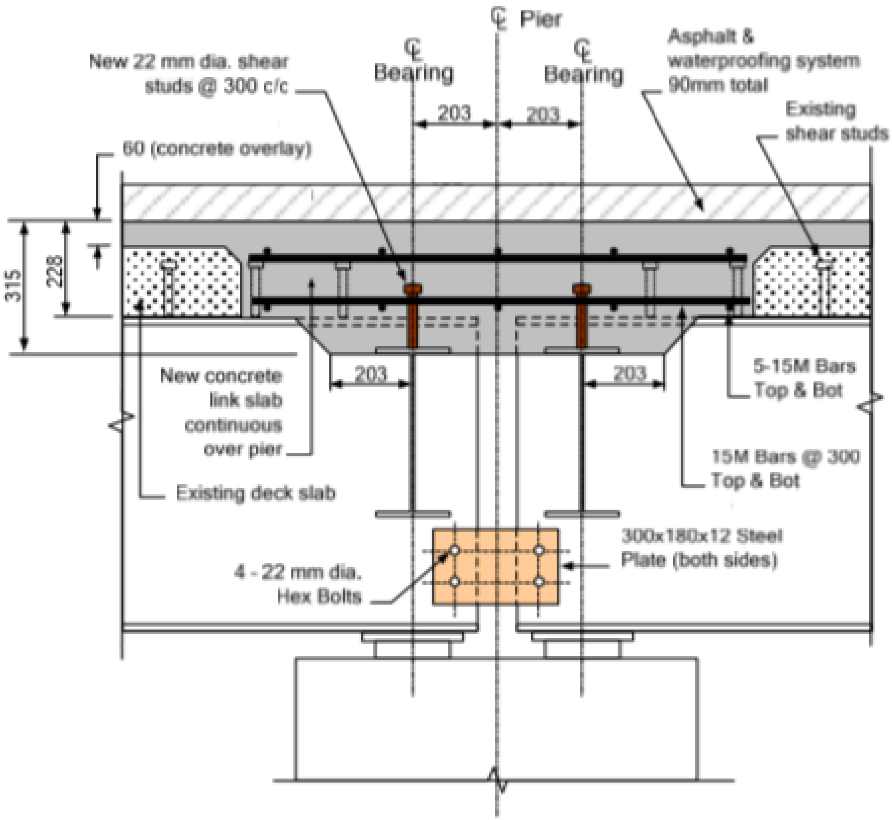

Figure 2.41. Trent Canal Bridge link slab detail, reprinted from Lam et al. (2008).

A flexible link slab design was implemented in 1987 on a bridge on the Gardiner Expressway (see Figure 2.42). The system consisted of a slender slab bridging between beam haunches, which were poured above the beam end diaphragms. The beams were not made continuous. This design became popular on multiple other bridges. The goal of the thick-thin design was to restrict flexure and corresponding cracking in the slender link slab. The top flanges of the connecting beams were also coped at their end regions to facilitate rotation. The link slab was covered with a rubber coating to prevent chemical infiltration. It was reinforced with mats top and bottom of 15M bars, spaced longitudinal at 75 mm (2.95 in.) and transversely at 150 mm (5.9 in), and 6-mm (0.24-in) diameter shear ties were added at 75-mm (2.95-in.) spacing.

The slab was designed to limit rotation to 0.17 degrees, which would comply with the Ontario Highway Bridge Design Code cracking requirements. A bond-breaking film was used on the barrier over the link slab. During construction, the reinforcement placement was found to be cumbersome. In a later inspection, the structure was performing well, but water seepage was noticed near the unbonded barrier.

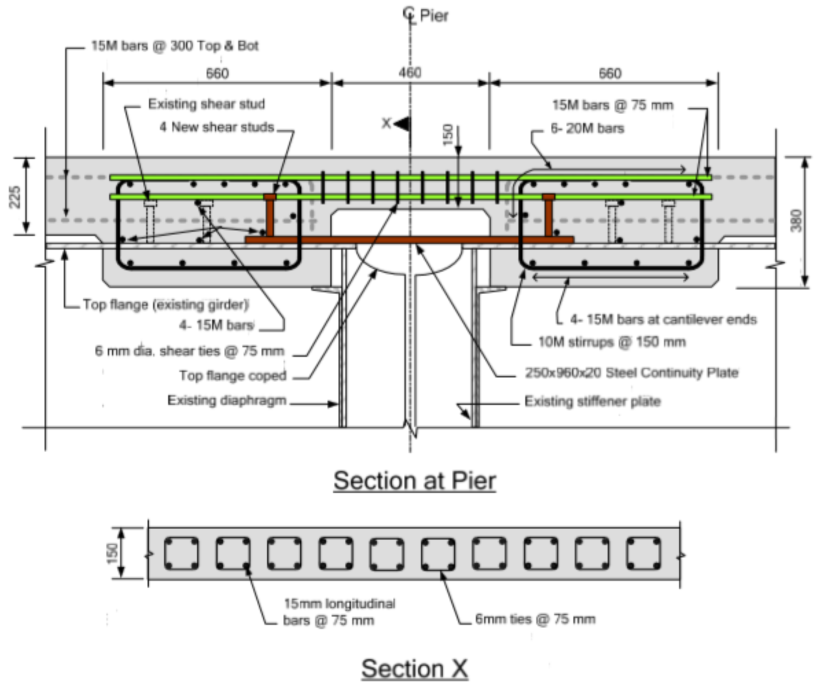

Figure 2.42. Hwy 401 Underpass link slab detail, reprinted from Lam et al. (2008).

Given the success and lessons learned from the above structures, MTO recommended design provisions for future link slab systems. These provisions include the dimensions of the link slab and deck haunch, reinforcing spacing and size, and continuity of reinforcing bars in barriers. The rotations of the girders, the bridge's skew, and its girder depth are all limited. Structures not meeting these criteria were marked for retrofits with girder continuity.

These design suggestions were applied to the Dixon Road Overpass, another four-span bridge with 12 steel girders spaced at 2.1 m (6.9 ft). Link slabs with the suggested dimensions and reinforcement, with the addition of shear reinforcement, were added as part of a widening project (see Figure 2.43). Upon later inspection, the link slabs were performing well, but water infiltration was still an issue at the barriers.

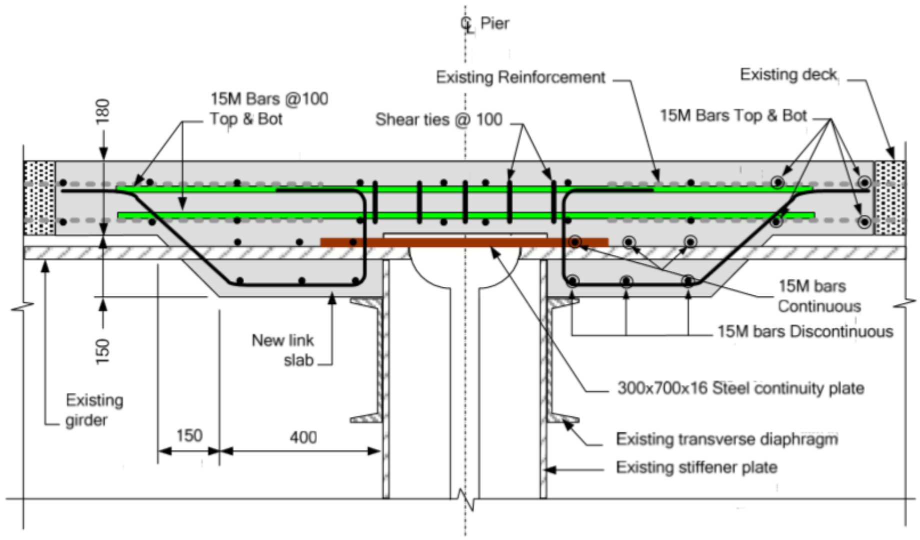

Figure 2.43. Dixon Road Overpass link slab detail, reprinted from Lam et al. (2008).

Snedeker et al. (2011) performed an evaluation of the bonded continuous deck detail used by the Georgia Department of Transportation (GDOT). At the time, the detail used a construction joint in the center of the link slab, with the normal deck reinforcement terminated on either side of the joint and additional #6 bars placed continuously across the joint between the normal reinforcement (see Figure 2.44). The surface of the slab at the construction joint features a filleted groove, sealed to prevent moisture infiltration (see Figure 2.45).

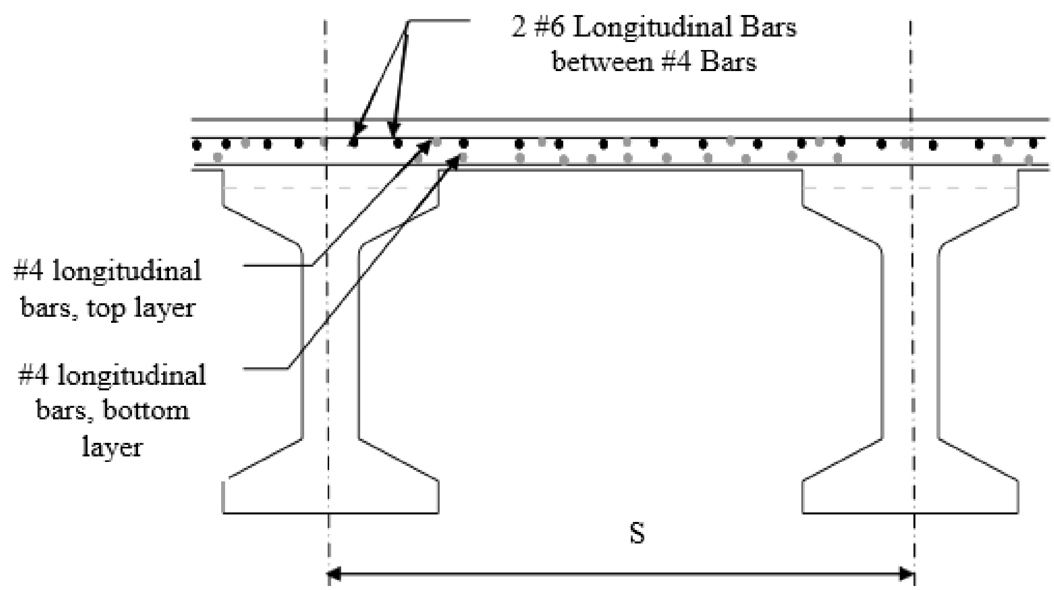

Figure 2.44. Reinforcement placement at continuous deck detail, reprinted from Snedeker et al. (2011).

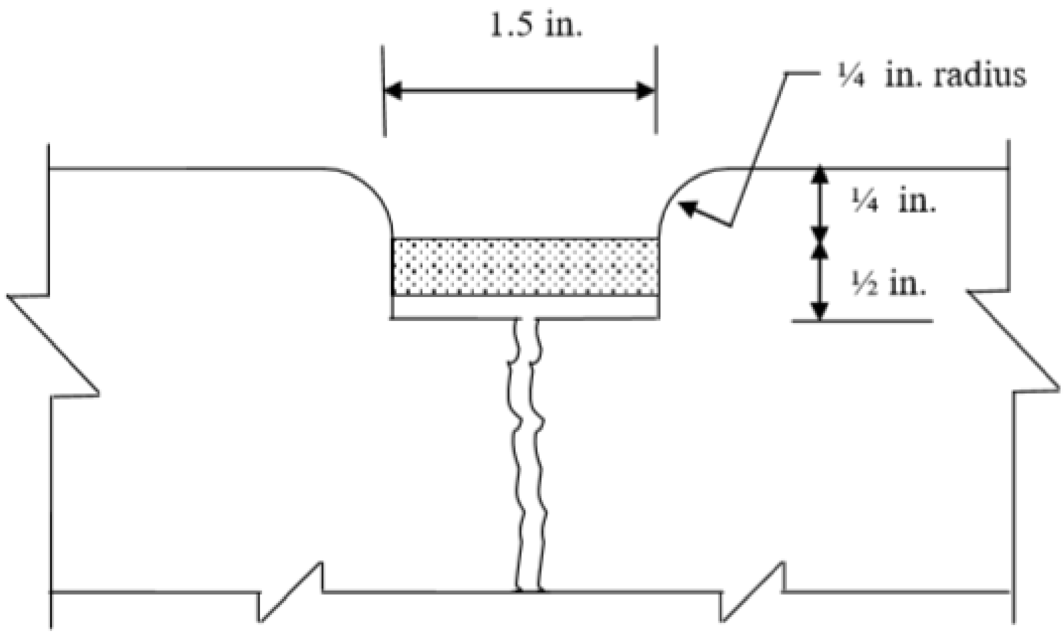

Figure 2.45. Surface detail at construction joint, reprinted from Snedeker et al. (2011).

A survey of inspection reports for the 244 GDOT bridges with the continuity detail found few issues, indicating good performance. Snedeker et al. (2011) visually inspected two complete bridges and observed construction at three other bridge projects with the continuity detail. Contractors noted that the header of the construction joint was time and labor intensive to produce since the bars must be continuous through the header, and bar spacing varies for different bridge decks. Support formwork must also be attached to brace the header.

Saw cutting or otherwise forming the crack-control joint after pouring the deck allows for a much faster continuous concrete pour. A saw-cut control joint is not included in specifications since the joint must be cut in a specific time frame between concrete set and the onset of shrinkage cracking. The construction joint is required to have 0.25-in. radius fillet edges to prevent spalling. The detail, including the nonstructural joint filler placed between the girder ends, is shown in Figure 2.46.

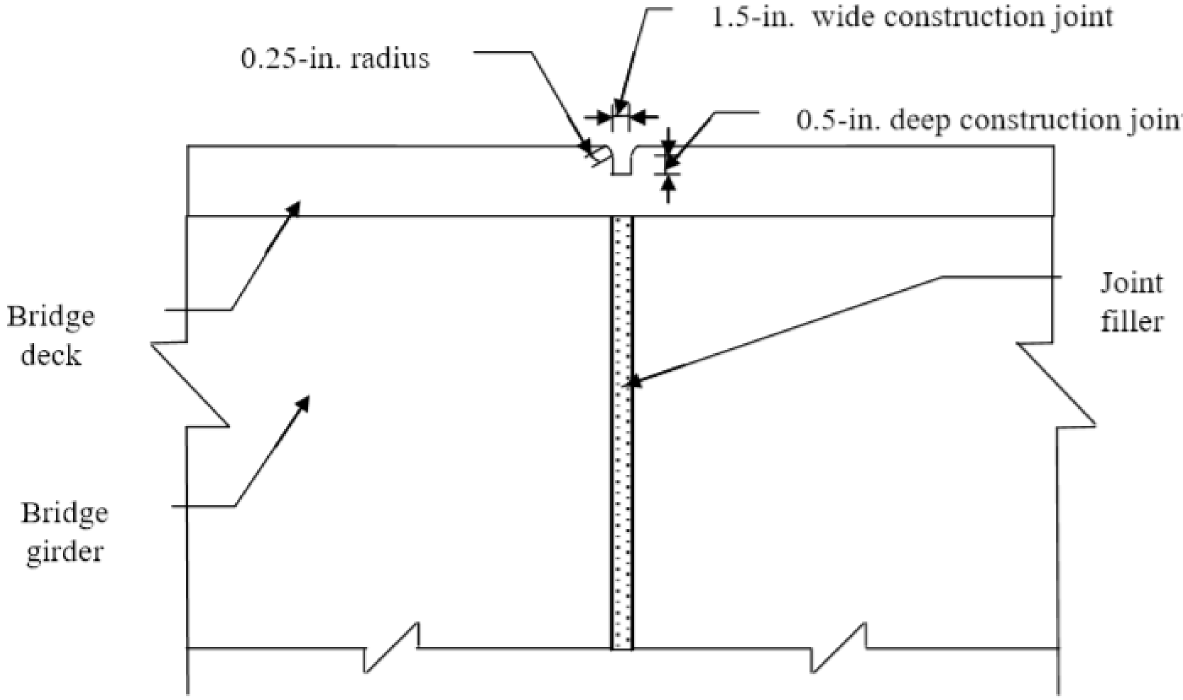

Figure 2.46. Construction joint and girder joint filler, reprinted from Snedeker et al. (2011).

Researchers conducted a simplified beam theory analysis of a single-span deck and girder section to find an upper-bound value for the rotations of the girder ends. The analysis used linear elastic behavior for the girder and a fiber section analysis for the deck including cracking behavior. Shrinkage, temperature, and live load effects were included.

The researchers also analyzed beam and link slab mechanics with fixed and free bearing support conditions simplified to pin and roller supports, respectively. Girder on each side of the link slab rotate about the neutral axis of the composite section. The translation of girder ends is restricted for pin supports. However, the bottom flanges of girder ends with roller-type supports are able to move inward toward one another, causing tension in the link slab. Dowel bars extend from the support into a cavity in the girder at some supports. These dowels are capable of transmitting longitudinal force once they come into contact with the girder's interior faces.

Researchers theorized that the continuous slab detail would not experience significant axial tension since they did not find evidence of significant cracking in their review of bridges. The extra space in the dowel bar cavity makes it such that the girders are able to translate by as much as 0.75 in. without the dowel bars contacting the edges of the cavity (see Figure 2.47). Thus, if the bearing pads beneath the girders are able to deform easily, longitudinal movements in the girders will not produce significant axial force in the link slab. Continuous deck units with multiple spans also allow longitudinal movements to redistribute over many supports, preventing longitudinal forces from developing due to the disproportionate deformation of any one bearing.

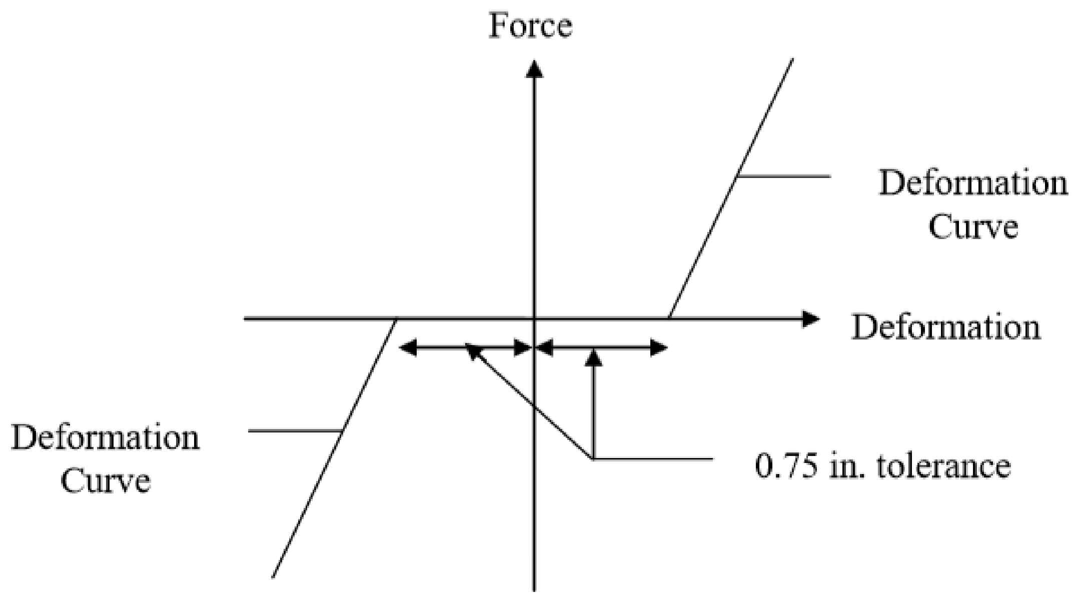

Figure 2.47. Bearing pad force-deformation behavior, reprinted from Snedeker et al. (2011).

Since the GDOT continuous slab detail does not include debonding of the slab at the girder ends, researchers compared girder end rotations calculated with the beam theory analysis to determine whether such debonding might be advisable to prevent excess flexure in the link slab. Using the assumption of negligible axial forces in the link slab, the researchers found the expected strain values for flexure in the continuous deck.

Researchers considered both an initially uncracked deck section and a section cracked from shrinkage, and varied the length of the link slab. Assuming a linear strain profile with the neutral axis at the center of the slab, researchers estimated the required area of steel to resist the tensile demand in the slab. However, the analysis did not produce realistic results. Researchers theorized that shrinkage cracking or camber may reduce the flexural strain in the link slab. Furthermore, literature suggested that girder end rotations in the field may be smaller than calculated rotations.

Davidson et al. (2012) continued the investigation of the GDOT link slab design by instrumenting five bridges and analyzing finite element models of the continuous deck. Initial inspection of the bridges found some damage at the construction joints that was largely attributed to improper construction. The girder ends were fitted with dial gages mounted to the supports beneath to measure the relative longitudinal movement of the girder ends. Demountable mechanical (DEMEC) type gages were used to measure movements across a gage length of

10 in. centered on the construction and expansion joints. The instruments were in place for over a year, with temperatures ranging from 97°F to 26°F.

Two bridges were instrumented at girder ends and abutments with wax scratch plate displacement devices, which leave grooves in wax indicating the magnitude of maximum movement. After a year, the maximum ranges of movement at the bottom flanges of girders on either side of the continuous slab were 0.38 in. and 0.5 in. for expansion type bearings. At fixed bearings, no movements were recorded. Comparing expansion joint movements to values predicted with AASHTO equations found that AASHTO predicted movements were 69 percent larger.

DEMEC and deck surface temperature measurements showed expansion and joint closure with an increase in temperature. The dial gages showed that the rotation of the girder ends is centered at the level of the deck. This confirms that bearing deformation allows the bottom girder flange to translate, thereby preventing a couple moment between the bottom flange and the link slab, which would cause axial forces in the link slab. For both expansion and fixed bearings, dial gage readings showed that the bottom flange of the girders was able to translate.

Researchers developed a finite element model of half of a girder span with an attached deck and edge beam. The bearing support did not resist longitudinal translation. The link slab was modeled as a fully cracked section. The model was loaded with AASHTO temperature gradient, and researchers theorized that deformation caused by temperature would not be sufficient to close cracks caused by shrinkage. Thus, low moment in the deck may be caused by shrinkage cracking. Researchers recommended that the continuous deck detail be changed to reduce the joint reinforcement to #4 longitudinal bars with the top layer of bars continuous across the joint.

Gergess (2019) investigated the design and behavior of a continuous deck that is bonded to its adjacent girders, in contrast to the more common practice of debonding link slabs. The structure considered was a two-span bridge with a CIP concrete deck over simply supported, precast, prestressed AASHTO girders. Elastomeric bearing pads were considered as pin supports for moment calculations but were analyzed with estimated stiffness for shear calculations. The structure was analyzed under AASHTO dead and live loads, including the HL-93 truck and tandem, and lane load.

A basic analysis was conducted using elastic beam theory, considering cracked section properties for the singly reinforced link slab and gross section properties for the prestressed beams and deck slab. Differential equations were developed for each segment and loading condition and solved using Wolfram Mathematica software. This analysis was used to develop closed-form solutions for the ratio of link slab moment to girder span moment (see Figure 2.48) and the ratio of link span shear force to a point load applied in the girder span (see Figure 2.49). Notably, the analysis did not consider longitudinal deformations or compression reinforcement in the slab.

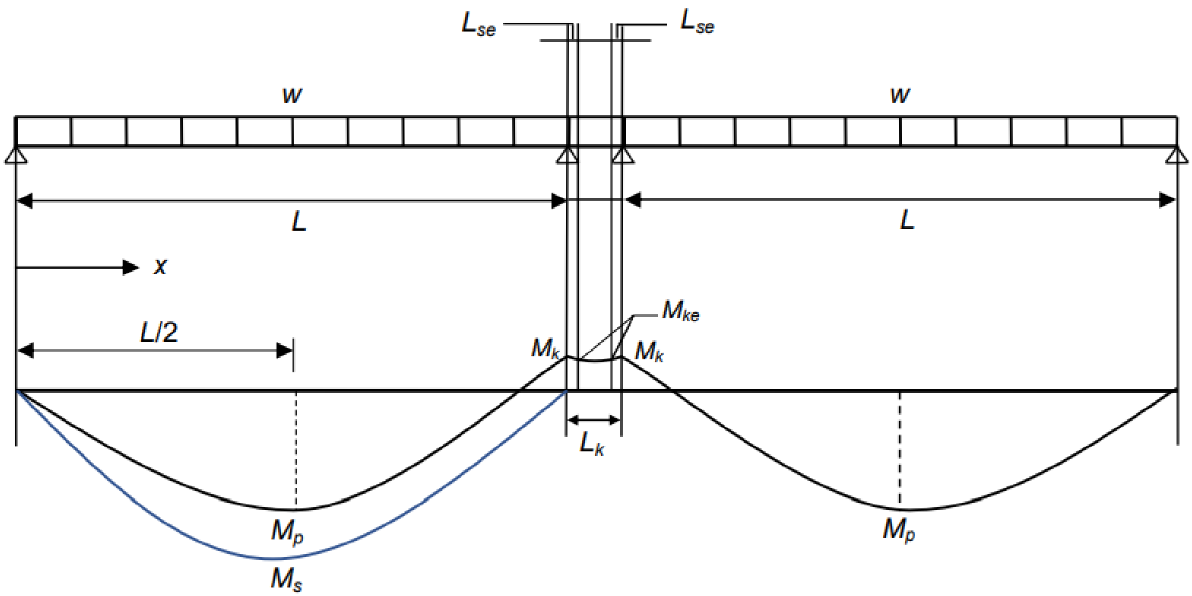

Moment diagram due to a uniformly distributed load w applied continuously

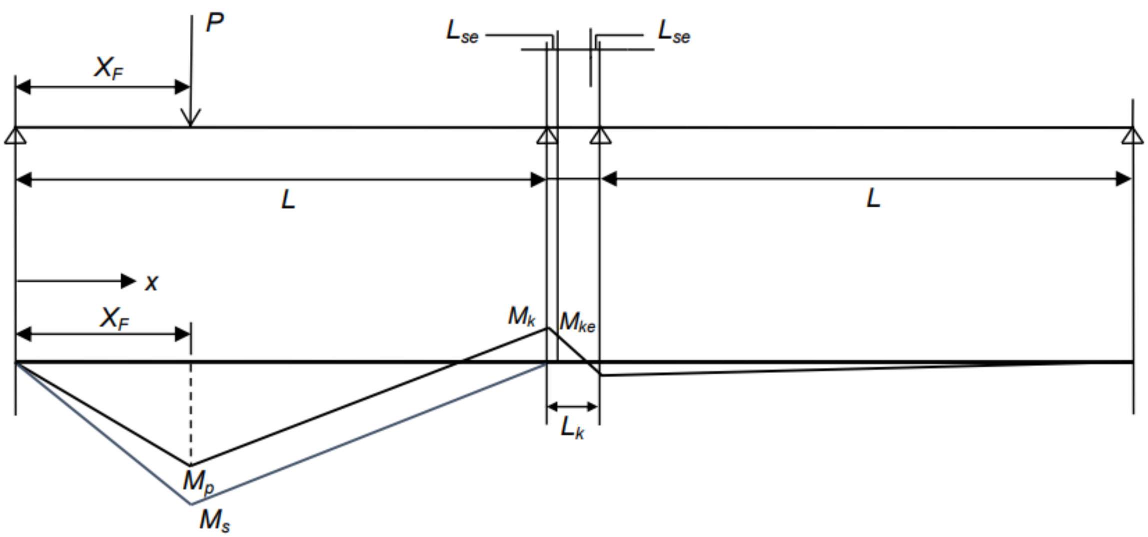

Moment diagram due to a concentrated load P applied at distance X_F

Figure 2.48. Moment diagrams, reprinted from Gergess (2019).

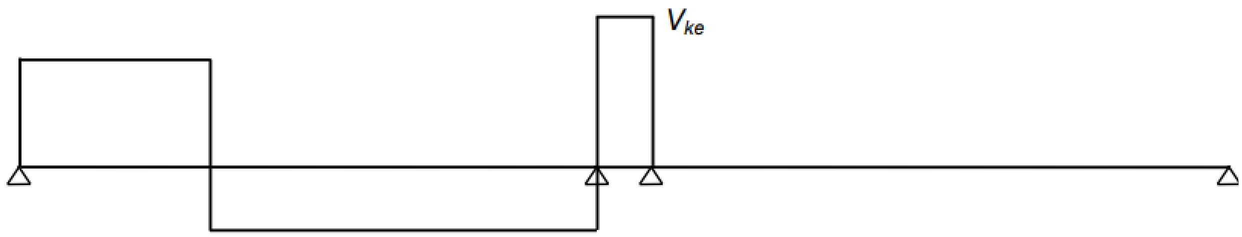

Shear force diagram due to a concentrated load P applied at distance X_F
(also representative of the case where the uniform load w is applied in one span)

Figure 2.49. Shear force, reprinted from Gergess (2019).

A parametric study was conducted by varying the reinforcement ratio, modular ratio, and reinforcement depth of the link slab. The AASHTO girder sections, concrete strength, span length, link slab length, and girder spacing were also varied.

Increasing the deck thickness caused an increase in force redistribution, particularly increasing shear forces. Increasing girder size and decreasing link slab reinforcement ratio reduces the ratio of link slab moment to girder moment. In general, changes that increase girder flexural stiffness and decrease link slab flexural stiffness reduce the ratio of link slab moment to girder moment. Increasing the length of the link slab does the same.

For shear analysis, forces are amplified in the link slab by asymmetrically applied loading with pinned support conditions. However, including the flexibility of the elastomeric bearing support decreases the shear across the link slab. For certain AASHTO girders, shear capacity was found to limit the slab's reinforcement ratio.

Given the parametric study results, a procedure for a bonded link slab design was developed, including a design example. The basic procedure involves choosing the proper ratio of link slab moment to span moment based on characteristics of the structure, then finding the moment values based on applied loads, and finally verifying moment capacity, steel stress, and crack-control requirements.

2.4.2 Debonded Continuous Deck Details

El-Safty (1995) studied the effect of debonding link slabs from the ends of girders designed as simply supported spans with the goal of formulating a finite element solution for analysis of such systems, including linear, nonlinear, immediate, and long-term behavior. The deck ends were modeled as integral with the abutment supports. Constitutive relationships that were used included bilinear or Hognestad models for concrete, a bilinear model for mild steel reinforcement, and a trilinear model for prestressing reinforcement. The general FE model makes use of isoparametric beam elements and uses smeared cracking fracture theory. El-Safty detailed expressions for concrete cyclic loading, aging, temperature effects, and creep, as well as expressions for steel relaxation and elastomeric bearing stiffness.

The finite element model was validated against existing results from literature. The program was run for various support conditions. The debonded deck concept was shown to satisfy strength requirements while providing for sufficient flexibility to prevent a significant change in structural behavior. However, for beams supported on bearing pads, debonding was not found to have a beneficial effect.

Zia et al. (1995) and Caner and Zia (1998) tested early concepts of a link slab with the deck debonded from the simply supported beams. The researchers also made finite element models of the system and developed a design procedure for debonded link slabs.

One specimen with concrete girders and another with steel girders were fabricated. Both specimens used two 20.5-ft spans beneath a 4-in. thick composite deck reinforced with three #6 epoxy-coated reinforcing bars oriented longitudinally. Including the gap between spans, the total length of the link slab was 26 in. Figure 2.50 shows the layout of these specimens, including the region of slab debonded from the girders for a length of 5 percent of the girder span on each side of the support.

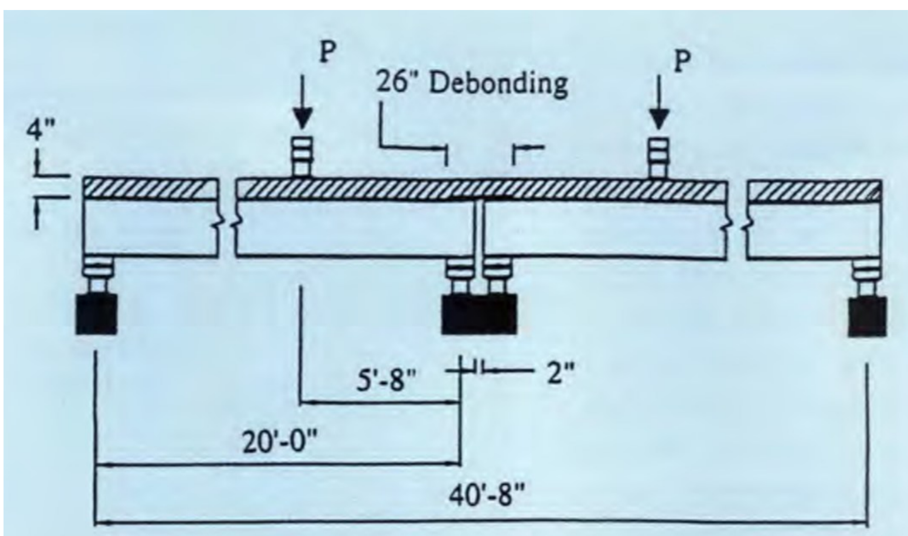

Figure 2.50. Elevation view of specimens, reprinted from Caner and Zia (1998).

The girder specimens were tested with a concentrated load in each span. The specimens were instrumented with load cells to measure applied load and reaction forces. Foil strain gages were installed on reinforcing bars in the concrete beam and slab. A mechanical strain gage was used on the top of the link slab. End conditions for the concrete specimen were altered in each of three load tests to determine the difference in behavior with different combinations of hinge and roller supports. The steel specimen was tested with four different support configurations of roller (R) and hinge (H) supports: HRRH, RHRH, RRRR, and RHHR. The concrete specimen was tested with three of the conditions, excluding the RRRR condition. The specimens were loaded to a maximum of 40 percent of ultimate load for each condition, with a final ultimate load test for the RHHR condition.

In the elastic range, changes in the support configurations did not produce different results. The stresses in the link slab were dominated by bending behavior, and the link slabs failed in bending. The overall load-deflection behavior of the girders, however, was similar to that of noncontinuous simply supported spans since the link slab did not deliver significant moment continuity. Two visible cracks formed in the link slab, with average widths increasing to 0.038 in. at 90 percent of ultimate load. Since the girder depths were small compared to the slab thickness, bridges with thin slabs and deeper girders may be affected more significantly by axial stresses.

The researchers also developed a finite element model of the specimen using isoperimetric beam elements. These elements neglect direct transverse strain and stress, include the assumption that plane sections remain plane after displacing, and take shear stresses as constant. Prestressing and temperature effects were also included, along with a smeared cracking model and nonlinear, time-dependent analysis. The model results predicted that debonding the link slab from the girder for a distance of 5 percent of the span length was sufficient to prevent composite behavior.

The researchers developed a simplified analysis method for the design of link slabs, assuming that the continuity in the slab was minimal, which allows the assumption of simply supported girder behavior. It is assumed that the rotations of the girder ends, calculated for simply supported conditions, will cause a bending effect in the link slab. Potential axial tension in the link slab, a result of the slab being offset from the neutral axis of the girders during bending, was not considered. The majority of transverse cracks in the test specimens occurred in the center of the link slab, while the debonded lengths of slab had only scarce, minor cracks. Thus, the middle length of link slab was analyzed using cracked section properties, while the debonded lengths of link slab were analyzed with the mean of the cracked and gross section properties. The surface crack width was estimated with an empirical equation by Gergely and Lutz (1968). A structural analysis program was written to analyze the system, calculating crack width and updating cracked section properties at each load step.

The results were also compared to those of an FEA program. The stress levels in the rebar were consistently lower than those from the simplified analysis program and the finite element program. The simplified analysis method was found to be conservative. Compared to simply supported conditions, the addition of the link slabs was not found to cause significant continuity.

Based on the results, the researchers developed a design method for link slabs. The link slabs are designed with the same simply supported conditions, debonded length, and end rotation demand calculations as in the simplified analysis method. Taking a conservative approach, the gross section properties of the link slab are used when calculating the link slab moment, and the reinforcement is designed to reach a maximum stress of 40 percent of the yield stress. The steel stress is calculated using design equations and used to confirm that the reinforcement meets AASHTO crack width requirements.

Kumar (1998) described the debonded link slab concept, referred to as the deckslab continuity method. It was suggested that an elastic distribution of the rotation of the link slab could be considered, with reinforcement provided to prevent cracking and resist wheel loads. Kumar theorized that continuous slab lengths may be limited to 350 m (1150 ft) to prevent excess load on bearings, longitudinal deck forces, and lateral forces. Transverse diaphragms are suggested at the beam ends to promote load distribution and reduce relative moments, but are not a necessity.

Kowalsky and Wing (2003) instrumented a bridge in North Carolina that was retrofitted with debonded link slabs to reduce the number of deck joints to evaluate the performance of the link slab concept. The structure was a four-span, simply supported steel girder bridge. The joint over the center bent was left unchanged, while the other joints were replaced with link slabs.

Wing and Kowalsky (2005) used the link slab design method by Caner and Zia (1998) as a basis for retrofits of bridges using link slabs. This method included designing the link slab reinforcement for girder end rotation assuming simply supported behavior and debonding the slab for a length of 5 percent of the girder spans. The bridges were instrumented with thermocouples and strain gages on the top and bottom of the deck and on the girders. Linear variable displacement transducers (LVDTs) were placed at the girder ends, as shown in Figure 2.51, to capture end rotations and displacements. The researchers conducted live load tests to generate maximum positive in-span moments and maximum negative moment at the link slab.

Researchers also built girder line models using the program Visual Analysis in order to predict the end rotations observed in the load tests. The abutment connection was assumed to be a fixed joint, while the expansion joint was assumed as a roller condition. The girder ends beneath the link slab were modeled with pinned supports. The girder and slab stiffness were found by transforming the concrete section into an equivalent steel area. The simulated and experimentally measured rotations were mostly similar but did vary in magnitude at some locations.

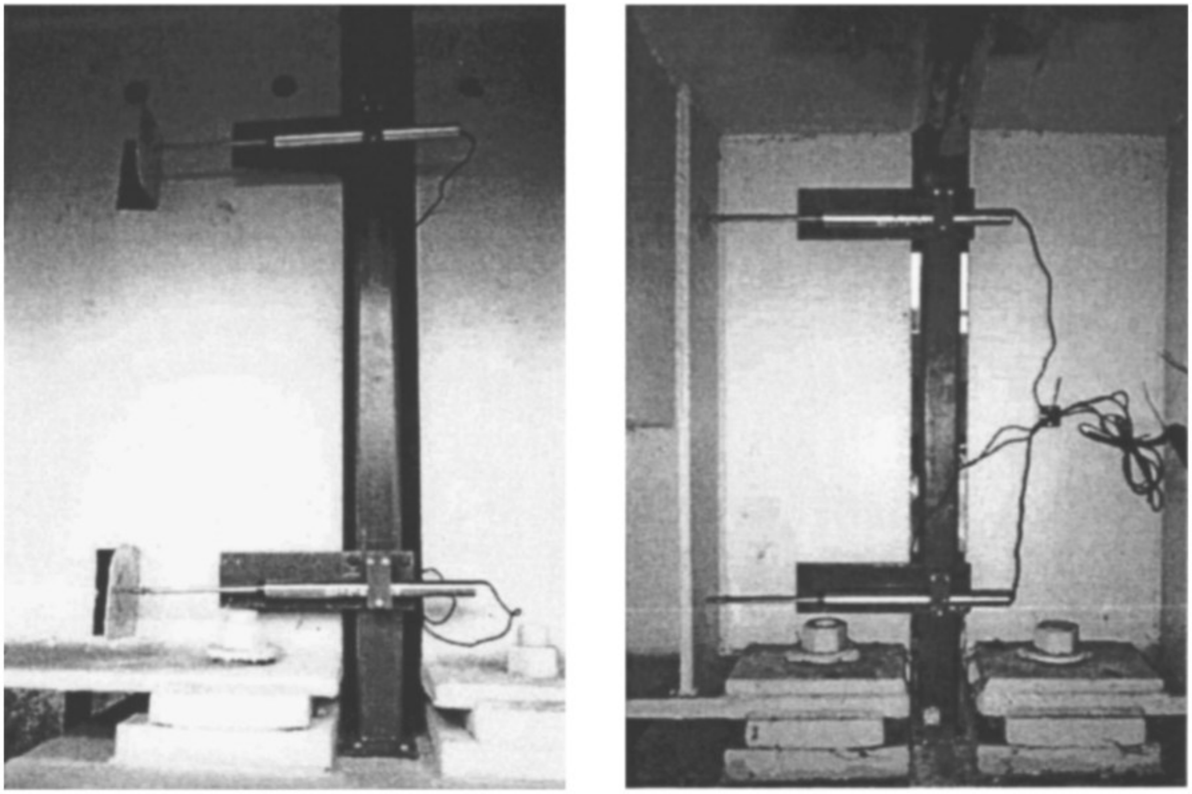

Exterior stand on girder line 5 **Interior stand on girder line 4**

Figure 2.51. LVDT placement at girder ends, reprinted from Wing and Kowalsky (2005).

The instrumentation was used to record bridge behavior for one year at two-hour intervals, with around 40 readings over the course of two minutes for each interval. Maximum daily and yearly temperature variations were approximately 15°C and 45°C, respectively. Traffic-induced rotations were found to be small compared to temperature-induced rotations. The maximum rotation in the link slab never exceeded the design rotation of 0.002 that assumed simply supported behavior. Theoretical rotations calculated using the measured thermal gradient had much larger magnitude than the measured rotations, indicating that the recorded surface temperatures may have varied significantly from internal temperatures. Researchers summarized the limit state design method with a step-by-step process.

Researchers wished to examine a design process for the link slabs that used girder end rotations to predict moment demand and steel reinforcement requirements. The stress in the steel may be found using the design moment in the link slab and cracking moment. Then, selecting a maximum desired crack width, it is possible to solve for the area of uncracked concrete in tension. This area may then be transformed to solve for the required number and spacing of reinforcing bars. Both the design process and the assumptions of the structural model were verified by the test results.

A transverse crack approximately 1.6 mm (0.0630 in.) wide was measured in the link slab at the location of an intentional saw cut to control crack location. This crack was larger than the 0.33 mm (0.0130 in.) design crack limit for exposed conditions. The crack width did not noticeably change during live load testing. Because the cracking in the link slab was localized to the saw cut, causing the crack width to be much larger than calculated, a different expression is needed to find crack widths for link slabs with saw cuts or similar crack-forming details.

Mothe (2006) conducted a parametric study on the effects of bearing pad stiffness, skew, girder size, span length, and debonding length on link slab behavior. Three-dimensional (3D) finite element models of a two-span bridge were developed and subjected to live loads. The bearing pads were represented using multiple springs at the girder ends.

The results of the study showed that increased support stiffness caused a corresponding increase in moment continuity for the system while link slab moment decreased. It was suspected that the link slab was subjected to higher tensile forces instead. Increased debonding length also reduced link slab moment and the maximum tensile stress in the top of the link slab. Mothe modified a three-moment equation for girder and link slab systems to include the contribution of bearing pad stiffness.

Aktan et al. (2008) surveyed bridges with debonded link slabs in Michigan and developed finite element models and link slab designs to improve the use of continuous decks. A total of eight bridges were inspected for damage in the link slabs, approach slabs, decks, abutments, piers, and bearings. A common damage state was full-depth cracks in the link slabs.

Finite element models of a two-span girder and link slab were created to investigate characteristics such as debonded length, girder size, span length, skew, and support stiffness. Additionally, full-width models were created to evaluate the effects of unsymmetrical loading and torsion. The three support conditions used were HRRR, RHHR, and RRHR. The models were subjected to live load, positive and negative thermal gradients, and uniform thermal load. Vertical and horizontal springs were added at the girder ends to include the effect of elastomeric bearing pads.

Debonding a length of the link slab effectively reduced link slab moment but led to only a limited reduction after about 5 percent span length debonding (see Figure 2.52). Increased girder depth caused additional axial force in the link slab. Increased girder stiffness, however, reduced the force and moment in the link slab as girder end rotations decreased.

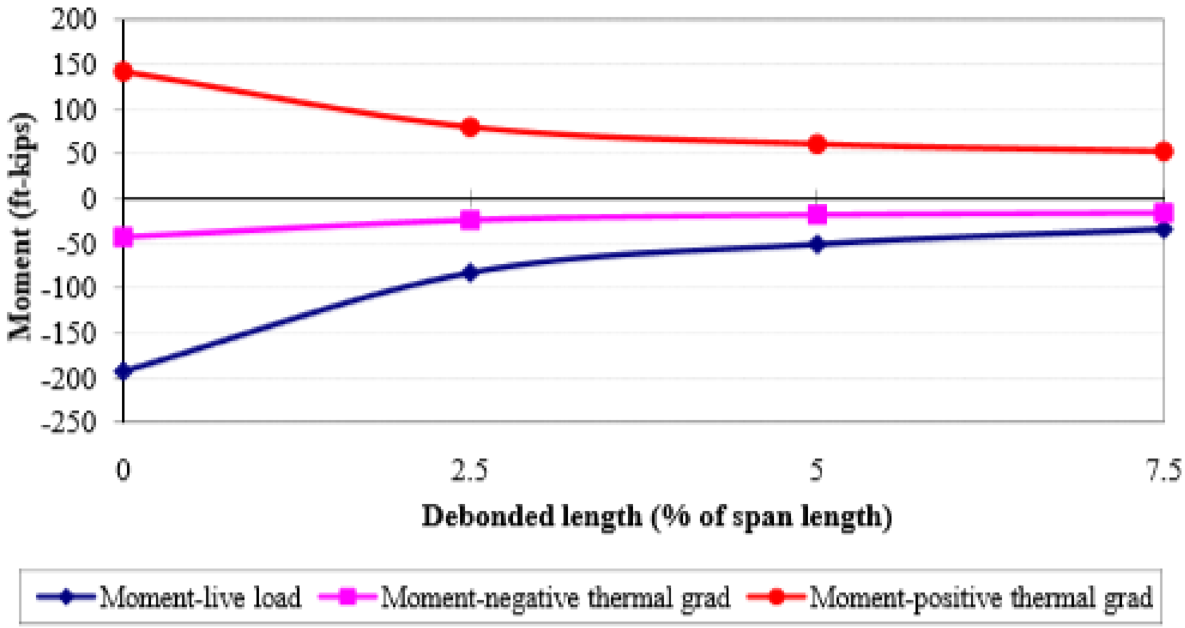

Figure 2.52. Moment demand for different debonded lengths, reprinted from Aktan et al. (2008).

Shrinkage cracking width and live load cracking width were calculated for the link slabs but were not used to reduce the moment in the link slabs. Due to thermal gradient loading, using continuous reinforcement through the link slab in both the top and bottom mats was recommended. Using the minimum debonded length was recommended to limit shrinkage cracking. Three saw cuts, two at the ends of the debonded length and one between the girder ends, were recommended to control cracking in the link slab detail (see Figure 2.53). Since the link slab is under a combination of axial and bending loads, researchers suggesting using moment interaction diagrams in link slab design.

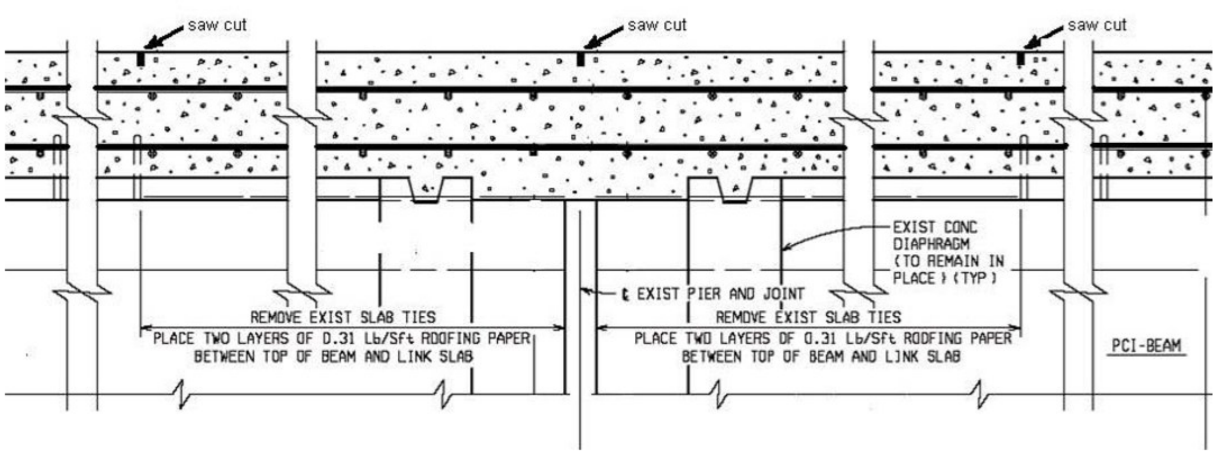

Figure 2.53. Debonded link slab design, reprinted from Aktan et al. (2008).

The full-bridge analysis showed that torsion increased in skewed bridges and with different support conditions beneath the link slab, such as a roller and a hinge. Twisting increased with greater support stiffness. The skewed bridge model was found to have increased link slab forces and moments.

Lam et al. (2008) described the use of a debonded link slab concept in Ontario for situations where a bonded link slab was impractical due to serviceability conditions or bridge geometry. This concept was applied at the Orford Road Underpass, a four-span bridge using steel I-girders and conventional abutments (see Figure 2.54). The slab was retrofitted in 2006 with a 180 mm (7.1 in.) thick debonded link slab, reinforced with 20M longitudinal bars at 100 mm (3.94 in.) and 15M bars in the transverse direction at 150 mm. (5.91 in.), in both the top and bottom mat. Bars were spliced into existing bars with straight laps. Rubber membrane reinforcement was laid over the link slab for water protection in anticipation of cracking. To control cracking, a saw cut was provided in both the slab and topping layer (see Figure 2.55). The structure was later inspected and found to be performing well, outside of hairline cracks in sidewalks above the link slabs. Providing a control joint in the sidewalk was suggested as a solution.

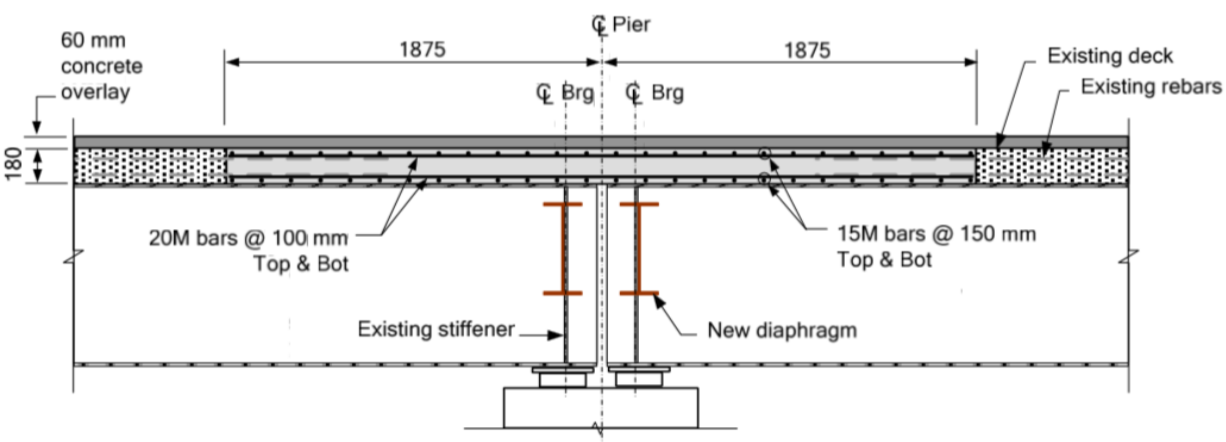

Figure 2.54. Orford Road Underpass link slab detail, reprinted from Lam et al. (2008).

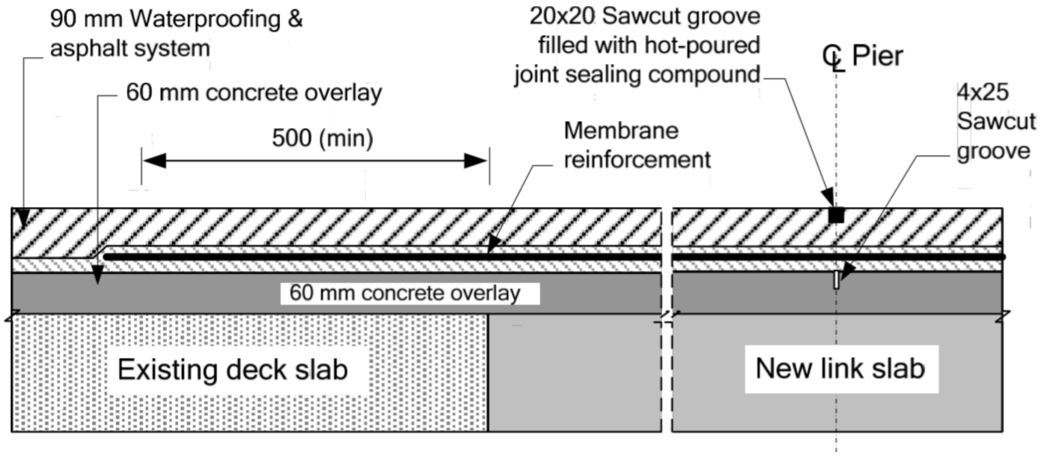

Figure 2.55. Water protection and crack-control details, reprinted from Lam et al. (2008).

A second case of debonded link slabs was implemented at the Mull Road Overpass above Hwy 401 in Ontario. The steel girder bridge also included a 180 mm. (7.1 in.) thick slab and four simply supported spans. In addition to the replacement of joints with link slabs, the abutments were made semi-integral, and the entire deck was replaced with a composite slab with full-depth PCPs. The debonded link slabs themselves were also PCPs with 20M longitudinal bars at 100 mm (3.94 in.) and 15M transverse bars at 225 mm (8.86 in.), both top and bottom mats (see Figure 2.56). PCPs were made continuous after placement with 300 mm (11.8 in.) wide closure pours. Mechanical couplers were used to splice reinforcement within the closure pours, and shear studs were made to fit into pockets in the precast slab to generate composite action. As with the Orford Road Underpass, rubber membrane reinforcement was added above the link slab and below an asphalt wearing surface. In the following year, an inspection of the structure found it in good condition, with small transverse cracks noticeable in the link slab and the sidewalk above the link slab.

(a) Reinforced continuity provided by mechanical couplers

(b) Prefabricated link slab panel showing expansion joint in parapet well

Figure 2.56. Prefabricated link slab construction, reprinted from Lam et al. (2008).

A final rehabilitated structure, the Camlachie Road Underpass crossing Hwy 402 in Ontario, was examined. The bridge consisted of two simple spans of steel box girders beneath a composite CIP slab. The retrofit included a debonded link slab installed over the pier and discontinuous girders, as well as modifications to make the abutments semi-integral. The link slab section was 6 m (19.7 ft) wide, with 4 m (13.1 ft) debonded and without shear reinforcement. The slab was reinforced with a rubber membrane to prevent water infiltration above 15M bars at 100 mm (3.94 in.) in the longitudinal direction and 20M bars at 200 mm (7.87 in.) in the transverse direction in both the top and bottom mat. Fiber-reinforced concrete with a peak tensile stress of 5.7 MPa was used to control crack widths.

The use of debonded link slabs was noted for being four to eight times more cost-effective than the more complicated retrofits involving continuity between girders. The flexible link slab system was less expensive than the debonded link slab for longer spans that required more retrofitted area of slab but more expensive for shorter spans with smaller link slab areas.

Romkema et al. (2011) discussed the use of link slabs in bridges with support skews over 20 degrees based on the behavior of 3D finite element models. The modeled structure was a two-span girder bridge with a debonded link slab. The support skews were varied from zero degrees to 45 degrees, and the girder supports were varied between idealized HRRH, RRHR, and RHHR conditions. The models were subjected to vehicle live loads and temperature gradients.

Torsion in the link slab decreased with increase in skew, while twisting forces varied for different support conditions. Increasing skew also caused bending moment and axial forces to decrease under live load but increase under positive temperature gradient. Girder end rotations increased with skew for HRRR and RRHR conditions. The researchers recommended the use of factors to account for these effects in link slab design for skewed bridges.

MTO conducted ⅓-scale experimental tests and field examinations of debonded link slab (DLS) systems in order to evaluate their utility in the rehabilitation of deteriorated expansion joints in multiple-span, simply supported bridges (Au et al. 2013). DLS systems replace expansion joints by linking the existing deck slab on either side of the support with a section of continuous slab debonded from the supporting girder (see Figure 2.57). The debonded slab section can cope with the girder end rotations across the simple support.

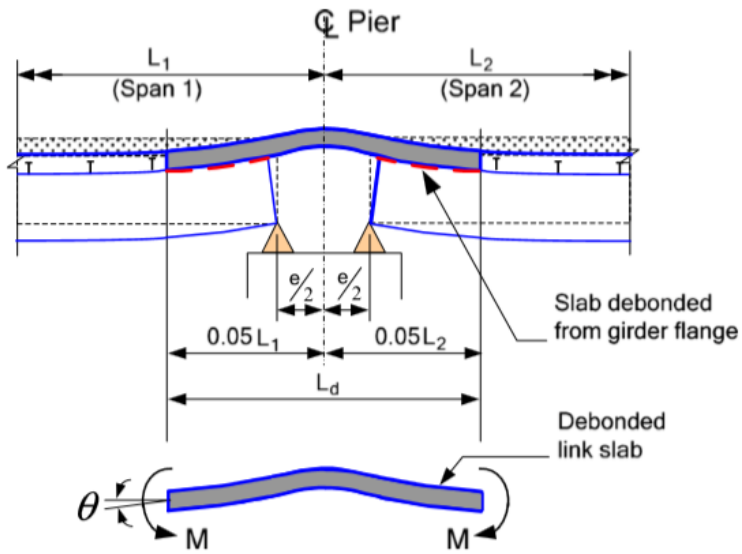

Fig. 1. DLS system

Figure 2.57. DLS system, reprinted from Au et al. (2013).

Simple design of such slab systems involves calculating the end rotation of the girders and using these rotations to find the moment demand in the link slab, assuming uniform curvature in the slab. However, an analysis this simple ignores longitudinal displacement of the girder ends and fails to accurately represent the deformation of the system. A modification factor that is a function of the link slab length and the gap distance between girder ends may be used to correct this.

The goals of the test program were to evaluate the performance of the link slab under repeated traffic loading and serviceability limits, and to determine whether the debonding dimension of 5 percent of the span was reasonable. The ⅓-scale specimens consisted of two steel girders connected to a strip of CIP slab and joined by a DLS (see Figure 2.58). One specimen approximated the 5 percent span requirement, and the second specimen approximated a 3 percent span length condition. The specimens were instrumented to record deflection and rebar strain. They were loaded cyclically in order to plot their response after increasing numbers of load cycles, up to 4 million.

The cracking in the 5 percent specimen consisted of hairline cracks in a fairly regular pattern (see Figure 2.59). There was minimal change in specimen stiffness with an increasing number of load cycles. Deflections were underestimated by the theoretical model.

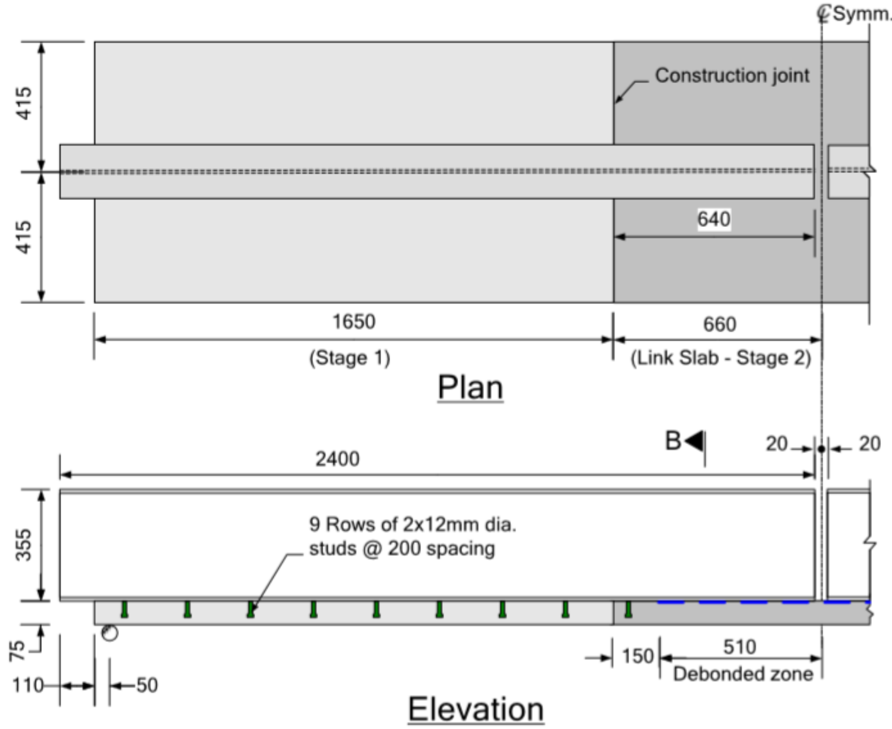

Figure 2.58. Diagram of test specimen, reprinted from Au et al. (2013).

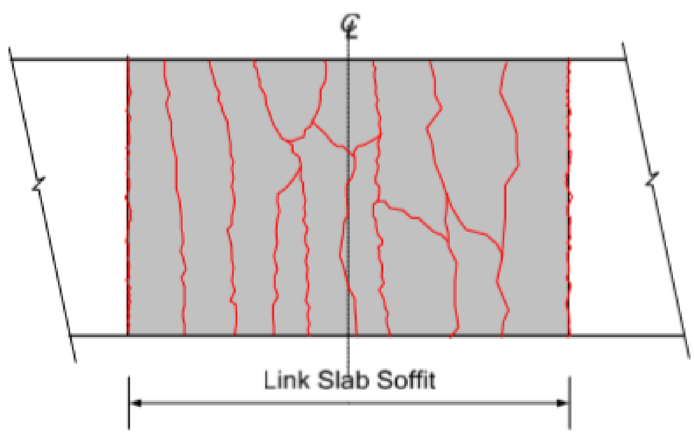

Figure 2.59. Slab crack pattern, reprinted from Au et al. (2013).

The 3 percent model displayed inelastic behavior prior to repeated load cycles. The cracks in the link slab were slightly larger. Since the debonded length of the slab was reduced, the link slab was not able to deform adequately to avoid the application of focused load by the deformed ends of the girders on the center of the slab. Thus, the crack pattern shows evidence of punching behavior, with cracks emanating from the location of load application (see Figure 2.60). Therefore, the feasibility of reducing the 5 percent requirement was not confirmed without further investigation.

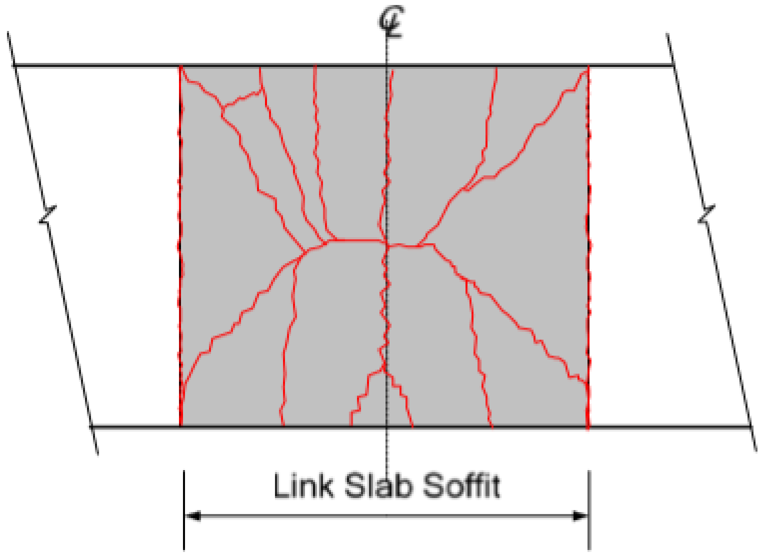

Figure 2.60. Slab crack pattern, reprinted from Au et al. (2013).

An in-service bridge in Ontario was load tested before and after rehabilitation with DLSs to observe its deformation behavior and compare the results to those calculated with analytical models. The bridge consists of two simply supported spans of CIP slab over steel box girders (see Figure 2.61). The rehabilitation project included removing expansion joints at the abutments and bent in favor of integral abutments and a DLS. The structure was instrumented with 44 strain gages over the slab, girder, and on some of the reinforcement within the link slab. Ten LVDTs and two inclinometers measured the bridge's vertical deflection and end rotation, respectively. Trucks were positioned on the span to create maximum structural responses.

The results were compared to the output of an S-FRAME 7.02 model, which utilized tensionless, rigid spring elements to simulate the debonded connection (see Figure 2.62). Axial loads were not considered, but this effect was considered negligible based on prior findings. The link slab model included an estimate of cracking in the negative moment region based on a reduced moment of inertia. This reduced section was calculated iteratively for each load step based on the value of the applied moment. After the strains in the rebar were calculated from the moment, crack width was estimated based on the strain listed in the Canadian Highway Bridge Design Code provisions.

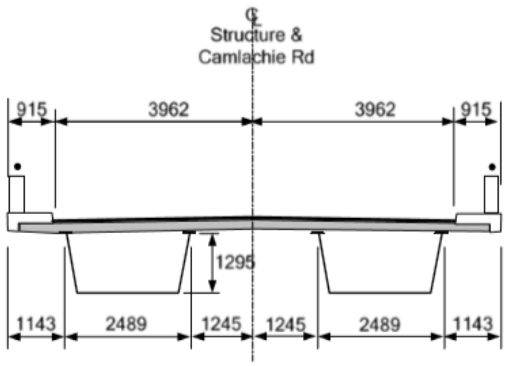

(a) Typical section

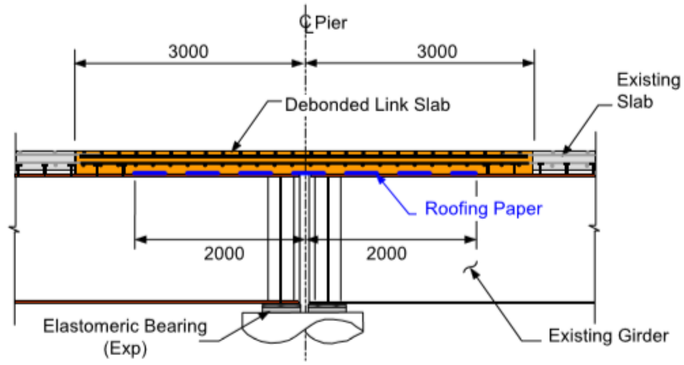

(b) Debonded link slab details

Figure 2.61. Bridge details, reprinted from Au et al. (2013).

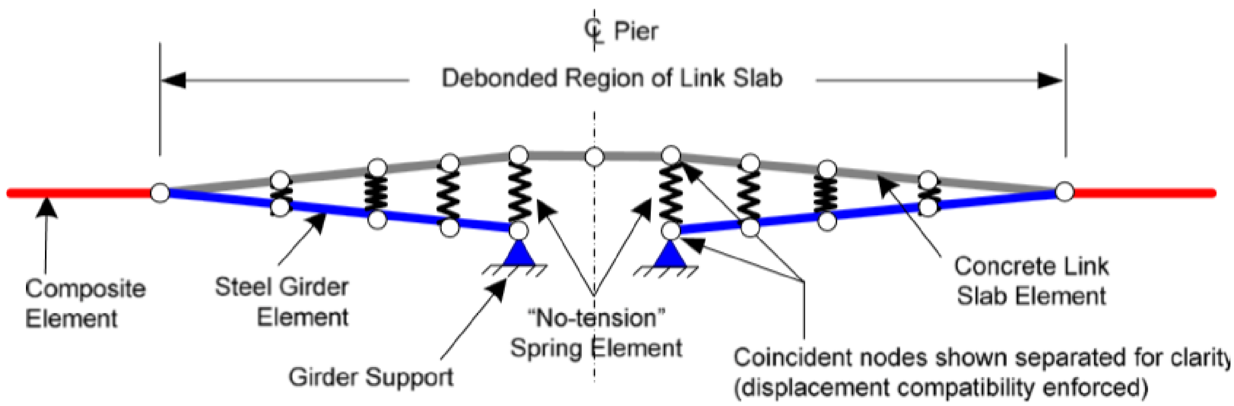

Figure 2.62. Spring model of link slab, reprinted from Au et al. (2013).

The theoretical and experimental results showed that experimental deflections, girder end rotations, and strains were consistently smaller than the predicted values. Strain in the top bars showed that the link slab was partially cracked. The axial effect was found to be minimal when compared to the bending effect, as shown in the small difference between the measured and test data curves. The vertical distribution of strain across the link slab section was not found to be linear, with researchers theorizing that contact with the girder flange in the debonded region caused this deviation. Experimental girder end rotation was also found to be lower than analytical values.

The link slab did, however, cause noticeable continuity between the spans, leading to a revision of the procedure by Caner and Zia (1998) to better model slab and girder deformations in order to capture this behavior. Maximum moment decreased by 16 percent with the addition of the link slab.

Wang et al. (2019) calculated stresses in link slabs for vertical displacement of girder ends due to differential support settlement, as well as longitudinal translation and rotation. The prospect of vertical deflection had a significant effect on stresses in the top of the link slab. The researchers developed a design for a composite link slab with reinforced concrete atop steel sections. The steel section includes a void above the girder ends, such that they are able to rotate without contacting the link slab above. The steel section is able to translate atop polytetrafluoroethylene (PTFE) plate supports, and reinforcing bars are welded to the steel, leaving an intentional gap in the concrete at the ends of the link slab (see Figure 2.63).

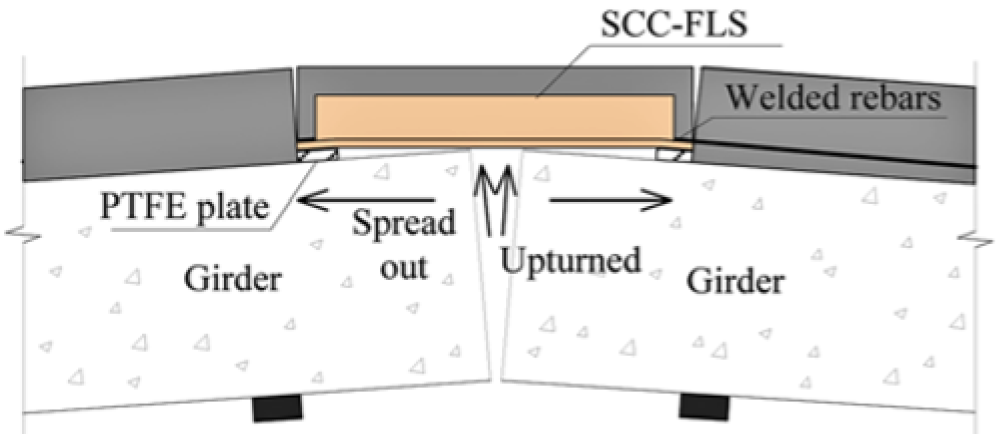

Figure 2.63. Composite link slab design, reprinted from Wang et al. (2019).

The concept was modeled using finite element software and was exposed to thermal gradient and live loads. The concept was then tested between a full-scale, two-span girder system. Results showed that the steel and welded rebar successfully transmitted tensile forces through the link slab, sparing the concrete above from cracking. The axial stiffness of the steel section resulted in small tensile strains.

2.4.3 Link Slabs Using Alternative Materials

Engineered cementitious composites (ECCs) are fiber-reinforced materials with microstructures tailored to induce strain-hardening behavior after initial cracking, in contrast to conventional concrete materials, which also have a tensile strain capacity 500–600 times lower than ECCs (see Figure 2.64). Additional benefits of ECCs include superior toughness, shear ductility, and damage resistance (Keoleian et al. 2005).

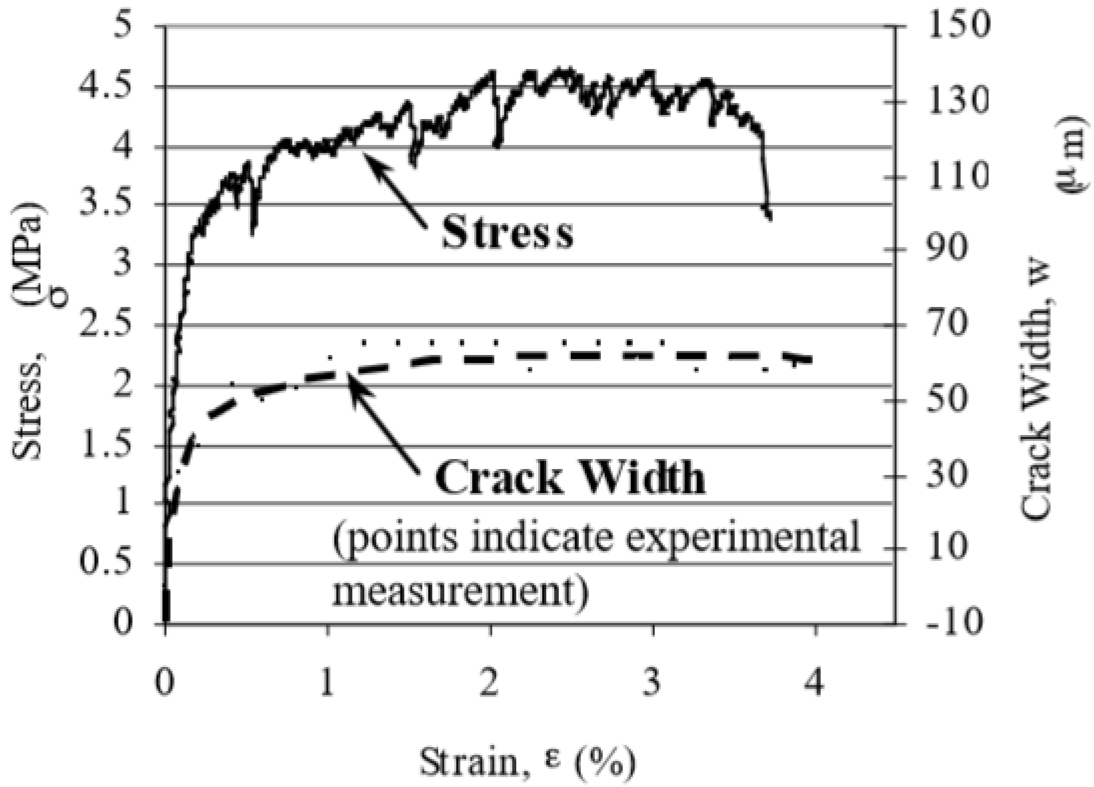

Figure 2.64. ECC stress-strain plot and corresponding crack width, reprinted from Lepech and Li (2005).

The tensile capacity of ECC materials makes them an attractive option in link slab designs since cracks in the deck that would allow the intrusion of deleterious substances may be minimized. Kim et al. (2004) utilized ECCs in the design of a link slab to enhance the durability of the system. By adding only 2 percent volume fraction of steel fibers, ECC materials can offer 370 times the tensile strain capacity of everyday concretes. The researchers formulated an ECC mix design and poured three full-scale link slab specimens, one with standard concrete and two with ECC (see Figure 2.65).

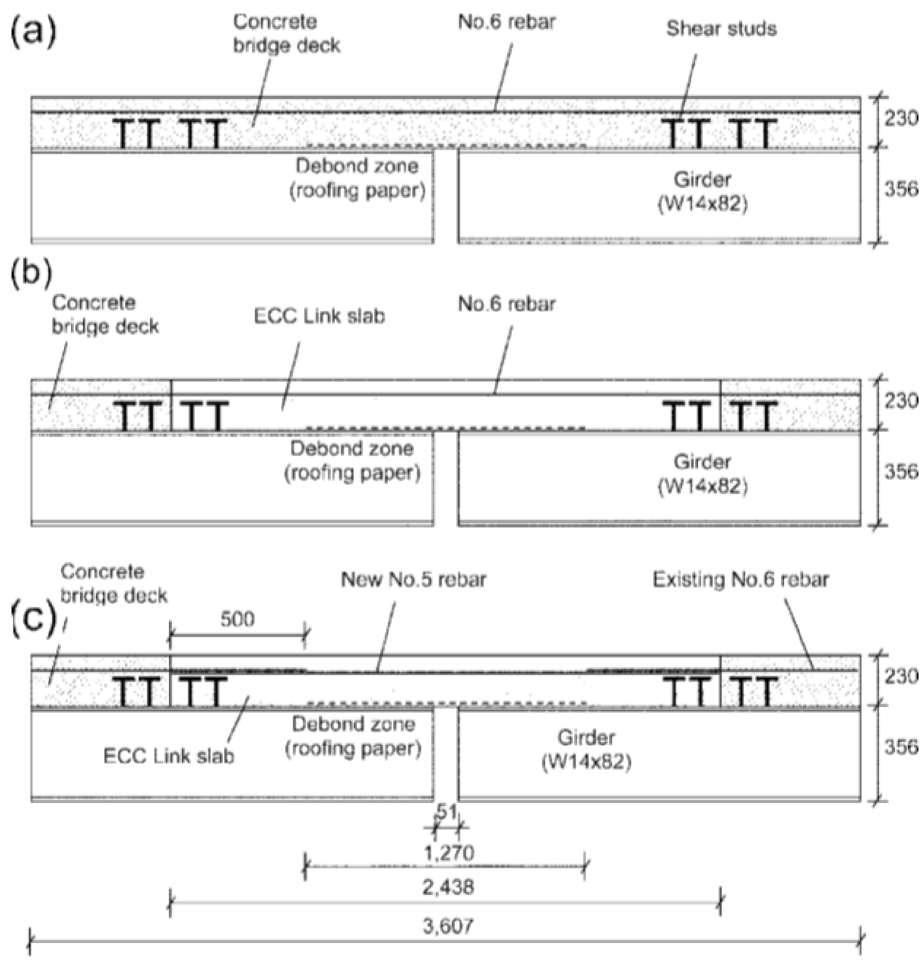

Figure 2.65. Diagrams of the three link slab specimens, dimensions in mm (1 in. = 25.4), reprinted from Kim et al. (2004).

Test results showed that the tensile contribution of the ECC results in a reduced stress in reinforcing steel. The ECC also performed more than adequately in preventing significant cracks, another function of reinforcing steel. Since less steel is required for strength and crack control, the link slab's stiffness may also be reduced. Cyclic loading tests also showed beneficial behavior of the ECC link slab when compared to normal concrete link slab since crack widths did not increase in the ECC material with mounting load cycles. Thus, after 10,000 load cycles, final crack widths for the concrete slab measured 640 µm, compared to just 50 µm in the ECC link slab. Interface cracking at the end of the link slab was prevented by installing shear studs within both the ECC link slab and adjacent normal concrete at their interface, shifting the location of stresses.

Lepech and Li (2005) described the use of debonded ECCs in link slabs in Michigan (see Figure 2.66). Using ECCs makes possible a reduction of reinforcing steel that would be used for crack control, which reduces the stiffness of the link slab. While normal concrete link slab designs were found to deteriorate quickly due to poor placement of steel and construction issues, ECC link slab behavior is more controlled by the material than by careful reinforcement placement.

The link slab's transition from an ECC to normal concrete was designed with 50 percent more shear stud reinforcement than the deck slab to account for the high-shear stresses near the interface. The design of the link slab followed standard methods, using the rotation of the girder ends to calculate the moment in the link slab. The steel reinforcement was then chosen based on a working stress design and assuming elastic-perfectly-plastic behavior of the ECC. After selecting reinforcement, the link slab was checked to ensure that maximum material strains were not exceeded due to live load, temperature, or shrinkage.

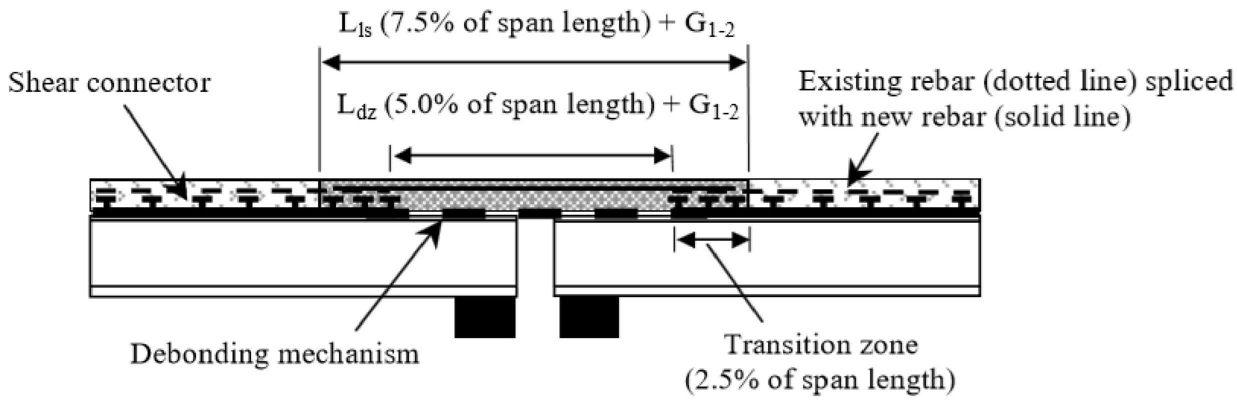

Figure 2.66. Debonded ECC link slab diagram.

These designs were put into practice on a demonstration bridge (see Figure 2.67) (Lepech and Li 2009). Since the structure was designed according to AASHTO standards, the link slab included almost three times the calculated necessary reinforcing steel. After the deck cured, the link slab was proof tested with live load. Recorded girder end rotations were similar to values found with a finite element model. Strain measurements at the link slab surface also were similar to values calculated using end rotations and were well below the tensile capacity of the ECC. Two years after construction, the detail was still performing well.

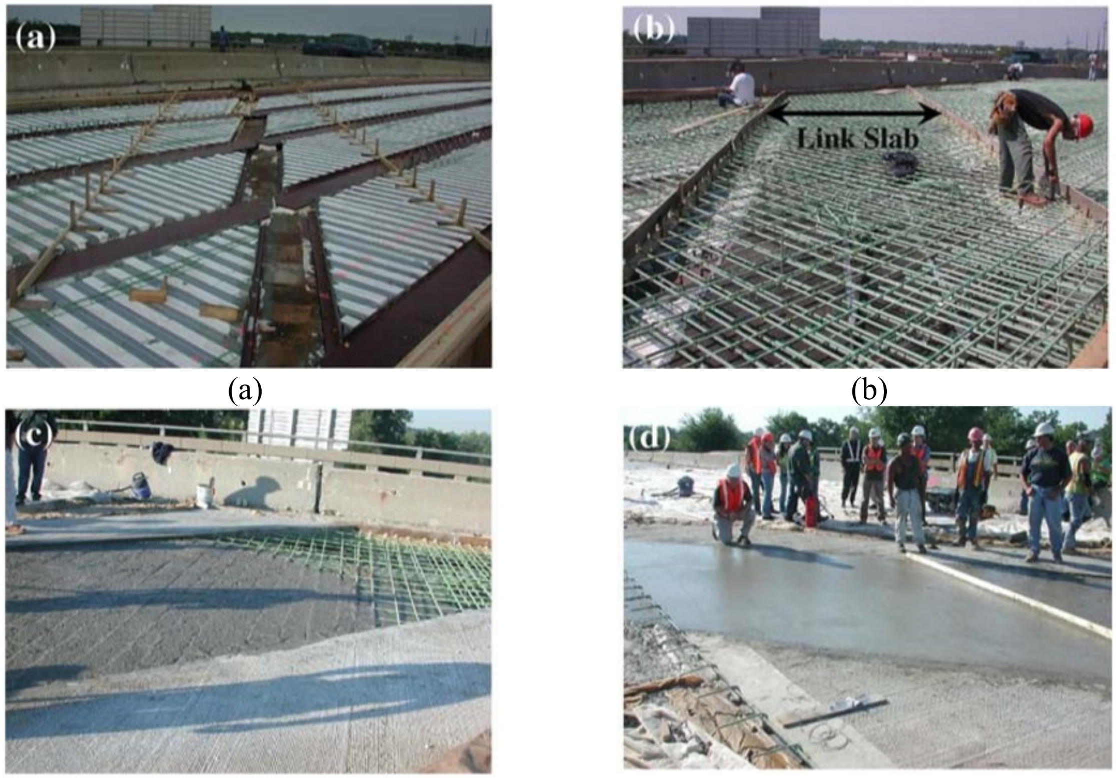

(a) (b) (c) (d)

Figure 2.67. Construction of the ECC link slab, showing the (a) girder ends beneath, (b) placement of reinforcement, (c) ECC pour, and (d) ECC finishing; reprinted from Lepech and Li (2009).

Keoleian et al. (2005) compared a conventional bridge deck built with expansion joints to a deck built using ECC link slabs in a life-cycle assessment. The expected benefits of an ECC link slab include longer service life, more innovative designs, and less maintenance and associated lost time. However, ECC cost is double or triple that of normal concrete.

The life-cycle assessment was carried out assuming a 60-year bridge life for the ECC system and a 30-year life for the normal concrete system, and included material, construction, service, and demolition factors as well as environmental impacts. Results showed that the bridge with ECC link slabs performed very well compared to the conventional concrete link slab bridge in various environmental factors.

Qian et al. (2009) developed designs for the transition regions of ECC link slabs where the ECC materials terminate and the normal concrete deck begins. This abrupt transition between materials generates stress concentrations and is vulnerable to cracking. The researchers proposed using shear studs and splicing reinforcing bars within the ECC transition zone (see Figure 2.68). Both elements encourage shear transfer between the different cementitious materials.

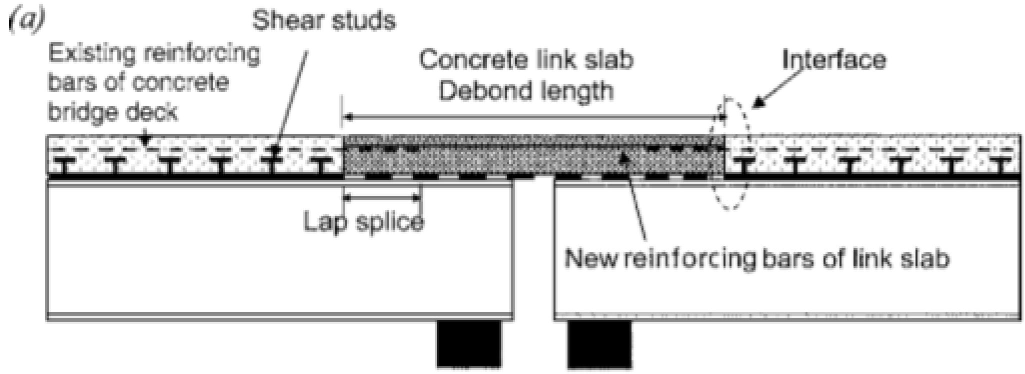

(a)

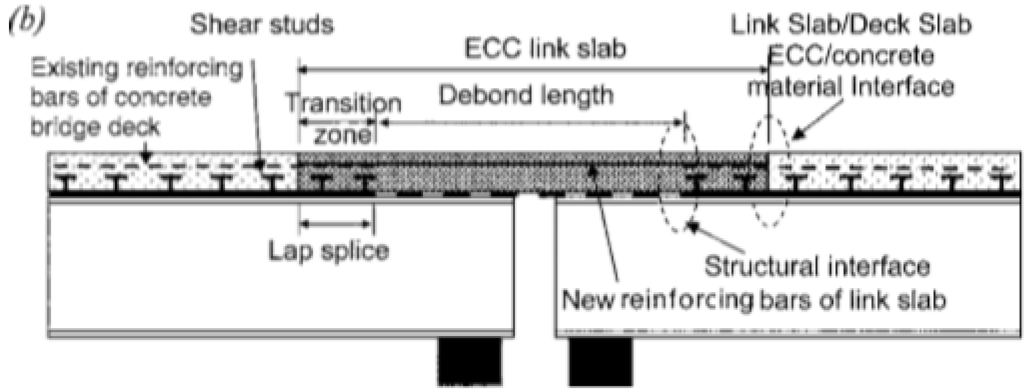

(b)

Figure 2.68. Link slab design for (a) normal concrete and (b) ECC with a reinforced transition zone to protect the discontinuity between materials; reprinted from Qian et al. (2009).

Experimental testing was conducted using three full-scale link slab units (see Figure 2.69). The specimens were built to represent (a) new construction with conventional materials, (b) new construction using ECC in the link slab, and (c) a retrofit using an ECC link slab. The slabs were subjected to 100,000 load cycles. The ECC link slabs successfully prevented cracking in the transition zones. Microcracking was limited to the debonded zones of the ECC slabs, while much wider cracks were generated in the normal concrete link slab.

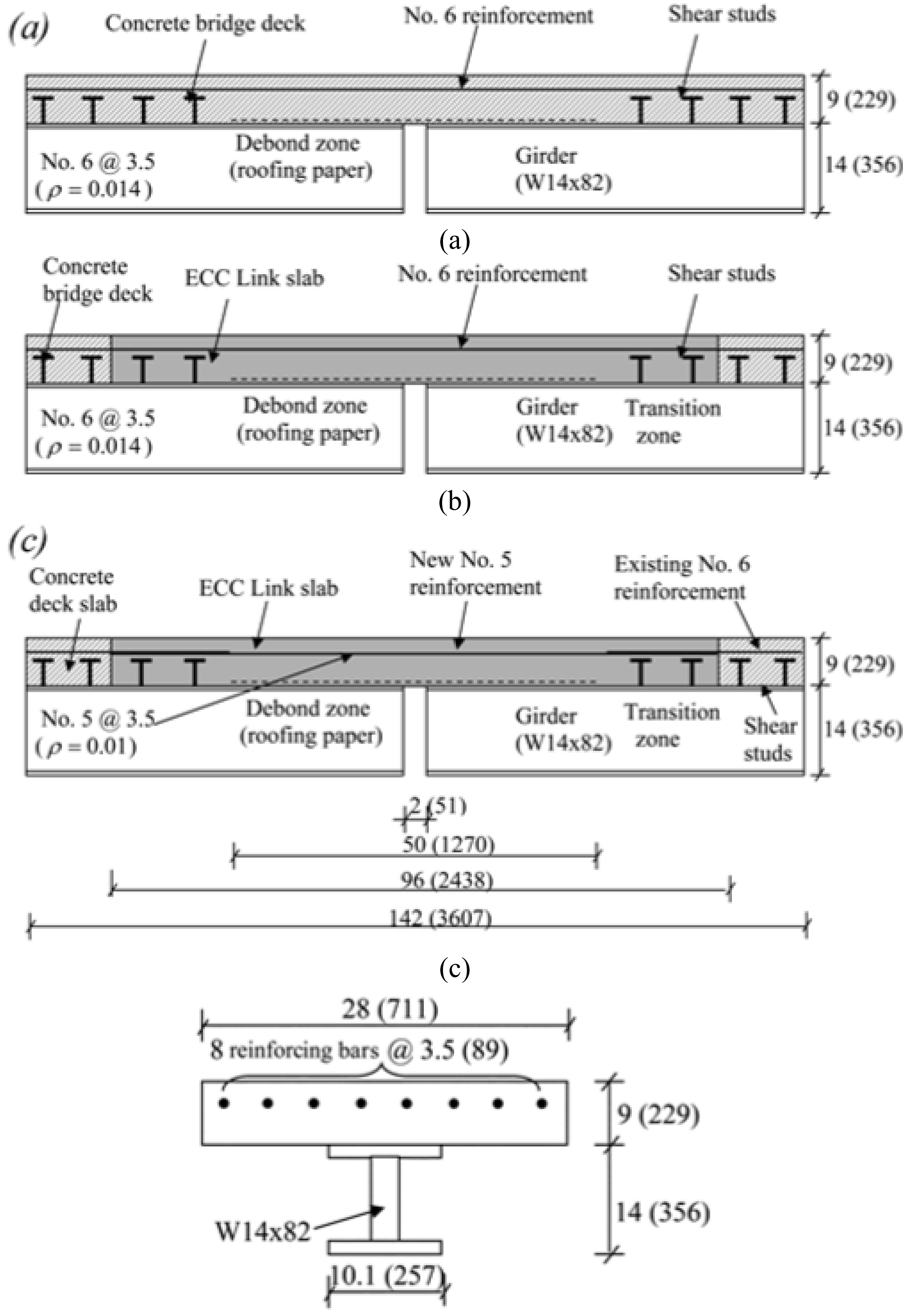

Figure 2.69. The three experimental link slab specimens (a, b, c) and a section view of the specimens (d), reprinted from Qian et al. (2009).

Pullout tests of reinforcement were conducted to verify the lap splice length within the ECC link slab, and pushout tests of the shear studs were conducted to verify their capacity in ECC. The design of the shear studs in the transition region involves finding the total force demand calculated from strain in the slab and choosing the number of shear studs to resist this force. These ECC link slab designs were implemented in the field, and after a year of service, they were found to be performing exceptionally well.

Samani (2015) considered fatigue loading on debonded ECC link slabs with an experimental test program. Three ECC mixtures and one self-consolidating concrete (SCC) mixture were fatigue tested in ¼-scale link slabs (see Figure 2.70). Seven ECC mixtures and two SCC mixtures were tested statically.

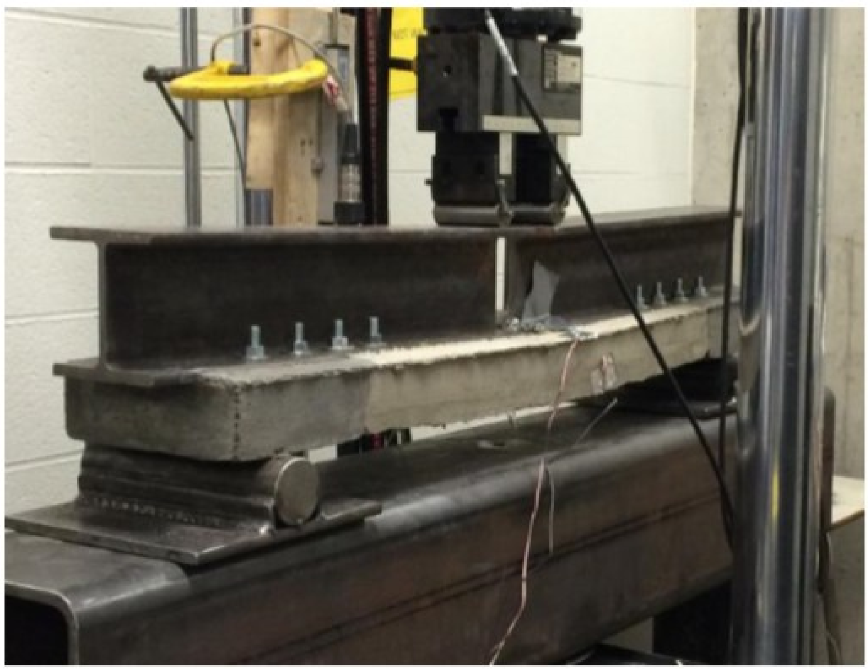

Figure 2.70. ECC link slab specimen under load test, reprinted from Samani (2015).

When compared to the SCC specimens, ECC specimens performed better in their cracking behavior, strain behavior, ductility, ultimate strength, and energy absorption capacity.

Both ECC, with its desirable tensile strain capacity, and fiber-reinforced polymer (FRP), with its beneficial noncorrosive properties and low stiffness, make a link slab built with these materials durable and flexible. Saber and Aleti (2012) investigated the use of FRP reinforcement in link slabs with finite element modeling and flexural testing of beam-like concrete specimens reinforced with FRP grid reinforcement. It was found that the ductility of the FRP reinforcement can result in lowered flexural stiffness of the link slab.

Lárusson et al. (2013) used ECC and glass fiber-reinforced polymer (GFRP) reinforcement to design a flexible, debonded link slab with advantageous cracking behavior. The link slab concept consists of a thin, prefabricated ECC panel, which is grouted on its ends to the surrounding bridge deck and debonded for the rest of its length (see Figure 2.71). Prefabrication of the link slab makes manufacturing and curing possible in a controlled environment while also accelerating construction. Reinforcement protruding from the ends of the link slab into the deck provided the connection that would typically be achieved with shear studs. The added reinforcement at the ends of the prefabricated link slab also stiffened and strengthened the connected ends, which helped to control the location of deformation. The use of GFRP, which has much lower tensile stiffness than reinforcing steel, allows the prefabricated section to be fully anchored to the surrounding deck concrete without using an excessive number of bars.

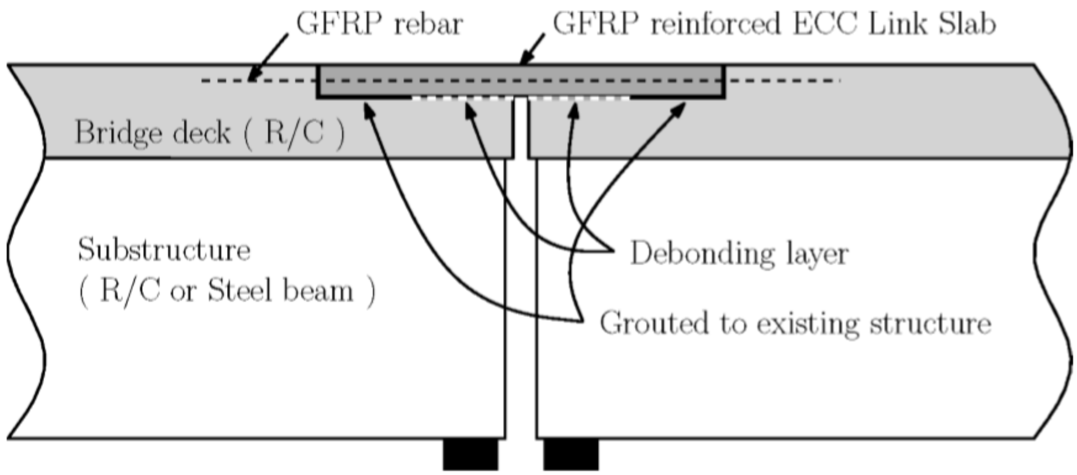

Figure 2.71. Prefabricated ECC link slab concept with GFRP reinforcement, reprinted from Lárusson et al. (2013).

Four test specimens were constructed with a prefabricated section attached to reinforcement prior to the main concrete pour (see Figure 2.72). The specimens were subjected to both static and cyclic axial loading only since bending tests were out of the scope of the project. The specimens achieved satisfactory strength and cracking behavior.

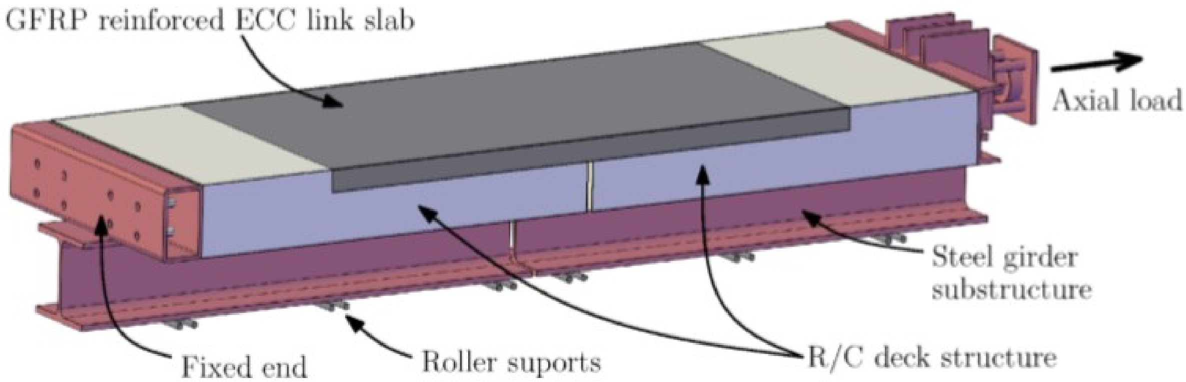

Figure 2.72. ECC link slab specimen characteristics, reprinted from Lárusson et al. (2013).

Zheng et al. (2018) designed and tested debonded ECC link slabs that included FRP reinforcement in the form of bars or grids. The ECC mix was designed for desired crack widths and ductility. Three two-span, single-girder and link slab test models were built to test the design in flexure. Results of the load tests showed that the low flexural stiffness of FRP grid reinforcement caused the specimen to perform similarly to an unreinforced EEC specimen. The unit reinforced with FRP bars was stiffer and had a better distribution of smaller cracks than the unreinforced or grid-reinforced specimens.

Yang et al. (2015) investigated early-age cracking in a link slab in Michigan constructed with a strain-hardening cementitious composite (SHCC). The cracks in question were between 0.006 in. and 0.01 in., which was larger than the design width of 0.004 in. The researchers conducted a restrained shrinkage test, restrained prism test, and finite element investigation to determine what factors may have caused the cracking. It was determined that both material and structural issues contributed to the cracking. The SHCC components, mixing process, and placement process make the material sensitive to high curing temperatures and water loss. Reinforcing bar stress concentrations and added restraint from skewed conditions can also cause cracking.

Shafei et al. (2018) conducted a feasibility study on rehabilitation of bridge decks by replacing expansion joints with link slabs. Researchers modeled a pre- and post-rehabilitation bridge in Iowa using ABAQUS FEA software. The bridge included nine spans, with two expansion joints over interior piers. The bridge was 37 years old at the time of the analysis. Aging of the bearing pad supports led to a reduction in their shear stiffness, causing the pads to behave similar to a pinned connection rather than a roller connection as they were originally designed. As such, researchers compared models with pinned supports to those with roller supports in order to establish the extreme cases for a link slab retrofit design.

The structure was modeled with linear beam elements for the girders and shell elements for the concrete deck. A main focus of the study was the effect of removing deformation capacity by installing link slabs, which causes higher stresses at piers. The models showed that the case of pinned support conditions beneath a link slab caused little change in pier stresses when compared to the pier stress for the pre-retrofitted structure. However, the use of roller support conditions with retrofitted link slabs caused significant increases in pier stress. These observations indicate a trade-off in design. While increased restraint in bearing pad supports causes higher stresses in the concrete deck and link slab, they appear to reduce stresses in the substructure. Since an aged bridge typically has stiffer bearing pads, a retrofit of such a bridge with link slabs was considered to have a minor effect on substructure stresses, while the focus of retrofit design may be concentrated on providing adequate reinforcement for the highly stressed link slabs themselves.

Hou et al. (2018) used ultra-high ductility cementitious composites (UHDCCs) in link slab design, studying their performance under fatigue loading. UHDCCs use polyethylene fiber to achieve a tensile strain capacity between 6 percent and 12 percent, and tensile strengths up to 20 MPa (2.9 ksi). Researchers produced a UHDCC mix and fabricated three steel-reinforced link slab specimens—two with UHDCC and one with normal concrete (see Figure 2.73).

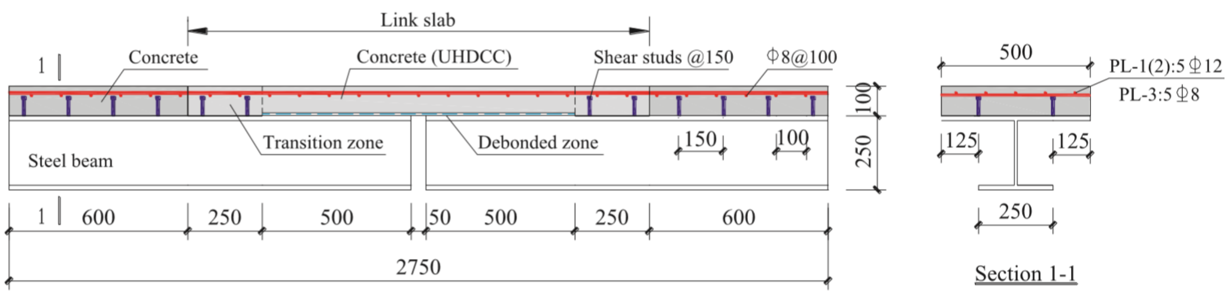

Figure 2.73. UHDCC link slab design, reprinted from Hou et al. (2018).

The UHDCC link slabs exhibited decreased flexural stiffness and triple the fatigue life of the normal concrete specimen. Enhanced fatigue performance was related to the cracking and strain-hardening behavior of the UHDCC. Since the cracks in UHDCCs are much smaller and more widespread, steel rebar bridging the cracks are subjected to smaller strain fluctuations in each load cycle. The strain-hardening behavior causes the UHDCC to assume higher bending loads with deformation, again reducing the magnitude of strain fluctuation in the reinforcing bars.

2.5 JOINTLESS BRIDGES

An alternative to the use of joints is integral construction. According to Burke Jr. (1989), while eliminating joints entirely may offer a significant cost savings, engineers must then account for secondary stresses in the restrained structure. Especially for bridges with short or moderate span lengths, the increased demand on abutments and foundation elements may be a cost-effective trade-off.

Zuk (1980) began a study of jointless bridge construction by conducting a survey of 12 states with existing jointless designs. The proper design of integral abutments, approach pavements, and systems such as railings attached to the structure must accommodate bridge movements. The structures provided the participating states with significant construction cost savings and were projected to save money in long-term maintenance over bridges with joints. Zuk (1981) continued the study by formulating and solving differential expressions for the forces in continuous, jointless decks. Slender transverse cracks are intended to propagate throughout continuous bridge decks but to not reach a width that readily allows the penetration of damaging substances that could lead to corrosion. Zuk determined that the stresses induced in the decks were not too high for practical design in bridge systems with the deck composite near midspan and non-composite near the span ends.

Thippeswamy and Gangarao (1995) studied five existing jointless bridges of composite slab on steel girder construction. It was found that using one row of piles, oriented in weak-axis bending, was an effective way to reduce stresses in jointless bridges. Support settlement also caused increased stress.

Husain and Bagnariol (2000) discussed the use of jointless bridges in Ontario, Canada. While the design of rigid structures less than 20 m (65 ft) in length is economical, longer spans can be expensive to construct. Integral abutment bridges eliminate the need for costly joints over piers and at abutments. Control joints are provided in the approach slab (see Figure 2.74) so that water infiltration will not damage the bridge substructure. Secondary stresses are relieved by making the foundations less rigid. Abutments may also be semi-integral, with the superstructure detached from the abutments but the deck remaining continuous. Cost benefits of these methods arise in the reduced abutment size and construction without the need for bearings. The structures were a design option in Ontario for bridge lengths up to 150 m (490 ft).

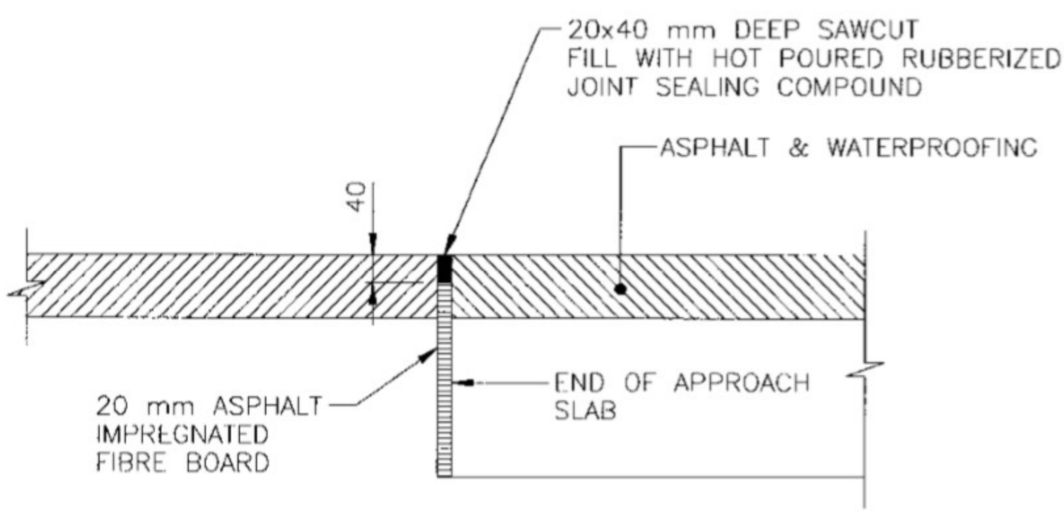

Figure 2.74. Approach slab expansion joint detail, reprinted from Husain and Bagnariol (2000).

Paraschos and Amde (2011) conducted a survey of U.S. states on experience in the design and performance of integral abutment bridges (IABs). The use of IABs began in the 1920s, with several states adopting such systems in subsequent decades. Most states prioritize constructing IABs when conditions allow due to their beneficial performance. States with over 1000 IABs include Missouri, Tennessee, California, Iowa, Illinois, Kansas, Washington, and Wyoming. States have a wide variety of reasons for preferring or excluding the use of IABs:

- In Alaska, soil liquefaction concerns cause engineers to prescribe the use of open circular piles rather than H-piles. The circular piles are typically stiffer, which can cause problems with integral abutments due to lack of deformation.
- In Arizona, the use of IABs was discontinued because longitudinal deformation caused expensive approach slab settlement damage.
- In California, seismic force dissipation is a benefit of IABs. Issues with approach slabs were noted.
- In Colorado, consistent issues were noted in approach slab fill for long approach slabs (7.5 m–10 m) and for approach slabs without expansion joints. Pavement damage was also noted for approach slabs.
- Florida discontinued the use of IABs because they were not found to be a better option than other designs. The need for approach slab joints and details offset the benefit of the jointless deck at the abutment.
- Kansas noted issues with mechanically stabilized earth (MSE) walls used with IABs, and Kansas now uses MSE walls with semi-integral abutments.
- Maine noted riprap settlement, which may expose the abutment and foundations.
- Mississippi had issues with IABs on expansive soils.
- Missouri noted issues with restricted abutment movement caused by rigid fill in abutments designed to slide over rock beneath the foundations.
- Nebraska noted the need to anchor wingwalls in order to prevent wingwall displacement.
- New Mexico noted issues with bearings between the abutment cap and diaphragm. The bearings must be thick enough to accommodate girder rotations.
- New York reported issues with cracking at the approach and deck slab interface, a problem that was addressed by making rebar discontinuous at the approach and deck slab joint. Highly skewed bridges have experienced twisting. Differing deflections are a concern between different stages of construction. This issue is addressed with an abutment closure pour that allows the deck to undergo prior deflection.
- Texas stopped constructing IABs after deciding that they were not advantageous. Because of soil characteristics, drilled shaft or prestressed concrete piles are typically used as more cost-effective foundation elements than more flexible steel piles. Thus, integral abutments are not an economical choice in most Texas environments. When integral abutments were used, their cost and performance was not found to be better than that of conventional designs.
- Virginia solved issues with soil-related rotation in skewed IABs by incorporating a buttress force. Approach slab cracking issues were solved by extending the reinforcing

bars that pass through the deck and approach slab, allowing the approach slab to settle without rotations causing cracking at the ends of the reinforcing bars.

In many cases, issues with IABs are avoided by departments of transportation (DOTs) by imposing limits on bridge length, skew curvature, pile type, soil conditions, and structure type. Research is needed to better understand the theoretical side of IABs, such that such structures may be used in a wider variety of conditions that are currently avoided because of empirically based limitations.

Stringer and Burgueño (2012) investigated the issue of deck cracking in jointless bridges. Such structures may be classified by the level of connection at their abutments. Integral bridges have the abutment and girder cast together, while non-integral bridges have only the continuous deck connecting into the abutment (see Figure 2.75).

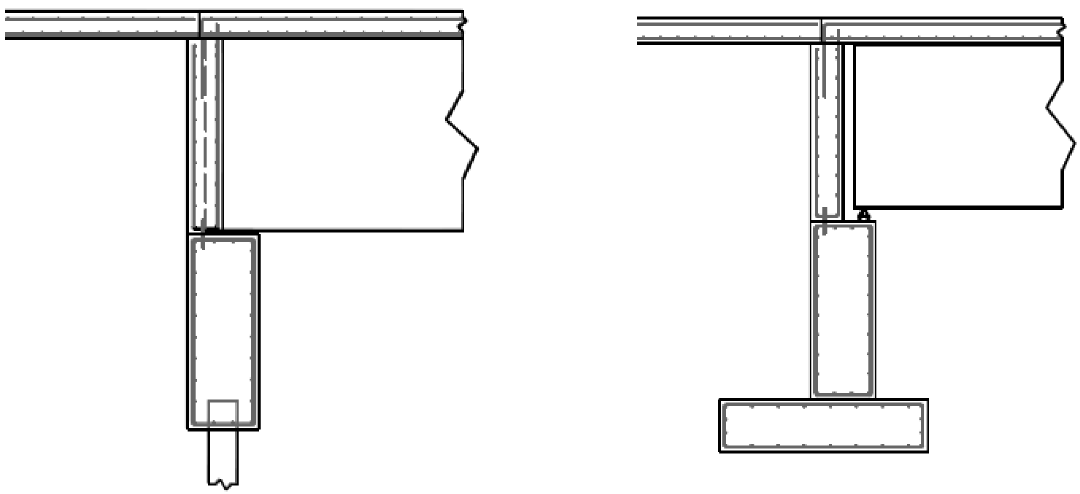

(a) Integral bridge abutment detail

(b) Non-integral bridge abutment detail

Figure 2.75. Abutment details: (a) integral and (b) non-integral; reprinted from Stringer and Burgueño (2012).

Furthermore, integral bridges may be subdivided into those with fully integral abutments that transfer both moment and shear to the foundation and those with semi-integral abutments that only transfer shear force to the pile or footing (see Figure 2.76). H-piles are typically used, oriented in their weak axis to facilitate some movement at the abutment. Typically, concrete girder bridges designed with jointless decks are between 150 ft and 800 ft in total length.

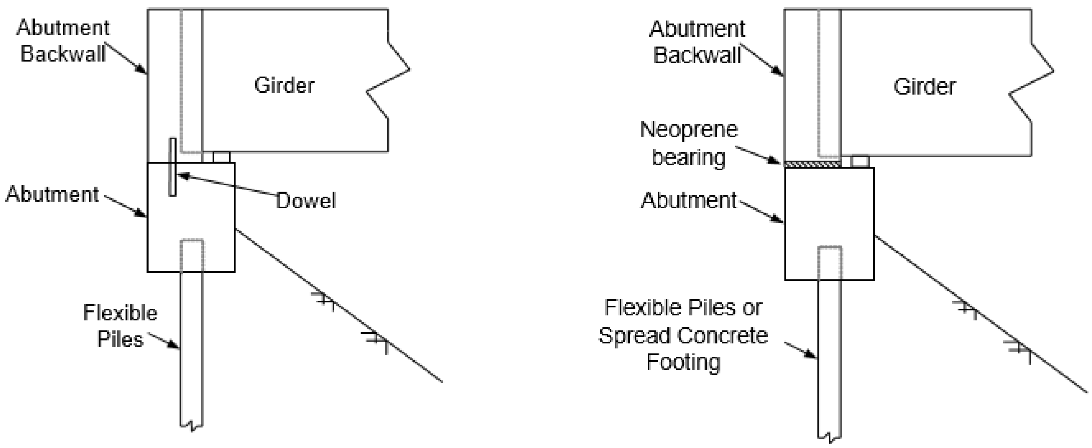

(a) Fully integral abutment (b) Semi-integral abutment

Figure 2.76. Abutment types in integral bridges, reprinted from Stringer and Burgueño (2012).

Azizinamini et al. (2014) surveyed DOTs to identify current practice in regard to bridge system construction. For jointless bridges, design practice varies widely when it comes to length restrictions, materials, skew considerations, piles, and details at abutments and piers. Cracking at abutments is a common issue. Despite the need for continued research and standardization of details, jointless bridges are an increasingly advantageous system.

The connection of pier and superstructure is typically designed in three different ways: integral, pinned, or roller. Integral connections do not require bearings, but must be designed to endure the superstructure's movements without fostering deleterious cracking. Pinned connections, otherwise referred to as fixed connections, allow rotation of the superstructure. Roller connections, or expansion connections, use bearings to incorporate both transverse and rotational deformations, but not longitudinal deformations. Pile design is key because these members must have proper strength while maintaining the flexibility and stability necessary to incorporate bridge deformations and fatigue cycles. The maximum bridge length for fully integral abutments is between 250 ft to 400 ft.

An issue with prestressed concrete girder bridges made continuous over supports is cracking in the girders near interior diaphragm locations, which were weaker than the strengthened diaphragms. Designers of girders made continuous must consider such issues with cracking, as well as secondary moments at piers.

2.6 SUMMARY

Gergess (2019) noted that bonded link slabs, such as TxDOT's poor boy detail, have not been widely studied like their debonded counterparts. More extensive numerical and experimental analysis of bonded link slabs is needed to better understand their behavior. This includes bonded link slabs that use nonstandard materials, such as ECC, UHDCC, ultra-high-performance concrete, and FRP reinforcement. The use of prefabricated link slab elements requires further study, as does the effect of expansion joint replacement on substructure stresses.

While studies have examined the mechanical behavior of some link slab designs, researchers have yet to use nondestructive evaluation techniques to determine the level of damage within in-service link slabs caused by cracking and corrosion. The effects of TxDOT building practices, such as the use of PCPs and the typical crack-forming detail, require further analysis. The cracking and shrinkage behavior noted by Davidson et al. (2012) may be further analyzed to determine its effect on link slab moment reduction. Link slab use in highly skewed bridges, which is not allowed in some states, is another area of future study.

Previous research on the behavior of continuous slabs included multiple analysis studies and experimental test programs that have investigated the impact of support conditions on the demands and deformations that must be accommodated in designs. However, these studies have focused on ideal conditions. While some field studies have monitored deformations, the bridge characteristics and support conditions have a significant impact on behavior. In this study, the characteristics of Texas bridges were explored, including structural health monitoring of several bridges.

3. PERFORMANCE OF POOR BOY JOINTS IN EXISTING BRIDGES

To characterize common characteristics and to provide an understanding of the performance of PBJs in Texas, the Poor Boy Joint Performance Database (PBJPD) was created. The database considered only prestressed I-girder bridges in the Panhandle (Lubbock and Amarillo Districts) and 215 bridges in Northeast Texas (Atlanta and Tyler Districts). These regions were selected because of the frequent use of deicing measures and the high rainfall, respectively.

To create the database, National Bridge Inventory System (NBI) data were filtered to identify prestressed concrete girder bridges that were likely to have PBJ continuous slab details. The age of bridges was limited to 1980 and later because this was the estimate of when the poor boy detailing began to be used. At least two spans were needed for PBJ details to be present over interior bents. Only simply supported girders were considered. Once a preliminary list had been verified, images from Google Earth and as-built drawings were used to confirm that bridges had continuous deck details; those without were eliminated from the database. The final database consisted of 258 bridges in the Panhandle and 216 bridges in Northeast Texas.

Section 3.1 provides a summary of bridge characteristics considered in the evaluation of existing bridges. Section 3.2 summarizes how the PBJ performance is characterized. Section 3.3 provides an evaluation of the database. Section 3.4 provides an overall summary of the chapter.

3.1 BRIDGE CHARACTERISTICS

The PBJPD was created by expanding the NBI database information to include additional information from as-built drawings. The final PBJPD included the following structural characteristics:

- Span lengths, configurations, skews.
- Girder type and spacing, bearing types.
- Deck reinforcement type, size and spacing.
- PBJ details, including type of link slab and additional reinforcement.
- Abutment era, presence of diaphragms.
- Calculated demand/capacity ratios.

When creating the database, sufficient information from the NBI database and the as-built drawings was not always available to characterize the PBJ, calculate capacities, or establish baselines for assessing the condition. Thus, some assumptions were made about details based on the age and other information.

Figure 3.1 and Figure 3.2 show the locations of bridges used in the database. Figure 3.3 through Figure 3.6 provide histograms summarizing characteristics of bridges in the database.

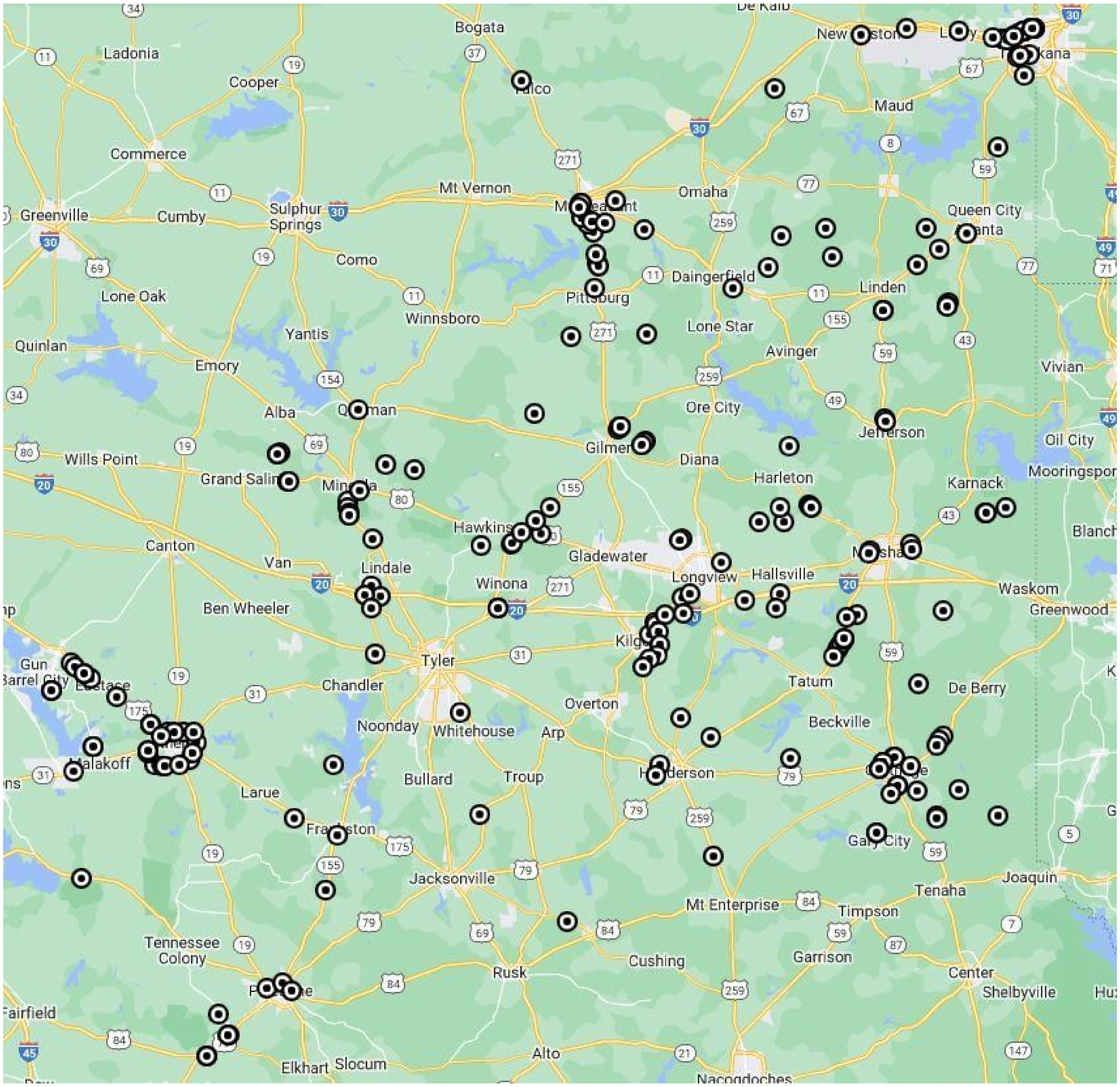

Figure 3.1. Locations of bridges in Atlanta (ATL) and Tyler (TYL) Districts.

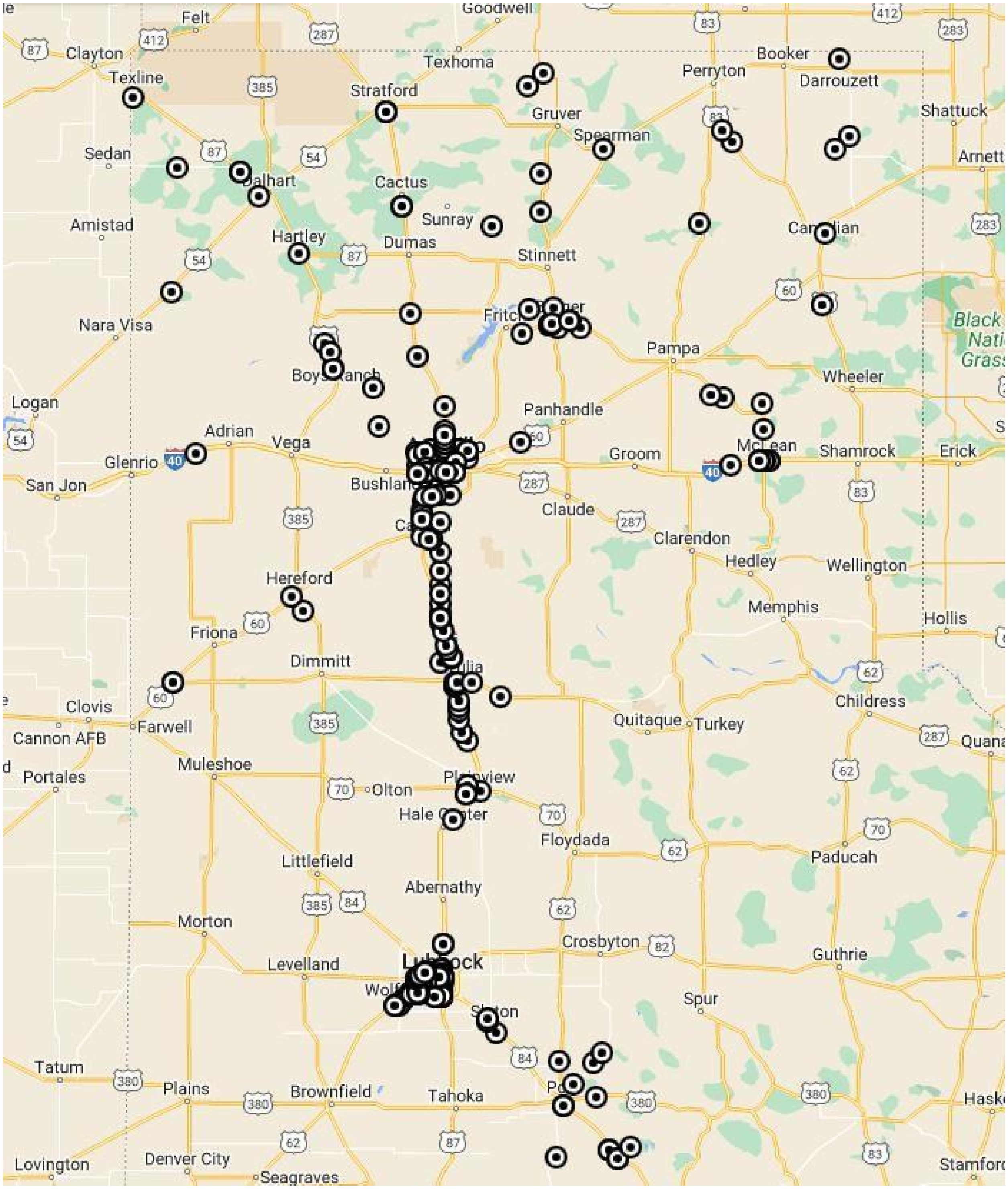

Figure 3.2. Locations of bridges in Amarillo (AMA) and Lubbock (LUB) Districts.

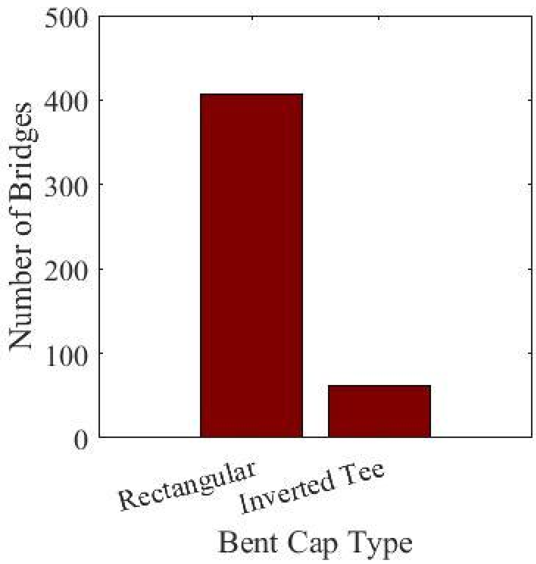

(a)

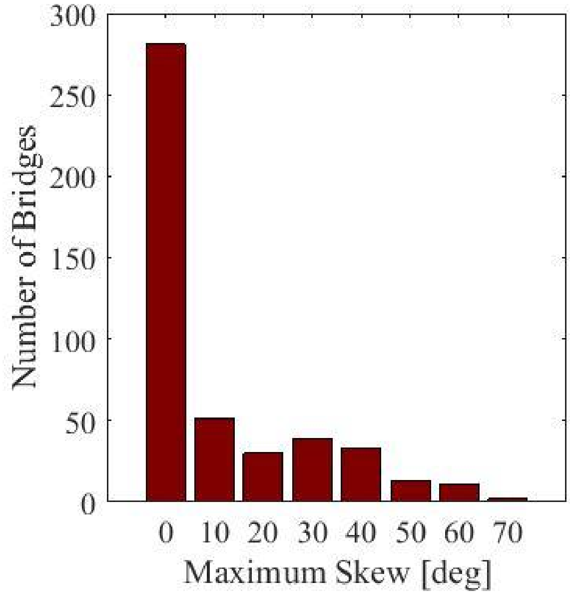

(b)

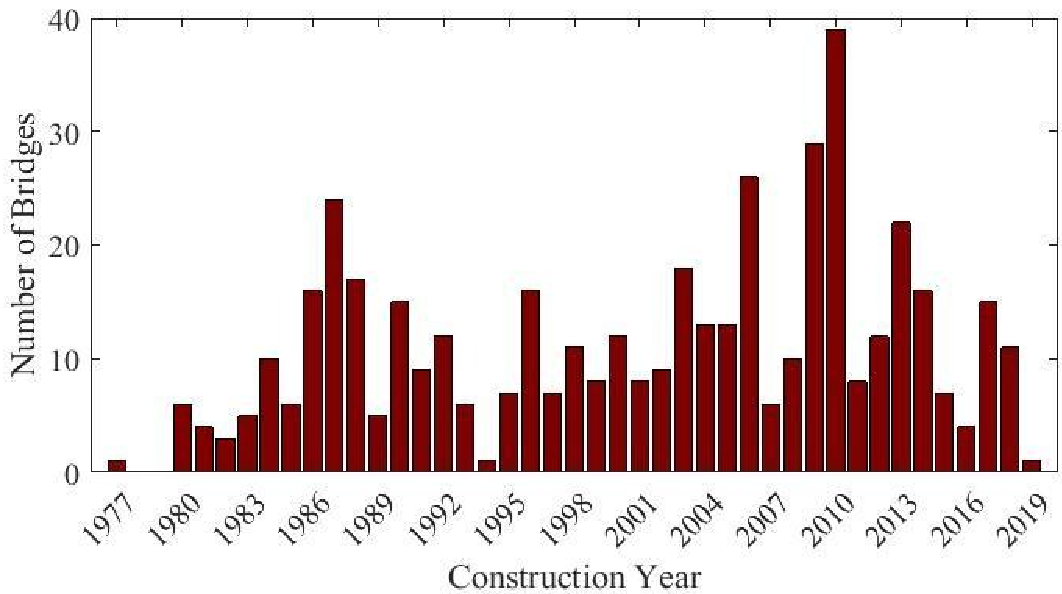

(c)

Figure 3.3. Histograms of overall bridge characteristics.

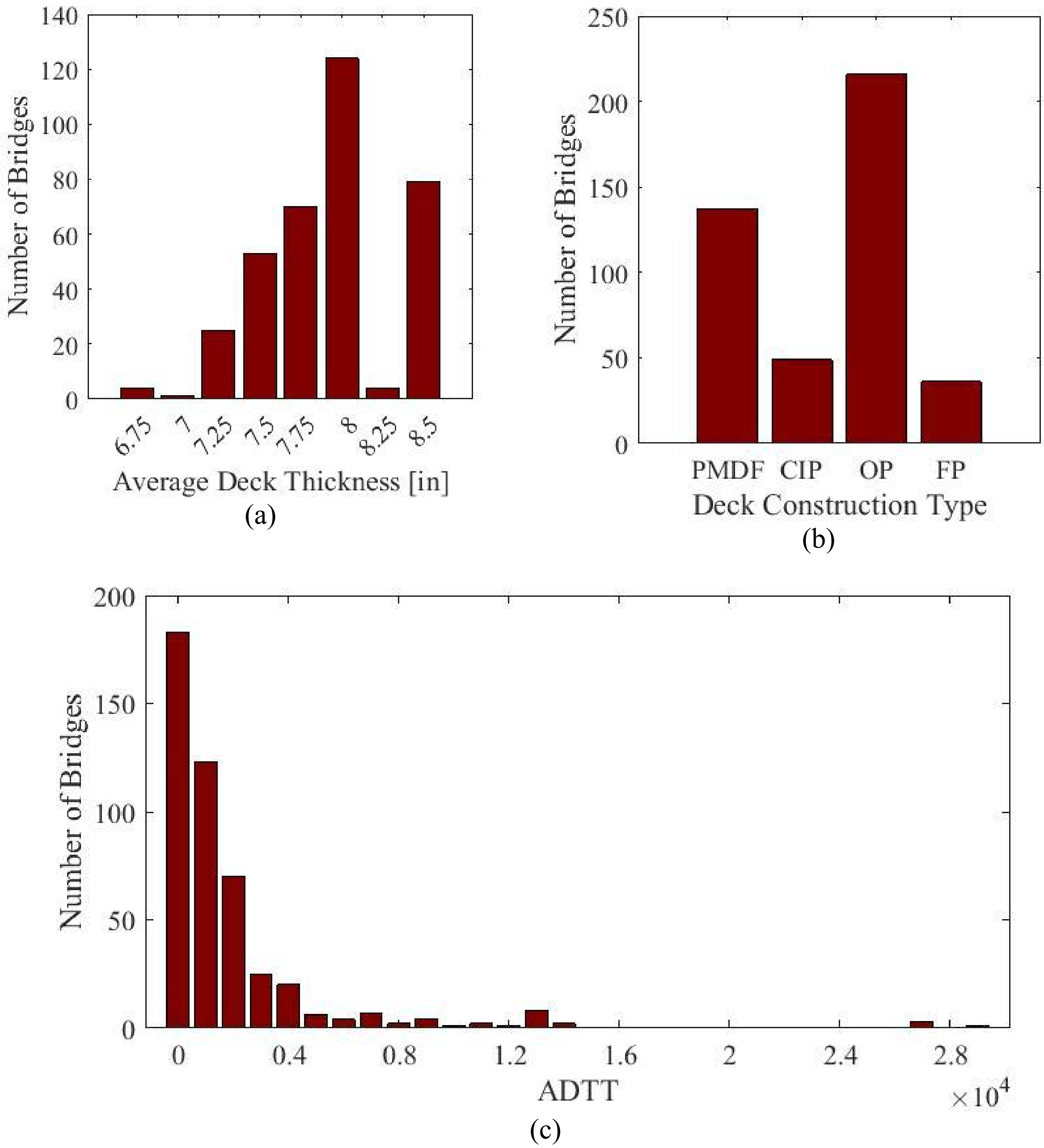

Figure 3.4. Histograms of deck characteristics.

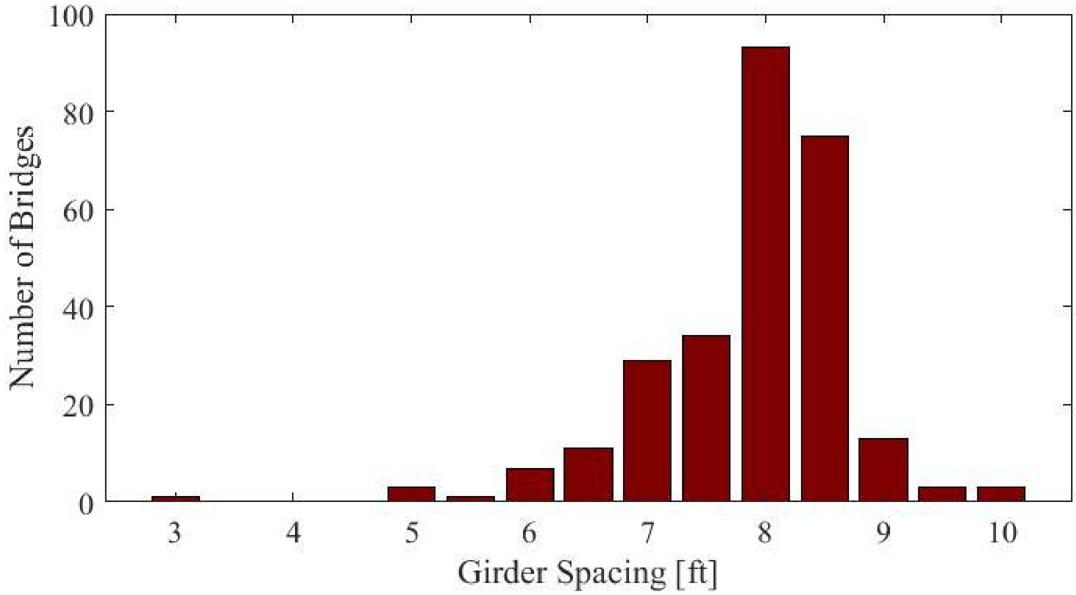

(a)

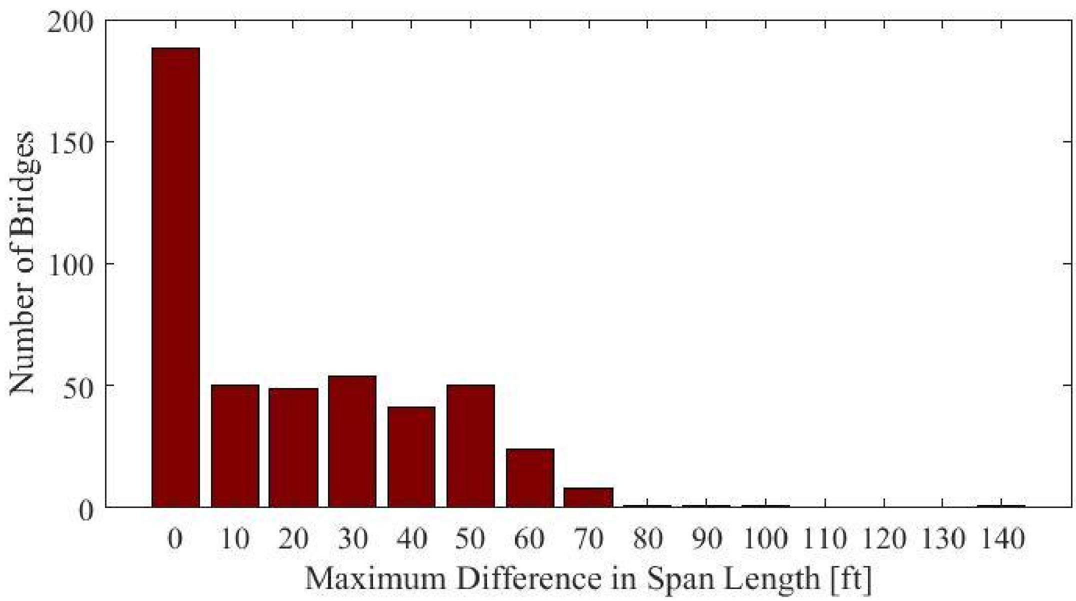

(b)

Figure 3.5. Histograms of span characteristics.

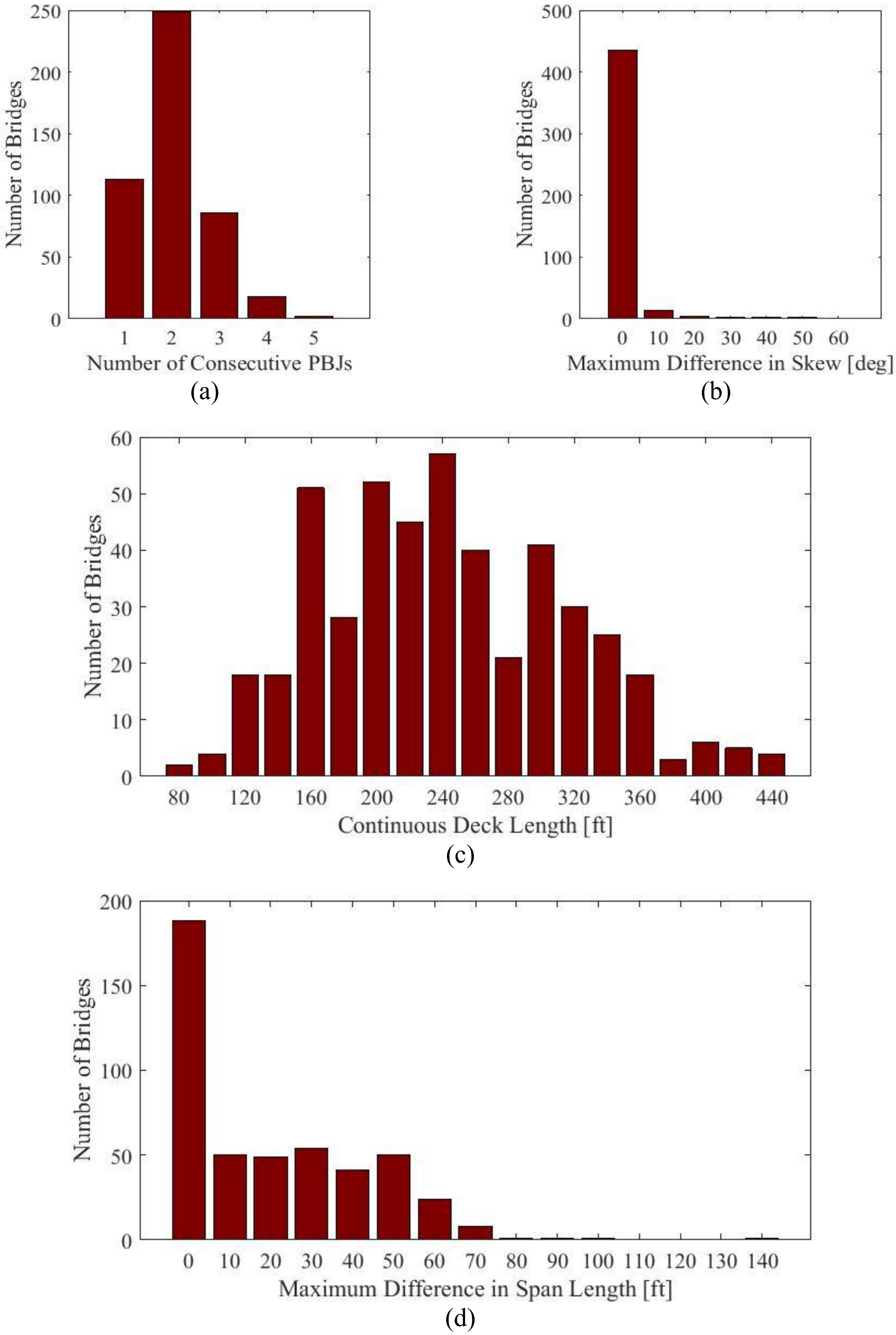

Figure 3.6. Histograms of continuous unit characteristics.

3.2 POOR BOY JOINT PERFORMANCE

As a part of the database assembly, inspection reports were obtained with the intent of establishing a score to describe the performance of link slabs. Each inspection report provides condition ratings for the different components of the structure. Condition ratings range from 9 (excellent condition) to 0 (failed condition—bridge closed but beyond repair). A rating is provided for the overall deck for all bridges and different aspects of the deck (e.g., curbs, wearing surface, expansion joints, other joints, etc.). The condition of interest to this study should fall under the "Joints, Other" item; however, inspection reports do not consistently address the condition of the continuous deck details in this item. For some, comments on damage are indicated in the overall deck condition rating and the score does not separate out the condition of the link slab from the rest of the deck. Further, the condition ratings merely document the condition of a component and do not address the types of damage associated with link slab deterioration.

To meet the desired goals of this study, a unique poor boy joint rating (PBJ-R) was created for each bridge. The PBJ-R is on a scale of 1–4, with 4 being the highest and indicating no reported damage. For each bridge, a rating of 4 was initially assumed, with the score then reduced by 1 for each reported instance of cracking, spalling, rust, or delamination in the deck or for damage at the end of the girders. Examples are shown in Figure 3.7.

To eliminate age bias when evaluating the damage rating, the raw PBJ-R was modified to create a poor boy joint age-adjusted rating (PBJ-AAR) in which the rating was normalized by an average rating for bridges of similar age. A similar approach has been taken by other researchers for the assessment of overall deck conditions. For adjustment of the PBJ-R, the ratings from the full database were used. Figure 3.8(a) shows the average PBJ-R versus year. A best-fit line was matched to the data and used to normalize the PBJ-R to a PBJ-AAR. A PBJ-AAR of zero indicates that the performance of the link slab is that of the average link slab for its age. A positive value indicates a performance that is better than expected based on the average performance. A negative value indicates the performance is worse than the average of all link slabs of the same age.

An initial linear fit for the PBJ-AAR using the average PBJ ratings for all bridges in the database is shown in Figure 3.8(a). However, subdividing the rating by region, shown in Figure 3.8(b), reveals that there is a significant difference in average PBJ ratings between the north region (Amarillo and Lubbock Districts) and the east region (Atlanta and Tyler Districts).

Because of the distinct difference in PBJ ratings between the two regions, the PBJ-AAR for each bridge was calculated using the linear fit for its region. This helped account for factors such as construction or maintenance practices, weather conditions and deicing practices, and other unforeseen differences between the regions that affect bridge deterioration. Figure 3.9 provides a histogram of age-adjusted ratings.

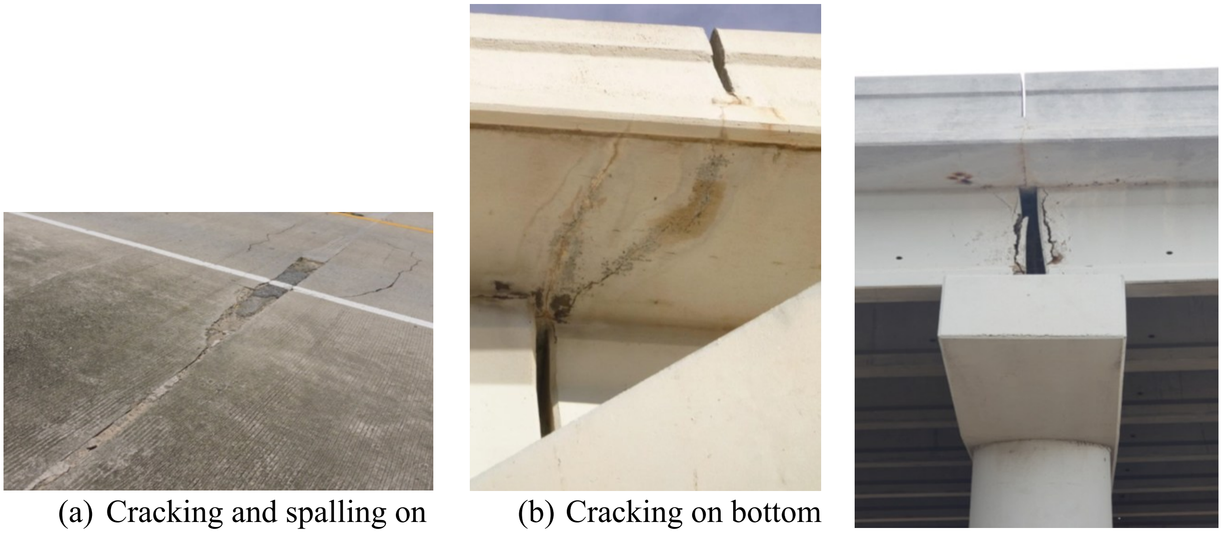

(a) Cracking and spalling on top of deck

(b) Cracking on bottom of overhang

(c) Girder end damage

Figure 3.7. Example of damage reducing the PBJ-R.

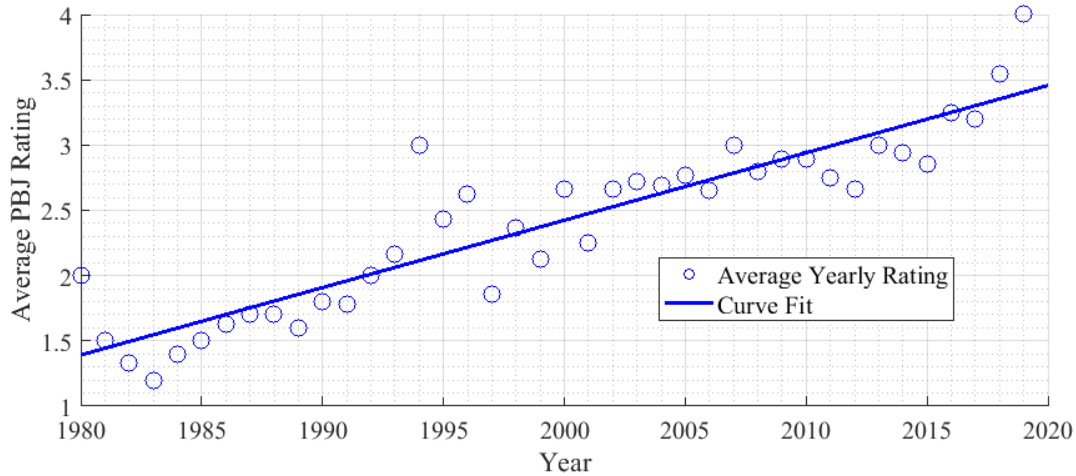

(a)

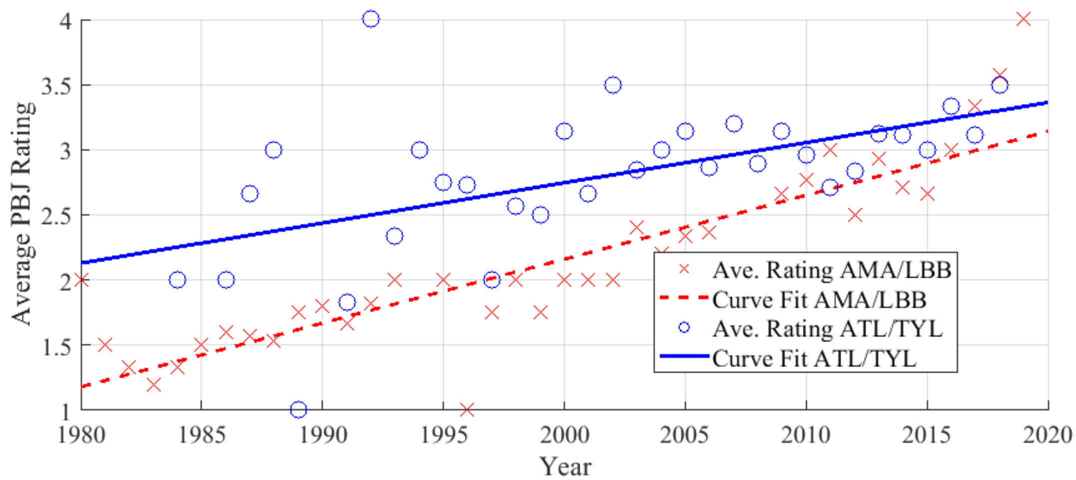

(b)

Figure 3.8. Linear fit of the PBJ-AAR for (a) the entire database and (b) split by region.

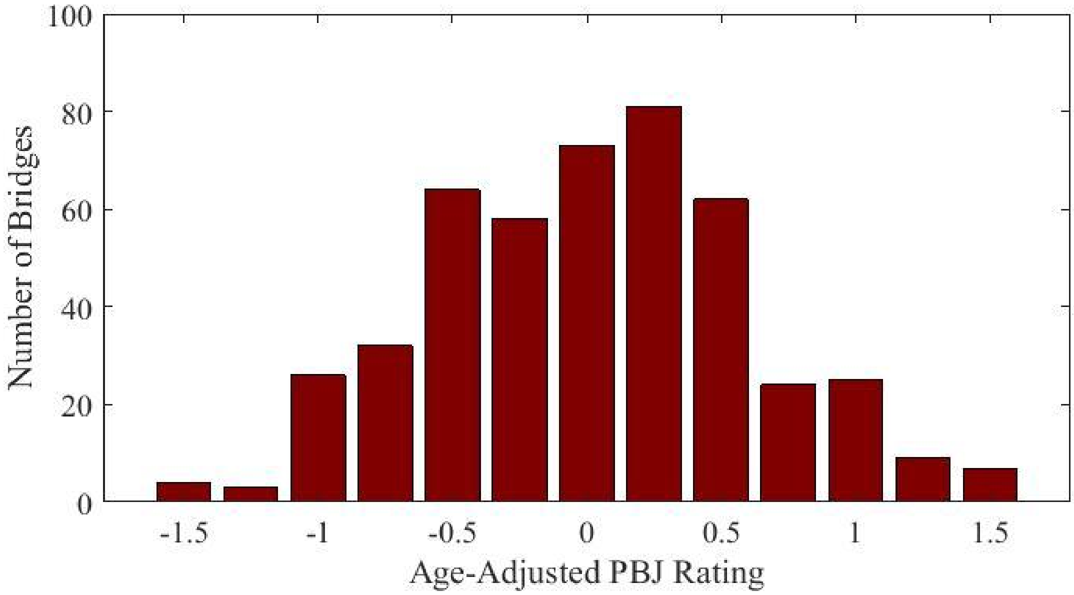

Figure 3.9. Histogram of age-adjusted PBJ ratings.

3.3 EVALUATION OF DATABASE

The PBJPD was evaluated to identify trends between performance rating (PBJ-AAR) and bridge/link slab characteristics. A summary of the most significant findings is presented here.

In addition to the characteristics previously summarized, rotations were estimated and then used to estimate service demands that were compared to the service capacity. Figure 3.10 summarizes these demands.

Table 3.1 provides the correlation coefficients between the AAR and the various bridge characteristics. While the total number of spans has the most negative correlation with PBJ-AAR, it is notable that the damage rating system was based on any damage noted on the bridge, not damage on a per-span or per-PBJ basis. In other words, bridges with many spans and continuous joints may be more likely to have PBJ damage reported on inspection reports since a large number of spans provides a larger opportunity for damage to be present.

Still, the negative correlation between PBJ-AAR and continuous deck length or total number of spans raises questions about damage caused by support conditions and girder end rotation. Structures with large numbers of spans and long continuous decks may be more at risk of damage if support conditions do not properly allow for longitudinal girder end deformation. FEA models have shown that pinned support conditions at the PBJ can produce large tensile stresses in the link slab. Decks with large continuous lengths, long spans, or a high number of consecutive PBJs may face larger girder end rotations or larger longitudinal girder end displacements on their bearing pads. These cases have the potential to cause higher tensile stresses in the link slab, leading to wider deck cracks and greater potential for damage.

Estimated calculations for rotation demand across the PBJ is also negatively correlated with PBJ-AAR. Link slabs with higher rotation demands have greater potential for cracking.

Characteristics such as deck skew, the maximum difference in skew between spans, average daily truck traffic (ADTT), average daily traffic (ADT), girder spacing, and deck thickness showed negligible correlation to PBJ-AAR. It is of note that bridges with higher skews were not found to negatively correlate with damage rating. When the data were further subdivided by deck construction type, only CIP slabs had a significant negative correlation of −0.096 between mean skew and PBJ-AAR. Slabs using PMDF, offset PCPs, and flush PCPs did not have a negative correlation with skew. Upon further investigation, the average age of CIP details was observed to be much older than the other detail types. It is possible that old practices in the design or construction of skewed bridges led to more negative outcomes, which primarily affects older CIP decks.

Table 3.2 provides the average age of construction for each type of detail. Examination of the performance of skewed decks by decade of construction (Table 3.3) showed the correlation between PBJ-AAR and skew changed from negative in the 1980s to positive in the 2010s. For bridges constructed in the 2010s, there was a relatively strong, positive correlation between bridge skew and PBJ-AAR. This finding suggests that, while past designs or construction practices in the 1980s and 1990s for skewed decks may have had negative effects on performance, current skewed deck designs appear to be performing well for PBJs when compared to non-skewed decks.

Increasing top longitudinal deck reinforcement and larger differences in span lengths on either side of the PBJ showed a minor positive correlation with PBJ-AAR. Finally, the ratio between estimated moment capacity and moment demand was positively correlated with PBJ-AAR. Decks with higher moment capacity relative to their moment demand appeared to perform better, as expected.

Bent cap type did not show a major difference in PBJ performance. Bridges with inverted tee bent caps had a slightly higher average PBJ-AAR. Deck details, however, showed more of a difference. Bridges with CIP details had the highest average PBJ-AAR, while bridges with offset panel details had the lowest.

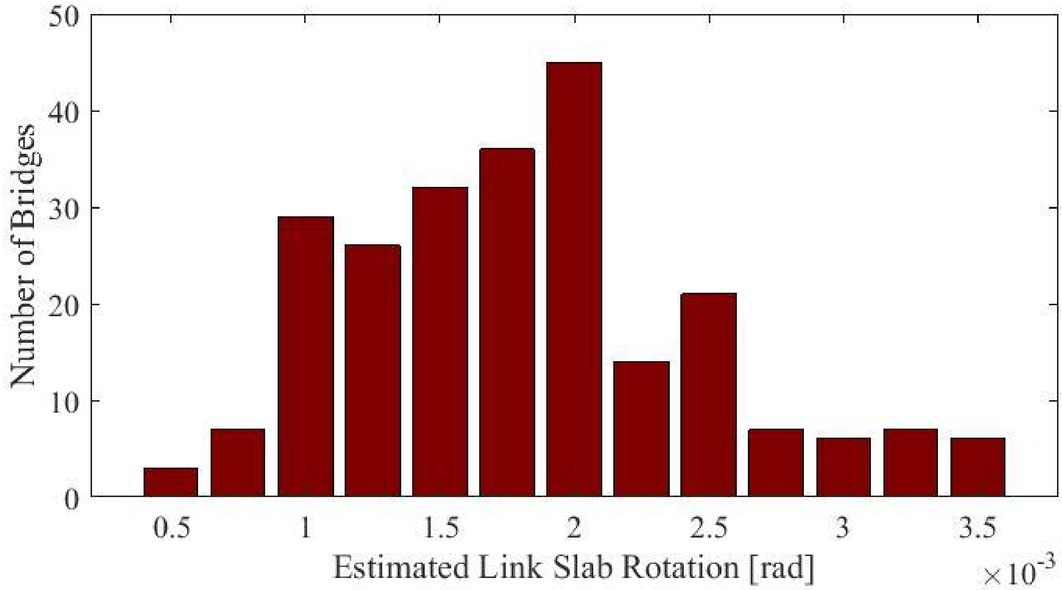

(a)

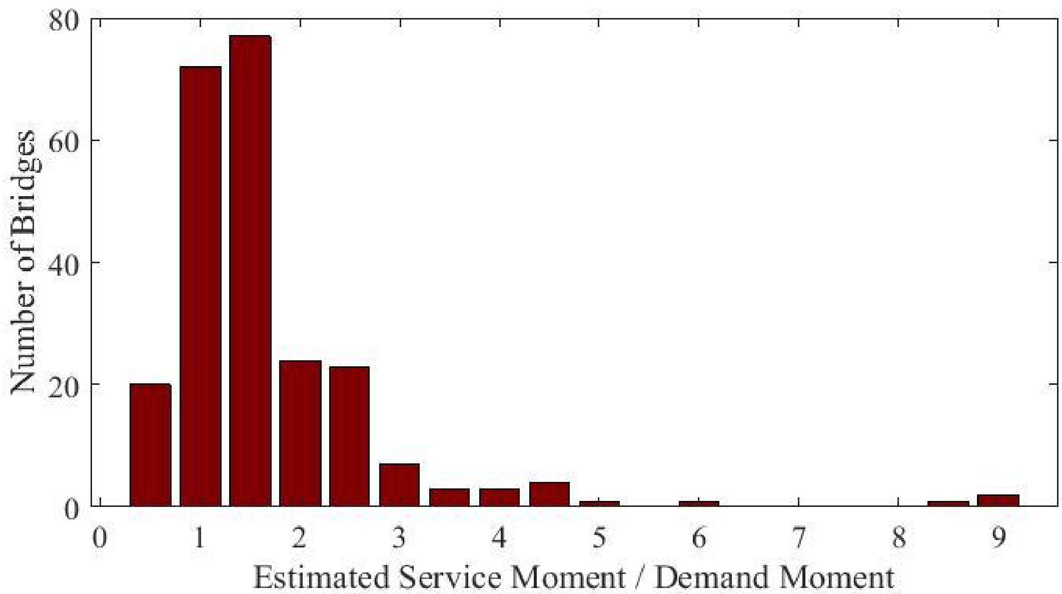

(b)

Figure 3.10. Histograms of link slab response.

Table 3.1. Correlation coefficient between PBJ-AAR and various bridge characteristics.

Bridge Database Characteristic	Correlation Coefficient
Total Number of Spans	−0.247
Continuous Deck Length	−0.207
Mean Span Length	−0.170
Maximum Rotation across PBJ	−0.126
Number of Consecutive PBJs	−0.065
Difference in Skew	−0.018
ADTT	0.004
Girder Spacing	0.007
Average Deck Thickness	0.011
ADT	0.034
Maximum Skew	0.035
Top Longitudinal Steel per ft	0.054
Difference in Span Lengths	0.067
Moment Capacity/Moment Demand	0.101

Table 3.2. Average year of construction for bridges in the database by deck detail type.

PBJ Detail Type	PMDF	CIP	OP	FP
Year Built	1997	1987	2003	2015

Note: OP = offset panel; FP = flush panel.

Table 3.3. Correlation between skew and PBJ-AAR, split by decade of bridge construction.

Decade of Construction	1980s	1990s	2000s	2010s
Correlation between skew and PBJ-AAR	−0.037	−0.091	−0.005	0.184

3.4 SUMMARY

To develop a preliminary understanding of the performance of poor boy joints in Texas bridges, as-built drawings and inspection reports were evaluated for nearly 500 bridges, with specific focus on the conditions of the link slab region. Structural characteristics expected to relate to the performance of the link slabs were identified from as-built drawings and added to the database. Damage ratings were developed for the link slab region, with adjustments made based on region and age. The database was evaluated for trends linking structural characteristics to age-adjusted ratings. A reduced performance was identified for bridges with longer continuous deck lengths and longer span lengths.

4. FIELD EVALUATION OF POOR BOY JOINTS

To understand the behavior and performance of PBJs, a multitiered evaluation of existing bridges was conducted. First, a survey of TxDOT's bridge inventory was conducted to establish characteristics and conditions of link slabs. The bridge inventory was then used to select bridges for nondestructive evaluation (NDE) in two regions of Texas to further assess the condition beyond what could be established from inspection reports. To provide further insight into the condition, NDE was utilized to detect discontinuities such as voids, delamination, and cracks.

This chapter presents details on the field evaluation of PBJs. Section 4.1 presents relevant notation and terminology information. Section 4.2 summarizes the process for selecting bridges and provides general details of the eight bridges evaluated. Section 4.3 provides an overview of the NDE methods utilized. Section 4.4 presents details of each bridge, including the regions surveyed. Section 4.5 provides a summary of findings.

4.1 NOTATION AND TERMINOLOGY

The continuous deck detail used by TxDOT is informally referred to as a poor boy joint, but the term "link slab" is often used in the literature. In this chapter, any continuous deck detail is referred to as a poor boy joint (or PBJ), and expansions joints, either at abutments or interior spans, is referred to as a sealed expansion joint (SEJ). PBJ and SEJ are used in labeling the types of joints on the bridges evaluated. When discussing the specifics of the continuous deck detail, it is described as a link slab (e.g., link slab length is 4 ft long or link slab is 8 in. thick). An actual construction joint may be intentionally formed (e.g., with a zip strip), or this crack may be allowed to crack naturally. In either case, the crack at the center of the link slab is referred to as the main PBJ crack. For some link slabs, additional cracks form parallel to this and are referred to as secondary PBJ cracks to distinguish them from other transverse cracks that may be present in both the link slab region and the regular deck.

4.2 OVERVIEW OF BRIDGES

Bridges were selected to provide a good distribution of characteristics considered to influence performance of the continuous deck detail. Accessibility was factored into the finalized selection to minimize the impact of traffic control.

Table 4.1 and Figure 4.1 provide locations for the bridges. Table 4.2 provides general characteristics of the bridges. Table 4.3 provides details on the continuous deck details.

Table 4.1. Location of bridges for nondestructive evaluation.

District	Bridge No.	NBI Bridge ID	Description	Coordinates
Atlanta	ATL1	19-032-1019-01-009	FM 556 over Lilly Creek, Camp County	32.928463, −95.016501
	ATL2	19-034-0946-01-013	FM 250 over Black Cypress Creek, Hughes Springs	33.049421, −94.603076
	ATL3	19-103-0402-04-040	FM 154 over Little Cypress Bayou, Harleton	32.627368, −94.515294
	ATL4	19-103-1575-02-022	FM 968 over Clarks Creek, Longview	32.446670, −94.588190
Lubbock	LUB1	5-152-00783-02-106	SB Loop 289 over Slide Rd./4th St.	33.596483, −101.923483
	LUB2	5-152-00067-11-198	Erskine St. over I-27	33.606849, −101.845036
	LUB3	5-152-00380-01-236	EB US 62 over Research Blvd.	33.499114, −102.026347
	LUB4	5-152-00783-01-090	WB Loop 289 over University Ave.	33.529412, −101.870437

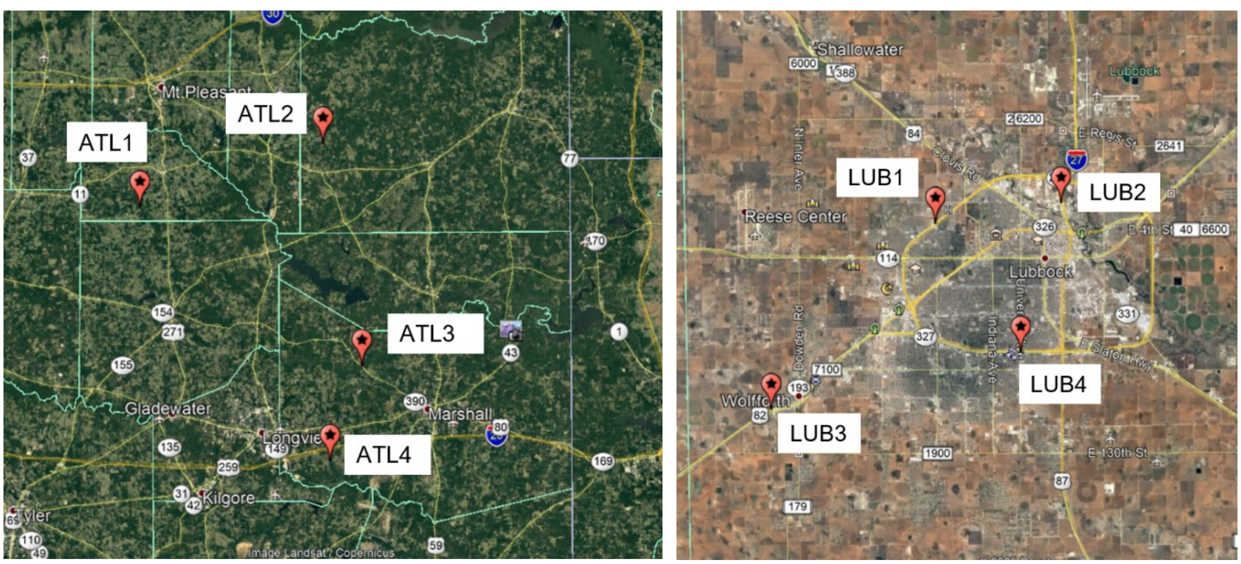

(a) Atlanta District Bridges (b) Lubbock District Bridges

Figure 4.1. Locations of bridges for nondestructive evaluation (from Google Earth).

Table 4.2. General characteristics of bridges for nondestructive evaluation.

Bridge No.	Year Built	ADT	Skew	Bent Cap Type	Girder Type	Number Girders	Girder Spacing, ft	Overhang Length, ft	Deck Type	Deck Reinforcement
ATL1	2012	1130	0	Rect.	C	7	6.667	3.000	PMDF	ECR
ATL2	2003	830	15	Rect.	C	4	8.667	3.000	PMDF	Black
ATL3	2010	1650	0	Rect.	C/IV	6	8.000	3.000	PMDF	Black
ATL4	1996	1820	0	Rect.	B	4	8.000	3.000	PCP	Black
LUB1	2010	8200	0	Rect.	Tx46	8	7.500	3.000	PCP	ECR
LUB2	1990	27,920	9	Inv-T	54	10	7.333	3.000	PMDF	Black, ECR
LUB3	2017	11,892	19.1	Rect.	Tx40	5	8.500	3.000	PCP	ECR
LUB4	1992	20,540	9	Rect.	C	8	7.250	3.229	PMDF	ECR

Table 4.3. General characteristics of link slabs of bridges for nondestructive evaluation.

Bridge No.	PBJ Type	Number Consecutive PBJs	Continuous Deck Length, ft	PBJ Condition Rating	Adjusted PBJ Rating	Service Moment Capacity/Demand
ATL1	PCP Offset w/ PMDF	1	160	3	−0.108	0.833
ATL2	PCP—Offset w/ CIP	2	220	2	−0.911	0.606
ATL3	PMDF	2	270	2	−1.075	0.210
ATL4	PCP—Offset w/ CIP	3	200	4	1.326	1.681
LUB1	PCP—Flush	2	266	2	−0.610	0.626
LUB2	PMDF	1	185.8	1	−0.586	2.265
LUB3	PCP—Flush	2	195	4	0.699	0.331
LUB4	PMDF	3	254	2	0.375	1.204

4.3 OVERVIEW OF NDE METHODS

The objective of the NDE was to evaluate damage in the poor boy region of decks. Information on the location, severity, and type of damage was used to inform designs of improved poor boy continuous deck details. For each bridge, a single lane was investigated to minimize the traffic control needed and the impact on use of the bridge. On bridges with more than one lane in a single direction, the outer lane was investigated to provide more working room and access to the overhang for evaluation. Four methods of NDE were conducted: visual analysis, infrared (IR) thermography, ground-penetrating radar (GPR), and ultrasonic tomography (UST).

Visual inspection was conducted first and done for all PBJs on a bridge to determine the potential regions for detailed evaluation. For all bridges, the deck surface in the poor boy regions was evaluated. For some bridges, inspection from below was also possible; however, heights and/or obstacles below (bodies of water or roadways) limited the data that could be collected. Cracks were mapped and widths were measured with a crack comparator card; generally, crack width measurements were limited to the NDE regions, but for some bridges, widths were also measured at other regions and/or other PBJ regions. Where zip strips were used to form the main PBJ cracks, crack widths were not measured.

Following visual inspection, infrared thermography was used to further narrow down the potential regions. Defects and/or damage will create a disturbance in the thermal flow and appear as regions of elevated temperature compared to the adjacent concrete. This area is detected through the IR camera as zones with an elevated temperature compared to the surrounding surface (i.e., a high temperature signature reveals a subsurface discontinuity). Delamination can be detected with IR thermography since the delamination are perpendicular to the thermal flow. Note that the infrared thermography does not supply information about the depth of the damage. The IR pictures were taken at the bridge immediately after arrival. This way local heat sources or sinks from the personnel on the bridge or shadows were eliminated.

Using the results of the visual inspection and infrared thermography, the researchers selected regions for GPR and UST. Regions were limited to 2-ft by 4-ft or 2-ft by 2-ft rectangles to accommodate equipment settings. For all bridges, a main NDE region was located along a 4-ft length of the PBJ between two girders. The transverse location of the main region varied based on the location of traffic lanes relative to the girders and observed damage. For some bridges, the main NDE region was a 2-ft by 4-ft grid centered on the joint. In other bridges, the main NDE region consisted of two adjacent 2-ft by 4-ft grids to create a larger 4-ft by 4-ft region; this was done in bridges where a longer region was of interest based on the structural characteristics (inverted-T bent cap), the full length of the link slab region could be captured, or observed damage would not fall within a 2-ft dimension centered on the main PBJ crack. In some bridges, an additional NDE region was done in the overhang. The decision to conduct NDE in the overhang was based on time constraints, structural conditions, and observed damaged. Each NDE region was marked with a 2×2 grid to guide placement of the GPR and UST equipment.

Three-dimensional GPR scans were conducted for all NDE regions. GPR was used to identify section breaks, locate rebars, and detect subsurface defects such as voiding and water-based deteriorations. A handheld GPR antenna GSSI mini with a frequency of 2.6 GHz was used in runs perpendicular to each other. The data were then processed in the software RADAN from GSSI.

UST was primarily restricted to the main NDE region, although data for overhang regions were completed for some bridges. UST incorporates advanced pulse-echo ultrasonics with tomography representation of a test field. It employs an array of low-frequency shear wave transducers with a center frequency of 50–55 kHz. The device can fit the profile of a rough concrete testing surface with a variance of approximately 0.4 in. and has no need for a coupling agent.

With this linear array of elements, there is a wide coverage of shear wave pulses that reflect at internal interfaces where the material impedance changes. With the help of a digitally focused algorithm, a 3D volume is presented with each point of possible reflection in half-space represented by a color scheme, scaled according to reflecting power. This 3D image can also be dissected into each of the three planes representing its volume: the B-scan, C-scan, and D-scan. With the intensity scaling, it is easy to see any discontinuities with distinctly different wave speeds, such as voids, delaminations, debonding of overlays, honeycombing, steel reinforcement, and other abnormalities. The data are processed using a synthetic aperture focusing technique.

4.4 DETAILS AND RESULTS FOR BRIDGES

4.4.1 Bridge ATL1 (FM 556 over Lilly Creek, Camp County)

Bridge ATL1, shown in Figure 4.2, was built in 2012; it carries FM 556 over Lilly Creek in Camp County, Texas. The 46-ft wide bridge has seven Type C prestressed concrete I-girders spaced at 6.667 ft with 3-ft overhangs. The bridge carries two 12-ft wide traffic lanes, with 10-ft wide shoulders on both sides.

The bridge is 320 ft long and is made up of four simple spans forming two continuous deck units. Both units consist of two 80-ft long spans. Expansion joints separate the units from each other and the abutments. The deck is shown as 8-in. thick CIP in the as-built drawings, but it was constructed using PCPs. Based on the age of the bridge, it is presumed to be made up of 4-in. thick PCPs with a 4-in. thick CIP top. The overhangs are fully CIP. The deck reinforcement is specified as #4 at 9 in. in the longitudinal direction and #5 at 6 in. in the transverse direction. At PBJ joints, the link slab is fully CIP with PMDF. Reinforcement details for the link slab were not available in the as-built drawings. During the field visit, it was confirmed that PCPs were used for the bridge deck, with offset panels and PMDFs used at the link slab regions. While it was not possible to take exact measurements, the length of the PMDF was approximately the width of the bent cap (2 ft 9 in.).

The inspection report for Bridge ATL1 indicated that minor spalling was present at the construction joints, with random hairline cracking in the deck overall. The minor spalling resulted in an unadjusted PBJ rating of 3; while this is a good condition overall, the bridge is only eight years old, leading to an age-adjusted rating of −0.11, indicating it is slightly lower performance than the average for bridges of similar age.

Visual inspection of the bridge confirmed the inspection report damage of minor spalling at the construction joint. The conditions of the continuous deck regions at Bent 2 and Bent 4 were similar. Figure 4.3 shows the condition of the link slab region at Bent 4 from below the deck and the top of the deck at Bent 2. The PMDF was in good condition, with no indication of rust or other damage. In the overhang, some minor spalling was observed at the PBJ crack, but no cracking was noted. Visual observations on the top side of the deck indicated that zip strips were used to form the main PBJ crack. The zip strip was still intact, but some minor spalling was observed at several locations along the length. Figure 4.3(c) shows the marked cracks in the NDE region. Secondary PBJ cracks were present at approximately the end of the portion of the deck where PMDFs were used. The secondary PBJ cracks were 0.014–0.016 in. wide in the NDE region. Hairline cracks were present in the link slab region and in the main deck, and they were primarily longitudinal, with an occasional transverse crack.

The NDE region was a 4-ft by 4-ft region at Bent 2, shown in Figure 4.4, located at the edge of the northbound lane and between Girders (G) 2 and 3. The region was off center relative to the main PBJ crack to capture the reinforcement at the main crack and one secondary crack, plus an extension beyond the secondary crack. At the time of the evaluation, rain had resulted in the deck being wet at the time of the GPR and UST data collection.

Figure 4.5 through Figure 4.9 show 2D views of GPR and UST scans at various depths. Figure 4.5 confirms longitudinal reinforcement spacing at 9 in., while Figure 4.6 and Figure 4.7 confirm transverse reinforcement spacing of 6 in., as specified in the as-built drawings. Transverse reinforcement is shown in two views for clarity; evaluation of 3D images reveals the transverse reinforcement to be at the same depth throughout the link slab region.

Figure 4.8 does not show clear images of the bottom reinforcement due to the presence of PMDFs, which obscure the GPR and UST signals. Still, longitudinal reinforcement at 9 in. can be made out from the GPR images of Figure 4.8(a) and Figure 4.9(a). The UST image in Figure 4.9(b) clearly shows the ribs of the PMDF laid out vertically in the figure, especially with the strong signal from zero to 10 in. horizontally in the image.

UST images were less distinct than GPR images at the same depth. This finding was typical for subsequent bridges as well. Factors such as the roughness and cleanliness of the concrete surface may have contributed to the lack of clarity in images since the UST data collection is dependent upon the physical contact between the transducers and the deck. Grooved or roughened pavement surfaces can prevent good contact between the deck and transducers. The deck surfaces were swept clean of dust and debris, but material caught within pavement grooves may have detracted from scan clarity. In order to complete the grid of UST scans in a timely manner, scans were taken from one direction only. While taking a second set of scans for each grid from a perpendicular direction may have increased the clarity of the results, doubling the number of scans for each UST session was avoided due to time constraints.

The IR images captured did not reveal abnormal thermal regions that would indicate voids or delaminations in the deck.

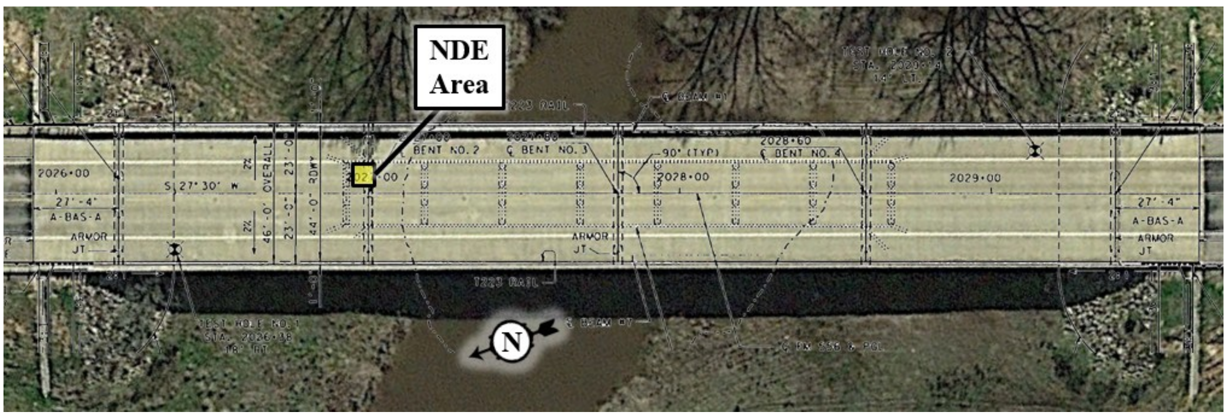

(a) Top view


(b) Elevation view

Figure 4.2. Site conditions at Bridge ATL1 (FM 556 over Lilly Creek).

(a) PMDF at Bent 4

(b) Bottom of overhang at Bent 4

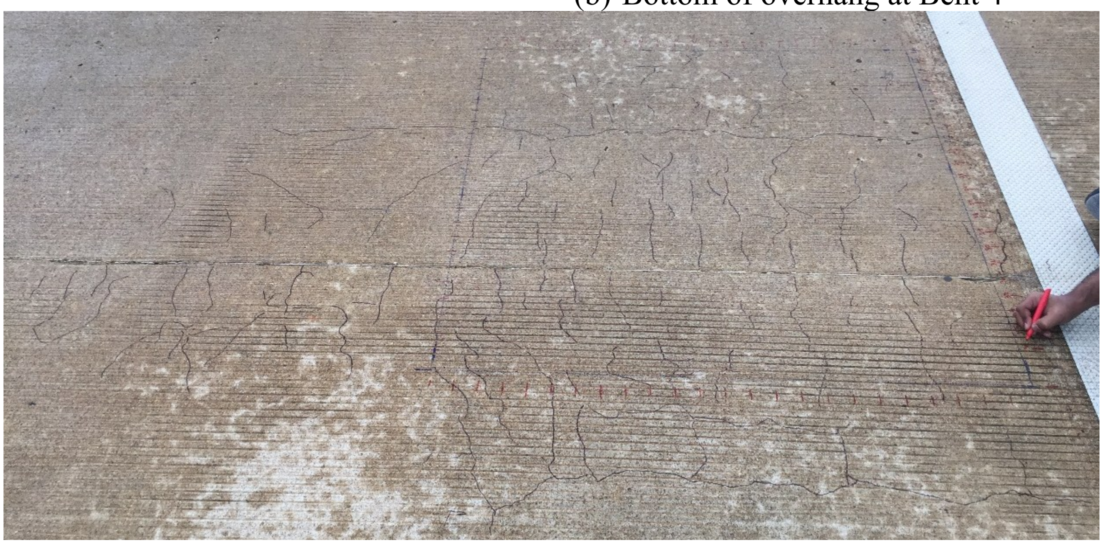

(c) Marked cracks in the NDE region at Bent 2

Figure 4.3. Link slab condition for Bridge ATL1 (FM 556 over Lilly Creek).

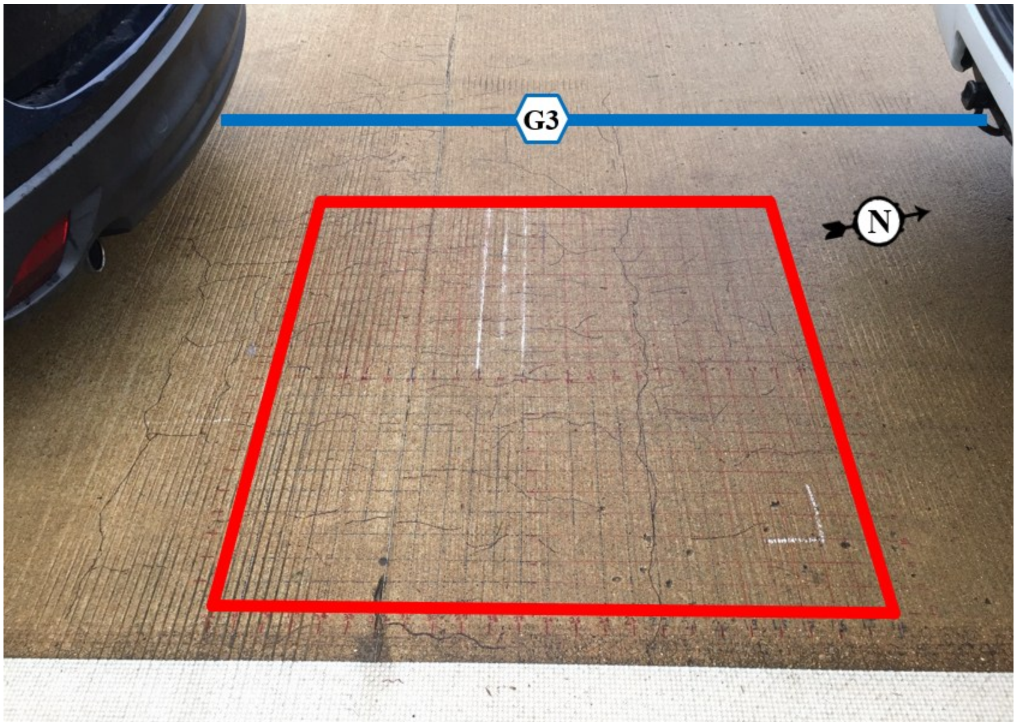

Figure 4.4. NDE region at Bent 2 for Bridge ATL1 (FM 556 over Lilly Creek).

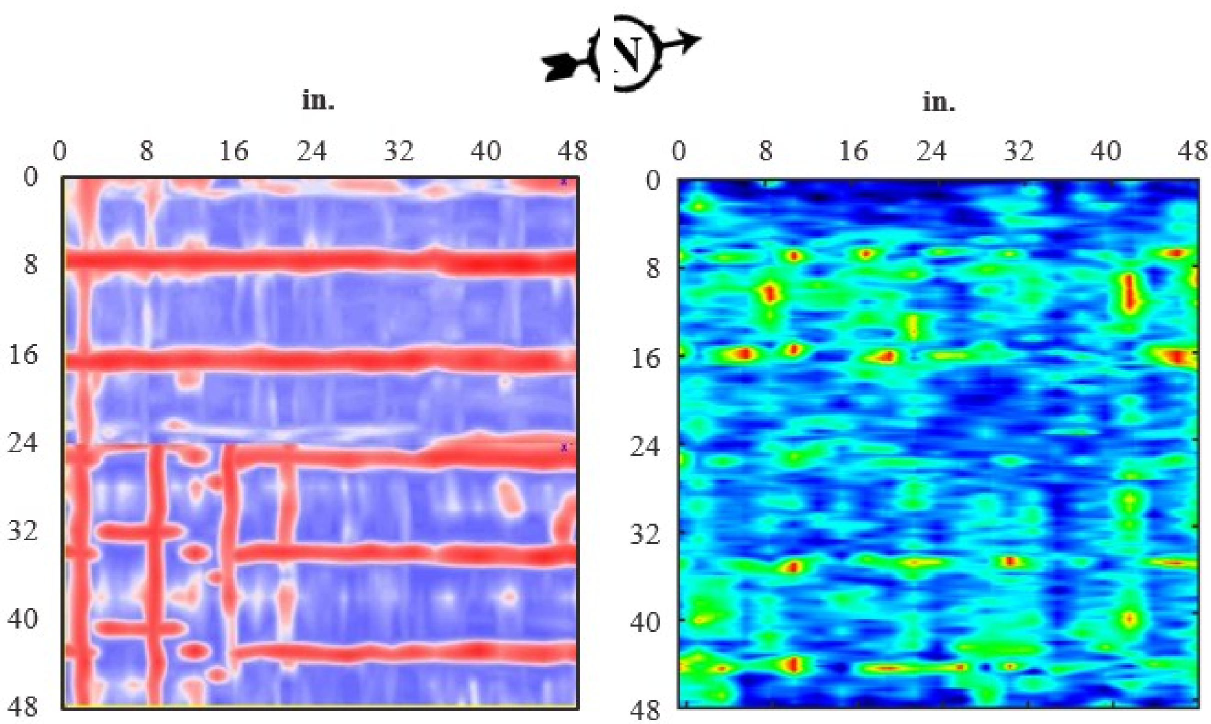

(a) (b)

Figure 4.5. ATL1 results for (a) GPR and (b) UST of top longitudinal reinforcement at depth 2.73 in.

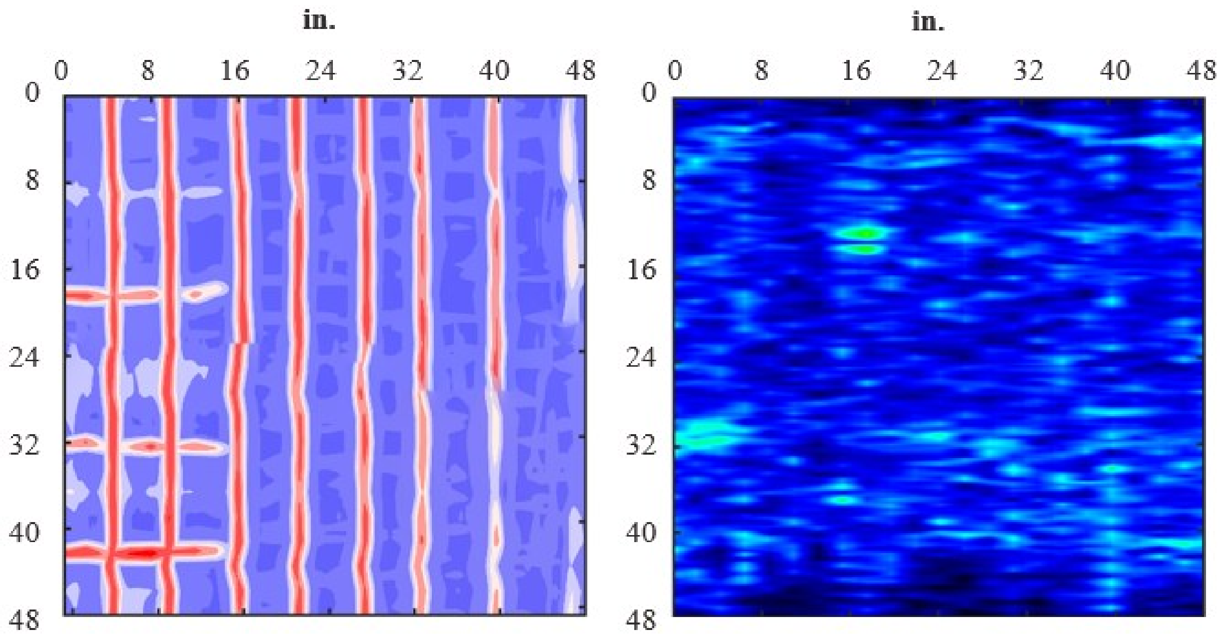

(a) (b)

Figure 4.6. ATL1 results for (a) GPR and (b) UST of top longitudinal reinforcement at depth 1.48 in.

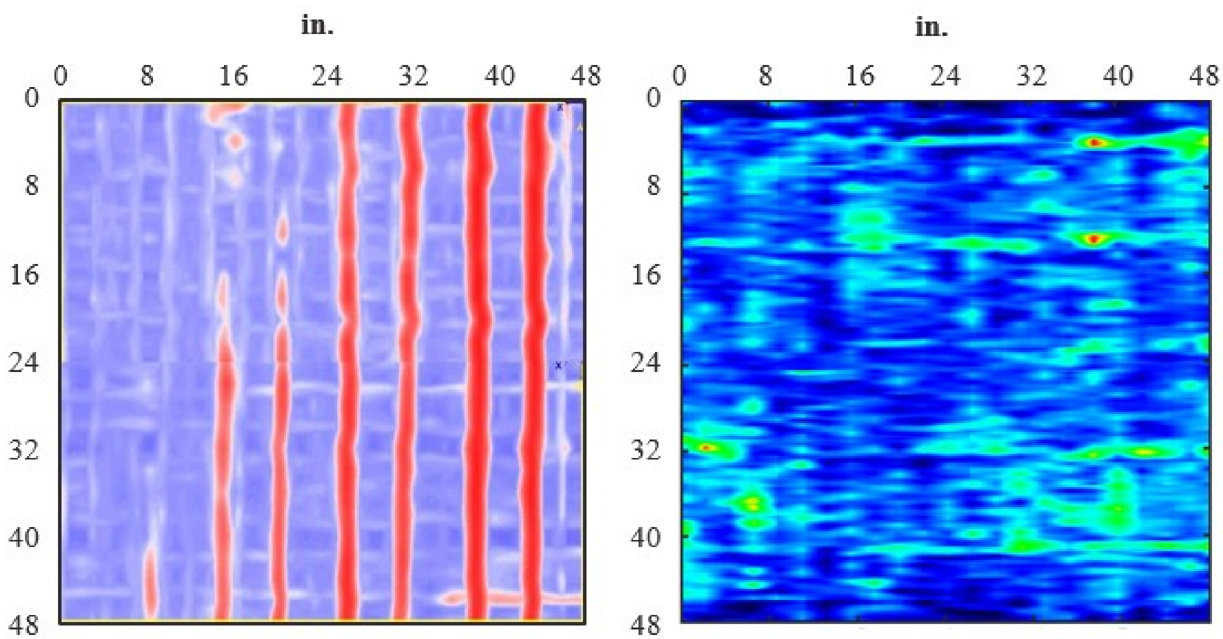

(a) (b)

Figure 4.7. ATL1 results for (a) GPR and (b) UST of top transverse reinforcement at depth 2.23 in.

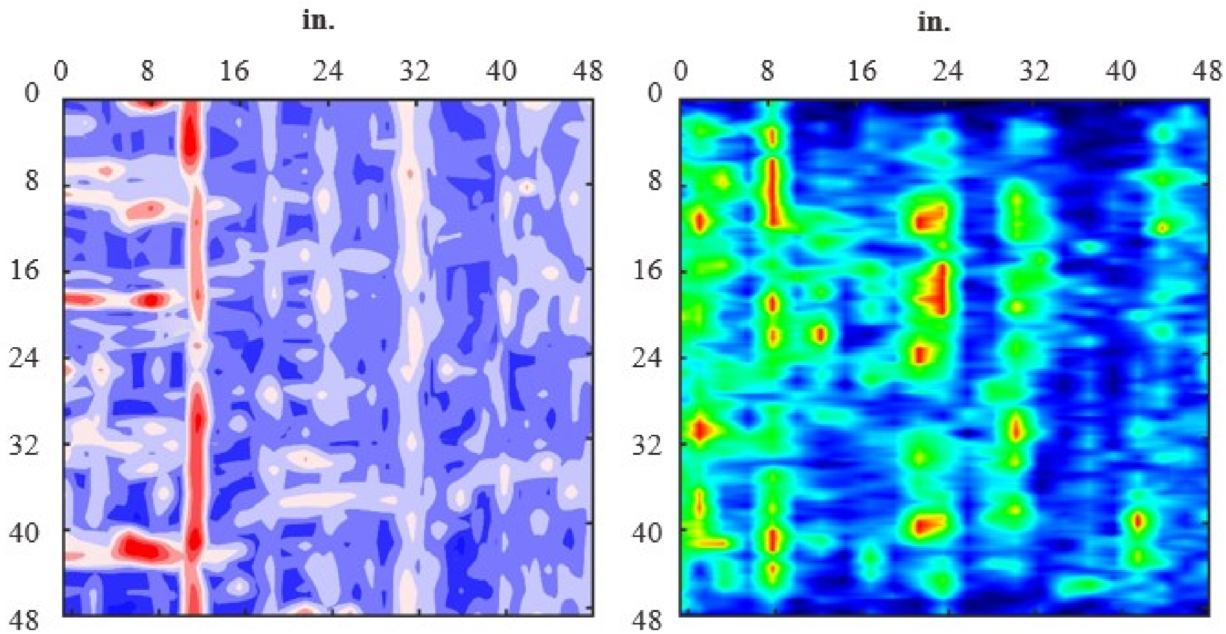

(a) (b)

Figure 4.8. ATL1 results for (a) GPR and (b) UST of bottom reinforcement at depth 7.48 in.

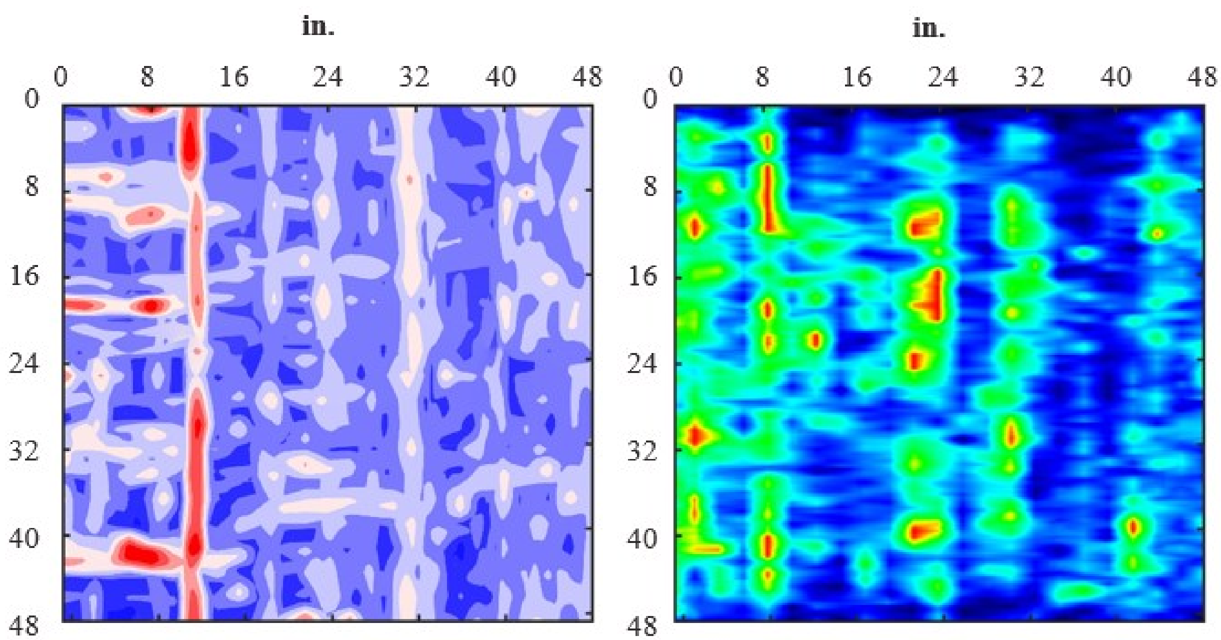

(a) (b)

Figure 4.9. ATL1 results for (a) GPR and (b) UST of PMDF at depth 8.5 in.

4.4.2 Bridge ATL2 (FM 250 over Black Cypress Creek, Hughes Springs)

Bridge ATL2, shown in Figure 4.10, was built in 2003 and carries FM 250 over Black Cypress Creek near Hughes Springs, Texas. The 32-ft wide bridge has two lanes on four Type C prestressed concrete I-girders spaced at 8.667 ft with 3-ft overhangs. The bridge is curved with a 15-degree skew.

The bridge is 350 ft long and is made up of five simple spans forming two continuous deck units. Unit 1 is 130 ft and consists of 60-ft and 70-ft spans separated by a poor boy region. Unit 2 is 220 ft and consists of one 80-ft and two 70-ft spans separated by two poor boy regions. Expansion joints separate the units from each other and the abutments. The deck is shown as 8-in. thick CIP in the as-built drawings but was constructed using PCPs. Based on the age of the bridge, it is presumed to be made up of 4-in. thick PCPs with a 4-in. thick CIP top. The deck reinforcement is specified as #4 @ 9 in. in the longitudinal direction and #5 @ 6 in. in the transverse direction. At PBJ joints, the link slab is fully CIP (formwork removed after construction). Reinforcement details for the link slab were not available in the as-built drawings. During the field visit, it was confirmed that PCPs were used for the bridge deck, with offset panels and full-depth CIP for the link slab regions. The CIP concrete was slightly thicker than the deck with PCPs. A main PBJ crack was formed using a zip strip that was still intact. On the bottom of the deck, a notch was formed beneath the zip strip location.

The inspection report for Bridge ATL2 indicated spalling along the edge of construction joints and showed that the soffit of overhangs and the CIP regions had efflorescence, with cracks less than 1⁄16 in. The cracking, spalling, and efflorescence resulted in an unadjusted PBJ rating of 2 and an age-adjusted rating of −0.91, indicating the bridge is lower performance than the average for bridges of similar age.

Visual inspection of the bridge confirmed the inspection report damage. The condition of all continuous deck regions was similar. Figure 4.11 shows representative conditions of the link slab regions. Visual observations on the top side indicated that zip strips were used to form the main PBJ crack. The zip strip was still intact, but some minor spalling was observed at several locations along the length. There were no distinct secondary PBJ cracks. Aside from the main PBJ crack, random cracks were present. The maximum cracks were 0.008 in. near the exterior side of the girder, but most cracks were 0.007 in. or less.

The NDE region was a 4-ft by 4-ft region at Bent 4 (in Unit 2), shown in Figure 4.12, located at the edge of the southbound lane and between G1 and G2 and was oriented parallel to the girder lines. The region was off center relative to the main PBJ crack to capture the reinforcement at the main PBJ crack and also extend beyond the CIP region. Figure 4.13 and Figure 4.14 confirm the spacing of longitudinal and transverse reinforcement in the as-built drawings as 9 in. and 6 in., respectively. Figure 4.15 and Figure 4.16 confirm the reinforcement spacing for the bottom reinforcement. No evidence of voids or delaminations was discovered using IR images.

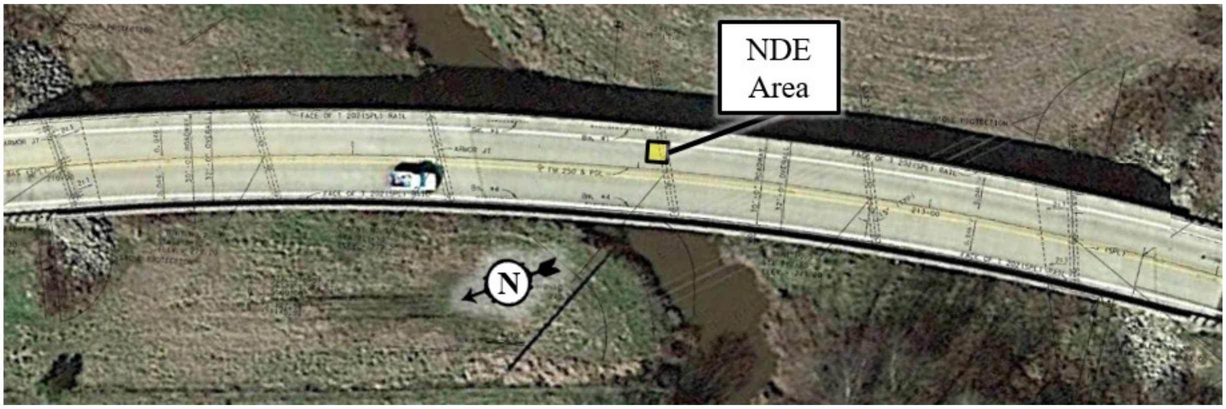

(a) Top view

(b) Elevation view

Figure 4.10. Site conditions at Bridge ATL2 (FM 250 over Black Cypress Creek).

(a) CIP at continuous deck detail

(b) Cracks in NDE region

Figure 4.11. Typical link slab condition for Bridge ATL2 (FM 250 over Black Cypress Creek).

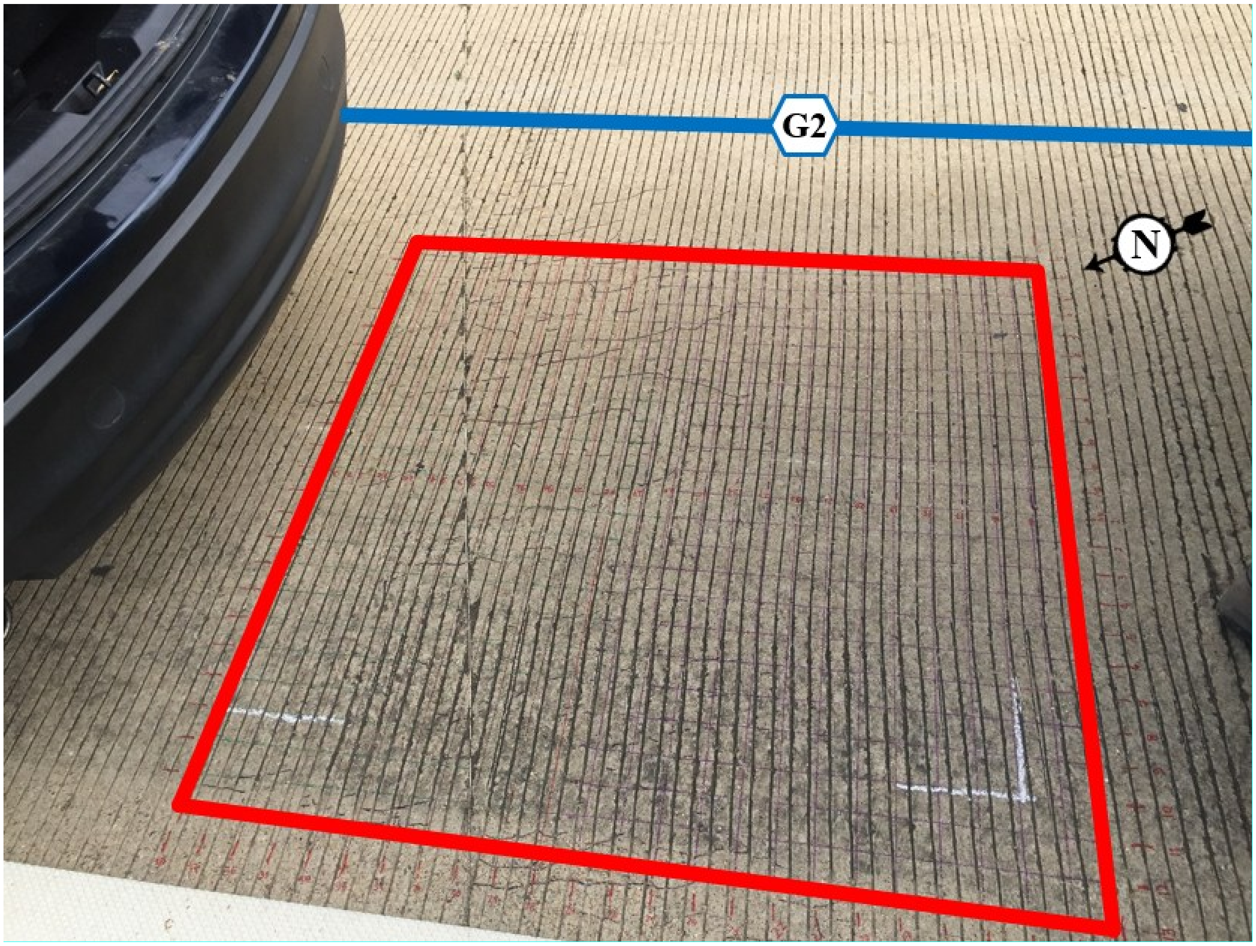

Figure 4.12. NDE region at Bent 3 for Bridge ATL2 (FM 250 over Black Cypress Creek).

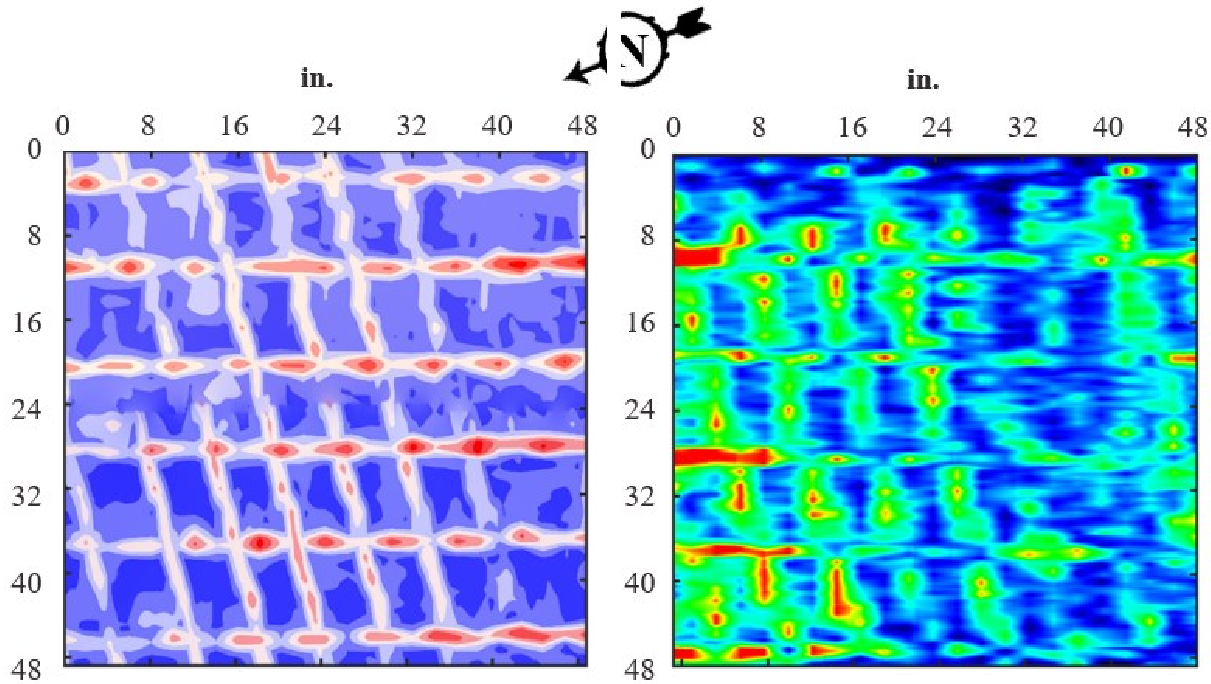

(a) (b)

Figure 4.13. ATL2 results for (a) GPR and (b) UST of top longitudinal reinforcement at depth 3.73 in.

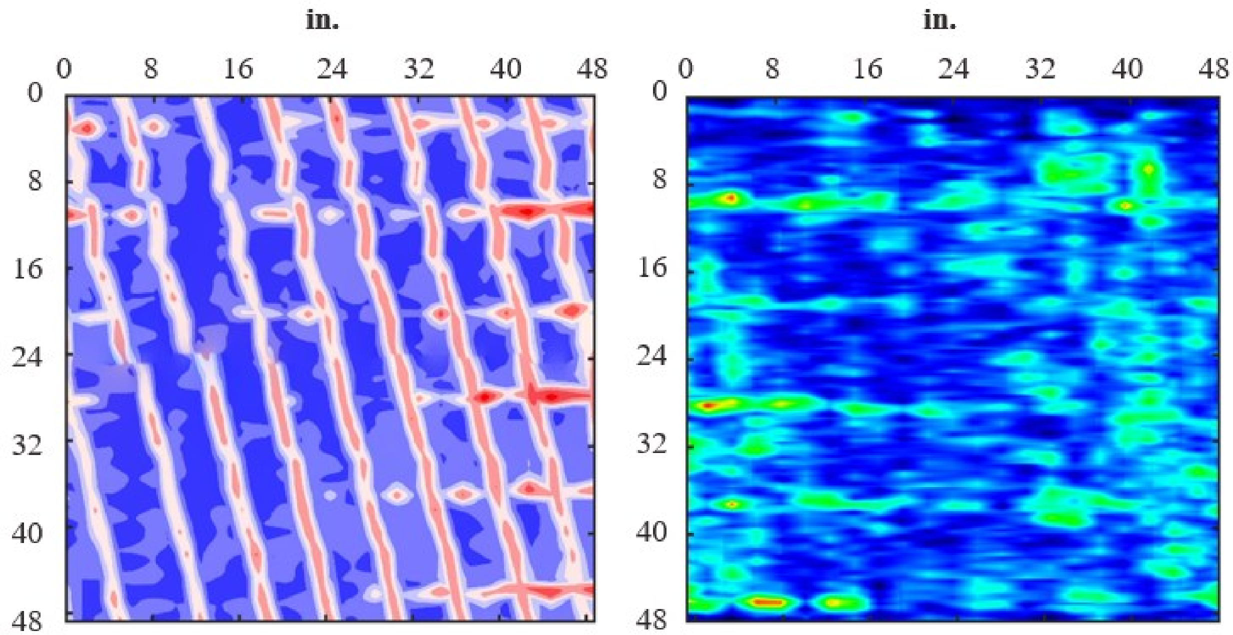

(a) (b)

Figure 4.14. ATL2 results for (a) GPR and (b) UST of top transverse reinforcement at depth 2.98 in.

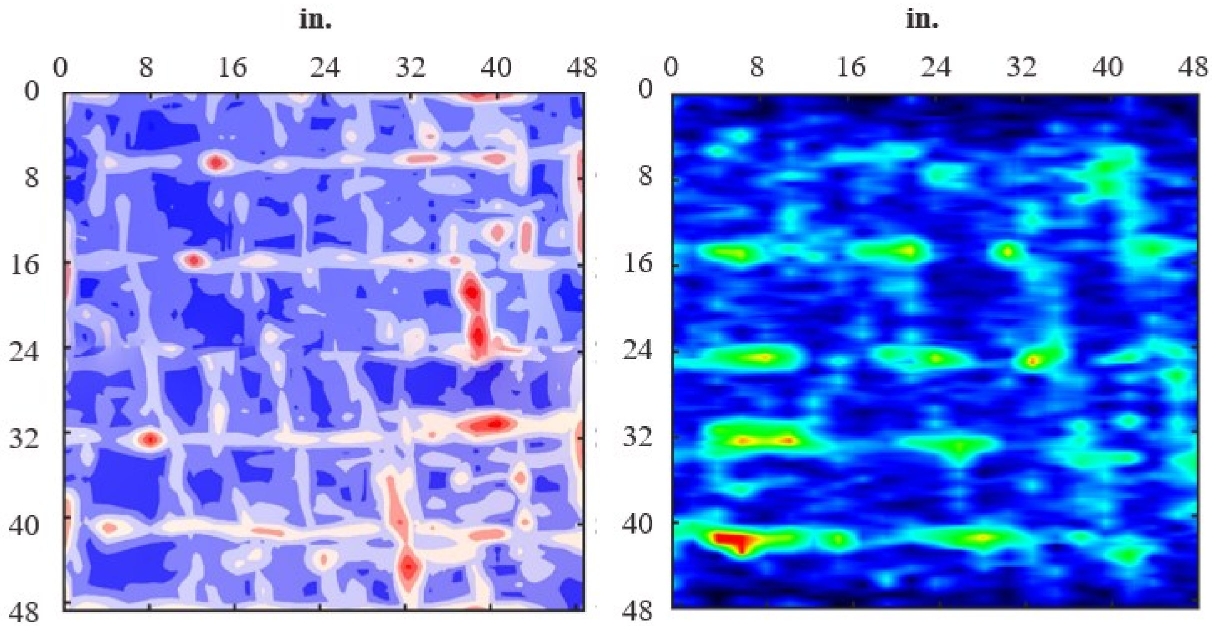

(a) (b)

Figure 4.15. ATL2 results for (a) GPR and (b) UST of bottom longitudinal reinforcement at depth 7.23 in.

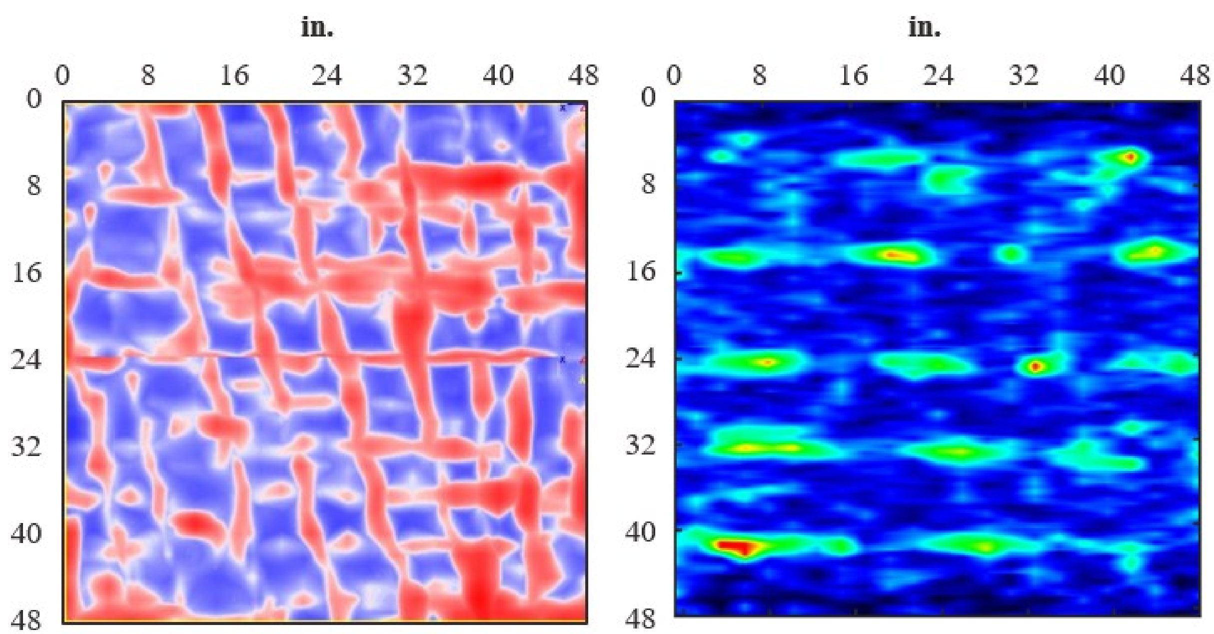

(a) (b)

Figure 4.16. ATL2 results for (a) GPR and (b) UST of bottom transverse reinforcement at depth 6.73 in.

4.4.3 Bridge ATL3 (FM 154 over Little Cypress Bayou, Harleton)

Bridge ATL3, shown in Figure 4.17, was built in 2010 and carries FM 154 over Little Cypress Bayou near Harleton, Texas. The 46-ft wide bridge has two lanes on six prestressed concrete I-girders spaced at 8 ft with 3-ft overhangs. Type C girders are used for four of five spans, with Type IV girders at the middle span.

The bridge is 430 ft long and is made up of five simple spans forming two continuous deck units. One unit has one poor boy region, and the other has two poor boy regions. Unit 1 is 160 ft long and consists of two 80-ft spans (Type C). Unit 2 is 270 ft long and consists of a 110-ft span (Type IV) and two 80-ft spans (Type C). Expansion joints separate the units from each other and the abutments. The deck is shown as 8-in. thick CIP in the as-built drawings but was constructed using a PMDF. The top deck reinforcement is specified as #4 @ 9 in. in the longitudinal direction and #5 @ 6 in. in the transverse direction. The bottom deck reinforcement is specified as #5 @ 9 in. in the longitudinal direction and #5 @ 6 in. in the transverse direction. During the field visit, it was confirmed that a PMDF was used for the bridge deck.

The inspection report for Bridge ATL3 indicated that transverse cracks less than ⅛ in. wide were present near the construction joints and that minor cracking with efflorescence was present in the overhangs, leading to an unadjusted PBJ rating of 2. Built in 2010, this bridge is significantly lower performing than other bridges of similar age, with an age-adjusted rating of −1.075.

Visual inspection of the bridge confirmed the damage indicated in the inspection reports, with all PBJ regions having similar damage characteristics. Figure 4.18 shows the condition of the PMDF below the continuous deck and the pattern of cracking on the top of the deck. Efflorescence was observed at the ends of the girders, and small gaps in the PMDF were present below the location of the main PBJ crack. Otherwise, the PMDF was in good condition with no indication of rust.

Figure 4.18(b) shows the main and secondary PBJ cracks typical of all continuous deck joints. The main PBJ crack was formed with a zip strip that was still located in the deck. There was moderate spalling along the main crack, larger than observed in the other bridges inspected in the Atlanta District. The location of the secondary cracks relative to the main PBJ crack varied, occurring as close as 5 in. at the girders or as far as 11 in. between the girders. The width of the secondary cracks varied from 0.020–0.025 in. and was smallest over the girders. Similar crack patterns were observed in the overhang, but the widths were 0.014–0.016 in. Figure 4.18(c) shows the marked cracks in the NDE region. In addition to the main and secondary PBJ cracks, cracking was consistent with the rest of the deck, with most of the cracks being longitudinal cracks and measuring as hairline cracks.

The NDE region was a 4-ft by 4-ft region at Bent 3, shown in Figure 4.19, located in the east/southbound lane. The region was centered on the main PBJ crack and captured both secondary cracks, plus an extension beyond the secondary cracks.

Figure 4.20 and Figure 4.21 confirm the spacing of top longitudinal and transverse reinforcement in the as-built drawings as 9 in. and 6 in., respectively. Figure 4.22 and Figure 4.23 confirm the reinforcement spacing for the bottom reinforcement, but it is less distinct due to interference from the PMDF, which is identifiable in Figure 4.24(b). Using the IR camera, differences in heat at the PBJ over the girders and between the girders are visible. However, no evidence of voids or delaminations was discovered using IR images.

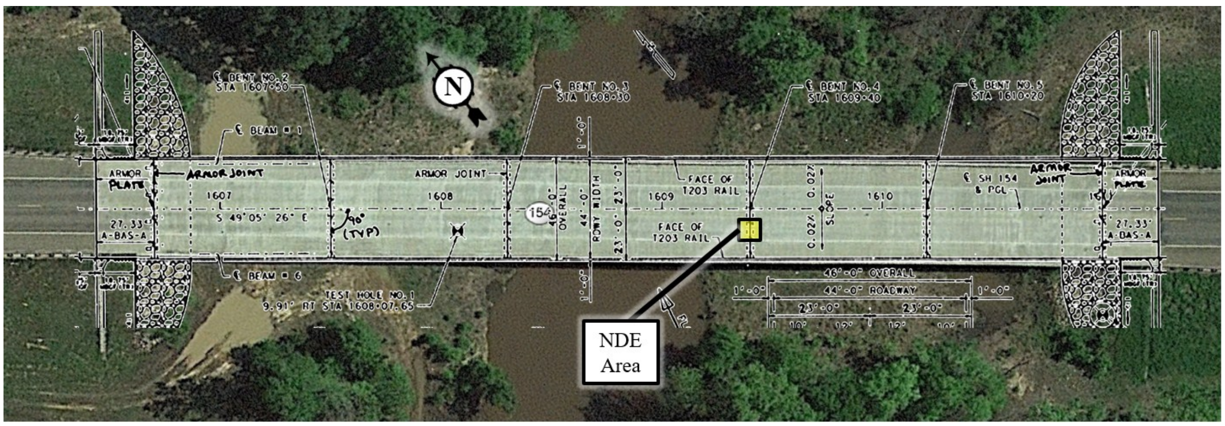

(a) Top view

(b) Elevation view

Figure 4.17. Site conditions at Bridge ATL3 (FM 154 over Little Cypress Bayou).

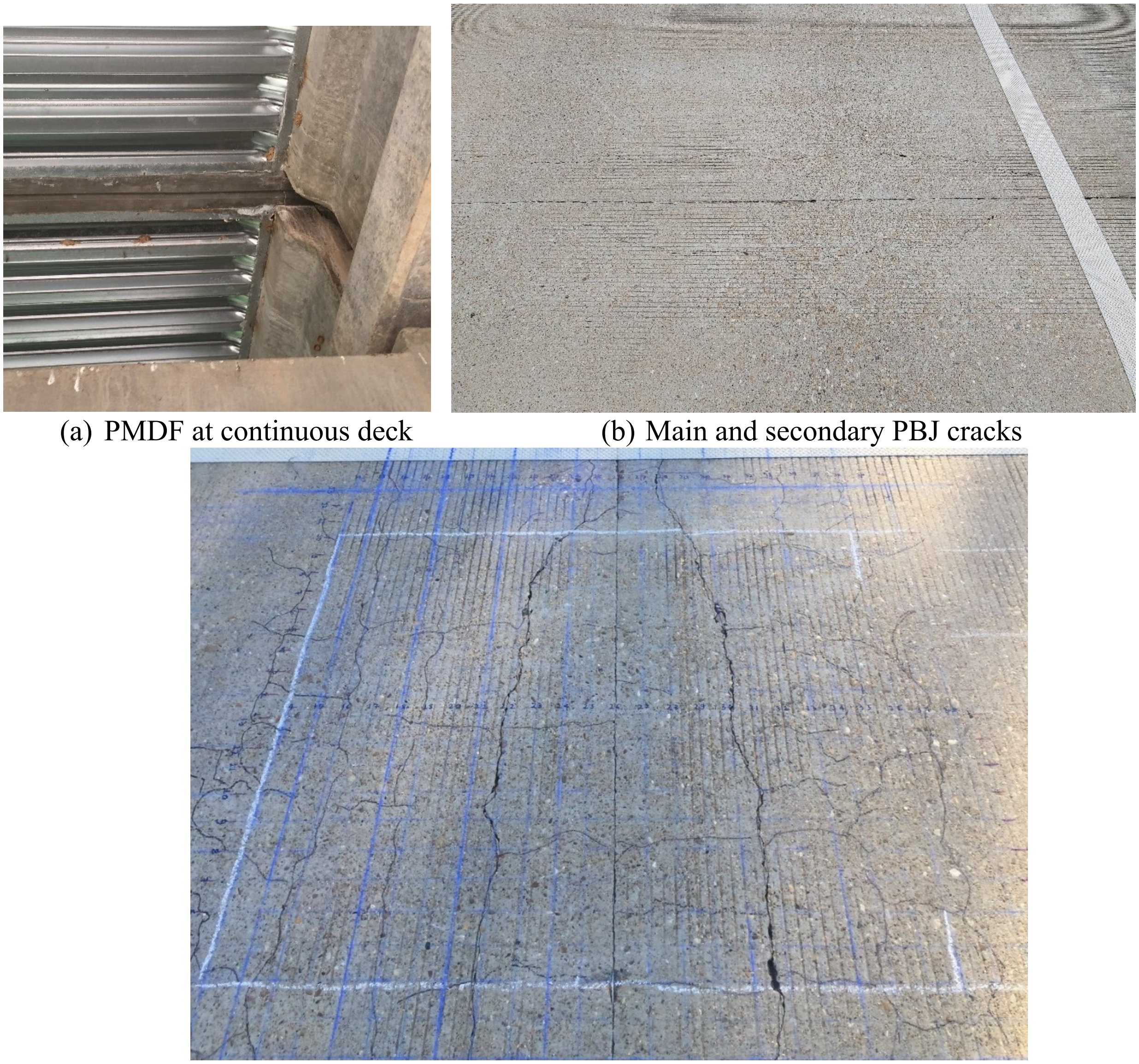

(a) PMDF at continuous deck

(b) Main and secondary PBJ cracks

(c) Cracks in NDE region

Figure 4.18. Typical link slab condition for Bridge ATL3 (FM 154 over Little Cypress Bayou).

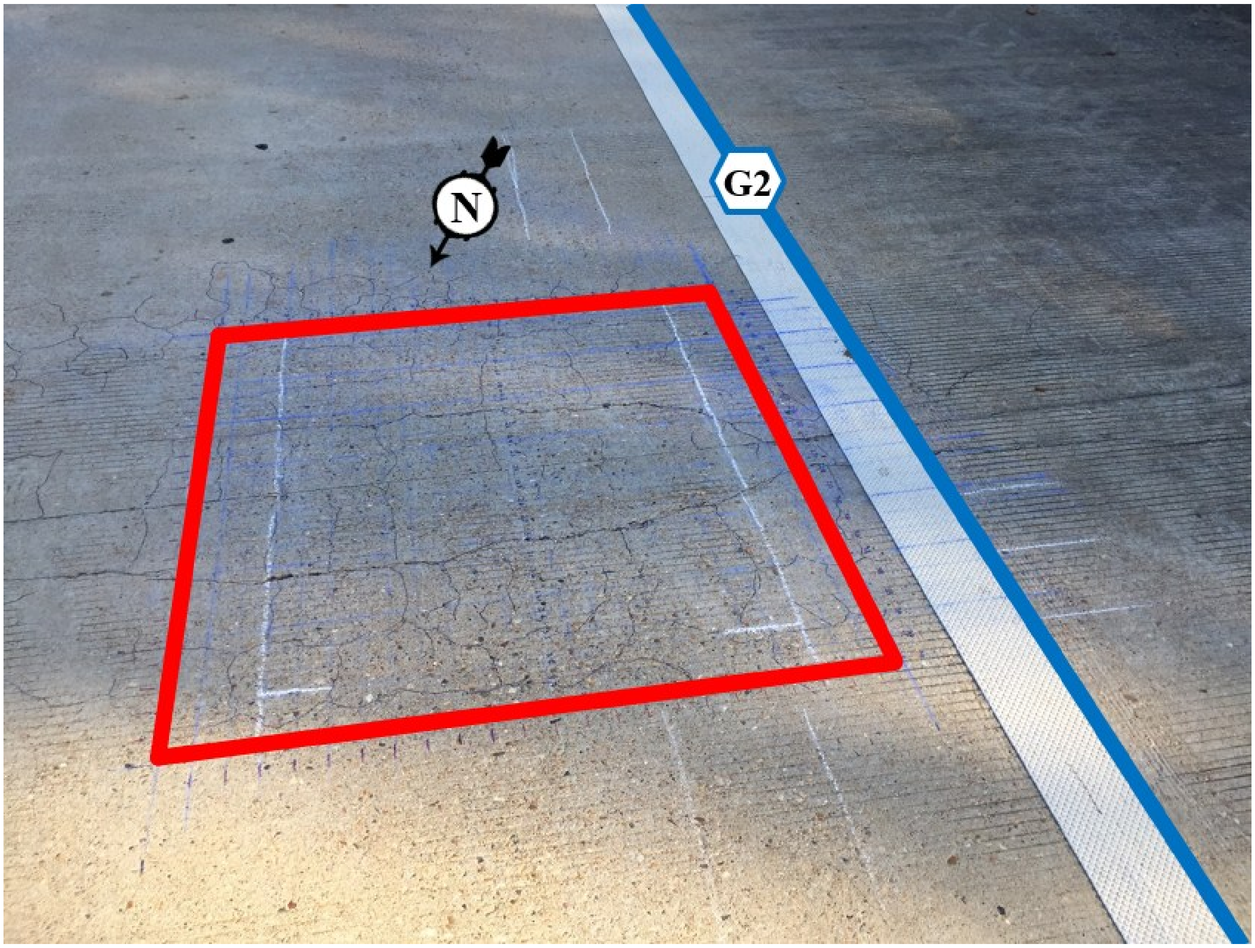

Figure 4.19. NDE region at Bent 3 for Bridge A3 (FM 154 over Little Cypress Bayou).

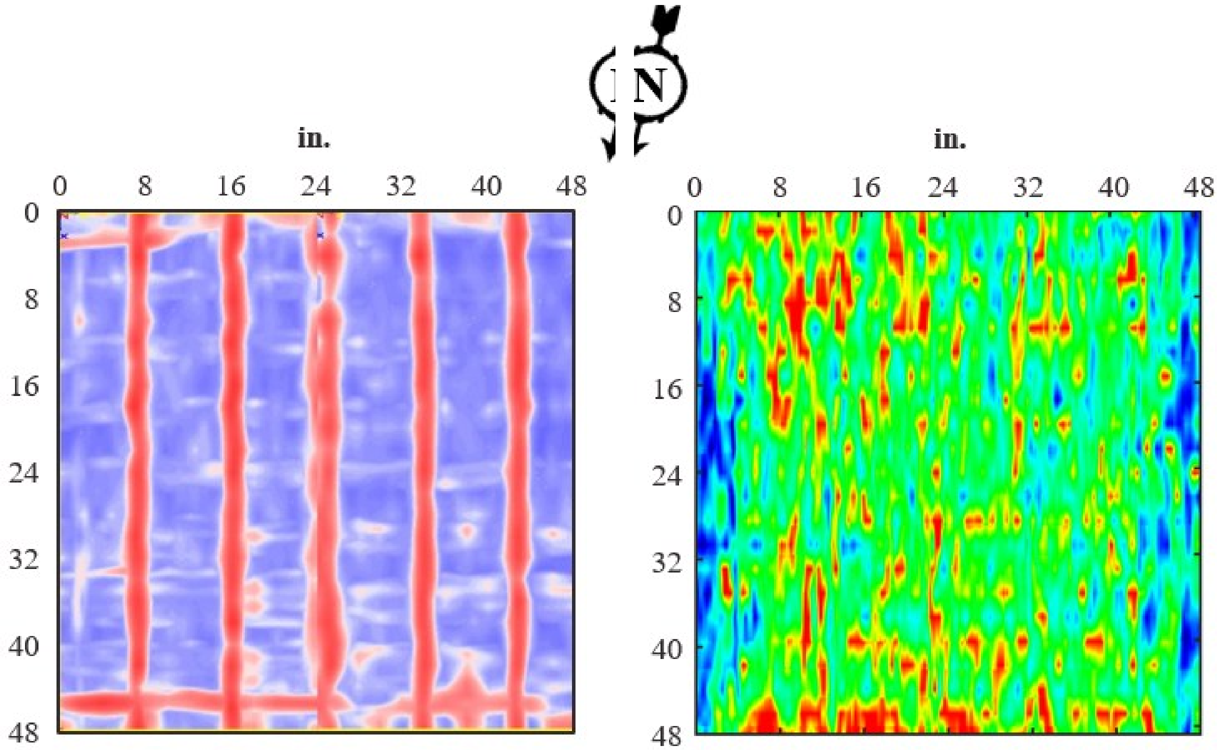

(a) (b)

Figure 4.20. ATL3 results for (a) GPR and (b) UST of top longitudinal reinforcement at depth 2.72 in.

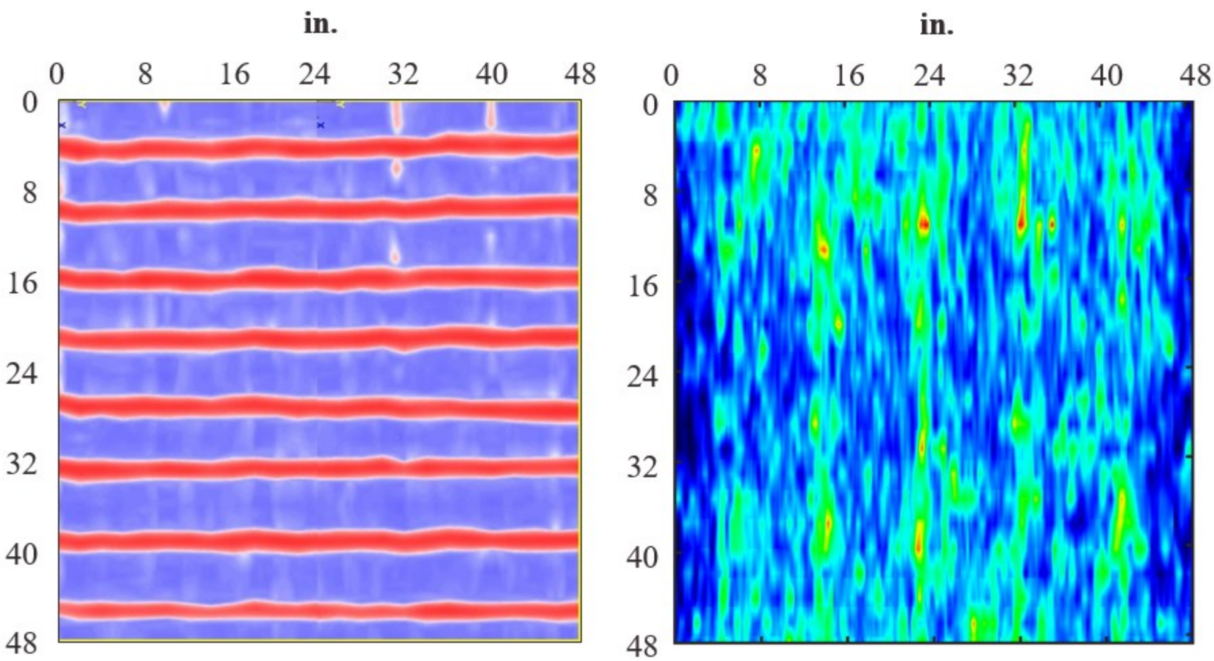

(a) (b)

Figure 4.21. ATL3 results for (a) GPR and (b) UST of top transverse reinforcement at depth 1.98 in.

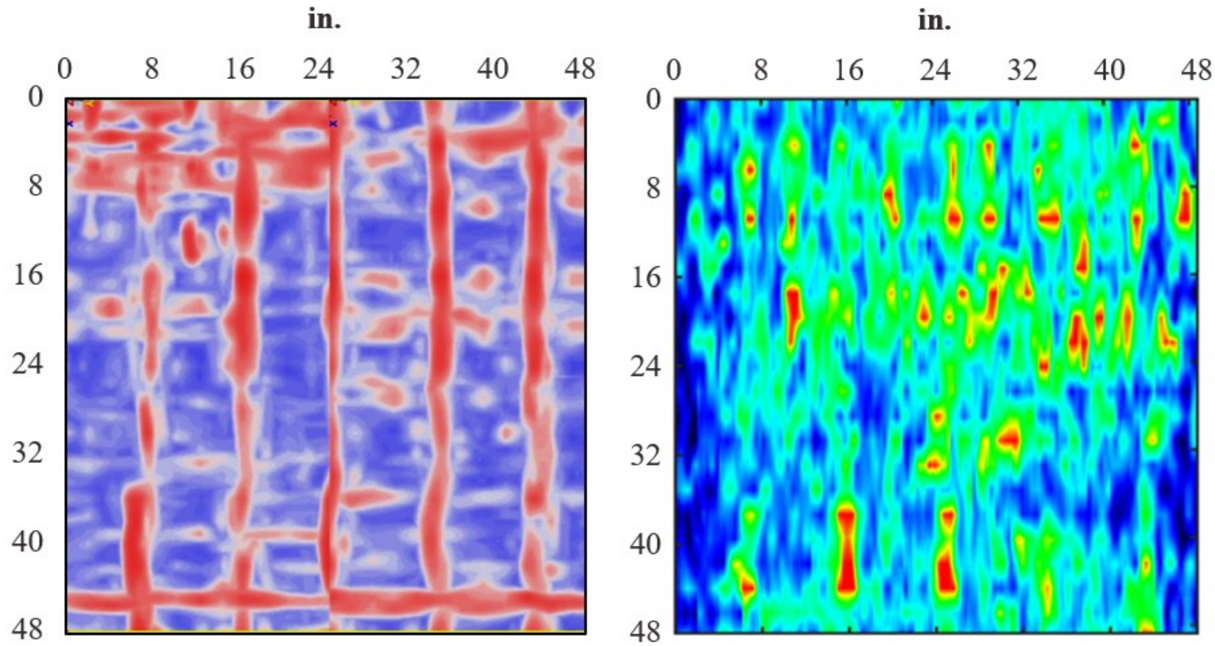

(a) (b)

Figure 4.22. ATL3 results for (a) GPR and (b) UST of bottom longitudinal reinforcement at depth 5.98 in.

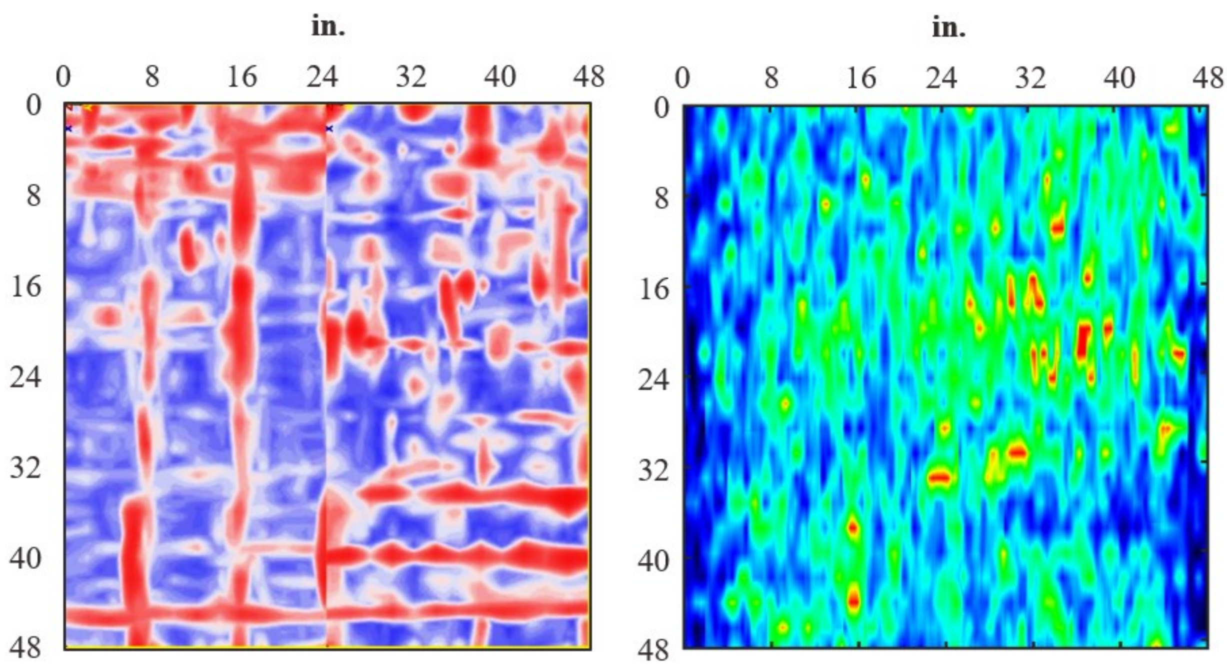

(a) (b)

Figure 4.23. ATL3 results for (a) GPR and (b) UST of bottom transverse reinforcement at depth 5.48 in.

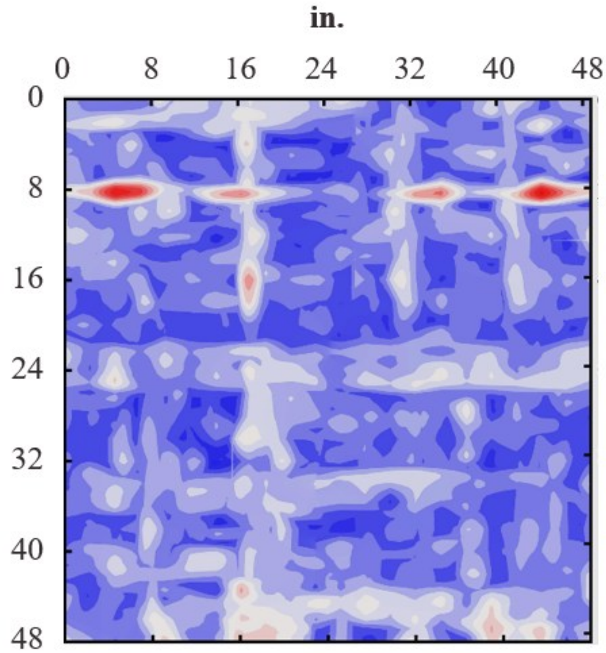

(a)

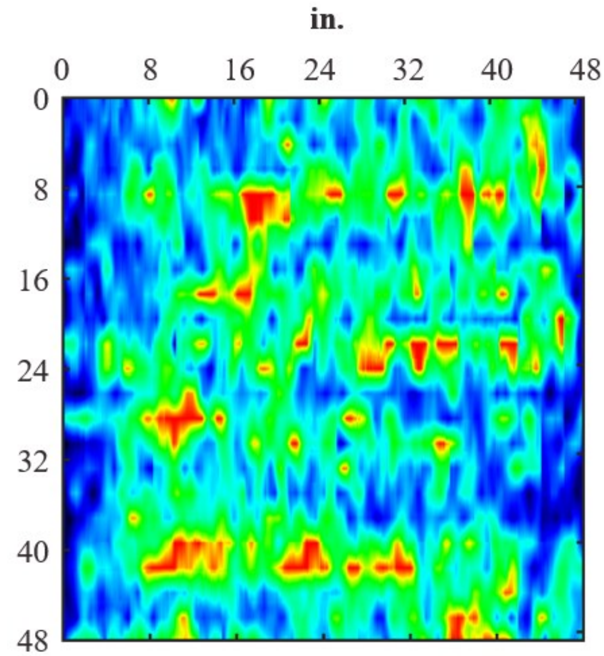

(b)

Figure 4.24. ATL3 results for (a) GPR and (b) UST of the PMDF at depth 8.5 in.

4.4.4 Bridge ATL4 (FM 968 over Clarks Creek, Longview)

Bridge ATL4, shown in Figure 4.25, was built in 1996 and carries FM 968 over Clarks Creek near Longview, Texas. The 32-ft wide bridge has two lanes on four Type B prestressed concrete I-girders spaced at 8 ft 8 in. with 3-ft overhangs.

The bridge is 200 ft long and is made up of four 50-ft simple spans forming one continuous deck unit. Expansion joints separate the unit from the abutments. The deck is shown as 8-in. thick CIP in the as-built drawings but was constructed using PCPs. Based on the age of the bridge, it is presumed to be made up of 4-in. thick PCPs with a 4-in. thick CIP top. The overhangs are fully CIP. The deck reinforcement is specified as #4 @ 12 in. in the longitudinal direction. In the transverse direction, #5 @ 9.5-in. top and bottom are included, with bent #5 bars at 9.5 in. spaced between. At PBJ joints, the link slab is fully CIP (formwork removed). Reinforcement details for the link slab were not available in the as-built drawings. During the field visit, it was confirmed that PCPs were used for the bridge deck, with offset panels. While it was not possible to take exact measurements, the length of the CIP region was approximately the width of the bent cap. The main PBJ crack was formed with a zip strip, and a notch was formed at the bottom of the deck in the same location. The CIP region at the PBJ was thicker than the rest of the deck formed with PCPs.

The inspection report for Bridge ATL4 did not indicate any damage related to the PBJ, resulting in an unadjusted PBJ rating of 4 and an age-adjusted rating of 1.326, indicating the bridge has performed far better than the average bridge of similar age. The good condition of the PBJ is consistent with the minimal cracking observed in the deck overall.

Visual inspection indicated that the condition of the three continuous deck regions was similar, and while the PBJs were overall in great condition, there was some very minor damage not indicated in the inspection report. Minor efflorescence was observed on the overhang shown in Figure 4.26(a). Between the girders, link slabs were in excellent condition, without any visible cracks or other damage, as shown in Figure 4.26(b). Visual observations on the top side indicated that some longitudinal cracks were present in the NDE region. The cracks were mostly hairline and measured 0.007 in. at the most. Zip strips were used to form the main PBJ crack. The extent of cracking and spalling along the main PBJ crack was much less than observed in other bridges evaluated. Figure 4.26(d) shows the marked cracks in the NDE region. Secondary PBJ cracks formed at approximately the end of the portion of the deck where PMDFs were used. The secondary PBJ cracks were 0.014–0.016 in. wide in the NDE region. Hairline cracks were present in the link slab region and in the main deck, and they were primarily longitudinal, with an occasional transverse crack.

The NDE regions are shown in Figure 4.27. The main NDE region was a 4-ft by 4-ft region at Bent 2, located in the northbound lane and between G1 and G2. The region was off center relative to the main PBJ crack to capture the reinforcement at the main crack plus an extension beyond the CIP region.

Figure 4.28 confirms the spacing of the top longitudinal reinforcement in the as-built drawings as 12 in. Figure 4.29, however, only shows transverse bars at 9.5 in. Transverse bent bars at 9.5-in. spacing were not found in GPR or UST images. Figure 4.30 and Figure 4.31 show that the reinforcement is deeper in the slab by approximately 1 in. at the PBJ than in the rest of the deck. A thickened CIP slab and a different depth of reinforcement at the PBJ are not specified in drawings or details. The spacing of the bottom longitudinal steel, seen in Figure 4.31(a), is approximately 7 in., which is a reasonable value given that bottom longitudinal steel is not shown on drawings as being placed over the girder lines and is instead clustered between the girder lines.

Figure 4.32 shows GPR images of the reinforcement placement in the overhang NDE region. Figure 4.32(a) and (b) show similar top-layer reinforcement spacing as in the primary NDE region between the girders. Figure 4.32(c) and (d), however, are less conclusive for the bottom reinforcement but still show that bottom transverse reinforcement appears to be placed deeper in the PBJ region. No evidence of voids or delaminations was discovered using IR images.

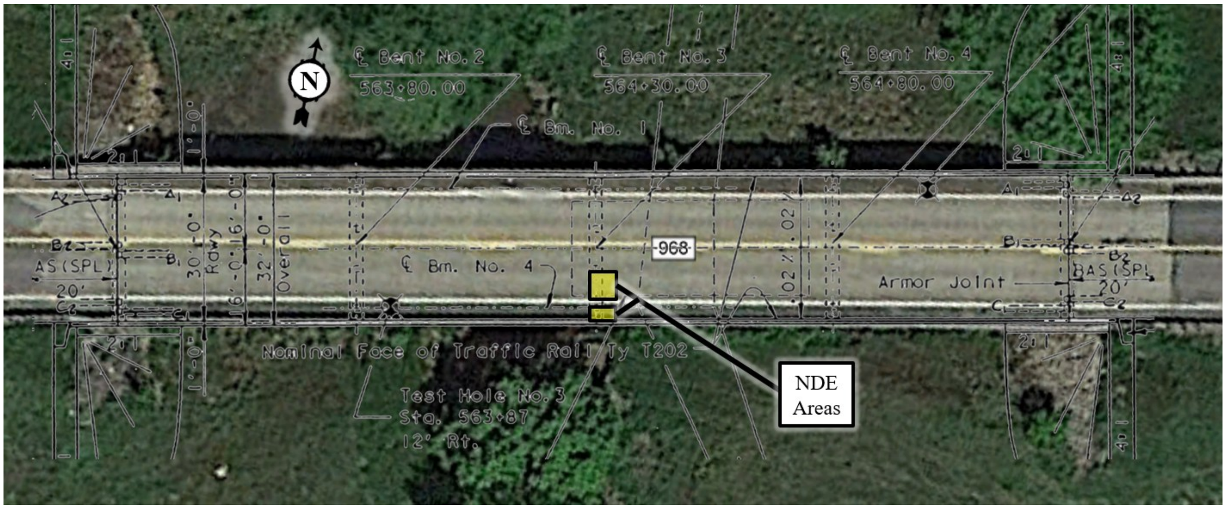

(a) Top view

(b) Side view

Figure 4.25. Site conditions at Bridge ATL4 (FM 968 over Clarks Creek).

(a) Bottom of overhang

(b) Bottom of CIP region between girders

(c) Main PBJ crack

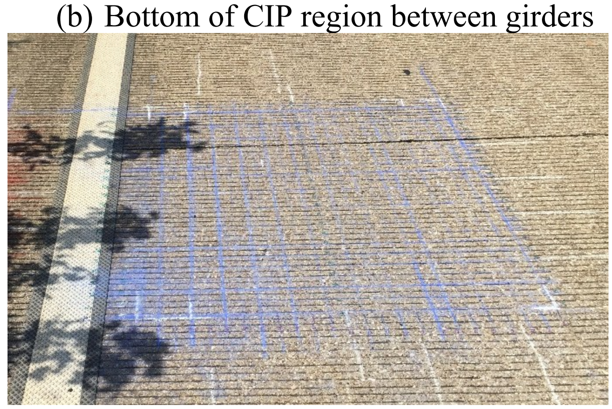

(d) Main NDE region

Figure 4.26. Typical link slab condition for Bridge ATL4 (FM 968 over Clarks Creek).

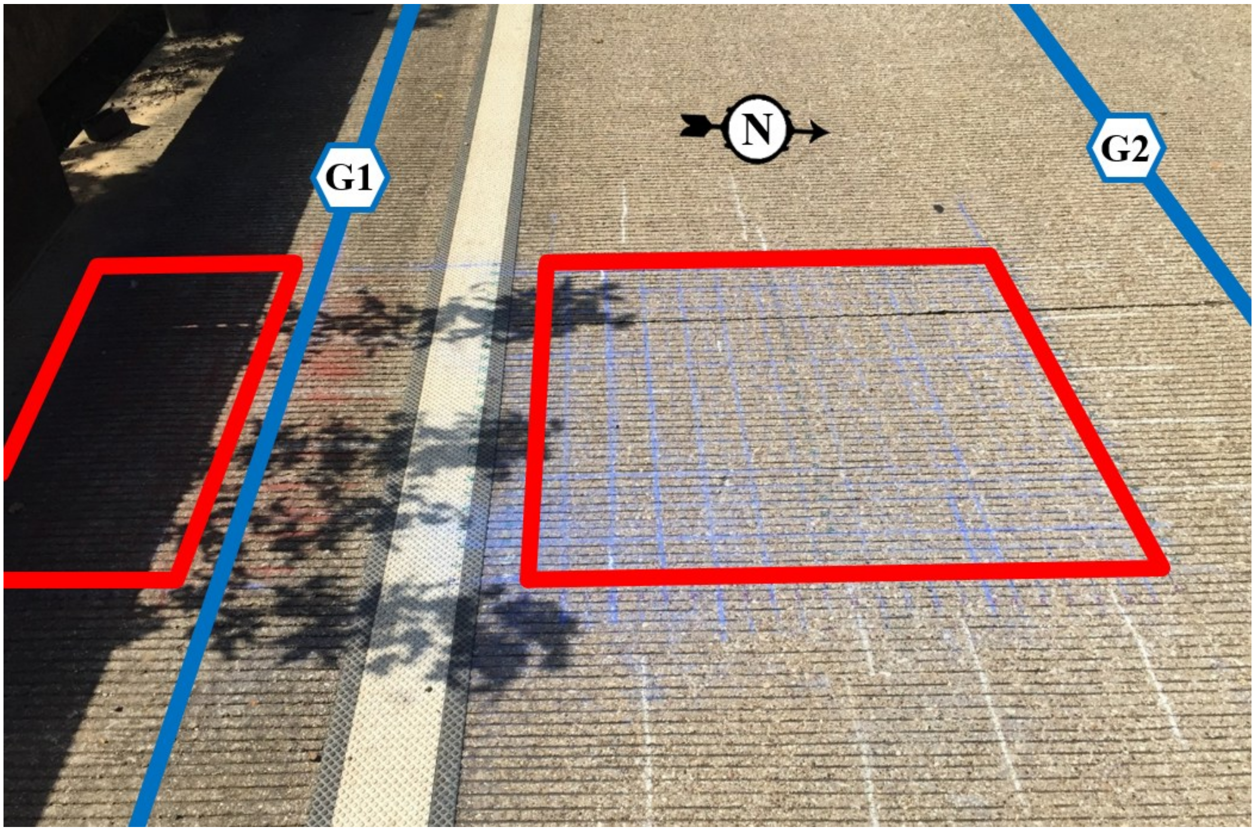

Figure 4.27. NDE region at Bent 3 for Bridge ATL4 (FM 968 over Clarks Creek).

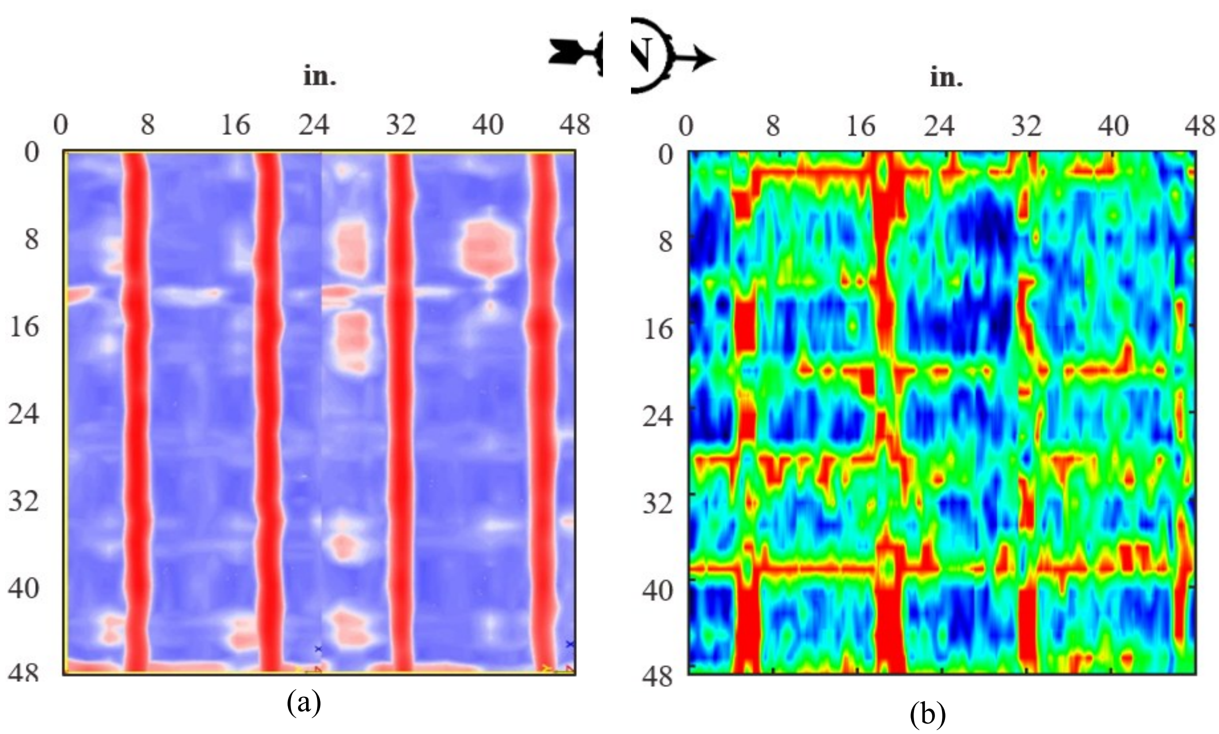

Figure 4.28. ATL4 results for (a) GPR and (b) UST of top longitudinal reinforcement between the girders at depth 4.95 in.

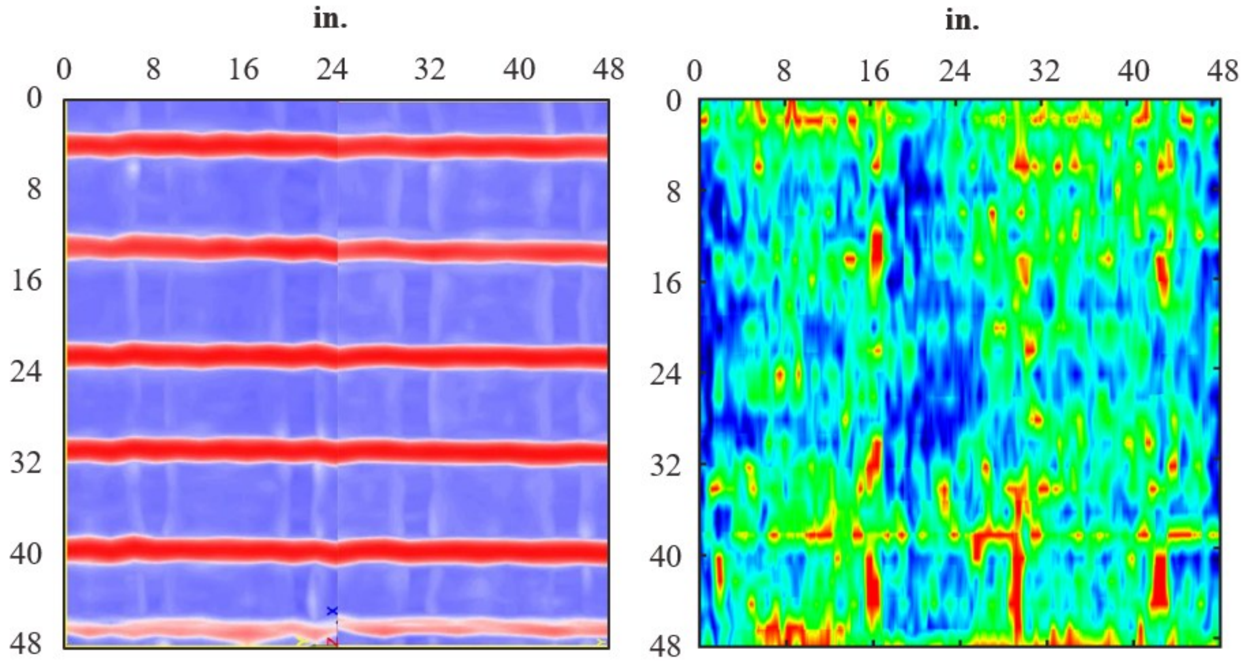

(a) (b)

Figure 4.29. ATL4 results for (a) GPR and (b) UST of top transverse reinforcement between the girders at depth 3.95 in.

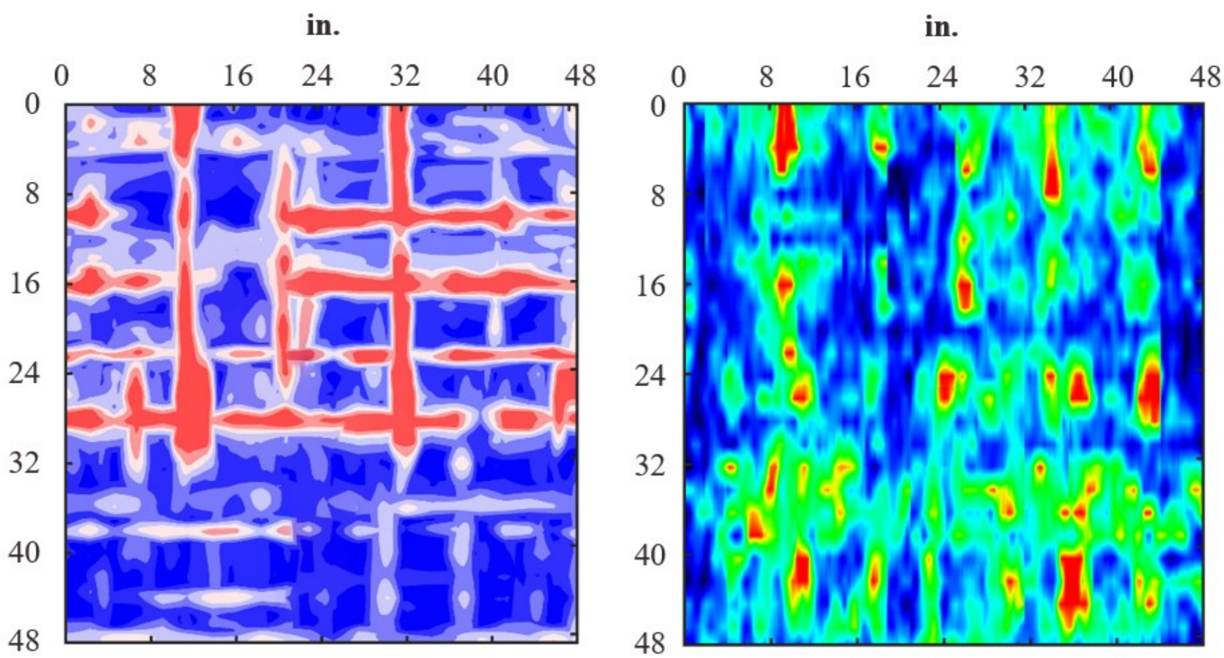

(a) (b)

Figure 4.30. ATL4 results for (a) GPR and (b) UST of bottom reinforcement between the girders at depth 8.48 in.

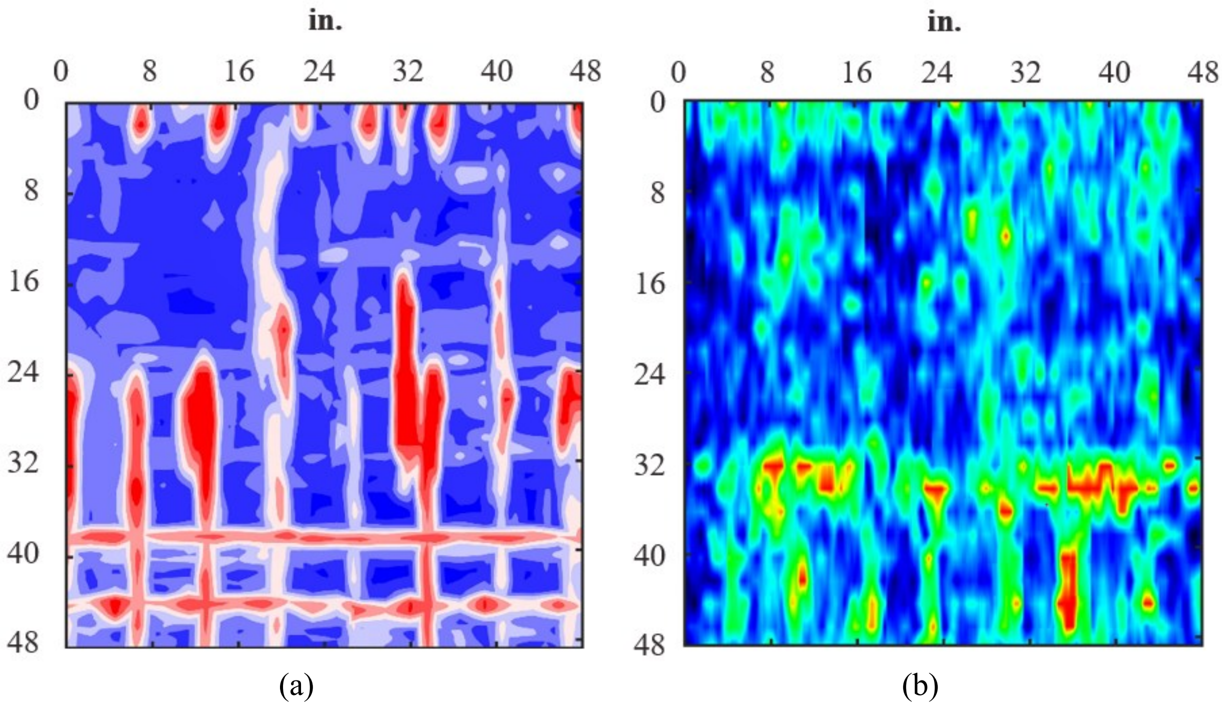

Figure 4.31. ATL4 results for (a) GPR and (b) UST of bottom reinforcement between the girders at depth 7.48 in.

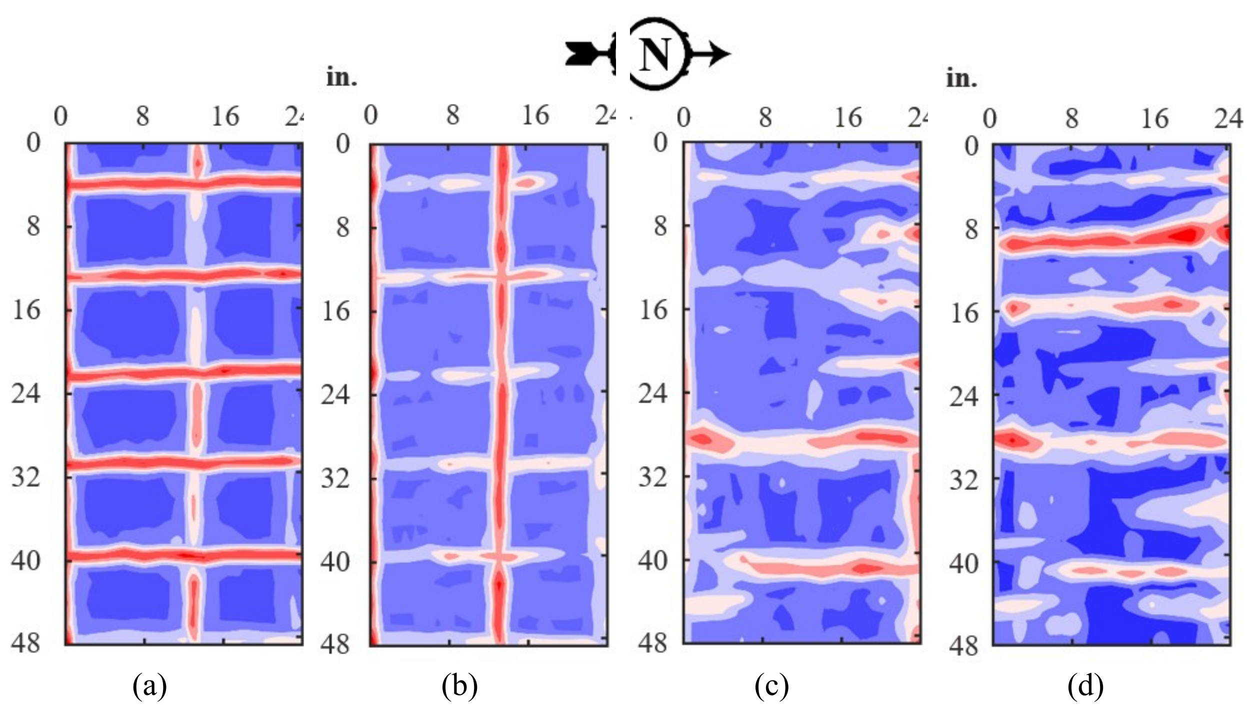

Figure 4.32. ATL4 GPR results in the overhang for (a) top transverse reinforcement at depth 4.23 in., (b) top longitudinal reinforcement at depth 4.98 in., (c) bottom reinforcement at 8.23 in., and (d) bottom reinforcement at 8.73 in.

4.4.5 Bridge LUB1 (SB Loop 289 over Slide Rd./4th St., Lubbock)

Bridge LUB1, shown in Figure 4.33, was built in 2010 and carries the southbound lanes of Loop 289 over Slide Rd./4th St. in Lubbock, Texas. The 58-ft 6-in. wide bridge has three lanes on eight Tx46 prestressed concrete I-girders spaced at 7.5 ft with 3-ft overhangs; a center barrier is shared with the adjacent bridge carrying northbound lanes, and a CIP region of deck connects the two bridges (Figure 4.34a).

The bridge is 266 ft long and is made up of three simple spans forming one continuous deck unit, with poor boy continuous deck regions providing deck continuity over interior supports. Expansion joints separate the unit from the abutment. The center span is 96 ft, and the end spans are both 85 ft. The deck is shown as 8.5-in. thick CIP in the as-built drawings but was constructed with PCPs. Based on the age of the bridge, it is presumed to be made up of 4-in. thick PCPs with a 4.5-in. thick CIP top. The deck reinforcement is specified as #4 @ 9 in. in the longitudinal direction and #5 @ 6 in. in the transverse direction. Prior to field inspection, it was believed that the continuous deck detail was offset PCPs, but inspection in the field revealed the PCPs were flush at the continuous deck joints (Figure 4.34b). The as-built drawings do not indicate if the reinforcement details are different in the link slab region.

The inspection report for Bridge LUB1 showed minor transverse, longitudinal, and map cracking on the deck and hairline cracks along joints in the outside lane and cracking and efflorescence in the deck overhangs. The indicated damage resulted in an unadjusted PBJ rating of 2 and an age-adjusted rating of −0.61, indicating the bridge has a lower performance than the average for bridges of similar age.

Visual inspection of the bridge confirmed the inspection report damage, and the condition of all continuous deck regions was similar. Figure 4.34 shows representative conditions of the link slab regions. Visual observations below the deck indicated confirmed cracking and efflorescence in the CIP overhangs. While the PCPs were in excellent condition, the gap between flush panels had some material hanging loss, and water stains were clearly present on the bent caps. On the top of the deck, the extensive cracking was confirmed. The main PBJ crack formed naturally (no zip strip). Between girders, the maximum width was 0.030 in. In the overhang, the maximum width was 0.025 in. Minor spalling was present in several locations along the main PBJ crack. Aside from the main PBJ crack, extensive cracks were present in the link slab region and the overall deck. Most cracks were no larger than 0.008 in., but one longitudinal crack was measured as 0.012 in. and several other longitudinal cracks as 0.010 in. While there were no distinct secondary PBJ cracks spanning the width of the bridge, NDE Area #3 contained a large transverse crack located 35.625 in. from the main PBJ crack with a width of 0.016–0.025 in.

Three NDE regions were investigated, all in the outside lane/overhang over Bent 3. Region 1 is a 2-ft by 4-ft region centered on the main PBJ crack over G2 and between G2 and G1 (42-in. mark is centered over G2). Region 2 is another 2-ft by 4-ft region centered over the main PBJ crack and captures the overhang, over G1, and part of the region between G1 and G2. Regions 1 and 2 are shown in Figure 4.35. Region 3 (2 ft by 2 ft) was selected to capture a region away from the main PBJ crack and was centered over the largest transverse crack away from the main PBJ crack. This region is shown adjacent to Regions 1 and 2 in Figure 4.36.

Figure 4.37 and Figure 4.38 confirm the spacing of the top longitudinal and transverse reinforcement in the as-built drawings as 9 in. and 6 in., respectively. Additionally, the dark horizontal areas in Figure 4.37(b), Figure 4.38(b), and Figure 4.39(b) at approximately 32 in. on the vertical axis appear to show a reflection caused by the edge of the girders. Figure 4.39 confirms that bottom longitudinal reinforcement is clustered between the girder lines, while bars are not placed directly over the girders, which is consistent with the design drawings. No evidence of voids or delaminations was discovered using IR images.

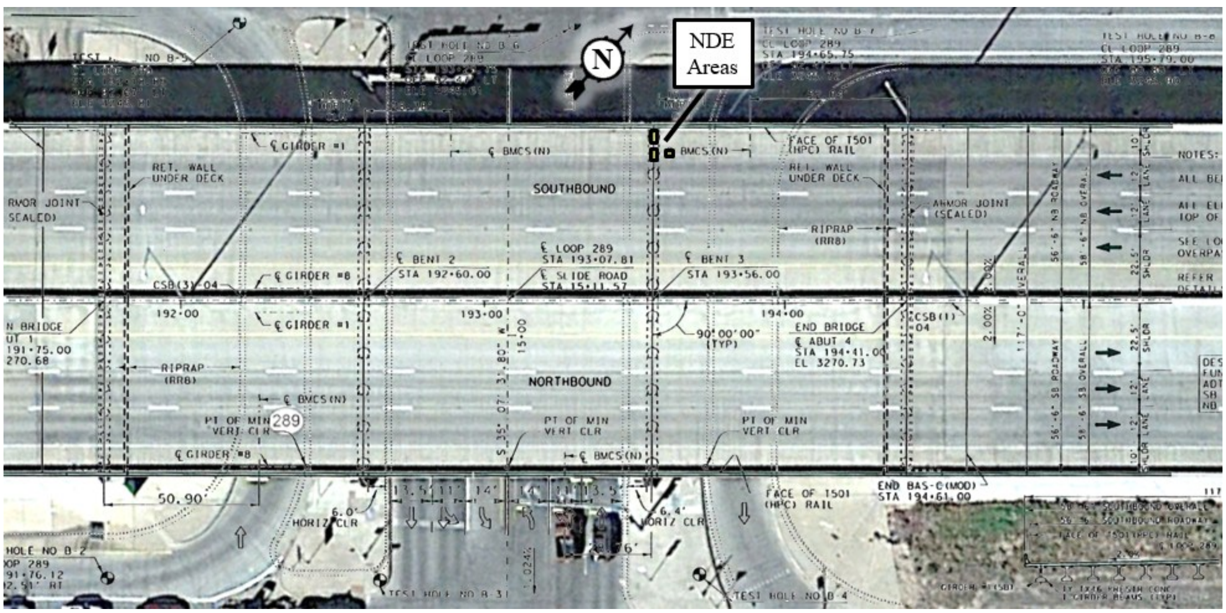

(a) Top view

(b) Elevation view

Figure 4.33. Site conditions at Bridge LUB1 (SB Loop 289 over Slide Rd./4th St.).

(a) CIP deck between northbound and southbound lanes

(b) Cracking and efflorescence in overhang

(c) Panels at interior bent

(d) Main PBJ crack

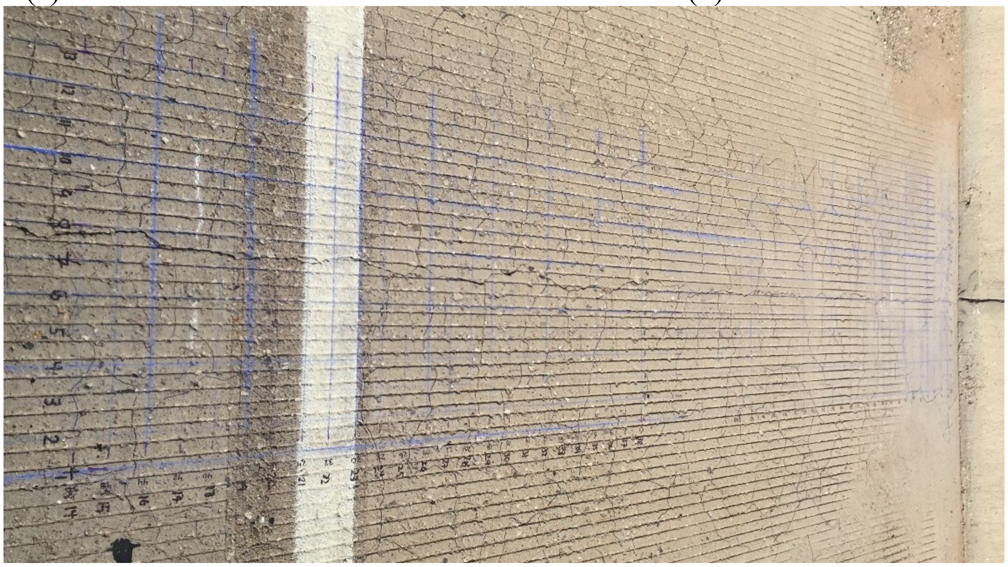

(e) Marked cracks in NDE regions

Figure 4.34. Typical link slab condition for Bridge LUB1 (SB Loop 289 over Slide Rd./4th St.).

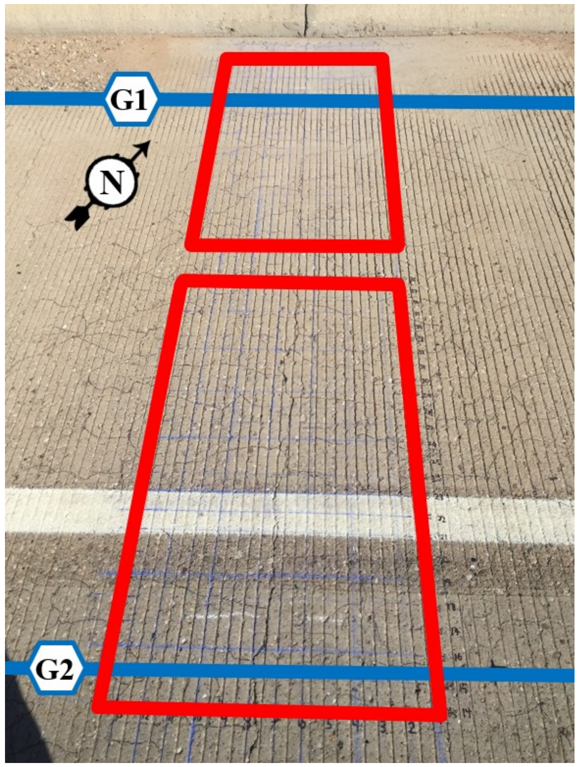

Figure 4.35. Primary NDE regions (Region 1 and 2) at Bent 3 for Bridge LUB1 (SB Loop 289 over Slide Rd./4th St.).

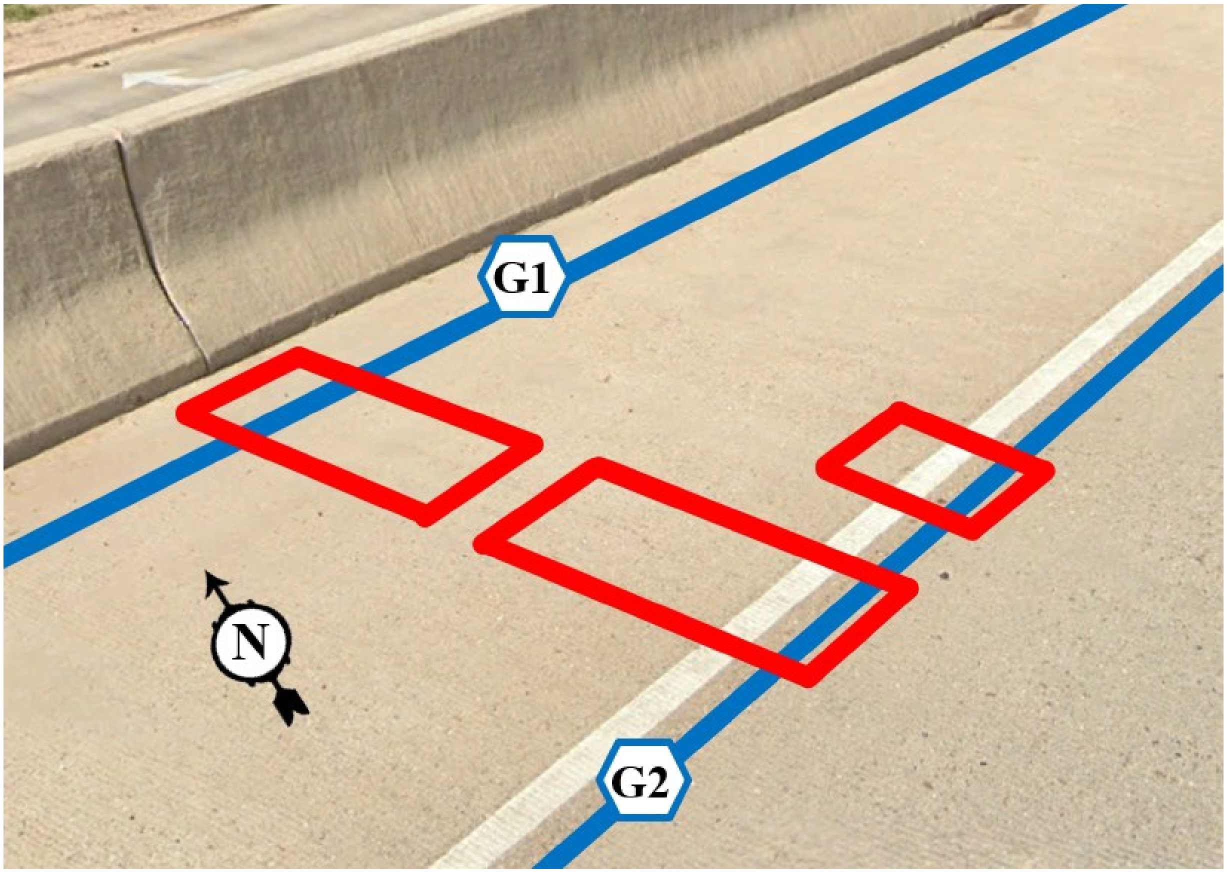

Figure 4.36. Primary NDE regions (1 and 2) at Bent 3 for Bridge LUB1 (SB Loop 289 over Slide Rd./4th St.) with the smaller secondary NDE region (Region 3) east of the primary regions adjacent to G2.

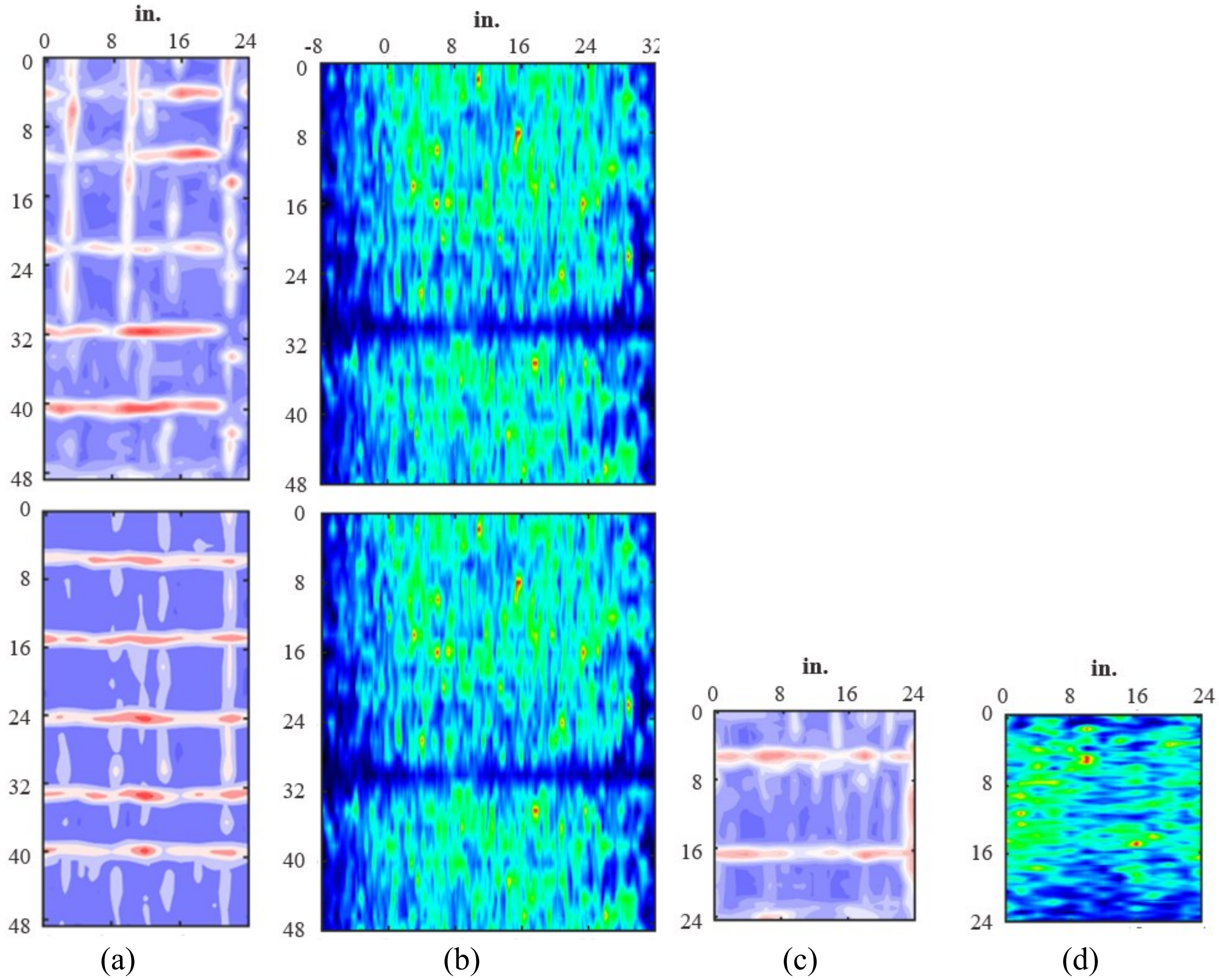

Figure 4.37. LUB1 results for top longitudinal reinforcement at depth 3.73 in. for (a) GPR in NDE Regions 1 and 2, (b) UST in Regions 1 and 2, (c) GPR in Region 3, and (d) UST in Region 3.

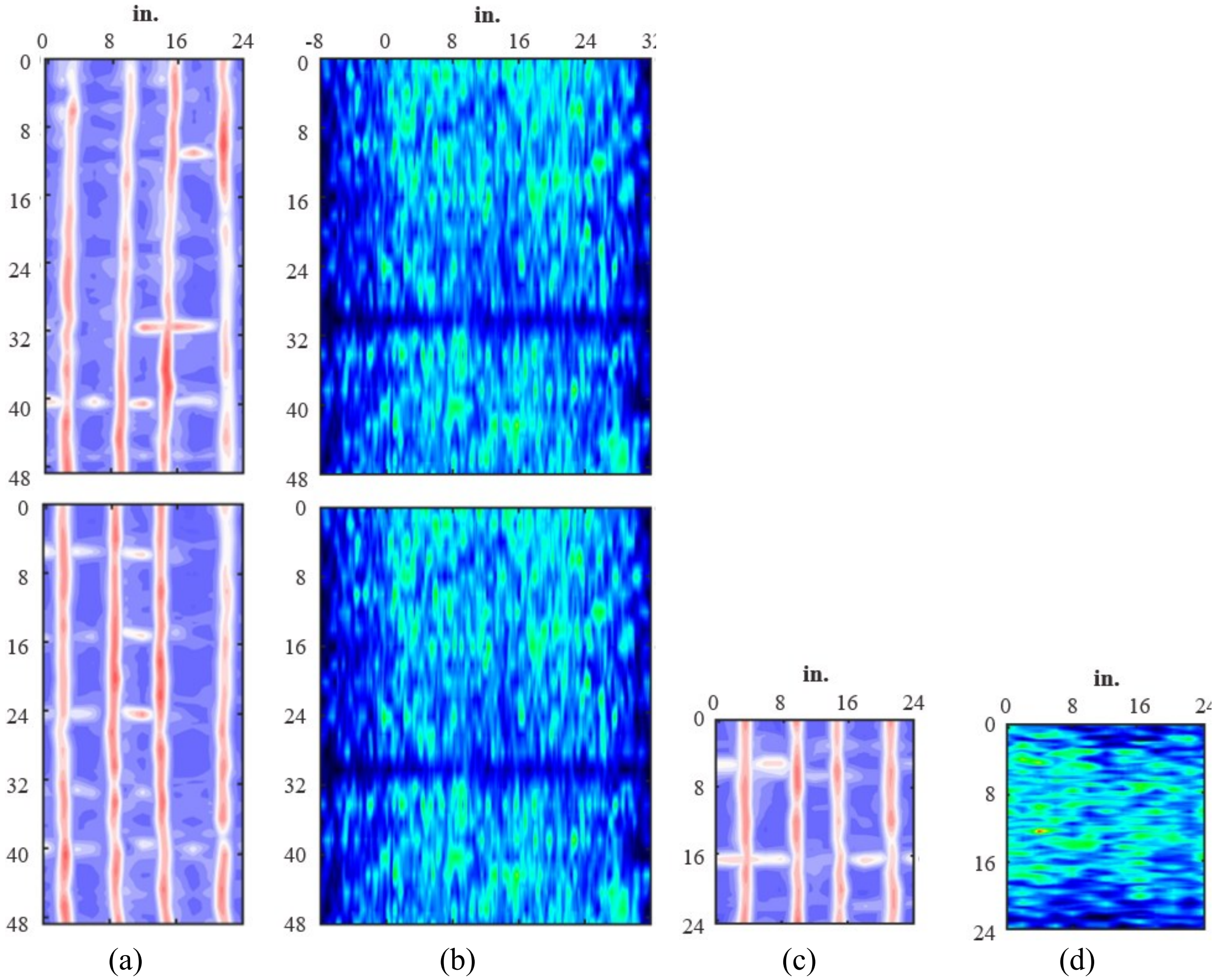

Figure 4.38. LUB1 results for top transverse reinforcement at depth 2.73 in. for (a) GPR in NDE Regions 1 and 2, (b) UST in Regions 1 and 2, (c) GPR in Region 3, and (d) UST in Region 3.

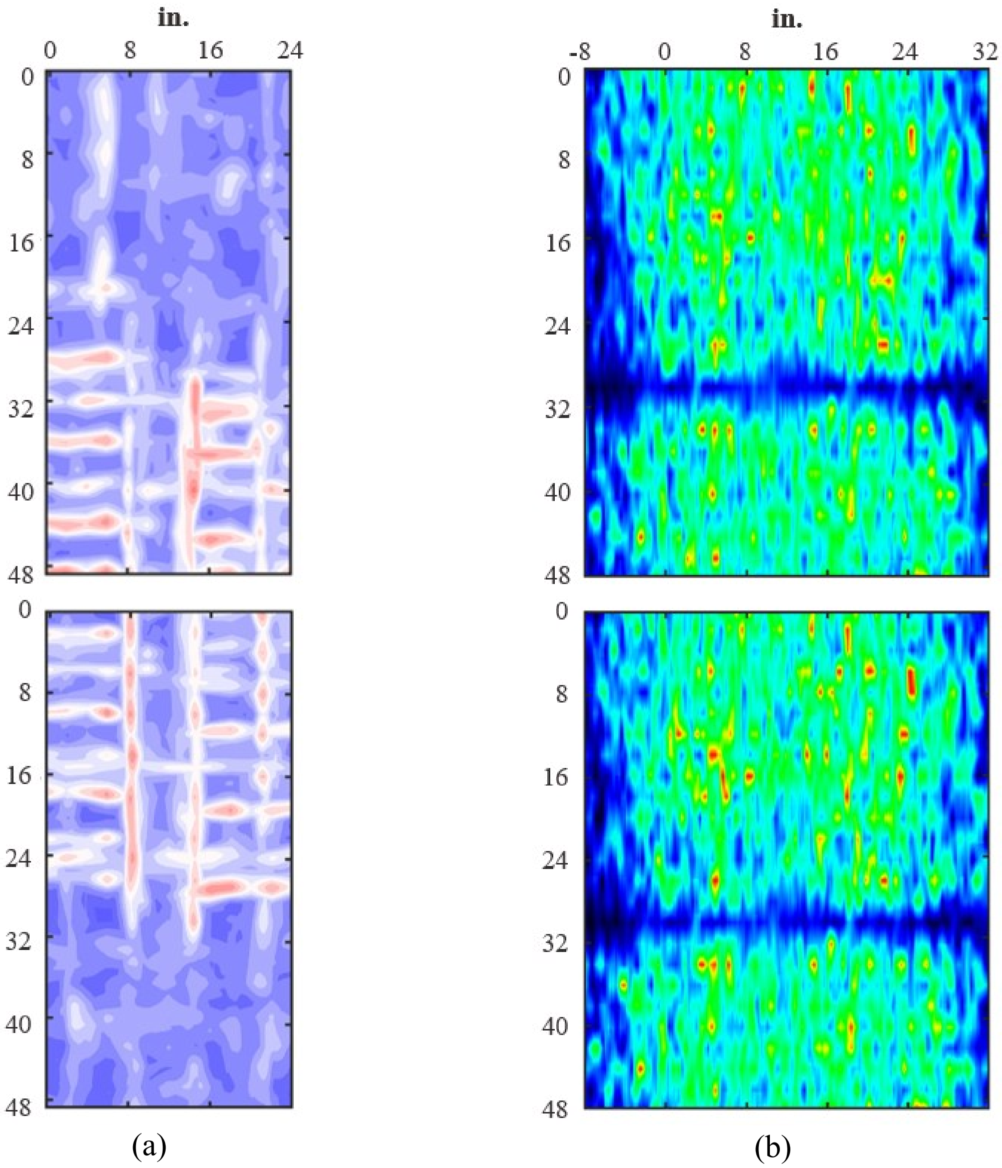

Figure 4.39. LUB1 results for bottom reinforcement at depth 6.98 in. for (a) GPR in NDE Regions 1 and 2, and (b) UST in Regions 1 and 2.

4.4.6 Bridge LUB2 (Erskine St. over I-27, Lubbock)

Bridge LUB2, shown in Figure 4.40, was built in 1990 and carries Erskine St. over I-27 in Lubbock, Texas. The 72-ft wide bridge has five lanes (two continuous each direction with a split turn lane) on 10 Type 54 prestressed concrete I-girders spaced at 7.333 ft with 3-ft overhangs. A 7-ft wide, 1-ft 2.5-in. thick (beyond the thickness of the deck) sidewalk is located on the westbound side of the bridge. The bridge is 185.7 ft long and is made up of two 92.85-ft simple spans forming one continuous deck unit with poor boy continuous deck regions providing deck continuity over interior supports. The interior bent is an inverted-T bent cap with a stem width of 2.5 ft. Expansion joints separate the unit from the abutment.

The deck is shown as 7.5-in. thick CIP in the as-built drawings but was constructed with a PMDF. The top longitudinal reinforcement is specified as #4 @ 10.5 in., and bottom longitudinal reinforcement is #4 @ 11 in. Transverse reinforcement is #5 @ 10.5 in. in the top layer, #4 @ 10.5 in. in the bottom layer, and #5 bent bars at 10.5 in. spaced between the top and bottom layer bars. The as-built drawings do not indicate if the reinforcement details are different in the link slab region.

The inspection report for Bridge LUB2 indicated minor longitudinal cracking (< ⅟32 in.), hairline map cracking, and transverse cracks adjacent to the control joint. The indicated damage resulted in an unadjusted PBJ rating of 1 and an age-adjusted rating of −0.586, indicating the bridge has a lower performance than the average for bridges of similar age.

Access below the bridge for visual inspection was limited; however, photographs taken from the shoulder of I-27 show spalling at the tops of the stems (Figure 4.41a). The bridge was sloped down toward the eastbound lane. At the time of visual inspection, water had pooled against the rail over the bent. Visual inspection below the bridge revealed dusting of the PMDF around and adjacent to a drainpipe (Figure 4.41[b]). Figure 4.41(c) shows the cracking at the top of the deck. Significant spalling was present along the main PBJ crack. The main PBJ had been formed at the time of construction (wider than a zip strip) and was not measured. The secondary PBJs were 2 ft 6 in. apart, aligning with the edges of the inverted-T bent cap stem and measured 0.03 in. wide in a couple of locations within the NDE region but were mostly 0.01–0.014 in. wide. Other transverse cracks in the NDE region were no more than 0.006 in., and longitudinal cracks did not exceed 0.012 in. wide. Adjacent to the sidewalk, diagonal cracks formed as shown in Figure 4.41(d).

One 4-ft by 4-ft NDE region was investigated in the westbound lane between G2 and G3. The NDE area consisted of two adjacent 2-ft by 4-ft grids centered on the main PBJ crack and oriented perpendicular to the control joint. GPR was conducted in the full area. UST was conducted in a reduced area. Figure 4.42 shows the NDE region.

Figure 4.43 and Figure 4.44 confirm the specified top reinforcement spacing. The top end of the bent transverse bars can be seen on the right side of the GPR and UST images in Figure 4.44, spaced between the straight transverse bars. The bottom end of the same bent transverse bars can be seen on the left of the GPR image in Figure 4.45(a). The ribs of the PMDF are visible in the UST image in Figure 4.46(b). No evidence of voids or delaminations was not found on the deck.

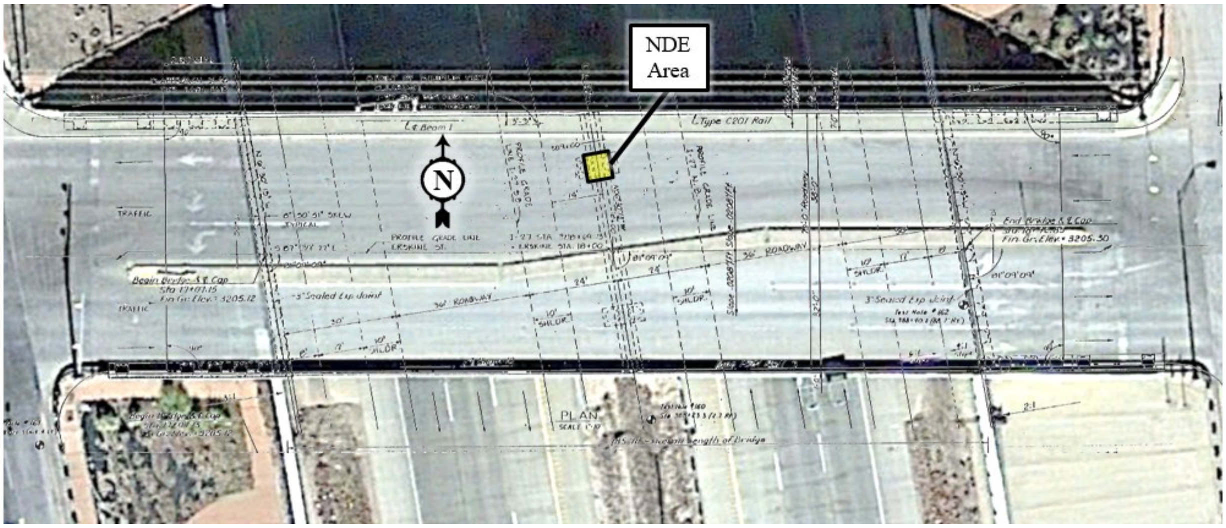

(a) Top view

(b) Elevation view

Figure 4.40. Site conditions at Bridge LUB2 (Erskine St. over I-27).

(a) Inverted-T bent cap and PMDF between girders

(b) Rusting PMDF on eastbound side

(c) Marked cracks in NDE area

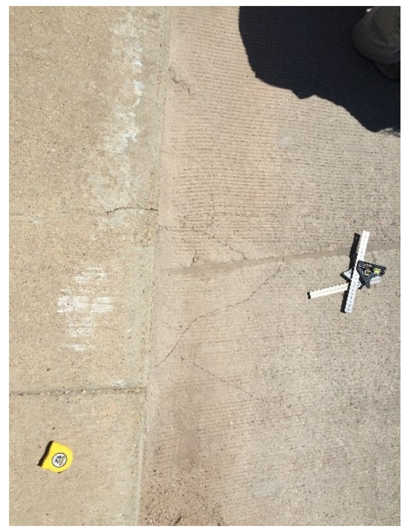

(d) Marked cracks adjacent to sidewalk

Figure 4.41. Typical link slab condition for Bridge LUB2 (Erskine St. over I-27).

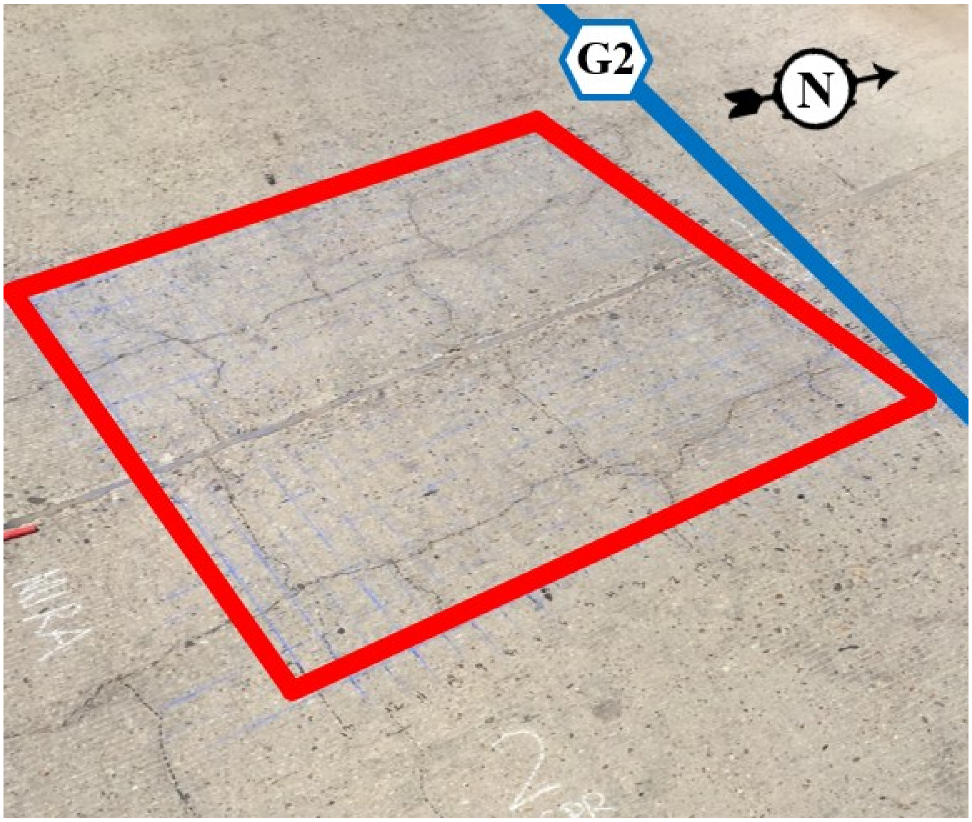

Figure 4.42. NDE region at Bent 2 for Bridge L2 (Erskine St. over I-27).

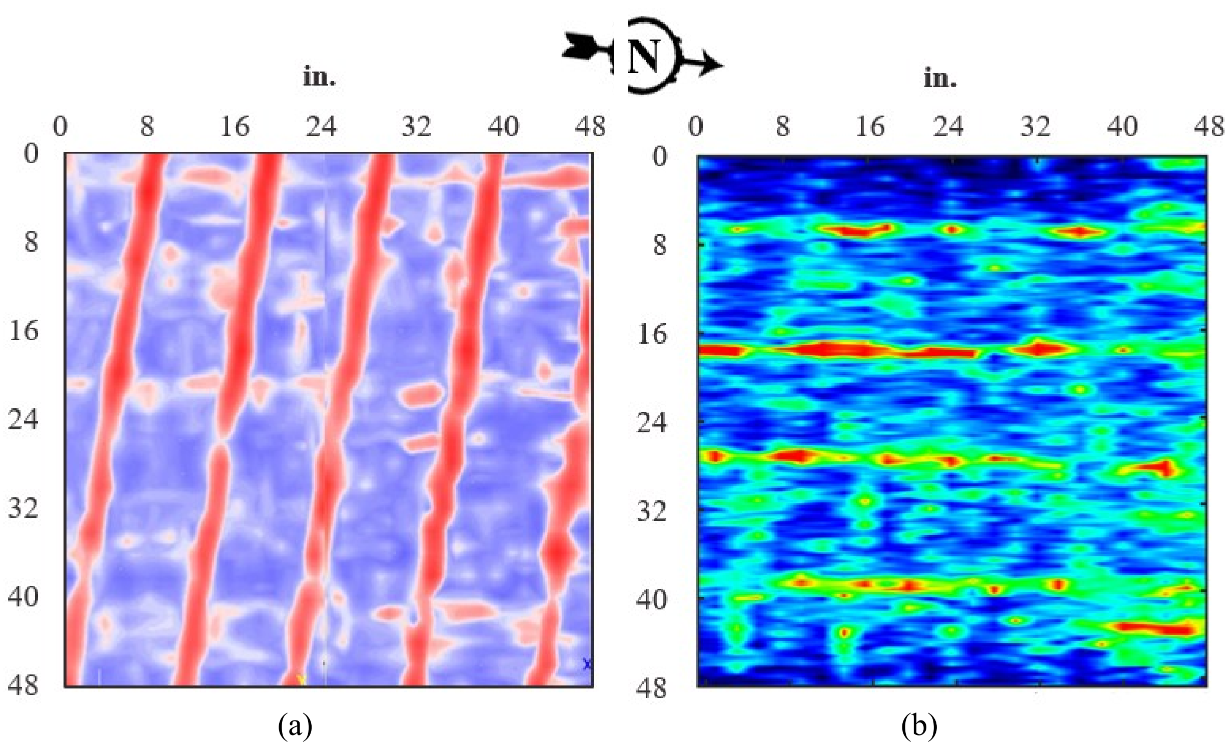

Figure 4.43. LUB2 results for (a) GPR and (b) UST of top longitudinal reinforcement at depth 3.48 in.

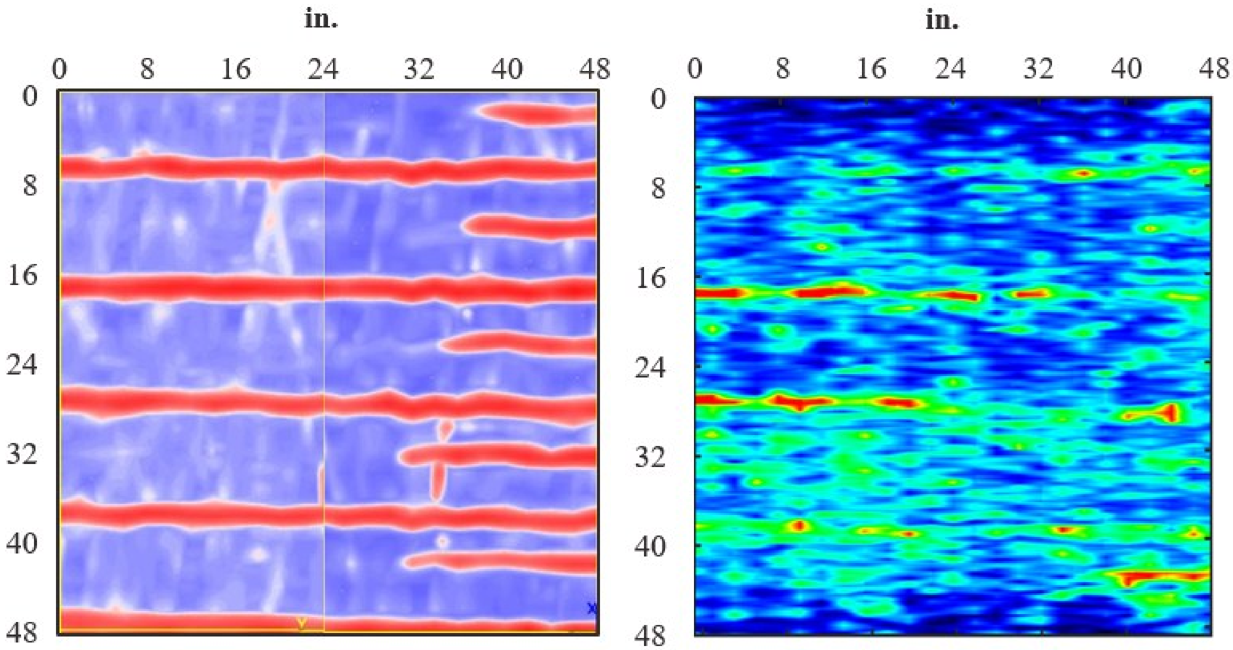

(a) (b)

Figure 4.44. LUB2 results for (a) GPR and (b) UST of top transverse reinforcement at depth 2.73 in.

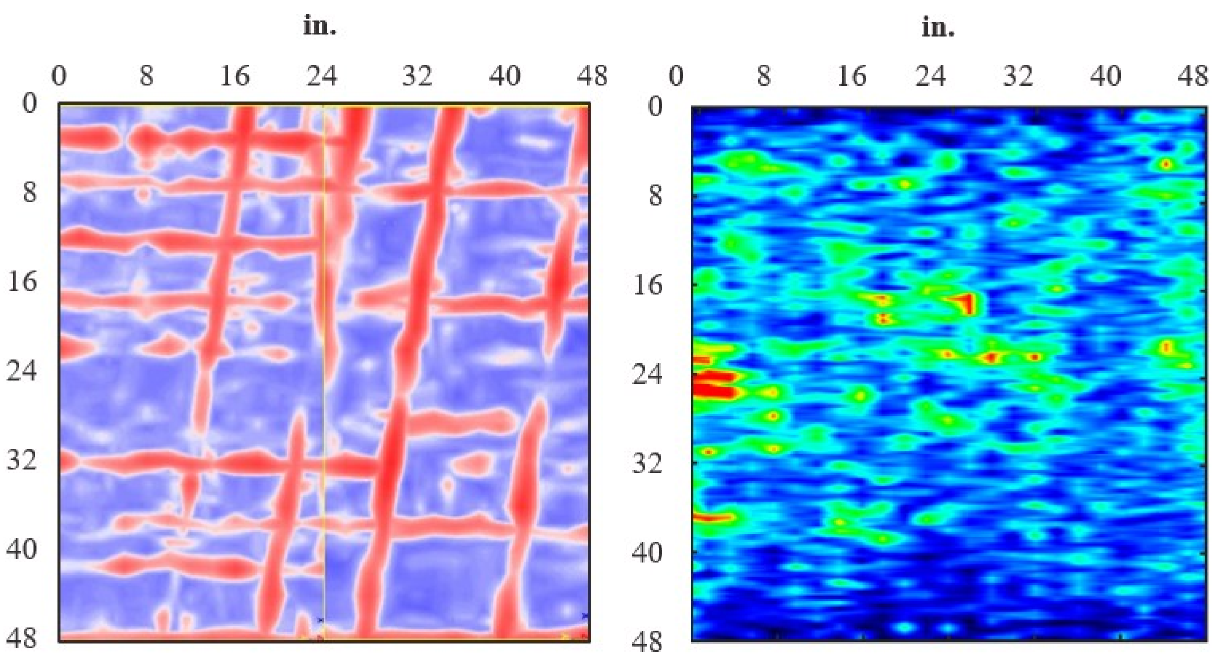

(a) (b)

Figure 4.45. LUB2 results for (a) GPR and (b) UST of bottom reinforcement at depth 5.73 in.

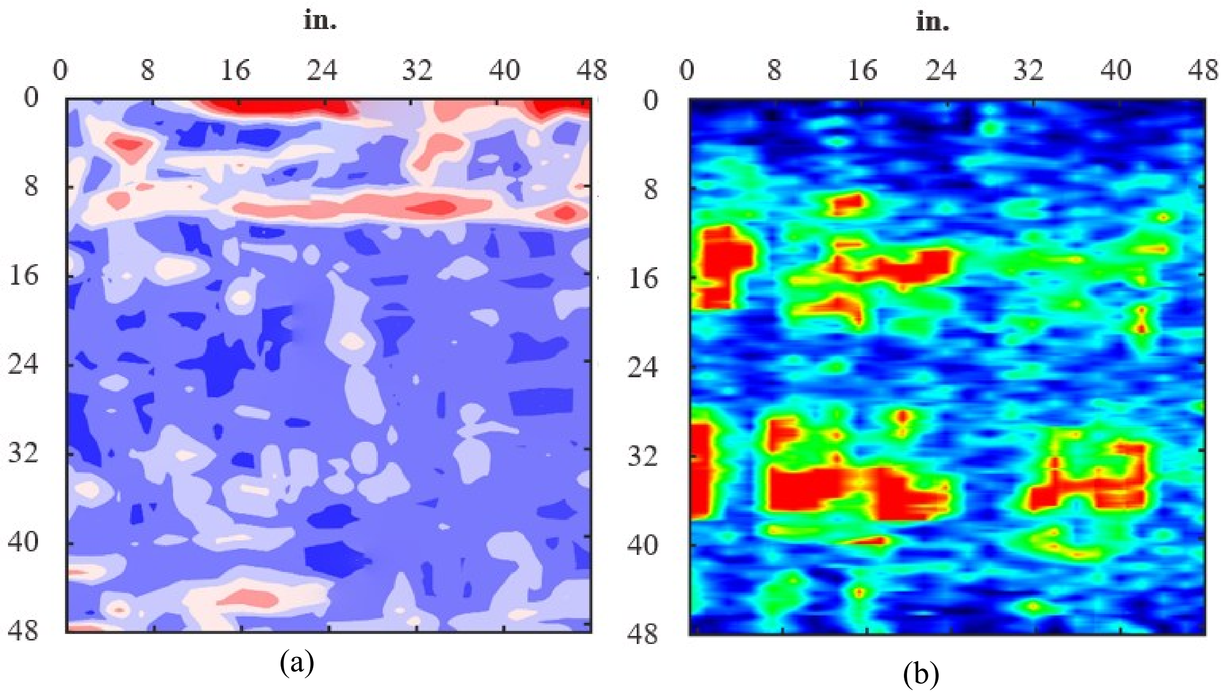

Figure 4.46. LUB2 results for (a) GPR and (b) UST of PMDF at depth 8.5 in.

4.4.7 Bridge LUB3 (EB US 62 over Research Blvd., Wolfforth)

Bridge LUB3, shown in Figure 4.47, was constructed in 2017 and carries eastbound US 62 over Research Blvd. in Wolfforth, Texas. The 40-ft wide bridge has two lanes with a 10-ft exterior shoulder on five Tx40 prestressed concrete I-girders spaced at 8.5 ft with 3-ft overhangs.

The bridge is 195 ft long and is made up of three simple spans forming one continuous deck unit, with two poor boy continuous deck regions providing deck continuity over interior supports. Both end spans are 50 ft, and the center span is 95 ft. Expansion joints separate the unit from the abutment. The deck is shown as 8.5-in. thick CIP in the as-built drawings but was constructed with PCPs except for CIP overhangs. Based on the age of the bridge, it is presumed the deck is constructed with 4-in. thick PCPs with a 4.5-in. thick CIP top. The deck reinforcement is specified as #4 @ 9 in. in the longitudinal direction and #5 @ 6 in. in the transverse direction. At the continuous deck joints, the PCPs are flush, consisting of partial-length panels on either side of the joint, as shown in Figure 4.48(a), with one end angled to accommodate the skew of the bridge. The as-built drawings do not indicate if the reinforcement details are different in the link slab region. On the top side of the deck, the main PBJ crack, shown in Figure 4.48(b), was formed with a zip strip that was still in place. Between the girders, the main PBJ crack was parallel to the bent cap, but in the overhang, it was perpendicular to the flow of traffic.

The inspection report for Bridge LUB3 did not indicate any damage related to the performance of the continuous deck regions, resulting in an unadjusted PBJ rating of 4 and an age-adjusted rating of +0.699, indicating the bridge has better performance than the average for bridges of similar age.

Visual inspection of the bridge confirmed the excellent condition. Some hairline cracks were present in the deck, consisting mainly of longitudinal cracks. Figure 4.48(c) shows the marked cracks in the NDE region. No spalling was observed along the main PBJ crack in the NDE region. The main PBJ crack measured 0.025 in. wide. Visual inspection from the ground beneath the bridge did not indicate any cracking or efflorescence in the overhang, and the panels and girder ends were all in excellent condition except for filler material between some panels hanging loose below the main PBJ crack.

Evaluation of LUB3 was done in a single NDE area at Bent 2 between G2 and G3, adjacent to G2 (Figure 4.49). The area consisted of two 2-ft by 4-ft grids, oriented with the 4-ft dimension parallel to the flow of traffic, with the main PBJ crack centered in the region.

Figure 4.50 appears to show that the top longitudinal reinforcement was doubled in the PBJ region since the bars are spaced at approximately 4.5 in. Figure 4.51 confirms that the top transverse bars are spaced according to the design drawings. The diagonal gap between the PCPs can be faintly seen in Figure 4.52, crossing the image at approximately 16 in. on the left to 32 in. on the right on the vertical axis. Figure 4.49 shows the diagonal PBJ crack and longitudinal cracks extending from the PBJ. No evidence of voids or delaminations was found in the IR images.

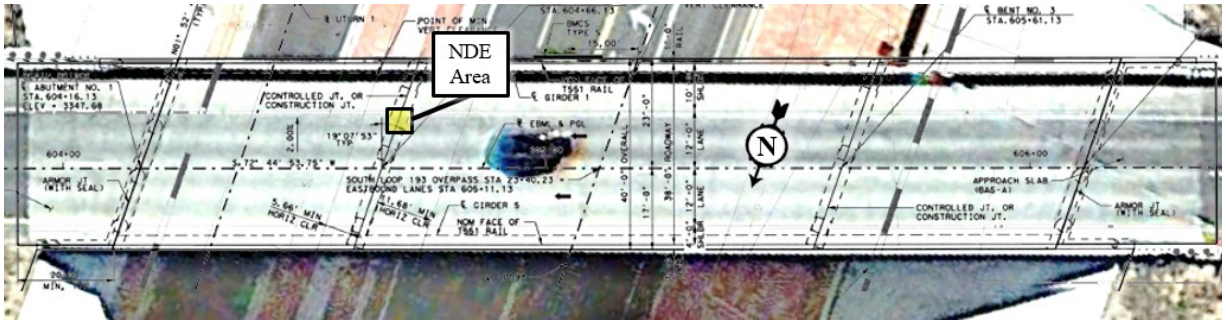

(a) Top view

(b) Elevation view

Figure 4.47. Site conditions at Bridge LUB3 (US 62 over Research Blvd.).

(a) Flush panels at continuous deck joint

(b) Continuous deck region in shoulder

(c) Marked cracks in NDE region

Figure 4.48. Typical link slab condition for Bridge LUB3 (US 62 over Research Blvd.).

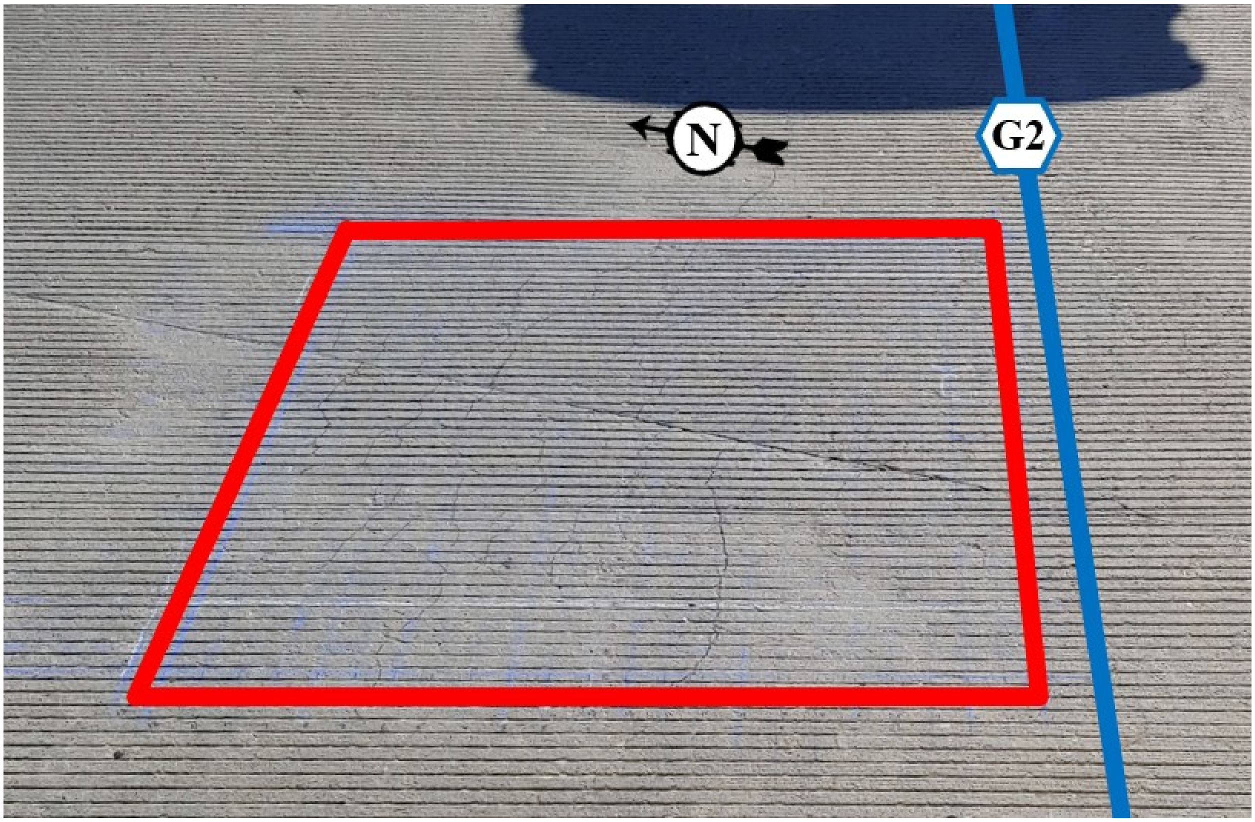

Figure 4.49. NDE region at Bent 2 for Bridge LUB3 (US 62 over Research Blvd.).

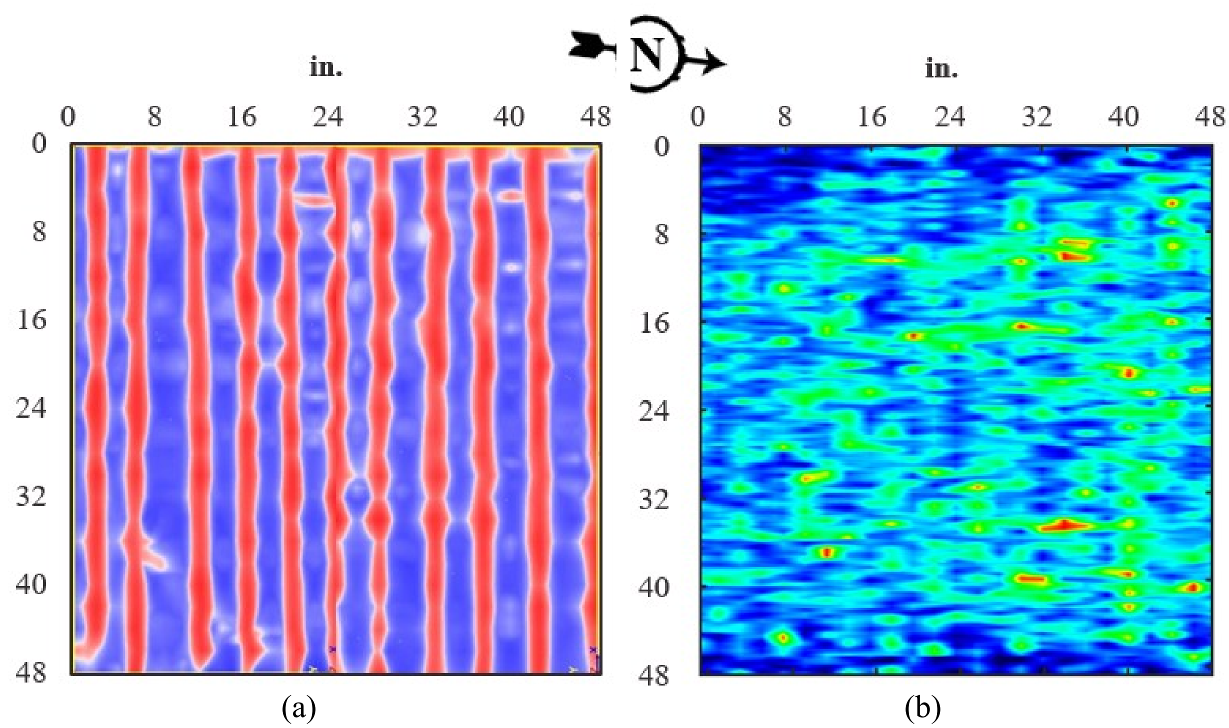

Figure 4.50. LUB3 results for (a) GPR and (b) UST of top longitudinal reinforcement at depth 4.73 in.

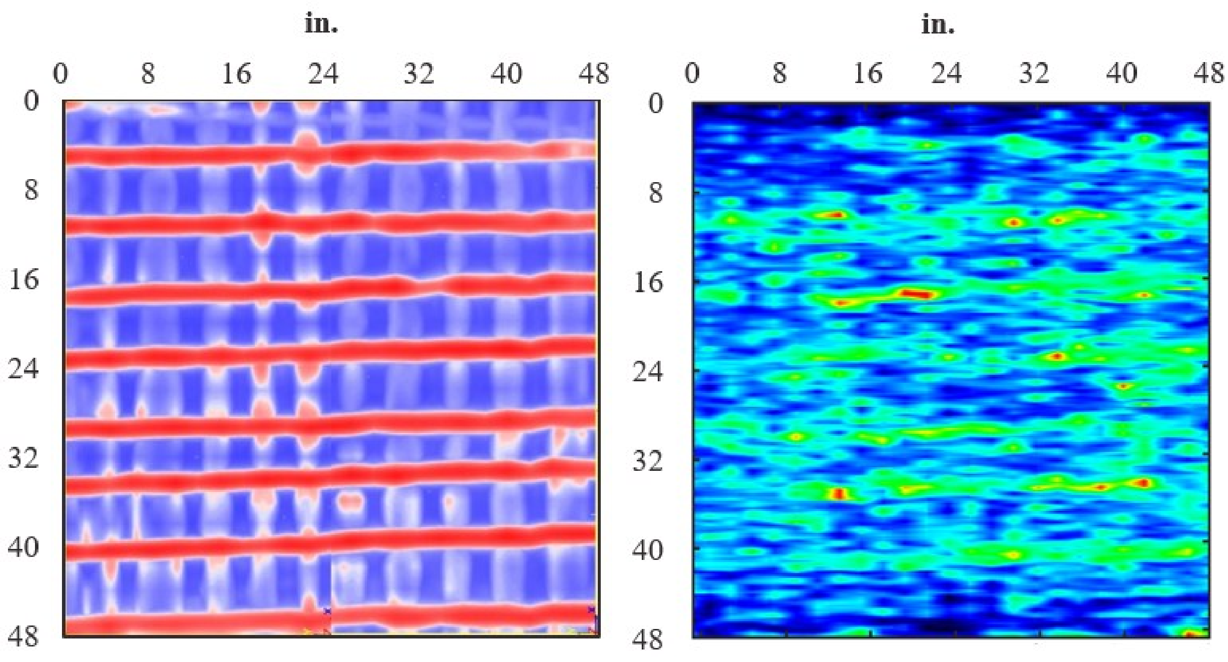

(a) (b)

Figure 4.51. LUB3 results for (a) GPR and (b) UST of top transverse reinforcement at depth 3.73 in.

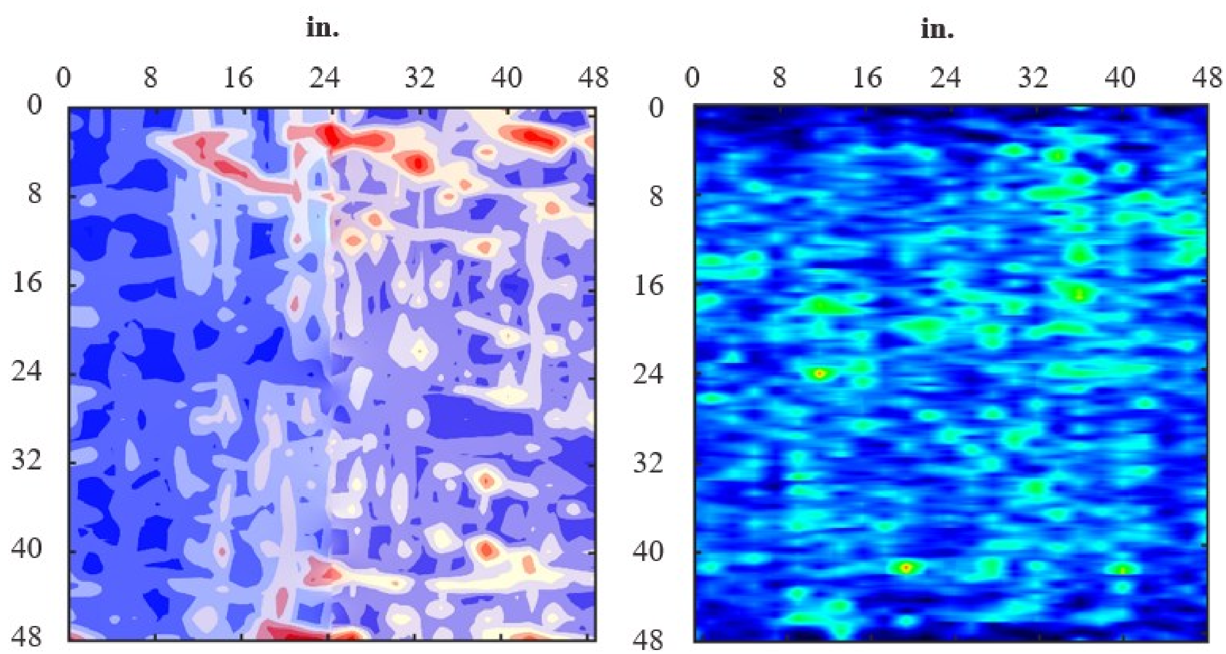

(a) (b)

Figure 4.52. LUB3 results for (a) GPR and (b) UST of the PCP end gap at depth 8.5 in.

4.4.8 Bridge LUB4 (Westbound [WB] Loop 289 over University Ave., Lubbock)

Bridge LUB4, shown in Figure 4.53, was built in 1992 and carries WB Loop 289 over University Ave. in Lubbock, Texas. The 57-ft 2-in. wide bridge has three lanes on eight Type C prestressed concrete I-girders spaced at 7.25 ft with 3.229-ft overhangs; a center barrier is shared with the adjacent bridge carrying eastbound lanes.

The bridge is 254 ft long and is made up of four simple spans forming one continuous deck unit, with three poor boy continuous deck regions providing deck continuity over interior supports. The two end spans are 65 ft, and the two interior spans are 62 ft. Expansion joints separate the unit from the abutment. The deck is shown as 7.5-in. thick CIP in the as-built drawings but was constructed with a PMDF. The deck reinforcement for both the top and bottom of the deck is specified as #4 @ 9 in. in the longitudinal direction and #4@ 9 in. in the transverse direction. Additional reinforcement is provided in the exterior overhangs. The as-built drawings do not indicate if the reinforcement details are different in the link slab region.

The inspection report for Bridge LUB4 indicated longitudinal and diagonal cracks in the deck, with additional transverse cracks along the construction joints, with efflorescence at the cracks. Minor rust was reported on the PMDF under the construction joints. The indicated damage resulted in an unadjusted PBJ rating of 2 and an age-adjusted rating of +0.375, indicating the bridge has a better performance than the average for bridges of similar age.

Visual inspection of the bridge confirmed the inspection report damage on the top of the deck; visual inspection below the bridge was not possible. The condition of all three continuous deck regions was similar. Figure 4.54 shows representative conditions of the link slab regions. The main PBJ crack had been formed as a construction joint, with the material no longer present. Considerable spalling was present along the main PBJ crack. Where measurable, the main crack was as wide at 0.030 in. Secondary PBJ cracks formed approximately 18 in. on either side of the main PBJ crack, measuring as wide as 0.025 in. in the NDE region. Outside the main NDE region, the secondary PBJ cracks were diagonal and joined with the main PBJ crack over the girder. Other cracks in the main NDE region measured no more than 0.01 in. except for one longitudinal crack outside the east secondary PBJ crack. Diagonal cracks were also present in the overhang, as shown in Figure 4.54(b).

Three NDE regions were investigated at Bent 3, shown in Figure 4.55, Figure 4.56, and Figure 4.57. The 4-ft by 4-ft primary region, shown in Figure 4.55, was located between G2 and G3 and was made up of two 2-ft by 4-ft grids centered on the main PBJ crack, with the 4-ft dimension parallel to the girders. Both GPR and UST were conducted in this region. Region 2, shown in Figure 4.56, was a 2-ft by 4-ft region centered on the main PBJ crack in the overhang. GPR was conducted in this region. Region 3, shown in Figure 4.57, is a smaller section of Region 2 and was used for conducting UST.

Figure 4.58, Figure 4.59, and Figure 4.60 show that the top and bottom longitudinal and transverse reinforcement appears to be spaced according to the design drawings. Figure 4.61 shows the PMDF at the bottom of the link slab. The longitudinal reinforcement spacing is consistent in the overhang, shown in Figure 4.62 and Figure 4.64. However, Figure 4.63 shows doubled transverse bars in the overhang, which is consistent with design drawings. The single rib of PMDF visible in Figure 4.65 indicates that the PMDF section directly below the PBJ is at a slightly different depth. No evidence of delaminations or voids was found in the IR images.

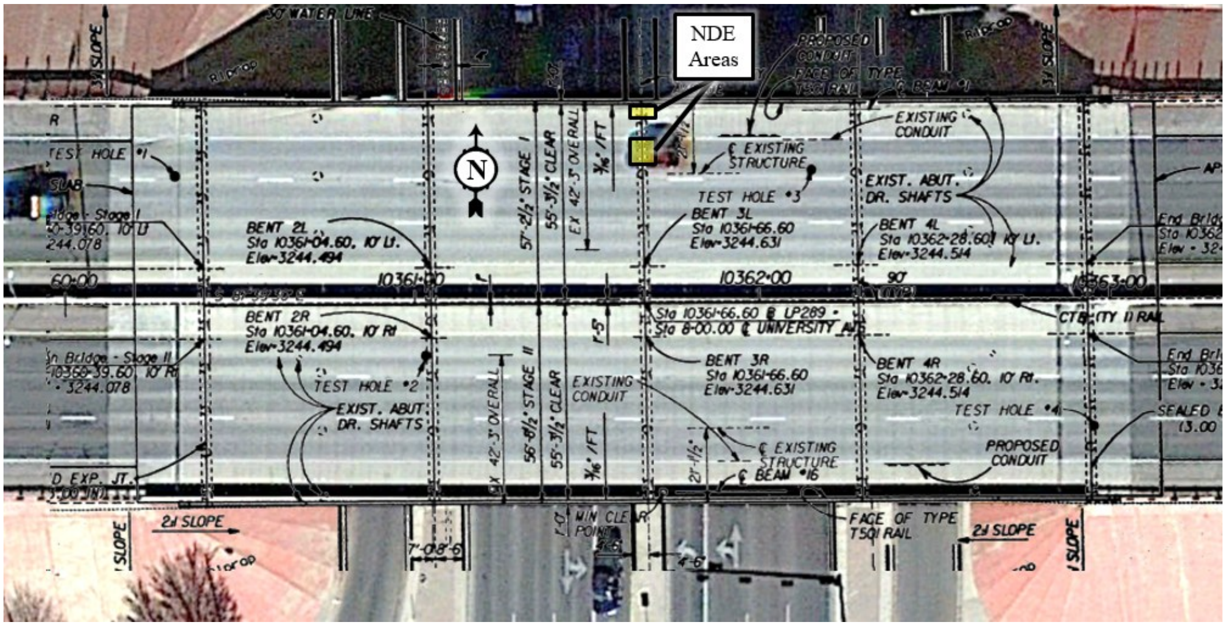

(a) Top view

(b) Elevation view

Figure 4.53. Site conditions at Bridge LUB4 (WB Loop 289 over University Ave.).

(a) CIP at continuous deck detail (b) Marked cracks in overhang

Figure 4.54. Typical link slab condition for Bridge LUB4 (WB Loop 289 over University Ave.).

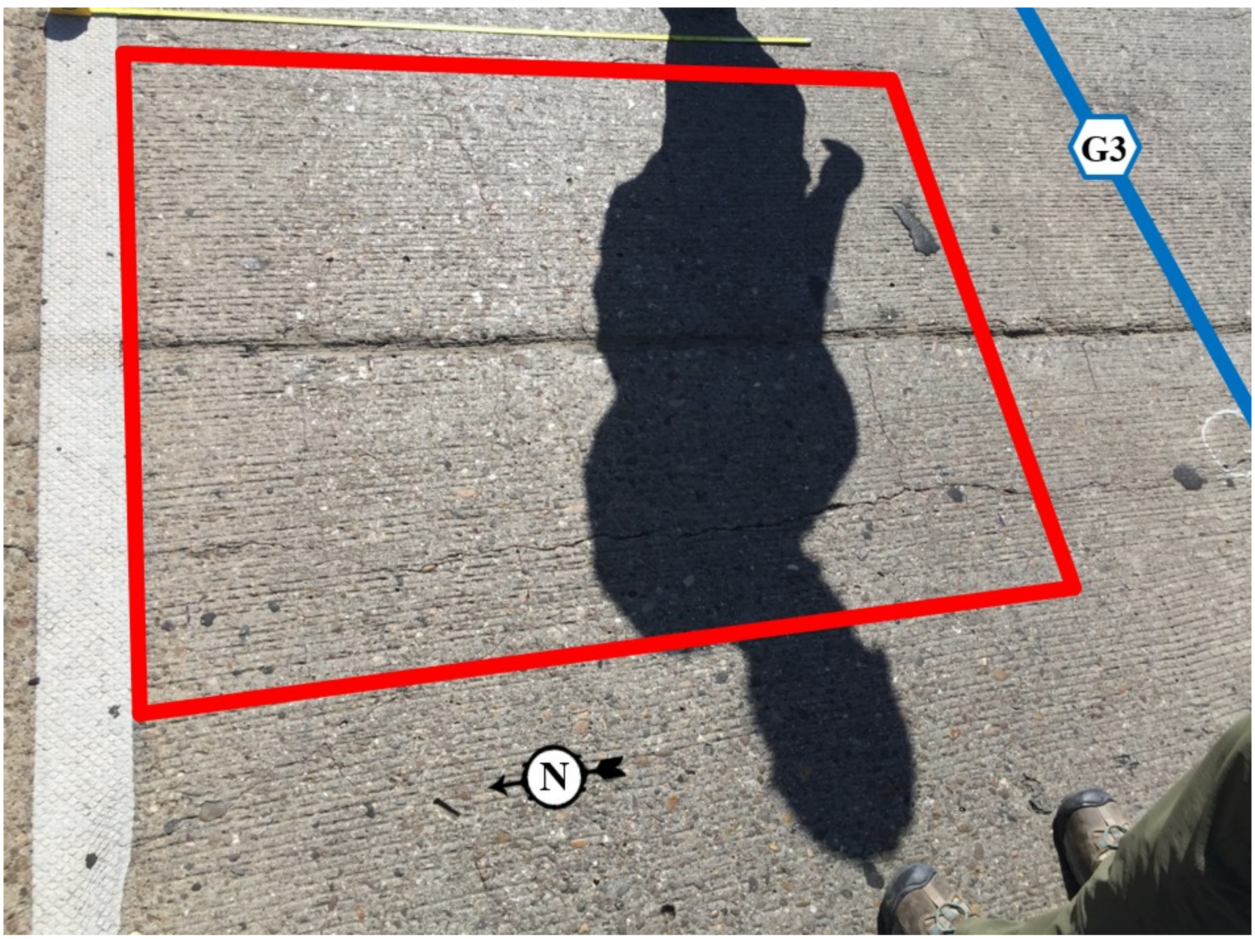

Figure 4.55. Primary NDE region at Bent 3 between G2 and G3 at Bridge LUB4 (WB Loop 289 over University Ave.).

Figure 4.56. Secondary NDE region for GPR at Bent 3 in the overhang at Bridge LUB4 (WB Loop 289 over University Ave.).

Figure 4.57. Secondary NDE region for UST at Bent 3 in the overhang at Bridge LUB4 (WB Loop 289 over University Ave.).

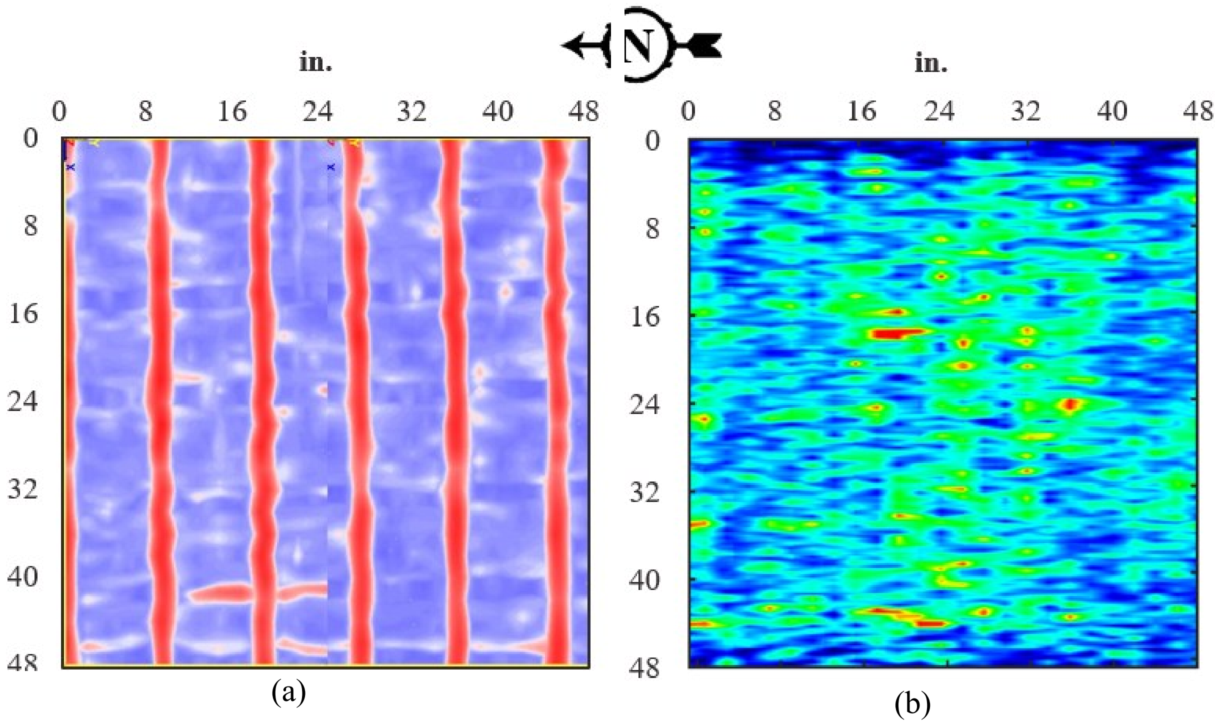

Figure 4.58. LUB4 results for the primary NDE area for (a) GPR and (b) UST of top longitudinal reinforcement at depth 2.73 in.

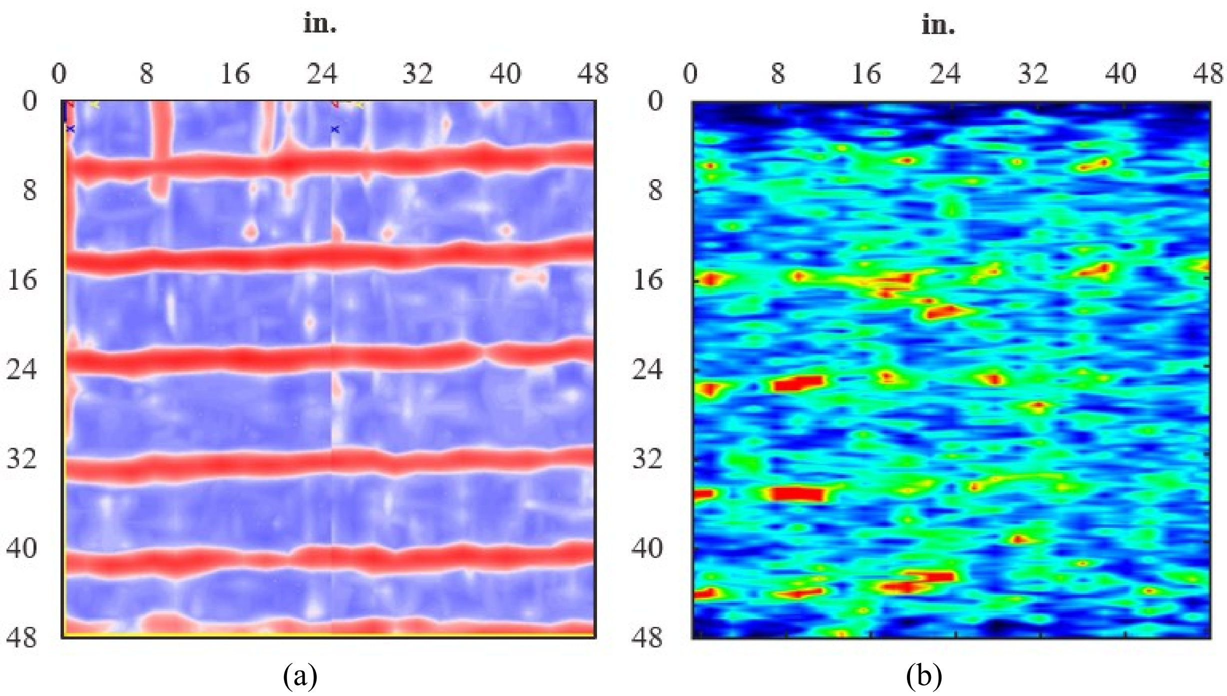

Figure 4.59. LUB4 results for the primary NDE area for (a) GPR and (b) UST of top transverse reinforcement at depth 3.5 in.

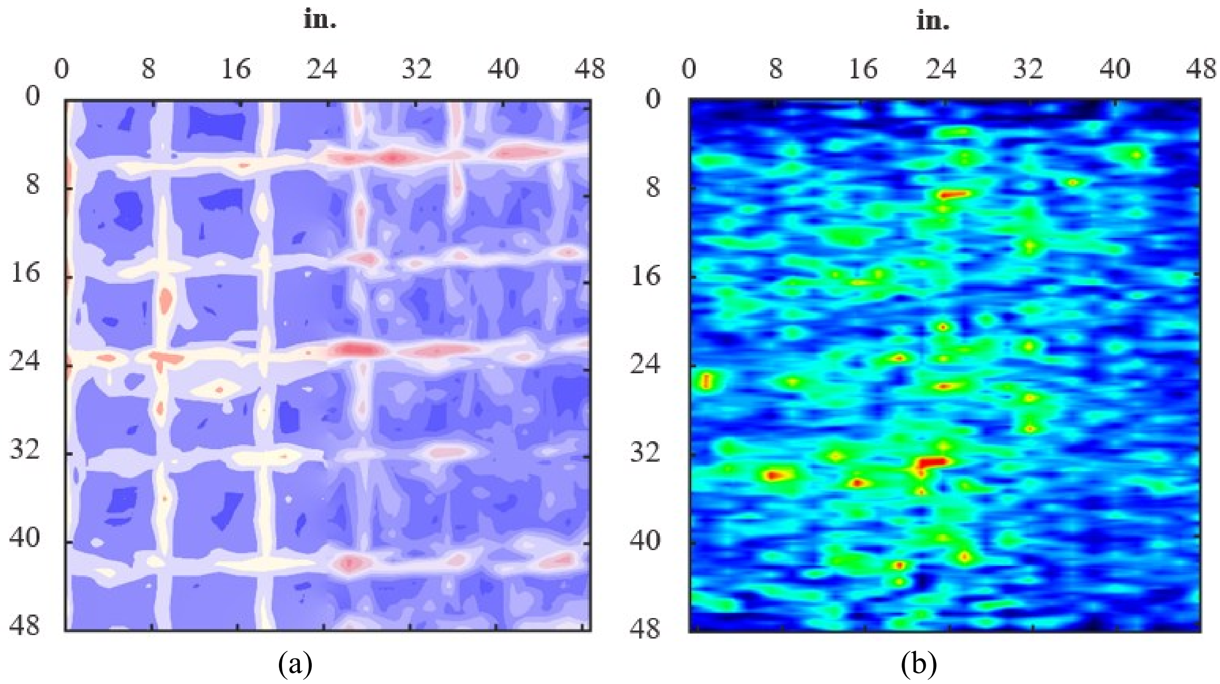

Figure 4.60. LUB4 results for the primary NDE area for (a) GPR and (b) UST of bottom reinforcement at depth 6.5 in.

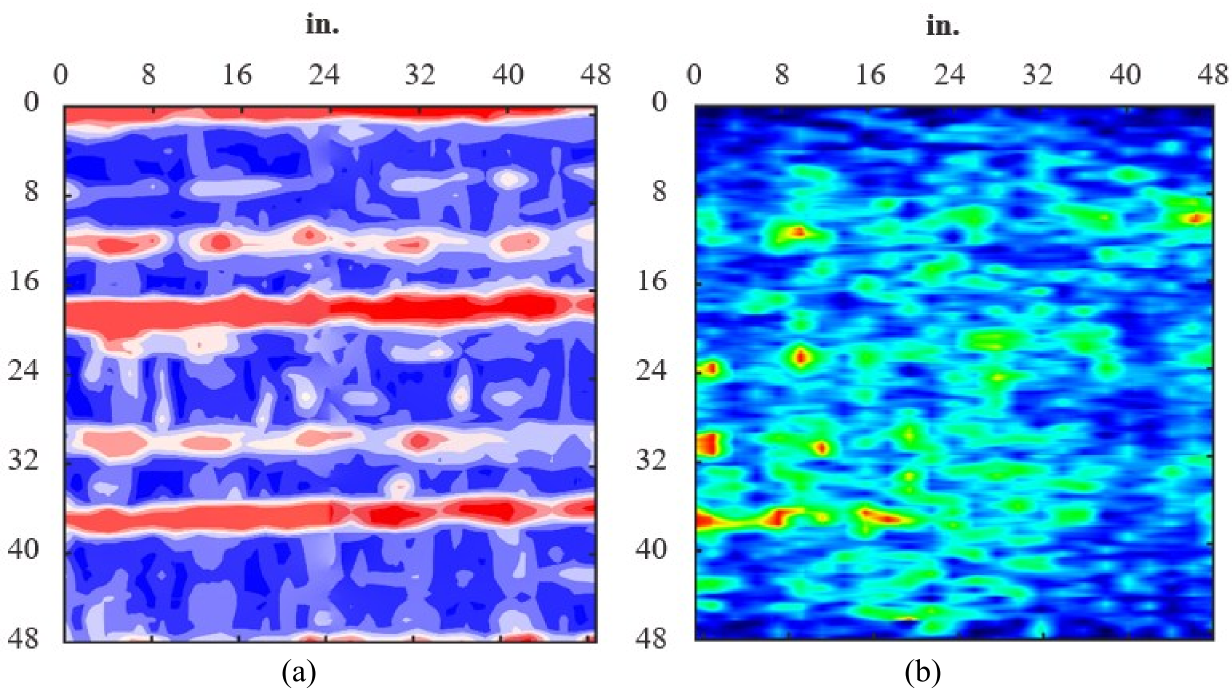

Figure 4.61. LUB4 results for the primary NDE area for (a) GPR and (b) UST of PMDF at depth 8.5 in.

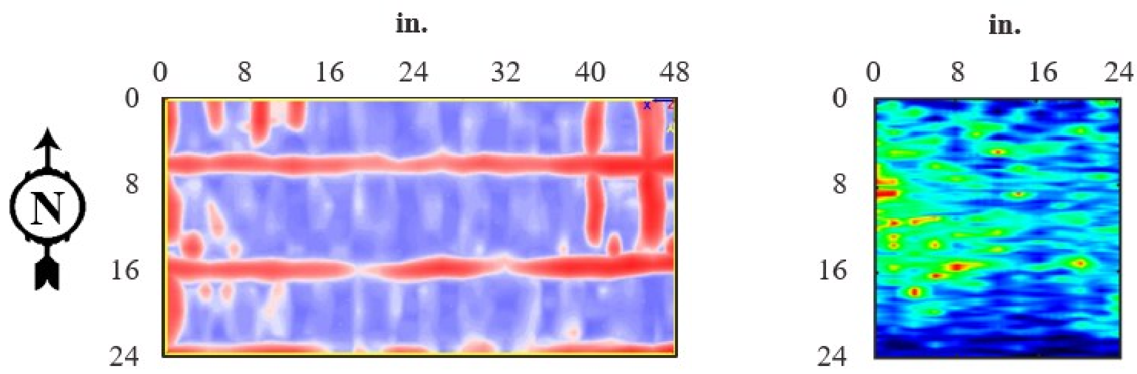

(a) (b)

Figure 4.62. LUB4 results for the secondary NDE area for (a) GPR and (b) UST of the top longitudinal reinforcement in the overhang at depth 2.73 in.

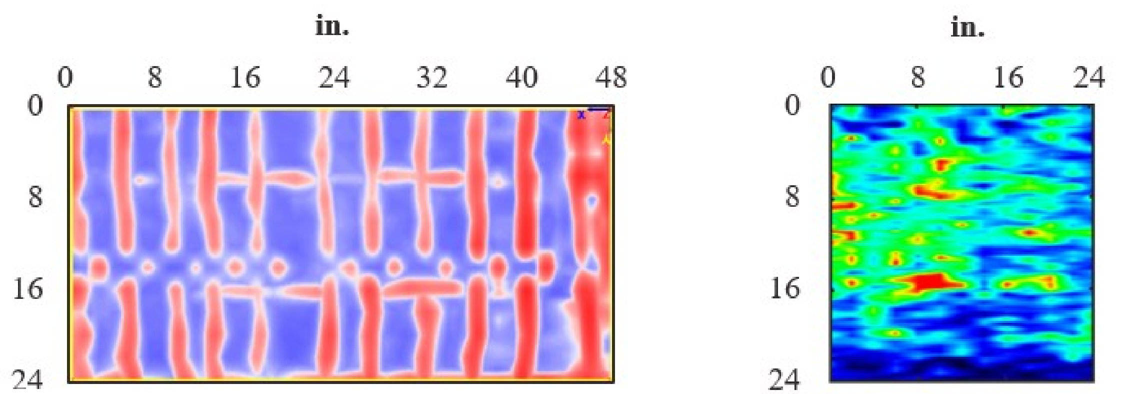

(a) (b)

Figure 4.63. LUB4 results for the secondary NDE area for (a) GPR and (b) UST of the top transverse reinforcement in the overhang at depth 3.48 in.

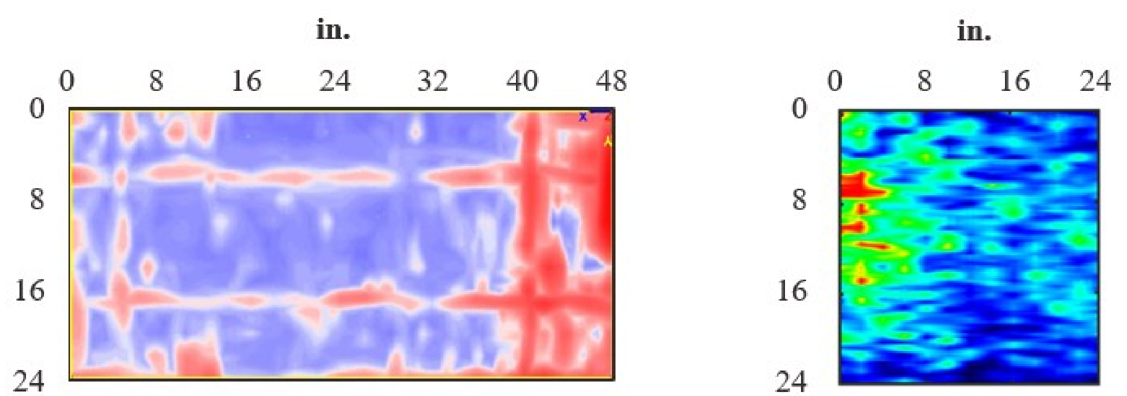

(a) (b)

Figure 4.64. LUB4 results for the secondary NDE area for (a) GPR and (b) UST of the bottom reinforcement in the overhang at depth 5.98 in.

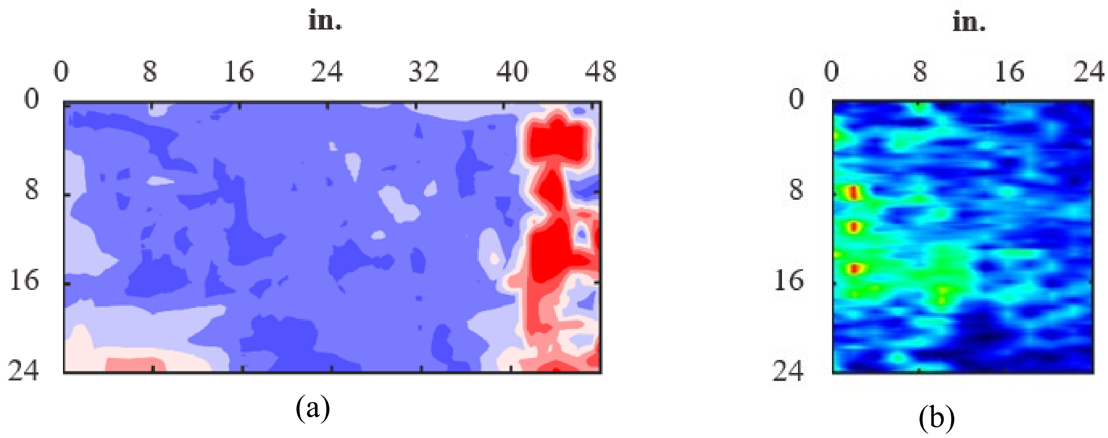

Figure 4.65. LUB4 results for the secondary NDE area for (a) GPR and (b) UST of the PMDF in the overhang at depth 8.5 in.

4.5 SUMMARY

This chapter provided a summary of visual inspections and findings from GPR, UST, and IR data for four bridges in the Atlanta District and four bridges in the Lubbock District. The processing of the data indicates that, while reinforcement placement was generally as indicated in design drawings, some bridges had reinforcement missing, spaced differently, or at different depths than designed. ATL4 did not appear to have bent bars in the PBJ region, and the depth of the reinforcement was different in the PBJ region. LUB3 showed doubled longitudinal reinforcement in the PBJ region. Bridges such as LUB4 with PMDF or ALT4 and ATL2 with offset PCPs had thicker decks at the PBJ than specified in design drawings. These observations are of value since the performance of the PBJ region may change with a thicker slab and increased or decreased reinforcement. Thickened slabs beneath the PBJ, which have been observed at bridges in the Bryan District as well, may be indicative of a misunderstanding of existing standard details.

UST images typically were less successful than GPR images at showing reinforcement locations and potential damage. Taking scans of each grid from a single direction rather than from two perpendicular directions allowed researchers to complete the testing in a timely manner but may have decreased the clarity of the results. Each bridge had grooved pavement surfaces with embedded debris that are known to prevent optimal contact between the deck and transducers of the UST array. However, UST images were useful in indicating the locations of girder edges and PMDFs. While IR images did not reveal delaminations or voids, visual analysis of the deck with IR imaging is dependent upon factors such as weather conditions, existing thermal conditions, sunlight exposure, and grooved pavement. It is possible that unfavorable conditions for IR camera use prevented finding damage.

One observation made during the documentation of the visual inspections is that the PBJ ratings developed from inspection reports are not necessarily an accurate representation, and some ratings would be different after an in-person inspection. For example, ATL2 had a lower rating than ATL1 based on inspection reports indicating that ATL2 had efflorescence and larger cracks than ATL1, when in fact the cracks were smaller. Overall, the inspection reports did not provide a good indication of the extent of cracking in relation to the continuous slab detail. Cracks were simply labeled as transverse or longitudinal, and it was not clear if it was general cracking, a main PBJ if not intentionally formed, or if secondary PBJ cracks had formed. Another limiting factor of the PBJ ratings is the broad definitions of widths used in the inspection reports (i.e., specified as < ⅛ in., but was actually < 1⁄64 in., as indicated in other decks).

Table 4.4 provides a summary of key characteristics from visual inspection of the continuous deck details that were not easily determined from as-built drawings and inspection reports and are useful to evaluating the performance of different details. The information in the table includes maximum crack width, how the main PBJ crack was formed, if spalling was present along the main crack, and if secondary PBJ cracks were present. The maximum crack widths are for either the main or secondary PBJ cracks, whichever is largest; other crack widths are not summarized.

Table 4.4. Location of bridges for nondestructive evaluation.

Bridge No.	Max PBJ Crack Width, in.	Control Joint for Main PBJ Crack	Spalling along Main PBJ Crack	Secondary PBJ Cracks
ATL1	0.016	Yes	Minor	Yes
ATL2	0.008	Yes	Minor	No
ATL3	0.025	Yes	Moderate	Yes
ATL4	0.007	Yes	Very Minor	Yes
LUB1	0.030	No	Minor	No
LUB2	0.030	Yes	Moderate	Yes (Inv-T)
LUB3	0.025	Yes	No	No
LUB4	0.030	Yes	Moderate	Yes

Three bridges (ATL2, LUB1, and LUB3) did not have secondary PBJ cracks. These bridges had flush or offset PCPs. In terms of trends related to whether or not secondary cracks were present, it appears that the secondary cracks formed in all offset PCP bridges where PMDF was used in the CIP region. ATL2 had CIP regions that used removable formwork; however, it is not possible to conclude that the PMDF directly resulted in the secondary cracks because ATL4 had secondary cracks with CIP with removable formwork, although the CIP region was notably shorter than that in other bridges, so the secondary cracks may be more a function of the length of the CIP region. The two bridges with flush PCP details (LUB1 and LUB3) did not have secondary PBJ cracks form, but it is worth noting that the measured crack widths were among the widest measured, although other bridges in the same district had widths that were similar widths, despite also have secondary cracks.

In decks with PCPs, either flush or offset, any secondary PBJ cracks formed at a consistent distance from the main PBJ crack. In bridges with PMDF and square bent caps (LUB4 and ATL3), the secondary cracks were farther from the main crack between the girders. Closer to the girders, the secondary cracks were spaced more closely, or in the case of LUB4, joined with the main crack. The widths of the secondary cracks were smaller at/near the girders and widest near the center of the deck between girders.

A comparison of LUB1 and LUB3 is interesting because they both have flush panels with the same depth of deck, but LUB3 has a much better rating than LUB1, which is confirmed with field evaluations. While the better bridge is much newer, there is still a notable difference when adjusting for age. The better condition of the PBJ region is consistent with the better overall condition of the deck, so it is difficult to know if it is more an issue of concrete quality or if LUB3 may deteriorate at a rapid rate. While both have flush PCPs at the PBJs, LUB3 has closer spacing of longitudinal reinforcement. Additionally, there are other structural characteristics that differ in the two bridges, with different girder sizes, span lengths, and overall length of continuous deck units.

5. MONITORING

Field monitoring of bridges representing common characteristics of TxDOT PBJs was conducted, with the objective of establishing the characteristics of the deformations due to live and thermal loads. At select locations in each bridge, instruments were attached to measure the relative deformation between girders, which was in turn used to establish the rotation demands and effective lengths of the link slab.

This chapter presents the details of the field monitoring. Section 5.1 provides an overview of the bridges monitored, and Section 5.2 provides details on the instrumentation of the bridges. The results from each bridge are presented in Section 5.3. Section 5.4 provides an analysis of the collected data, and Section 5.5 provides a summary and conclusions for this part of the study.

5.1 OVERVIEW OF BRIDGES

Table 5.1 provides location information on the bridges selected for response monitoring; locations are shown in Figure 5.1. Bridges were selected to provide measured responses for bridges with different link slab types, different girder types, and different skews. Characteristics of the bridges are summarized in Table 5.2. Details of the link slabs are provided in Table 5.3.

Table 5.1. Location of bridges for response monitoring.

Bridge No.	NBI Bridge ID	Description	Coordinates
BRY1	17-021-00050-02-135	SH 6 over Peach Cr., Millican	30.512610, −96.206461
BRY2	17-026-00648-03-020	Eastbound FM 60 over Old River, Snook	30.509512, −96.470340
BRY3	17-021-00117-02-046	Eastbound SH 21/ US 190 over Old Cedar Cr., Kurten	30.835810, −96.216628
BRY4	17-094-0-0643-05-067	FM 3090 at Spring/Holland Relief, Navasota	30.435992, −96.062868
BRY5	17-021-00050-02-182	SH 6 over Nantucket Dr., College Station	30.543552, −96.241862

Table 5.2. General characteristics of bridges for response monitoring.

Bridge No.	Year Built	ADT	Skew	Bent Cap Type	Girder Type	Number Girders	Girder Spacing (ft)	Overhang Length (ft)	Deck Details	Deck Reinforcement
BRY1	1996	36,468	15	CIP	C (40″)	14	6.77	3.0	4″ PCP & 3.25″ CIP	Black
BRY2	2010	3400	30	CIP	C (40″)	5	8.5	3.0	4″ PCP & 4″ CIP	Black
BRY3	2013	7900	0	CIP	B (34″)	5	8.5	3.0	4″ PCP & 4″ CIP	Black
BRY4	2017	5387	0	CIP	Tx28	4	9.33	3.0	4″ PCP & 4″ CIP	Black
BRY5	2006	37,905	0	CIP	IV (54″)	11	8.8	3.0	4″ PCP & 4″ CIP	Black

Table 5.3. General characteristics of link slabs of bridges for response monitoring.

Bridge ID	PBJ Type	Number Consecutive PBJs	Continuous Deck Length, ft
BRY1	Offset PCP	2	255
BRY2	Offset PCP	2	240
BRY3	Flush PCP	2	150
BRY4	Offset PCP	2	195
BRY5	PMDF	2	325

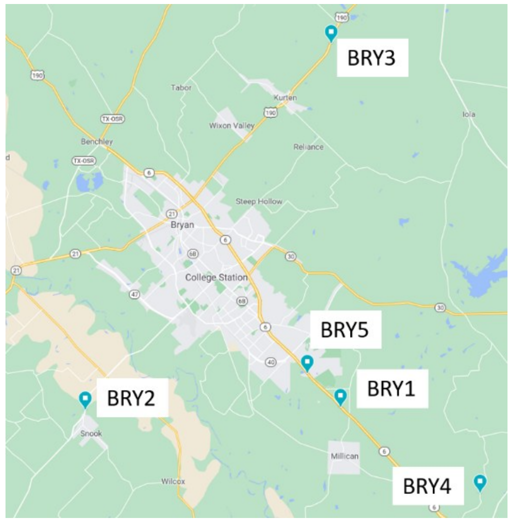

Figure 5.1. Locations of bridges for response monitoring (from Google Earth).

5.2 OVERVIEW OF INSTRUMENTATION AND DATA COLLECTED

The bridges were instrumented at the girder ends, and in some cases the bottom of the deck in the link slab region, to measure the movement under ambient traffic and temperature loads.

Figure 5.2 shows the general configuration of instrumentation for the bridges. Figure 5.3 shows an example of instruments attached in the field. Vibrating wire strain gages, indicated by diamonds on the instrumentation plans, were placed on the bottom of the deck spanning the location (or presumed location) of the main PBJ crack. Pairs of VW displacement gages, indicated by triangles on the instrumentation plans, were located at the top and bottom of the girders to capture the relative displacement between the girders ends at the bents, or the girder end relative to the abutment. Each sensor included a thermistor to measure temperatures. The pairs of displacement gages were used to calculate the relative rotation. Generally, these pairs were provided at the PBJs (referred to as PBJ pairs), but on some bridges were also provided at SEJs (referred to as SEJ pairs) to provide a comparison between the response at the two joint types. Where pairs were installed at PBJs, 1-in. stroke length gages were used; 4-in. stroke length gages were used at SEJs. At the abutments, 4-in. stroke gages were located on the bottom flange to capture the full change in length of the girders under thermal loads.

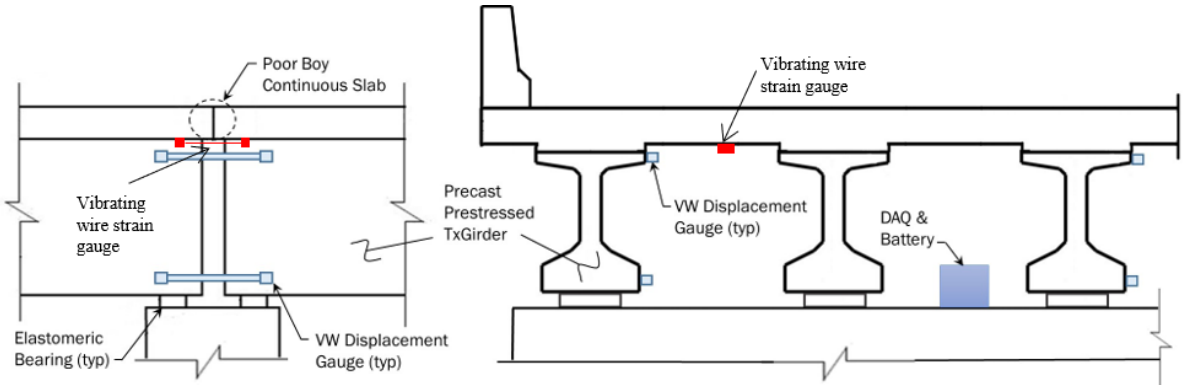

Figure 5.2. General layout of instrumentation at girder ends.

(a) Interior bent (b) At abutment

Figure 5.3. Example of gage attachment (shown installed on Bridge BRY3).

Instrumentation was left installed for approximately seven days, with the actual duration governed by weather and other schedule constraints. Thermal data were collected once per minute. To confirm temperature readings of the instrumentation, infrared thermography was utilized at some bridges. Comparisons of temperatures confirmed that the VW gages provided reasonable readings.

Live load events were recorded when a five-second moving average of displacement produced a change in excess of a specified threshold. Once triggered, the data were collected at a rate of 50 Hz. To verify accurate capture of the live load events, a limited time range of videos was taken of traffic crossing the bridge and synced to the recorded data.

The data from the displacement gages were used to calculate the rotation at the ends of the girders. Figure 5.4 shows the notation used for the calculations.

The rotation of a single girder end, θ, was calculated as:

$$\theta = \sin^{-1}\left(\frac{0.5(L_{top} - L_{bot}}{L_{vg}}\right) \tag{5.1}$$

where L_{top} is the length of the top gage, L_{bot} is the length of the bottom gage, and L_{vg} is the vertical distance between gage ends.

The rotation presented is for a single girder end, with the assumption made that the total rotation between two girders is split evenly between the connected girders. Figure 5.5 shows the sign convention used. Positive angles are based on positive bending in the girders and are associated with a concave down configuration of the link slab. Negative angles are based on positive bending in the girders and are associated with a concave up configuration of the link slab.

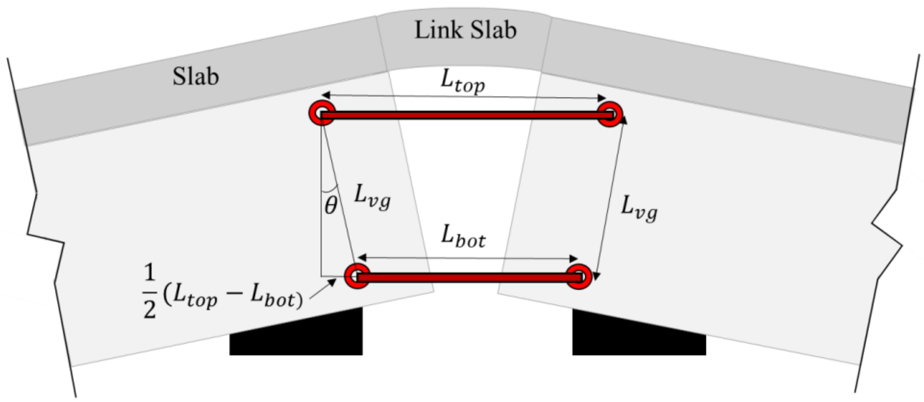

Figure 5.4. Variables used for the calculation of girder end rotations from displacement gages.

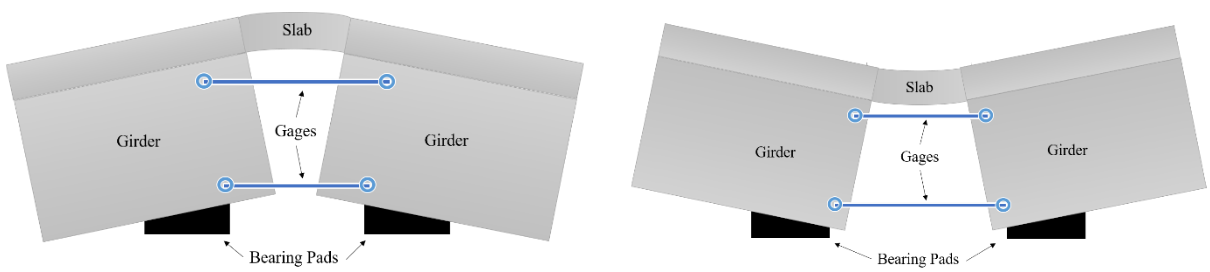

(a) Positive bending (b) Negative bending

Figure 5.5. Sign convention for rotations.

5.3 MONITORING DETAILS FOR BRIDGES

Details of each bridge, including photographs and instrumentation plans, are provided in the following subsections. A summary of the data for all bridges is provided in Section 5.4.

5.3.1 BRY1 (SH 6 over Peach Creek, Millican)

Bridge BRY1, shown in Figure 5.6, was built in 1996 and carries SH 6 over Peach Creek near Millican, Texas. The 94-ft wide bridge has four lanes with a median on 14 Type C prestressed concrete I-girders at 6.769-ft spacing with 3-ft overhangs. The bridge has a constant skew of

15 degrees. The bridge was built in two stages, with Stage I consisting of the southbound lanes and Stage 2 carrying the northbound lanes and median.

The bridge is 425 ft long and is made up of five simple spans forming three continuous deck units. Unit 1 and Unit 3 are single 85-ft spans. Unit 2 has three equal 85-ft spans. The deck is 7.25 in. thick, made up of 4-in. PCPs with a 3.25-in. thick CIP top. At PBJ joints, the link slab is fully CIP and is thicker than the adjacent deck. The thickened slab appeared to be implementation of the SEJ thickened slab detail at the PBJ. Overhangs are fully CIP.

Figure 5.7 shows the instrumentation plan for Bridge BRY1. The primary location of monitoring was at the continuous deck over Bent (B) 4. PBJ pairs of gages were installed at the top and bottom flange of girder lines G1 (west exterior), G5 (under southbound lanes), and G10 (under northbound lanes). Strain gages were placed on the bottom of the deck on the exterior side of G5 and G8. SEJ pairs of gages were installed on the top and bottom flanges of girder lines G1, G5, and G7 at B5 and G5 at the south abutment (B6 Abut.). Instrumentation was installed on June 8, 2020, and remained in place until June 15, 2020.

(a) Elevation view of bridge

(b) View beneath bridge

(c) Close-up at PBJ

(d) Close-up at SEJ

Figure 5.6. Overview of Bridge BRY1 (SH 6 over Peach Creek).

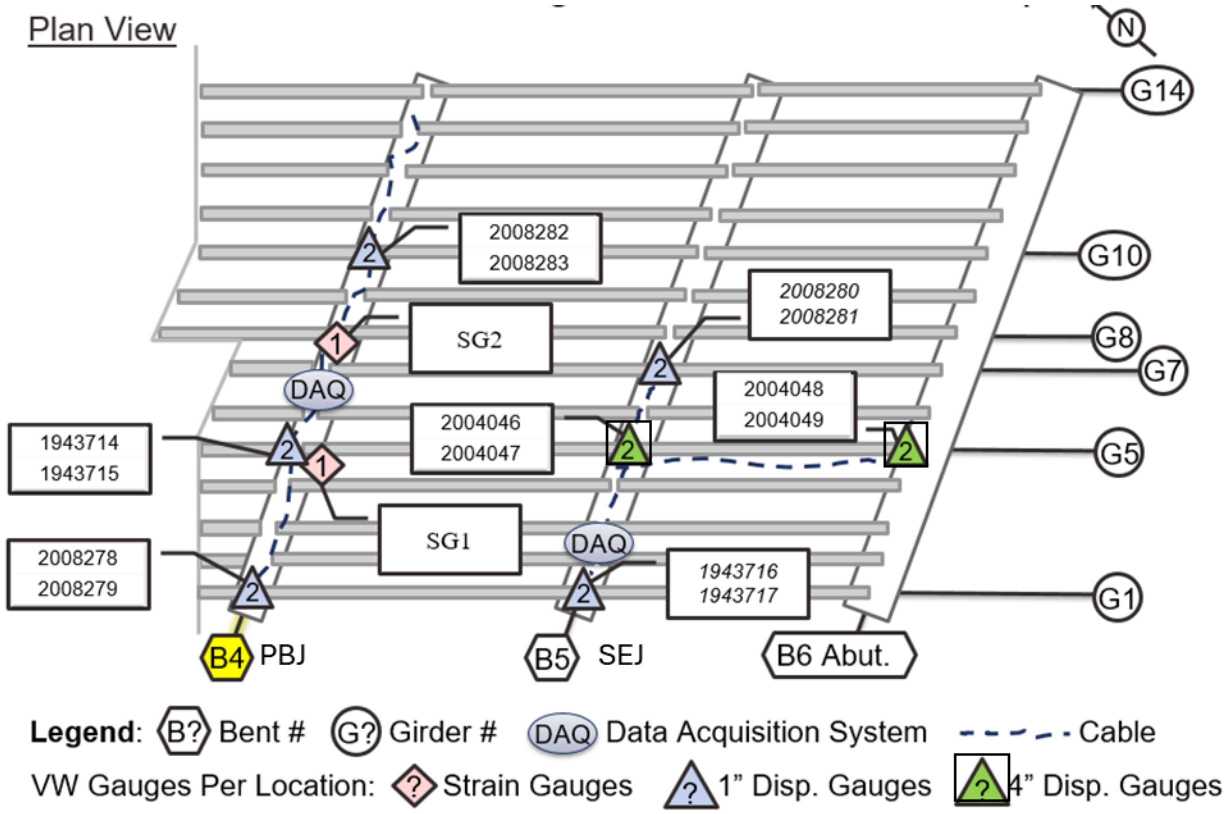

Figure 5.7. Instrumentation plan for Bridge BRY1 (SH 6 over Peach Creek).

5.3.2 BRY2 (FM 60 over Old River, Snook)

Bridge BRY2, shown in Figure 5.8, was built in 2010 and carries eastbound FM 60 over Old River near Snook, Texas. The 40-ft wide bridge has two lanes on five Type C prestressed concrete I-girders spaced at 8 ft 6 in. with 3-ft 0-in. overhangs. The bridge has a constant skew of 30 degrees.

The bridge is 400 ft long and is made up of five simple spans forming two continuous deck units. Unit 1 is three equal 80-ft spans, and Unit 2 is two equal 80-ft spans. The deck is 8 in. thick, made up of 4-in. thick PCPs with a 4-in. thick CIP top. At PBJ joints, the link slab region uses standard TxDOT details dated April 2006, which specify that the link slab should extend a minimum of 1 ft 6 in. beyond the end of the girder; visual inspection during the field visit indicated the slab was slightly thicker than the adjacent deck. PBJ top reinforcement is assumed the same as the adjacent deck. Bottom reinforcement is assumed to be #5 @ 6 in. in the transverse direction and #5 @ 9 in. in the longitudinal direction.

Figure 5.9 shows the instrumentation plan for Bridge BRY2. The primary location of monitoring is at the continuous deck over B3 (part of the three-span Unit 1). PBJ pairs of gages were installed at the top and bottom flange of both outer girder lines (G1 and G5) and the center girder line (G3). Strain gages were placed on the bottom of the deck between G2–G3 and G4–G5. The outer girder lines were also instrumented with PBJ pairs of gages at B5 (part of the two-span Unit 2). SEJ pairs of gages were installed at the top and bottom flange of the center girder line (G3) at B4 and the north abutment (B6 Abut.). Instrumentation was installed on June 18, 2020, and remained in place until June 25, 2020.

(a) Elevation view of bridge

(b) View beneath bridge

(c) Close-up at PBJ

(d) Close-up at SEJ

Figure 5.8. Overview of Bridge BRY2 (FM 60 over Old River).

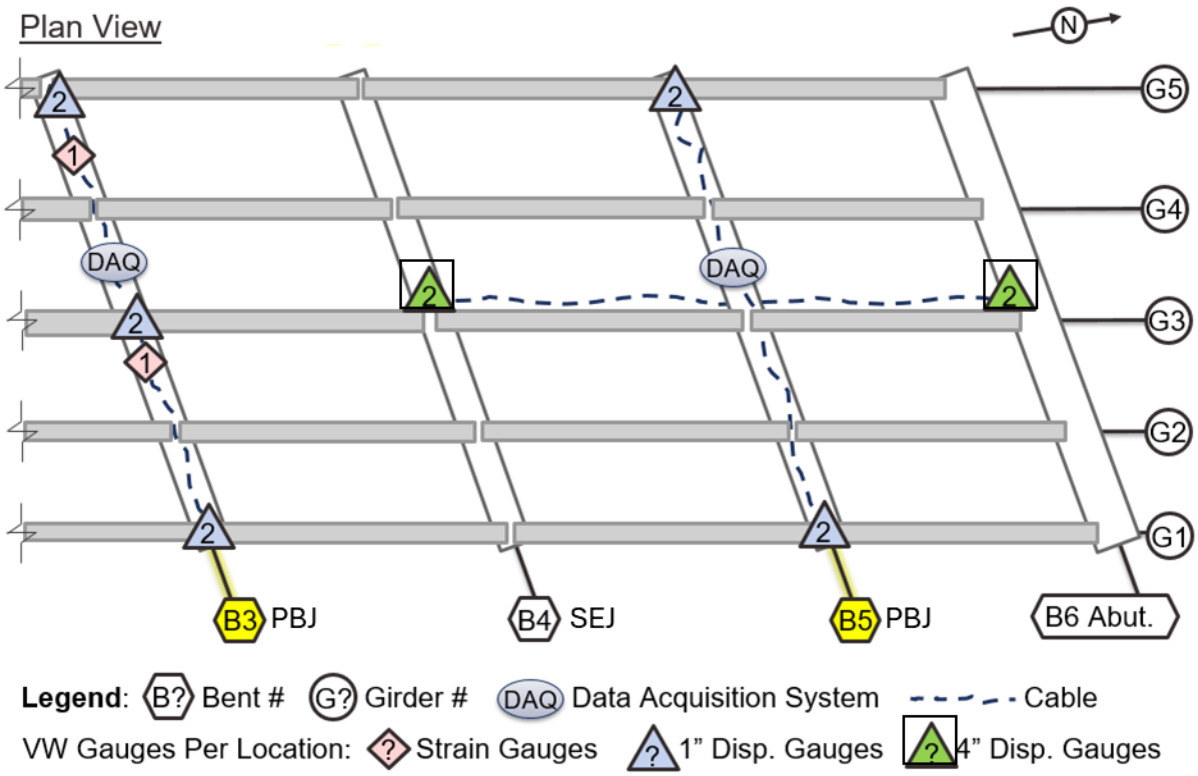

Figure 5.9. Instrumentation plan for Bridge BRY2 (FM 60 over Old River).

5.3.3 BRY3 (SH 21/US 190 over Old Cedar Creek, Kurten)

Bridge BRY3, shown in Figure 5.10, was built in 2013 and carries eastbound SH 21 over Old Cedar Creek near Kurten, Texas. The 40-ft wide bridge has two lanes on five Type B prestressed concrete I-girders spaced at 8 ft 6 in. with 3-ft 0-in. overhangs.

The bridge is 350 ft long and is made up of seven simple spans forming three continuous deck units. Unit 1 is two equal 50-ft spans, Unit 2 is three equal 50-ft spans, and Unit 3 is two equal 50-ft spans. The deck is 8 in. thick, made up of 4-in. thick PCPs with a 4-in. CIP top. At PBJ joints, flush PCPs are used. As-built drawings do not provide the details used; it is assumed that the top deck reinforcement in the link slab is the same as that in the decks.

Figure 5.11 shows the instrumentation plan for Bridge BRY3. The primary locations of monitoring were at the continuous deck over B5 and B7 (part of the three-span Unit 2 and the two-span Unit 3). Instrumentation was identical at these bents, with PBJ pairs of gages installed at the top and bottom flange of girder lines G3 (center) and G5 (east exterior). Strain gages were located at the bottom of the deck adjacent to the interior side of G5 and the east side of G3. SEJ pairs of gages were installed at the top and bottom flange of the center girder line (G3) at B6 (between Unit 2 and Unit 3) and abutment at the north end of Unit 3 (B8 Abut.). Instrumentation was installed on July 21, 2020, and remained in place until July 30, 2020.

(a) Elevation view of bridge

(b) View beneath bridge

(c) Close-up at PBJ

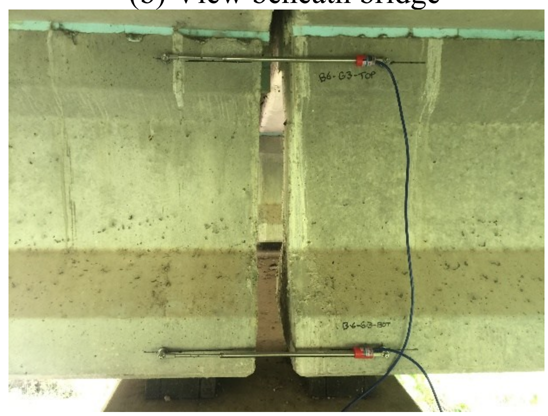

(d) Close-up at SEJ

Figure 5.10. Overview of Bridge BRY3 (SH 21/US 190 over Old Cedar Creek).

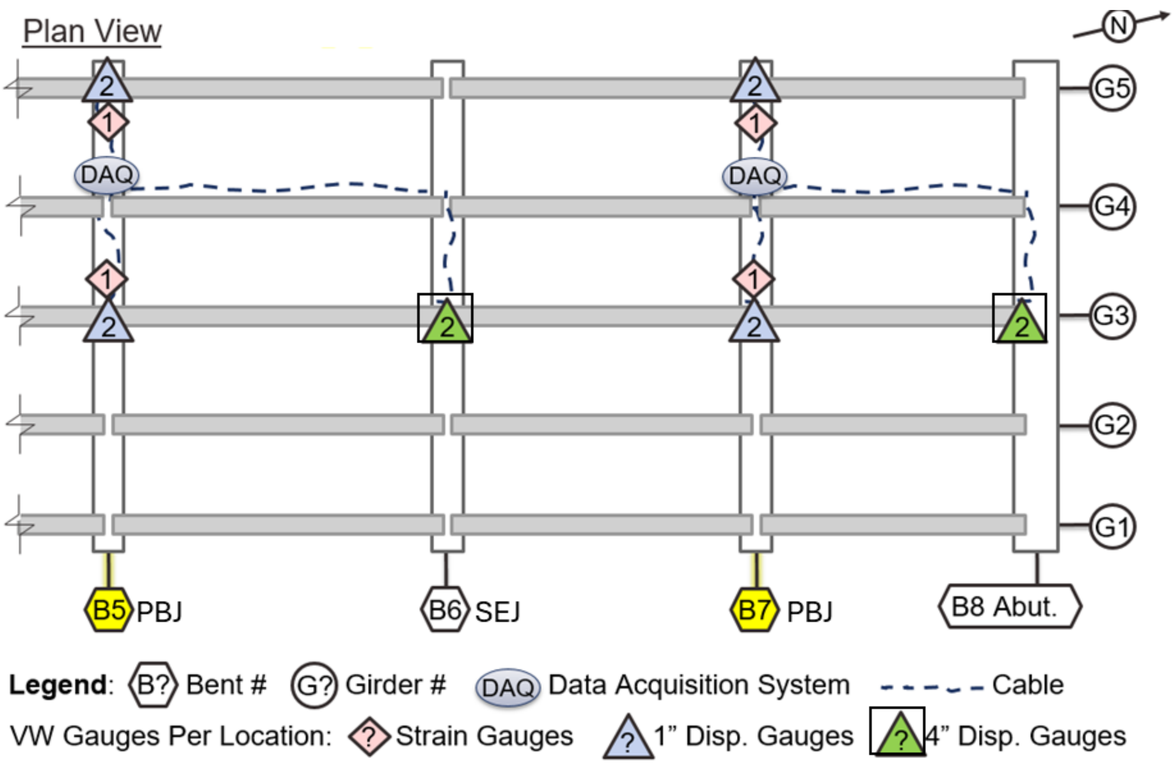

Figure 5.11. Instrumentation plan for Bridge BRY3 (SH 21/US 190 over Old Cedar Creek).

5.3.4 BRY4 (FM 3090 at Spring/Holland Relief, Navasota)

Bridge BRY4, shown in Figure 5.12, was built in 2017 and carries FM 3090 over a relief area for Spring Creek and Holland Creek near Navasota, Texas. The 34-ft wide bridge has two lanes on four Tx28 prestressed concrete I-girders at 9-ft 4-in. spacing with 3-ft 0-in. overhangs.

The bridge is 195 ft long and is made up of three 65-ft long simple spans forming one continuous deck unit. The deck is 8 in. thick, made up of 4-in. thick PCPs with a 4-in. CIP top. At PBJs, fully CIP link slabs are used; while the as-builts do not include the details used, from the age of the bridge, it is assumed that details similar to those in Bridge BRY2 were used. PBJ top reinforcement is assumed the same as the adjacent deck. Bottom reinforcement is assumed to be #5 @ 6 in. in the transverse direction and #5 @ 9 in. in the longitudinal direction.

Figure 5.13 shows the instrumentation plan for Bridge BRY4. With the bridge being only three spans and having no skew, instrumentation was installed at all bents and abutments. PBJ pairs of gages were installed on the top and bottom flanges of girder lines G3 (interior) and G4 (east exterior). SEJ pairs of gages were installed at the abutments (B1 Abut. and B4 Abut.) on girder line G3. At both interior bents, strain gages were installed on the interior side of girder lines G3 and G4. Instrumentation was installed on September 10, 2020, and remained in place until September 18, 2020.

(a) Elevation view of bridge

(b) View beneath bridge

Figure 5.12. Overview of Bridge BRY4 (FM 3090 at Spring/Holland Relief).

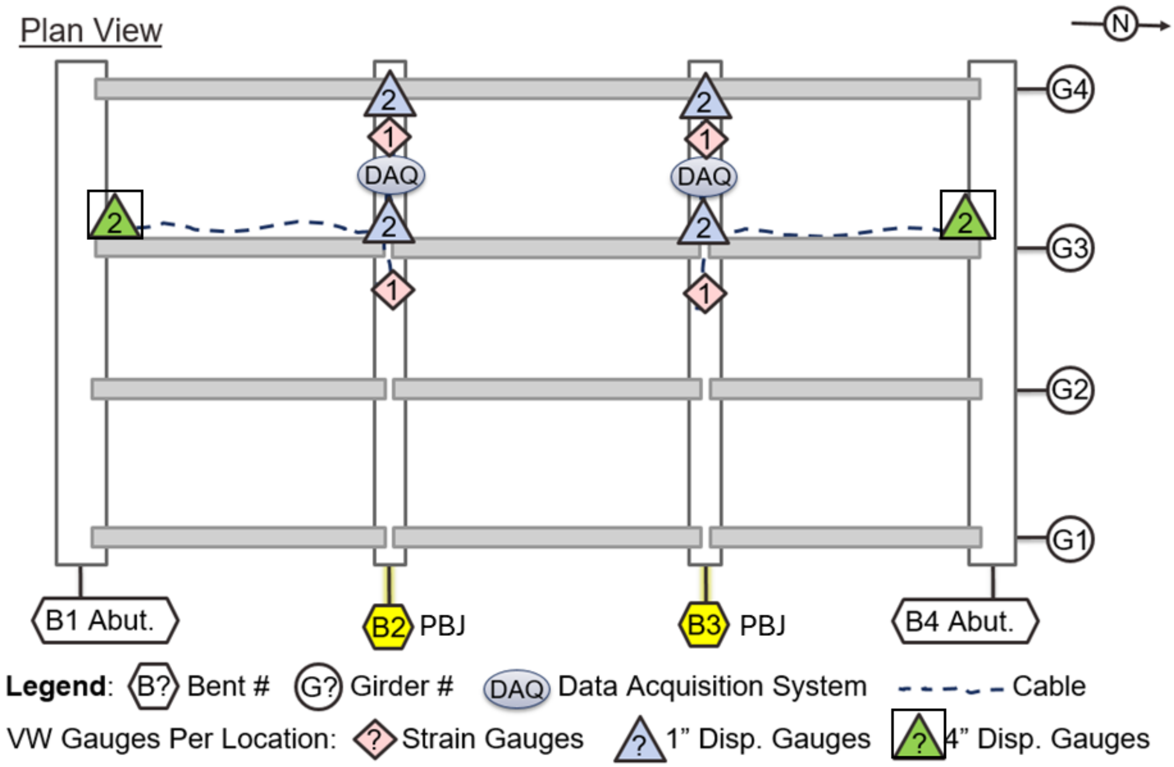

Figure 5.13. Instrumentation plan for Bridge BRY4 (FM 3090 at Spring/Holland Relief).

5.3.5 BRY5 (SH 6 over Nantucket, College Station)

Bridge BRY5, shown in Figure 5.14, was built in 2006 and carries SH 6 over Nantucket Dr. near College Station, Texas. The 94-ft wide bridge has four lanes on 11 Type IV prestressed concrete I-girders at 8.8-ft spacing with 3-ft overhangs.

The bridge is 795 ft long and is made up of eight simple spans forming three continuous deck units. Unit 1 is one 115-ft span and two 105-ft spans, Unit 2 is three equal 105-ft spans, and Unit 3 consists of a 90-ft span and a 65-ft span. The deck is 8 in. thick made up of 4-in. thick PCPs with a 4-in. thick CIP top. At PBJ joints, the link slab region is full-depth CIP on PMDF. PBJ top reinforcement is assumed to be the same as the adjacent deck. Bottom reinforcement is assumed be #5 @ 6 in. in the transverse direction and #5 @ 9 in. in the longitudinal direction.

Figure 5.15 shows the instrumentation plan for Bridge BRY5. Monitoring was limited relative to the other bridges since the primary objective was to capture deformations in a bridge with PMDF detail. The primary location of monitoring was at the continuous deck over B5 (part of the three-span Unit 2). PBJ pairs of gages were installed at the top and bottom flange of an outer girder line (G11) and an interior girder line (G9). Strain gages were placed on the bottom of the deck in the overhang because this was the only location where it was practical to attach the gage since between girders had PMDF. An SEJ pair of gages was installed at the top and bottom flange of interior girder line (G9) at B4.

(a) Elevation view of bridge

(b) Close-up at PBJ

Figure 5.14. Overview of Bridge BRY5 (SH 6 over Nantucket Dr.).

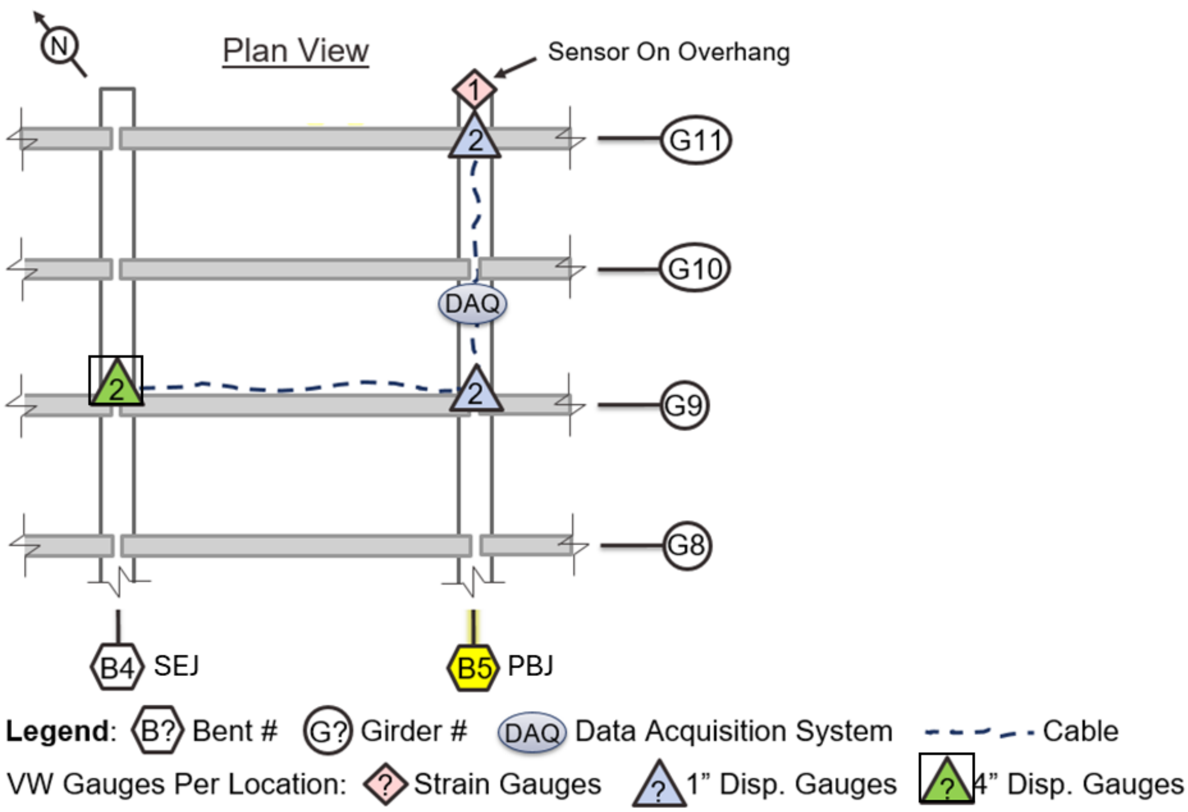

Figure 5.15. Instrumentation plan for Bridge BRY5 (SH 6 over Nantucket Dr.).

5.4 ANALYSIS OF COLLECTED DATA

This section presents a summary of the data analysis from all bridges monitored. Section 5.4.1 and Section 5.4.2 discusses the thermal and live load response, respectively. Section 5.4.3 discusses use of the data to estimate the effective link slab length and Section 5.4.4 discuses estimated strains.

5.4.1 Thermal Response

Each gage on a bridge provided a temperature reading, with measured values varying at locations throughout an individual bridge. When examining the data holistically, researchers observed a noticeable difference in temperatures at the interior bents and those as the abutments. Figure 5.16 provides an example of the temperatures collected for the BRY3 bridge. The yellow area provides an envelope of temperatures at the interior bents. The blue and red lines provide the temperatures measured at the abutments. The higher temperatures at the abutment are a result of the abutment backwall retaining heat and resulting in slower drops in temperature in the evening and morning, compared to that of the interior bents. Temperatures are highest in the evening and lowest in the morning hours.

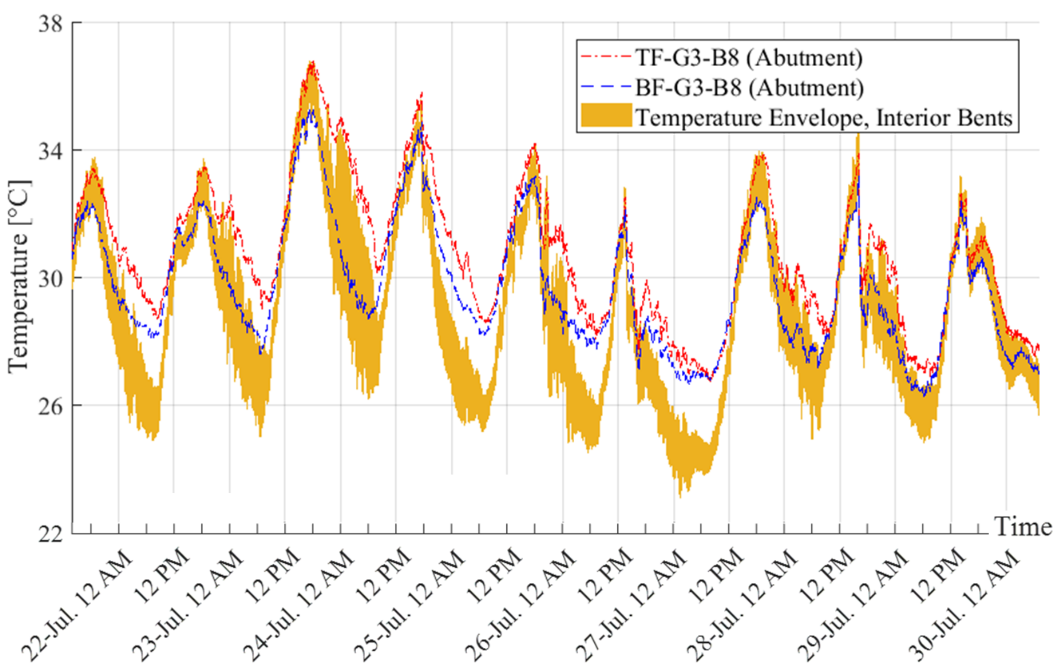

Figure 5.16. Temperature envelope for BRY3.

Deformation histories for gages on BRY3 are provided in Figure 5.17 and Figure 5.18 at PBJ locations and Figure 5.19 for SEJ locations. Figure 5.20 shows the strain history for strain gages located on either side of G3.

A comparison of the deformations at the PBJ and SEJ indicates a difference in the general trends of deformation in the top and bottom gages. At the PBJ locations, displacements of the top gages (those starting with TF and shown as a solid red line) are smaller than those of the bottom gages (those starting with BF and shown as a dashed blue line). For SEJ, the displacements are larger at the top flanges. This fundamental difference in the response is an indication that the center of rotation is different between the two locations. At SEJs, the center of rotation is located within the height of the girder. For PBJs, the continuity provided by the deck shifts the center of rotation higher toward or within the slab.

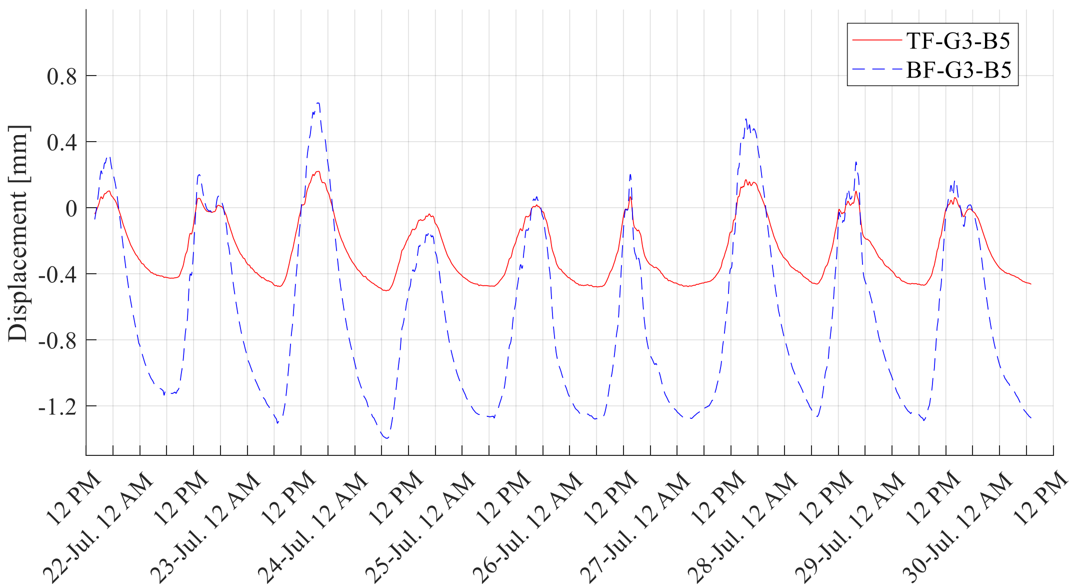

(a) G3

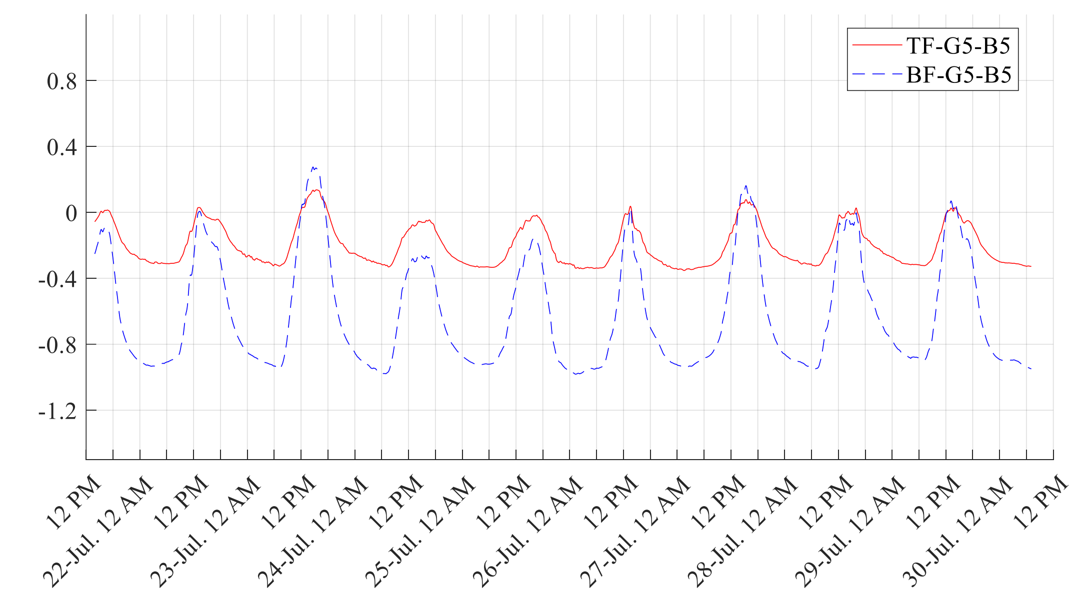

(b) G5

Figure 5.17. Thermal deformations of gages in BRY3 at PBJs at B5.

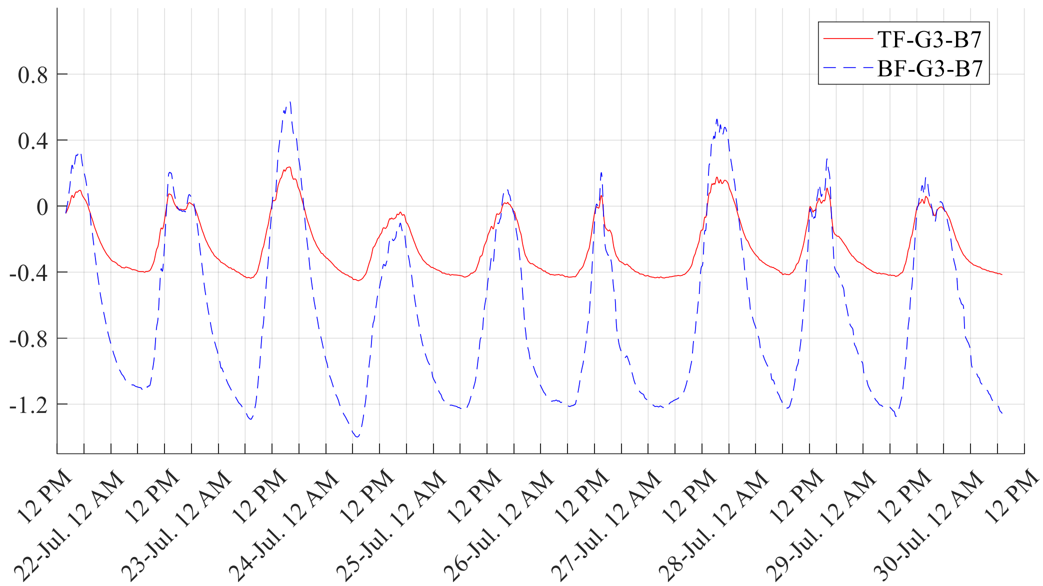

(a) G3

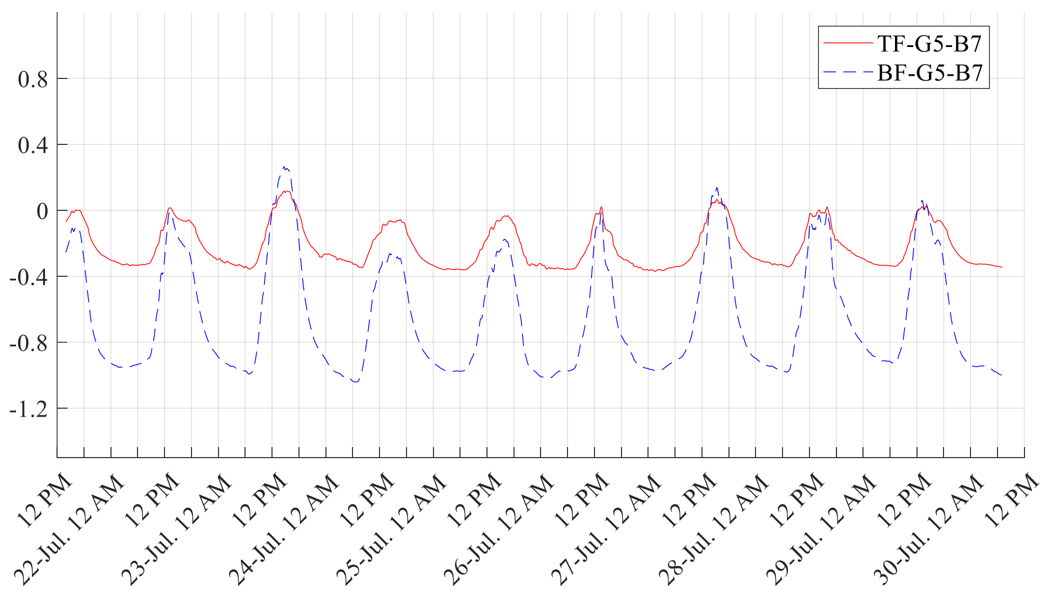

(b) G5

Figure 5.18. Thermal deformations of gages in BRY3 at PBJs at B7.

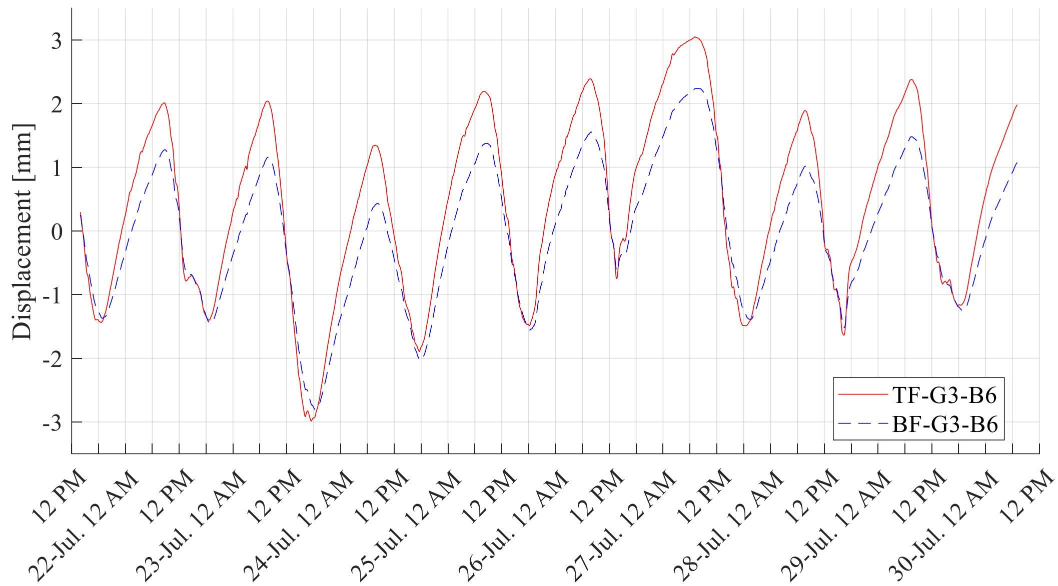

(a) B6

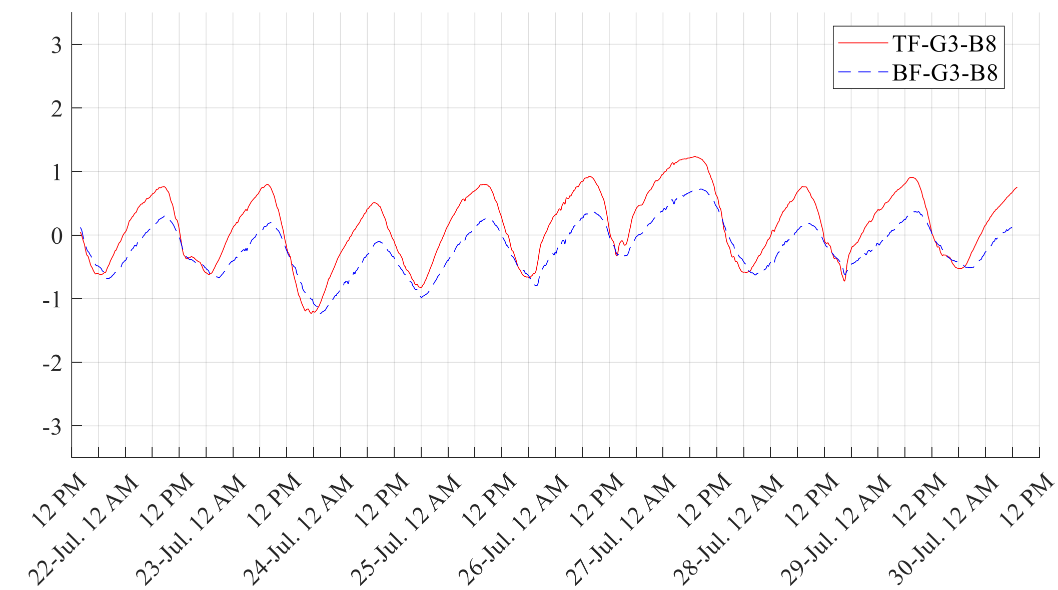

(b) B8

Figure 5.19. Thermal deformations of gages in BRY3 at SEJs along G3.

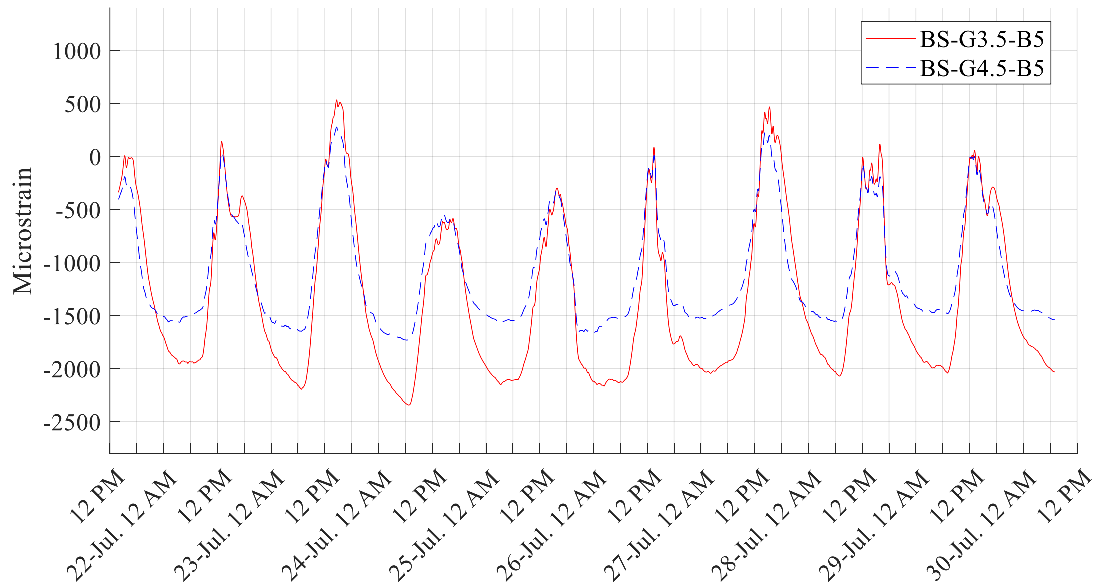

(a) B5

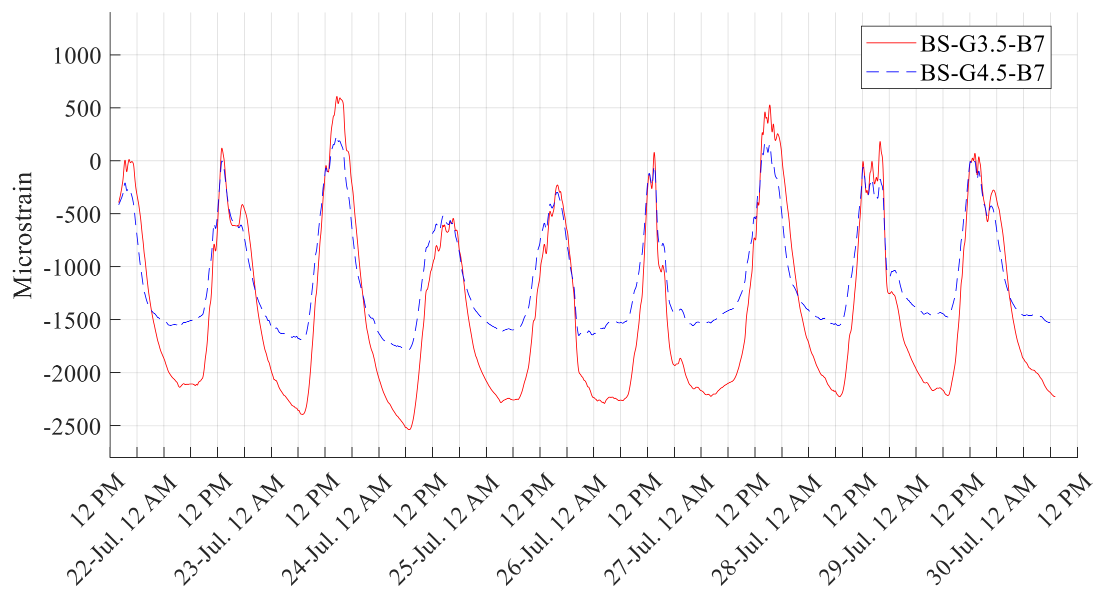

(b) B7

Figure 5.20. Thermal strains for BRY3 on either side of G3.

The deformations at each location were used to calculate the rotation using Equation 5.1. An example of rotations is shown in Figure 5.21 for BRY1. The rotation history cycles between peak negative values in the evening (when temperatures are highest) and positive values in the morning (when temperatures the lowest). The selected histories shown are for G5-B4 (PBJ) and G5-B5 (SEJ). Since both are along the same girder line, the comparison allows for a comparison of the influence of the slab continuity on the rotation. Under positive bending, the rotation varies by as much as 35 percent, illustrating the considerable impact of the slab continuity on the rotation demand used for design. For negative bending, the difference is much smaller.

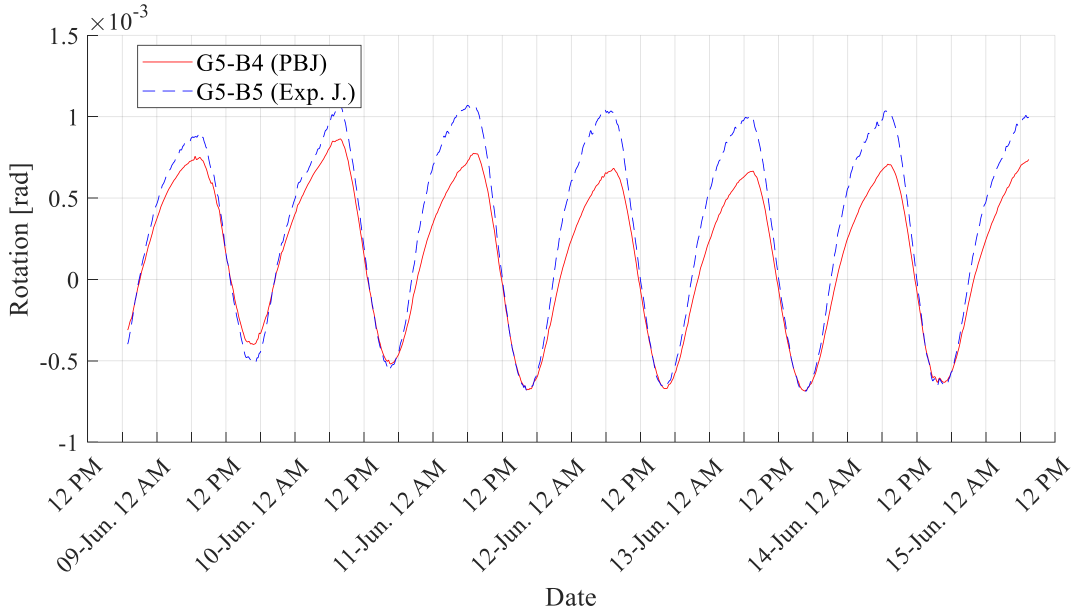

Figure 5.21. Example of thermal rotation time history, shown for BRY1.

The prior discussion shows the time history for individual bridges and limited locations. Similar trends in the history are seen in the time history for all collected and calculated data. To allow for a more comprehensive comparison of the data collected in relation to bridge characteristics and location of the measurements, the maximum positive and negative rotation values at each were identified and are shown in Figure 5.22. Each bar represents an individual monitoring location, with blue bars showing PBJ rotations and green bars showing SEJ rotations. Positive values are shown as solid, and negative values are shown as hatched. Below each bar, the transverse location is indicated, with E indicating an exterior girder and I indicating an interior girder.

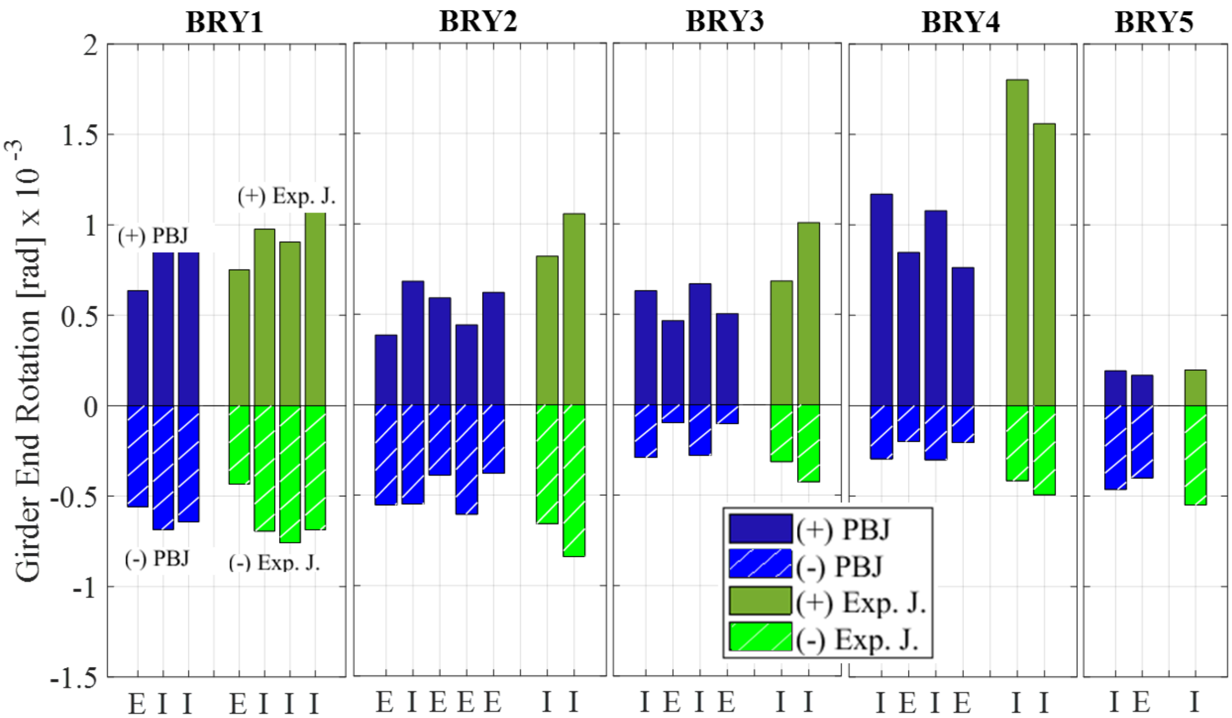

Figure 5.22. Maximum positive and negative thermal rotations.

For BRY1, the rotations at the PBJs are larger at interior girders. The interior girder rotation is measured under the median (G10) and under the traffic lane (G5). The larger positive rotations occur under the median, and the larger negative rotations occur under the traffic lane. At the exterior G1, the positive rotations are slightly larger at the SEJ, but the PBJ rotation is larger magnitude for negative bending. At the interior G5, the largest magnitude rotation occurs at the abutment SEJ.

For BRY2, PBJs were monitored at one interior girder (G3) and at four total locations along both exterior girders instrumented (G1 and G5). SEJs were monitored only on the interior G3. When comparing the SEJ and PBJ rotation along G3, researchers observed a noticeable reduction in rotation provided by the continuity of the slab, with the difference greater than observed for BRY1. For the exterior PBJ values, there is inconsistency between which locations have larger positive or negative values. Two bridge characteristics are captured in these four locations—the side of the skewed bridge and the number of units on the span. Figure 5.23 shows the relevant BRY2 data from Figure 5.22, with these details clarified. PBJ values are shown for two-span (yellow) and three-span (red) units. The x-axis labels indicate the specific exterior girder lines. The positive values are larger along G5 (north edge), and the negative values are larger along G1 (south edge). The positive rotations, regardless of location, are larger on the two-span units.

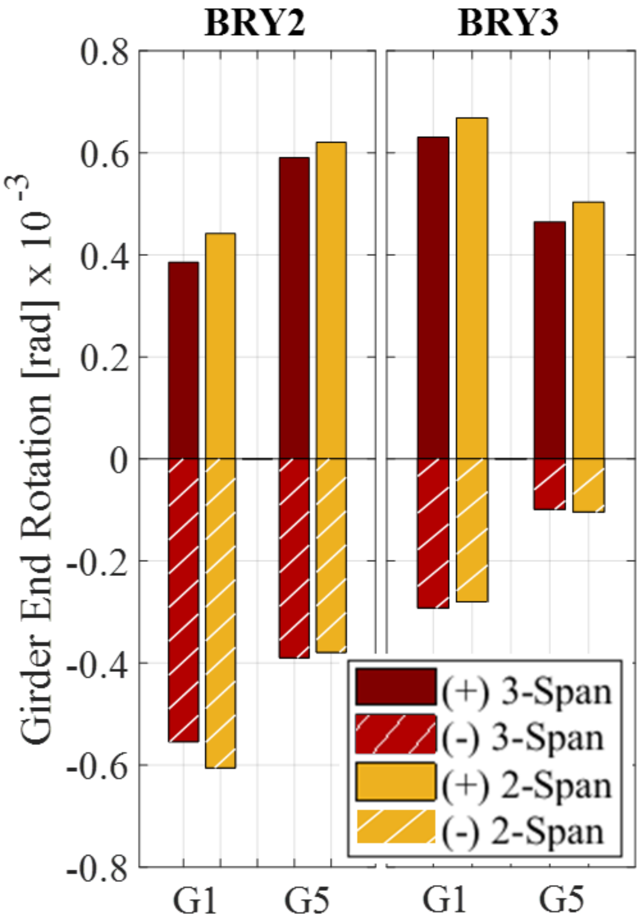

Figure 5.23. Thermal rotations for BRY2 and BRY3, with bars indicating number of continuous spans in a unit (red bars indicate three-span units and yellow bars indicate two-span units).

For BRY3, the center girder line (G3) provided rotations at both PBJ and SEJs, with the girders having slightly larger magnitude rotations at the interior SEJs. The smallest magnitude rotations are at the abutment SEJs. The exterior girder line was instrumented only at the PBJs, with both bents having similar rotations throughout the monitoring period. BRY3 provides another opportunity for comparison of two- and three-span units, with the relevant data included in Figure 5.22. As with BRY2, there is larger positive rotation in the two-span units. The negative rotation is similar or slightly smaller when negative bending is considered. This finding is slightly different than for BRY2, but it may be due in part to the inclusion of interior girder data and the fact that BRY3 is not skewed while BRY2 is skewed.

For BRY4, the largest positive and negative rotations occur at the interior girder (G3). The exterior girder line is instrumented at the PBJs only, with similar rotations throughout the monitoring period. The interior girder (G4) provides rotation at both PBJs and SEJs (abutment only), with the girders having larger magnitude rotations at the SEJs. Since the span lengths are the same for all spans, these observations were as expected. While the bridge is symmetric, there are slight differences in the PBJ rotations at the two interior bents. This is likely a result of different exposure to the sun at different locations on the bridge.

For BRY5, limited locations were monitored. Both PBJ rotations were at the same bent (B5), with the interior girder having slightly larger rotations. The same interior girder was monitored at an SEJ. The rotations were slightly larger at the SEJ for both positive and negative bending.

When looking at the five bridges collectively, researchers determined that the magnitude of the maximum rotation demand in the PBJs was larger for positive bending than for negative bending. The positive rotation demands are less than 0.001 radians (rad) for all but BRY4, which had slightly larger demands. For negative bending, all demands are less than 0.001 rad, with many less than 0.0005 rad. The difference in rotations for individual bridges should be considered in the context of the individual structures. Given the diversity of span lengths, girder spacing, and girder stiffnesses, a comparison of the rotation values is not meaningful. While these could be used to normalize the rotation demands, the comparison is further complicated by differences in temperatures for each bridge, along with the limited time window for the monitoring. A more useful evaluation of the influence of continuous deck detailing (e.g., offset panels, flush panels, or PMDF) is not in the girder rotations themselves but in the effective length and strains of the link slab, which are presented in a later section.

5.4.2 Live Load Response

An example of data from a live load event is shown in Figure 5.24 and Figure 5.25. Figure 5.24(a) and (b) show the displacements of gages at the PBJ and SEJs, respectively. At the PBJs, the data from all gages are shown. The gages on the bottom and top flanges of the location nearest the truck are shown by solid red and dashed blue lines, respectively. The other gages are not distinguishable as individual lines and are shown only to demonstrate that the magnitude is significantly smaller at those locations since the truck is not near to those locations at the time of the data collection. Figure 5.25 shows the strain data, with the two gages closest to the event highlighted.

While the trends in the thermal response were similar between all bridges, there is a greater range of responses in live load. A driving factor of this is the dynamic nature of the load. For BRY3, the truck event is positioned well relative to the instrumentation and thus provides very clear results. This is not the case for all bridges, where the instrumented locations may not directly correspond to the live load events triggered. Thus, the response for individual bridges is presented as the maximum magnitudes of the rotations in Figure 5.26. Each bar represents an individual monitoring location, with blue bars showing PBJ rotations and green bars showing SEJ rotations. Positive values are shown as solid, and negative values are shown as hatched. Below each bar, the transverse location is indicated, with E indicating an exterior girder and I indicating an interior girder. Both positive and negative rotations are calculated. The positive values are larger than the negative values, which occurs due to the dynamic nature of the load. Evaluation of the data is focused on the positive rotations since this factor is what is considered when establishing design demands and results in the most critical scenario for design (top of the deck in tension).

Overall, the relative observations for each bridge are similar to those made for thermal. For all bridges, PBJ rotations are smaller than the SEJ rotations. A comparison of interior and exterior locations shows that the interior rotations are larger magnitudes than the thermal demands.

Figure 5.27 shows the live load rotations for two- and three-span units in BRY2 and BRY3. Presentation of the data is the same as that for the thermal loads shown in Figure 5.23. Rotations are generally larger for three-span units under positive bending and larger for two-span bridges under negative bending.

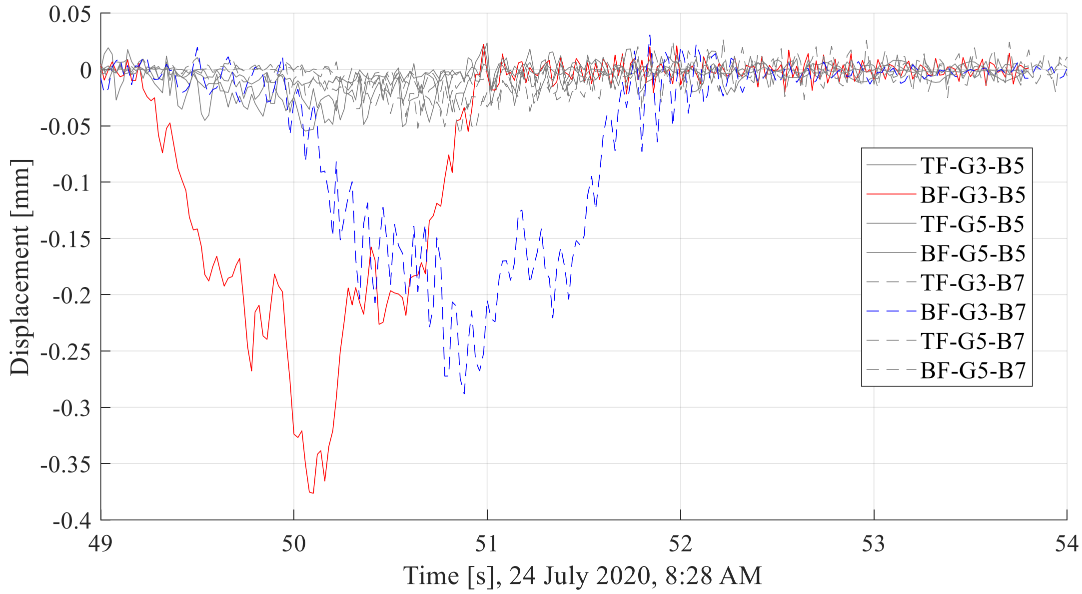

(a) Displacements at PBJ closest to truck event

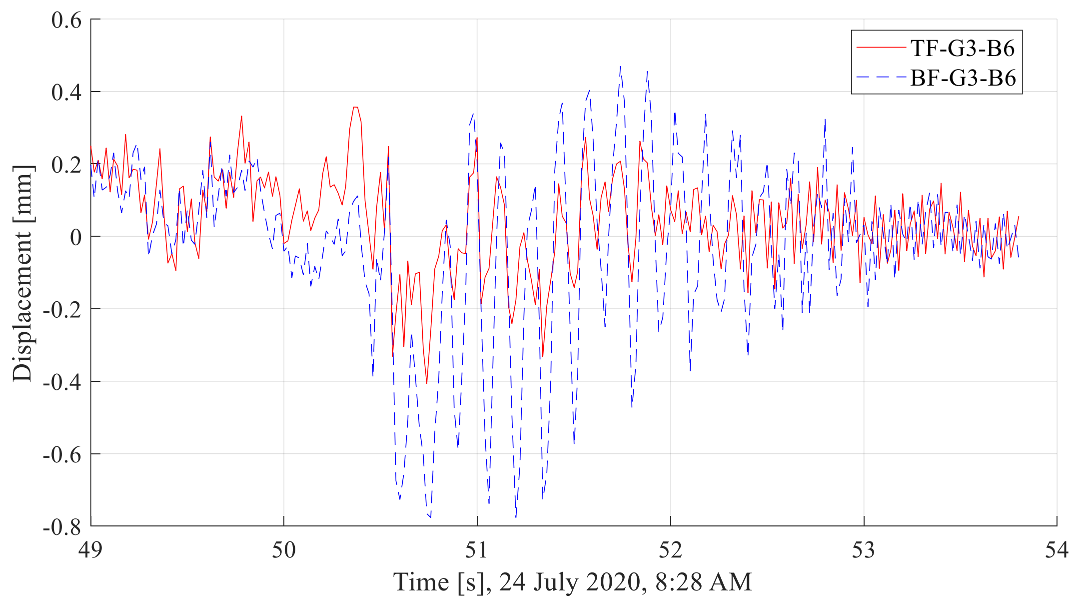

(b) Displacements at SEJ closest to expansion joint

Figure 5.24. Displacement data for sample live load event for truck on BRY3 above G3.

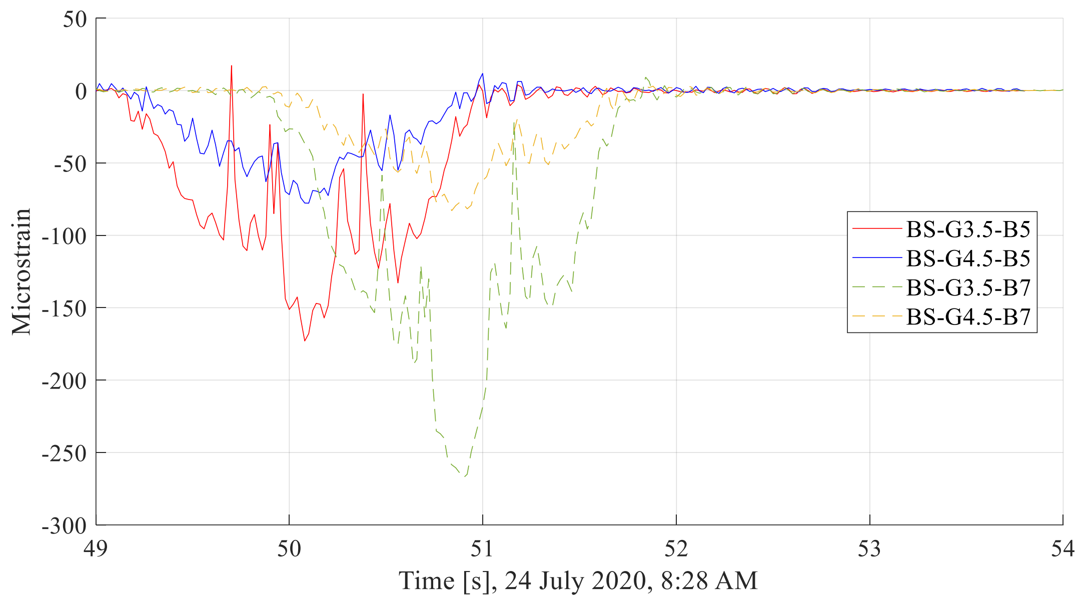

Figure 5.25. Strain data for sample live load event for truck on BRY3 above G3.

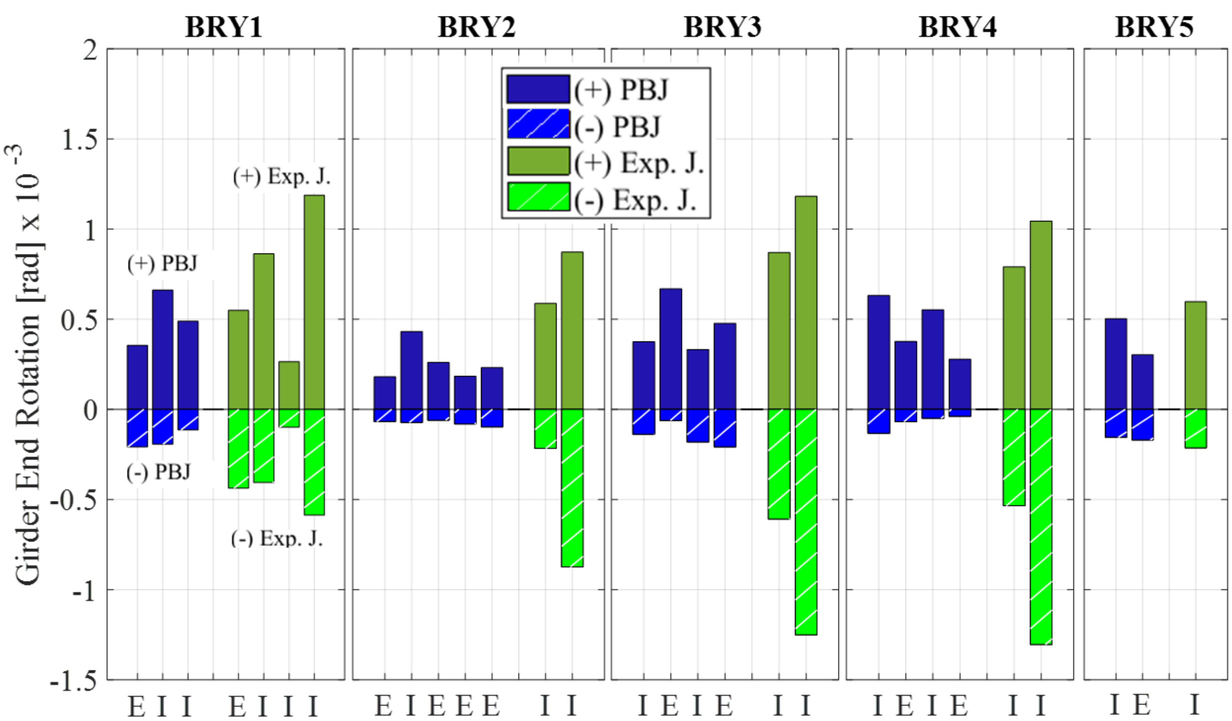

Figure 5.26. Maximum positive and negative live load rotations.

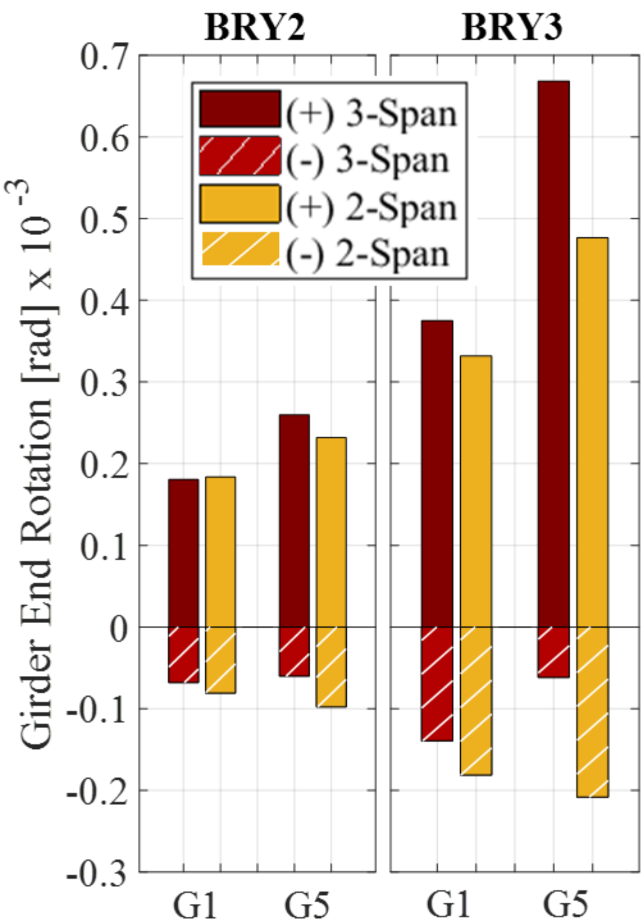

Figure 5.27. Thermal rotations for BRY2 and BRY3, with bars indicating number of continuous spans in a unit.

5.4.3 Effective Link Slab Length

In establishing design demands for bridges, a link slab length is needed to calculate the slab moment given a girder rotation demand. The design procedures for link slabs are typically presented for debonded link slabs, in which the length used is the debonded length. For bonded link slabs (including PBJs), it is less clear what the appropriate value is. Potential values that might be used for design include the distance between the ends of girders or the distance between the center of the bearing pads.

To evaluate the appropriate lengths to use for TxDOT bridges, including consideration for the different types of deck in the PBJ region, a concept of effective link slab length is considered. The effective link slab length, L_{link}, is considered to be the length between inflection points, thus isolating the portion of the slab experiencing rotation opposite that of the girders (i.e., top of the deck in tension for positive bending of the girders), thus mimicking the design concept used for debonded link slabs.

Figure 5.28 provides an overview of the variables describing the deformed and undeformed configuration of the link slabs. The undeformed configuration is shown in Figure 5.28(a). L_{link} is the effective link slab length and does not necessarily align with the location of the ends of the gages. The distance between the top displacement gage and the point of interest for calculation of the strain is d_{gage}. This is shown as the top of the slab but can be the bottom of the slab, which is used for comparison to the measured data.

Figure 5.28(b) shows the deformed configuration of the link slab. The measured displacement of the top gage is x_{gage}. The projected elongation at the location of the desired strain, x_{proj}, is calculated as:

$$x_{proj} = \frac{x_{gage}}{2} + \mathrm{d_{gage}} \sin\theta \tag{5.2}$$

where θ is the calculated rotation of a single girder.

The radius of curvature, r_{arc}, and the length of the arc, s, at the desired location in the slab are calculated as:

$$r_{arc} = \frac{x_{proj} + 0.5L_{link}}{\sin\theta} \tag{5.3}$$

$$s = r_{arc} 2\theta \tag{5.4}$$

The strain is then calculated as:

$$\varepsilon = \frac{s - L_{link}}{L_{link}} \tag{5.5}$$

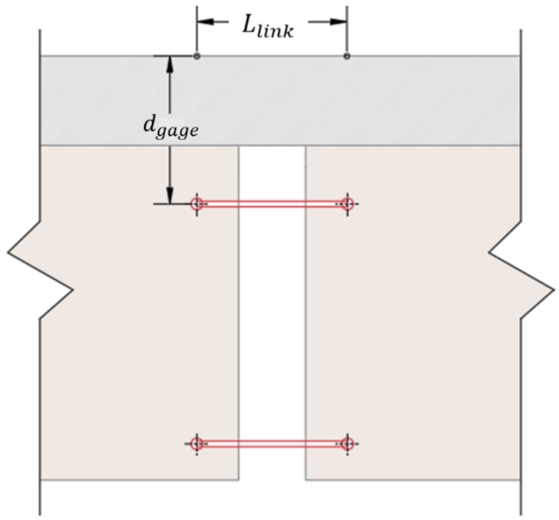

(a) Undeformed configuration

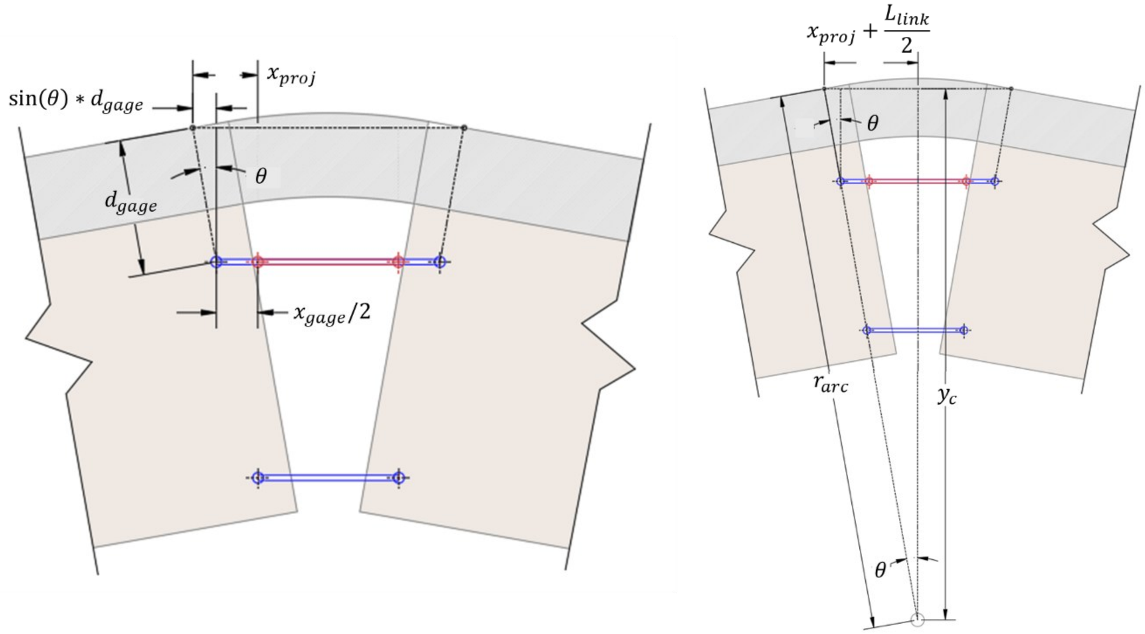

(b) Deformed configuration

Figure 5.28. Variables and deformed shape of link slab used for calculating deck strains from measured displacements at the ends of girders.

From gage displacements and girder rotation, the strains in the deck can be estimated and compared to the measured strain. The measured strains were located slightly off from the girder edges, but it was assumed that the strains were similar to those immediately over the girder line. By estimating strains for a range of possible effective link slab lengths in 0.5-in. increments, the effective length could be identified as the length that minimizes the difference between the measured and estimated strains. An example of the estimated and measured strains is shown for BRY1 in Figure 5.29.

Table 5.4 provides the effective lengths, along with the detail type, for each bridge. For offset panels, the effective link slab length is 16.5 to 17.5 in. For flush panels, the effective link slab length is noticeably shorter, ranging from 5.5 to 6.5 in. This is a very useful observation because it demonstrates that when flush panels are used, the link slab deformation is concentrated near the joint between panels, whereas for offset panels, the deformation is spread over a greater range, thereby reducing the demand. Only one bridge was monitored with PMDF: BRY5. This bridge had the longest effective link slab length (26.5 in.). This finding may be influenced by the much larger stiffness of the Tx54 girders compared to those in other bridges. Thus, additional data are needed before it is possible to conclude that there is a longer effective link slab length in bridges with PMDF link slabs.

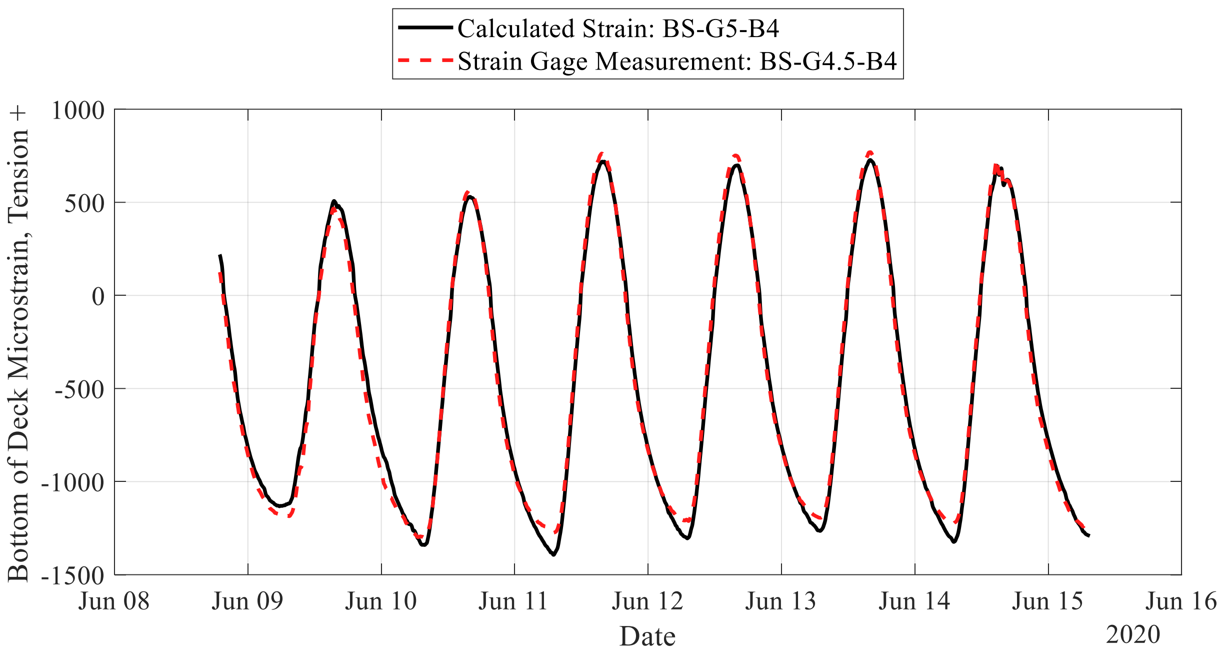

Figure 5.29. Comparison of measured and estimated strains for BRY1.

Table 5.4. Effective link slab lengths for monitored bridges.

Bridge No.	Detail Type	Effective Link Slab Length (in.)
BRY1	Offset PCP	16.5
BRY2	Offset PCP	17.5
BRY3	Flush PCP	5.5
BRY4	Flush PCP	6.5
BRY5	PMDF	26.5

5.4.4 Estimated Strains in Bridge Decks

Evaluation of the performance of PBJs is based largely on the extent of cracking in the deck, and thus the potential for more rapid deterioration of the deck at that location. Since monitoring was not possible on the surface of the deck or at internal locations in the deck, estimates of the strains at the top of the deck were made to allow for consideration of the performance of different deck details. Using the procedure for estimating strains discussed in Section 5.4.3, researchers estimated the strains at the top and bottom of the deck at all PBJ rotation locations; strains were not estimated for SEJ locations.

For thermal strains, it was not possible to establish the true point of zero strain; thus, the range of strains is presented in Figure 5.30. Figure 5.30(a) shows the strain range at the top (green) and bottom (cyan) of the deck. Figure 5.30(b) shows the strain range in the longitudinal reinforcement bars. For the flush panel bridges (BRY3 and BRY4), only top steel is shown because there is no bottom reinforcement at the center of the link slab. Thermal strains are larger at the bottom of the deck for both steel and concrete. While the strain range exceeds the anticipated yield strain of the longitudinal reinforcement, it is not expected that yielding is occurring since the range of strain is expected to be split between positive and negative strains.

Live load strains are shown in Figure 5.31. Bridges are grouped as non-flush panels (BRY1, BRY2, and BRY5) and flush panels (BRY3 and BRY4). The strains for individual events are considered and include both positive and negative strains. Note that this is the strain due to the live load event, not the total strain. The strains are larger magnitude in the flush panel bridges, indicating concentration of deformation where the panels meet.

Only in BRY3 do the estimated strains indicate that yielding may be occurring in the reinforcing bar. Non-flush details do not indicate strains near yield for either thermal or live load.

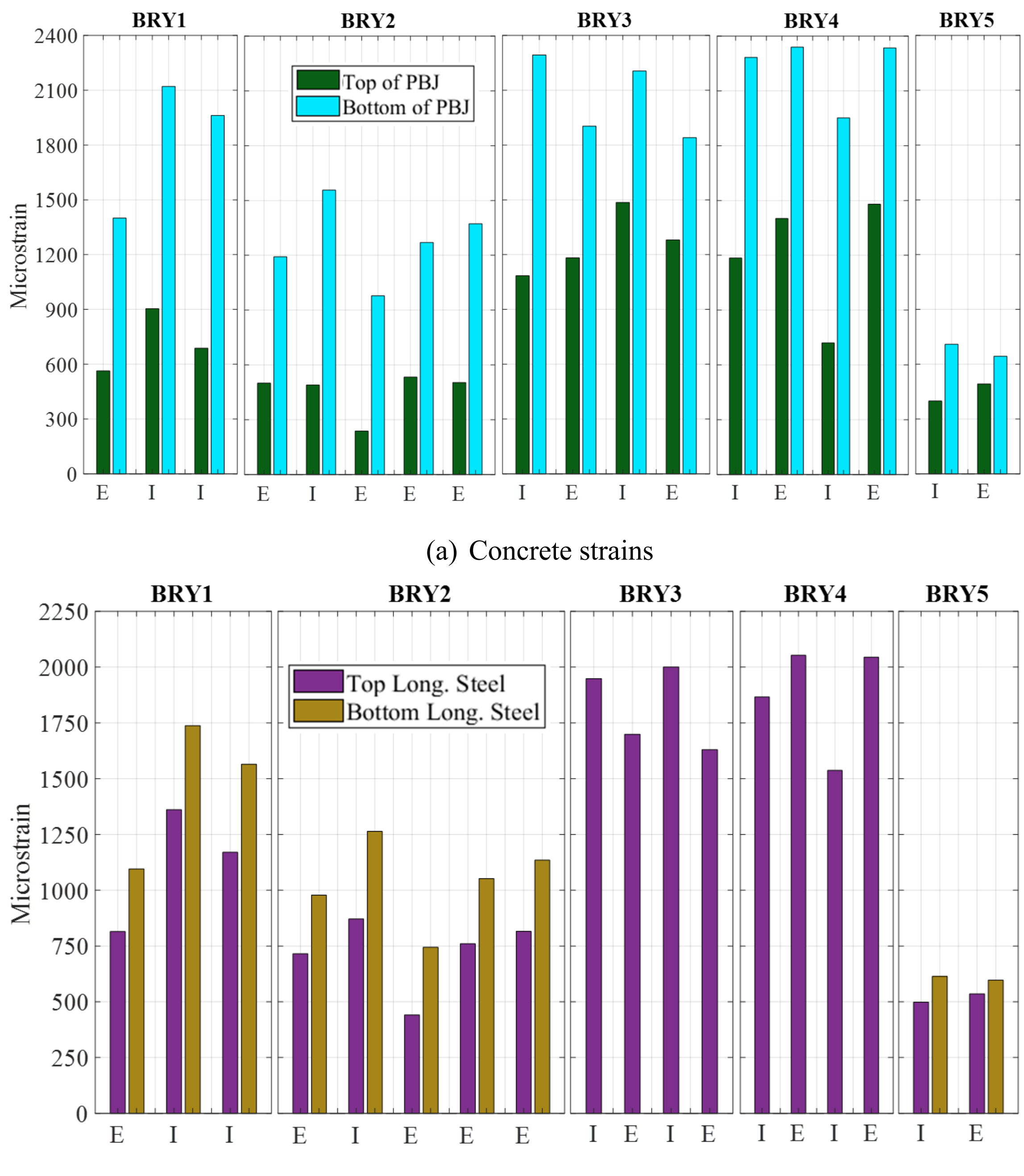

(a) Concrete strains

(b) Longitudinal rebar strain

Figure 5.30. Thermal strain range estimated at each PBJ for each bridge (E = exterior girders and I = interior girders).

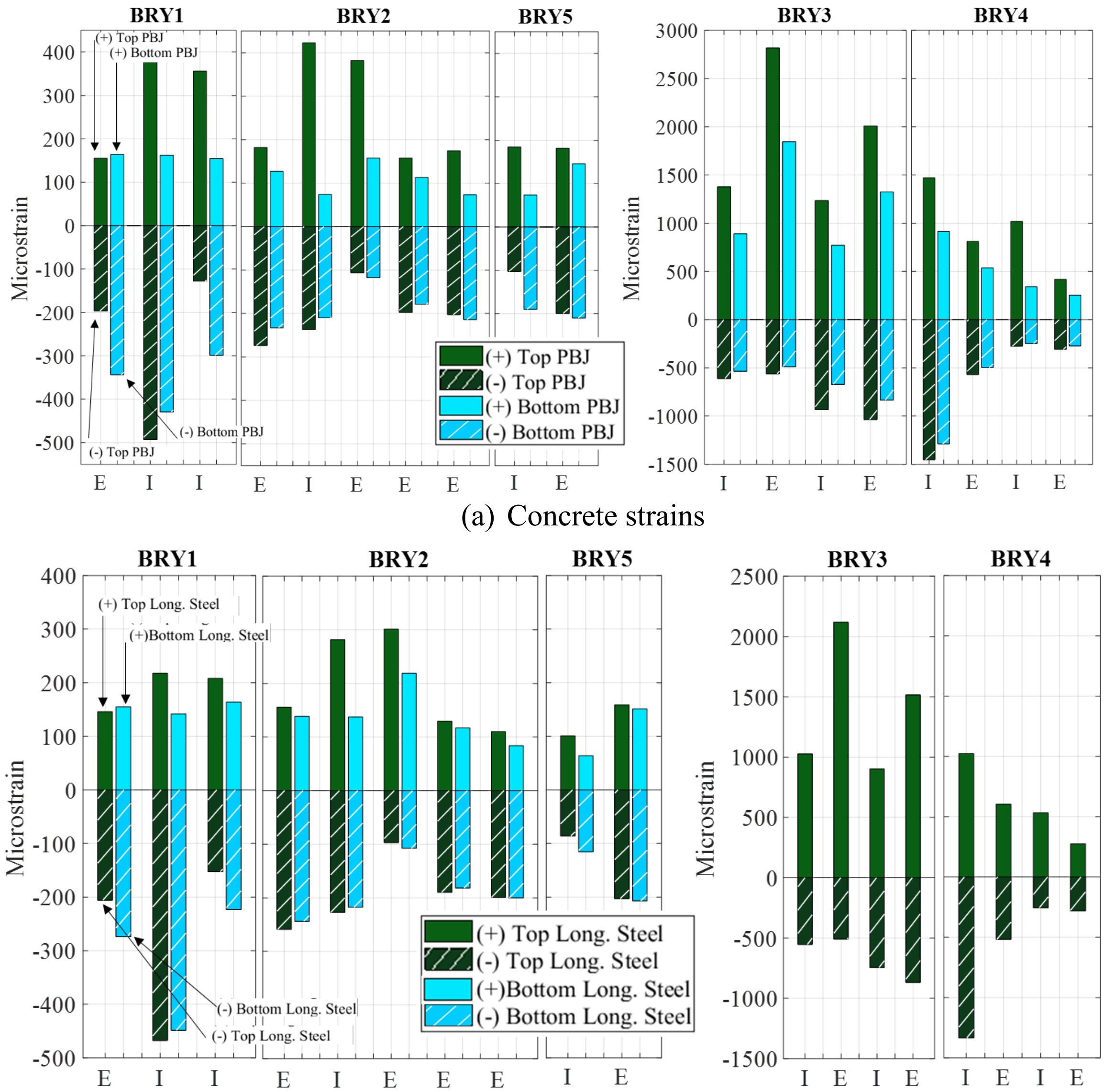

(a) Concrete strains

(b) Longitudinal rebar strain

Figure 5.31. Thermal strain range estimated at each PBJ for each bridge (E = exterior girders and I = interior girders).

5.5 SUMMARY

Five bridges were monitored for approximately one week to characterize the deformation under live and thermal loads. The selected bridges included those with diverse characteristics, including (a) both older AASHTO girder shapes and current Tx girder shapes, (b) skewed and non-skewed bridges, and (c) various span lengths and continuous deck unit lengths. The continuous deck details included two offset panels, two flush panels, and one PMDF. Locations of measurements included PBJs and SEJs at interior and exterior girder lines.

The rotations were found to be smaller at PBJs than at similar locations with SEJs, indicating that the continuity provided by the continuous deck provides a reduction in the moment. This is expected since the spans act as continuous members when a link slab is present, thus reducing the rotation relative to that of an identical girder that is a single simply supported span. Overall, the rotations are larger at interior girders.

The rotations are larger for thermal loads than for live loads, indicating the need to include this factor in the design and evaluation of continuous deck details. The largest truck event rotations are from BRY3, a result of the location of the instrumentation relative to the lane. The second largest rotations occurred in BRY1, for which spans are longer and for which the thermal rotations are slightly larger than those of other bridges. A preliminary comparison to other field studies indicates the magnitudes of the thermal and event rotations measured are on par with those observed by other research teams.

The influence of two- and three-span continuous units was evaluated to establish if one provided more favorable demands. Researchers found that thermal loads had larger positive rotations in two-span bridges. For live load, the opposite was true. Given the small differences in rotation for the number of spans, there is no need for consideration of the number of spans as a factor in design of link slabs in the future, and three-span units should be utilized where possible to reduce the number of expansion joints in a bridge.

Effective link slab lengths, defined as the distance between inflection points, was determined using the calculated rotation data and the measured strains. The effective lengths were found to be smallest for flush panel details and were approximately the distance between the ends of the girders. In offset panel details, the effective length was larger, and similar to the distance between the center of the bearing pads. Thus, in design procedures needing a link slab length, it is recommended to use the length between the ends of the girder for the design length for flush panel bridges and the distance between the center of the bearing pads for offset panel designs.

The effective lengths were in turn used to estimate the strains at a greater number of locations on the bridges. It was not possible to establish the total magnitude of the strains since the point of zero strain for thermal loading is not known. For thermal loading, the total range of strains was evaluated. For live load, the maximum positive and negative strains from all events were determined. The strains were well below the expected yield strain of the steel with the exception of BRY3, which has flush panel details.

6. OBSERVATIONS ON CONSTRUCTION DETAILS

Field visits to bridges for nondestructive evaluation and field monitoring provided the opportunity to closely examine the construction details of bridges containing link slabs. The observations made are summarized in this chapter. Section 6.1 provides a summary of observations made at bridges with offset and flush panel details. Section 6.2 provides an overview of skewed end details as documented in standards and those observed in the field. Finally, Section 6.3 discusses potential implications for performance and needs for further investigation.

6.1 PANEL DETAILS

TxDOT standards offers two options for continuous deck detailing when partial-depth PCPs are used: offset panels and flush panels (see Figure 6.1).

When offset panels are used (Figure 6.1[a]), the panels end a minimum of 1 ft 6 in. from the end of the girders, with the deck full-depth CIP between the ends of the panel. The top reinforcement is the same as that in the remainder of the deck, while bottom reinforcement is provided spliced with dowel bars extending from the panels. Per the standard details, the intent of the detail is that the deck in the link slab region be the same thickness as the deck elsewhere. This is notably different than for a thickened deck at the ends of girders where expansion joints are used. At bridges with offset panel detailing visited as part of this project, researchers observed a slight thickening of the slab where there were continuous decks. Although measurement of the thickness increase was not possible, it appeared to be similar to the increase in thickness at expansion joint locations. While such a deviation will have limited impact on the stiffness and strength of the deck, it is worth considering in making recommendations for future changes to standard details.

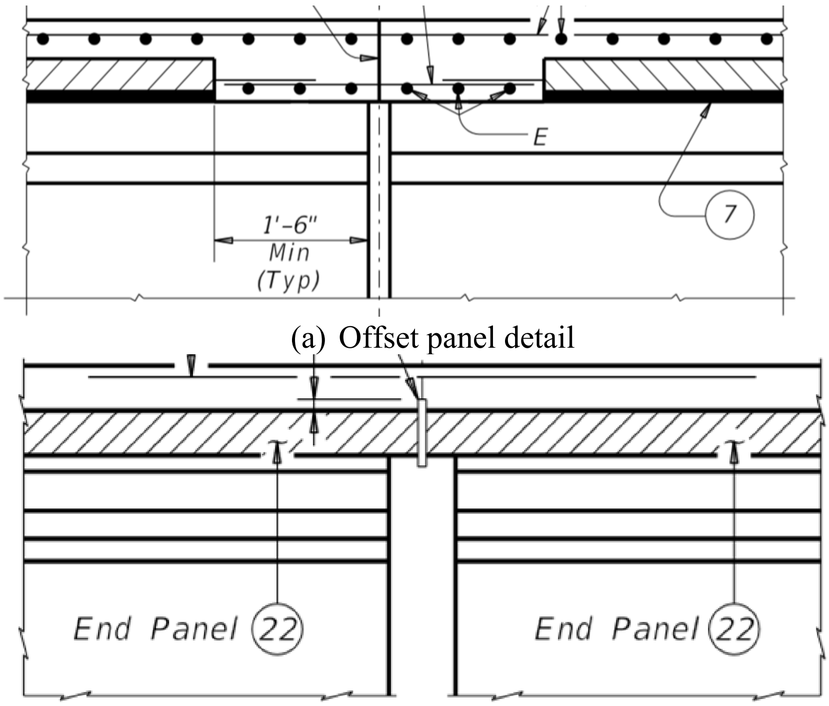

(a) Offset panel detail

(b) Flush panel detail

Figure 6.1. TxDOT PBJ detailing with partial-depth PCPs.

The current flush panel detail (Figure 6.1[a]) utilizes a ¾-in. redwood board, chamfered at the top to act as a crack former, between the panels from either span of the girder line. During field visits for BRY3 and BRY4, flush panel details were observed to have been constructed differently than in the current standards, utilizing bedding strip foam for the gap between the panels (Figure 6.2). It is not clear what the design drawings or approved change orders were for these bridges, only that the constructed detail is different than the current standard.

Figure 6.2. Observed flush panel detail for BRY4.

6.2 SKEWED DETAILS

Highway bridges with prestressed concrete girders have a long history in Texas. For skewed bridges with discontinuous concrete girders, TxDOT has long provided optional details to contractors for the treatment of girder ends. The details address the problem of the corners of girders with squared ends protruding beneath the deck of the adjacent span.

6.2.1 Overview and History of Skewed End Details

To prevent the girder and bridge deck from interfering with one another as the bridge deforms under load, there are two main detail types: a skewed girder end detail and a foam insert detail. The skewed girder end detail consists of a girder end face design that is trimmed to match the support skew. The foam insert detail uses typical squared girder end faces but includes a strip of polystyrene foam over the protruding corner of the girder to prevent concrete-to-concrete contact with the deck. In 1959, TxDOT's prestressed concrete beams GPC1 standard detail (see Figure 6.3) included a skewed end detail with a 1-in. deep notch cut into the girder end.

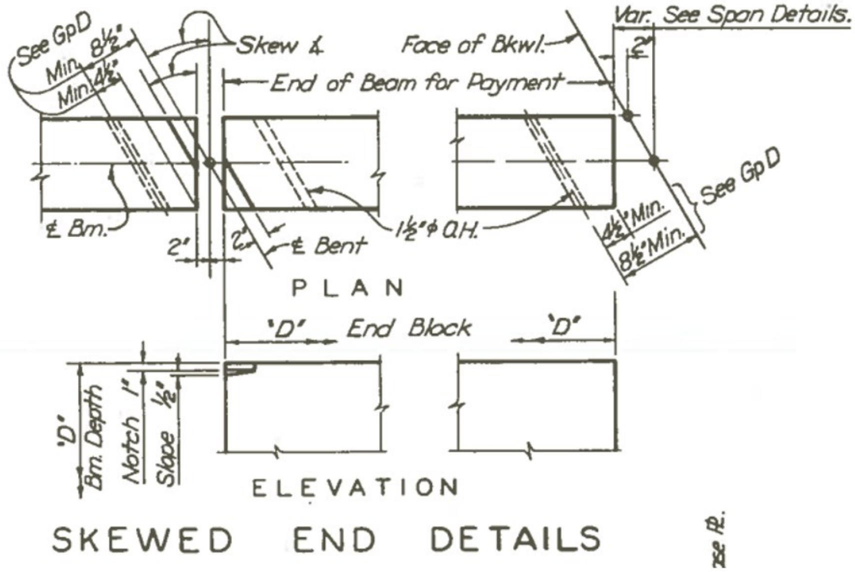

Figure 6.3. Prestressed concrete beams GPC1 standard detail of 1959.

In 1968, both types of end details were present (see Figure 6.4). Rather than using a partial-depth notch in the girder end, the end face was skewed for the whole depth of the girder. The foam insert detail appeared for the first time, mandating a minimum of ½ in. of clearance.

The prestressed concrete beam span details of 1971 (see Figure 6.5) continued the use of the foam insert. In 1998, the foam insert detail changed slightly to mandate 3 in. of foam extension past the edge of the girder, as shown in Figure 6.6.

The current iteration of the two girder end detail options at skewed supports includes direction on reinforcement placement (Figure 6.7) and bearing pad placement (Figure 6.8) for the skewed end detail. The current foam insert detail, shown in Figure 6.9, is similar to the detail from 1998.

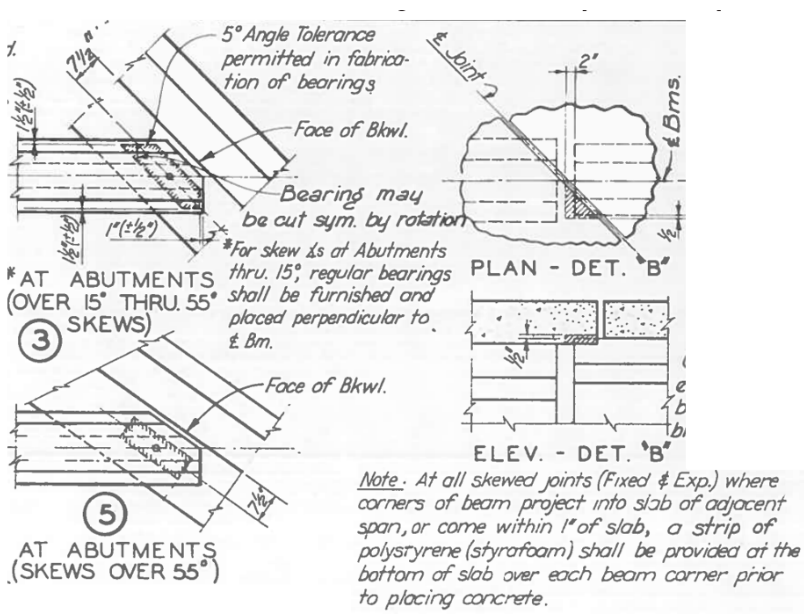

Figure 6.4. Prestressed concrete beam span details, AASHTO Type IV standard detail of 1968.

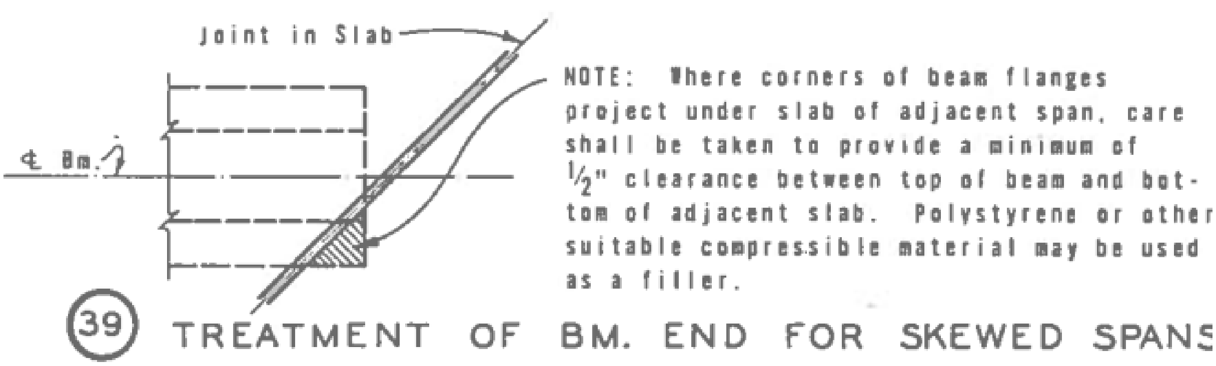

Figure 6.5. Prestressed concrete beam span details of 1971.

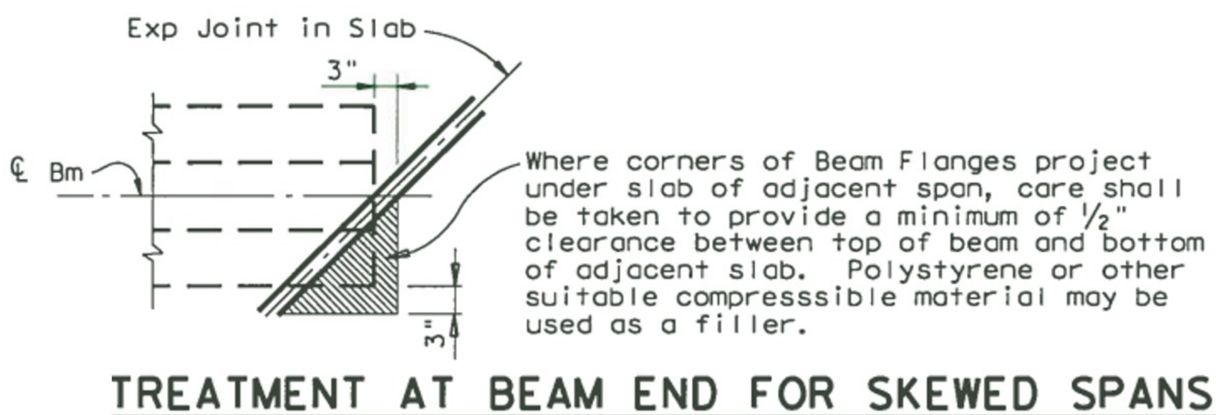

Figure 6.6. Miscellaneous slab details of 1998.

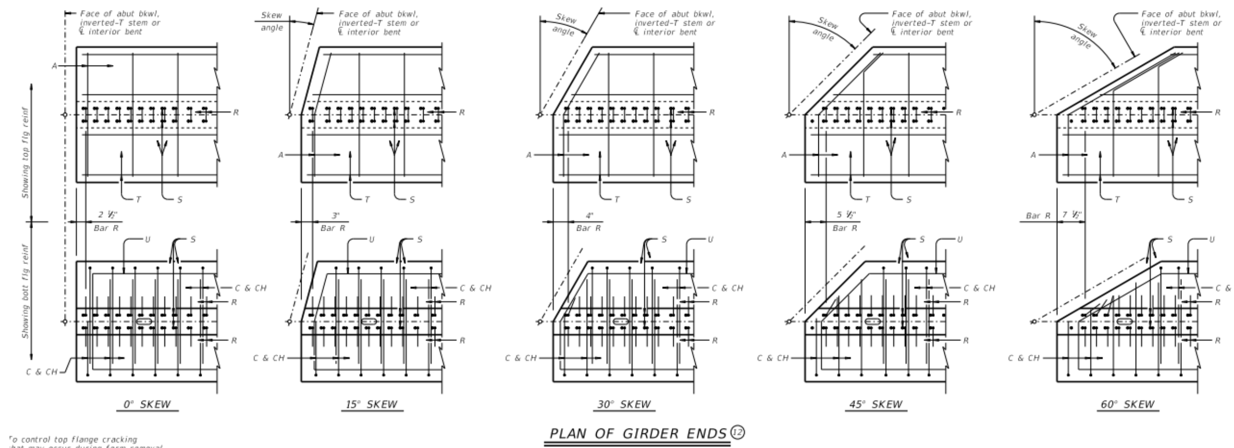

Figure 6.7. Current standard details for skewed ends from prestressed concrete I-girder details sheet.

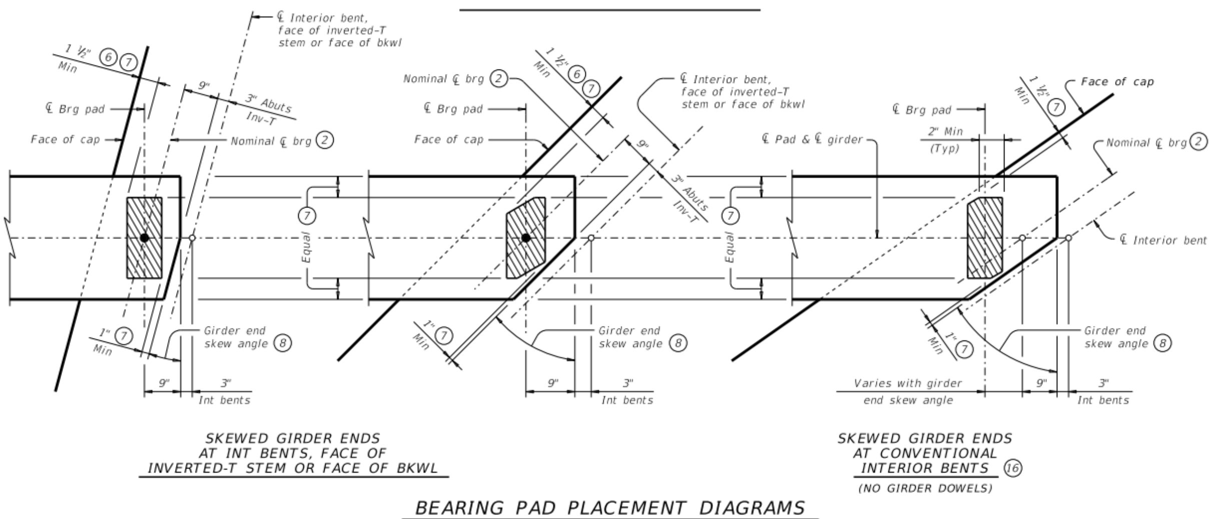

Figure 6.8. Current standard details for skewed ends from elastomeric bearings and girder end details sheet.

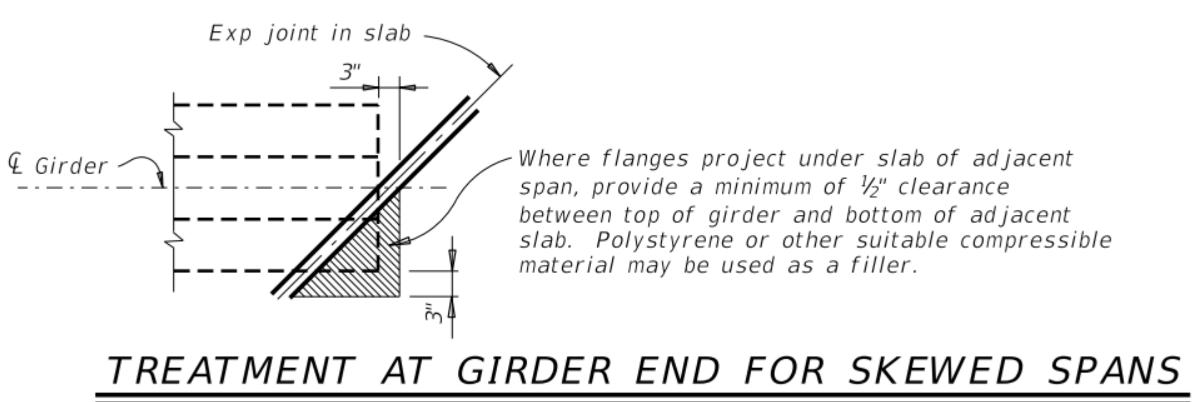

Figure 6.9. Foam insert detail from current miscellaneous slab details sheet.

6.2.2 Field Observations of Skewed Details

Despite the availability of two standard detail options, there is evidence that contractors have not provided either detail at some bridges. For instance, at Old River Bridge (Bridge ID 17-026-0648-03-020), neither skewed girder ends nor a visible foam insert was used to prevent the girder ends from contacting the slab of the adjacent span, as shown in Figure 6.10. The skew at all bents of Old River Bridge is 30 degrees. Figure 6.11 shows possible damage from contact between the slab and protruding girder at an expansion joint. At Peach Creek Bridge (Bridge ID 17-021-0050-02-135), no skewed girder or foam insert detail is visible, despite the deck crack between spans running beneath the edge of the girder end (see Figure 6.12). Peach Creek Bridge has supports with 15-degree skew. At Bridge 2.2 in the Atlanta District (Bridge ID 19-034-00946-01-013), which has a 15-degree skew, no skewed girder of foam insert detail is visible at the girder ends (see Figure 6.13).

An as-built example of a skewed girder end detail is shown in Figure 6.14 on a bridge in the Lubbock District on Highway 62 (Bridge ID 5-152-00380-01-236). This bridge has a 19-degree skew. Of the four skewed bridges with visible details that the project team assessed as part of Task 3, only one had a visible skewed end detail. The application of these details appears to be inconsistent.

Figure 6.10. A poor boy continuous deck above girder ends on a skewed support at Old River Bridge, without the use of foam insert or skewed end girder detail.

Figure 6.11. Contact between girder end and the deck of the adjacent span at an expansion joint on Old River Bridge.

Figure 6.12. Cracking in the deck above the girder ends at skewed supports on Peach Creek Bridge.

Figure 6.13. Atlanta District bridge without a foam insert or skewed girder end detail.

Figure 6.14. Lubbock District bridge with skewed girder end details.

6.3 SUMMARY

The detailing of the bridge deck in the continuous deck region and at the girder ends is important to consider in evaluating the performance of PBJs and making recommendations for design. The detailing introduces locations for stress concentrations and therefore cracks to form. From the standpoint of making detailing recommendations, consideration should be made for how observed construction deviates from design detailing, and thus impact performance. From a construction standpoint, it is critical to ensure that detailing meets that intended to ensure the best performance of the structure.

7. DESIGN CONSIDERATIONS

This chapter provides a summary of design considerations for the design of link slabs in Texas bridges. Section 7.1 presents a summary of design demands for bridges, and Section 7.2 summarizes the different factors considered in exploring designs. Section 7.3 provides a summary of design considerations.

7.1 DESIGN DEMANDS

Numerous studies have been done on the design and performance of link slabs. The most common and simplest approach to determining the design demands is found in the recommendations in the AASHTO *LRFD Guide Specifications for Accelerated Bridge Construction* (AASHTO 2018). The link slab reinforcement is designed for a moment, M_{ls}, calculated as:

$$M_{ls} = \frac{2E_{ls}I_{ls}\theta}{L_{ls}} \tag{7.1}$$

where E_{ls} is the modulus of elasticity of the link slab; I_{ls} is the moment of inertia of the link slab using gross section properties; L_{ls} is the length of the link slab, taken as the length of the region of slab debonded from the girders, with a recommended minimum of 5 percent of the span length; and θ is the girder end rotation.

The AASHTO *LRFD Guide Specifications for Accelerated Bridge Construction* indicates that (a) the girder end rotation should be based on the demands after casting and curing, implying only the live and thermal loads need to be considered; and (b) the appropriate load factors should be used for strength and serviceability. A common simplification of the girder end rotation for design is to use an upper-bound value based on a maximum deflection of L/800 acting at one-third the span length, leading to a design rotation of 0.00375 rad (Lepech and Li 2009).

The calculation of the moment is based on the length of the link slab, which in turn is affected by debonding length (if any) and compatibility conditions at the girder/deck interface. Various recommendations are available to determine what the specific moment should be in the slab, including recommendations for link slab lengths, girder end rotations, and modifications to account for deformation compatibility at the girder ends. An in-depth evaluation of recommendations was not the scope of the task discussed in this chapter, although it is important to note that much of the literature focuses on debonded link slabs. Instead, the focus was on the appropriate end rotations of the girders in TxDOT bridges.

For both the design demands and the laboratory setup, the girders are assumed to be simply supported single spans. While this is not fully accurate since the deck provides some continuity and the actual rotation is expected to be a bit smaller, this will be true for both the experimental test setup and actual bridges. Thus, it is reasonable to make this simplification in the planning process.

Design demands were found for I-girder bridges based on the characteristics in the TxDOT bridge standards. Bridge widths considered were 24, 28, 30, 32, 38, 40, and 44 ft. For each width, all girder sizes from Tx28 to Tx54 were considered to establish common ranges of demands in the link slabs. For each girder size, a minimum, intermediate, and maximum span length (based on those in the bridge standards) were considered.

The effect of temperature gradient is accounted for using Section 3.12.3 of the AASHTO specifications. The profile of AASHTO's temperature gradient is shown in Figure 7.1. To simplify rotation calculations, this nonlinear gradient was simplified as a linear gradient with endpoints T1 at the top of the superstructure and T3 equal to zero at the bottom of the superstructure. For positive bending in the girders, a negative gradient is used, which applies a factor of −0.30 to the AASHTO specified values. For each prototype bridge, rotations due to thermal loading were found by integrating the temperature gradient. Values are shown as absolute values in Figure 7.2. Positive thermal values are for positive thermal gradients and correspond to negative girder bending. Negative thermal values are for negative thermal gradients and correspond to positive girder bending. The magnitudes of thermal rotations are typically larger than live load rotations, except for very flexible bridges, in which the live load values exceed the negative thermal loading values.

Live load criteria for deflection calculations are detailed in AASHTO (2012) Section 3.6.1.3.2. Two load cases are considered: the design truck alone, and lane load with 25 percent of the design truck. AASHTO Section 2.5.2.6.2 specifies that deflections for straight girder bridges should consider all design lanes loaded. Thus, a live load distribution factor may be taken as the total number of design lanes divided by the total number of girders in the span. Load combination Service I is used, including the dynamic load factor and multiple presence factor. PGSuper was used to complete the analysis for the bridges considered. The resulting rotation is for a single girder.

In considering the spans on both sides of the link slab, the lane load is assumed to act in both spans, with the truck load in a single span. While the girder end rotations are different in each span, the link slab need only consider the total rotation, which amounts to the lane load from both spans and the truck load for one span. To simplify analysis and present values as a single girder rotation, the girder end rotation is specified as half the link slab rotation (lane plus one-half truck). This final rotation for the live load is shown in Figure 7.2. Note that some of these exceed the rotation of 0.00375 recommended by some researchers. To assess if the design simplification made by using one-half of the rotation from the truck load is appropriate, asymmetric loading patterns are considered for experimental tests.

The rotations from live plus impact and thermal demands were combined using the AASHTO LRFD Service I load combination. In accordance with the AASHTO specifications, service combinations use the maximum of (a) thermal and (b) one-half thermal plus live. Figure 7.3 shows the positive and negative bending service combinations. Negative bending values are typically larger. However, this is a different load scenario than what is tested in the lab tests. Strength combinations use live only with a factor of 1.75 (thermal is not included in strength combinations); therefore, only positive bending is relevant. Figure 7.4 compares the service and strength combinations for positive girder bending. Appendix A provides tables containing rotation values used for the suite of standard bridges considered here.

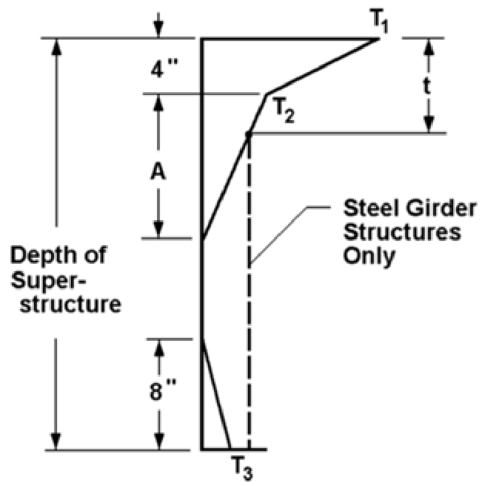

Figure 7.1. Temperature gradient from AASHTO LRFD specification.

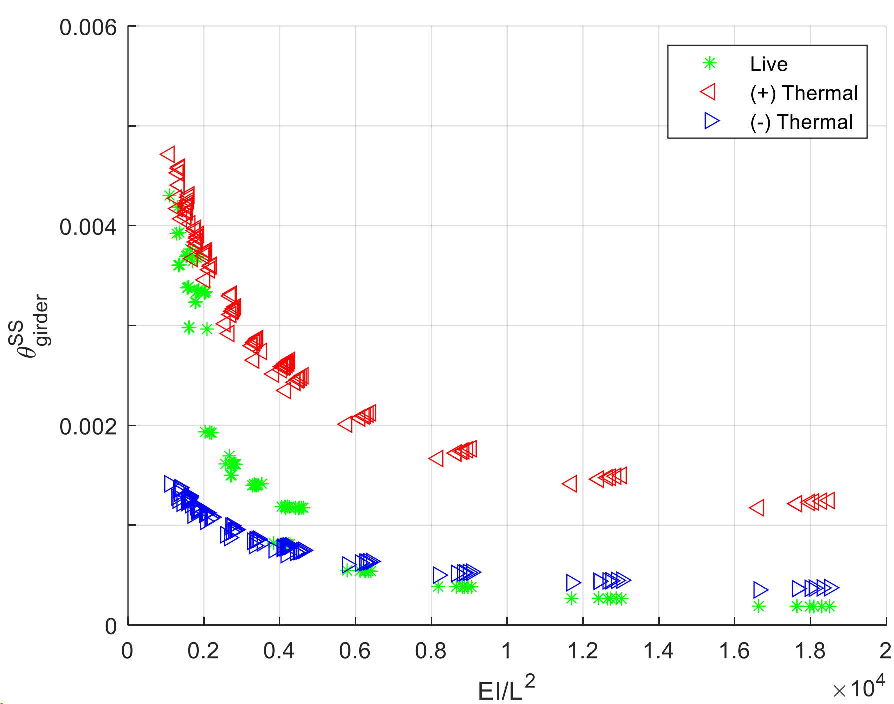

Figure 7.2. Girder end rotations for live and thermal loading.

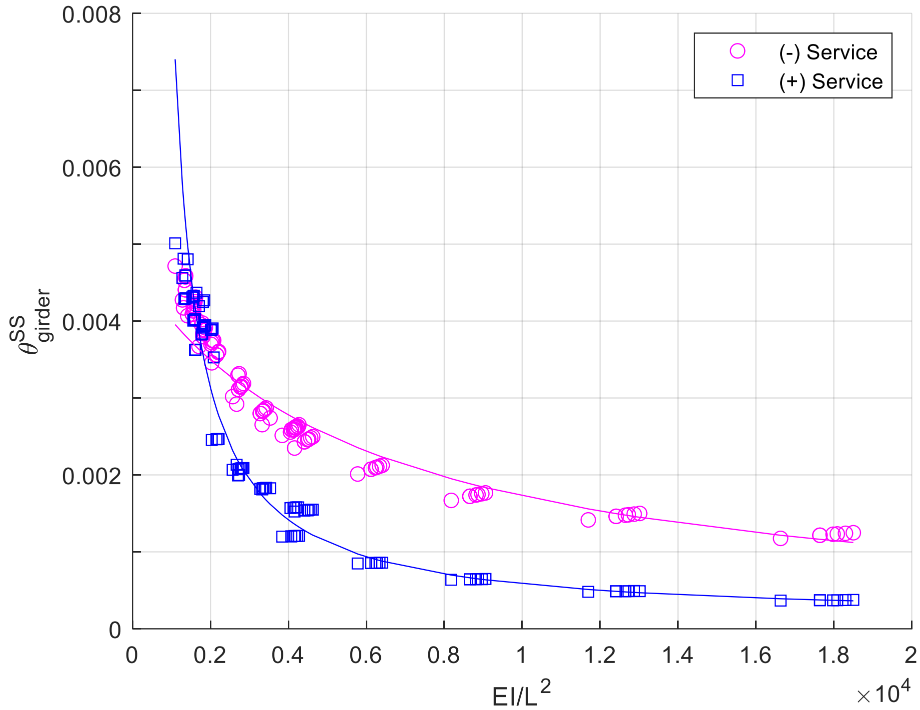

Figure 7.3. Girder end rotations for service load combinations.

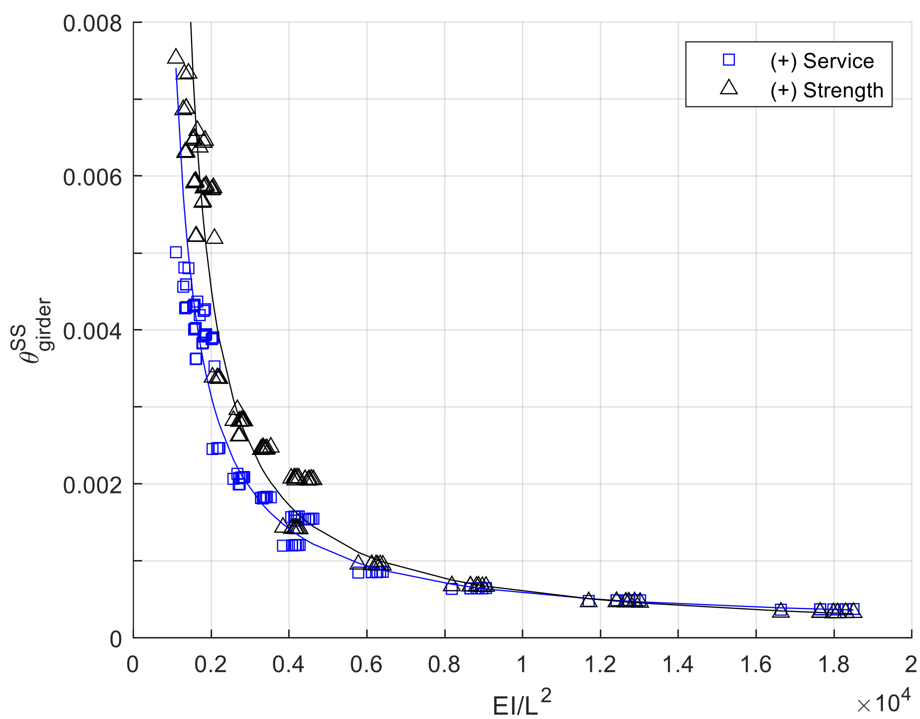

Figure 7.4. Girder end rotations for design of TxDOT standard I-girder bridges (only positive bending shown).

7.2 DESIGN CONSIDERATIONS

In this project, the existing TxDOT details were considered, as well as recommendations for new design details and for retrofit of existing decks. There are two aspects that must be considered: (a) overall aspects of the design, and (b) detailing. Engineers must assess the design procedure, construction, cost, and performance, where performance is determined by distribution of cracking that occurs in the link slab and the widths of the cracks.

The overall aspects of the design include if the slab is bonded or debonded from the top of the girder and the amount of reinforcement in the link slab. For debonded design options, consideration must be made for the length of the debonded region and the impact on the composite action of the girder with deck. Typical recommendations for debonded length are 5 percent of the girder length because this will ensure that composite behavior of the girders is not impacted. However, limited investigations have been done to investigate the impact on debonded length on the performance of full-scale link slabs with detailing representative of actual construction. In this study, the impact of debonded length was considered to balance the improved performance with minimizing construction effort and not requiring changes to girder designs. Reinforcement is often designed using the recommendations in Section 7.1. For bonded link slabs, the appropriate length to use is less clear and was a consideration of this research project. In this study, considerations were made for guaranteeing consistency with current TxDOT deck reinforcement and ensuring that the AASHTO crack width limits were met for excepted rotation demands.

Detailing considerations include panel details, use of crack formers, and detailing at girder ends. In current TxDOT standard details, offset and flush panel options are available (see Figure 1.1). The differences in performance of these should be considered when evaluating the expected performance of the details. For flush panels, this includes the detail as designed and the observed field conditions in bridges monitored and documented in Chapter 6. An additional option of a continuous panel is also explored. The objective of the continuous panel is to provide continuity of the bottom portion of the deck and thus eliminate a potential plane of weakness at the panel gap in the flush panel option. The continuous panel would also provide prestressed concrete in the bottom, which may contribute to avoiding full-depth cracking of link slab designs. A disadvantage of the continuous panel relative to offset panel designs is the need to coordinate the correct panel length prior to construction. However, this is no different than that needed for flush panels.

Current TxDOT details use a crack former, often a zip strip, on the top of the deck to provide a controlled location of the crack. While this improves the appearance of the cracks, as was documented in field evaluations Chapter 4, cracks may naturally form at the girder ends in addition to or instead of at the center of the link slab. Thus, an investigation of the appropriateness of a crack former should be undertaken. This is done in finite element models. On the bottom of the deck, chamfers serve the same purpose of the crack former, providing a location for deformation, and potentially damage, to concentrate. The use of bottom chamfers is explored in both the finite element models and experimental tests presented in later chapters.

Finally, the detailing of the deck-girder interface at the girder ends should be considered. Standard link slab details in some jurisdictions utilize compressive materials to form a small gap at the bottom of the deck haunch. The objective of this is to prevent the cracking that occurs from stress concentrations where the top of the girder bears into the bottom of the deck. This is similar to the polystyrene gaps used at the ends of girders for skewed bridges in current details. The use of a small gap in the haunch at the ends of the girders is explored by finite element modeling and experimental tests in later chapters.

7.3 SUMMARY

The demands in link slabs are deformation controlled by the rotation of the girder ends due to thermal and live load. In Section 7.1, service and strength rotation demands were presented for a suite of typical TxDOT I-girder bridges. These demands provide a more accurate value than the rotation of 0.00375 rad commonly recommended in the literature, with many bridges in the suite having lower rotation demands. Another value needed for the design is the length of the link slab. While the debonded length is often used, guidance for bonded link slabs is needed, particularly considering the detailing of TxDOT link slabs; further exploration of these topics is provided in the analysis of experimental data presented in Chapter 10.

Section 7.2 summarized design considerations for the design and detailing of new and retrofit designs. These considerations include bonded/debonded, debonded length, reinforcement, panel detailing type, crack formers, and girder/deck interface material. Each of these considerations was investigated through the finite element modeling presented in Chapter 8, with experimental investigation of some designs as presented in Chapter 9. Final design recommendations were compiled from the results of the finite element models and experimental tests, as presented in Chapter 11.

8. FINITE ELEMENT MODELING

This chapter describes the use of FEA to investigate the anticipated performance of the existing continuous deck detail, or PBJ, and the anticipated performance of design alternatives. Section 8.1 provides an overview of the model configurations. Section 8.2 presents details on common model details, modeling practices, and features used across many models. Section 8.3 summarizes findings for the full-depth CIP deck detail, and Section 8.4 provides an overview of the flush precast panel deck designs. Section 8.5 presents a summary of offset precast panel designs, and then Section 8.6 summarizes models using the continuous panel detail. Section 8.7 discusses material shrinkage effects, while Section 8.8 summarizes models loaded with thermal gradients. Section 8.9 discusses the effects of support stiffness on tensile forces in the deck, and Section 8.10 summarizes different skewed deck models. Section 8.11 compares cracking behavior across the various model types, while Section 8.12 summarizes model validation by comparing results to the experimental test program, as well as support for test setup and instrumentation. Finally, Section 8.13 provides a summary of all modeling work.

8.1 OVERVIEW OF MODEL TYPES

To investigate a multitude of designs and testing configurations, researchers needed to develop an array of finite element models. When prudent, simplified models were developed to ensure that the computing times were minimized. Larger, more complex models were developed for the purpose of modeling issues of asymmetrical decks or loading conditions. Section 8.1.1 provides an overview of different model types. The designs used by TxDOT utilize PCPs in two different configurations, which when combined with considerations for debonding and skew lead to numerous deck configurations. A third potential precast panel configuration was also tested. Section 8.1.2 summarizes how these are captured in the models.

8.1.1 Model Configurations

To maintain computing efficiency, multiple girder lines and girder parts were reduced to a single girder and slab section for some models. As shown in Figure 8.1, using a symmetrical single-girder model allowed for mirroring of the model along lines of symmetry. Thus, a single-girder model with symmetrical constraints across two directions of the slab could be used to obtain more efficient results. Both concrete faces and the ends of continuous reinforcement were marked as symmetrical using boundary conditions in the analysis, creating continuity along mirrored faces. The single-girder line model was used to study a variety of link slab cases. While material properties were simplified for the concrete girders, the deck and deck reinforcement used the nonlinear material models described in Section 8.2.1.

An important effect demonstrated using this mirroring technique was the hourglass behavior in stress distribution caused by shear lag. As shown in Figure 8.2, an hourglass shape formed when viewing a color gradient of longitudinal stresses in the deck, with stress concentrated over the girder ends and fading between the girders.

The dual-girder line model was used when a more in-depth investigation of differences at each girder line is needed, including (a) modeling of experimental test setups where different detailing is used in each overhang, (b) investigation of a bridge with more than two girder lines (using mirroring with two girders allows for consideration of a four-girder bridge), (c) modeling of asymmetrical loading conditions, and (d) investigation of skewed designs. A skewed support model, shown in Figure 8.3, had two girder lines with girder ends offset to model skew effects in the slab. The model was loaded by displacing the girder ends rather than by applying a load to the model.

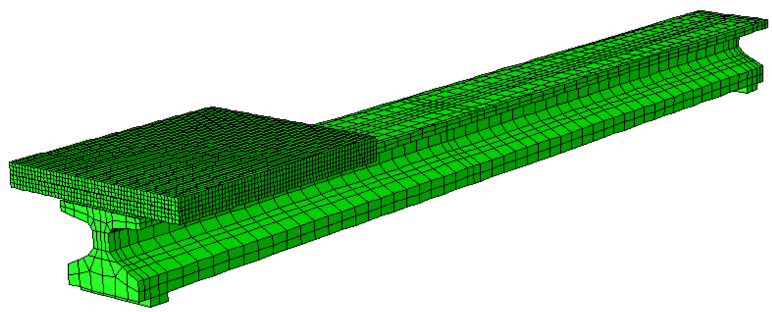

(a) Single girder modeled

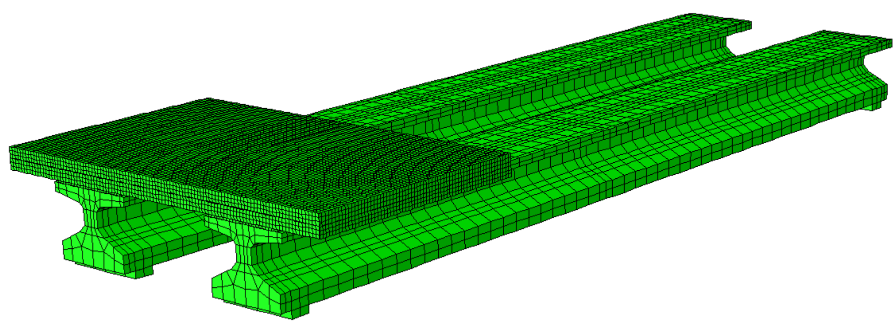

(b) Mirrored longitudinally

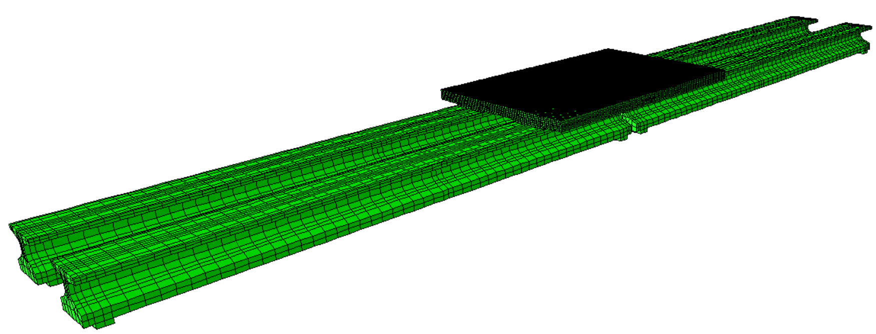

(c) Mirrored longitudinally and transversely

Figure 8.1. Mirroring of symmetric models.

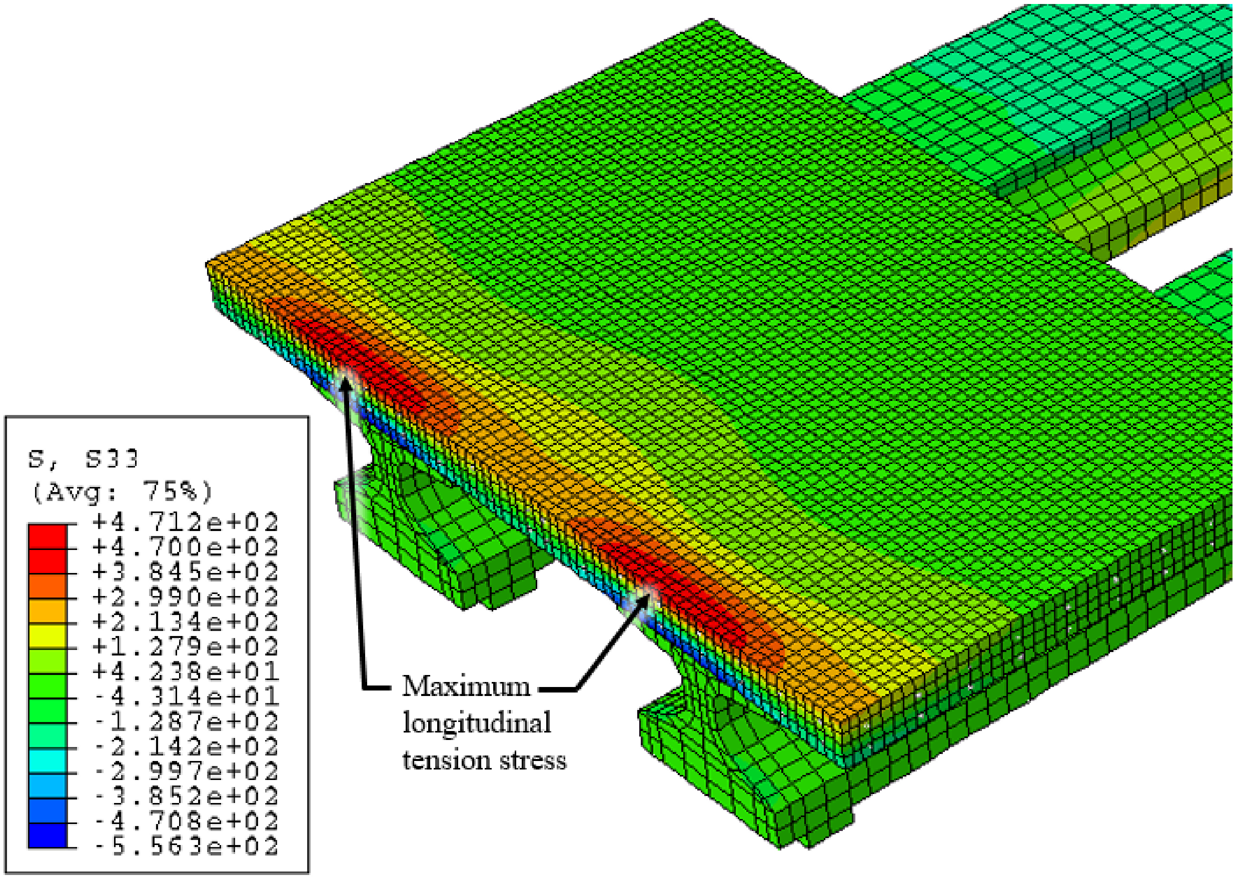

Figure 8.2. Shear lag effect shown by longitudinal stress distribution with hourglass shape over the girder ends.

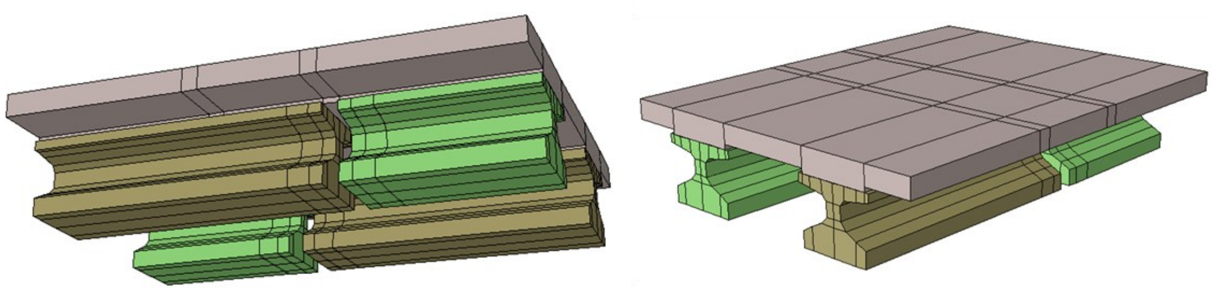

Figure 8.3. Dual-girder model for skewed girder configuration without clipped girders.

8.1.2 Deck Configurations

Given TxDOT's use of PCPs and the desire to investigate multiple design configurations, it was necessary to establish three baseline model types that are representative of TxDOT's common deck designs: (a) full-depth CIP concrete, (b) offset PCPs, and (c) flush PCPs. A fourth model type, continuous PCPs, was added to investigate potential design options. Then, the connection of the deck with girders used several variations: (a) fully bonded; (b) full-depth debonded, in which the deck is debonded from the girder; and (c) partial-depth debonded, in which the top portion of the deck is debonded from the lower portion of the deck.

A single-girder line flush precast panel model is shown in Figure 8.4. Half-sections of precast panel form the bottom of the PBJ crack with a timber board separating the panels. The top face of the CIP slab has an extra dividing line that can be used to create a crack-forming gap at the PBJ, similar to the gap that would be provided by a zip strip during construction.

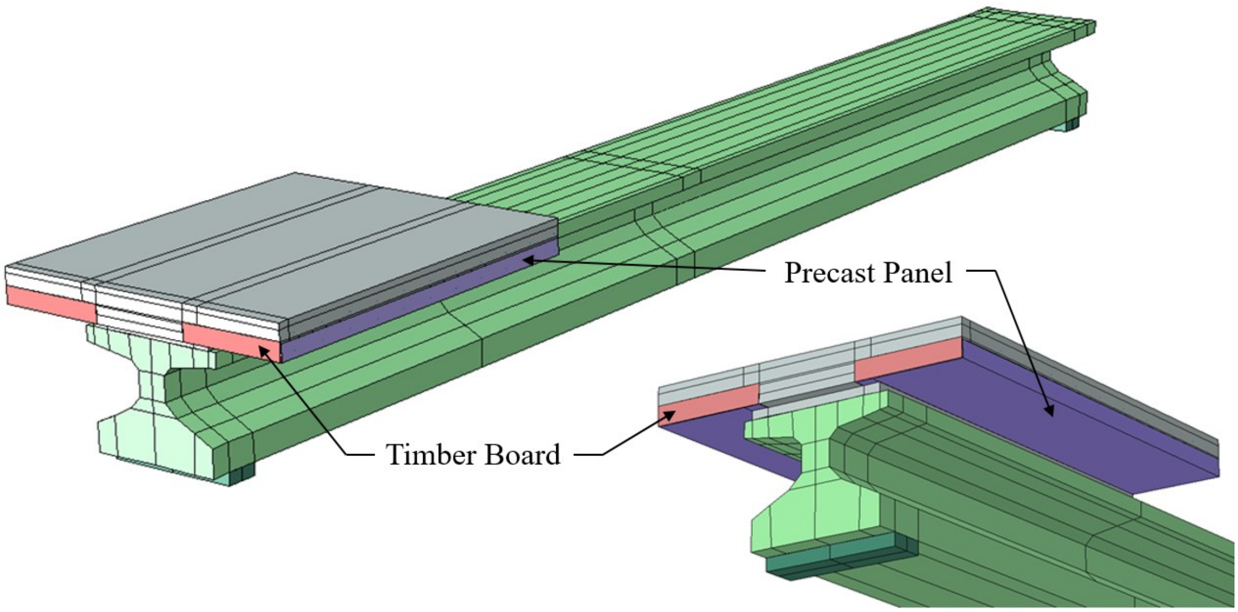

Figure 8.4. Flush panel model with timber board.

A single-girder line offset precast panel model is shown in Figure 8.5. This model also uses half-panels on each side of the girder, but the panels terminate 18 in. from the girder end (21 in. from the center of the PBJ). Models with and without a notch in the bottom of deck at the PBJ were considered.

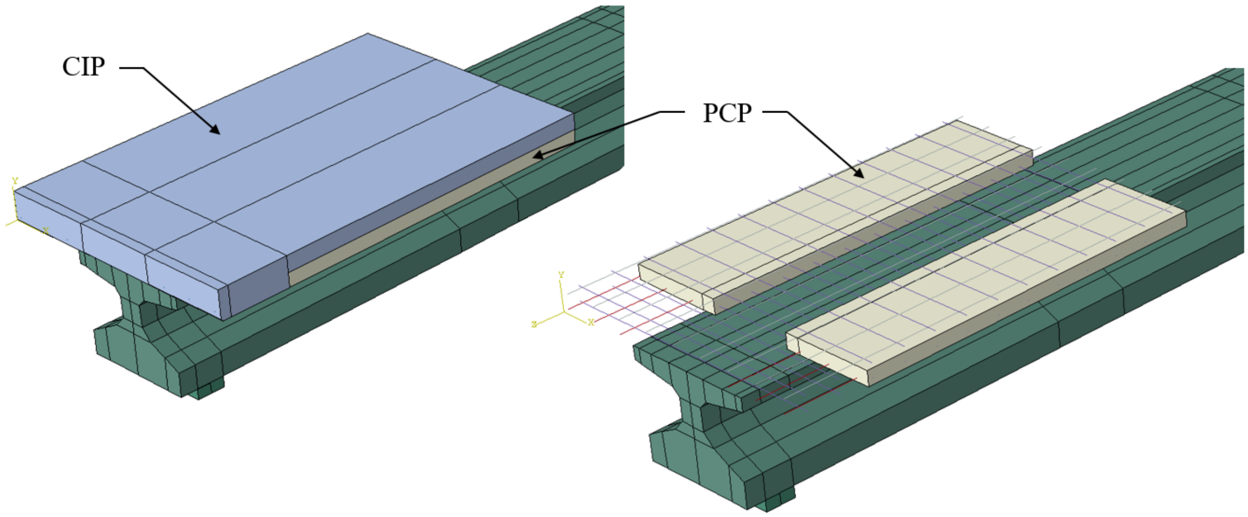

Figure 8.5. Single-girder offset precast panel model, showing the CIP topping slab (left) and without the CIP concrete, revealing the offset PCPs and reinforcement beneath (right).

A double-girder line model with continuous PCPs is shown in Figure 8.6. Continuous panels span across the girder ends. A full-width panel sits between the girder lines, while half-width panels rest on the exterior side of each girder. The continuous panel model includes no crack-forming notch or strip since a main intention of the continuous panel design is the reduction of crack severity.

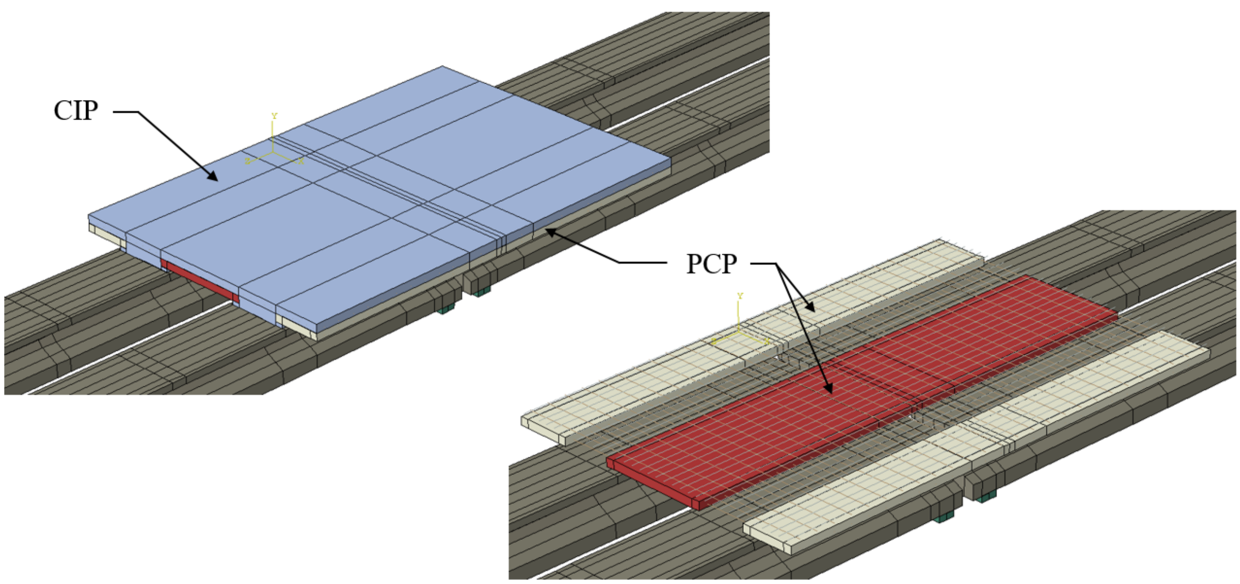

Figure 8.6. Double-girder continuous precast panel model, showing the CIP topping slab (left) and without the CIP concrete, revealing the continuous PCPs and reinforcement beneath (right).

DLS models simulate discontinuity between the slab and girder face, or between horizontal planes in the slab. This debonding allows the link slab to undergo deformations over a longer length, reducing bending curvature and delaying or eliminating cracking. A partial-depth debonded model, shown in Figure 8.7, has the upper section of slab debonded from the lower slab and PCPs at the level of the PCP top face. Figure 8.8 shows a full-depth debonded model, where a section of slab is debonded at the girder face.

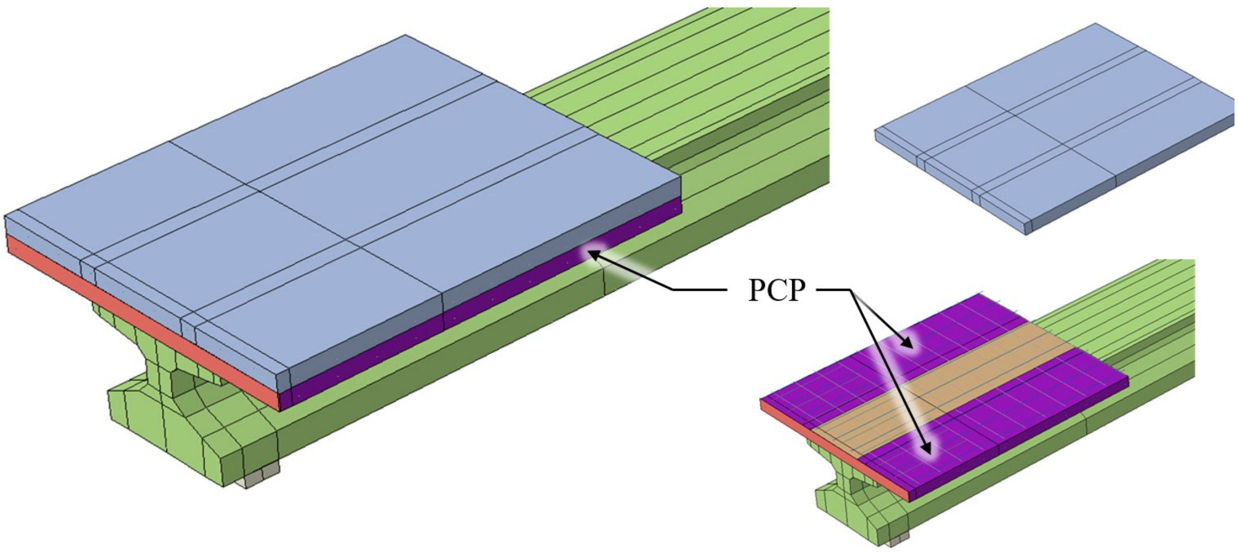

Figure 8.7. Partial-depth debonded model used with flush panel configuration.

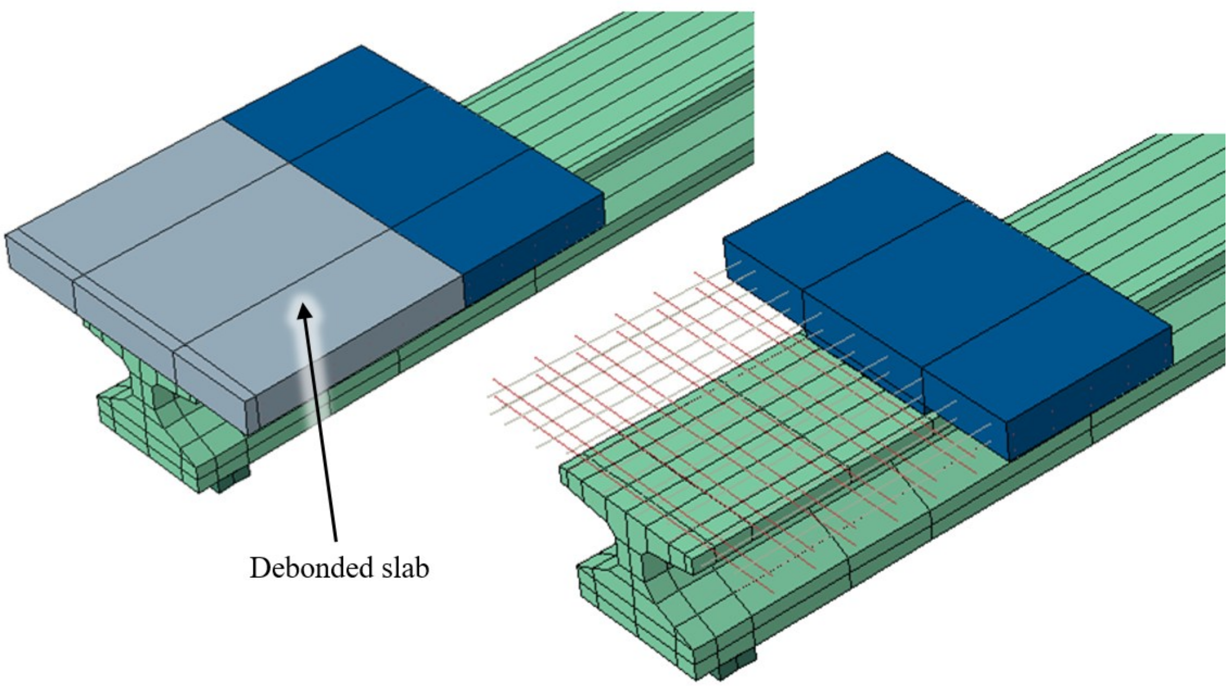

Figure 8.8. Full-depth debonded model.

In the process of modeling debonded details, researchers found that the geometry of the debonded region is critical to the performance of the link slab. Simply creating a disconnected plane between the slab and girder or layers of slab allows for minimal horizontal sliding between the disconnected segments. This is because the upward deflection of the girder ends under positive bending interferes with the slab above, as shown in Figure 8.9.

The principle behind debonding is to increase the radius of curvature, ρ, of the link slab to decrease the bending moment, M, thereby reducing bending stresses. According to beam theory,

$$M = \frac{EI}{\rho} \tag{8.1}$$

where E is elastic modulus and I is the moment of inertia. For negative bending in the girders, such as the deformation caused by thermal gradient, a gap is naturally formed between the debonded faces. Simply detaching the link slab from the girder ends allows the link slab to deform freely and produce a larger radius of curvature associated with debonding, as shown in Figure 8.10.

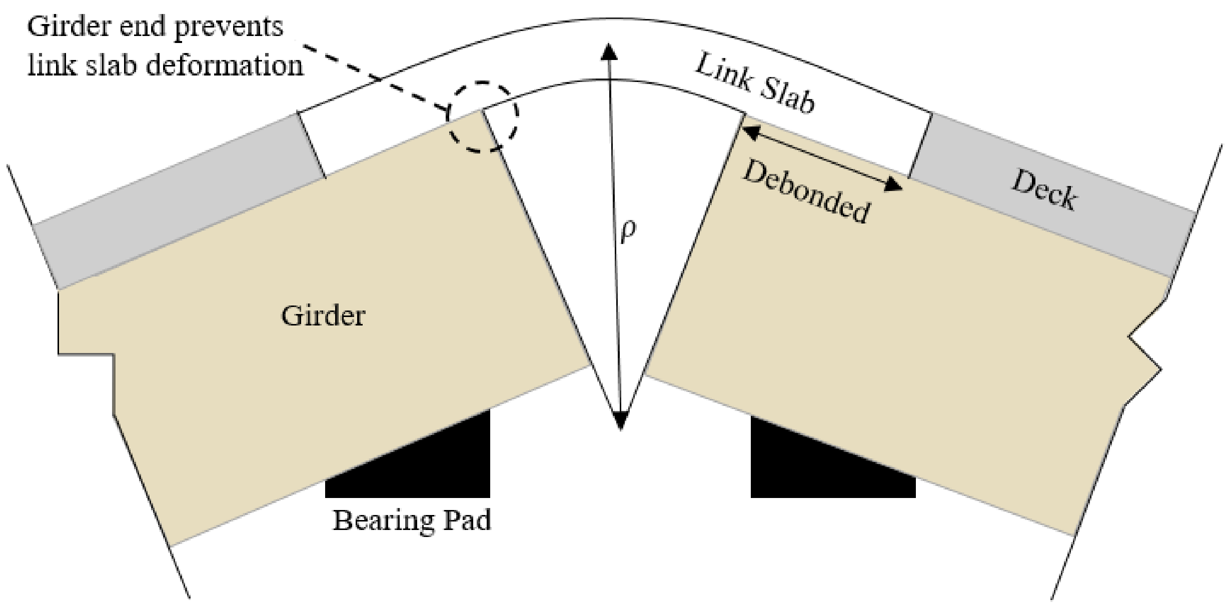

Figure 8.9. DLS diagram showing the girder ends interfering with intended link slab deformation, causing a short radius of curvature, ρ, for the link slab.

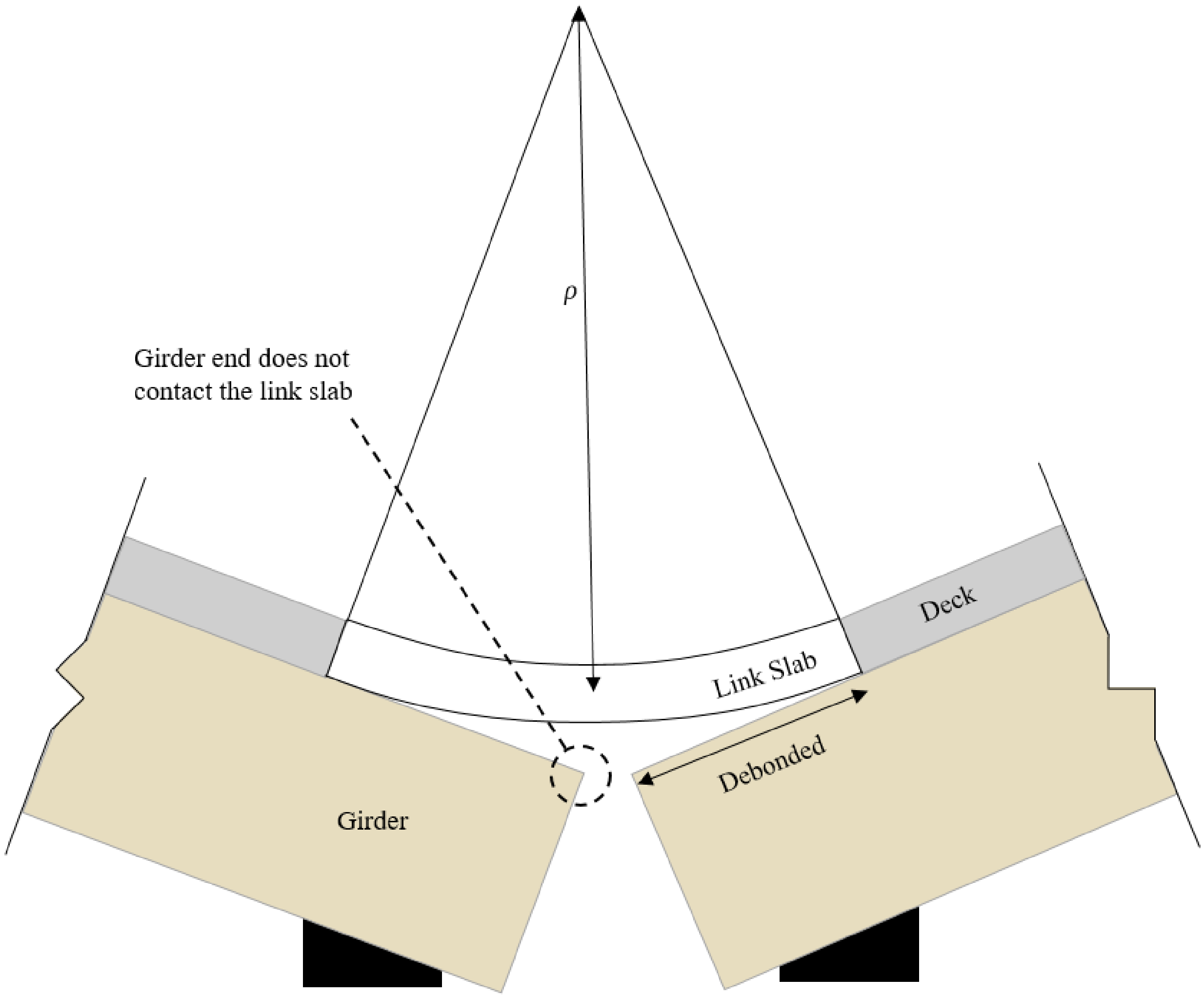

Figure 8.10. DLS diagram showing that the girder ends do not interfere with link slab deformation under negative bending, causing a longer radius of curvature, ρ, for the link slab.

Providing a vertical gap between the two debonded faces allows the link slab to deform as intended. The radius of curvature of the link slab is increased, reducing bending stress in the deck, as shown in Figure 8.11. Early finite element models were built without vertical gaps in the debonded region, leading to small improvements in cracking performance. Later models that included a debonded gap of 0.5 in. or larger showed much larger improvements in link slab cracking performance. Measuring the girder end vertical deflection on multiple models showed that a 0.5-in. gap would be sufficient to prevent the girder ends from contacting the bottom of the link slab at high rotations.

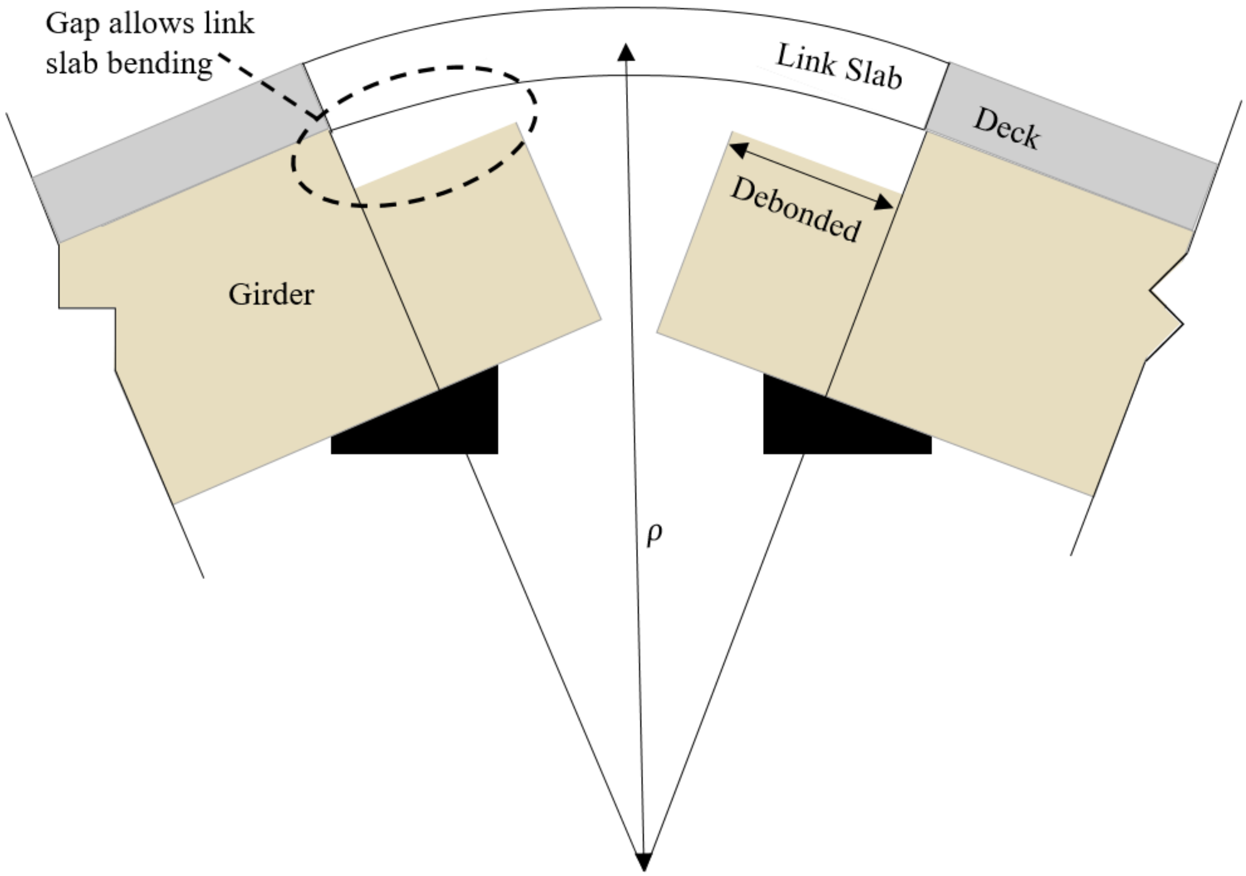

Figure 8.11. DLS diagram showing that the girder ends do not interfere with link slab deformation when a gap is provided along the debonded length, causing a longer radius of curvature, ρ, for the link slab.

8.2 MODEL DETAILS

ABAQUS models were primarily designed to mimic the qualities of the laboratory test program and the Spring/Holland Relief Bridge in the Bryan District. As such, Tx28 girders with 6-ft 4-in. spacing were used with a typical slab depth of 8.5 in, with 4-in. PCPs and 4.5-in. CIP concrete. Reinforcement type and spacing matched current TxDOT designs (#4 @ 9", with supplemental bars at 9 in. in the flush panel designs). Steel was Grade 60. Concrete strength of 5 ksi was typically used in slab sections. While this is larger than the design value of 4 ksi, it is in line with the properties of concrete obtained when 4-ksi concrete was ordered from local ready-mix suppliers. Concrete sections were meshed using C3D8R elements, which are eight-node brick elements with reduced integration and hourglass control to prevent unrealistic deformations.

8.2.1 Material Properties

Material properties and models were selected to provide a balance between simulation accuracy and model flexibility and run time. In general, material and behavioral models for elements of lesser importance, such as the prestressed concrete girders, were simplified to promote faster run times. As such, girders were modeled as uncracked sections with linear material properties. Elements of the model with greater importance to this research, such as the link slab and slab reinforcement, used nonlinear material models to provide more accurate results, especially at high deformations.

Nonlinear concrete compressive models that were considered include the Hognestad model (shown in Figure 8.12) and the unconfined Kent-Park model (shown in Figure 8.13); presented results use the Kent-Park model. Both models utilize a parabolic rise in stress to ultimate strength, with linear post-peak behavior. While both models provided reasonable results and have been used in literature for concrete deck slabs (Al-Rousan et al. 2020; Chaudhari and Chakrabarti 2012), the unconfined Kent-Park model was chosen as the primary compressive concrete material model.

To model tensile behavior of concrete, the simple bilinear model shown in Figure 8.14 was chosen based on experience with convergence issues and suggestions for use with the concrete damaged plasticity model in ABAQUS. This bilinear example is for 5000 psi concrete and defines constant slope of stress before and after rupture. For steel reinforcement, a bilinear elastic-perfectly-plastic model was chosen for typical Grade 60 reinforcing bars.

Both tensile and compressive concrete behavior are used within a concrete material model incorporated into ABAQUS: the concrete damaged plasticity model. This incorporates tensile and compressive stress-strain data to calculate fracture or crushing behavior in elements, such that cracking locations and reasonable deformation and stiffness of the link slab may be calculated at each step of analysis. Common values for the model, shown in Table 8.1, were used to provide reasonable material results.

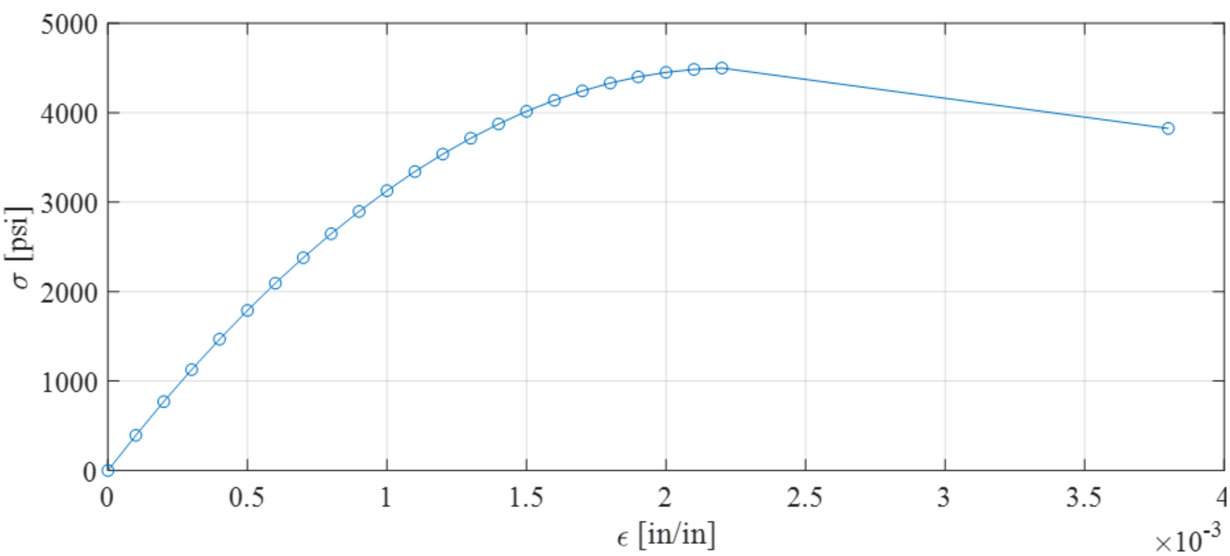

Figure 8.12. Hognestad concrete model for ultimate compressive strength of 4500 psi.

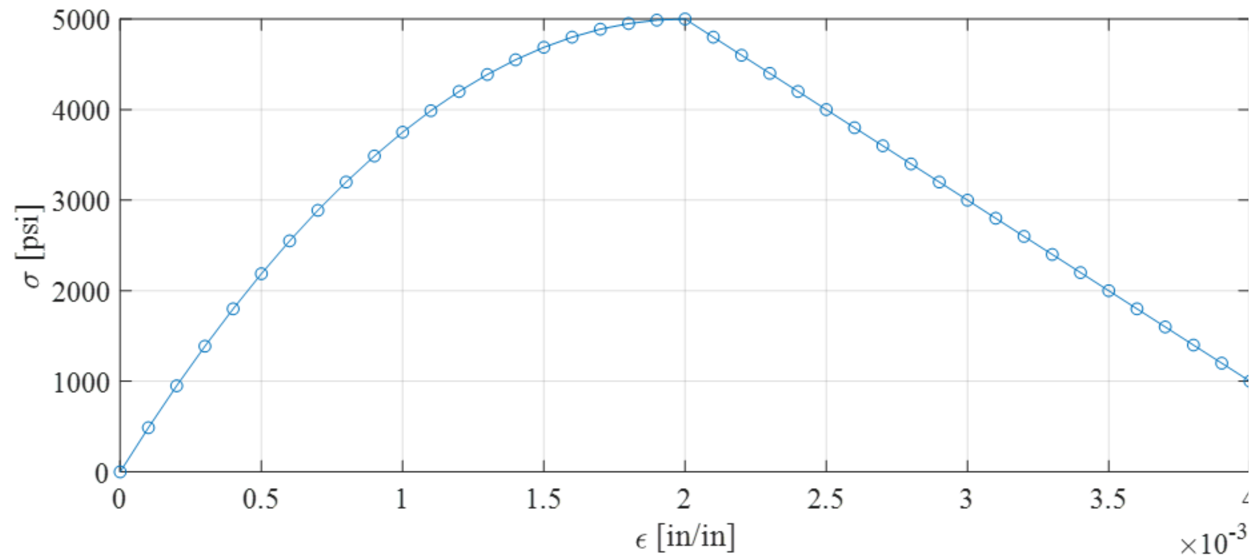

Figure 8.13. Unconfined Kent-Park concrete model for ultimate compressive strength of 5000 psi.

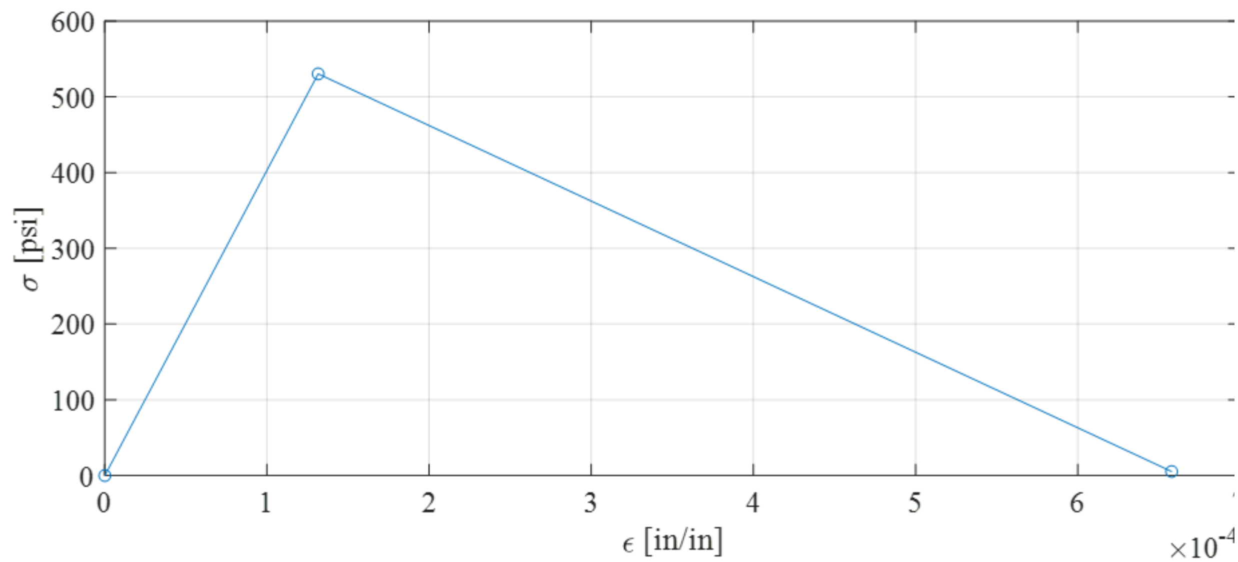

Figure 8.14. Bilinear tension model for concrete.

Table 8.1. Concrete damage plasticity parameters.

Coefficient	Dilation Angle	Eccentricity	Fb0/fc0	K	Viscosity Parameter
Value	35	0.1	1.16	0.67	0.001

8.2.2 Reinforcement

Reinforcement in the link slab was modeled using embedded truss elements. These elements are commonly used for reinforcement modeling in ABAQUS and assume a perfect, nonslip bond between the embedded elements (steel) and the host material (concrete). Longitudinal and transverse reinforcement layers for the slab, shown in Figure 8.15, were modeled with symmetric boundary conditions in two directions to simulate continuous reinforcement.

The typical bar configuration in these models, unless altered to investigate the effect of changing reinforcement conditions, was modeled to match the laboratory test specimens and typical TxDOT details. Grade 60, #4 steel rebar was placed in two mats, top and bottom, with bars in the longitudinal and transverse directions at 9-in. on-center spacing. Concrete cover of 2.5 in. was provided on top and 1.25 in. on the bottom of the slab.

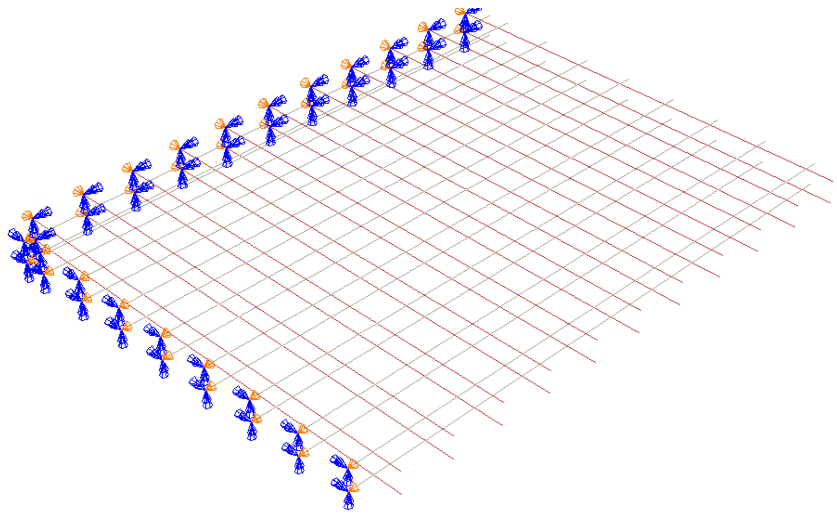

Figure 8.15. Rebar cage showing the mirrored end constraints on the reinforcement in two directions.

8.2.3 Miscellaneous Details

Bearing pad behavior was modeled using linear springs in three directions. Spring stiffness was estimated based on values from Terzioglu (2015) and Wassef et al. (2003) for typical elastomeric bearing pads (see Table 8.2). The location of all three springs was centered on the bottom of a stiff bearing pad part, shown with a spring element in Figure 8.16. The bearing pad part, shown attached to the bottom of the girder in Figure 8.17, was connected to the girder's bottom face with a tie constraint. This allowed girder ends to rotate on their supports with minimal resistance, but to deflect horizontally with resistance typical of the shear force provided by an elastomeric bearing pad. Using a bearing pad part instead of attaching the spring directly to the girder face prevents the formation of unrealistic stress concentrations at the girder ends.

Table 8.2. Elastomeric bearing pad stiffness values.

Spring Constant	Vertical	Longitudinal	Transverse
Value	6100 kip/in	10 kip/in	10 kip/in

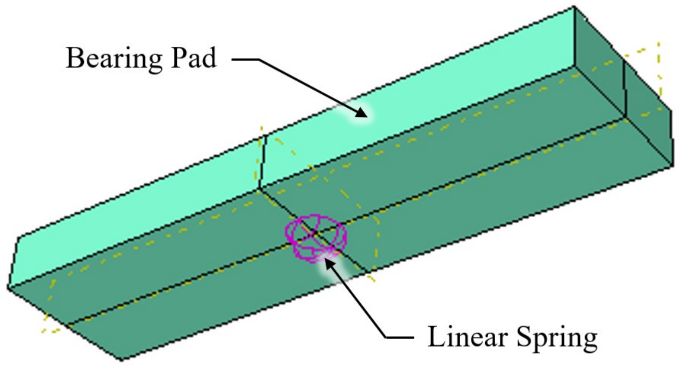

Figure 8.16. Bearing pad spring location.

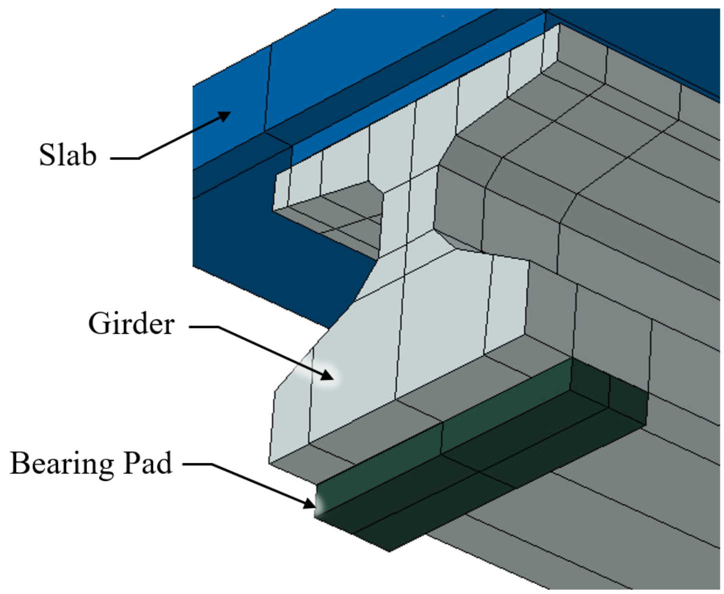

Figure 8.17. Bearing pad location at girder end.

A key variable that may be modeled is the use of debonding of the link slab, either at the girder face or within the slab depth. Debonded surfaces are modeled to have frictionless contact, such that the surfaces will resist normal contact but provide no resistance due to tangential friction. This simulates the use of a debonding agent such as roofing paper that provides negligible friction between debonded concrete surfaces.

8.2.4 Loading

Loading of the model was designed to simulate the loading conditions of the experimental test setup, as shown in Figure 8.18. A pressure load (b) was applied to the top girder face near midspan (a), far from the slab section in order to avoid localized effects due to loading. For single-girder models, the symmetrical boundary conditions meant that each mirrored span has an equivalent pressure load applied. Models with multiple girder lines required increased computing time but allowed for asymmetrical loading conditions. The vertical load on the girder face caused girder deformations that produced tensile forces at the top of the link slab and compressive forces at the bottom. Girder end displacement data were saved for each load step to record a relationship between load, rotation, and link slab behavior.

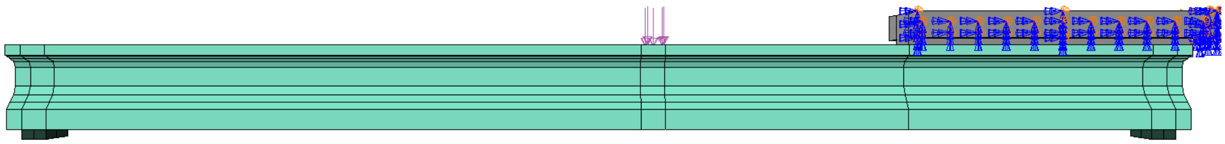

(a)

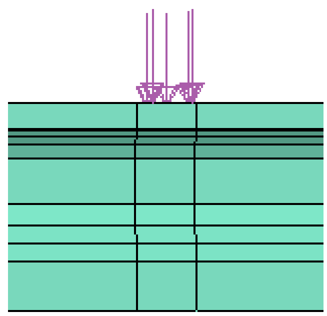

(b)

Figure 8.18. Loading on top girder face.

In order to investigate the effects of thermal gradient and negative bending of the girders, temperature loading was applied in some models. A preliminary analysis step was used to designate initial temperature conditions of the girders. During the loading step, the temperature of the bottom face of the girder was decreased, producing negative girder end rotations (see Figure 8.19) and tensile forces in the bottom of the link slab. Uniform temperature loading was also used to investigate deck shrinkage effects.

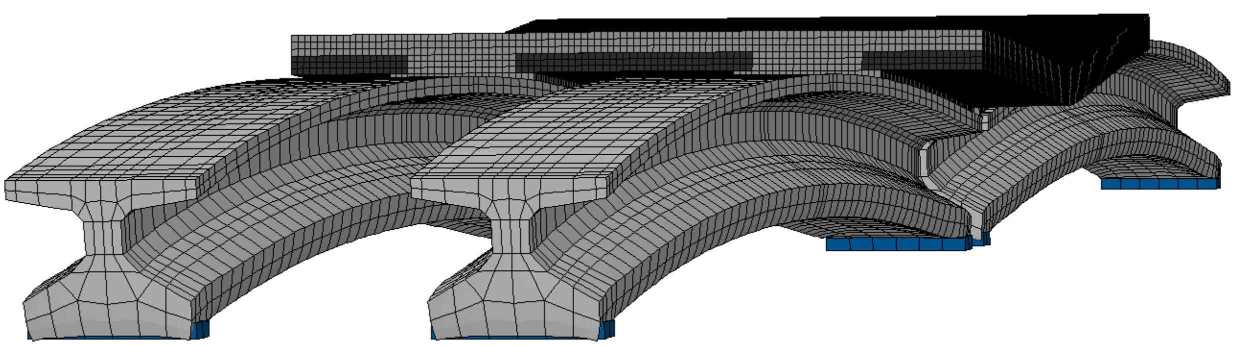

Figure 8.19. Negative bending due to thermal gradient with deformation exaggerated to show girder curvature.

Since midspan loading is not possible for girder stub models, the exterior girder ends were displaced using rotation boundary conditions for each girder line. This displacement loading (see Figure 8.20) rotates both exterior ends of one girder by 0.005 rad (a), and then rotates the second girder line in the same way (b) while the first girder line is held in its rotated state. Thus, stresses in the deck can be seen propagating from over one girder line to the next.

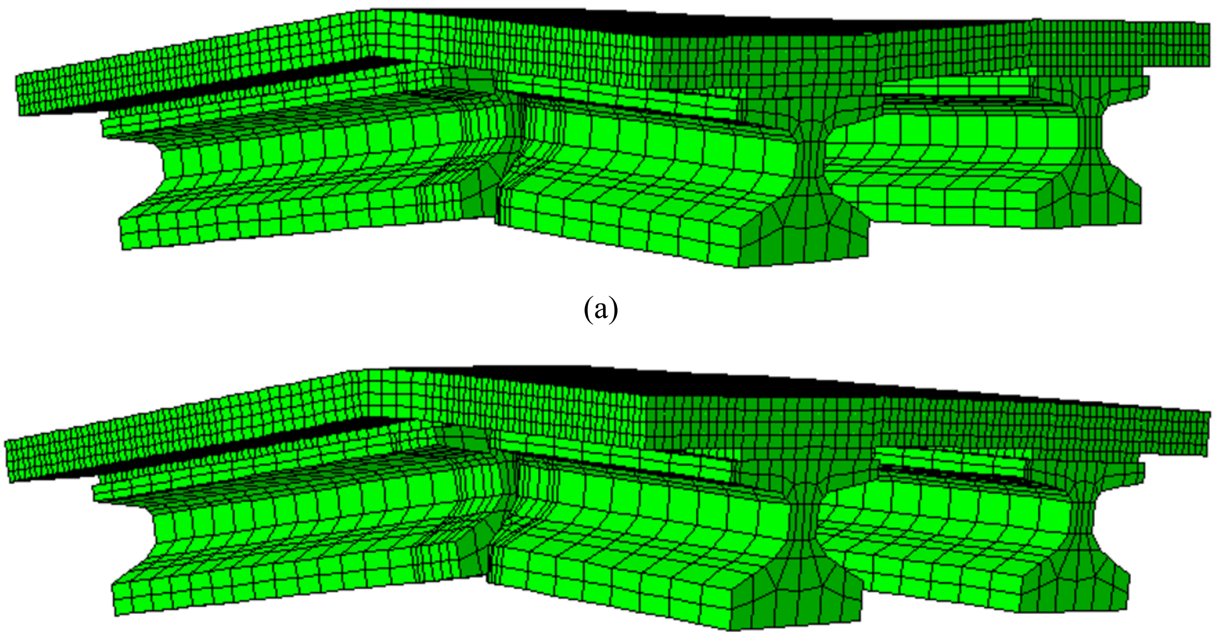

(a)

(b)

Figure 8.20. Deformation of girder stub model, at 20 times scale, showing deformation of (a) one girder line and (b) both girder lines.

8.2.5 Recorded Information

Results were recorded at each iterative step of the simulation. For all models, girder displacement was recorded in order to calculate girder end rotations. In the deck, stress, strain, and displacement were recorded for all deck, reinforcement, and attached elements. In order to verify the validity of results, values such as contact stresses were recorded to ensure that debonded faces in contact were behaving appropriately.

Maximum plastic principal strains were recorded to determine cracking patterns. Since tensile strains are modeled as elastic up to the cracking point, plastic strain in concrete elements indicates that the concrete has passed the rupture stress. The magnitude of plastic principal strain may be used as a proxy for crack width.

Maximum principal stresses are another useful tool for tracking potential cracking behavior. For steel reinforcement modeled by truss elements, the only stresses recorded were in the longitudinal direction.

8.3 FULL-DEPTH CIP DECK

The ABAQUS models were first used to investigate the behavior of full-depth CIP link slabs. Section 8.3.1 presents results for a preliminary model using a full-depth CIP deck.

8.3.1 Bonded Models

The most basic model developed in ABAQUS was a fully CIP deck, bonded completely to the girder below, with typical reinforcement. This model, which may be used to compare results of other model iterations, is shown in Figure 8.21 and Figure 8.22. Bonding is accomplished using tie constraints that model zero separation between the disparate surfaces. The effect of initial loading, shown in Figure 8.21(b), demonstrates the buildup of longitudinal tensile stresses in the top of the deck concentrated over the girder. In Figure 8.22(a), cracking initiates over the girders at the center of the link slab as the bottom of the slab is in compression. In Figure 8.22(b), the section is fully cracked, and some regions of compressive stress develop in the deck away from the girder ends. As the slab cracks to around half-depth, the neutral axis of the section falls closer to the bottom of the slab. Compressive forces in the bottom of the slab are still concentrated over the girders. Significant tensile forces in the slab are limited to about the first 6 in. of link slab length, corresponding to high stress in the reinforcement that is also limited to the area in the immediate vicinity of the PBJ crack.

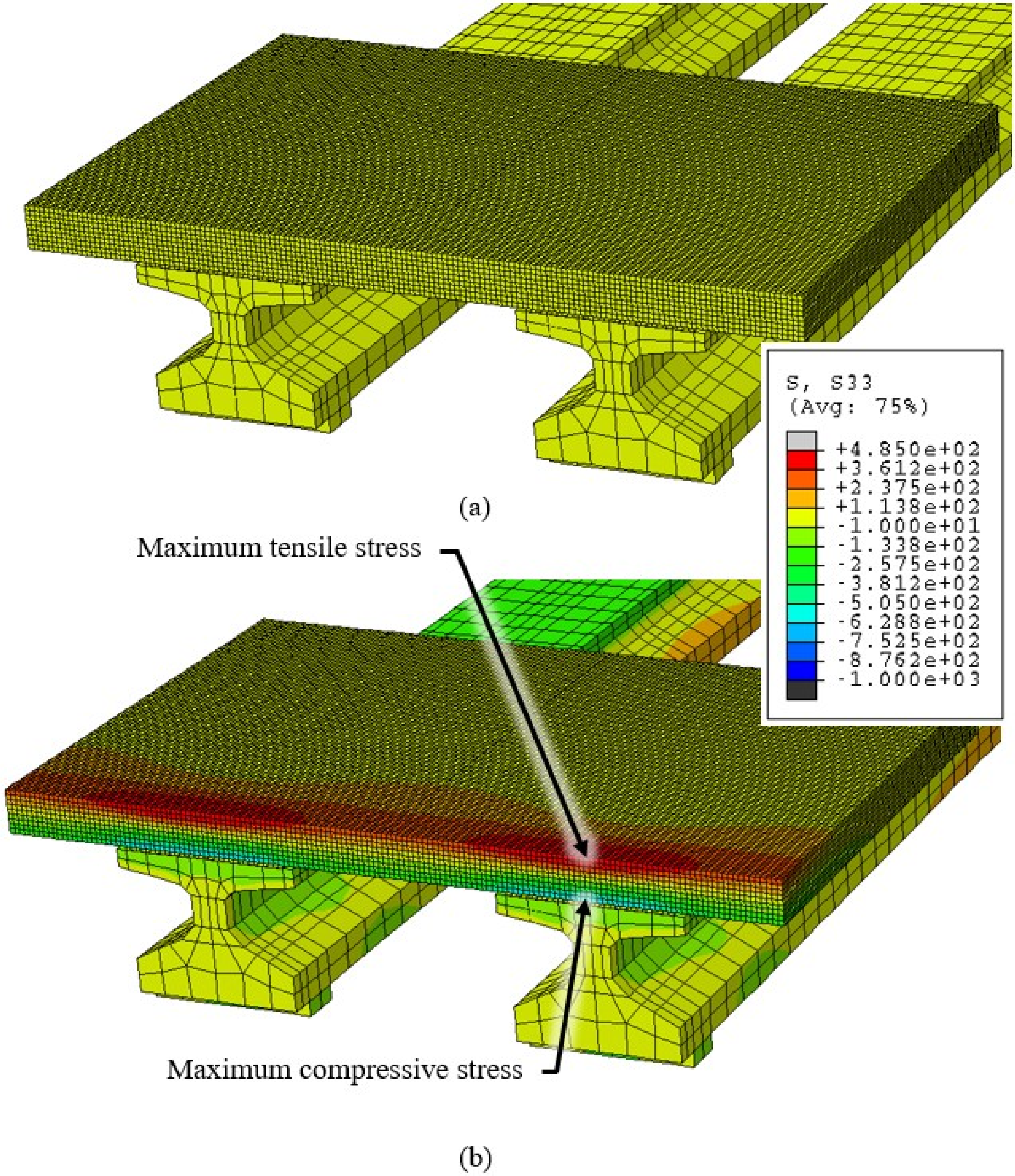

Figure 8.21. Longitudinal stresses in CIP deck concrete (psi), showing (a) the unloaded condition and (b) the formation of a force couple in the deck, concentrated over the girders.

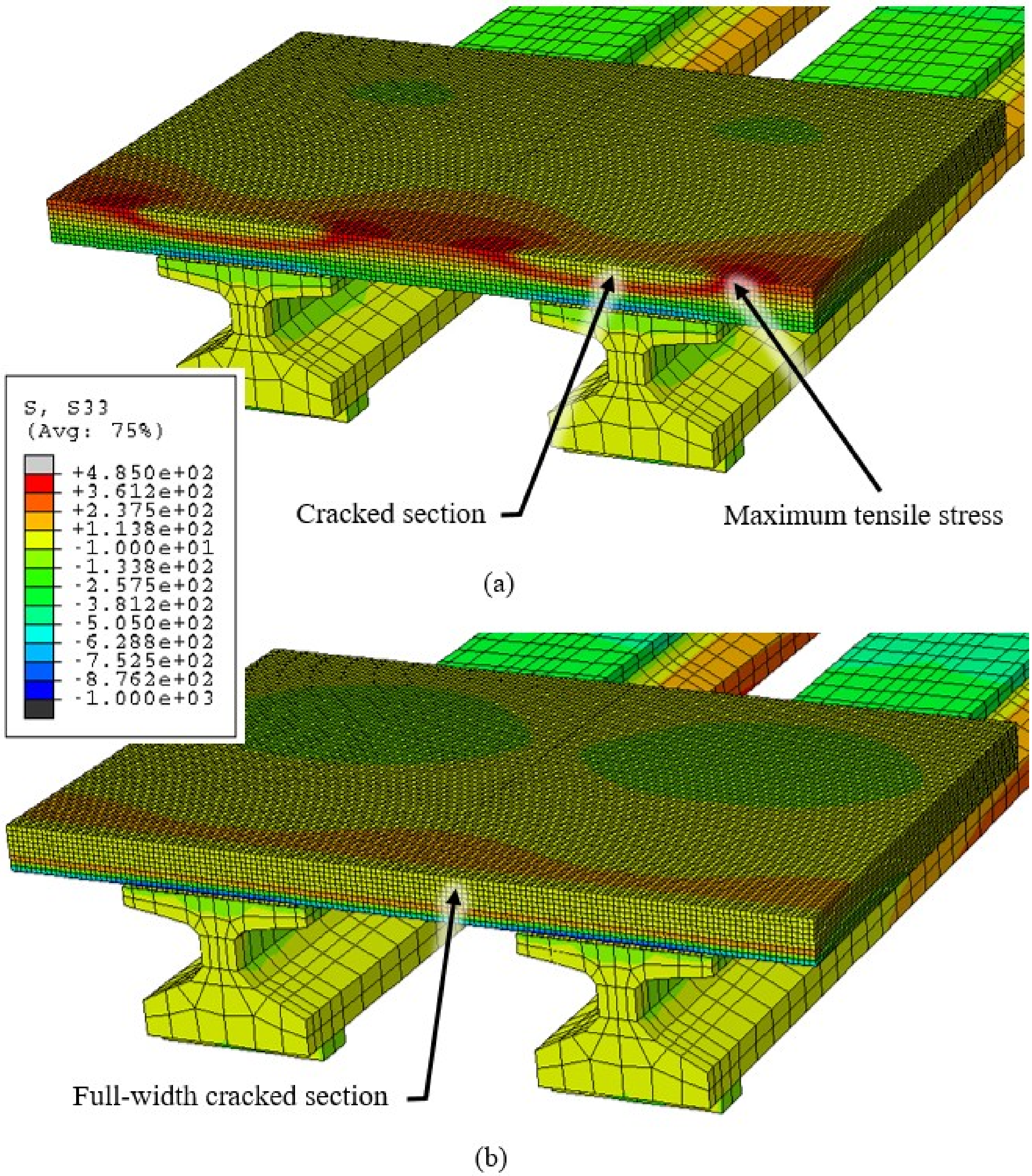

Figure 8.22. Longitudinal stresses in CIP deck concrete (psi), showing (a) initial crack propagation over the girders, which (b) continues until the entire deck width is cracked.

Figure 8.23 shows reinforcement stresses corresponding to the partial cracking in the slab over the girder in Figure 8.22(a). Figure 8.23(a) shows the transverse reinforcement at the PBJ developing mild tensile stresses between the girders and in the overhang, as well as mild compressive stresses over the girders. Figure 8.23(b) shows the top longitudinal reinforcement developing mild tensile stresses (around 330 psi), while the bottom longitudinal reinforcement develops higher compressive stresses (around 9200 psi). In Figure 8.24, steel stresses are shown for cracking across the entire width of the section, as shown in Figure 8.22(b). Figure 8.24(a) shows similar stresses in the transverse reinforcement as in the initial cracking phase. Figure 8.24(b) shows the top layer of steel developing larger tensile stresses close to the PBJ as the concrete no longer resists the rotation of the link slab across the crack. The stress drops in the bottom longitudinal steel.

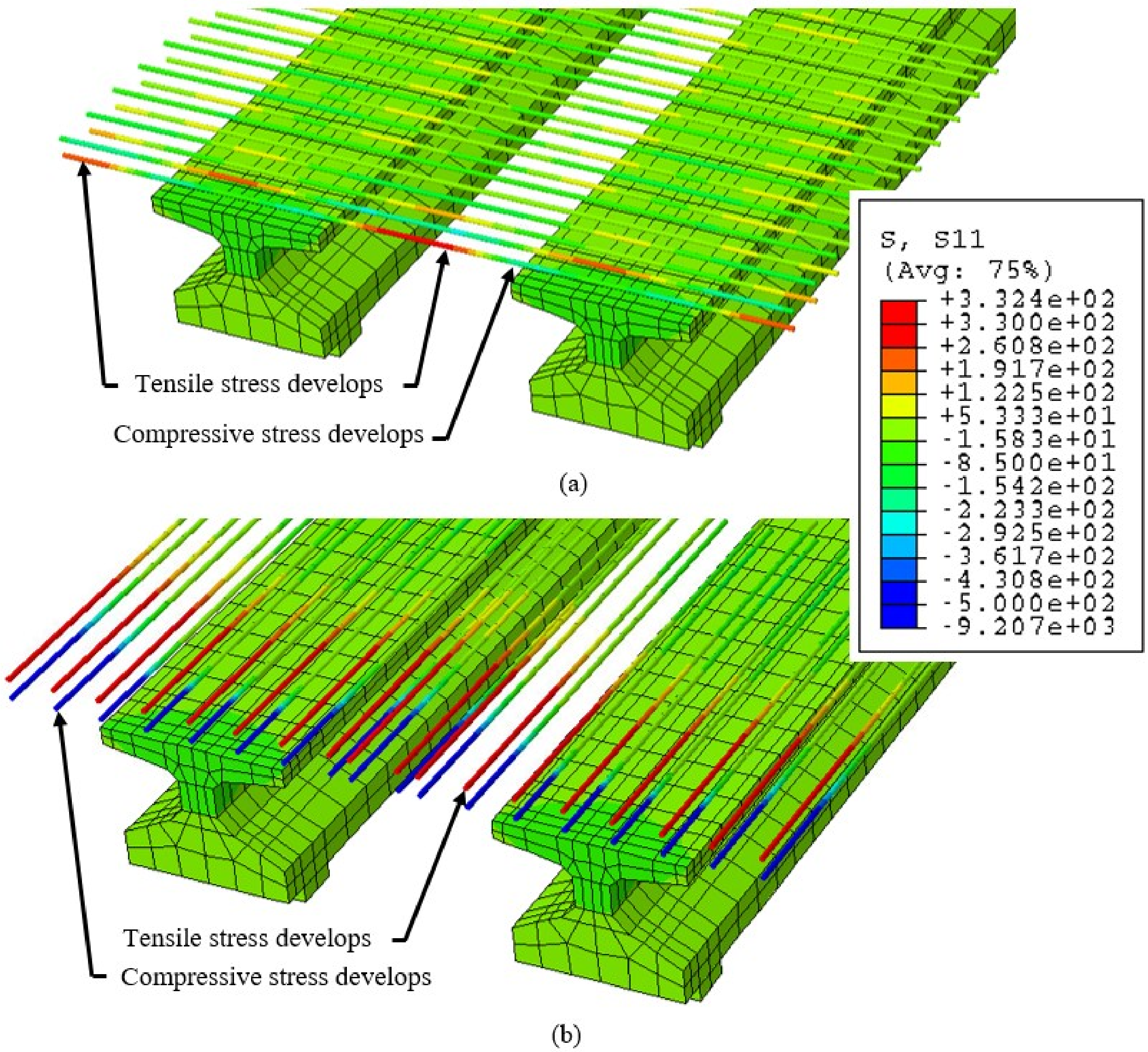

Figure 8.23. Longitudinal stresses in reinforcement (psi) for (a) transverse bars and (b) longitudinal bars at the onset of cracking.

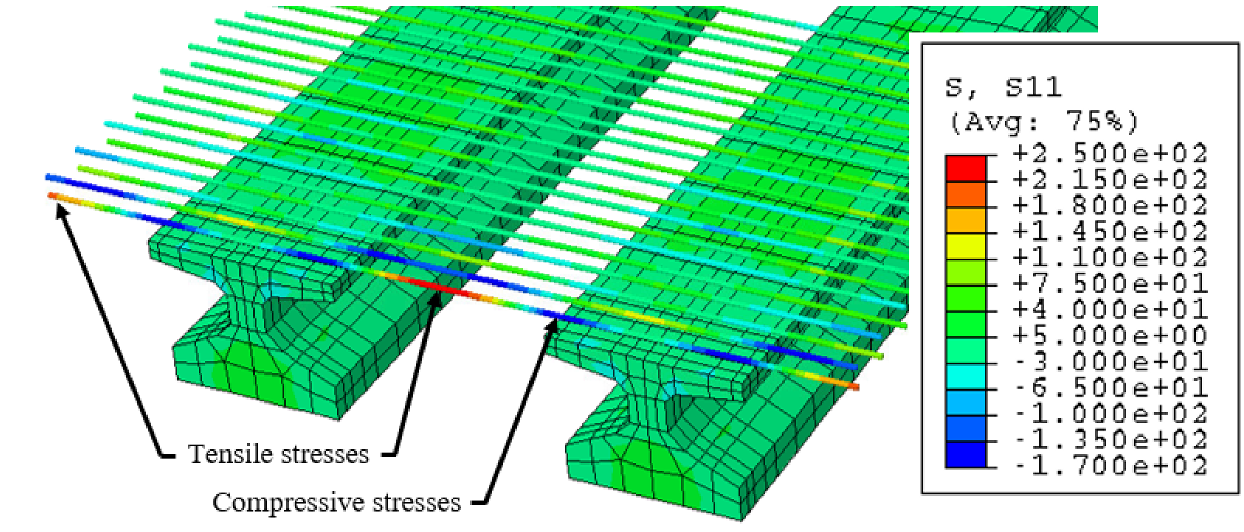

(a)

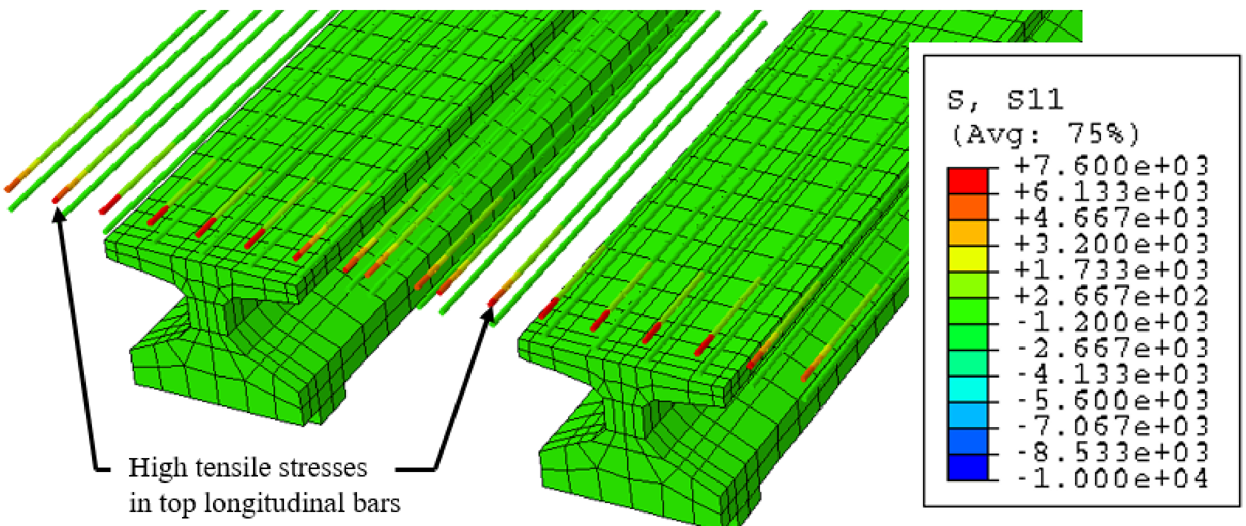

(b)

Figure 8.24. Longitudinal stresses (psi) in the reinforcement when the deck is cracked across the width of the section for (a) transverse bars and (b) longitudinal bars.

8.3.2 Debonded Models

While TxDOT PBJ details do not currently incorporate debonding of the link slab, debonding is a common practice in link slab construction to reduce or eliminate cracking of the slab. Finite element models are used to investigate debonding of the link slab at the girder ends for varying lengths in order to identify a practical length of debonding to prevent cracking. Other factors, such as stresses due to contact of the girder end and reduction of the interface reinforcement between the girder and slab, are discussed in later sections.

The single-girder line model was used to investigate the effect of different debonded lengths. Since a common practice in designing debonded link slabs is to debond for 5 percent of the girder span, debonded lengths were chosen in 5 percent increments of the span length of the laboratory specimen, 31 ft. However, since the girder span length used in the laboratory test setup is especially short compared to typical bridges, debonded lengths of 10 percent and 15 percent were also used for comparison. Not including the 6-in. gap between the girder ends, lengths of 0 in. (fully bonded), 16 in. (5 percent debonded), 35 in. (10 percent debonded), and 54 in. (15 percent debonded) are shown in the results.

Longitudinal concrete stresses at different longitudinal distances from the center of the PBJ are shown for each level of debonding in Figure 8.25. Stress was recorded over the girder at distances of 0 in. (the center of the PBJ), 3 in., 6 in., and 9 in. longitudinally from the center of the PBJ. Stresses increase until cracking with stress highest at the center of the PBJ. Post-cracking behavior shows minimal remaining stress in the concrete at the center and 3 in. from the PBJ. Increasing debonded length delays the onset of cracking.

Figure 8.26 shows the effect of debonding on the top longitudinal steel stresses within the section at the same distances from the PBJ. Stresses in the steel decrease dramatically within a few inches of the poor boy crack. The steel is barely engaged before cracking, but stresses near the PBJ increase toward the yield strength of the bars after cracking. Debonding delays when the bars are engaged until higher girder end rotations, as shown in Figure 8.27.

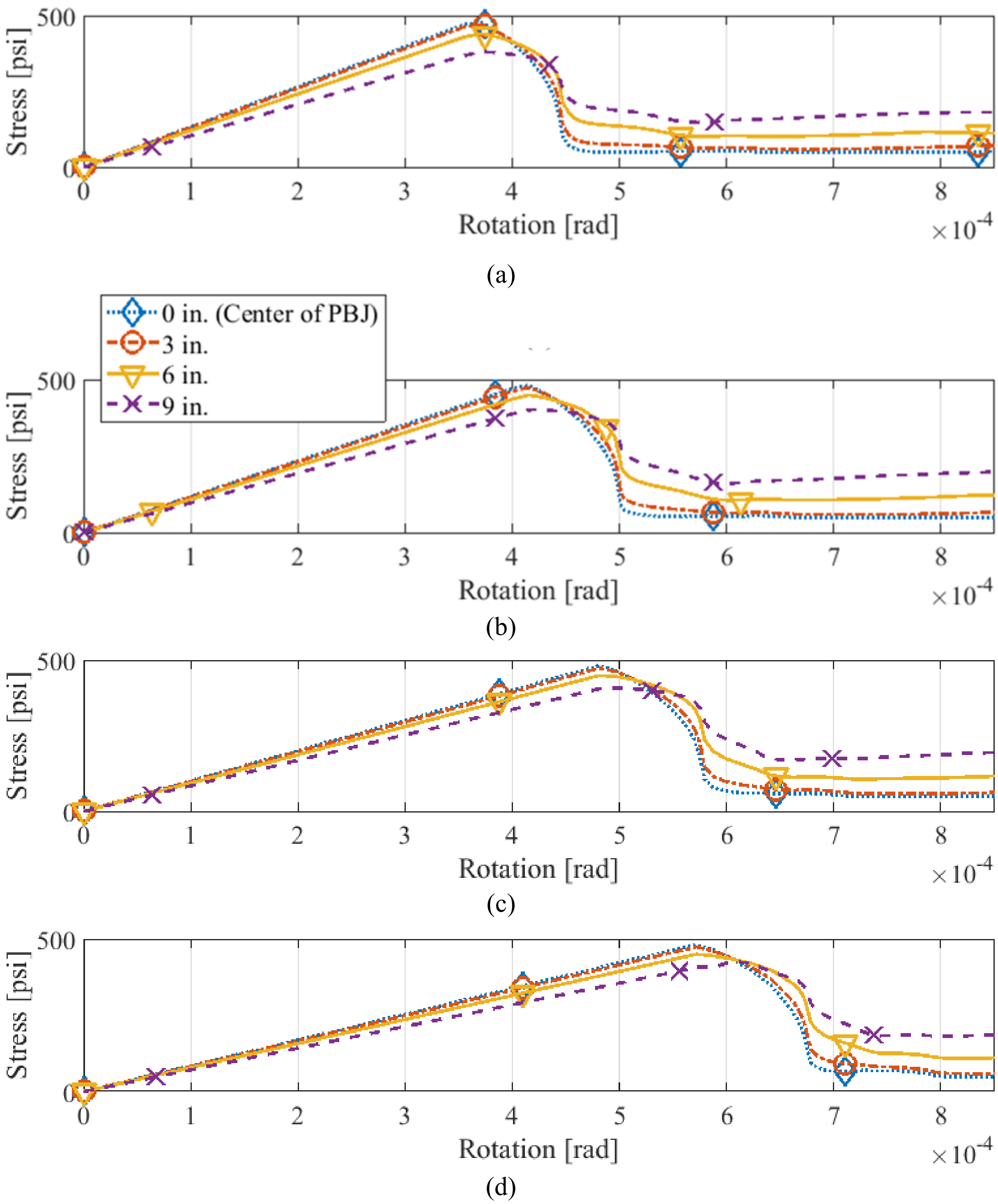

Figure 8.25. Effect of debonded length on longitudinal concrete stresses, showing (a) a fully bonded slab, as well as a slab debonded at the girder-slab interface for (b) 16 in., (c) 35 in., and (d) 54 in.

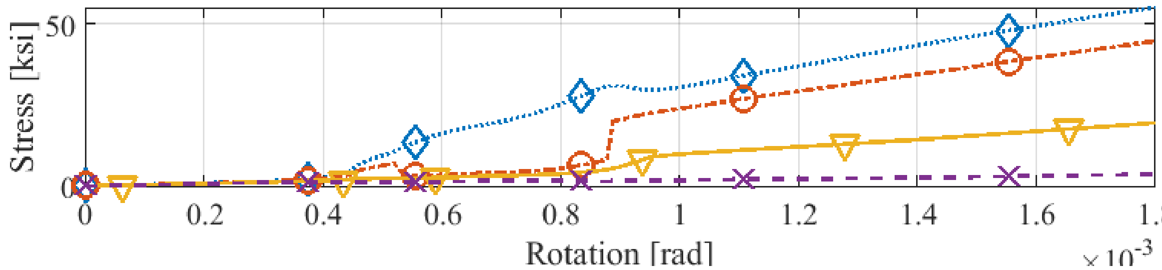

(a)

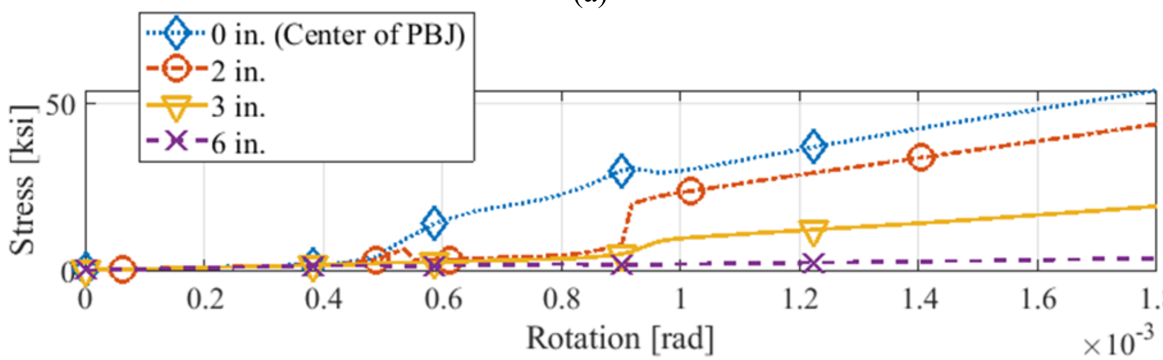

(b)

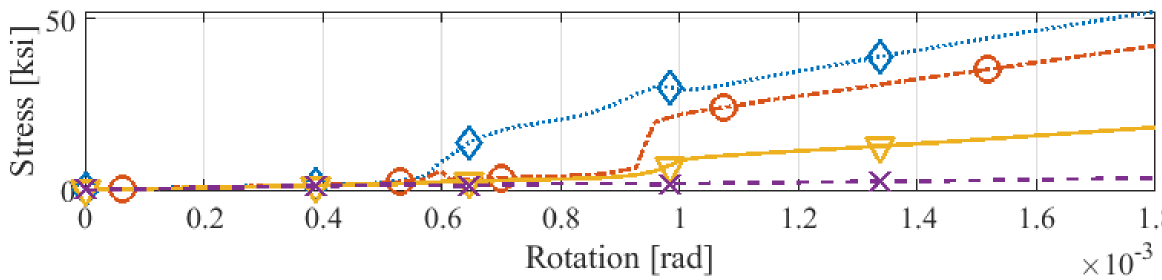

(c)

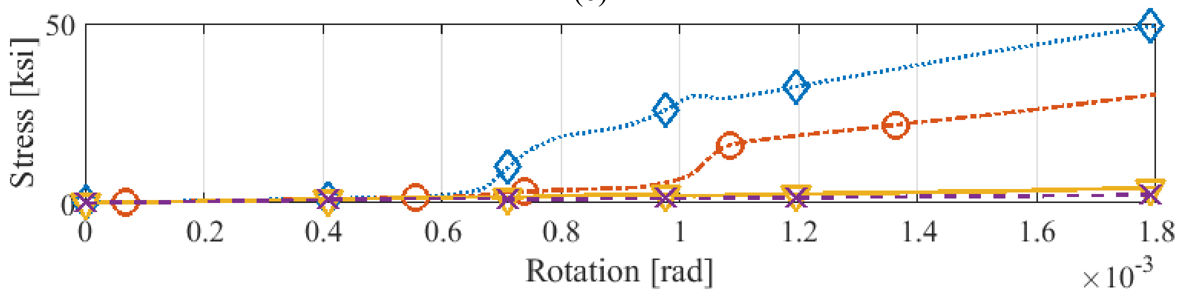

(d)

Figure 8.26. Effect of debonded length on top longitudinal reinforcing steel stresses, showing (a) a fully bonded slab, as well as a slab debonded at the girder-slab interface for (b) 16 in., (c) 35 in., and (d) 54 in.

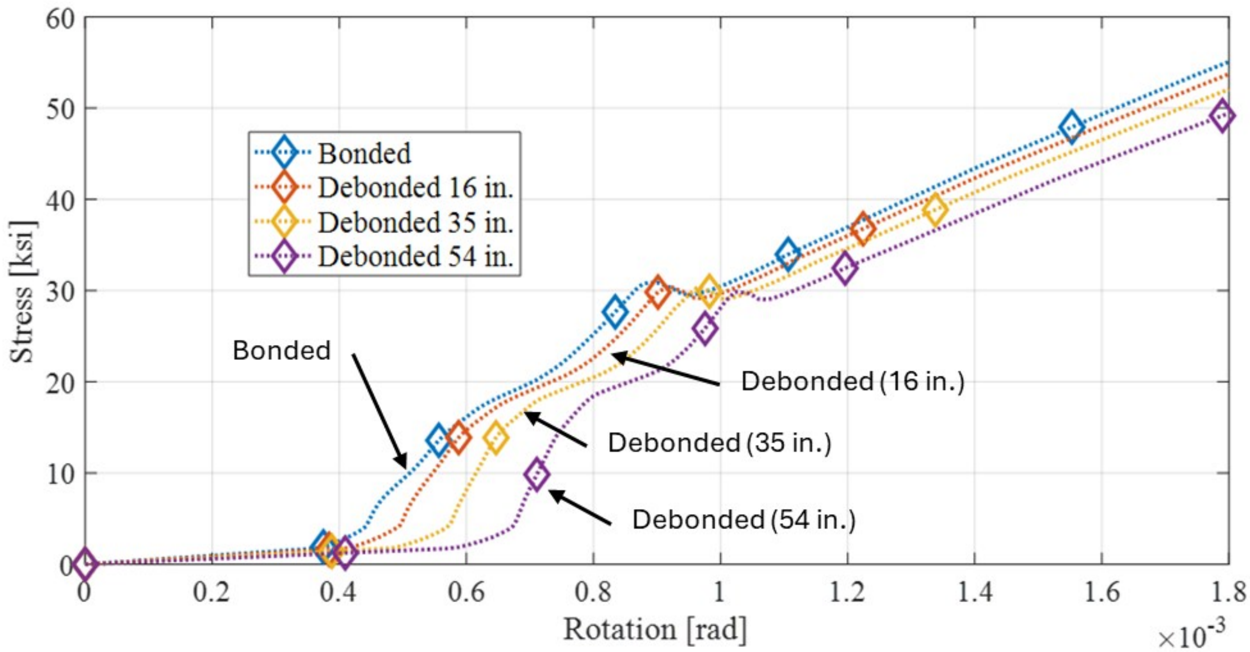

Figure 8.27. Comparison of top longitudinal steel stresses at different lengths of debonded slab, showing that debonding delays steel stress and crack formation.

8.4 FLUSH PANEL DECK

8.4.1 Bonded Model

The model was updated to include PCPs with the flush panel detail, including the timber board. The timber board spans the width of the joint and is tied to the surrounding concrete. A crack former in the top of the deck was considered by modeling the top section of the slab as discontinuous across the mirrored face of the PBJ.

The PCPs were modeled using concrete with a higher compressive strength but without prestressing force. It was assumed that stiffness of the panels could be approximated using proper material strengths but neglecting prestressing.

Selected results of a flush PCP model demonstrate stress and cracking patterns in the deck at rotations of approximately 0.005 rad. In Figure 8.28, the use of a crack-former detail including a timber board causes high longitudinal tensile stresses at the PBJ almost immediately after loading commences. The elements at the PBJ location reach their cracking stress, while the hourglass stress shape is noticeable, developing on both sides of the girder lines. Since the center of the PBJ is still the weakest point in the slab with the highest bending curvature, cracking still initiates at the center of the PBJ regardless of the use of a crack-former detail. Cracking is limited to this weak section at the center of the PBJ, even at higher rotations.

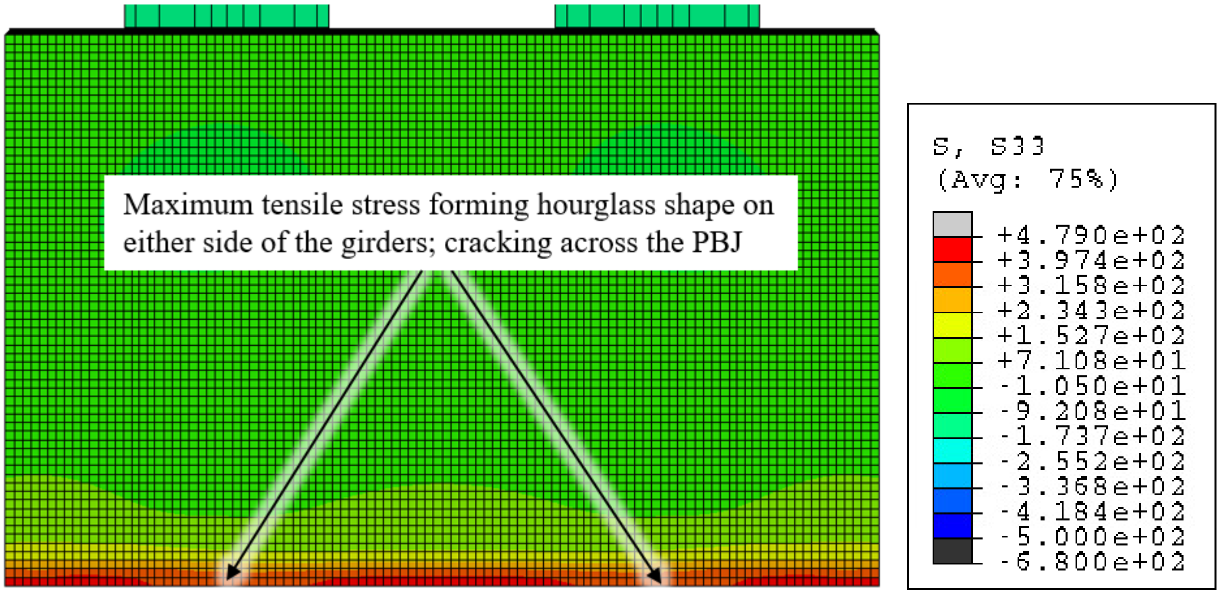

Figure 8.28. Initial cracking of the PBJ with the use of a control joint detail for a flush PCP model.

At higher rotations, with the PBJ long since cracked, longitudinal tensile stresses form over the reinforcement embedded within the slab, as shown in Figure 8.29. Furthermore, compressive stresses form farther back in the slab over the girders. The tensile stress within the top longitudinal steel, shown in Figure 8.30, reveals that the bulk of the tensile stress in the steel is constrained to the first 4 in. of bar length on each side of the joint. Cracking reaches the full depth of the CIP concrete over the timber board.

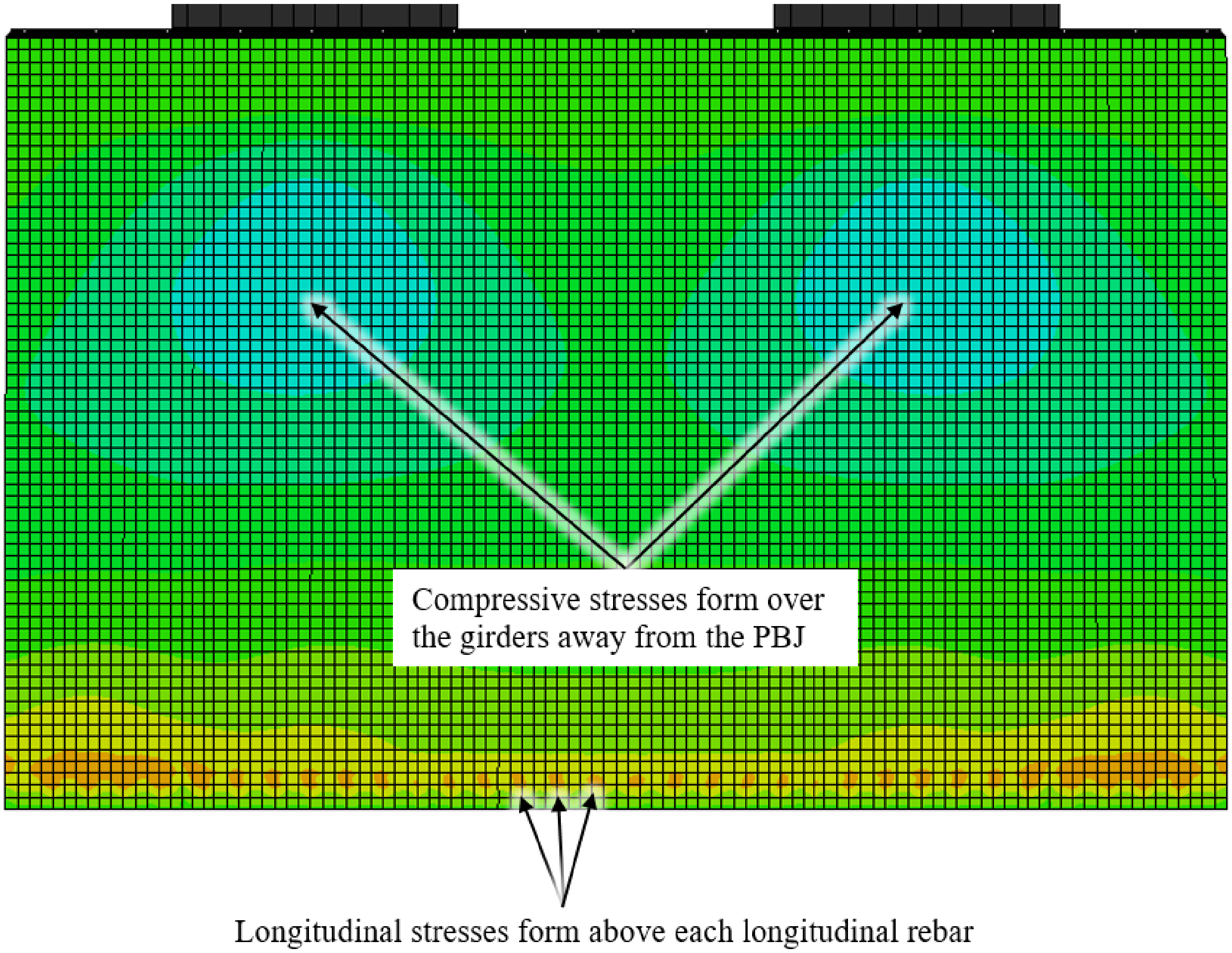

Figure 8.29. Longitudinal stresses form near the PBJ at the locations of longitudinal reinforcing bars, while compressive forces form away from the PBJ over the girder lines.

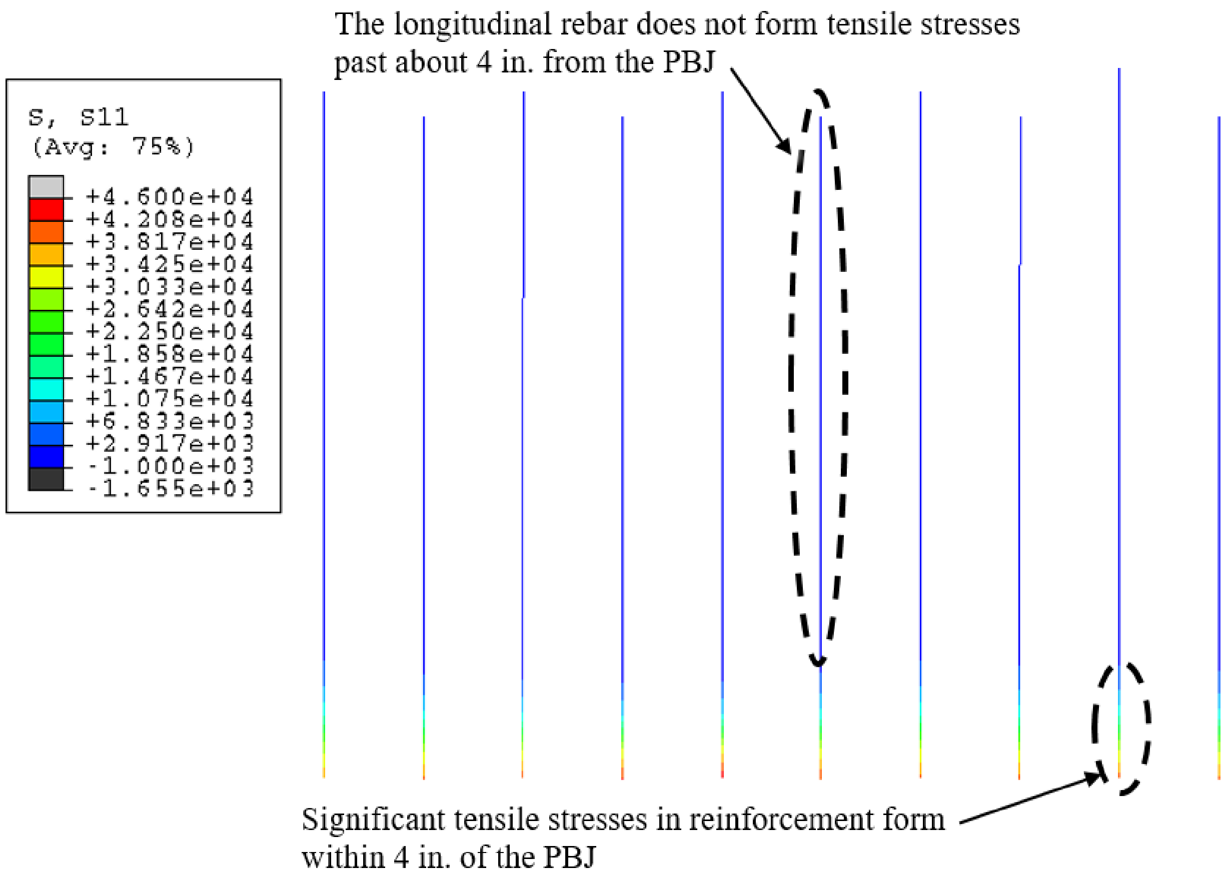

Figure 8.30. Close-up of embedded longitudinal steel reinforcement showing that tensile stresses are focused near the PBJ.

8.4.2 Full-Depth Debonded Slab

The full-depth debonded flush precast panel model shown in Figure 8.31 has a debonded length of 54 in. along the top face of the girder. This model did not include a vertical gap between the top of the girder and the bottom of the slab. Figure 8.32 shows the stress pattern for the deck, where cracking occurs at the center of the PBJ above the panel end gap. The weak plane in the deck caused by the panel end gap leads to a crack at low rotations above this feature despite debonding.

Figure 8.33 shows the principal stress in the concrete at the center of the PBJ and 6 in. longitudinally from the center for the bonded and debonded flush PCP models. The 6-in. curves show that concrete stresses dissipate quickly away from the center of the PBJ. The 0-in. curves show that this debonded detail delays cracking by a small amount—approximately 0.00003 rad. Figure 8.34 shows the longitudinal stress in top longitudinal steel at the center of the PBJ and 6 in. from the center, also for both the bonded and debonded flush PCP models. Prior to cracking, the top longitudinal steel is in compression. Due to the reduced section height at the PBJ because of the PCP gap, the tension zone in the concrete does not reach the steel reinforcement before cracking. Because of the limited improvement of the debonding, alternative lengths of debonding are not considered.

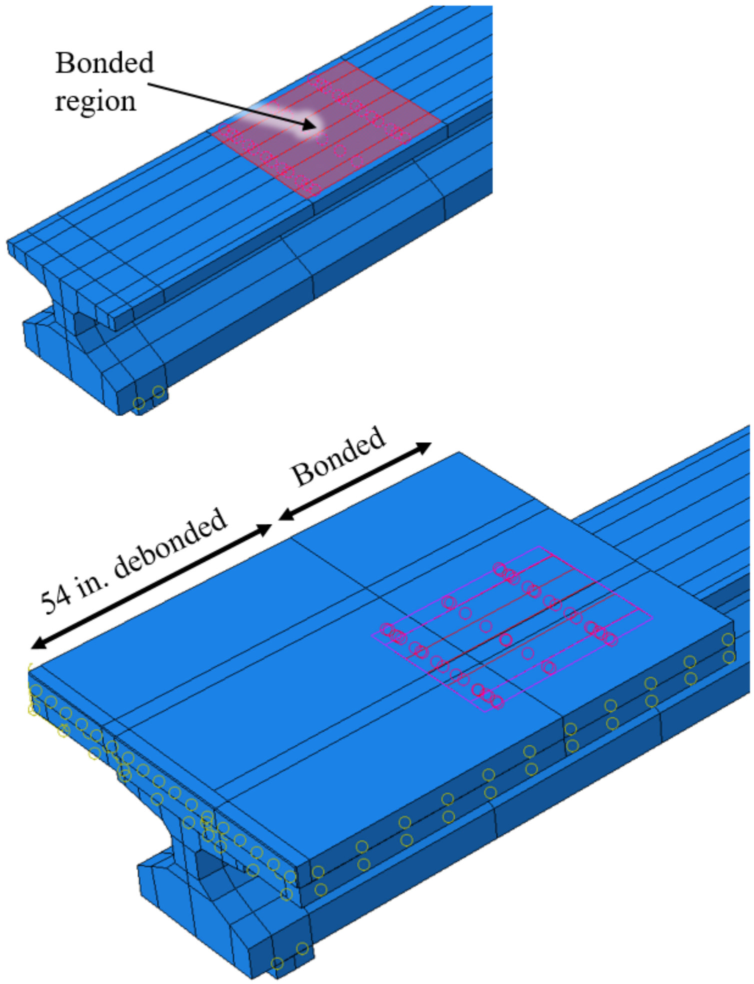

Figure 8.31. Flush precast panel model debonded from the top face of the girder for a length of 54 in.

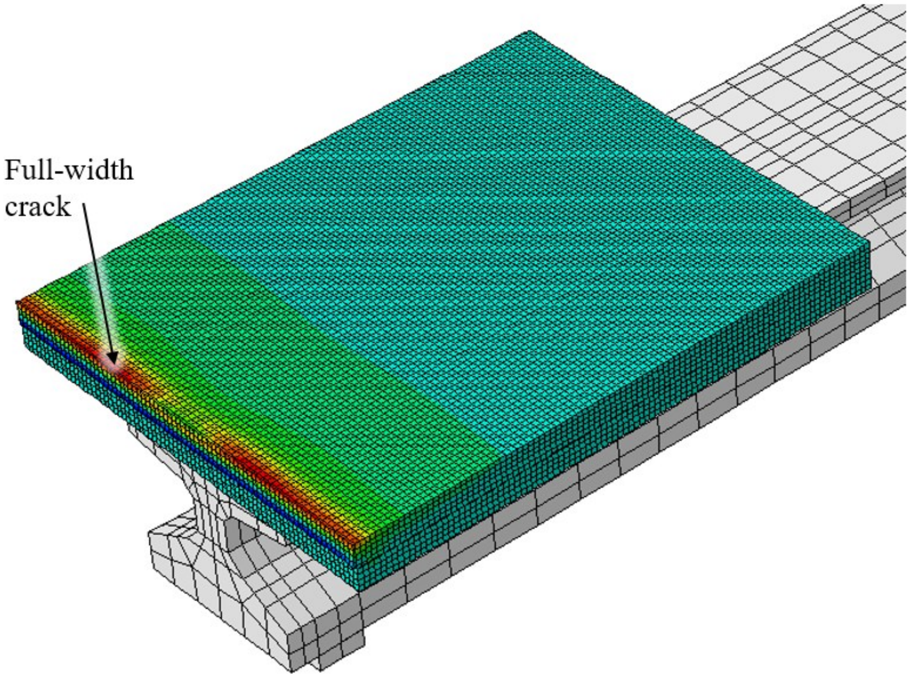

Figure 8.32. Debonded flush precast panel model with cracks across the full width of the deck above the panel gap.

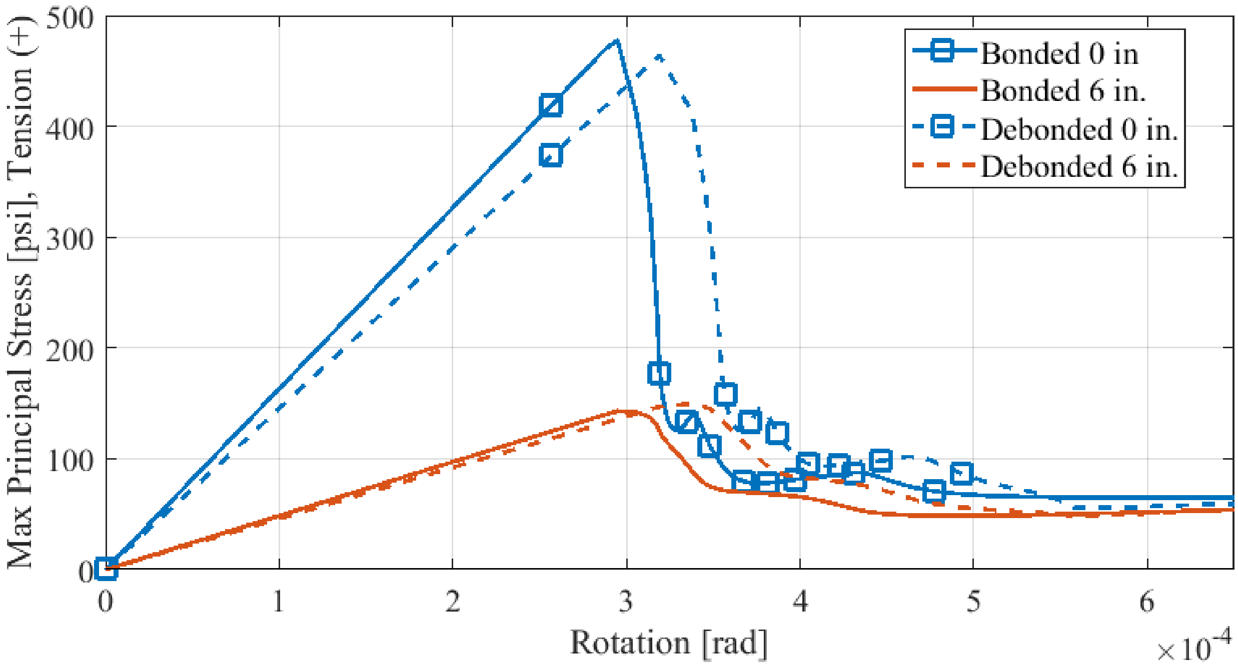

Figure 8.33. Bonded and 54-in. debonded flush precast panel model concrete stresses at the center of the PBJ (0 in.) and at 6 in. away longitudinally from the PBJ.

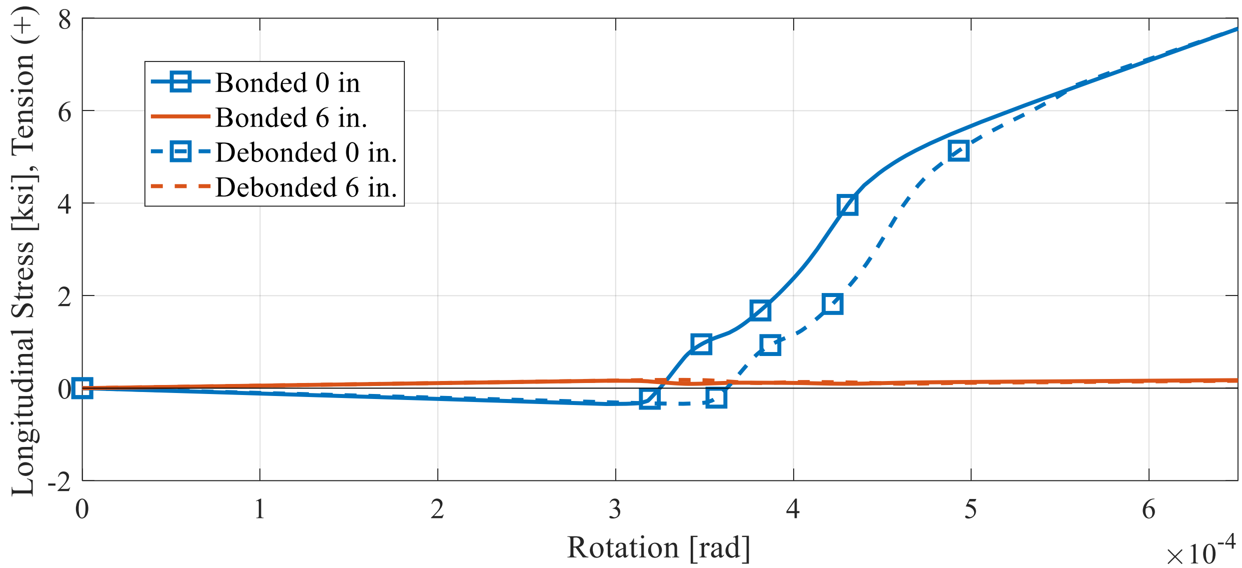

Figure 8.34. Bonded and debonded flush precast panel model steel stresses at the center of the PBJ (0 in.) and at 6 in. away longitudinally from the PBJ.

8.4.3 Partial-Depth Debonded Slab

Rather than debonding at the level of the top girder face, a secondary model considered debonding a slab for a length of 35 in. with PCPs at the level of the top of the panel face. The intent of the design was to explore options for retrofit of decks constructed. While such a design could be considered for new construction, challenges would be encountered with the PCPs not present over the girders.

Debonding the slab at the level of the PCP top face resulted in a continuous slab with no reinforcement in the tension zone at the PBJ before cracking under current designs, as shown in Figure 8.35 and Figure 8.36. Thus, a second model with alternative reinforcement was considered. The standard flush PCP detail included additional 5-ft lengths of longitudinal rebar, centered at the PBJ and placed between the continuous longitudinal bars. Raising these bars by 1 in. in the slab allowed for placement of reinforcement in the tension zone of the DLS while sacrificing concrete cover.

Results for the partial-depth debonded flush panel model and partial-depth debonded flush panel model with raised reinforcement are shown in Figure 8.37 and Figure 8.38, respectively. Concrete and steel stresses are presented at the center of the PBJ (0 in.) and at 3 in., 6 in., and 9 in. from the center.

The results of these two models show that there is minimal difference in concrete stress at the PBJ with the alternative reinforcement. The standard longitudinal reinforcement goes briefly into compression prior to cracking of the section. The raised longitudinal reinforcement, however, bears tensile forces throughout loading, before and after cracking.

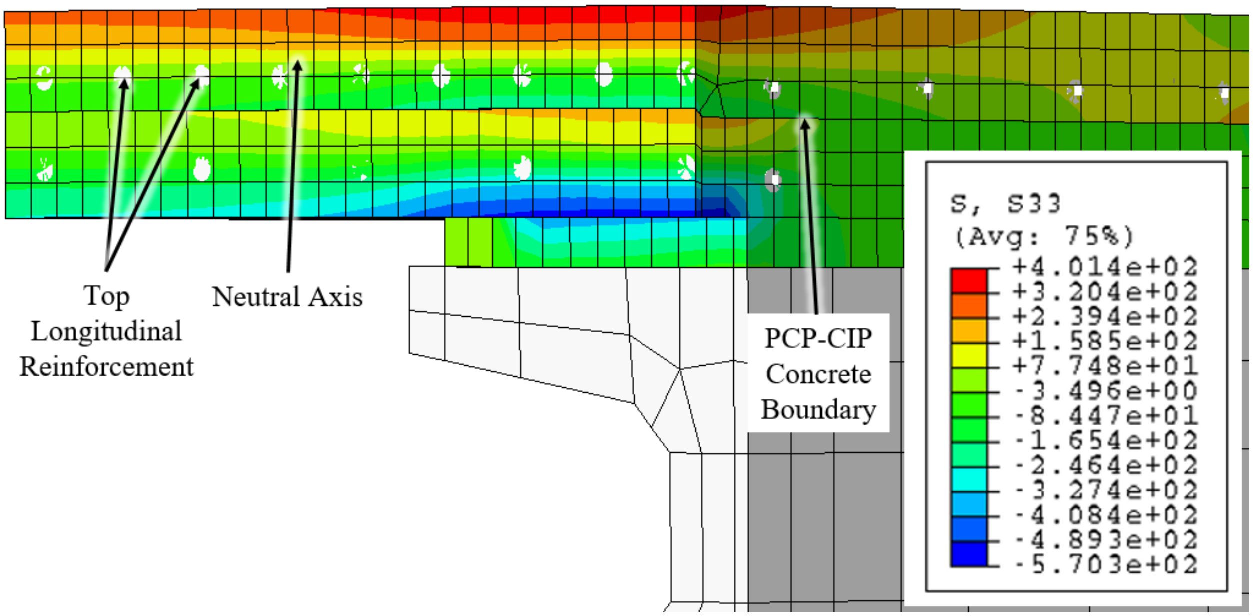

Figure 8.35. Cross-section of the slab for the partial-depth debonded model showing that the top longitudinal steel reinforcement is below the tension zone in the concrete prior to cracking.

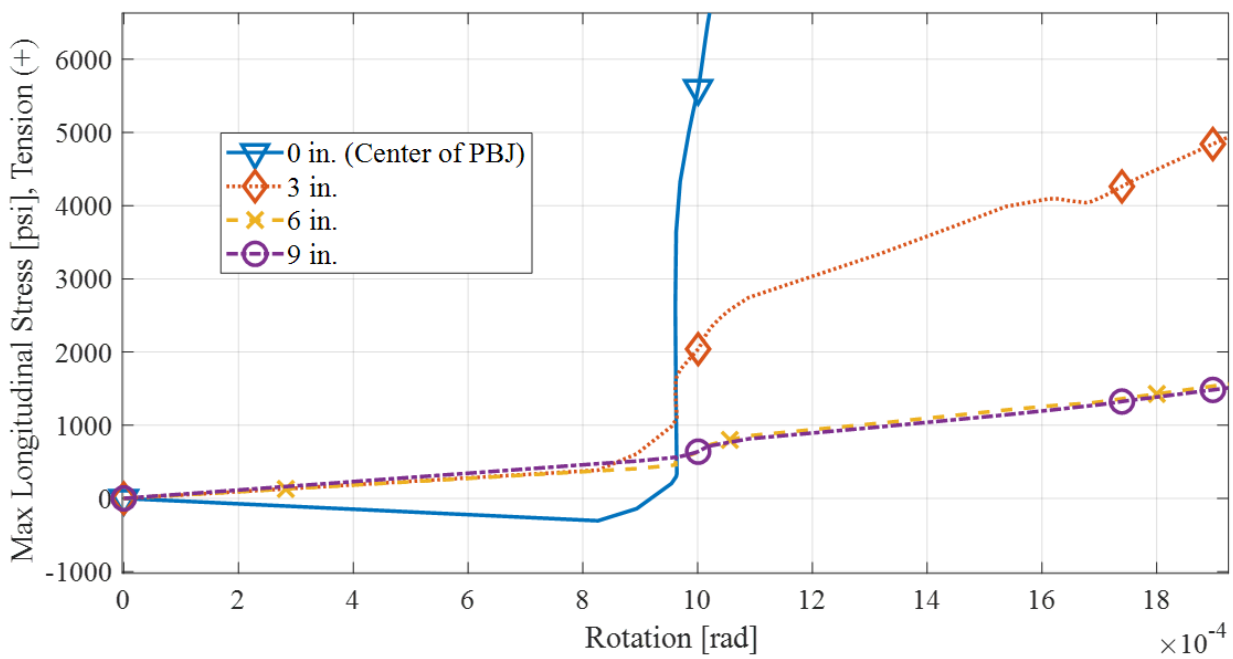

Figure 8.36. Top longitudinal steel stresses for the partial-depth debonded model showing that the bars at the center of the PBJ develop compressive stress prior to cracking.

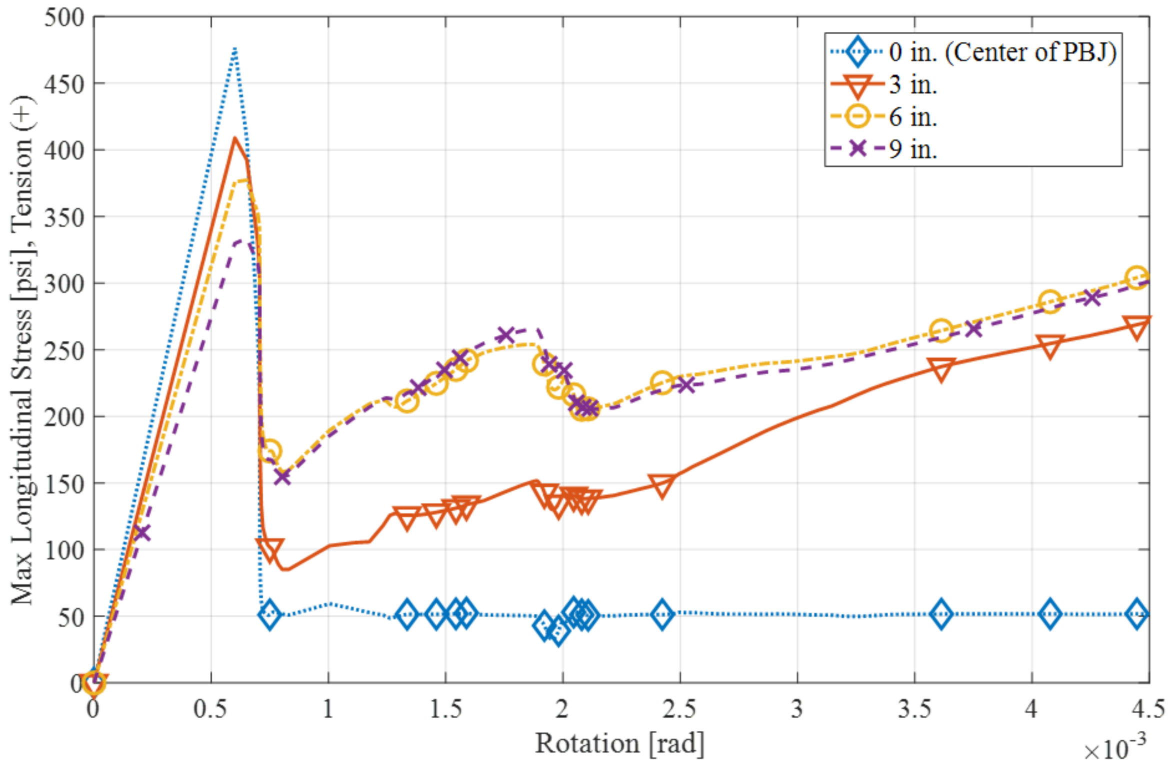

(a) Concrete stress, top of slab

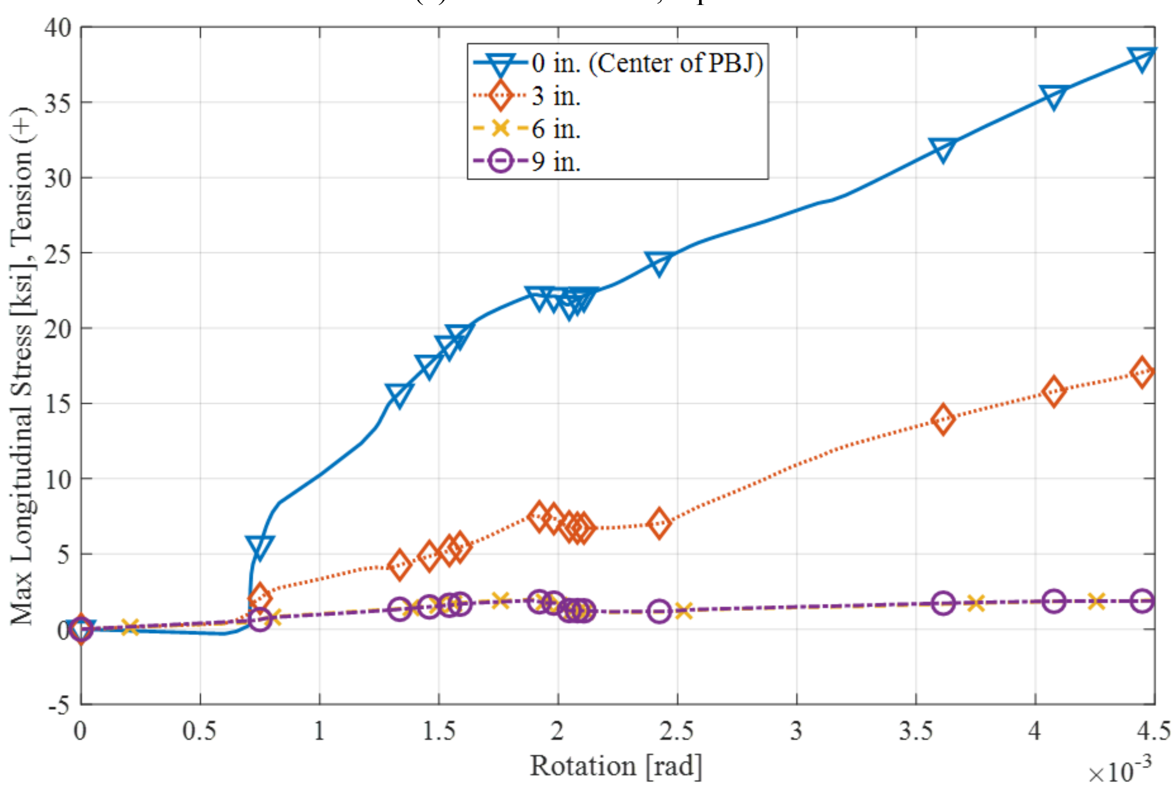

(b) Rebar stress (5 ft supplemental bars)

Figure 8.37. (a) Strains in the concrete and (b) supplemental top longitudinal bars for the 35-in. partial-depth DLS.

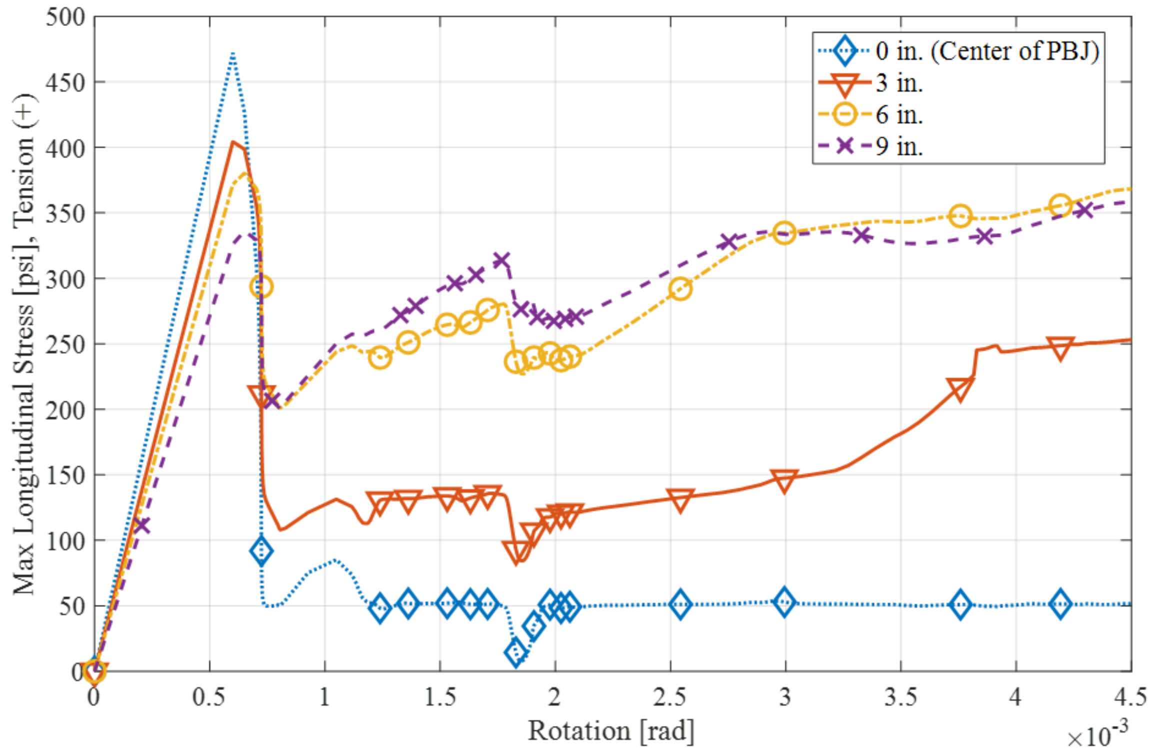

(a) Concrete stress, top of slab

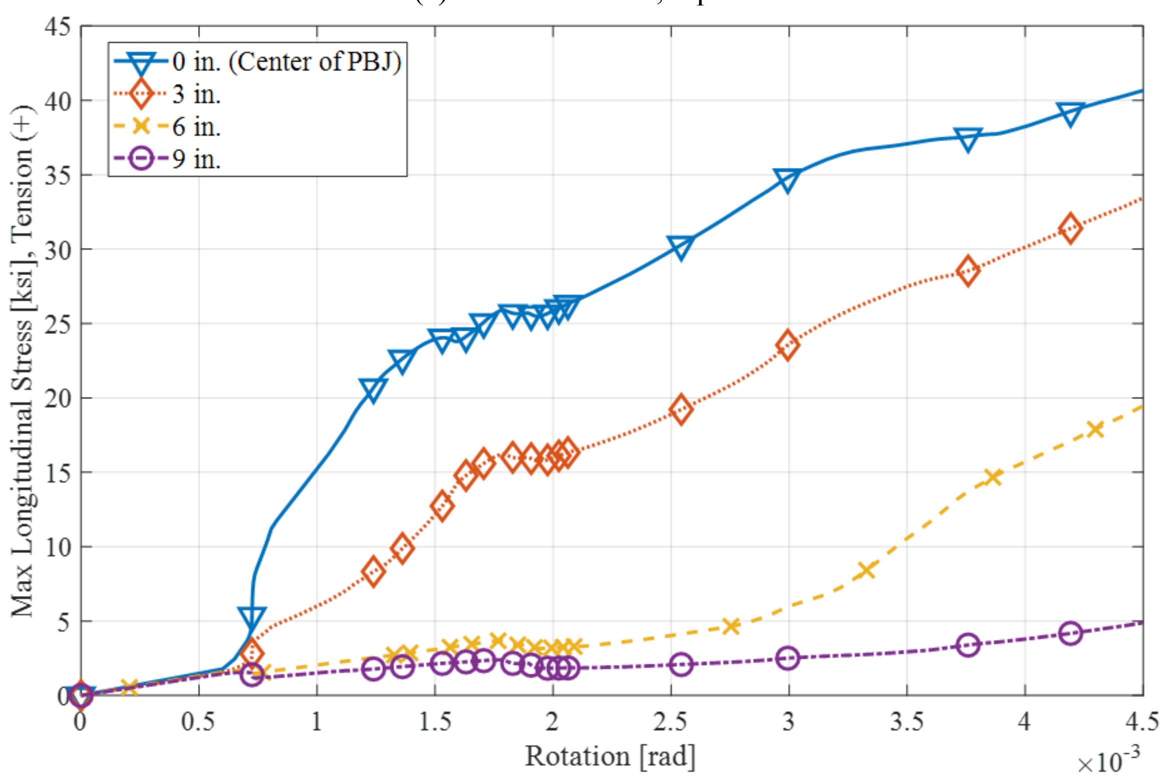

(b) Rebar stress (raised 5-ft supplemental bars)

Figure 8.38. (a) Strains in the concrete and (b) raised supplemental longitudinal bars for the 35-in. partial-depth DLS with elevated reinforcement.

8.4.4 Panel End Gap

Because the panel end gap creates a weak plane in the deck where cracking originates, a model that lengthens the panel gap to distribute cracking over a wider section of deck was considered. Figure 8.39 shows the difference in end gap between the standard 0.75-in. detail and an elongated 3-in. end gap detail. The deck still cracks over the center of the PBJ for both details. However, Figure 8.40 shows that the 3-in. detail performs better, with delayed cracking behavior and more distributed concrete stresses. While elongating a thinner slab section over the girder ends may lead to concerns with regards to design considerations such as punching shear, a longer end gap improves the general behavior of the link slab.

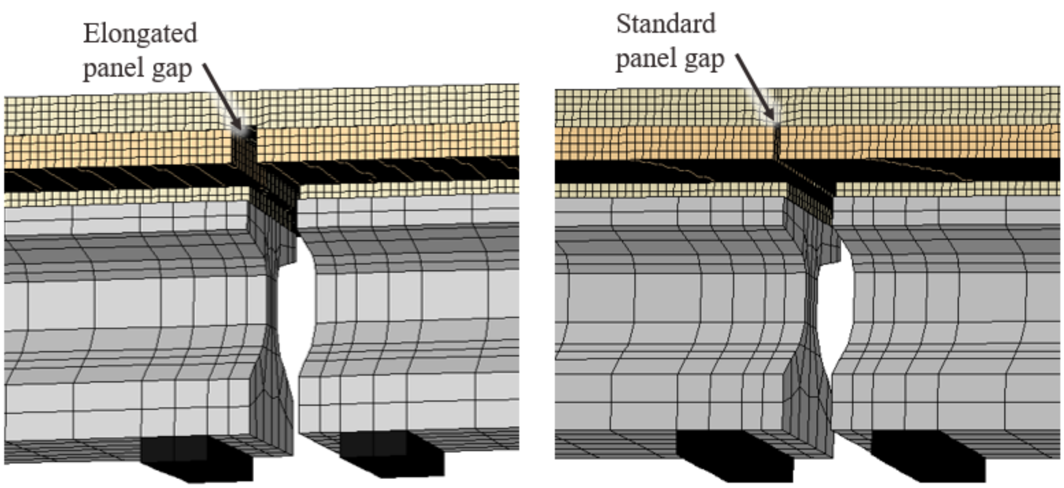

Figure 8.39. Flush precast panel models with a standard 0.75-in. end gap width (right) and an elongated 3-in. end gap width (left).

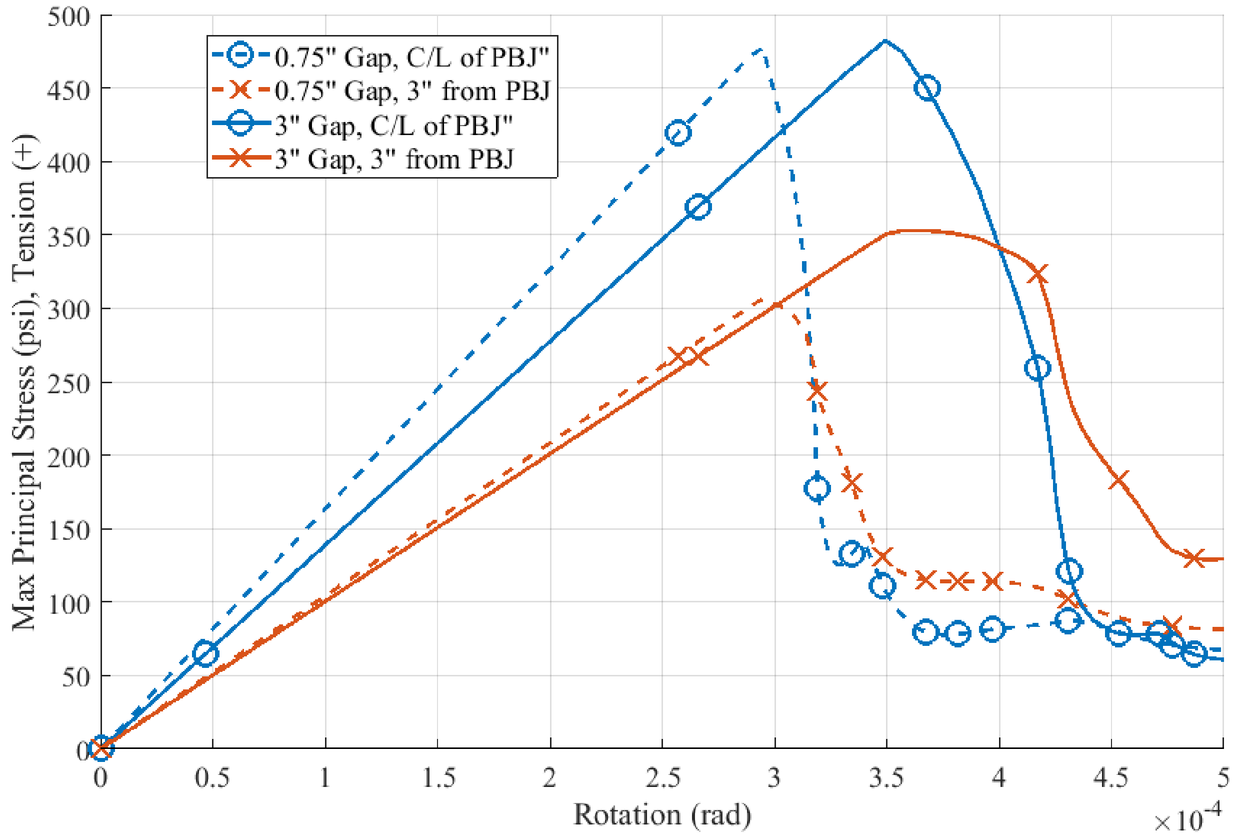

Figure 8.40. Concrete principal stress for flush precast panel models, comparing details of the standard 0.75-in. end gap with a longer 3-in. end gap.

8.5 OFFSET PANEL DECK

Offset precast panel models were used to investigate many potential debonding scenarios, reinforcement setups, and deck details. In particular, debonded models were shown to be effective with the offset panel model.

8.5.1 Bonded Models

A single-girder bonded offset panel model, utilizing mirroring to simulate a four-girder model, was used as a baseline for subsequent models (see Figure 8.41). Its cracking pattern was reminiscent of the bonded flush panel model under similar rotations (0.005 rad). The presence of a notch in the bottom of the deck created a weak section at the center of the PBJ, which focused cracking across the deck. However, secondary cracks were noticeable in the overhangs.

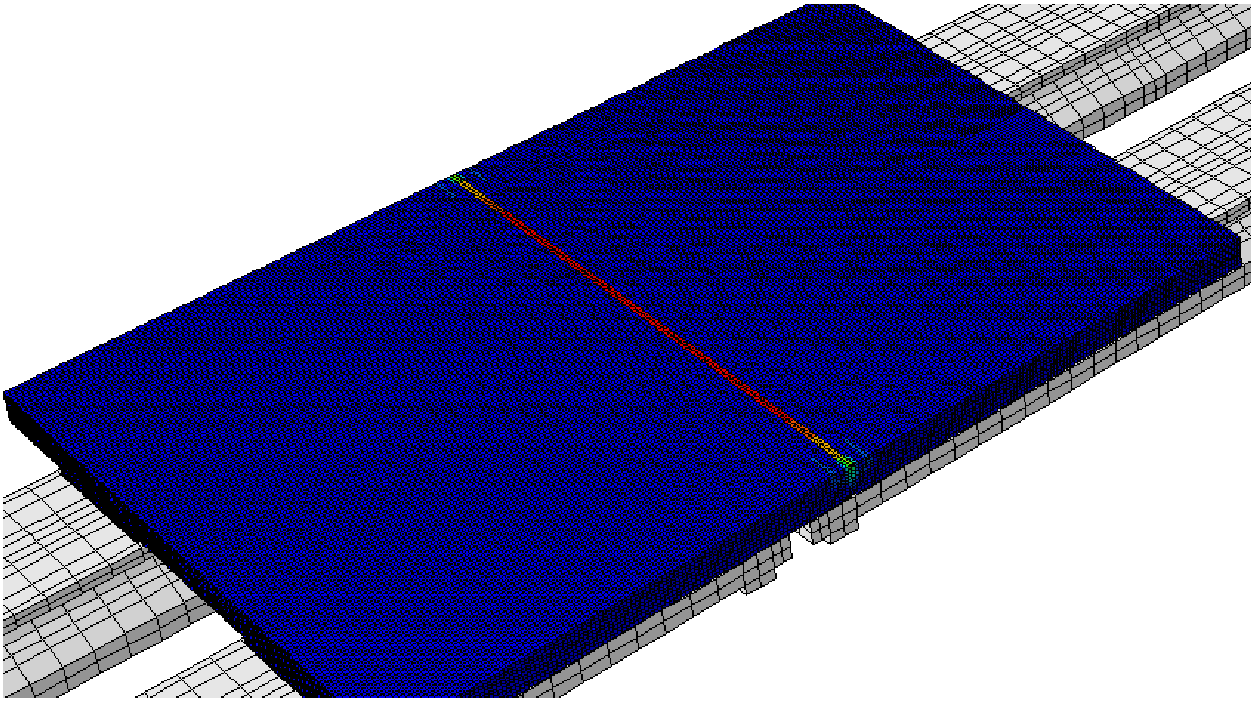

Figure 8.41. Cracking pattern for single-girder offset panel model, mirrored to show four girder lines and secondary cracking in the overhangs.

A four-girder bonded offset panel model was also developed as a baseline for subsequent models. This model was subjected to much higher rotations (up to 0.012 rad) under symmetric loading. In order to promote a more dispersed cracking pattern, the bottom notch in the PBJ was removed and the top longitudinal reinforcement was doubled over the PBJ. This model's cracking pattern, shown in Figure 8.42, is more distributed than flush panel cracking patterns. Cracking initiated transversely above the center of the link slab, and secondary cracks formed on either side as the girder ends continued to rotate. Still, while secondary and tertiary cracks formed at over double the rotation of the single-line model, the crack at the center of the PBJ still formed first and remained large. A more detailed analysis of the development of cracking and stresses is presented in Section 8.5.2 as a basis for comparing to debonded models.

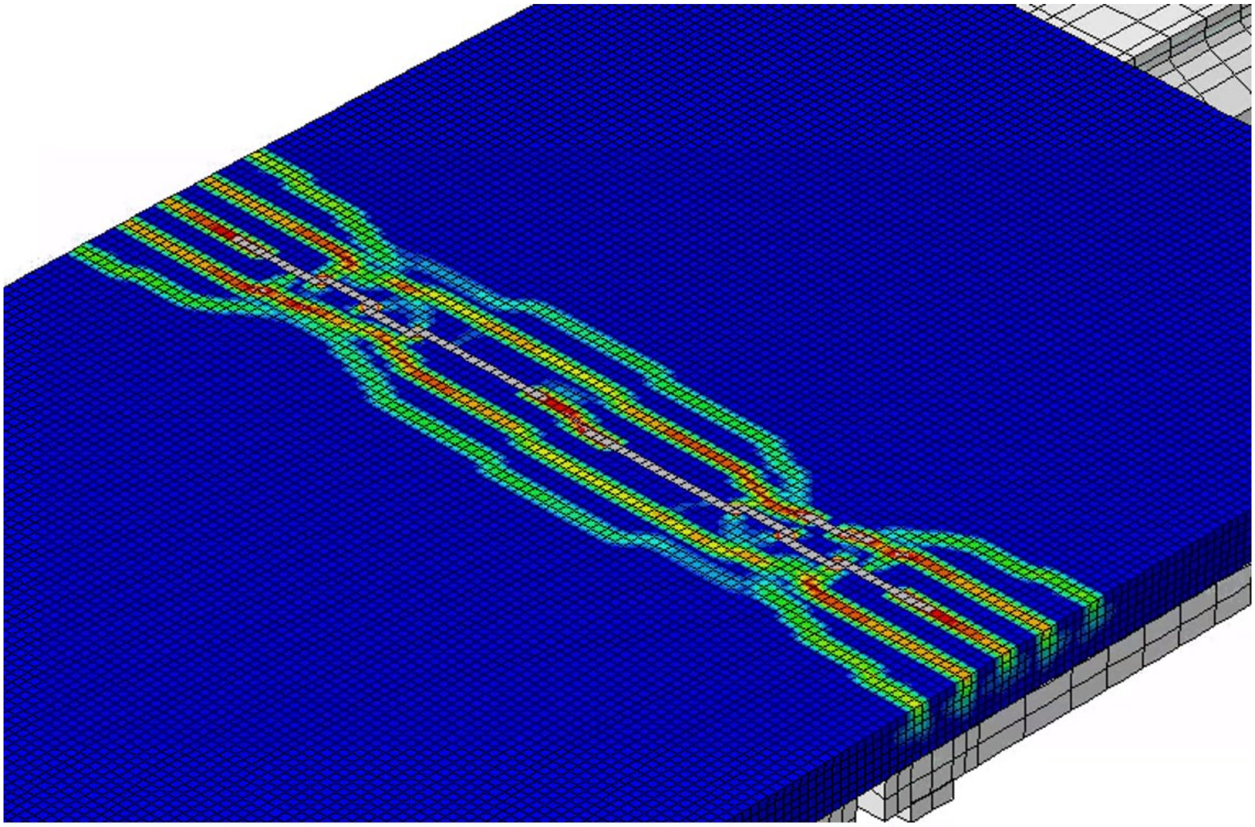

Figure 8.42. Cracking pattern for a bonded offset precast panel model, without a transverse notch in the bottom of the deck and with double the amount of top longitudinal reinforcement at the PBJ.

8.5.2 Debonded Models

Various offset panel debonded details were examined. First, a bonded model, shown in Figure 8.43(a), was compared with the three debonded details in Figure 8.43(b–d). Figure 8.43 (b) is debonded for a length of 54 in. Figure 8.43 (c) is also debonded 54 in. but does not include the standard crack-forming notch detail at the bottom of the PBJ. Figure 8.43 (d) is also debonded 54 in. without a bottom notch but has doubled top longitudinal rebar. All four models were loaded to girder end rotations of approximately 0.005 rad.

The cracking pattern in Figure 8.43(a) shows a large crack focused to a singular location, the center of the PBJ. The existence of the notch in the bottom of the slab consolidates cracking. Figure 8.43 shows that debonding causes a longer link slab length, allowing secondary cracks to form. Figure 8.43 (c) shows that the same debonded model without a notch in the bottom of the link slab at the center of the PBJ allows the central crack to split off into branched main cracks between the girders and in the deck edges. Finally, Figure 8.43 (d) shows that doubled top longitudinal rebar allows for further distribution of cracking, leading to four distinct transverse cracks.

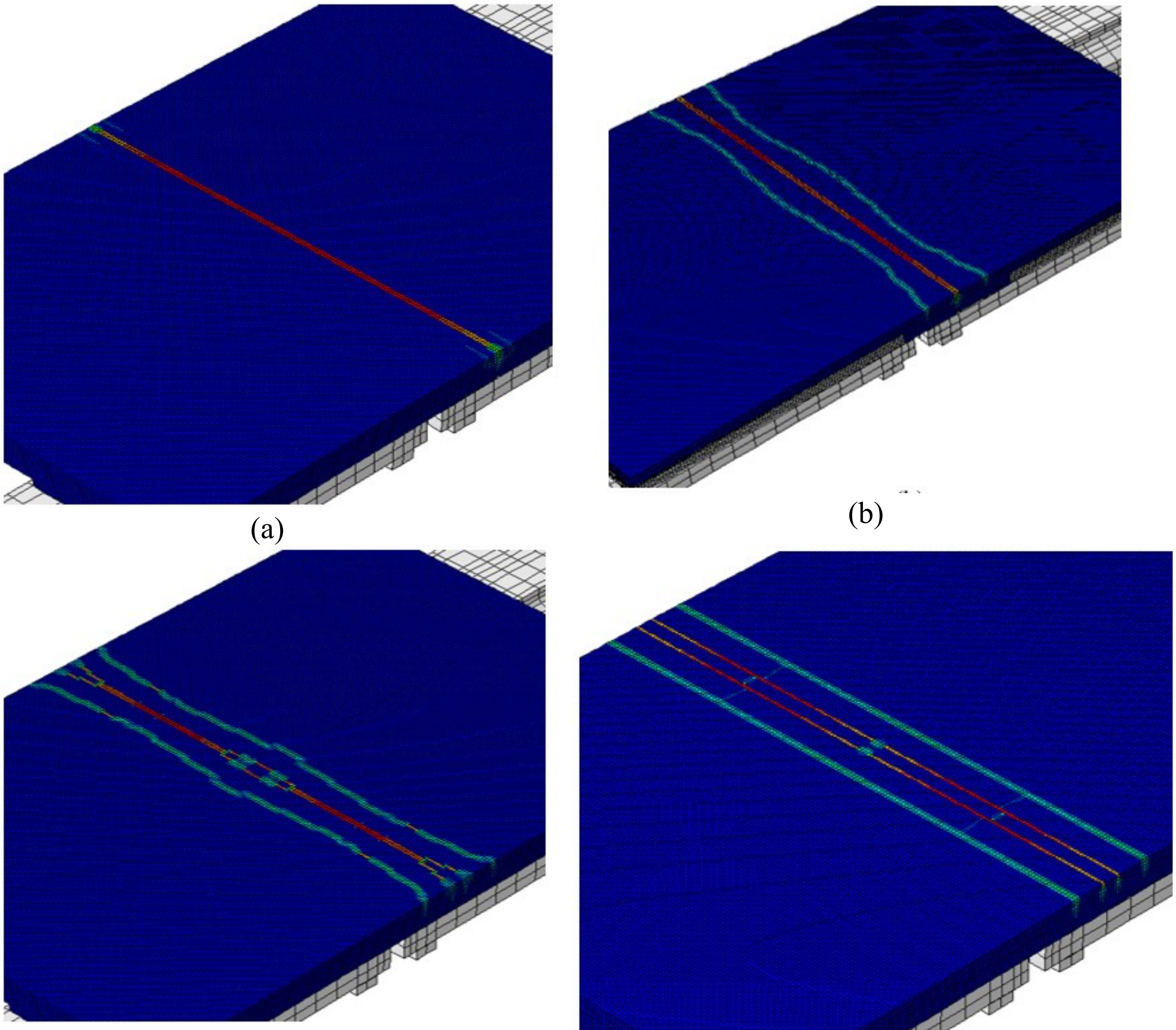

(a) (b) (c) (d)

Figure 8.43. Crack patterns for different offset precast panel models: (a) bonded, (b) debonded, (c) debonded without a bottom notch, and (d) debonded without a bottom notch and with additional top longitudinal rebar.

The vertical gap between the debonded concrete faces was found to be a key factor in the effectiveness of debonded details. Four dual-girder models were developed to investigate debonding length effects and the effectiveness of a vertical gap over the debonded length. One debonded model with the girder haunch removed was compared to the bonded detail and two debonded details with different debonded lengths. Figure 8.44 shows the debonded model with the girder haunch removed, creating a vertical gap of 2 in. in the debonded region. Figure 8.45 shows a comparison of the concrete stresses at first cracking for these four models. While increasing debonded lengths caused a small delay in the onset of cracking, including a vertical gap over the debonded length yielded large improvements to cracking behavior. Figure 8.46 shows the plastic principal strains for the same models. The magnitude of these plastic strains may be used as a proxy for crack width. The debonded model with a haunch gap was the most effective for limiting crack width.

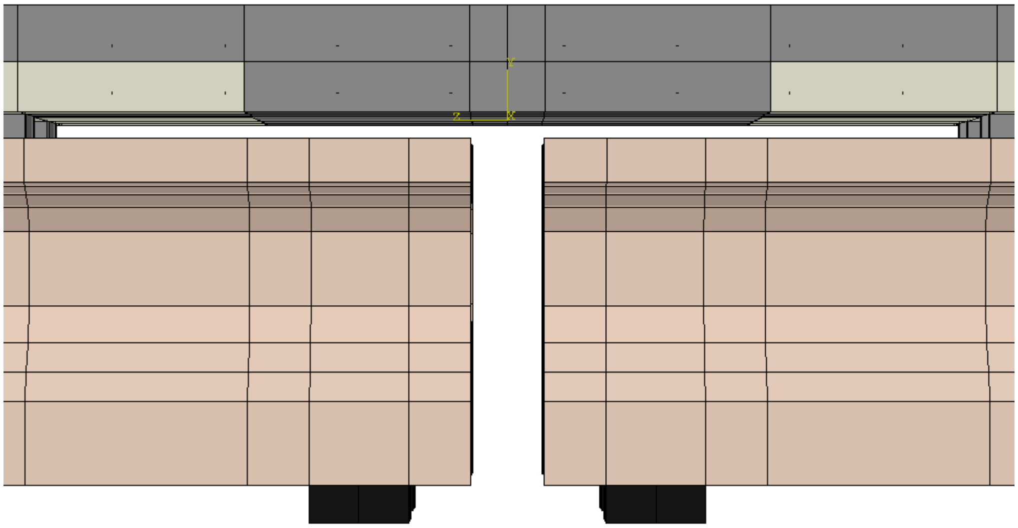

Figure 8.44. Debonded offset panel model with the girder haunch removed, creating a 2-in. vertical gap between the girder and the bottom of the slab.

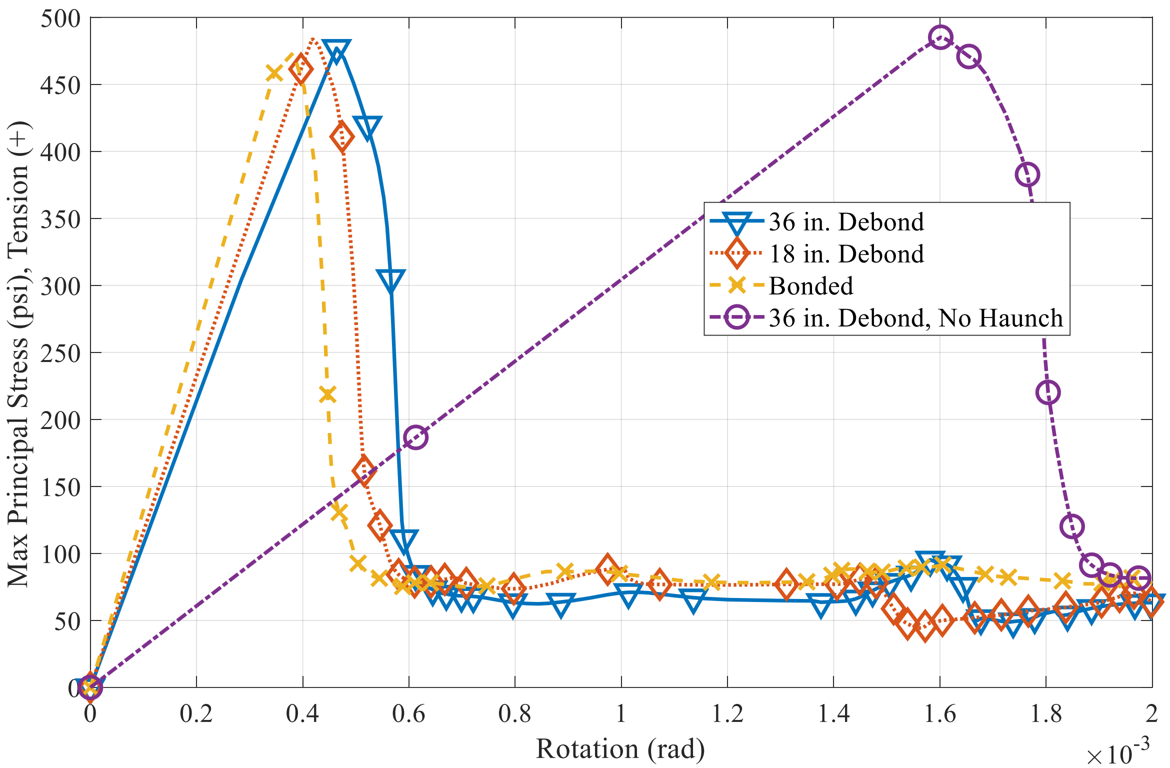

Figure 8.45. Maximum principal stress for various offset precast panel models at the location of first cracking.

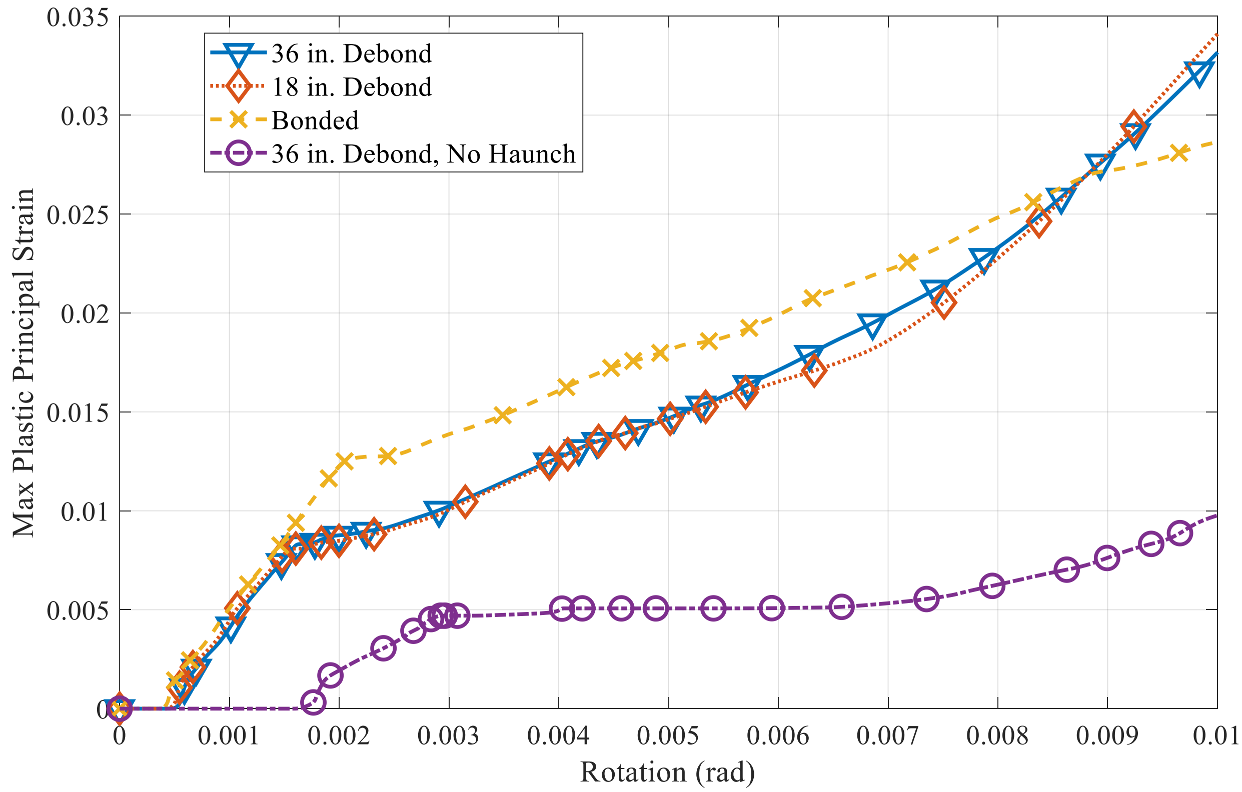

Figure 8.46. Maximum plastic principal strains for different offset panel models at the location of first cracking.

Furthermore, the geometry of the vertical gap over the debonded length was investigated to determine whether a tapered end to the debonded zone would improve performance, perhaps by avoiding stress concentrations at the end of the debonded region. Figure 8.47 shows a simple squared end to the haunch gap and the corresponding deck cracking pattern. Figure 8.48 shows a tapered end to the haunch gap and the corresponding cracking pattern. Little difference in cracking behavior can be seen between the two models. Figure 8.49 shows the principal stress at the location of first cracking for both models. The tapered haunch gap model does not delay the onset of cracking.

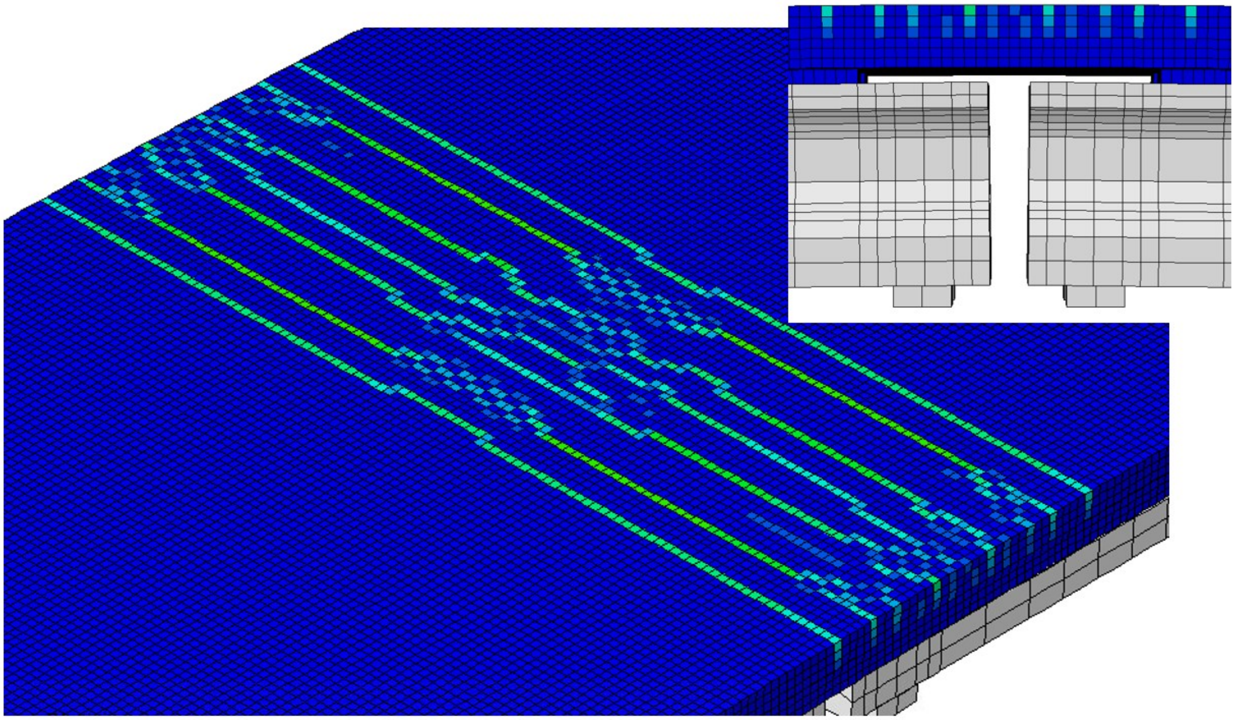

Figure 8.47. Cracking pattern for an offset precast panel model, debonded for 18 in. with a vertical gap along the debonded length, and squared ends of the debonded region.

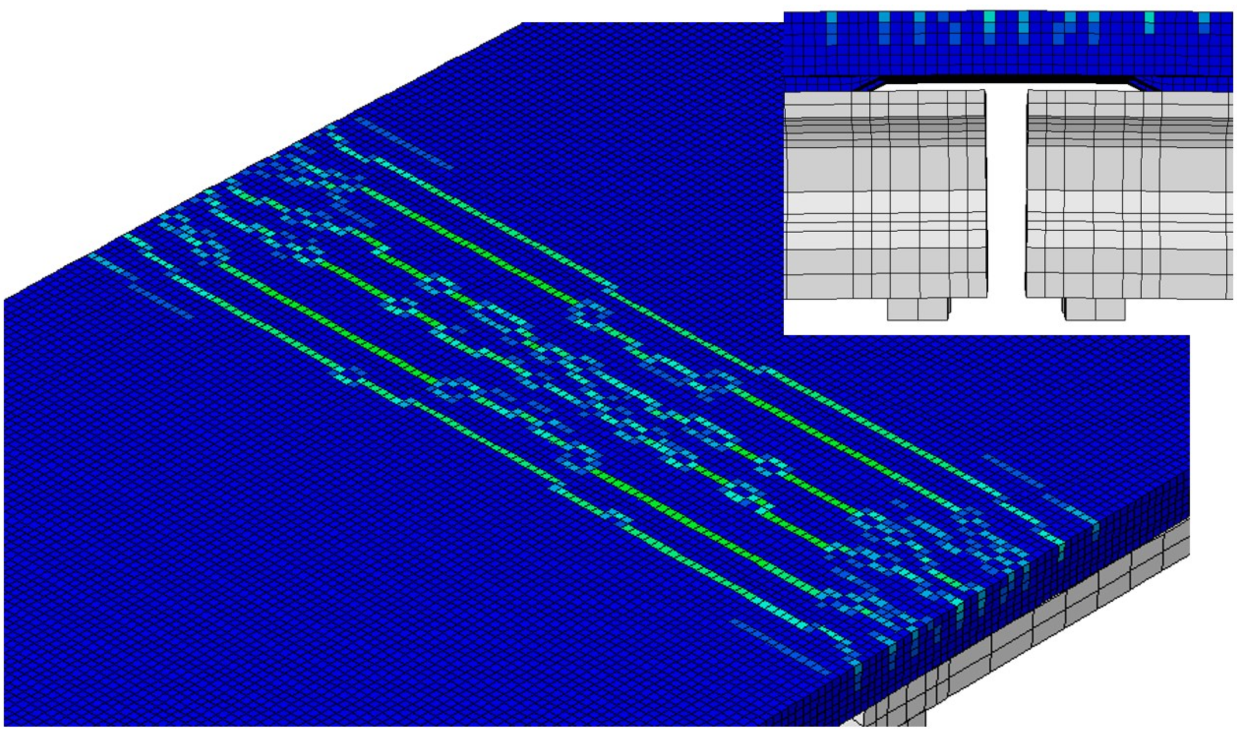

Figure 8.48. Cracking pattern for an offset precast panel model, debonded for 18 in. with a vertical gap along the debonded length, and tapered ends of the debonded region.

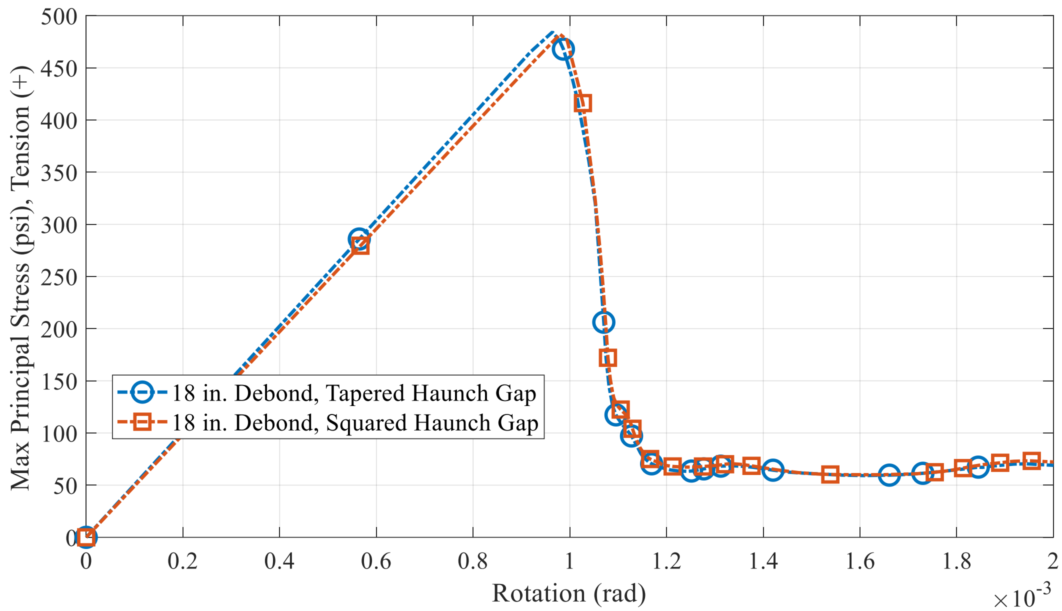

Figure 8.49. Comparison of concrete principal stress at the location of first cracking for debonded offset precast panel models with different haunch gap end conditions.

8.5.3 Reinforcement Placement Effects

Some models were used to investigate the effects of specific reinforcement placement for testing. For test PBJ-OP1R, the PCPs did not have protruding longitudinal reinforcement as specified in standard drawings. Single-girder models, shown in Figure 8.50, were used to compare the behavior of the PBJ with and without protruding PCP bars. Results showed similar behavior between the two models, indicating that the test specimen would be acceptable with spliced reinforcement.

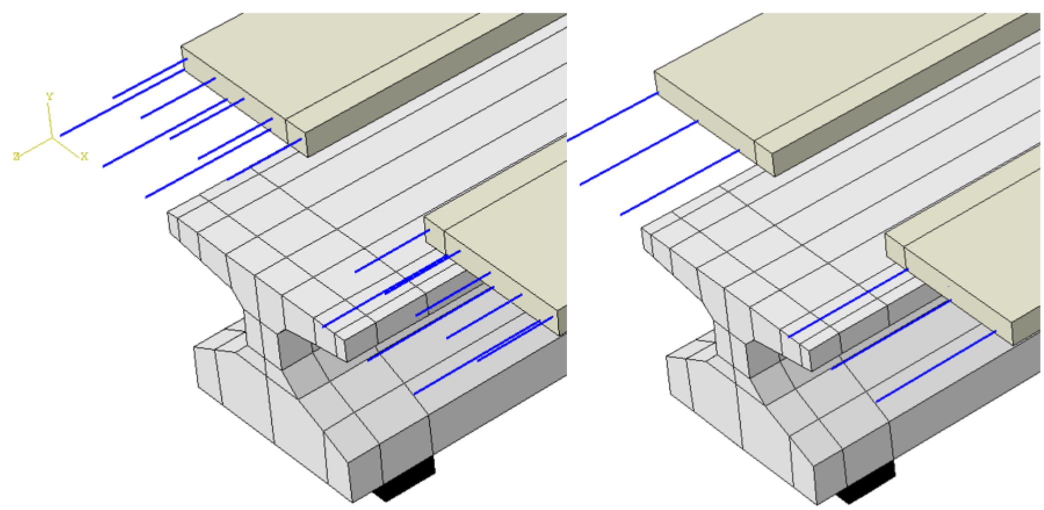

Figure 8.50. Offset panel models with bars protruding from the panels (left) and without bars protruding from the panels (right).

For test specimen PBJ-OP2, #4 bars were added to the north half of the deck in the longitudinal direction between existing longitudinal bars. A model matching this test setup, shown in Figure 8.51, indicated that the increased reinforcement in the north deck would cause a more distributed cracking pattern, while the south deck would see fewer, wider cracks.

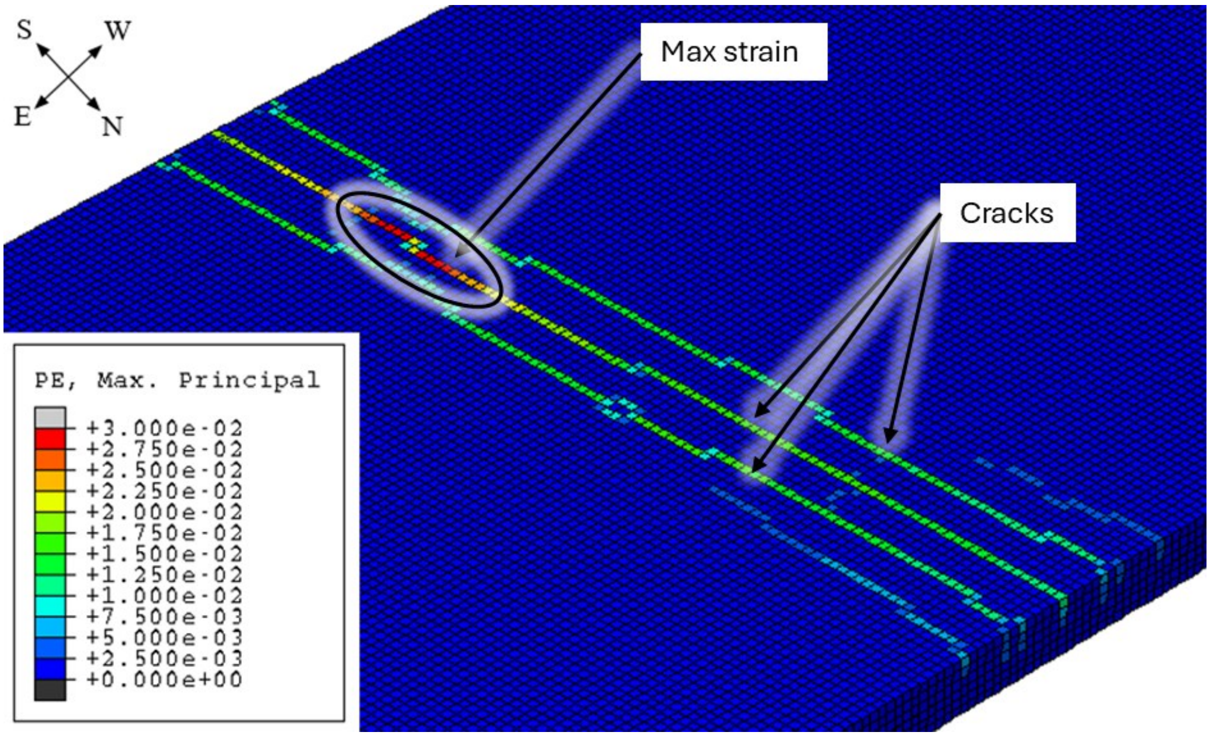

Figure 8.51. Cracking pattern for a model simulating PBJ-OP2, with added longitudinal reinforcement in the north half of the deck.

Since the largest crack widths tend to be consolidated over the girders, it was theorized that increasing reinforcement over the girder lines may lead to a more uniform distribution of cracks. Two models were developed to investigate crack patterns for decks with added #4 top longitudinal bars between existing bars above the girders.

Figure 8.52 shows the crack pattern for top longitudinal bar spacing of 4.5 in. over the girders. The crack pattern was not significantly more distributed than the pattern seen in the south end of the deck in Figure 8.51. Further increasing the amount of longitudinal reinforcement over the girders to 3-in. spacing over the south girder and 2.25-in. spacing over the north girder, shown in Figure 8.53, produced a modest improvement in crack distribution. However, the negligible difference in cracking behavior for the 2.25-in. spacing above the north girder and the 3-in. spacing above the south girder indicates that the benefit of adding reinforcement over the girders is limited.

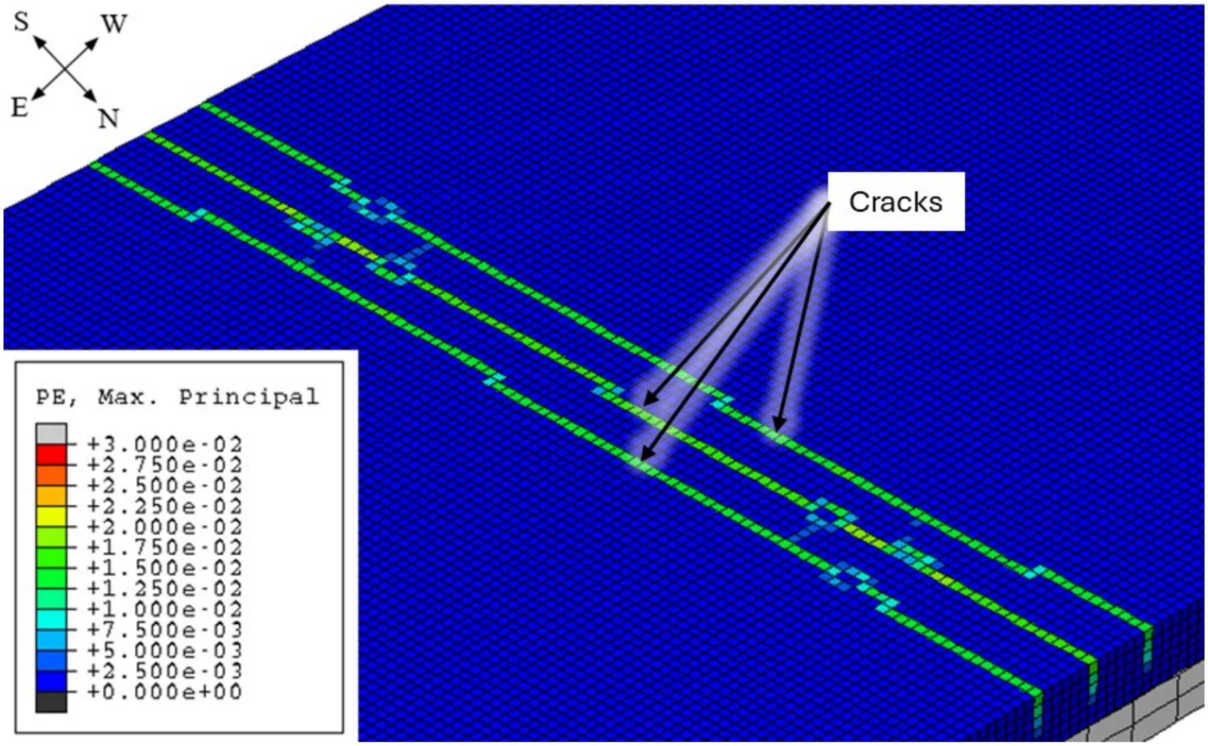

Figure 8.52. Offset precast panel model with longitudinal reinforcement added over the girders to provide 4.5-in. spacing.

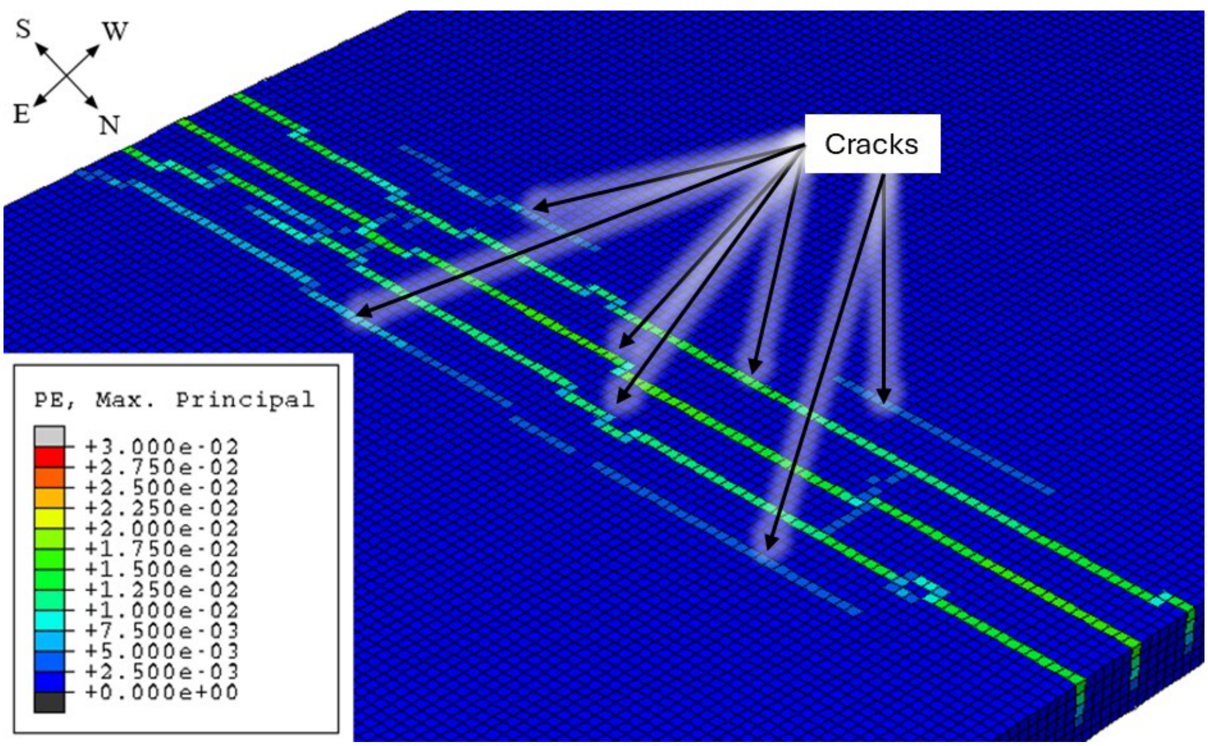

Figure 8.53. Offset precast panel model with longitudinal reinforcement added over the north girder to provide 2.25-in. spacing and over the south girder to provide 3-in. spacing.

8.6 CONTINUOUS PANEL DECK

The continuous panel model, shown in Figure 8.6, utilizes PCPs that span across the girder end gap and the PBJ. Each continuous panel model was developed with equal loading in the four girder spans. This setup has the potential to simplify PBJ construction by eliminating the need for the additional formwork associated with offset panel details. Furthermore, the continuous panel eliminates the weak plane at the PBJ associated with the flush panel details that promote cracking.

8.6.1 Bonded Model

The initial cracking behavior of the slab, shown in Figure 8.54(a), shows that initial cracking occurs between the girder ends in both girder lines. At high rotations (0.0068 rad), shown in Figure 8.54(b), cracks propagate over the width of the slab, branching out into secondary and tertiary cracks at the girder edges. Cracks are not full depth. The initial crack pattern appears to be more dispersed than flush panel details.

Concrete stresses at the point of first cracking are shown in Figure 8.55, which compares the bonded continuous panel model to its offset panel and flush panel counterparts. All three models have very similar behavior at the point of first cracking, but the flush panel model cracks at a slightly lower rotation than the continuous panel model.

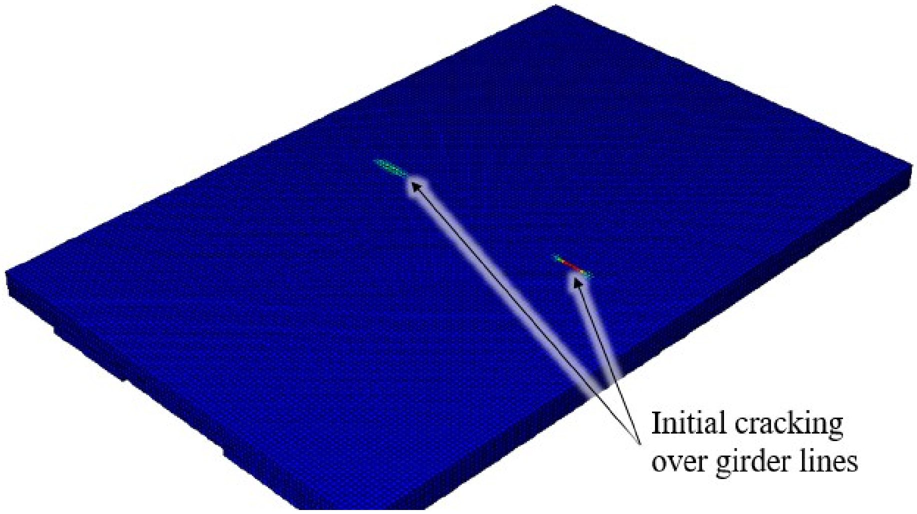

(a)

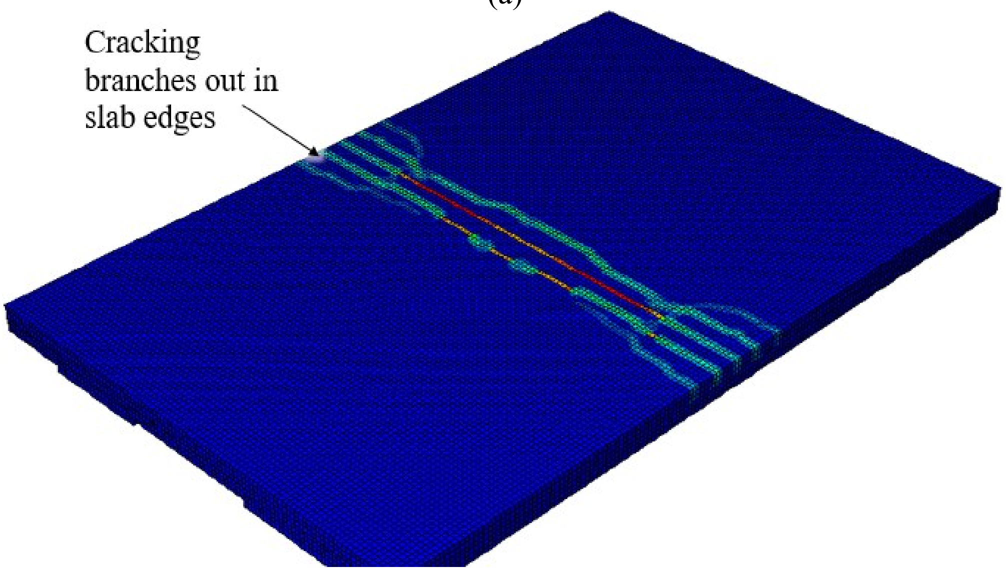

(b)

Figure 8.54. Bonded continuous panel model crack behavior, showing (a) initial cracking over the girder ends and (b) crack propagation.

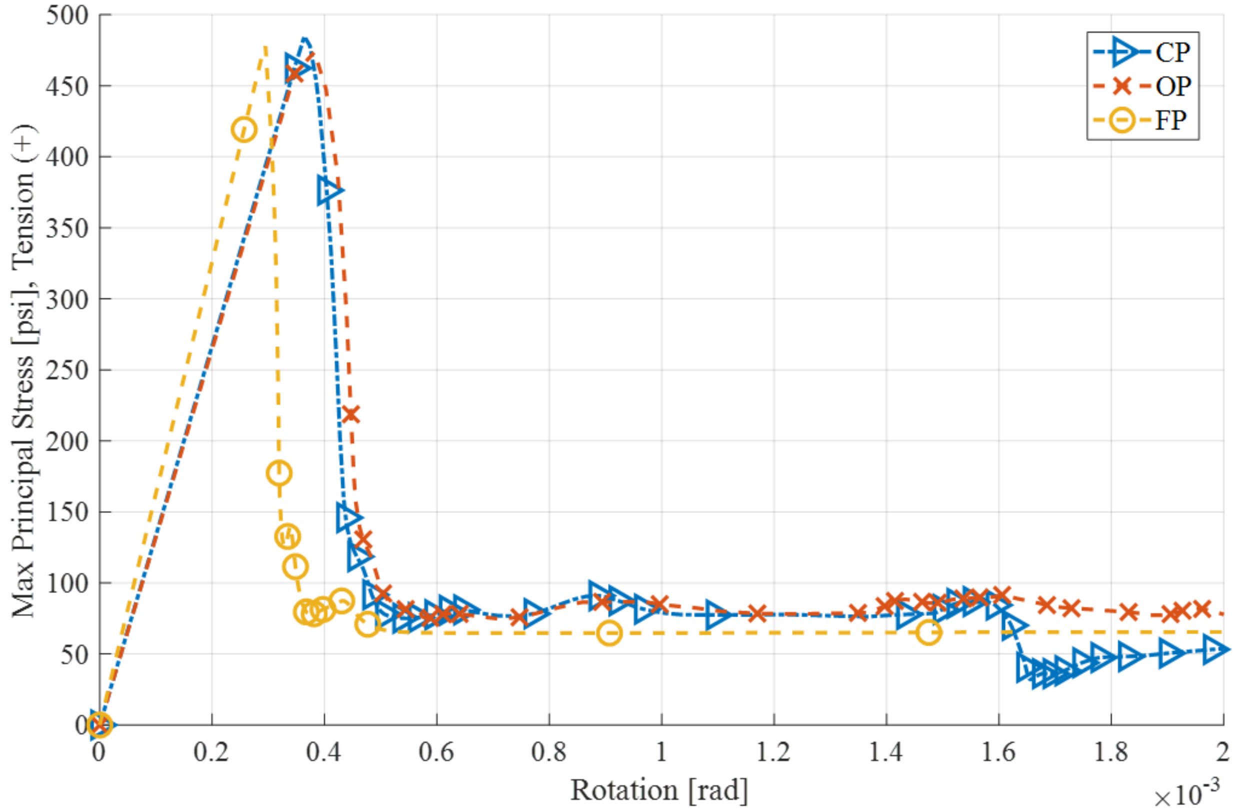

Figure 8.55. Maximum principal stress in the concrete at the point of first cracking for the continuous panel model, compared to the bonded offset panel and flush panel models.

8.6.2 Debonded Models

Two debonded models were developed for the continuous panel detail. The first model utilizes an 18-in. debonded length with a 0.5-in. gap in the girder haunch between the top face of the girder and the link slab for the entire 18-in. length, as shown in Figure 8.56. The second model is similar, but with the same 0.5-in. haunch gap for 18 in. over each girder, but with a 36-in. debonded length. Thus, only half of the debonded length includes the haunch gap.

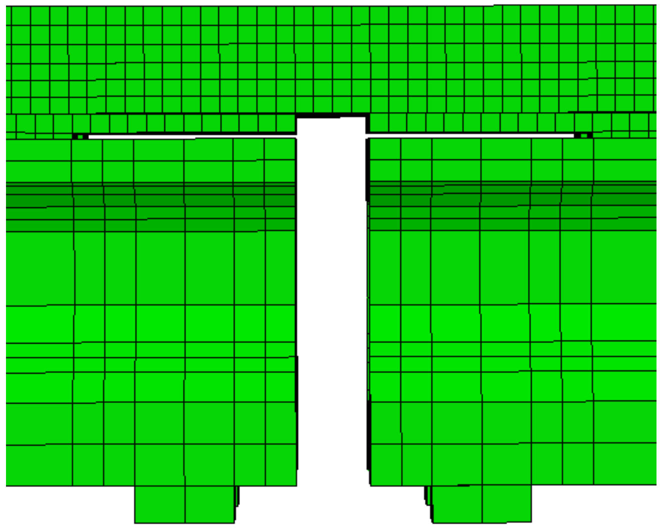

Figure 8.56. Side view of the DLS for the continuous panel models, showing the 0.5-in. gap between the slab and top faces of the girders.

The initial cracking behavior of the 18-in. debonded slab, shown in Figure 8.57(a), shows that cracking begins between the girder ends in both girder lines, as in the bonded model. At high rotations (0.0078 rad), shown in Figure 8.57(b), cracks propagate over the width of the slab, branching out into multiple layers of cracks at the girder edges. Cracks are not full depth. The crack pattern is significantly more dispersed than the pattern in the bonded model.

For the 36-in. debonded model with 18-in. length haunch gap, shown in Figure 8.58, the initial cracking also occurs between the girder ends. At high rotations (0.0072 rad), cracks propagate extensively over the width of the slab but do not branch out significantly in the deck edges. Instead, transverse cracks are mostly straight over the entire slab width. Cracks are not full depth. The crack pattern is again more dispersed than the pattern of the 18-in. bonded model.

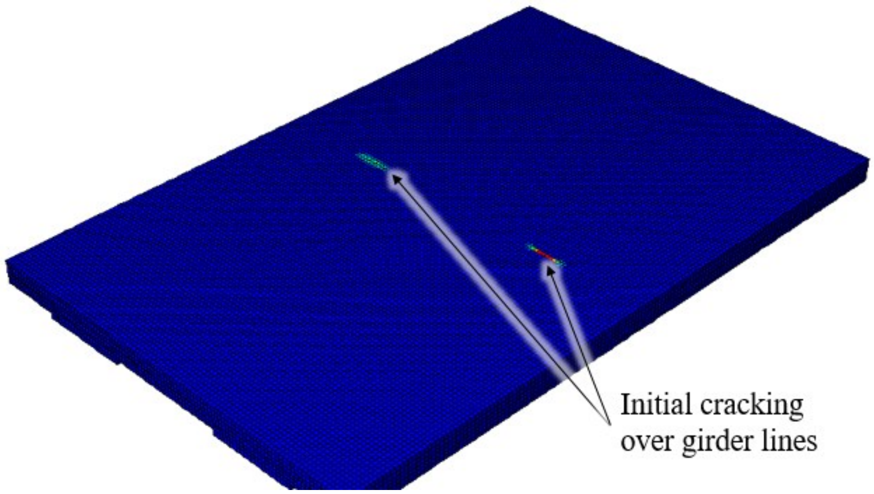

(a)

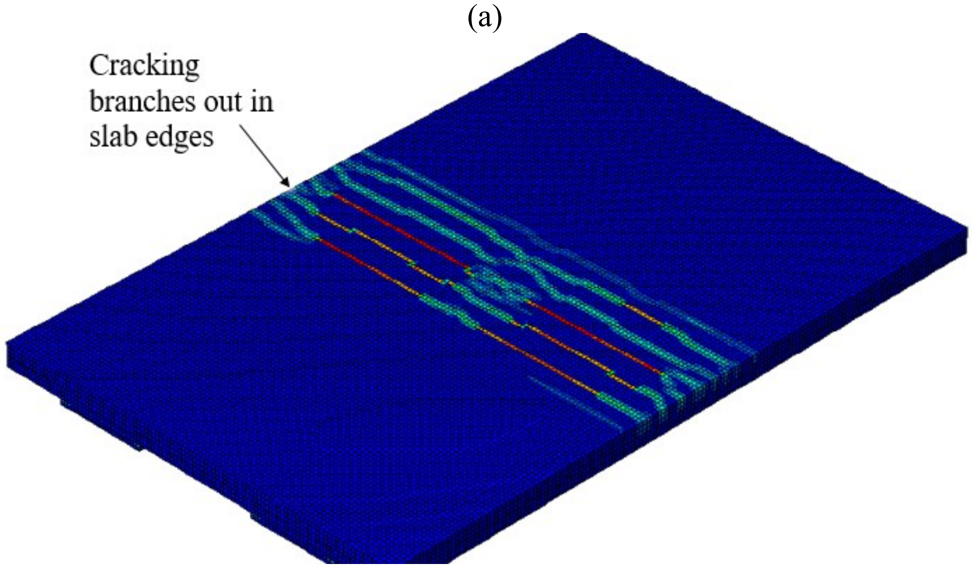

(b)

Figure 8.57. 18-in. debonded continuous panel model crack behavior, showing (a) initial cracking over the girder ends and (b) crack propagation.

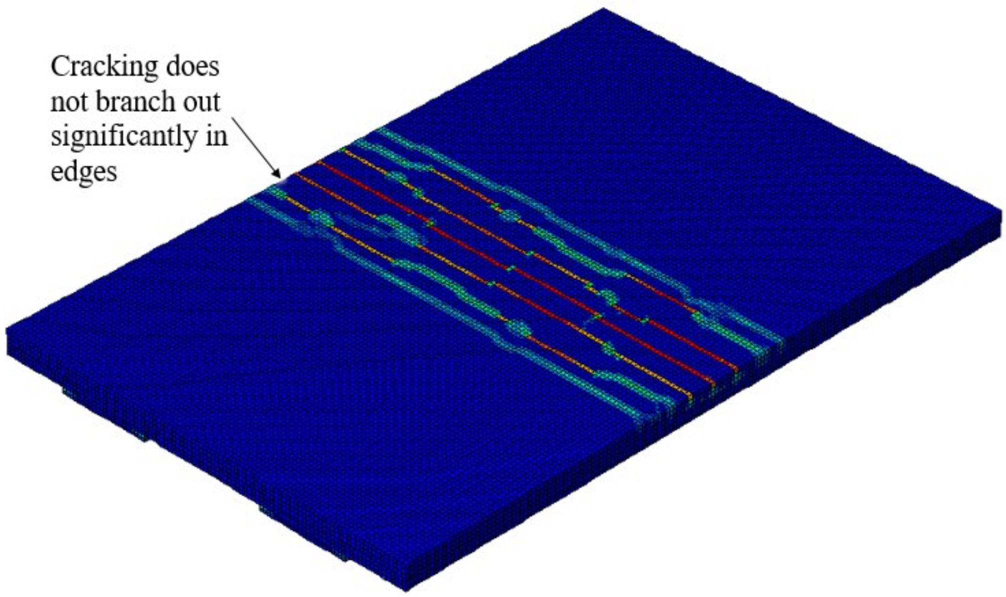

Figure 8.58. 36-in. debonded continuous panel model crack behavior, showing crack propagation at high rotations.

The initial cracking behavior of the three continuous panel models is compared in Figure 8.59. Debonding the continuous panel model for 18 in. on each girder with a 0.5-in. haunch gap for the full 18-in. length delays cracking in the slab for 0.00052 rad of girder end rotation. An increased debonded length of 36 in., but with a haunch gap for only 18 in. along that length, gives a modest improvement of 0.00009 rad of rotation before cracking. Debonding is effective in delaying the onset of cracking, but not including the haunch gap for the debonded length limits the effectiveness of debonding.

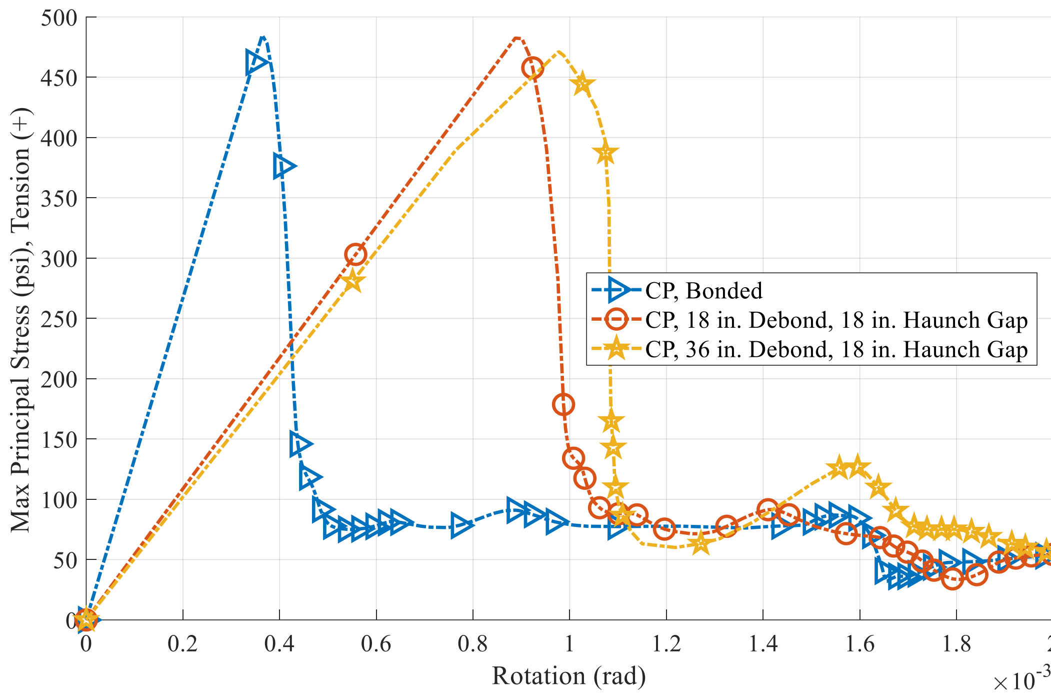

Figure 8.59. Comparison of first cracking behavior for continuous panel models.

8.7 SHRINKAGE EFFECTS

When evidence of cracking due to concrete shrinkage was noticed after fabrication of the flush panel laboratory specimens, a model was developed to investigate shrinkage. This model, shown in Figure 8.60, is built to mimic the laboratory test specimen with a flush precast panel detail. By imposing a uniform temperature change on only the CIP portion of the deck, it was possible to simulate the effect of drying shrinkage. Reducing the deck's temperature causes the deck to contract, which generates forces in the slab since the girders do not have a similar temperature change.

Results showed the potential for cracking in the deck, especially over the girders, which restrain the movement of the slab. Cracking initiates in the middle of the deck, rather than at the PBJ, suggesting that deformation at the supports prevents the buildup of stress in the deck between the girder ends. However, no such relief for deformation is possible at the interior of the slab since a perfect bond between the deck and girder is assumed.

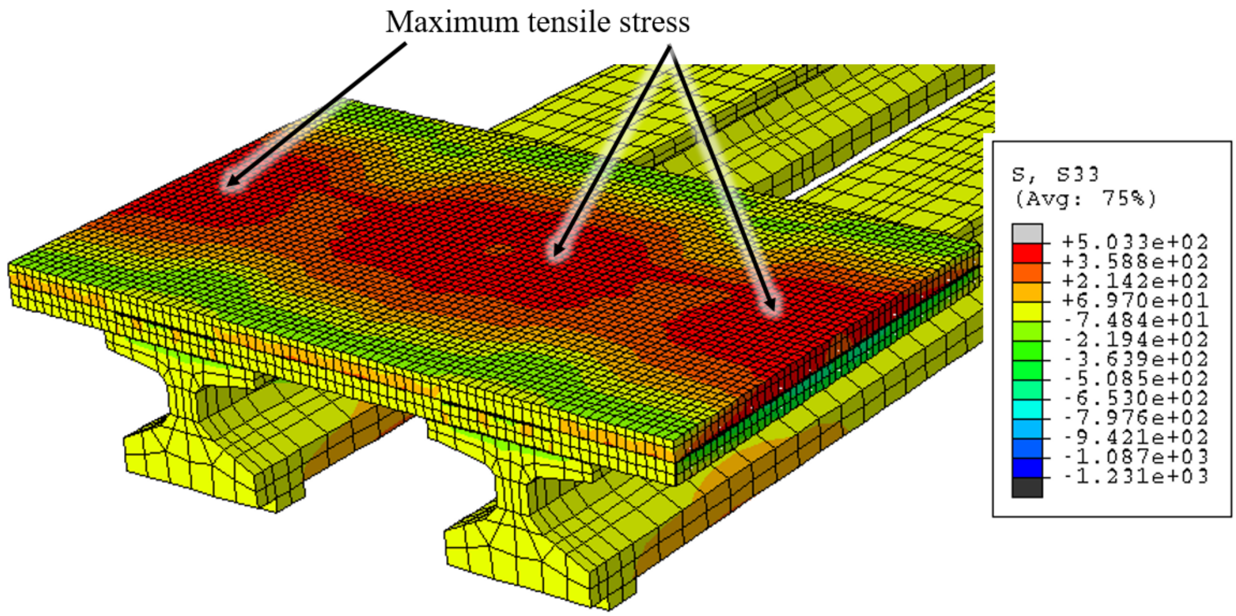

Figure 8.60. Longitudinal concrete stresses formed by uniform shrinkage in the deck, causing potential cracking within the section.

8.8 NEGATIVE BENDING

Thermal gradient in the girders was used to investigate negative bending of the girders and slab. A preliminary analysis step was used to designate an initial temperature for the girders. During the loading step, the temperature of the bottom face of each girder was decreased an equal amount, producing negative girder end rotations (see Figure 8.61) of around 0.001 rad and tensile forces in the bottom of the link slab. The results of three offset precast panel models loaded with thermal gradient are presented here. The first model is fully bonded, while the second and third are debonded at the girder-slab interface.

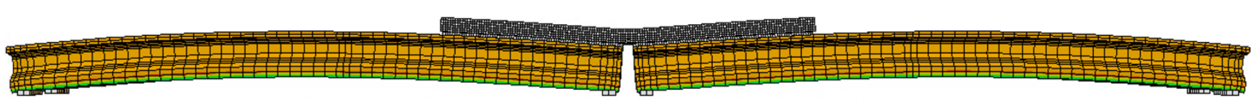

Figure 8.61. Exaggerated girder and slab deformation caused by thermal gradient, leading to tension in the bottom of the link slab.

Figure 8.62 shows the cracking pattern for the bonded model. Cracking begins over the girder lines at the girder edge at the change in cross-section depth. These cracks propagate in the transverse direction between the girders and out to the slab edges. The cracks are not full depth.

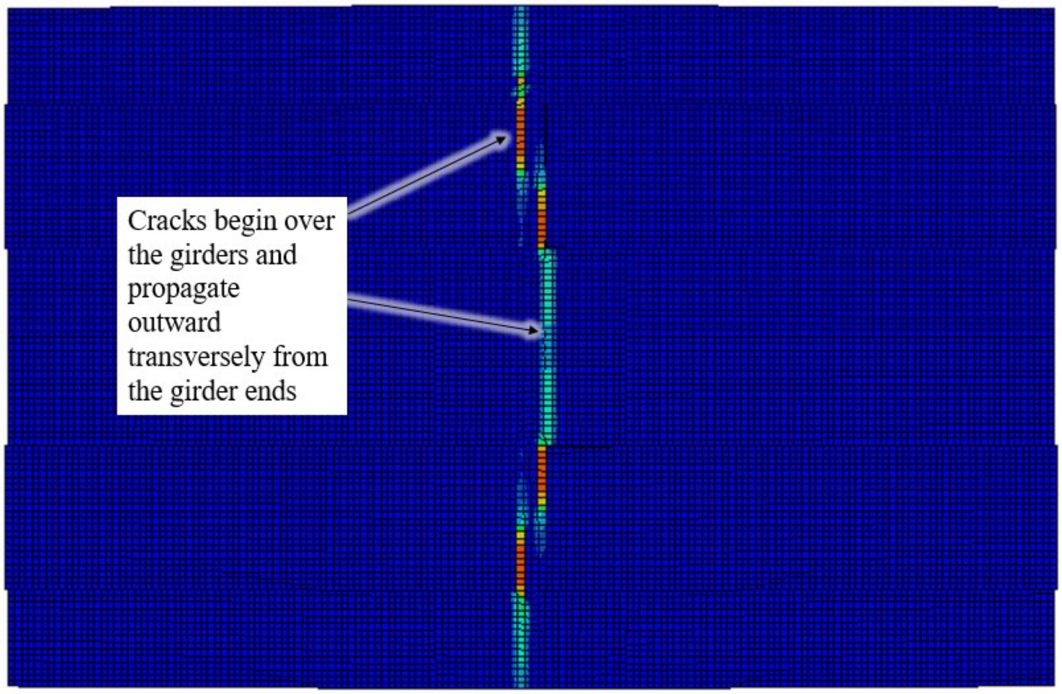

Figure 8.62. The crack pattern in the bottom of the slab for an offset precast panel model loaded with negative temperature gradient.

Debonded models were investigated with an 18-in. debonded length and a 36-in. debonded length, both without a vertical gap in the debonded region. As seen in Figure 8.63, a gap between the girder and the 36-in. debonded slab formed naturally due to negative bending of the girders. Debonding was so effective that the 36-in. debonded slab did not crack during the simulation. The bottom of the 18-in. debonded slab did crack, as shown in Figure 8.64. However, unlike for the bonded model, the cracks did not extend between the girders and out to the deck edges. Instead, cracks formed over the girder ends and at the end of the debonded region. These results show that even debonded details without vertical gaps are effective at reducing cracking under negative girder deformation.

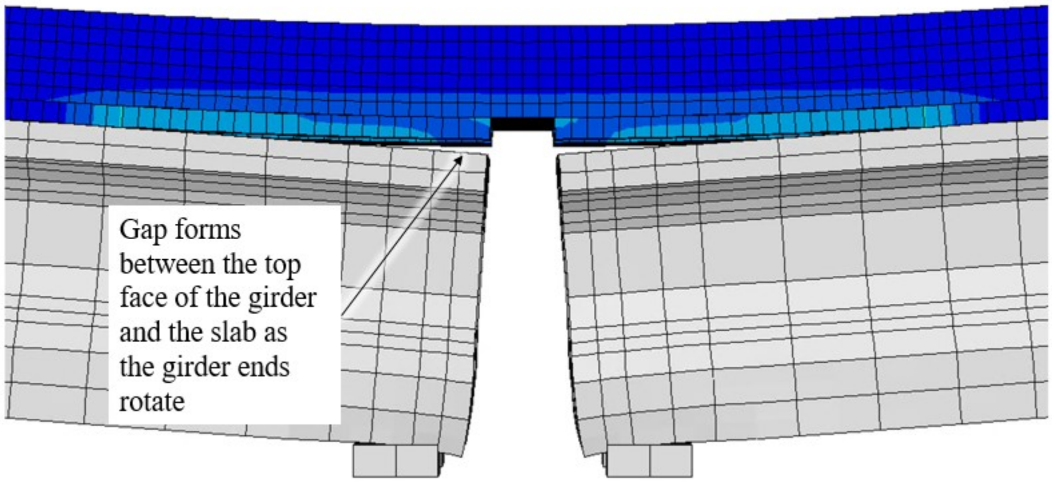

Figure 8.63. Exaggerated deformation of the girder ends for the 36-in. debonded model, causing a natural gap between the bottom of the DLS and the top face of the girder.

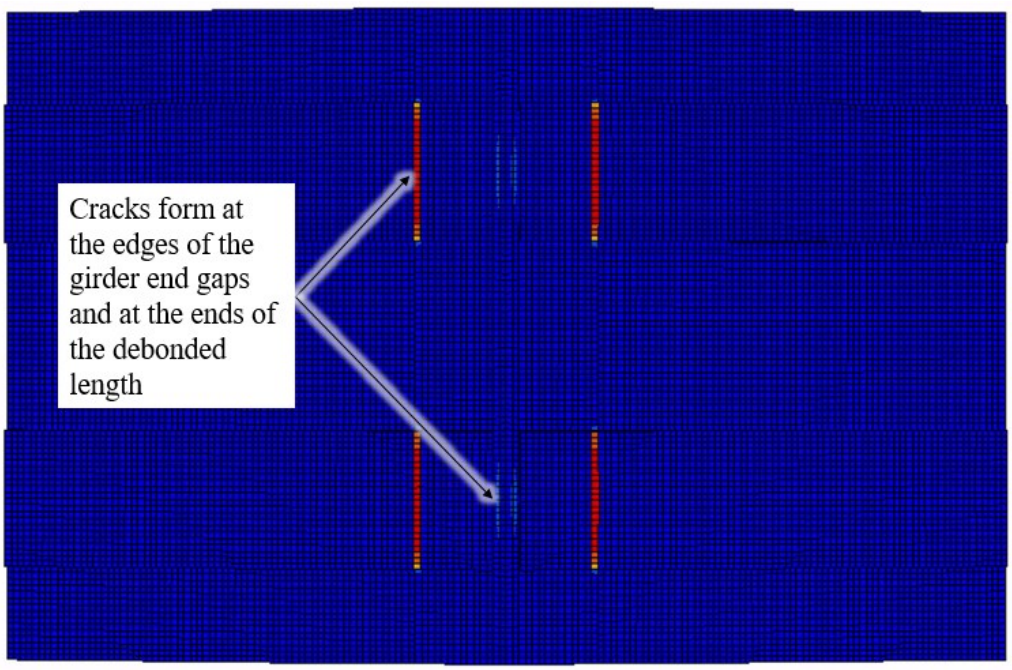

Figure 8.64. Crack pattern in the bottom of the slab for an 18-in. debonded offset precast panel model loaded with negative temperature gradient.

8.9 SUPPORT STIFFNESS AND DECK TENSILE FORCES

A concern for PBJ behavior is that additional tensile forces in the deck may worsen cracking. In order to investigate the longitudinal tensile force through the PBJ, researchers drew an analytical section through the center of the PBJ region. The section through the deck, shown in Figure 8.65(a), was used to sum longitudinal forces across all concrete elements bisected by the plane. When summed with the longitudinal forces from all rebars bisected by the plane, a total force in the deck could be calculated. The models were loaded on both girders in one span according to Figure 8.65(b).

Support conditions have the potential to affect the tensile force carried by the PBJ. The use of elastomeric bearings has the benefit of allowing the girder ends to displace longitudinally, thereby preventing a force couple between the supports and the link slab. However, if the supports are stiffened, it is possible that tensile forces will increase within the PBJ. To investigate this phenomena, three models were analyzed: one flush PCP and one offset PCP model with normal values for support stiffness, and one offset PCP model with pinned supports. If tensile forces are not formed across the PBJ for normal support conditions, then additional tension effects may not be a concern for most bridges. However, if pinned supports cause significant tension in the deck, then the presence of stuck bearings on bridges may be very harmful to PBJs.

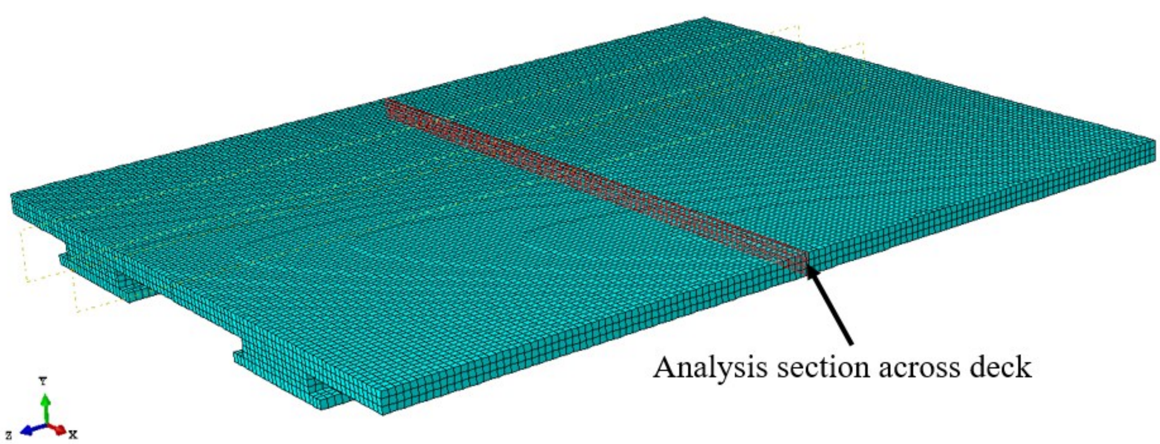

(a)

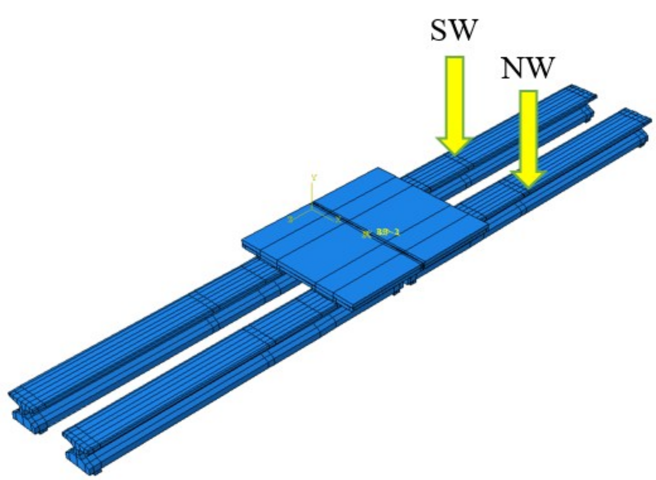

(b)

Figure 8.65. (a) Deck model used to analyze tensile forces across the PBJ, and (b) loading diagram for the flush PCP model.

The results of the analyses are shown in Figure 8.66. The simulations were taken to high rotations, up to 0.012 rad, in order to evaluate deck forces. Both the flush PCP and offset PCP models had net compression forces in the link slab with the support stiffness of a typical elastomeric bearing pad. However, large tensile forces were observed for the offset PCP model with pinned supports, simulating fixed or frozen bearing pads. This finding shows that typical support conditions do not result in deleterious tensile forces in the link slab. However, faulty bearing pad conditions that prevent the girder ends from translating longitudinally may cause significant tensile loads in the link slab, leading to deleterious cracking and subsequent damage.

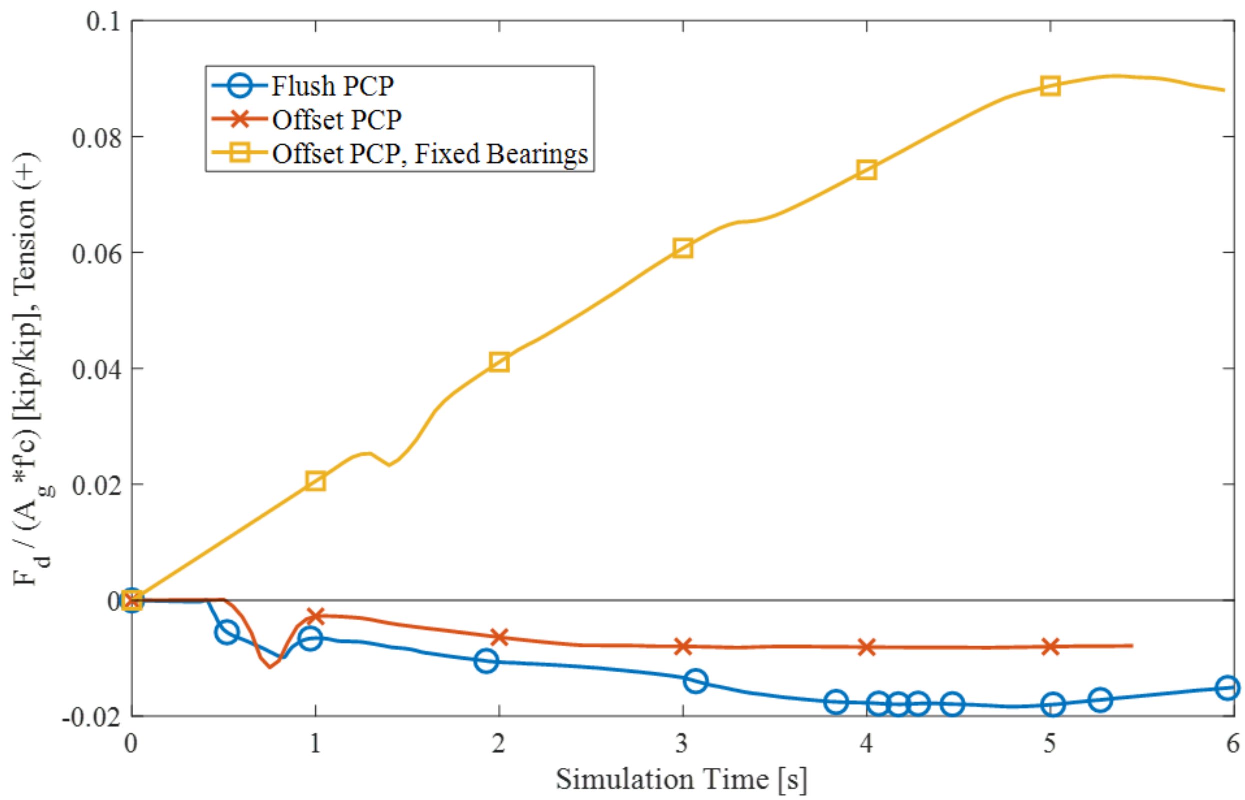

Figure 8.66. Longitudinal force in the deck, F_d, across the PBJ normalized by the gross section area at the PBJ and concrete compressive strength ($A_g * f'_c$) for models with flush PCP, offset PCP, and offset PCP with fixed bearings.

8.10 SKEW EFFECTS

An experimental test with skewed supports was outside the scope of the project. However, skewed bridges have different deck cracking and stress distributions than non-skewed structures. As such, PBJ details at skewed bridges required further study. Finite element models were used to examine link slab behavior between offset girder ends for a variety of skews. Particularly, the interface between precast panel edges and CIP concrete above the bents interacted with shear lag effects over the girder ends to produce a unique stress pattern.

Skewed structures lack mirrored symmetry, making the use of single-girder line models with symmetrical boundary conditions inappropriate for studying skew effects. Instead, girder stub models and dual-girder line models were developed to investigate skew effects at the PBJ.

8.10.1 Girder Stub Model

Two primary girder stub model types were developed: with and without coped girder ends. TxDOT design standards call for the use of either skewed girder ends or foam filler above girder ends above skewed supports. These standards provide clearance between the girder end and the slab in the adjacent span, preventing contact between the girder end and slab that could result in damage under repeated loading. However, field investigations in the Bryan, Lubbock, and Atlanta Districts showed that some existing structures used neither skewed girder ends nor foam inserts above the girder end corners. Case (a) in Figure 8.67 shows a model with skewed girder ends, while case (b) shows a model without skewed ends or inserts. These two models allowed for comparisons between the different conditions for skewed girder ends. Both models had a skew of 30 degrees. Each stub model included standard longitudinal and transverse reinforcement within a CIP slab.

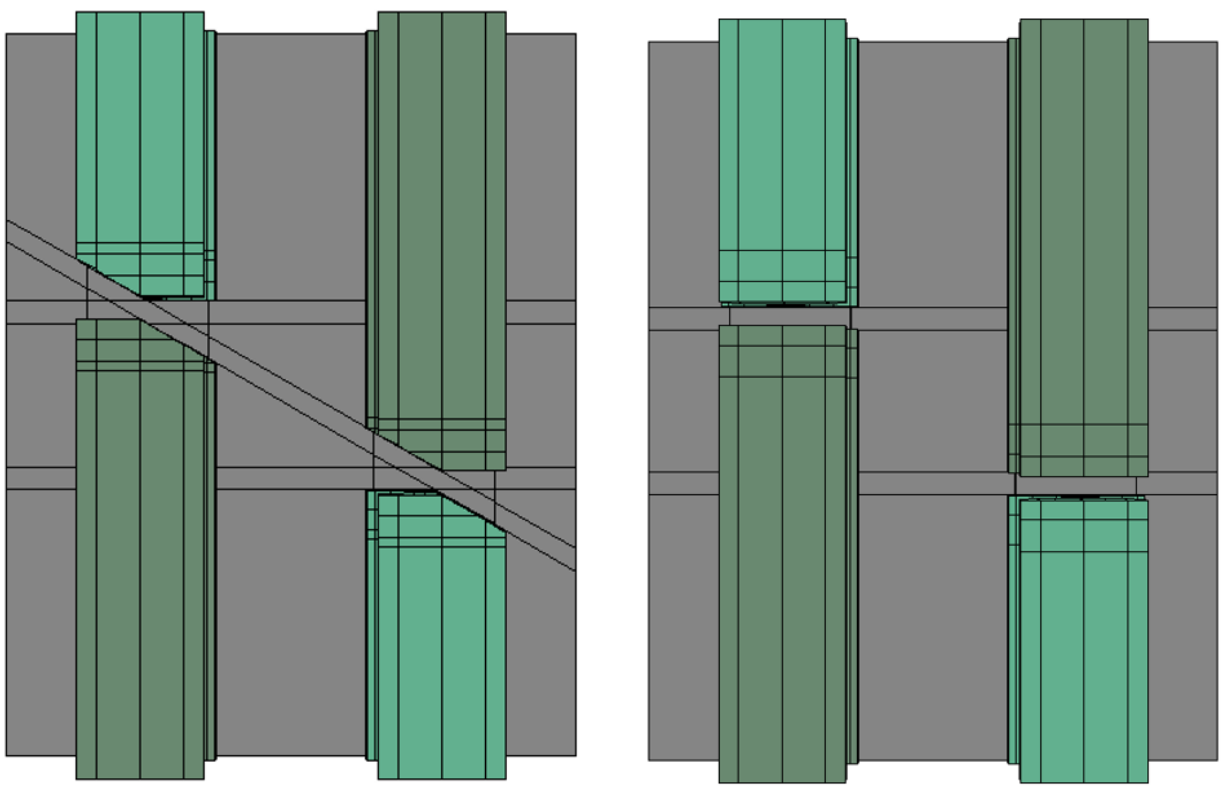

(a) (b)

Figure 8.67. Underside of skewed stub models, showing (a) a skewed girder end condition and (b) a flat girder end condition.

The stress propagation for the skewed girder end model is shown in Figure 8.68. As illustrated in Figure 8.68 (a), the left girder line's displacement produces initial cracking between the girder ends. Cracking initiates between the girder ends and propagates outward toward the other girder line and the edge of the deck. In Figure 8.68 (b), the movement of the left girder line causes crack propagation toward the right girder line. However, the cracking pattern does not directly follow the skew of the support but rather causes nearly longitudinal cracking between the girder lines. In Figure 8.68(c), the right girder line is rotated, causing cracking from between the girder ends to the edge of the slab. Isolated pockets of tensile stress develop over the longitudinal reinforcement in the cracked deck.

The non-skewed girder end model shows different cracking behavior, as displayed in Figure 8.69. Figure 8.69(a) shows that the initial cracking proceeds similarly to the skewed end model, with the left girder causing tensile stresses that spread out in the transverse direction from between the girder ends. In Figure 8.69(b), however, cracking begins between the right girder line, with scattered cracking stresses forming between the two girder lines rather than a distinct line of stress like that shown in the skewed girder end model. In Figure 8.69(c), the right girder line is displaced, causing cracking to spread to the right edge of the slab.

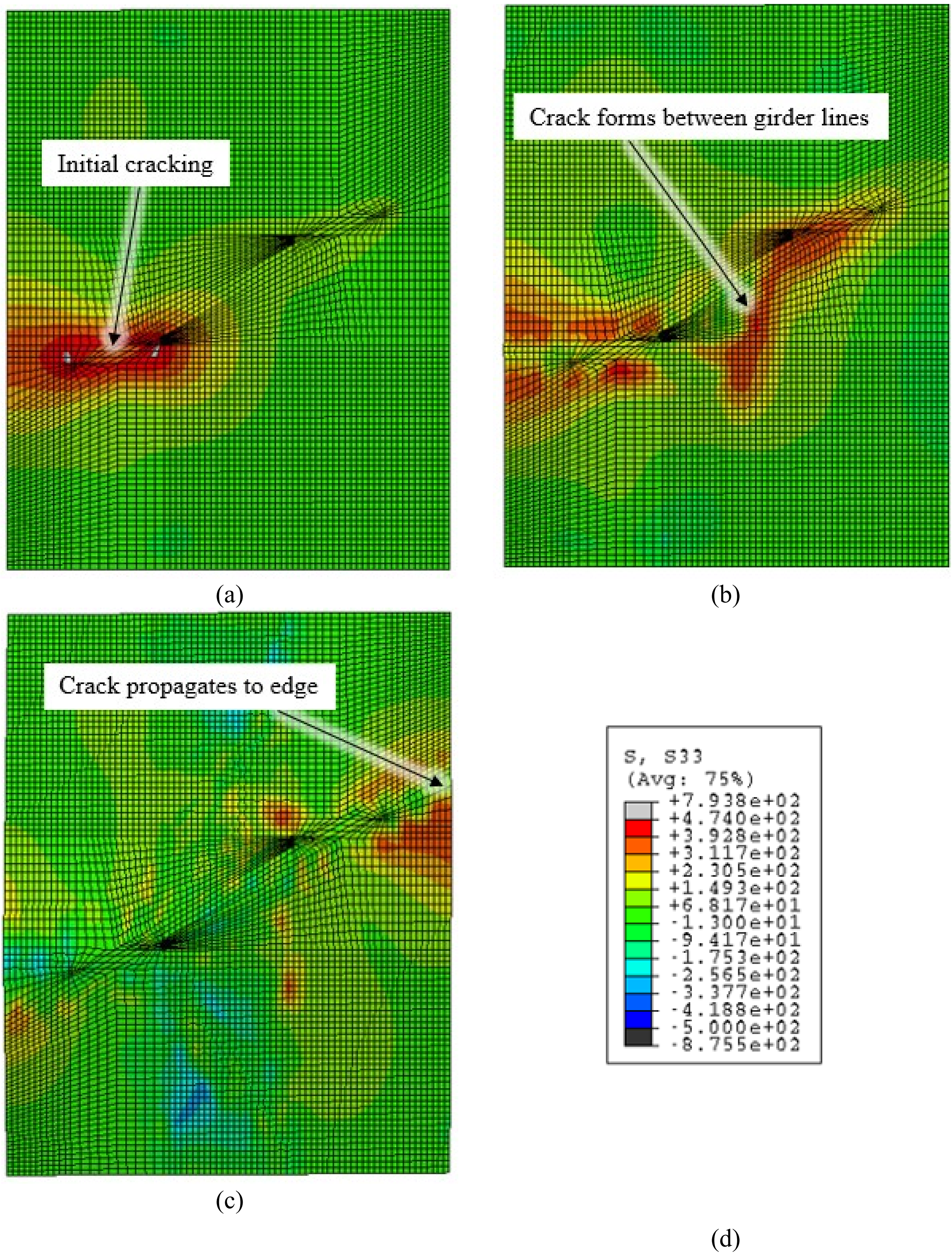

Figure 8.68. Longitudinal stress propagation in the deck of the skewed girder end model.

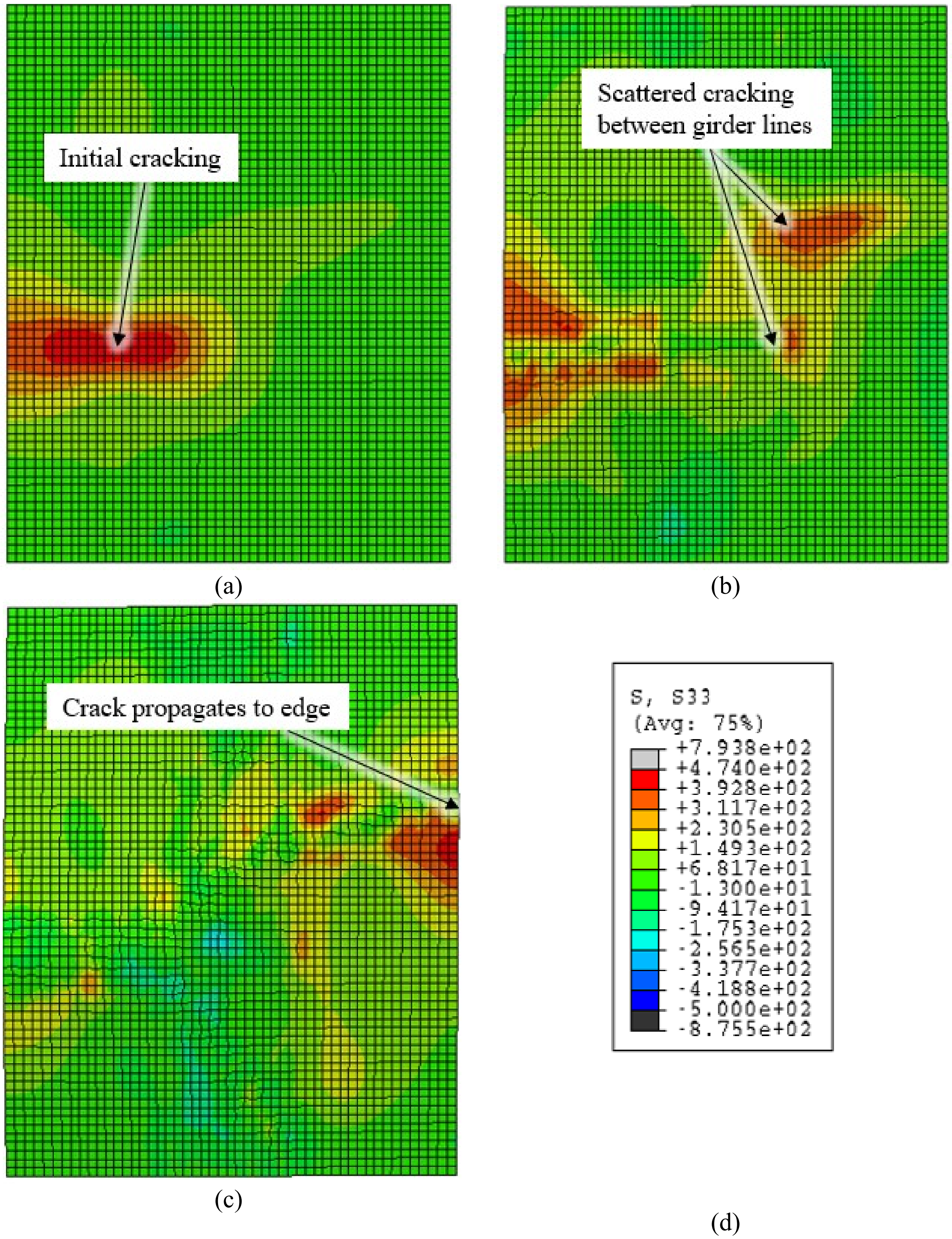

Figure 8.69. Longitudinal stress propagation in the deck of the non-skewed girder end model.

Comparisons of deck concrete and steel stresses at the point of first cracking did not reveal significant differences in initial cracking behavior between the two models. The use of skewed girder ends did not delay cracking, as shown in Figure 8.70. The girder stub model with standard girder ends reached first cracking slightly after the model with skewed ends. Longitudinal stresses in the top longitudinal reinforcing bars adjacent to the location of first cracking, shown in Figure 8.71, exhibited similar behavior between the two models. The reinforcing bars in both the skewed and non-skewed girder end models began increasing in stress and reached their yield stress at approximately equivalent girder end rotations.

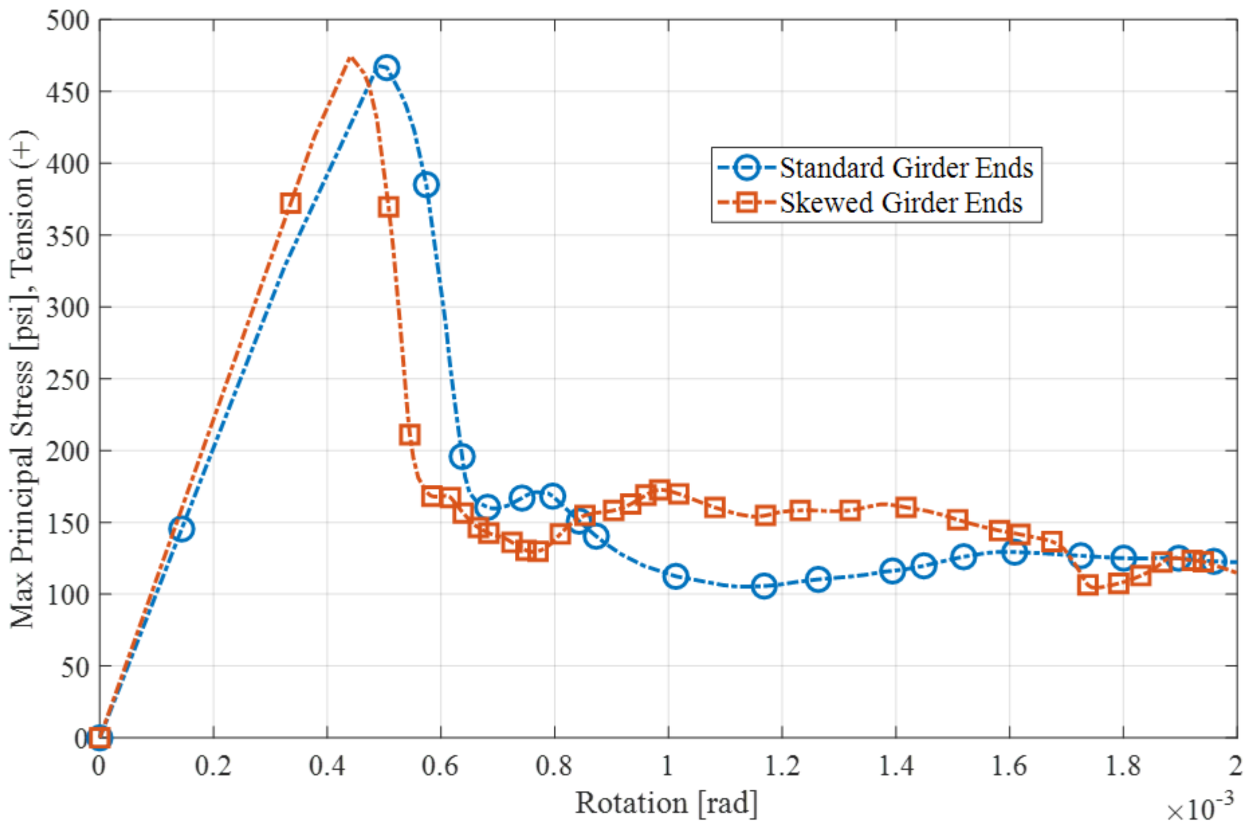

Figure 8.70. Comparison of maximum principal stresses at the point of first cracking for the skewed girder stub models with standard girder ends and skewed girder ends.

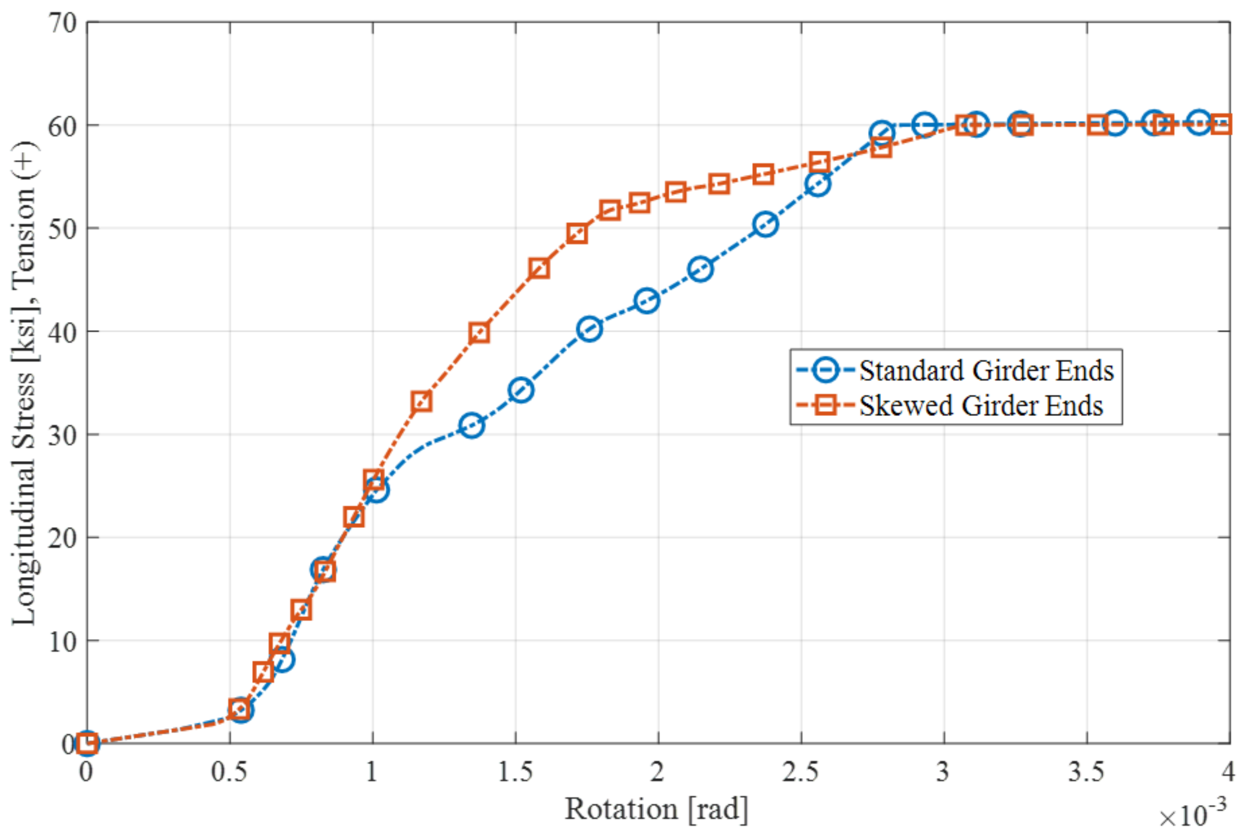

Figure 8.71. Comparison of longitudinal stress in the top longitudinal reinforcement adjacent to the point of first cracking in the deck for the skewed girder stub models with standard girder ends and skewed girder ends.

8.10.2 Dual-Girder Skewed Model

The dual-girder skewed model, seen in Figure 8.72, was set up in a similar fashion to the non-skewed laboratory setup, with four girders loaded with span loads at the top face of each girder. This model used the bonded offset panel detail with a 45-degree skew and no coped girder end details. The top of the deck, shown in Figure 8.73, used CIP concrete without a crack former. The standard reinforcement used in the deck is shown in Figure 8.74, while the precast panel locations are shown from beneath the deck in Figure 8.75.

The model was loaded in steps, starting with the northwest girder in Figure 8.76(a), then the southwest girder in Figure 8.76(b), and finally the northeast and southeast girders together in Figure 8.76(c). Load from the previous step was retained on the girder for subsequent load steps. The cracking pattern in step (a) begins between the girder ends, propagating to the north edge of the slab and curving in an L-shape above the edge of the precast panel to the west edge of the slab. Cracking continues in step (b) with a diagonal crack between the girder lines and a second horizontal crack between the girder ends that reaches the south edge of the slab. Finally, step (c) instigates a vertical crack toward the east end of the deck over the precast panel edge as well as Y-shaped secondary cracks at the slab edges.

The bottom of the deck shows cracking primarily along the girder edges, which reach full depth at high rotations, as shown in Figure 8.77.

Top reinforcement stresses follow the cracking pattern generally. Maximum stresses occur in the longitudinal bars over the girder lines, as shown in Figure 8.78. Cracking in the top slab forms diagonally between the girder lines, activating both the longitudinal and transverse bars. Transverse bar stresses also form along the girder edges. Bottom reinforcement stresses, shown in Figure 8.79, are much smaller in magnitude than top reinforcement stresses. Tensile stresses form in the transverse reinforcement along the girder edges.

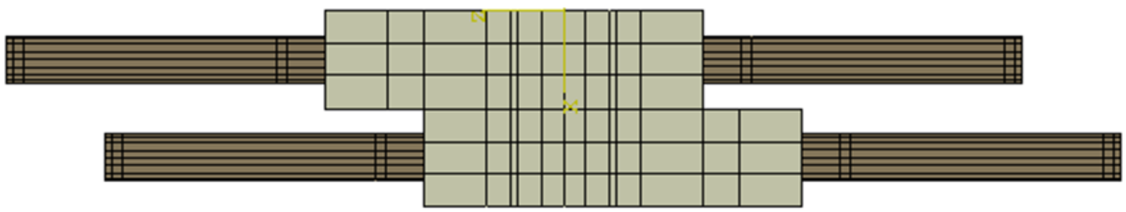

Figure 8.72. Top view of the dual-girder skewed model.

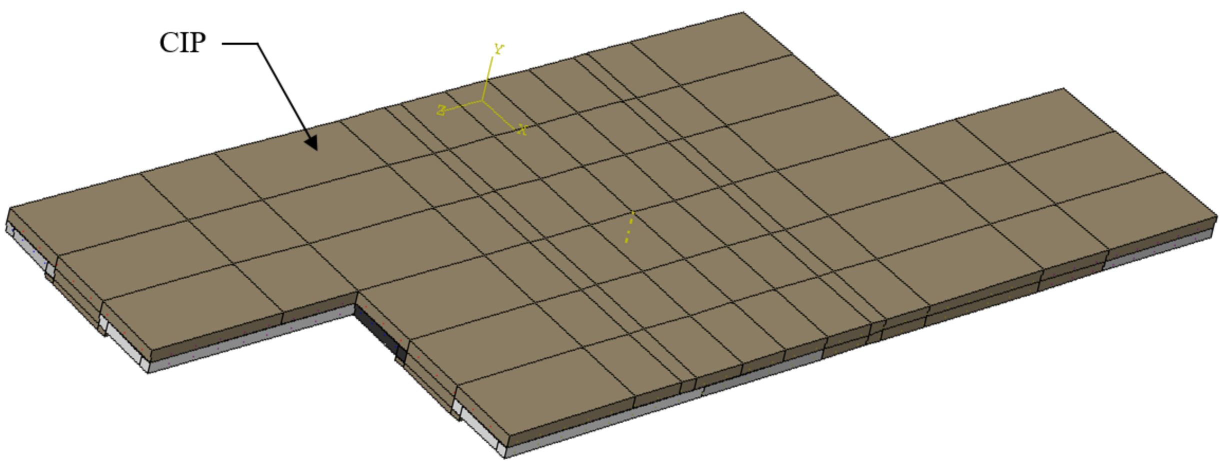

Figure 8.73. Top view of the deck for the dual-girder skewed model.

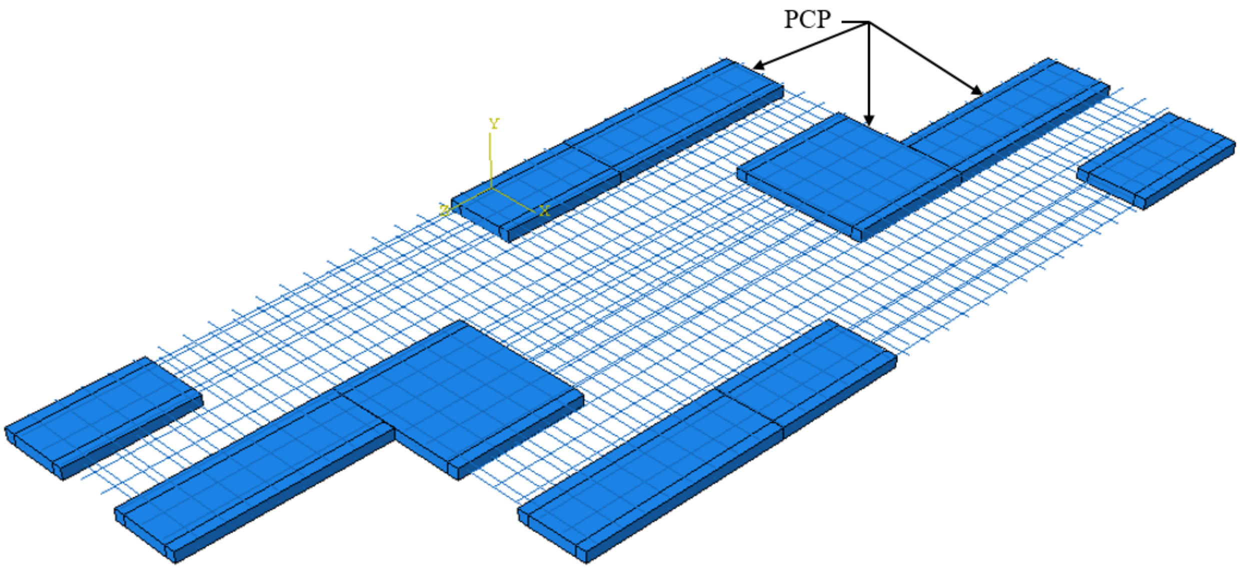

Figure 8.74. Top view of the PCPs and reinforcement for the dual-girder skewed model with the offset panel detail.

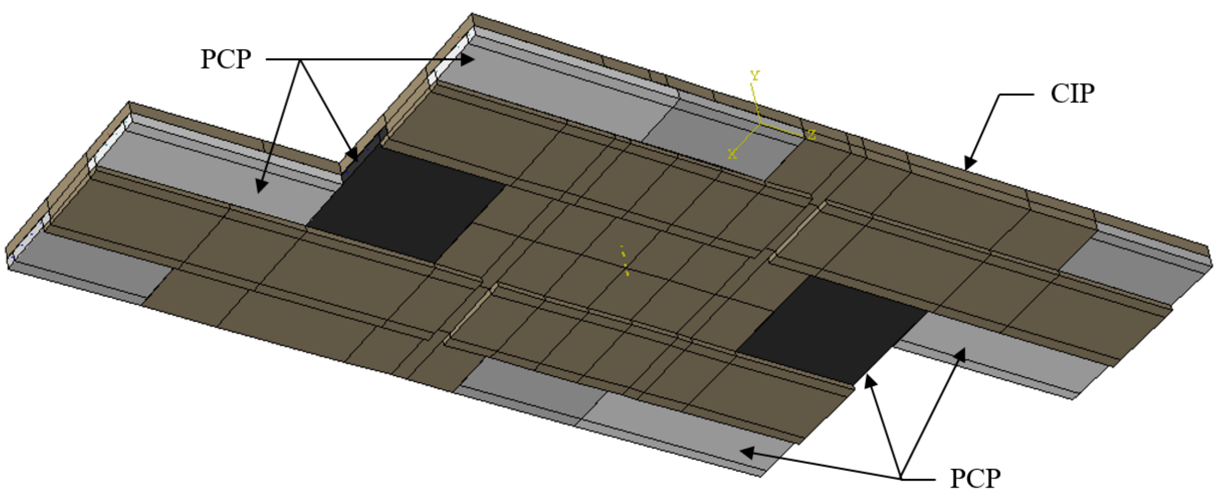

Figure 8.75. Bottom view of the deck for the dual-girder skewed model with the offset panel detail.

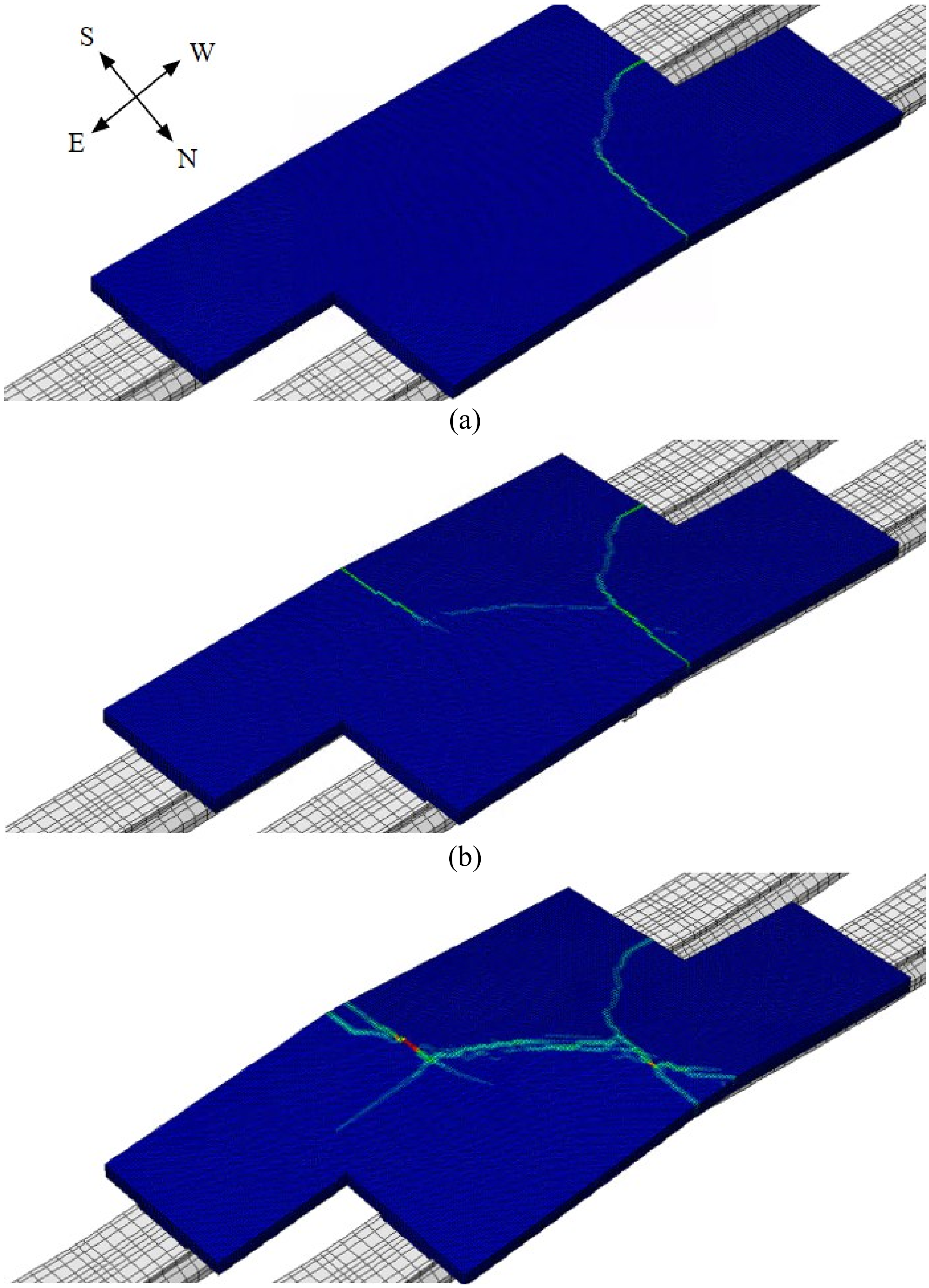

(a)

(b)

(c)

Figure 8.76. Crack propagation in the dual-girder skewed model with offset panels for loading progressing from the (a) northwest girder, (b) southwest girder, and (c) southeast and northeast girders.

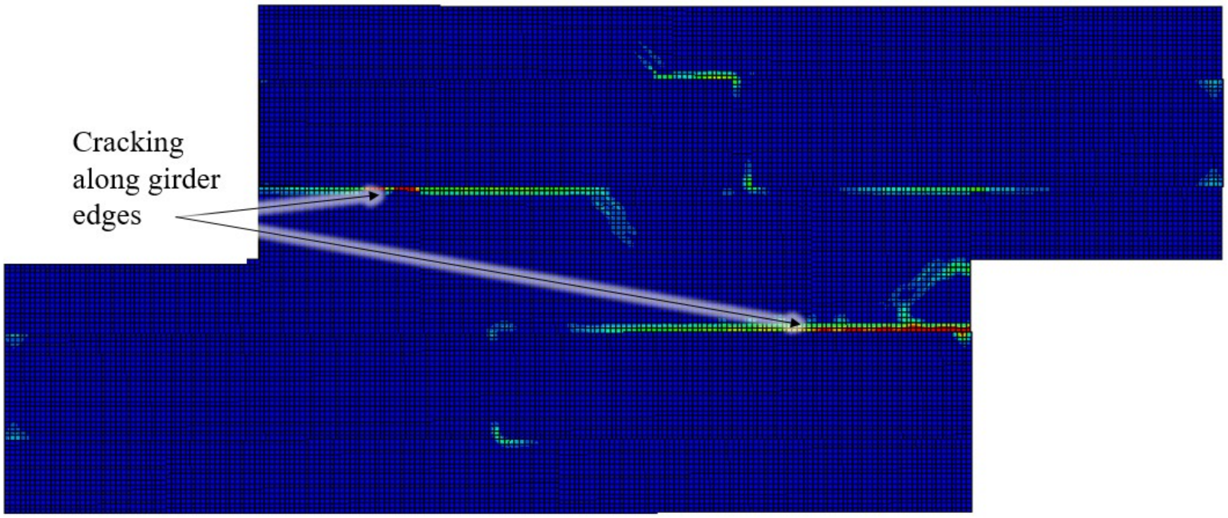

Figure 8.77. Cracking in the bottom of the deck for the dual-girder skewed model, primarily along the girder edges.

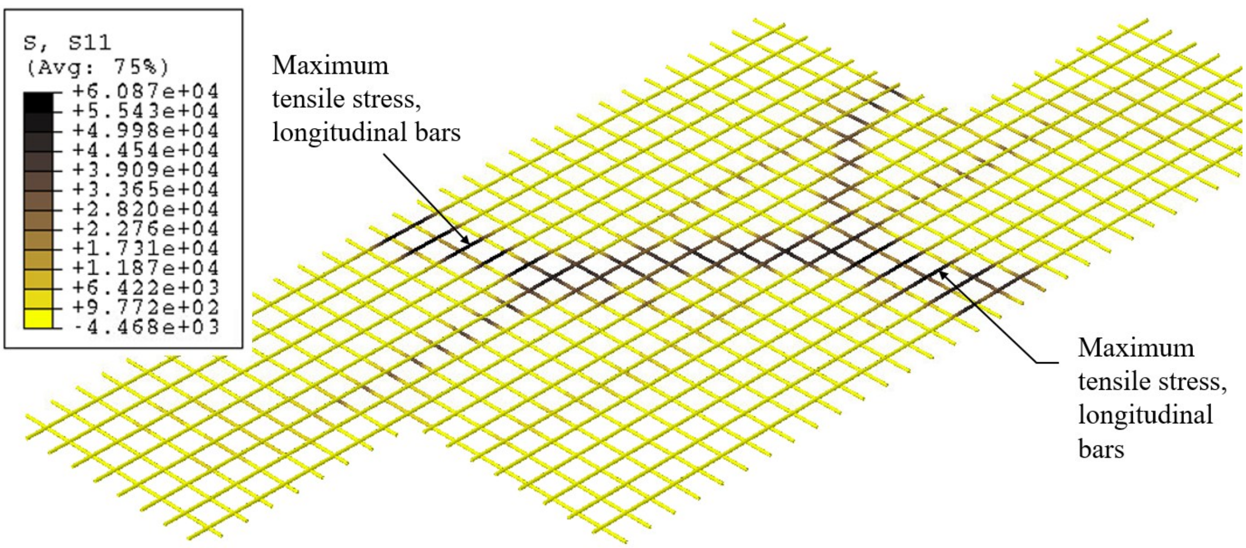

Figure 8.78. Stress in the top longitudinal and transverse bars for the skewed model, showing maximum tensile stresses forming over the girder, with stresses extending diagonally between girder lines following the cracking pattern.

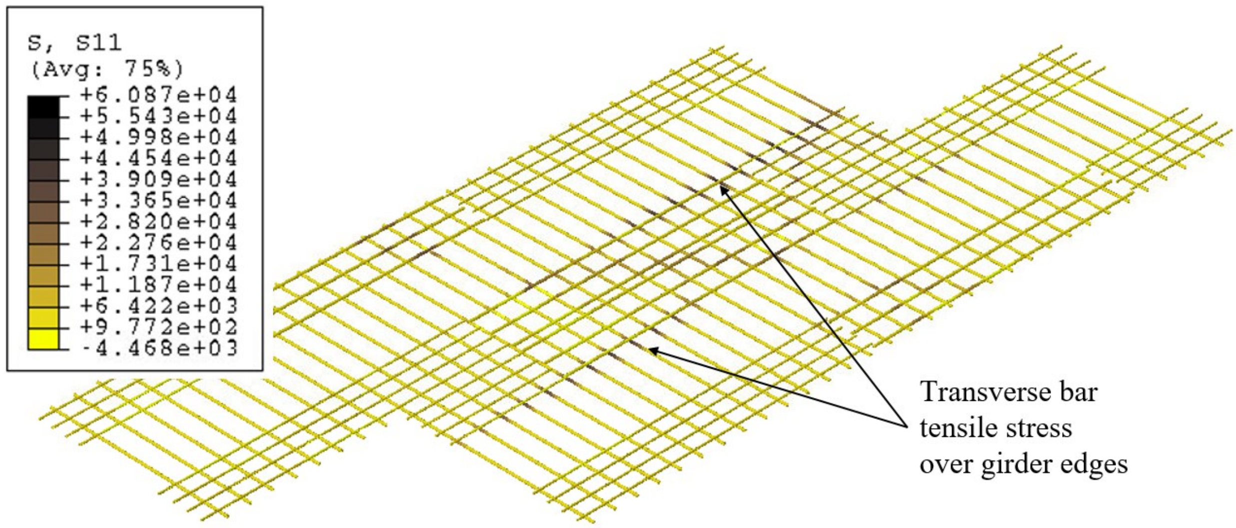

Figure 8.79. Stress in the bottom longitudinal and transverse bars for the skewed model, showing maximum tensile stresses forming in the transverse reinforcement over the girder edges.

8.10.3 Debonded Skewed Model

A debonded version of the dual-girder skewed model was created to evaluate the effects of debonding on skewed bridges. Similar to other debonded models, an 18-in. debonded length was chosen along with a 0.5-in. gap in the deck haunch between the top face of the girder and the bottom face of the link slab, as shown in Figure 8.80. The 0.5-in. haunch gap was chosen to match the gap constructed during lab testing. Since 0.5 in. of clearance prevented contact between the girder face and slab at practical rotations, there was no difference in performance from the larger 2-in. vertical gap used in other models.

The debonded skewed model was loaded in the same steps as the bonded skewed model, starting with the northwest girder in Figure 8.81(a), then the southwest girder in Figure 8.81(b), and finally the northeast and southeast girders together in Figure 8.81(c). Load from the previous step was retained on the girder for subsequent load steps. The cracking pattern in step (a) began over the girder at the end of the debonded region, propagating to the north edge of the slab and curving in an L-shape above the edge of the precast panel to the west edge of the slab. Cracks formed independently on the west edge of the slab over the girder edge and joined with the crack emanating from the PBJ. A secondary crack also formed over the northeast girder in the debonded region. This crack propagated to the slab edge in one direction and southwest to join the initial crack. The crack branches on the north edge of the deck were on either side of the girder end gap in the debonded regions.

Cracking continued in step (b) with a diagonal crack between the girder lines and a second horizontal crack over the debonded region of the southwest girder, reaching the south edge of the slab. A secondary crack then formed over the southeast girder in the debonded region. This crack ran diagonally across the deck to join the main PBJ crack. Finally, in step (c), additional secondary cracks formed on the north side of the slab past the northwest debonded region. Multiple branches also formed along the diagonal crack across the deck.

The bottom of the deck showed cracking primarily in the west deck, following the diagonal crack at the top surface. This crack reached full depth at high rotations, as shown in Figure 8.82. Separation between the girder and deck occurred at the end of the debonded regions.

Top reinforcement stresses followed the cracking pattern generally. Maximum stresses occurred in the longitudinal bars over the girder lines, as shown in Figure 8.83. Cracking in the top slab formed diagonally between the girder lines, activating both the longitudinal and transverse bars. Transverse bar stresses also formed along the southwest girder edge. Bottom reinforcement stresses, shown in Figure 8.84, were much smaller in magnitude than top reinforcement stresses. Tensile stresses formed in the transverse reinforcement along the girder edges and in the longitudinal reinforcement along the PBJ.

A comparison of the initial cracking behavior of the bonded and debonded skewed models showed the effects of debonding. Figure 8.85 shows that the debonded model delayed initial cracking by 0.00025 rad of girder end rotation. Furthermore, examination of Figure 8.76(c) and Figure 8.81(c) shows that the overall cracking pattern at high rotations was more dispersed in the debonded model. Debonding the link slab, even for a modest length of 18 in., caused multiple additional cracks to form within and outside of the debonded region. In the bonded model, cracking was more consolidated, forming larger singular cracks. Figure 8.86 shows the longitudinal stress in the top longitudinal steel adjacent to the point of first cracking in the decks. At higher rotations, stress in the steel of the bonded model exceeded that of the debonded model by as much as 20 ksi, indicating that crack widths are reduced with the dispersed cracking pattern.

In the area between the girder lines, more distinct cracks formed in the debonded model, but cracking still occurred over a small width. While crack patterns for skewed models are more complicated than non-skewed models, bonding is still beneficial for the purposes of delaying initial cracking and causing a more dispersed crack pattern.

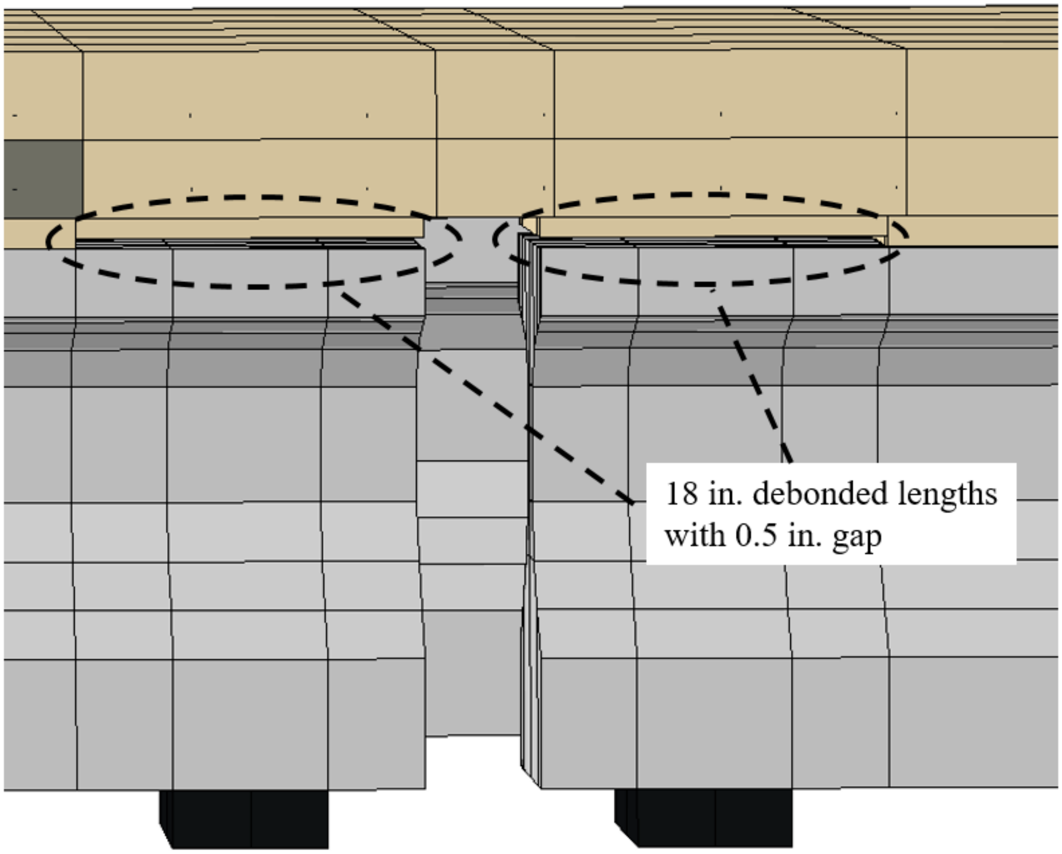

Figure 8.80. Debonded regions of the skewed model, with an 18-in. debonded length and a 0.5-in. gap between the girder face and the bottom of the deck.

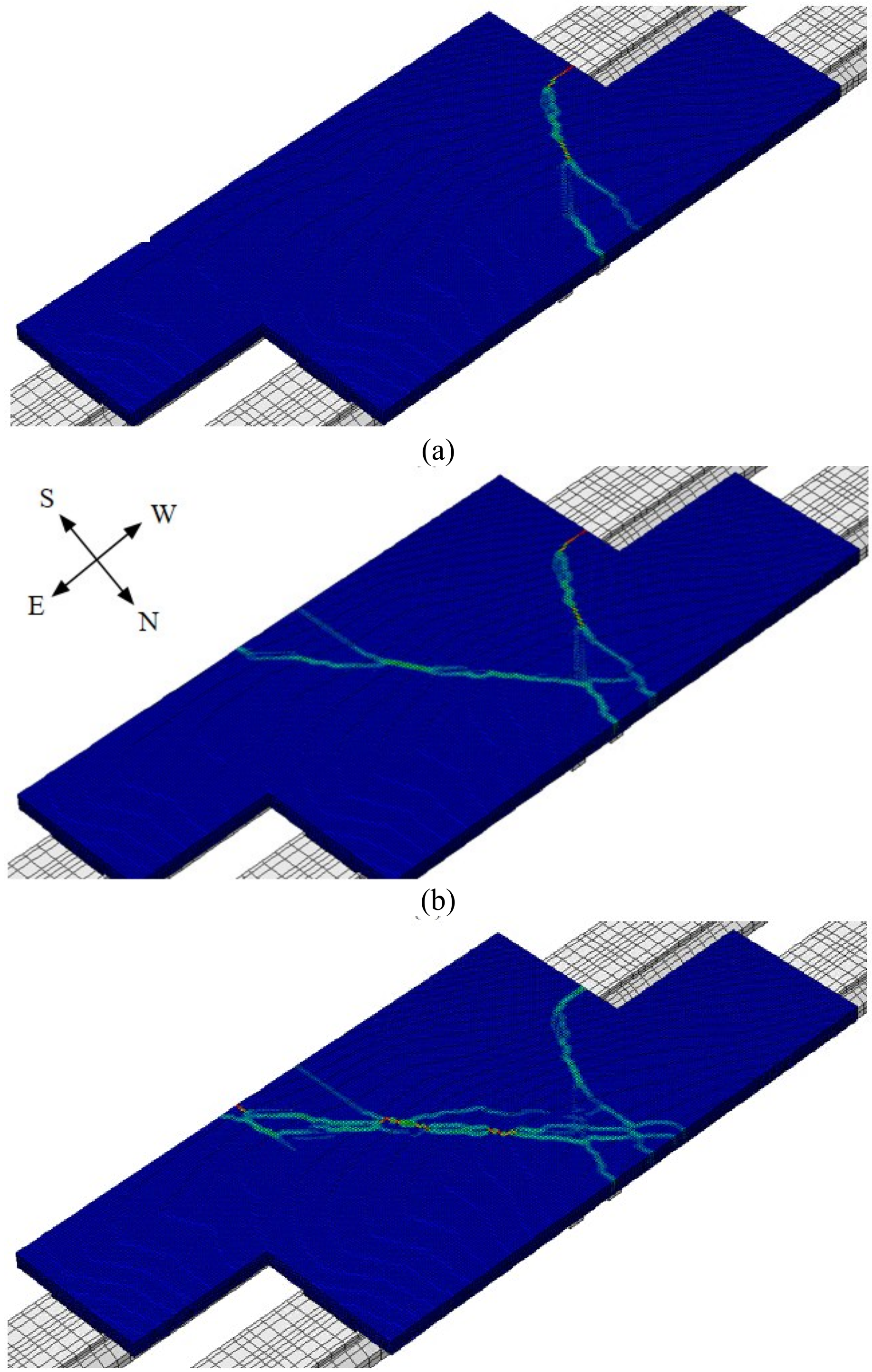

Figure 8.81. Crack propagation in the debonded dual-girder skewed model with offset panels for loading progressing from the (a) northwest girder, (b) southwest girder, and (c) southeast and northeast girders.

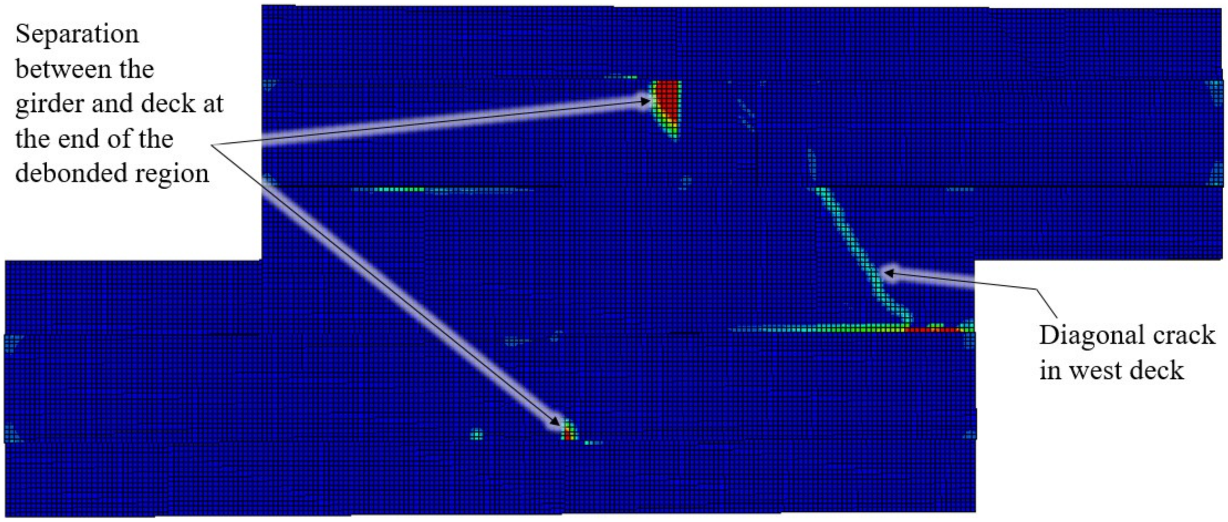

Figure 8.82. Cracking in the bottom of the deck for the debonded dual-girder skewed model, including a full-depth diagonal crack in the west deck, with separation between the girder and deck occurring at the end of the debonded regions.

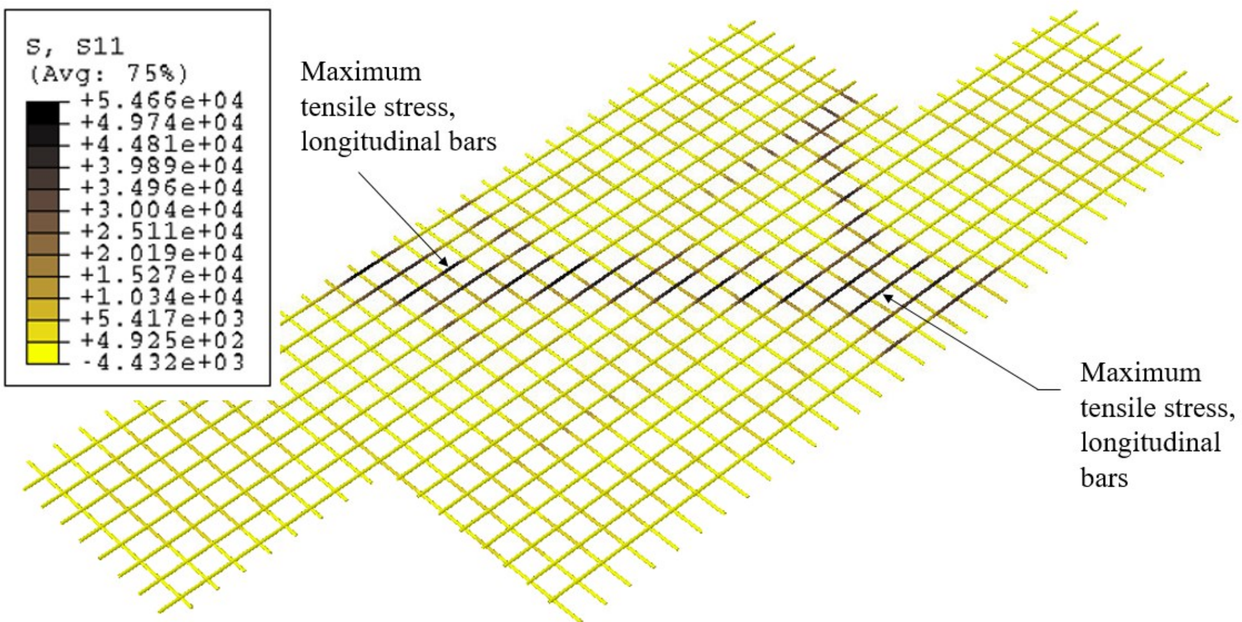

Figure 8.83. Stress in the top longitudinal and transverse bars for the debonded skewed model, showing maximum tensile stresses forming over the girder, with stresses extending diagonally between girder lines following the cracking pattern.

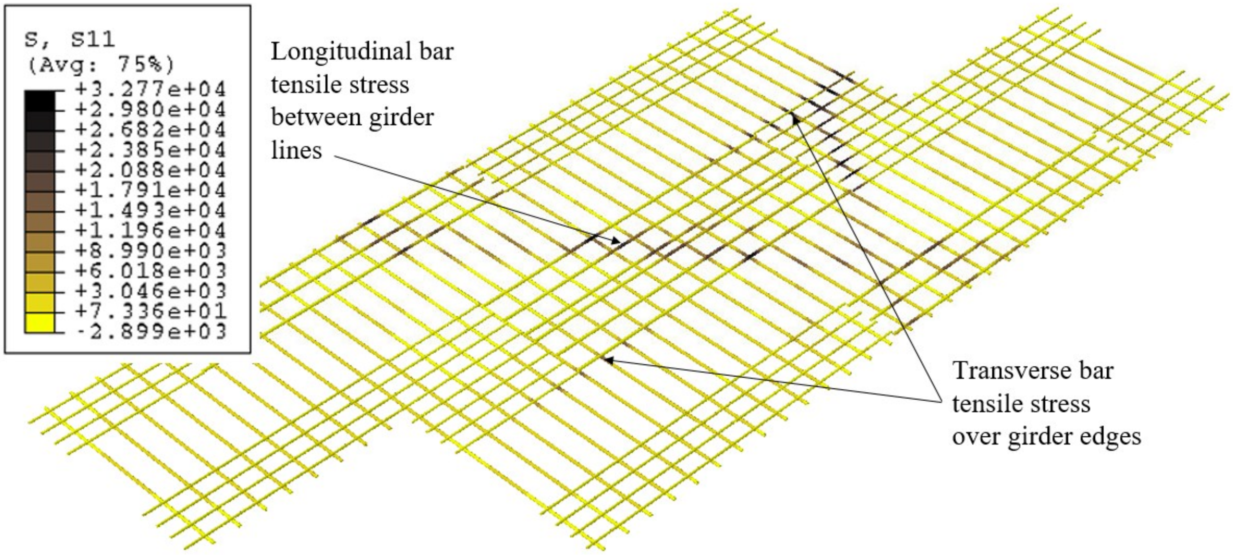

Figure 8.84. Stress in the bottom longitudinal and transverse bars for the debonded skewed model, showing tensile stresses forming over the girder edges, with stresses extending diagonally between girder lines following the cracking pattern.

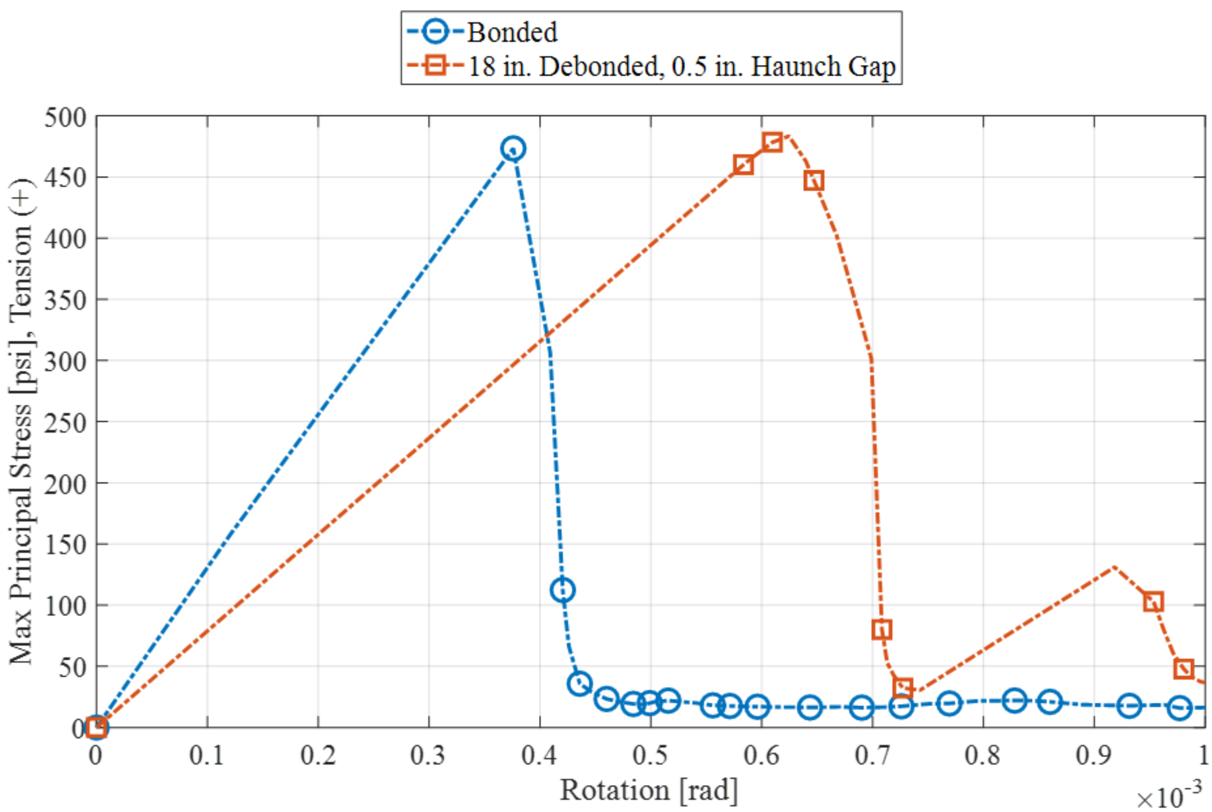

Figure 8.85. Bonded and debonded comparison of dual-girder skewed models, showing maximum principal stress at the location of first cracking in each deck.

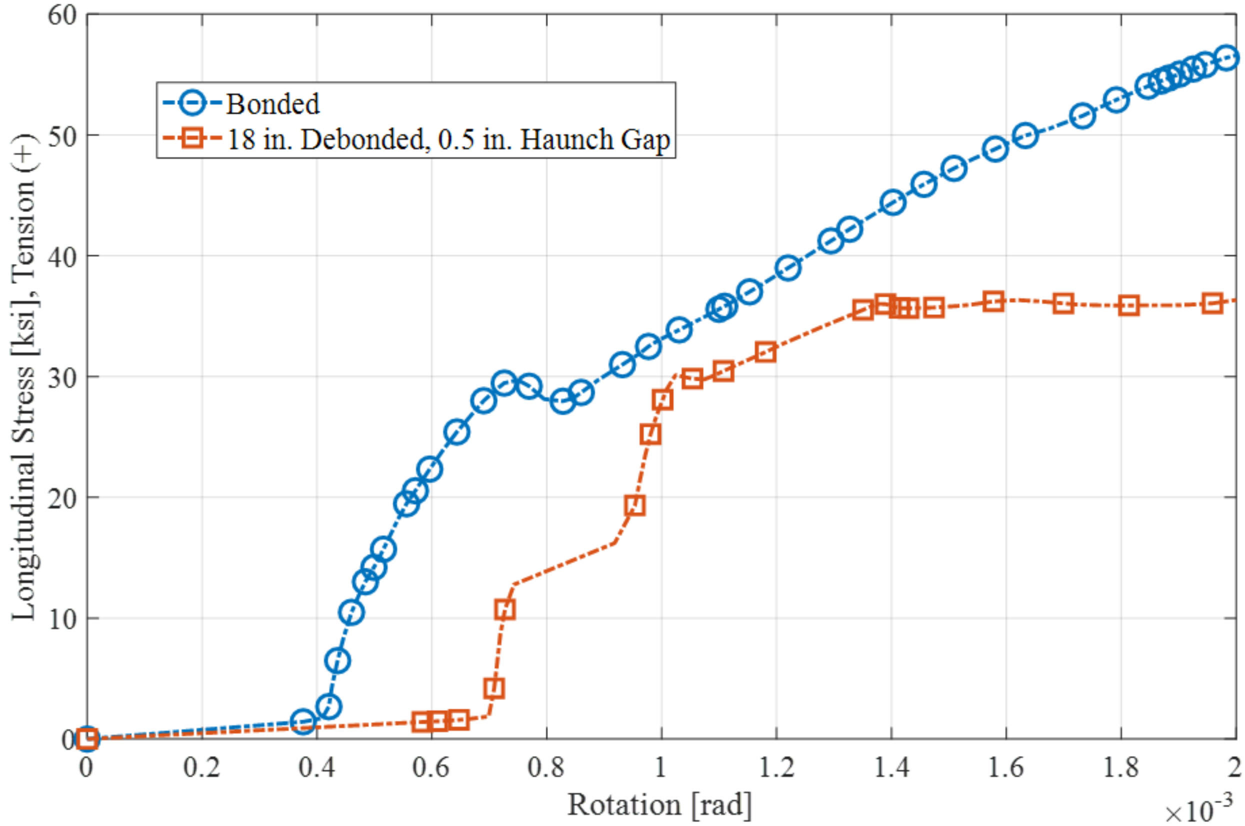

Figure 8.86. Bonded and debonded comparison of dual-girder skewed models, showing longitudinal stress in the top longitudinal reinforcement at the location of first cracking in each deck.

8.11 CONCRETE CRACKING COMPARISON

Cracking behavior varies with different PBJ details, debonded lengths, debonded gap details, girder end gaps, and support skews. Table 8.3 shows a summary of the rotations at the point of first cracking for a variety of models. It may be observed that the flush panel detail is most susceptible to early cracking. Increasing the girder end gap provides a modest improvement, but debonding at the girder-slab interface was not shown to significantly delay cracking. However, debonding at the PCP-slab interface doubled the cracking rotation.

Offset panel details showed modest improvement with simple debonding. However, when a vertical gap in the debonded region was combined with a 36-in. debonded length, the offset panel model realized the most significant gains, with the cracking point delayed by over four times that of the bonded model. With a debonded length of 18 in. and a vertical gap, the cracking point was delayed by 2.5 times the bonded cracking rotation. The continuous panel model showed a similar degree of benefit. Doubling the debonded length while maintaining the same length of the vertical gap further delayed cracking, but using a vertical gap for the entire debonded length is optimal. The benefit of debonding with a vertical gap in the debonded region is demonstrated visually in Figure 8.87.

Finally, for skewed models, an 18-in. debonded length with a corresponding vertical gap increased the cracking rotation by a factor of 1.6. Using skewed girder ends for the 30-degree skew model did not delay cracking when compared to the model with standard girder ends.

Table 8.3. Comparison of rotations at the point of first cracking for various models.

Deck	Debond Length (in.)	Debond Location	Other Features	Cracking Rotation (μrad)
CIP	Bonded			371
CIP	16	Girder-Slab		414
CIP	35	Girder-Slab		481
CIP	54	Girder-Slab		572
FP	Bonded		0.75 in. Panel End Gap	295
FP	Bonded		3 in. Panel End Gap	349
FP	54	Girder-Slab		319
FP	35	PCP-Slab		601
FP	35	PCP-Slab	Raised Longitudinal Reinforcement	600
OP	Bonded			382
OP	18	Girder-Slab		418
OP	36	Girder-Slab		464
OP	36	Girder-Slab	2 in. × 36 in. Debond Gap	1602
OP	18	Girder-Slab	2 in. × 18 in. Squared Debond Gap	980
OP	18	Girder-Slab	2 in. × 18 in. Tapered Debond Gap	964
CP	Bonded			364
CP	18	Girder-Slab	2 in. × 18 in. Debond Gap	887
CP	36	Girder-Slab	2 in. × 18 in. Debond Gap	977
CIP	Bonded		30 deg. Skew	505
CIP	Bonded		30 deg. Skew; Skewed Girder Ends	441
OP	Bonded		45 deg. Skew	376
OP	18	Girder-Slab	45 deg. Skew; 0.5 in. × 18 in. Gap	625

Note: CP = continuous panel.

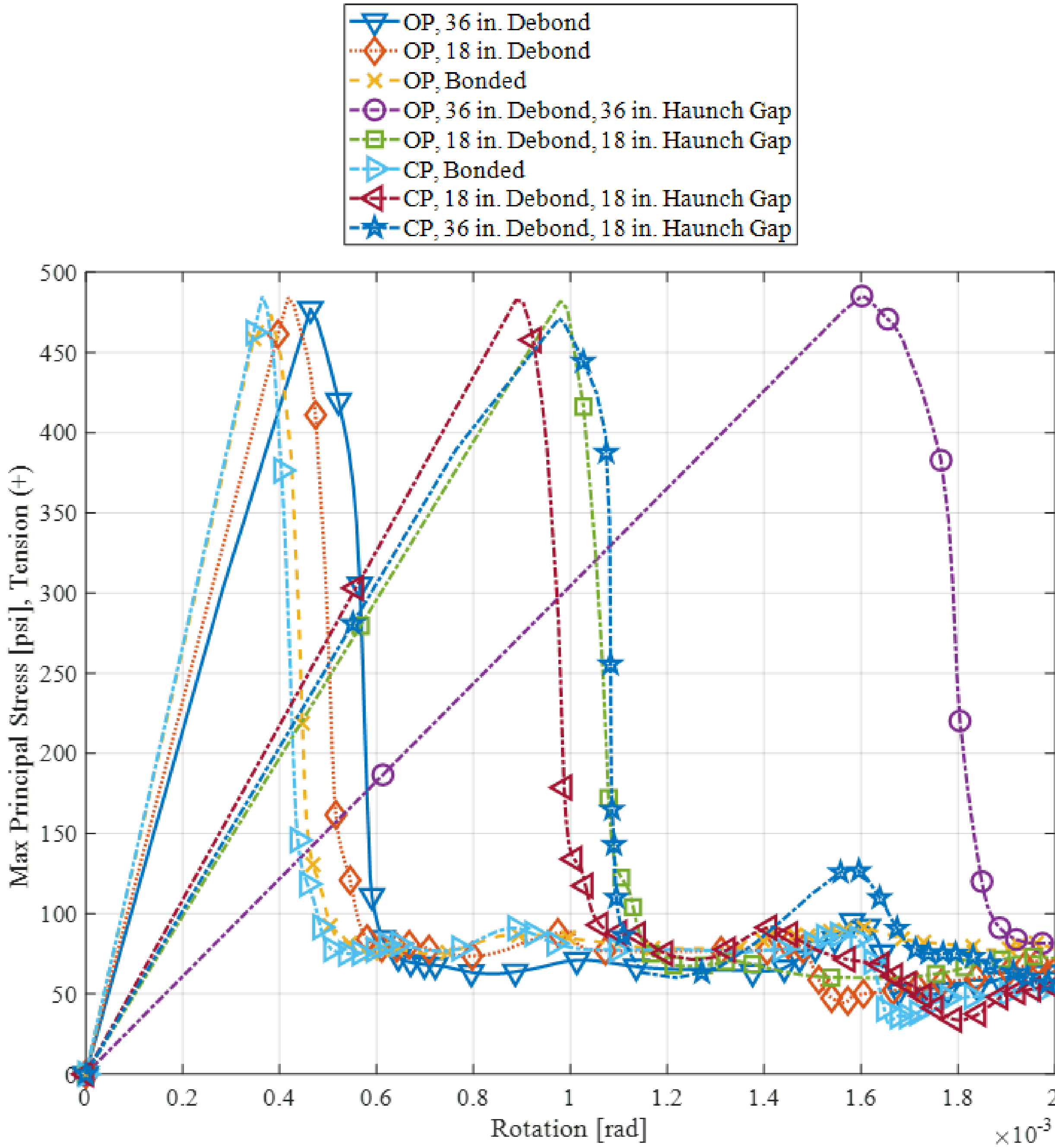

Figure 8.87. Comparison of cracking behavior between offset and continuous panel models, bonded and debonded, with differing haunch gap details.

8.12 VALIDATION AND EXPERIMENTAL TEST PROGRAM SUPPORT

Finite element models were used to inform the experimental test program by predicting and comparing results of many specimens. Analytical results were specifically compared to displacements and stresses while predicting cracking patterns. The results of these models were used to inform subsequent laboratory tests and prioritize the fabrication of specimens that demand additional study. An overview of the experimental test program, including the observed crack patterns, is presented in Chapter 9. Chapter 10 provides a discussion of data calculated from the measured experimental data, including the calculation of girder end rotations. Here, a comparison of the experimental and finite element models is presented to provide validation of the models. Section 8.12.1 presents a validation of the end rotations of the girders, which is the primary design value for assessing design demands in a link slab. Section 8.12.2 compares vertical displacements to provide validation of the overall deformations of the girders and deck. Section 8.12.3 compares the measured and modeled strains. Section 8.12.4 and 8.12.5 provide a comparison of crack patterns in the tests and models. Finally, Section 8.12.6 presents the SAP2000 model used to verify elements of the laboratory test program and ABAQUS results.

8.12.1 Girder End Rotation Validation

To validate the finite element models (FEMs) produced in ABAQUS, the researchers compared deformation and cracking behavior in the simulations with experimental test results. Since link slab loading is determined by girder end rotation, deformation of FEMs and test results were compared at equal girder end rotations.

While the initial input of both experimental testing and FEMs is span loading on the girders, girder end rotation is a more suitable basis for comparing test behavior to model behavior in the PBJ region. This is because the difference in girder stiffness between the test specimens and models causes differing load-deformation behavior. The stiffness of the deck—and the rotation of the girder ends that drive the deformation behavior of the link slab—are of primary importance. Girder stiffness and overall girder deformation are relatively unimportant when comparing PBJ behavior. As such, simplified models were used for the girders with elastic material properties to promote computational efficiency. Figure 8.88 shows an example of the difference in girder stiffness between test FP1 and the corresponding FEM, where the girders in the experimental test were less stiff. For each test program, the FEM was continued to higher levels of girder end rotation than in the test.

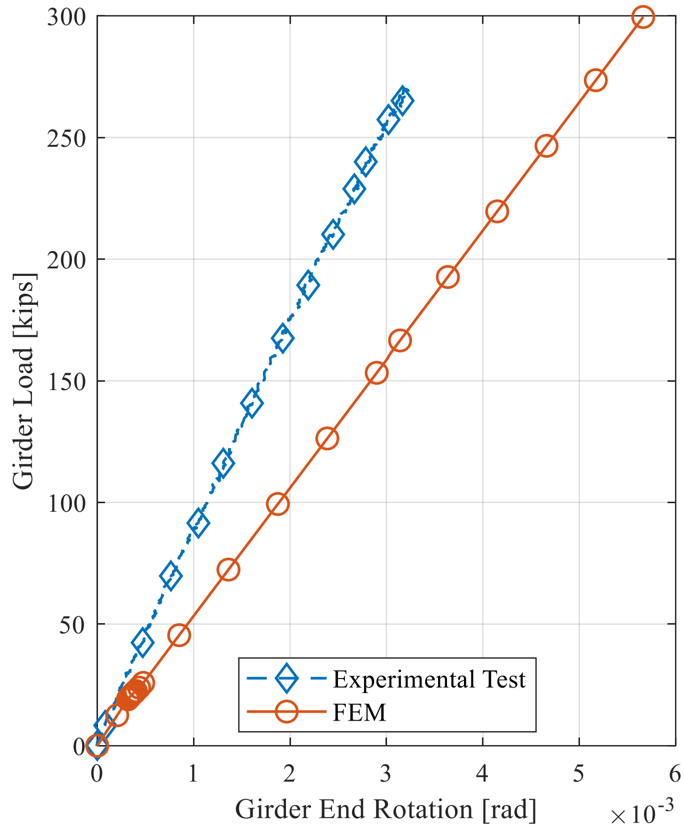

Figure 8.88. FP1 girder end rotation versus girder loading for the experimental test and FEM.

Since girder end rotation is the primary input for link slab deformation, comparing the deformation behavior in the PBJ region at different girder end rotations between the experimental test and FEM results reveals how well an FEM matches an experimental test. LVDTs installed at the girder ends, shown in Figure 8.89, may be used to make this comparison. The continuity provided by the link slab causes the girder ends to rotate about an axis in the link slab. If the stiffness properties and cracking behavior of the slab differ between the FEM and test, the location of this axis of rotation will also differ. Furthermore, differences in stiffness, cracking behavior, or support stiffness may cause differences in the axial deformation of the girder ends. These differences in the deformation characteristics of the link slab region cause different LVDT deformation values for a given rotation.

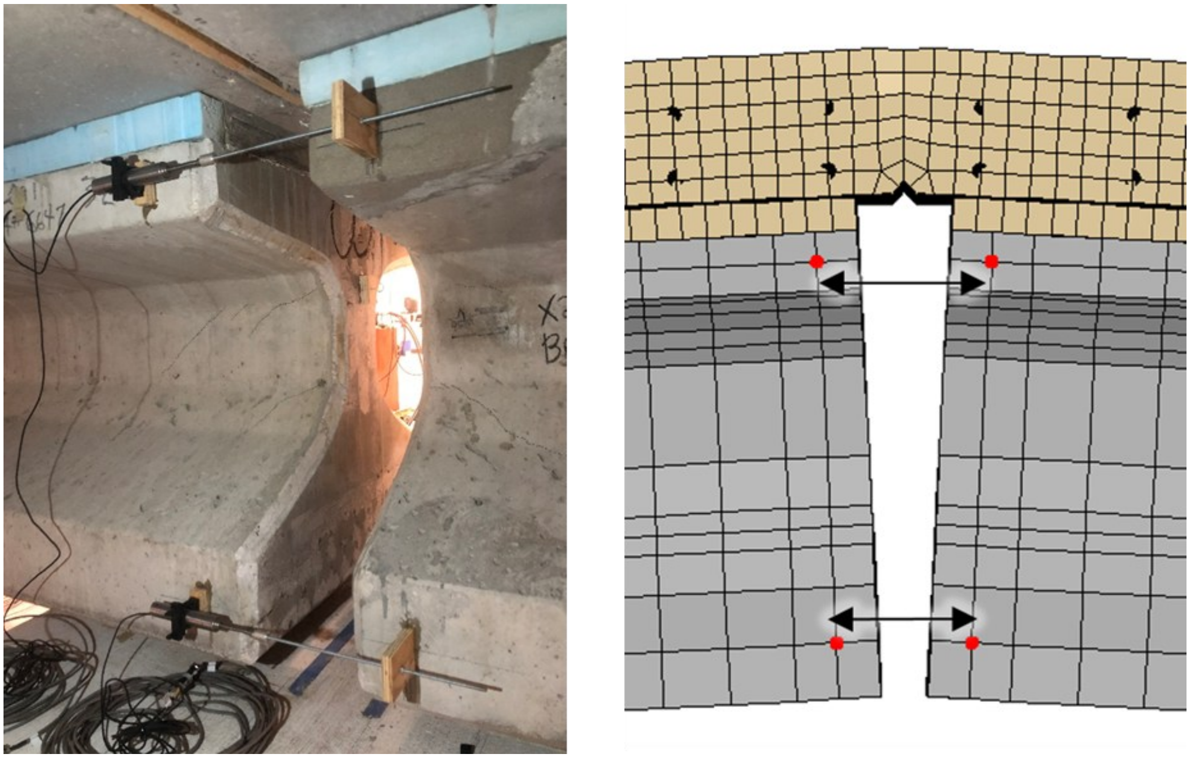

Figure 8.89. LVDTs recording deformation at the girder ends (left) and nodes of matching LVDT connection points on the FEM (right).

To verify that the link slab region is deforming similarly in the experimental test and FEM, LVDT displacements were plotted alongside the corresponding deformations at the same locations on the FEM, as shown in Figure 8.90. The FEMs continued to higher rotations than the experimental test. For tests FP1 (a), OP1 (b), and CP1 (c), there was strong similarity between the LVDT displacement and FEM results. This finding indicates that the link slabs' stiffness and deformation characteristics, before and after cracking, were similar in the experimental tests and computational models.

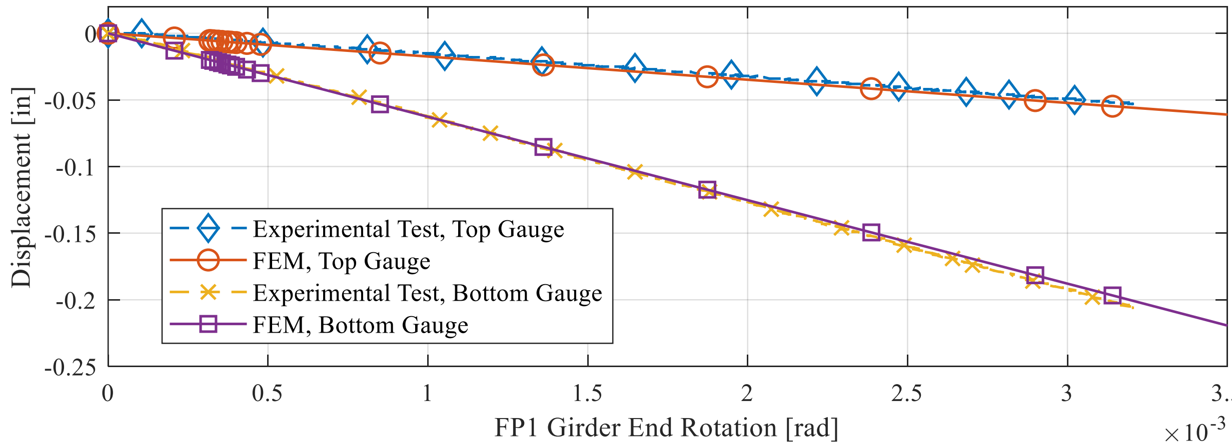

(a)

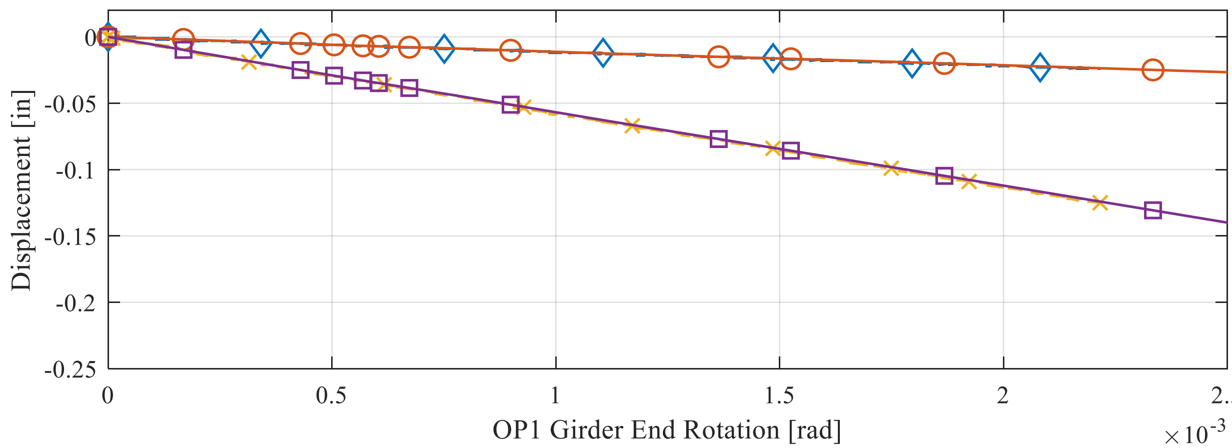

(b)

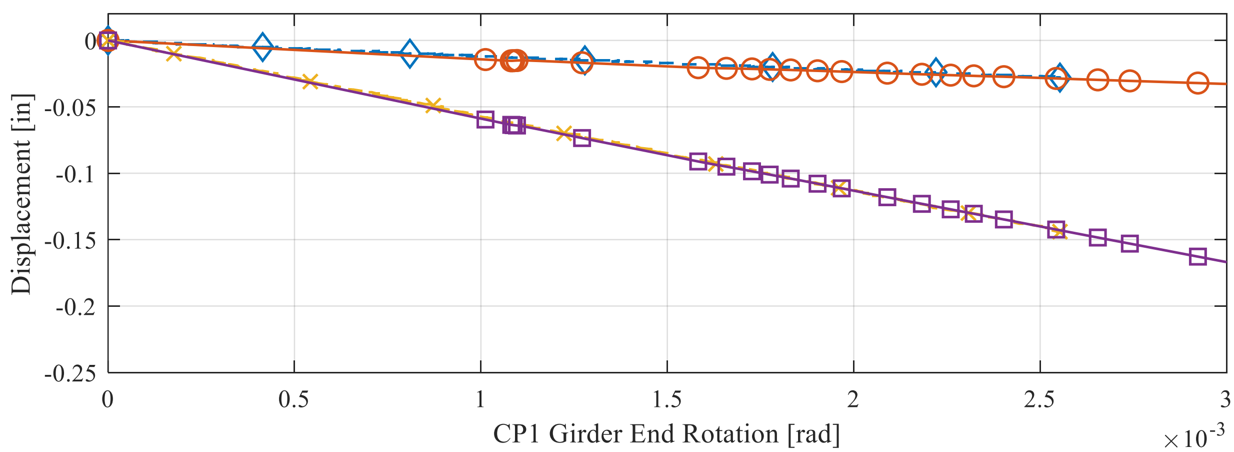

(c)

Figure 8.90. Comparison of LVDT displacement at the girder ends for experimental tests FP1 (a), OP1 (b), and CP1 (c), with corresponding displacements from FEMs.

8.12.2 Vertical Displacement Validation

Comparisons between the vertical deflection of test specimens FP1, OP1, and CP1 and their corresponding FEMs at three separate locations are shown in Figure 8.91. Figure 8.91(a), (d), and (g) show the vertical deflection under the loading point of the girder at the corresponding girder end rotation. Figure 8.91(b), (e), and (h) examine the deflection under the center of the deck at the PBJ. Figure 8.91(c), (f), and (i) show the deflection under the center of the deck, offset 3 ft from the PBJ. Typically, there is either negligible difference in deflection or slightly more vertical deflection in the experimental test than in the FEM. However, Figure 8.91(f) shows more deflection in the FEM than in test OP1. Increased vertical deflection in the tests may be explained by added vertical deformation at the bearing pads. Vertical bearing pad stiffness was neglected in the FEM since horizontal stiffness primarily affects link slab behavior.

8.12.3 Strain Comparisons

Comparisons of strain measurements were also considered, but the local effects of cracking made reasonable assessments difficult. In the FEM, a crack was often localized at a small number of elements. The existence of plastic strain in the element indicated whether or not the element had reached the cracking point. Once plastic strain had been reached, the strain in the element often grew quickly as a distinct crack according to the constitutive information associated with the concrete damaged plasticity model. However, strain gages in the experimental test did not measure strain at a distinct crack location. The gages, which were mounted on longitudinal reinforcement, recorded the strain behavior over a gage length that included both cracked and uncracked concrete. The placement of the gages within the deck also made it difficult to assess whether cracks crossed the strain gages. Thus, while the global deformation of the link slab region may have matched between experimental and computational results, strain measurements appeared differently at specific locations.

Figure 8.92 shows a comparison of strains from embedded strain gages and from cracked elements in the FEM at the same locations: over the longitudinal reinforcement at the PBJ between the girder lines (a), over the girder line (b), and in the overhang (c). While the embedded gages showed a gradual increase in strains over the gage length, the FEM results showed nonlinear cracking behavior indicative of a crack opening at a specific element.

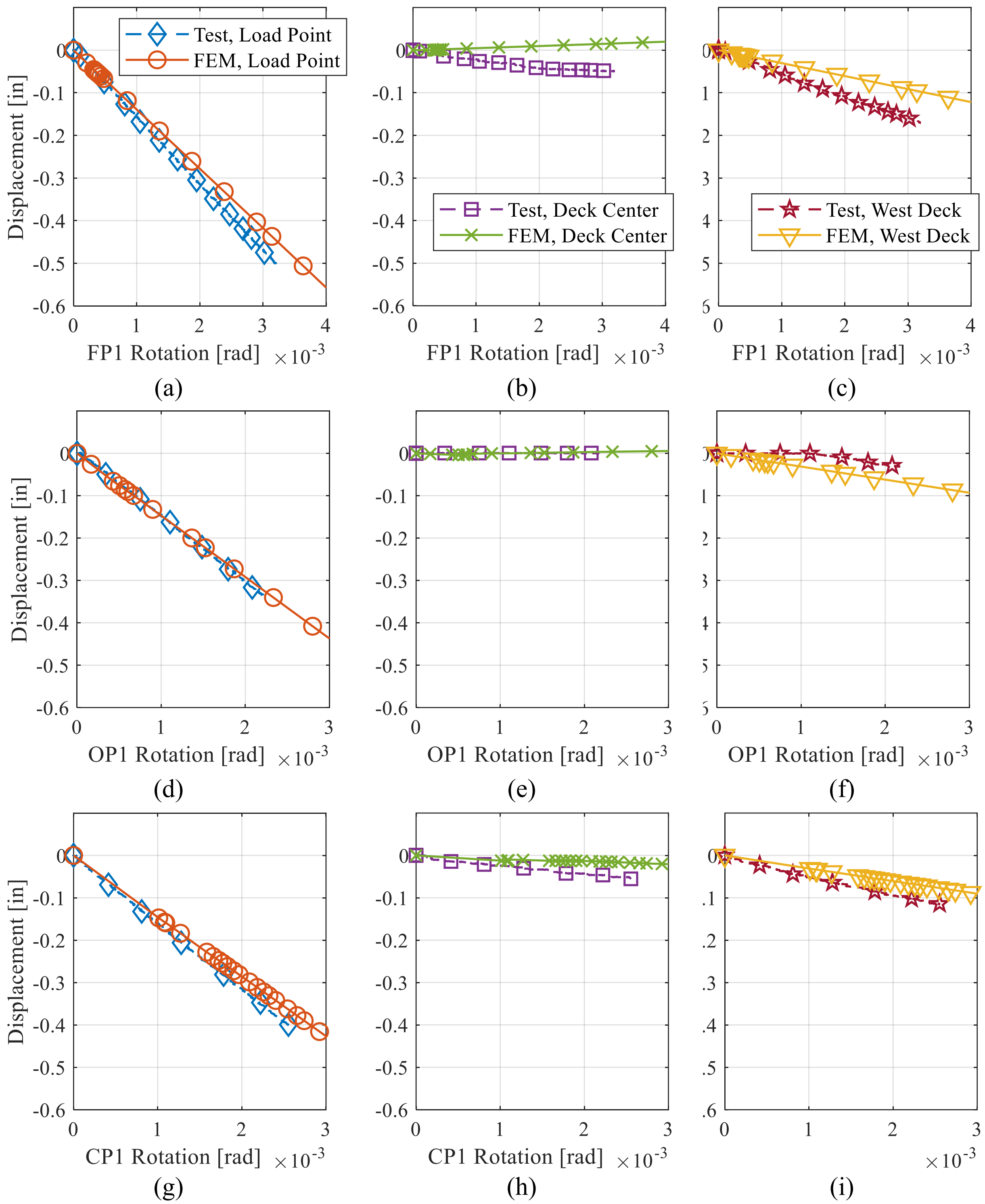

Figure 8.91. Comparison of vertical displacement beneath the loading point of the girder, the deck center beneath the PBJ, and the deck center 3 ft west of the PBJ for tests FP1, OP1, and CP1.

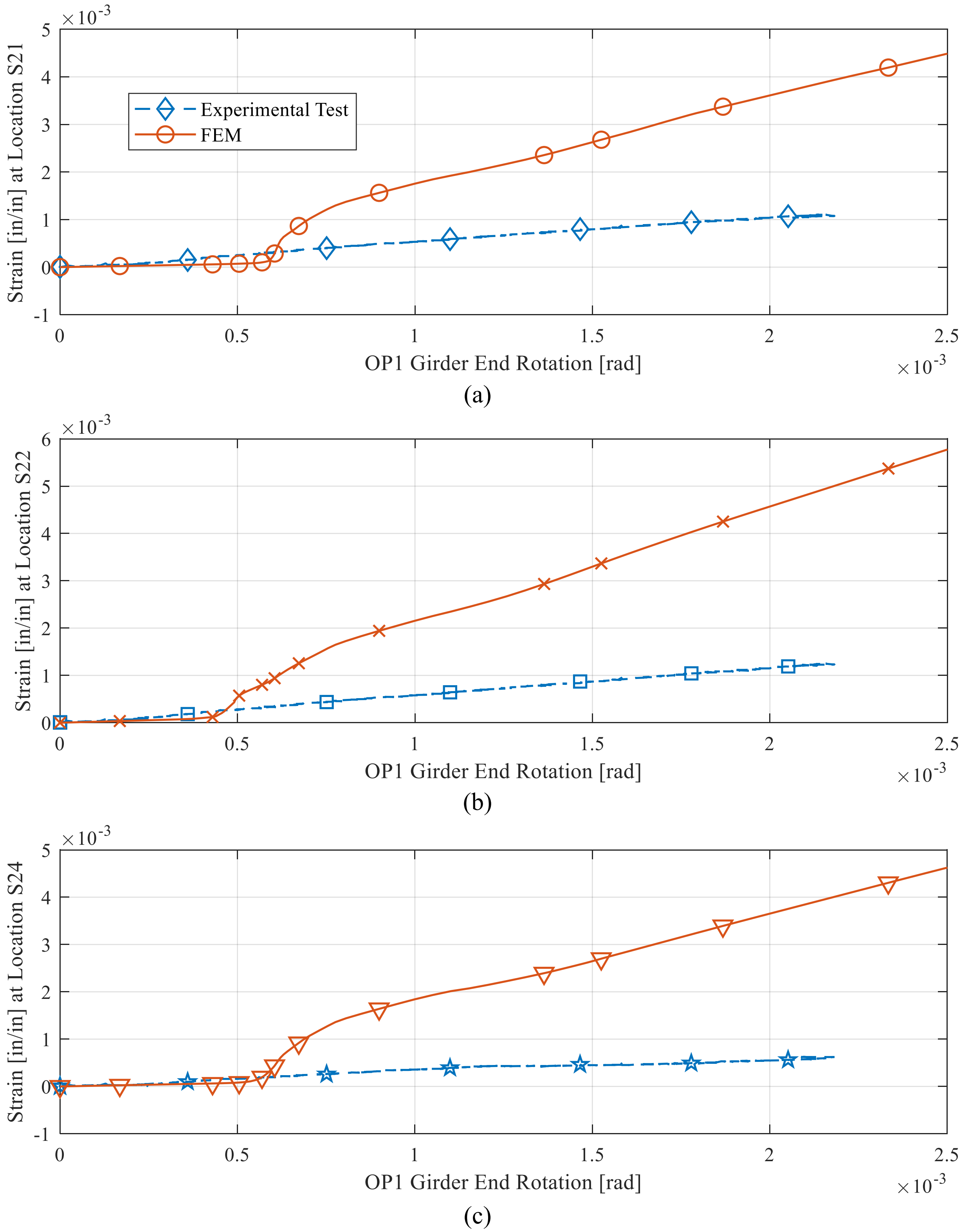

Figure 8.92. Comparison of strains (a) at the center of the deck, (b) over the girder, and (c) in the overhang at the level of the top longitudinal reinforcement.

8.12.4 Crack Pattern Validation

Crack patterns may also be used to confirm that the FEM is accurately capturing test behavior. Cracking in the top of the deck for model FP1, presented in Figure 8.93, showed a crack above the timber board at the center of the PBJ reaching the full depth of the reduced CIP section above the board. The crack pattern was similar between the test and FEM, with the primary difference being a branched cracking pattern in the overhang of the experimental test deck.

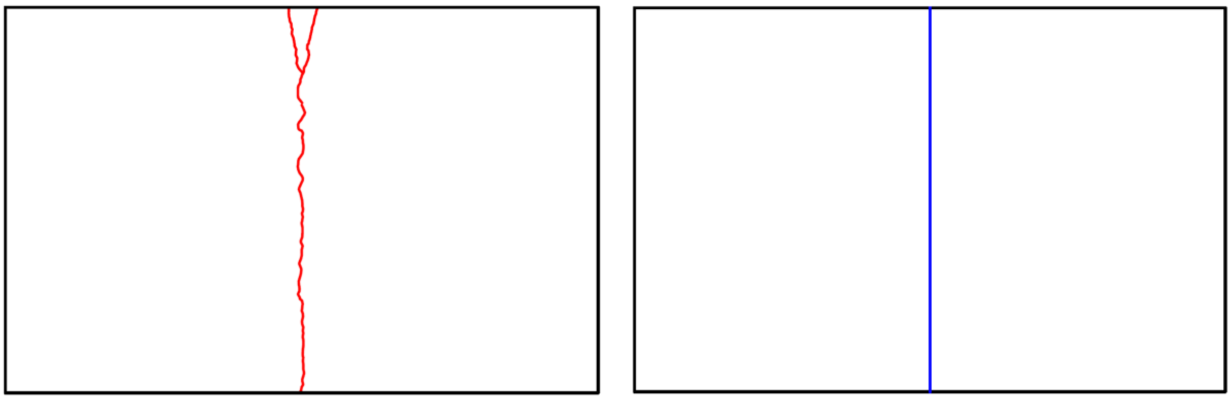

(a) (b)

Figure 8.93. Crack patterns of model FP1 for (a) the experimental test and (b) the FEM.

Similarly, for test OP1, a main crack ran over the center of the PBJ, as shown in Figure 8.94. Branched cracks formed in the overhang for both the experimental testing and FEM. Cracks in the FEM did not reach the full depth of the deck, while the overhangs in the experimental test showed a full-depth main crack and branched cracks.

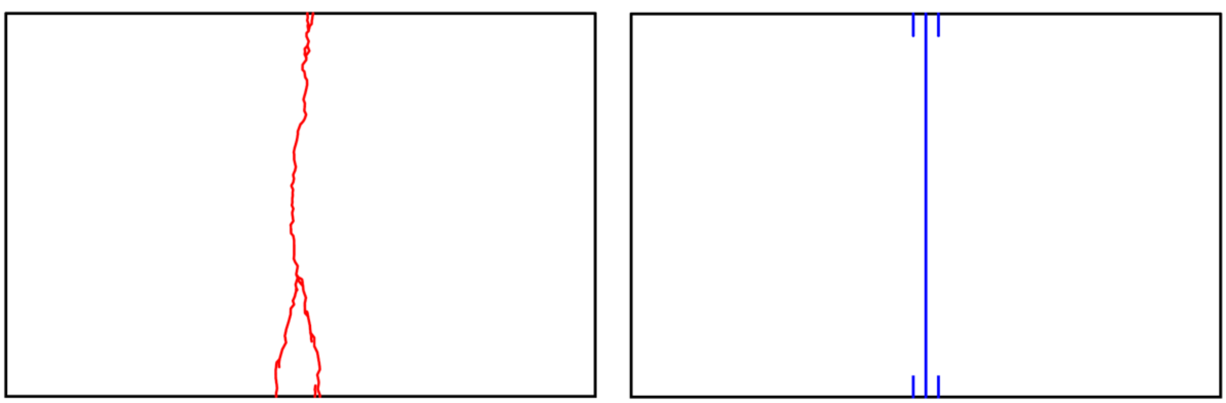

(a) (b)

Figure 8.94. Crack patterns of model OP1 for (a) the experimental test and (b) the FEM.

Comparison of cracking patterns for OP2 in Figure 8.95 showed similar secondary and branched cracking patterns. The addition of top longitudinal reinforcement in the northern side of the deck created a more dispersed crack pattern in the north deck in both the test and the FEM. The crack depth in overhang for OP2 was consistent between the experimental test and the FEM. Cracks did not reach full depth, and the center crack reached the deepest, while subsequent offset cracks were less deep.

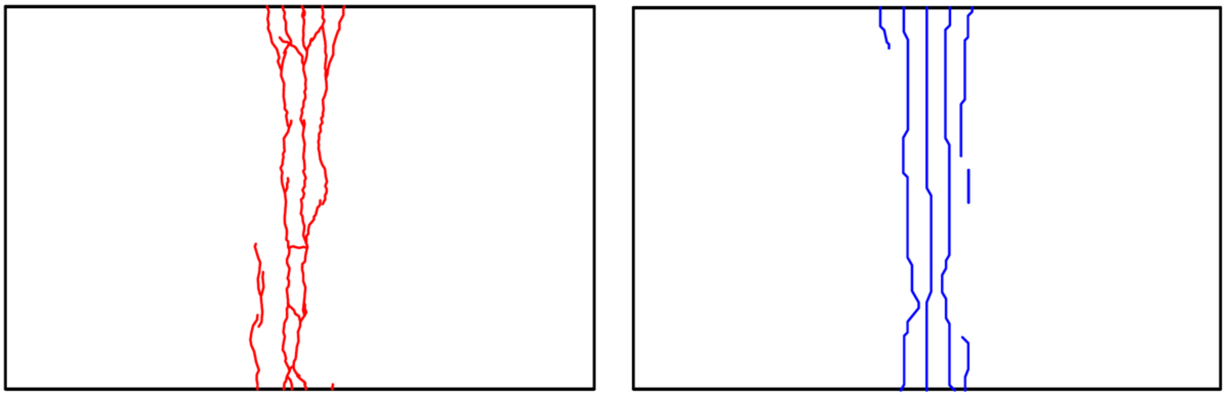

(a) (b)

Figure 8.95. Crack patterns of model OP2 for (a) the experimental test and (b) the FEM.

For test CP1, comparison of cracking patterns in Figure 8.96 showed a much more distributed pattern with secondary and tertiary cracks, as well as branches connecting these horizontal cracks. While cracks in the overhang did not reach full depth in the FEM, some full-depth cracks were visible in the experimental test. Furthermore, while offset tertiary cracks were not as deep as the primary and secondary cracks in the FEM, some tertiary cracks in the experimental test reached full depth.

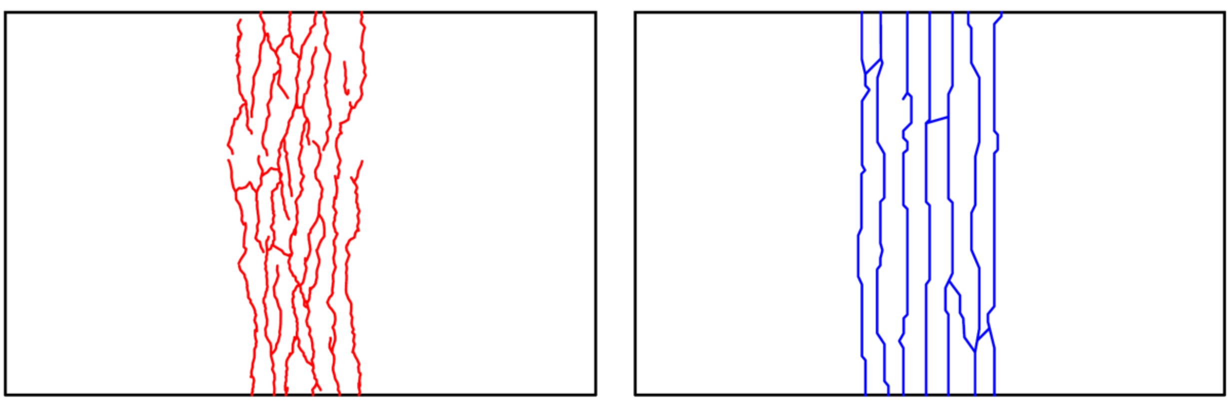

(a) (b)

Figure 8.96. Crack patterns of model CP1 for (a) the experimental test and (b) the FEM.

In general, the crack patterns were consistent between the FEMs and experimental tests. Secondary and tertiary cracks were generally less deep in the FEMs, but experimental results showed that these cracks may be full depth in practice. While FEMs showed a primary central crack in each simulation, tests FP1 and OP1 revealed that branched overhang cracking may be present without a central crack.

8.12.5 Angled Cracking Behavior

Experimental test specimen OP2 was observed to have peculiar cracking behavior over the girder edges at the poor boy joint. When the specimen was demolished after testing, a crack was observed on a cross-section of the deck that had formed below the top surface of the slab but did not extend to the top surface.

Finite element results for this test setup showed that taking a section cut at a slight angle to the top surface revealed similar behavior, as shown in Figure 8.97. Since the angle of cracks vary across the width of a specimen, taking an angled cross-section will intersect cracks beneath the surface while the concrete directly above is not visibly cracked.

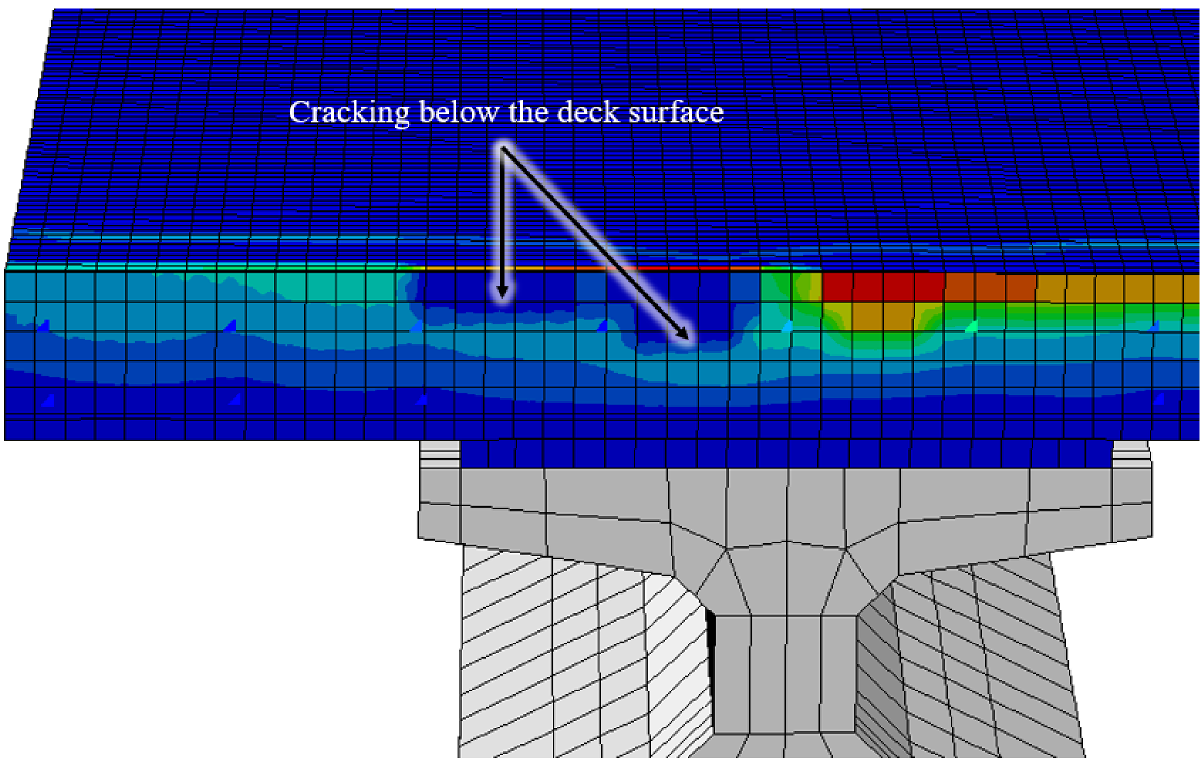

Figure 8.97. Angled section cut of the deck revealing cracking behavior below the deck surface similar to the behavior observed in laboratory testing.

8.12.6 SAP2000 Model

Simplified SAP2000 girder line models, such as the one shown in Figure 8.98, were used to verify elements of the laboratory test program and ABAQUS results. These models were limited to using concrete material properties in the elastic region (see Table 8.4) and therefore provided upper bounds for girder end deformation and slab rotation. SAP2000 models were not used to verify deck deformations and stresses from ABAQUS at high loads since material nonlinearity would lead to dissimilar results. Both the deck and girder were modeled with beam elements. Continuity between the girder and slab was provided by rigid links.

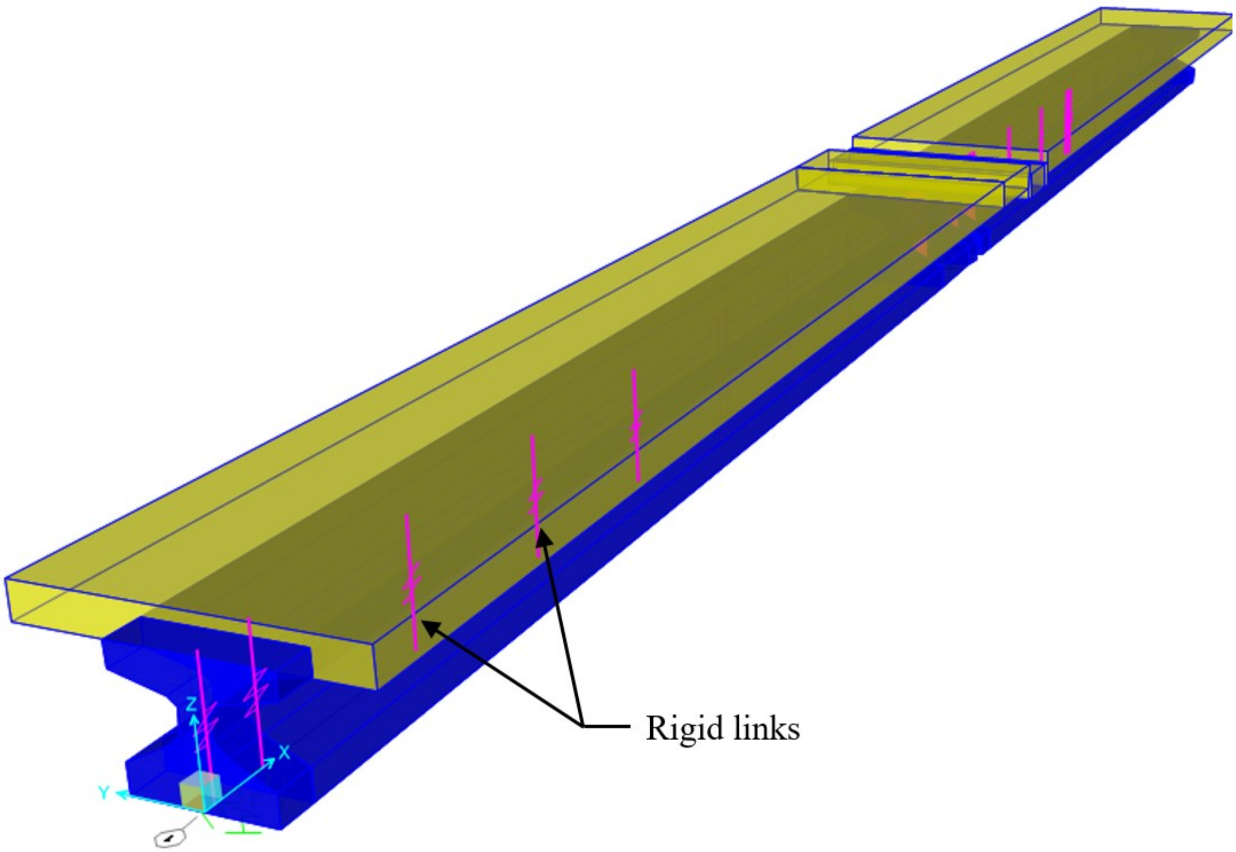

(a) 3D view

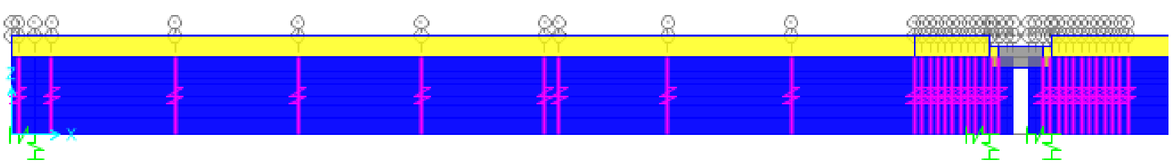

(b) Elevation, one girder and PBJ shown

Figure 8.98. Simplified SAP2000 model using a single girder line with offset beam elements connected with rigid links.

Table 8.4. SAP2000 model material properties.

Property	Value
Deck f'_c	4000 psi
Girder f'_c	8250 psi
Support stiffness, longitudinal	4.5 kip/in
Support stiffness, transverse	4.5 kip/in
Support stiffness, vertical	1270 kip/in
Deck uncracked stiffness (per ft width)	614 in^4
Deck cracked stiffness (per ft width)	51.2 in^4

The purpose of this model was to estimate the location of bending inflection points in the girders and link slab, approximating the effective length of the link slab for comparison with the results of field monitoring. The inflection point in the link slab was estimated to be 5 in. away from the first shear connection, suggesting that the link slab with a physical length of 6 in. between the girder ends and 17 in. between the first rows of shear reinforcement has an effective length of 33 in. This much longer effective length than the physical link slab length coincides with findings from field monitoring, where calculated deformations at the girder ends suggested lengths between slab inflection points that were much longer than the physical length of the link slab between the girder ends.

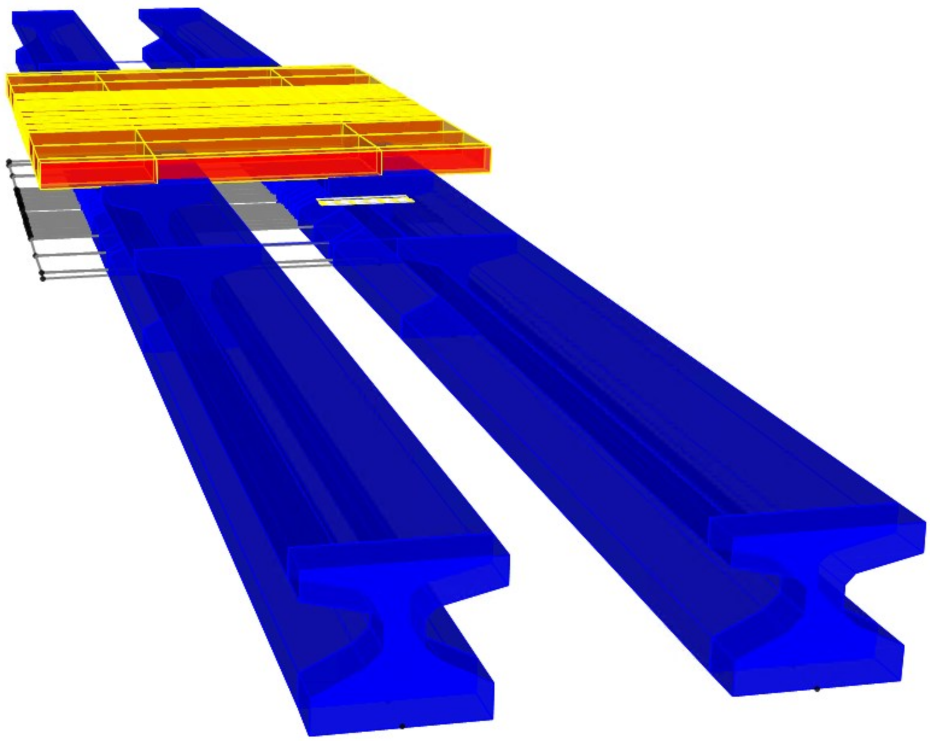

(a) 3D view

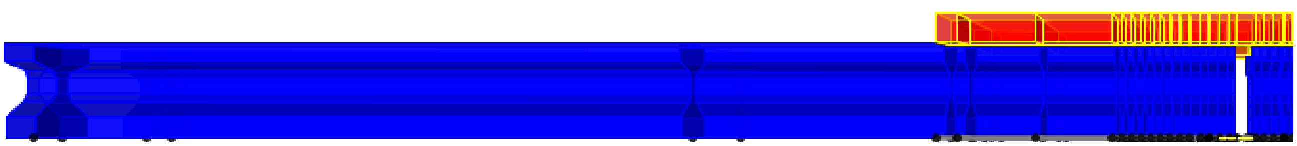

(b) Elevation, one girder and PBJ shown

Figure 8.99. Simplified SAP2000 model of experimental test setup with slab section modeled by offset shell objects at the PBJ region.

A dual-girder model, shown in Figure 8.99, was used to investigate torsional effects from loading girder lines individually or off center. Since the model showed minimal torsional deformations under load, the laboratory test setup was deemed adequate without additional restraint against torsion effects. Figure 8.100 shows the deformed shape of the shell model.

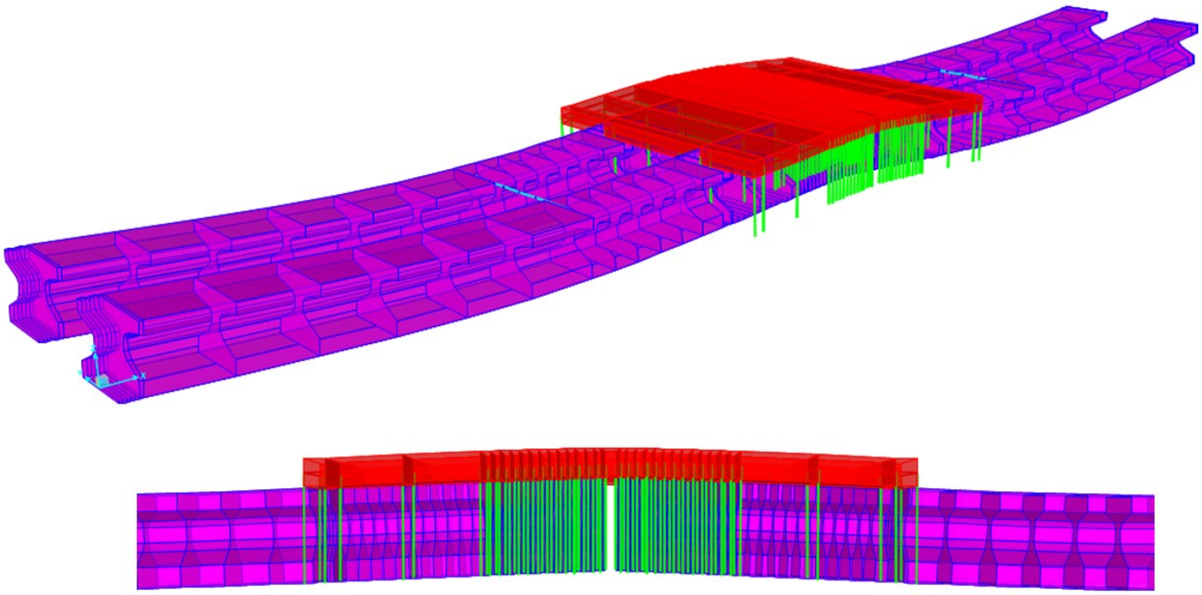

Figure 8.100. Deformed shape of the dual-girder and shell model used to investigate torsional effects.

8.13 SUMMARY

FEA using ABAQUS software was used to evaluate different PBJ designs. Single-girder line models utilizing mirrored boundary conditions were investigated under pressure loads within the girder span. Cracking patterns observed in the field were verified. Hourglass cracking caused by shear lag effects was demonstrated at the PBJ between girder lines and in overhangs.

Flush panel details were investigated with a series of models, showing that the panel end gap causes premature cracking in the link slab. The efficacy of debonding at the girder-slab interface is limited by the presence of the PCP end gap. However, debonding at the interface between the PCP and CIP slab significantly delays cracking. Another way to improve cracking behavior is by elongating the panel end gap.

Offset panel details were tested in a variety of models. Unlike the flush panel detail, debonding was shown to significantly benefit offset panel details. Using debonded details with vertical gaps along the length of the debonded region produced much better results since the vertical deflection of the girder ends no longer interfered with the link slab. Increasing top longitudinal reinforcement and omitting crack-former details improved behavior to a modest degree.

A new continuous panel detail was considered to improve behavior and streamline construction. The design showed beneficial cracking behavior, especially with debonded details, where cracks were smaller and more distributed longitudinally across the deck.

Debonding was shown to delay the onset of cracking. While cast-in-place, offset panel, and continuous panel details have the potential to limit and widely distribute cracking, flush panel designs showed less improvement with debonding due to the weak section caused by the panel gap at the center of the PBJ. Debonding at both the level of the top face of the girder and the top face of PCP sections was shown to be potentially effective. To facilitate debonding of a partial depth of the slab, a portion of the longitudinal reinforcement was raised into the tension zone of the slab. This did not significantly change the cracking behavior of the slab but allowed for the formation of tensile stresses in the longitudinal reinforcement before and after cracking. Stress concentrations were observed at the connection interface of the debonded section. While debonding the slab without the use of a vertical gap along the debonded length showed limited effectiveness under positive girder bending, it was found to be very effective for negative girder bending, such as deformations caused by thermal gradient. Under negative bending, the girder ends did not interfere with the bottom of the slab, and subsequent cracking patterns were more dispersed with smaller crack widths.

Shrinkage effects were considered using uniform temperature change in the deck. Tensile forces in the deck were found to be insignificant for models with functioning elastomeric bearing pad stiffness. However, frozen bearings, in the form of pinned supports, were shown to drastically increase tensile forces in the deck. PBJ health is therefore dependent upon functioning bearing pads. Since resultant tensile forces were not expected in the PBJ under normal bearing conditions, full-depth cracking was not observed for non-skewed cast-in-place, offset panel, and continuous panel designs. However, full-depth cracking was observed for flush panel models due to the panel end gap and in skewed models above the girder lines at panel edges.

Double-girder stub models were utilized to investigate skew effects by directly applying rotational deformations at the ends of the girder stubs. In skewed models, differences in girder end conditions led to different cracking patterns. Using skewed girder ends produced more linear and controlled cracking than using non-skewed ends. However, different girder end conditions did not produce significant differences in the onset of damage or crack widths. Dual-girder skewed models were used to understand deck behavior under asymmetrical loading. Diagonal cracking behavior between girder lines and longitudinal cracking over girder edges were observed, including full-depth cracking. A debonded dual-girder skewed model showed that debonding is also an effective means of delaying and distributing cracking for skewed bridges.

Various details were investigated to support the experimental test program. Torsion effects, reinforcement placement, and angled cracking behavior were all investigated with the use of finite element models. Comparisons between the analytical and laboratory tests for displacements at the girder ends, vertical displacements beneath the deck and girders, and cracking patterns were used to verify the finite element models.

9. EXPERIMENTAL TEST PROGRAM: OVERVIEW AND TEST OBSERVATIONS

A full-scale experimental test program was conducted to (a) investigate the behavior and performance of existing continuous deck details by taking measurements not possible in the field, and (b) investigate the behavior and performance of proposed design alternatives.

This chapter presents an overview of the experimental test program and a summary of the observed results. An analysis of measured data is then presented in Chapter 10. Section 9.1 provides an overview of the test setup and the design. Section 9.2 introduces the test matrix and discusses individual design variations. Section 9.3 provides an overview of construction. Section 9.4 summarizes material properties. Section 0 provides an overview of the instrumentation, while Section 9.6 presents the data collection. Section 9.6 summarizes the loading applied to the specimens. Sections 9.7–9.13 provide construction and loading details for each individual specimen, as well as a summary of the damage. Section 9.13 summarizes the experimental test program and observed results.

9.1 OVERVIEW OF EXPERIMENTAL TEST SETUP

Continuous decks between the ends of simply supported girders are referred to as link slabs and are commonly known in Texas bridges as poor boy joints (PBJs) due to the simplicity of providing the same deck thickness and reinforcement in the link slab as in the rest of the deck. When link slabs are explicitly designed, the design is commonly based on the calculated girder end rotations assuming a simply supported girder. The link slab deformation is determined by assuming compatibility with the girder deformations. The girder end rotations used are from live and/or thermal loads, depending on the specific recommendations of a department of transportation or research group studying link slabs. Live load and negative thermal gradients result in deformation, as shown in Figure 9.1(a), in which the girder has positive bending and the link slab has negative bending (top is in tension). This is referred to in this report as positive bending. Negative bending of the girders and positive bending of the link slab (bottom in tension) is the result of positive thermal gradients and is referred to as negative bending. Axial loads can also be a factor, resulting from the impact of restrained girder ends or thermal elongation/contraction of the girders.

In this study, positive bending was the most critical demand because it results in cracks at the top of the deck, allowing the ingress of moisture that can contribute to deterioration of the deck and potentially the bent caps below. Thus, the experimental test setup was designed to only induce positive bending. While this prevented a fully comprehensive set of loading scenarios, most experimental tests of link slabs used a similar test setup, with exceptions for fatigue testing of link slabs and axial-only loading.

Figure 9.2 shows a schematic overview of the experimental test setup. The specimen was designed as a two-span, two-girder bridge with deck only in the central portion of the specimen. One actuator was used in each span, with a spreader beam transferring load to each individual girder. Figure 9.3 through Figure 9.5 show generic cross-section, plan, and elevation views of the setup to provide dimensions; specific details for each link slab test are provided in Section 9.2, with full drawings of each specimen provided in Appendix B.

The two-span design allowed for inclusion of a continuous deck between the ends and was consistent with prior experimental investigations of link slabs. The use of two girder lines was a unique feature to this project's experimental test program and allowed for (a) investigation of the impact of deck continuity in the transverse direction on the behavior of the link slab, and (b) realistic construction using the partial-depth panels used by TxDOT. The spacing of the girders was 6 ft 4 in., which was slightly smaller than typical bridges but was necessary to accommodate laboratory constraints. The overhang lengths (measured from girder center to edge of deck) were one-half the girder spacing to provide a consistent effective flange width on each side of the girder. This was slightly larger than the 3-ft dimension used in standard TxDOT bridges but was not expected to influence the performance of the link slab.

The girders were 32 ft 6 in. long, with a 31-ft length from center to center of the bearing pads. The location of the bearing relative to the ends of the girders and the gap between the ends of the girders (approximately 6 in.) was consistent with TxDOT standards. The girder span length, girder size, and deck locations were determined to satisfy laboratory constraints (space and loading capacity) while maximizing the girder end rotation (the primary variable used in establishing the link slab demands). The length was maximized for the space available in the lab and considering the locations where the support pedestals representing the bent caps could be tied down. The girders were Tx28 girders to allow for the specimen to use realistic dimensions and detailing for TxDOT I-girders while minimizing the stiffness.

Since the deck provided additional stiffness to the girders and thus decreased the amount of rotation at the end of the girder, the deck was placed over only a portion of the girders. While this provided less longitudinal restraint than if the full deck was present, preliminary modeling at the time of setup design indicated that minimal axial demands would be generated by the proposed loading and the reduced deck length would not be expected to impact the general behavior of the link slab. As an additional benefit, this design allowed for the use of one set of girders for two link slab tests. The length of the deck on both girders was 9.5 ft, which is the length of a standard panel (8 ft) plus the minimum length of cast-in-place concrete in TxDOT offset panel details (1.5 ft). Including the gap between the ends of the girders, the full length of the deck was 19.5 ft.

The location of the actuators was determined to maximize the rotation at the interior end of the girders and fit within the laboratory constraints of tie-down locations. The location of the actuator was 14 ft from the center of the interior bearing pad. The girder designs were based on a maximum applied load of 250 kips at the loading location. This resulted in a larger number of strands and transverse reinforcement than what would typically be found in a Tx28 girder.

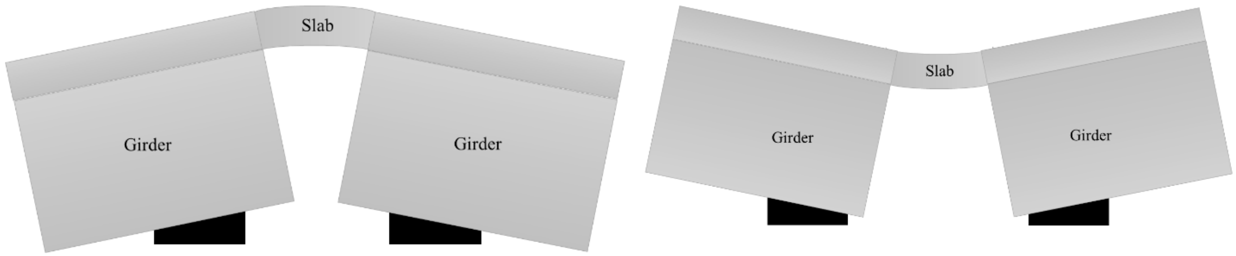

(a) (b)

Figure 9.1. Sign convention used for discussion of continuous deck demands: (a) positive bending and (b) negative bending.

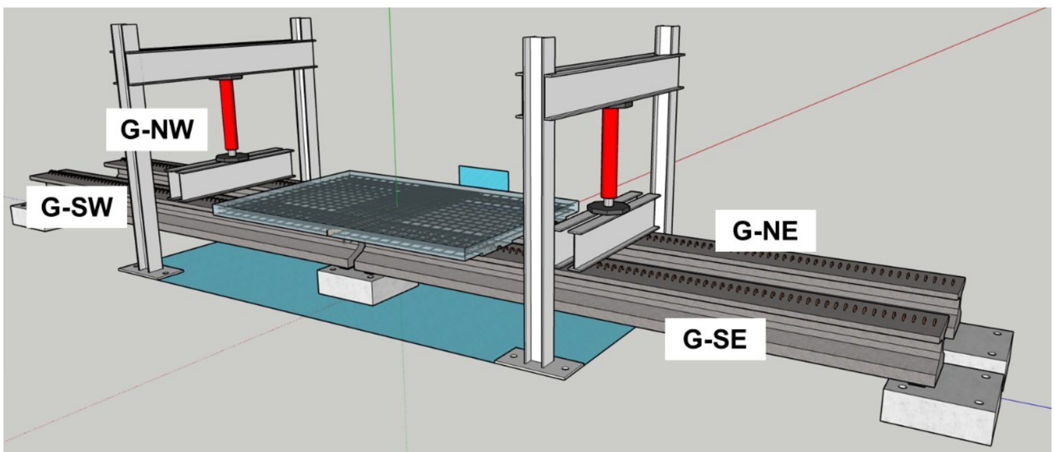

Figure 9.2. Schematic overview of test setup.

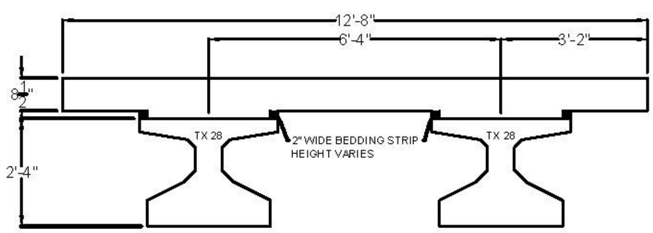

Figure 9.3. Generic cross-section of specimen.

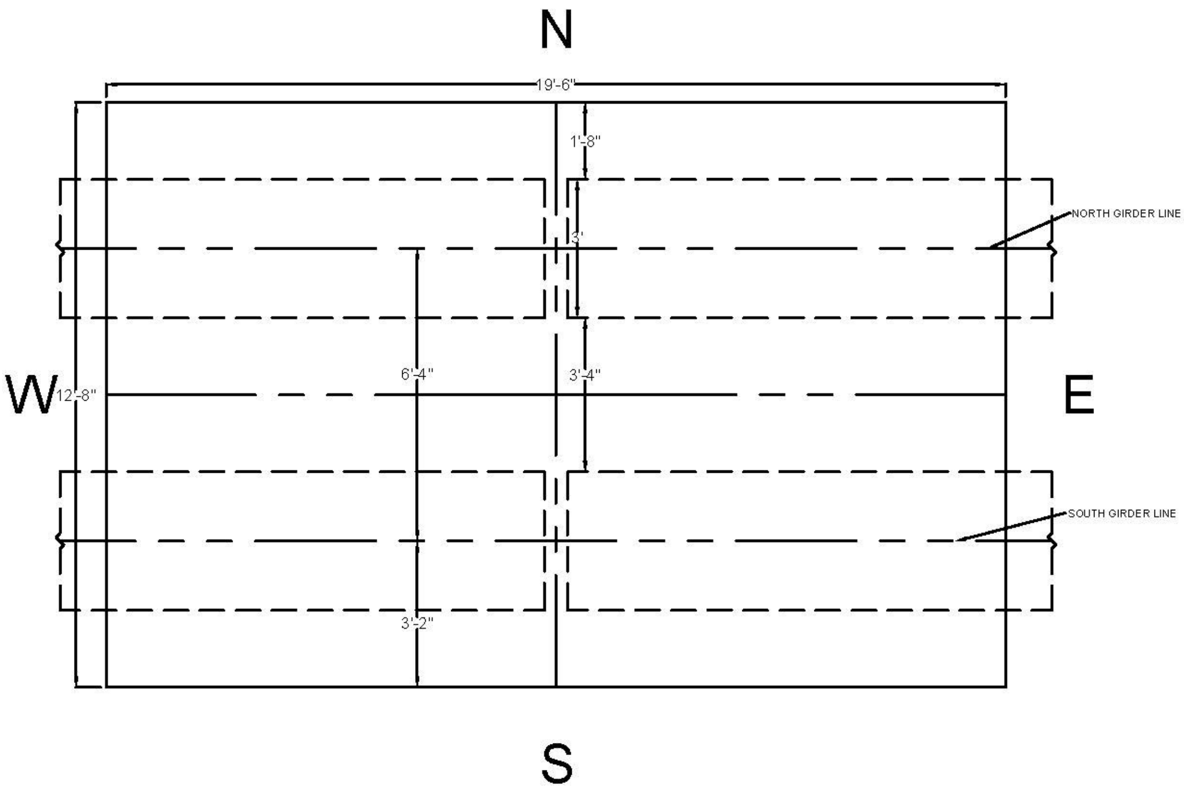

Figure 9.4. Generic plan view of specimens showing geometry.

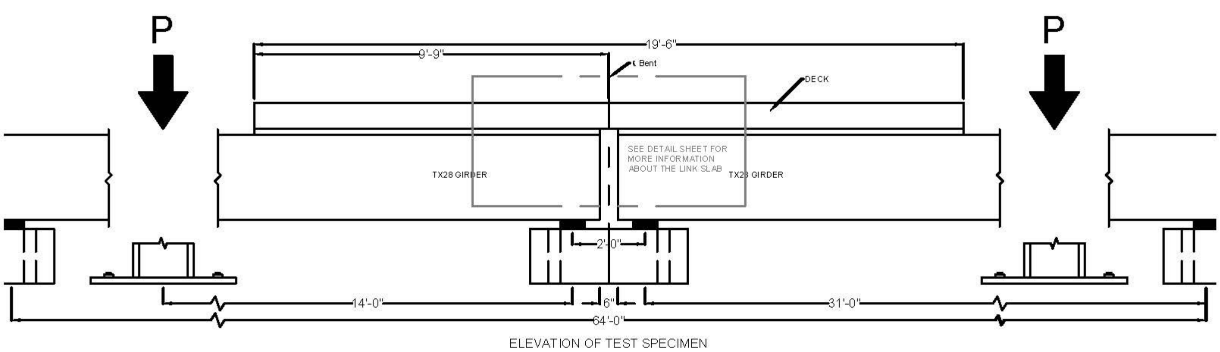

Figure 9.5. Generic elevation of specimens showing geometry.

9.2 OVERVIEW OF SPECIMENS

The details of the specimens are discussed here in relationship to the standard detail used by TxDOT at the time of this project. Figure 9.6(a) shows OP details that have been in place for many years. More recently, the use of the FP detailing shown in Figure 9.6(b) was introduced in response to preferences from contractors to avoid formwork for the CIP region.

Table 9.1 provides a summary of the test matrix, listed in the order the tests were conducted. In developing the designs for the test program, researchers desired first testing the two current details to establish a baseline for the behavior and performance of the current designs. The remaining specimens explored alternative designs. Details of each specimen are provided in the subsections that follow.

In all specimens, the top deck reinforcement was #4 @ 9 in. for both the transverse and longitudinal reinforcement, with a clear cover of 2.5 in. The longitudinal reinforcement was located above the transverse reinforcement, resulting in 2.75 in. from the surface of the deck to the center of the bars. In the full-depth CIP portion of the deck and overhang, the bottom longitudinal reinforcement was also #4 @ 9 in., with a clear cover of 1.25 in. The longitudinal reinforcement was above the transverse reinforcement. In the overhangs of actual bridges, additional transverse reinforcement is provided. Given that the overhangs are not directly loaded, this reinforcement was omitted for simplicity. As a result, overhang cracks that are longitudinal or diagonal may have greater widths than if standard overhang reinforcement had been used. This will be important to consider in assessing the performance of overhangs. For each specimen, variations to the deck reinforcement, if any, are described in the overview of the specimen design.

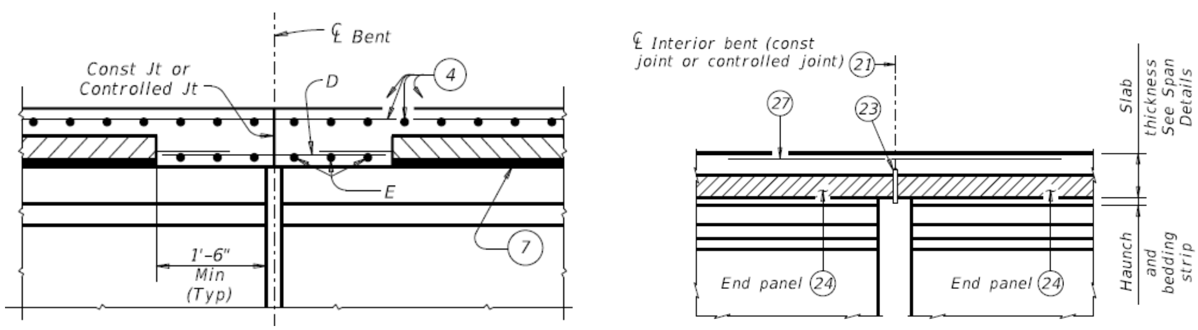

(a) Offset panels (b) Flush panels

Figure 9.6. TxDOT standard drawing options for continuous deck details.

Table 9.1. Test matrix for PBJ link slab tests.

Girder Set/Ends	Specimen Name	Panels	Material	Debonded?	Description
1-A	PBJ-FP1	Flush	Class S	No	TxDOT current flush detail
1-A	PBJ-FP1R	Flush	Class S	Top only	Retrofit w/ partial-depth debonded slab
1-B	PBJ-OP1	Offset	Class S	No	TxDOT current offset detail
1-B	PBJ-OP1R	Offset	HPC	No	Potential retrofit, pending available time
2-A	PBJ-OP2	Offset	Class S	3 ft	Offset panel with deck debonded from girders
2-B	PBJ-CP1	Continuous	Class S	3 ft	Continuous panels, debonded with girder end gap

9.2.1 PBJ-FP1 Overview

The flush panel reference specimen is named PBJ-FP1. Details are shown in Figure 9.7. The panels have a slight separation by a ¾-in. thick board placed vertically between the panels. In TxDOT standards, this is extended to the exterior face of the fascia girder. In other words, the board is present between the girder ends where the deck is full-depth CIP but not in the overhangs, which are full-depth CIP. According to the designs, the board should be redwood. Due to lack of local availability of a redwood board and because the bridge is not being exposed to the elements for decades, a cedar board was used instead.

The two overhangs have different detailing. The north overhang is detailed as a typical overhang, with full-depth CIP concrete. The only difference from a true overhang is the bedding strip on the exterior edge; this was done to provide a similar haunch on both girders. The south overhang is detailed to represent the effective flange width of an interior girder. It was not practical to use panels in the overhang; therefore, the south overhang is full-depth CIP. However, the board between the panels extends from the girder edge to the edge of the deck.

The typical detailing with flush panels uses a zip strip as a crack former on the top center of the continuous deck along the transverse direction of the deck. The objective of the zip strip is to encourage the crack that is expected to form under applied loading to do so cleanly in a controlled location. The zip strip on the top was not included in PBJ-FP1 to allow for (a) investigation of when and where the main crack(s) form without any starter, and (b) clear measurements of crack widths. On the bottom side of the deck, the typical flush panel detail also encourages the formation of the crack at the center of the link slab. In the full-depth CIP portion of the deck (overhangs), this is a ¾ in. notch. Where panels are present, this is in the form of a ¾ in. notch on the top of the board separating the panels. In PBJ-FP1, this bottom detail was included. In the north overhang, this is a ¾ in. notch. Elsewhere, a ¾ in. chamfer is used at the top of the board.

The flush panel detail has, in the continuous slab region, twice as much top longitudinal reinforcement as the typical deck reinforcement. This is accomplished by adding 5 ft long #4 bars halfway between each of the longitudinal deck bars. The length is adapted from the standard TxDOT detail. In the cast-in-place portion of the deck between girders at outer portions of the deck, longitudinal reinforcement was not included in the bottom of the deck over the girders; this is consistent with the standard TxDOT detail.

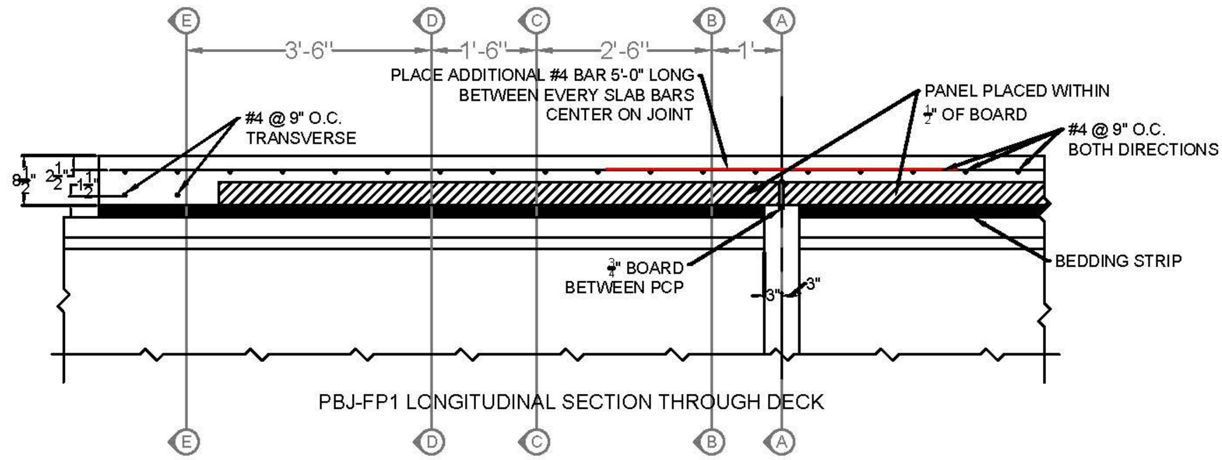

(a)

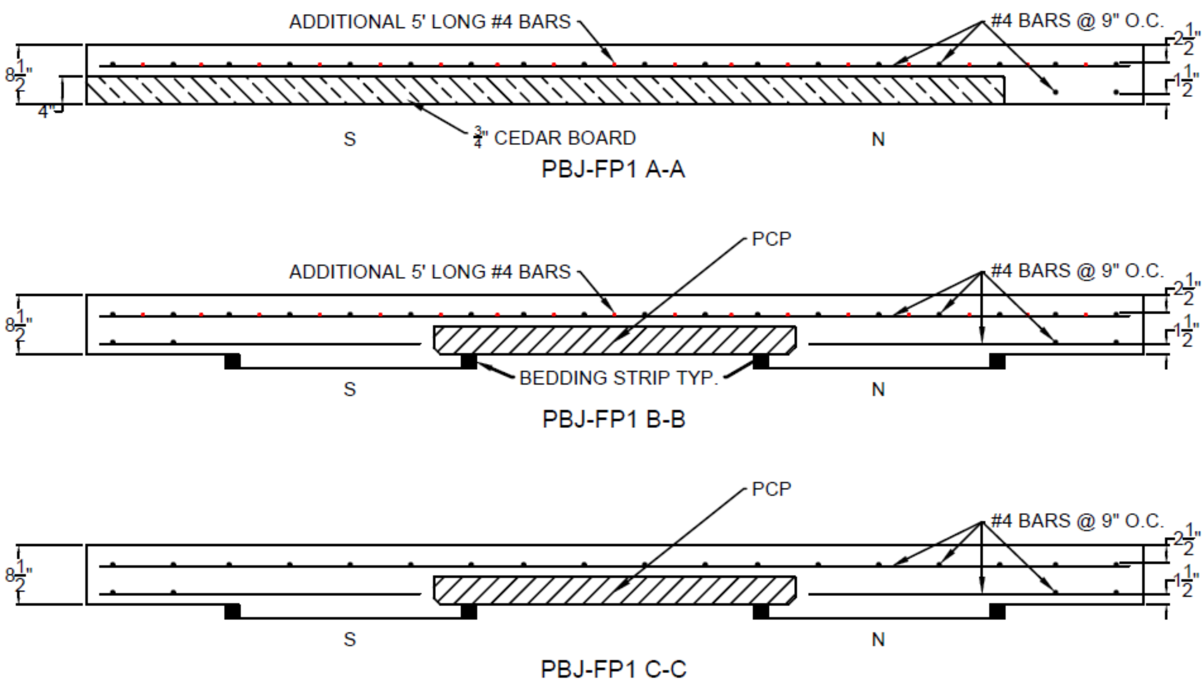

(b)

Figure 9.7. PBJ-FP1 geometry and reinforcement: (a) elevation view and (b) select cross-sections.

9.2.2 PBJ-FP1R Overview

After testing, PBJ-FP1 was retrofitted to specimen PBJ-FP1R; details are shown in Figure 9.8. The full depth of the CIP concrete (4.5 in.) is removed from the center 10.5 ft of the deck. The top rebar is replaced, with a 1 ft 9 in. splice with the existing reinforcement. The new concrete is debonded from the existing concrete, with the exception of 1 ft 6 in. at each end. The bonded region is where the splice is located and is referred to as the transition zone. The objective of this retrofit is to explore the impact of a more flexible link slab.

Special consideration must be given to the reinforcement for the retrofit, since top portion of the non-composite slab will be only 4.5 in. thick, leaving the rebar very near the compression face. This introduces the potential for excessive crack width. Thus, two different reinforcement designs were used. In the south half of the deck, the reinforcement was the same as PBJ-FP1. In the north half of the deck, the supplemental #4 bars in PBJ-FP1 were raised closer to the surface. The original intent was to provide 1.5 in. clear cover for this upper layer of reinforcement; however, supply chain challenges meant that the reinforcement chair with the proper height was not available prior to casting the concrete. Instead, a slightly shorter chair was used, providing 1.75 in. cover. While the cover provided is not sufficient for ordinary reinforcing steel, it would be appropriate if FRP reinforcing bars or alternative steel reinforcement, such as stainless steel, were used. Although these are more expensive options, the limited use of these materials in a link slab, particularly for the retrofit of an older, thinner deck, may be a worthwhile application if demonstrated to improve performance. The presence of additional reinforcement near the surface provides better crack control, with the trade-off of a greater flexural stiffness, and thus the potential to attract greater demands. This trade-off can be investigated analytically but measured response can offer additional insight. Thus, it was deemed worthwhile to explore both options in the FP1R retrofit.

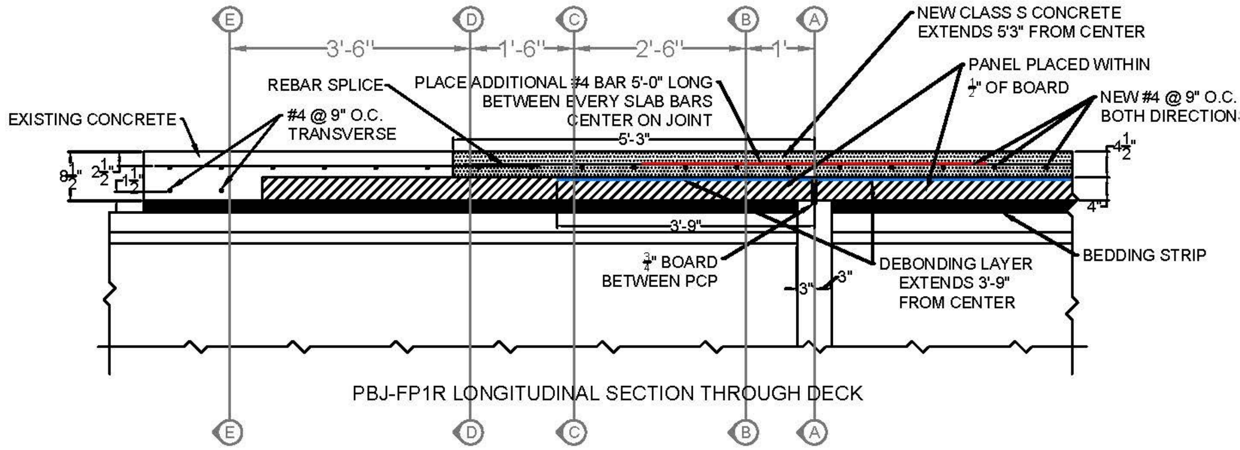

(a)

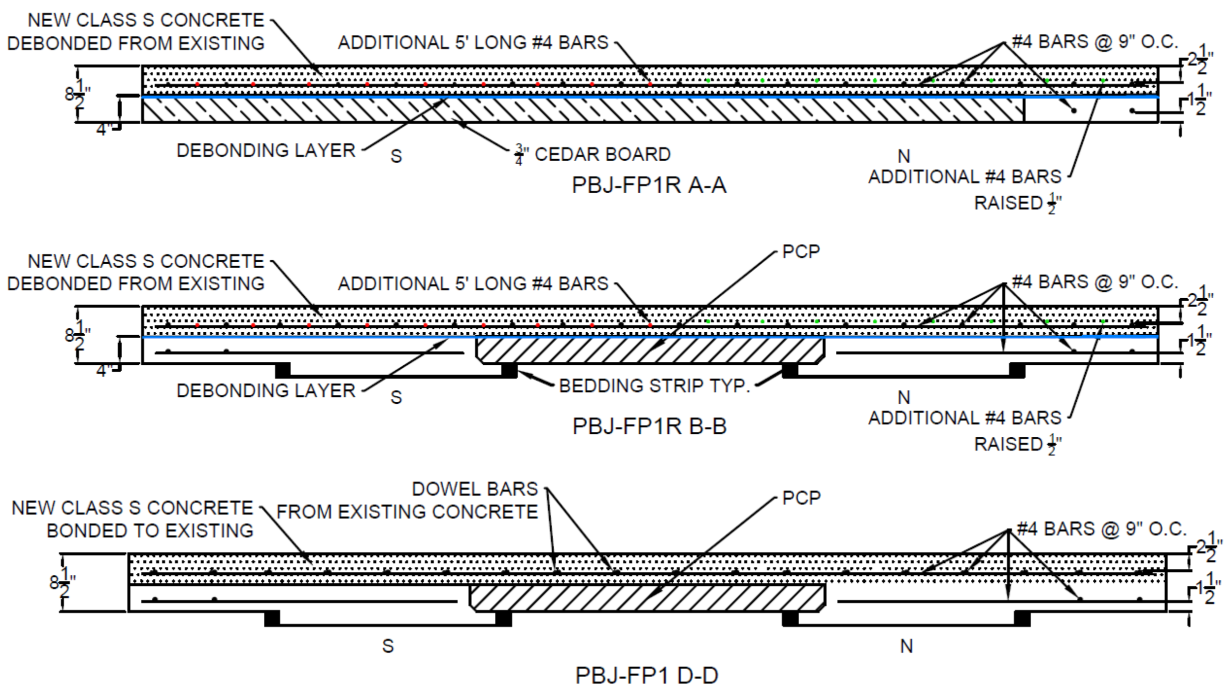

(b)

Figure 9.8. PBJ-FP1R geometry and reinforcement: (a) elevation view and (b) select cross-sections.

9.2.3 PBJ-OP1 Overview

The offset panel reference specimen is named PBJ-OP1; details are shown in Figure 9.9. The panels are set 1 ft 6 in. from the end of the girder, with full-depth cast-in-place concrete in the deck between the ends of the panel. At the bottom of the slab, a preformed notch is located at the center of the continuous deck. The result is that the two overhangs are the same, unlike on FP1 and FP1R. As with prior tests, the bedding strip on the exterior of the girder is the only difference from the overhang detailing in standard TxDOT bridges.

The top reinforcement is the same as the longitudinal deck reinforcement, #4 @ 9 in. The same reinforcement is specified in the bottom of the CIP region. Over the south girder line, there is no longitudinal reinforcement, consistent with the TxDOT standard detail in place at the time of this research. Over the north girder line, bottom longitudinal reinforcement was included to consider design recommendation for inclusion of reinforcement for the purpose of positive bending in the link slab. A plane of weakness at the panel edges are avoided by providing #3 dowel bars extending from the panels, spaced at 6 in. Due to miscommunication with the fabricator, these dowels were not provided. Dowel bars were post-installed at 9 in. on center. While this is slightly different from the standard detail, it provides continuity with the bottom reinforcement in the CIP region. The post-installed dowels were confirmed to provide adequate capacity for demands expected during testing. On the north end of the panel, a dowel bar was included over the edge of the girder; this was not done on the south side.

The typical offset panel detail specifies a zip strip as a crack former on the top center of the continuous deck and a ¾-in. chamfer on the bottom. Similar to the PBJ-FP1 test, PBJ-OP1 does not include the zip strip but does include the chamfer on the bottom of the detail.

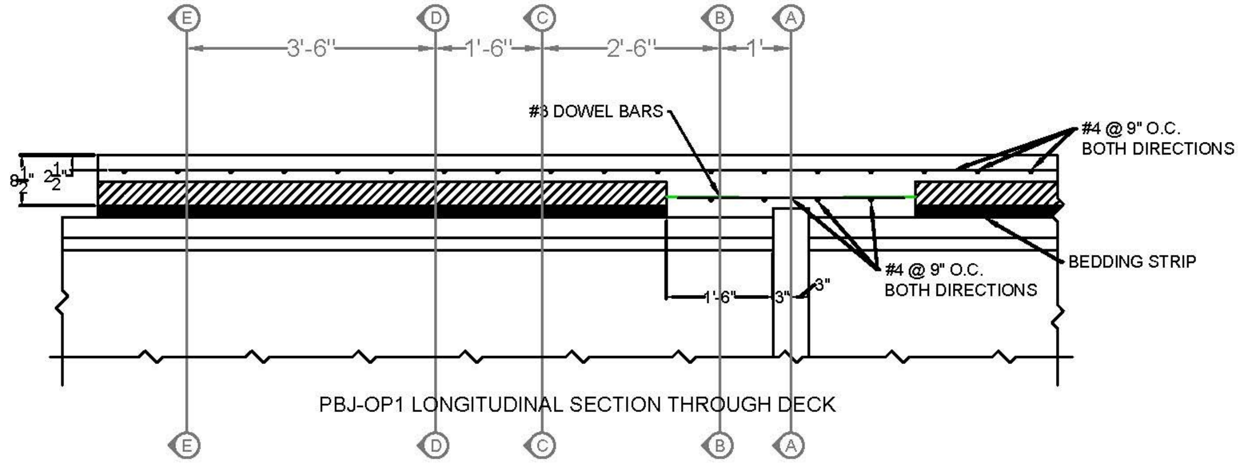

(a)

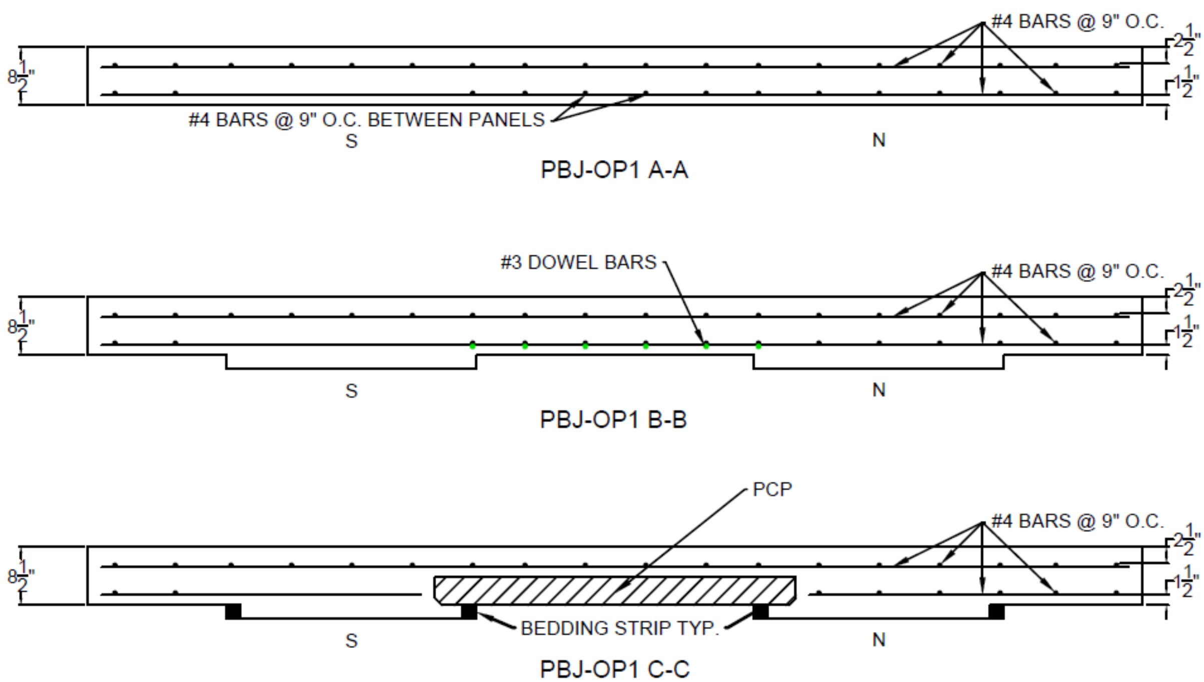

(b)

Figure 9.9. PBJ-OP1 geometry and reinforcement: (a) elevation view and (b) select cross-sections.

9.2.4 PBJ-OP1R Overview

After testing, PBJ-OP1 was retrofitted to specimen PBJ-OP1R. Figure 9.10 shows the elevation view of the retrofit. Figure 9.11 shows the cross-section. The objective of this retrofit was to investigate the behavior of a link slab with HPC. Such a link slab is expected to be stiffer and form multiple small cracks compared to a single large crack. The details of the retrofit were intended to enable a quick investigation of the performance of a link slab using HPC while minimizing the amount of demolition and new material placed. The girder lines were separated by a full-depth cut of the deck slabs. Only the north girder line was retrofitted and tested.

The length of the retrofit region extended 3 in. beyond the edges of the panels. This ensured that damage from prior testing (cracks at edge of panel) was removed and did not influence the retrofit behavior. The depth of the retrofit was sufficient to install new longitudinal reinforcement given that yielding occurred in PBJ-OP1. The depth of the removal was 3.75 in., which provided 0.75 in. below the top reinforcement, a requirement of the TxDOT Concrete Repair Manual.

The existing longitudinal bars were retained except for a 2-in. section in the middle. This provided a splice between the new bar and the existing deck steel. The transverse reinforcement was removed for simplicity of demolition and construction. It was not replaced given the nature of the planned loading. HPC was bonded to the existing concrete. A nonproprietary mix developed for TxDOT Research Project 0-6982 was utilized.

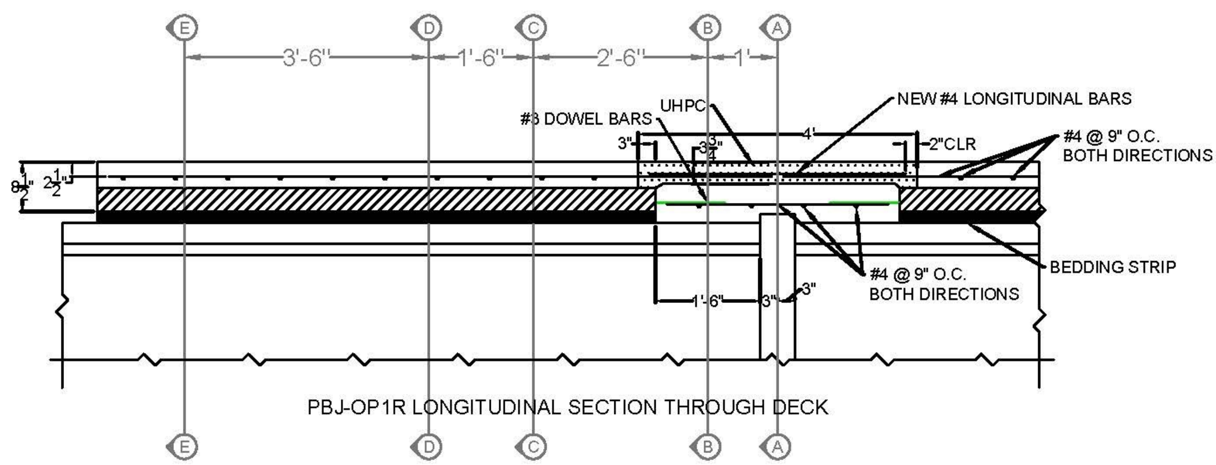

Figure 9.10. PBJ-OP1R elevation view.

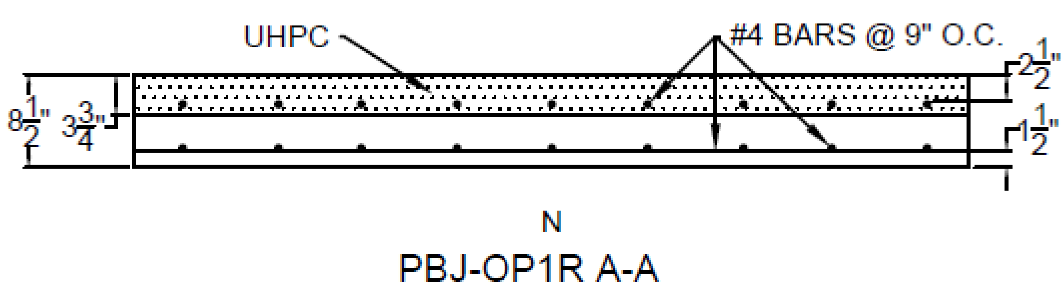

Figure 9.11. PBJ-OP1R cross-section at center of link slab (Section A-A).

9.2.5 PBJ-OP2 Overview

PBJ-OP2 is a proposed design alternative for link slabs with offset panel details. Figure 9.12 shows the elevation view of the design; drawings with full details are available in Appendix B. The objective here was to modify the existing offset panel design to improve the performance by increasing the length over which damage occurs and reduce stress. The design modification included debonding, increased reinforcement, and no chamfer on the deck bottom.

The key feature of the design was debonding of the deck from the girder. The debonded length was 3 ft from the end of the girder. This is a lower bound that would be used for TxDOT bridges since it is approximately d_v from the center of the bearing pad. The debonding was accomplished by cutting and grinding the R-bars in the debonded region. Roofing paper was used to prevent the deck concrete from bonding with the top of the girders.

The reinforcement in PBJ-OP2 was different in the north and south halves of the deck. Both contained #4 @ 9 in. in both the transverse and longitudinal directions. The difference in the reinforcement was that in the north half, additional longitudinal #4 bars were added between the deck longitudinal reinforcement. This was notionally the same as the reinforcement in the flush panel details and was selected due to the smaller crack widths in PBJ-FP1 compared to PBJ-OP1. The PBJ-OP2 north reinforcement was different from PBJ-FP1 in that the bars extended 10 ft on each side of the center to ensure adequate development in the DLS. Over both girders, no bottom longitudinal reinforcement was provided in accordance with the existing standard.

Finite element modeling of debonded designs indicated that the chamfer found in the existing offset panel detail contributed to concentration of damage/stresses at the center of the slab. To ensure the best performance of the proposed design, this chamfer was not included in the construction.

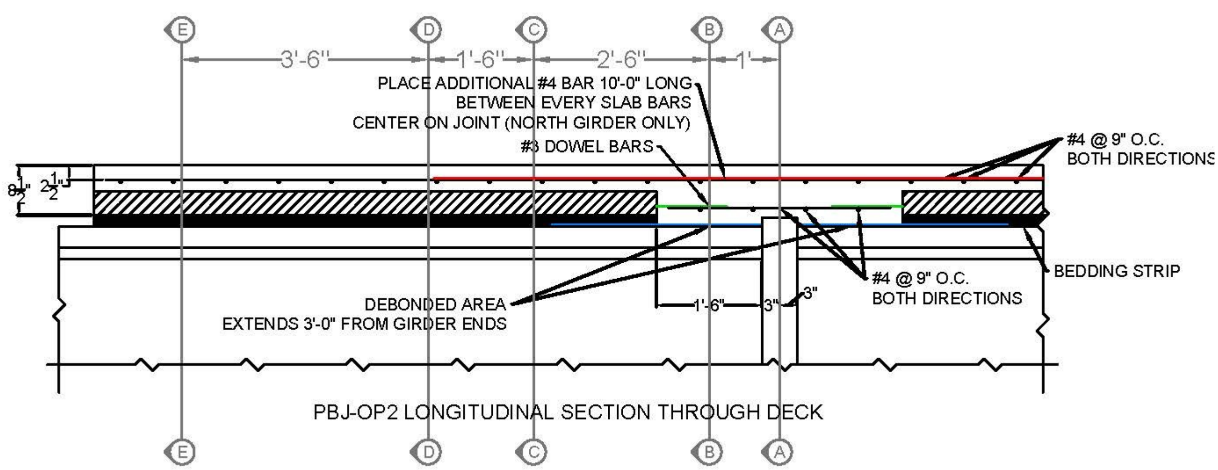

Figure 9.12. PBJ-OP2 elevation view.

9.2.6 PBJ-CP1 Overview

PBJ-CP1 is a proposed design alternative for link slabs with the precast panel continuous over the ends of the girders. This detail is referred to as the continuous panel detail. Figure 9.13 shows the elevation view of the design. The objective here was to eliminate aspects that contribute to the formation of cracks to allow for more distributed cracking. As a part of this, a small gap was included between the top of the girder and the haunch. The design modification included debonding, increased reinforcement, and no chamfer on the deck bottom. Figure 9.14 provides a cross-section at the gap; full drawings of the details can be found in Appendix B.

Like the PBJ-OP2 proposed design, a major distinguishing feature from existing tests was debonding the deck from the top of the girder. The debonding in PBJ-CP1 was the same as that for PBJ-OP2 and was done in the same manner. As with PBJ-OP2, the bottom chamfer was eliminated to support avoiding regions where deformation and therefore damage concentrate.

Two key features of the design differentiated it from the PBJ-OP2 proposed design alternative. The first was the continuous panel. The goal of this was to eliminate weak sections in the link slab that would provide a location for deformation, and therefore damage, to concentrate. A single panel was used in this test, with the panel length of 8 ft extending 4 ft on either side of the center of the link slab. The second was a 0.5-in. gap between the top of the girder and the haunch concrete. The goal was to eliminate the initiation of cracking from the girder end pushing into the deck concrete. Such detailing is used in standard details used by other jurisdictions. Since a physical gap is not practical to construct and provides potential location for water intrusion, the gap was formed with a weak polystyrene. The length of the polystyrene gap was 1.5 ft.

The reinforcement in PBJ-CP1 contained #4 @ 9 in. in both the transverse and longitudinal directions, with additional longitudinal #4 bars added between the deck longitudinal reinforcement. This was notionally the same as the reinforcement in the flush panel details and was selected due to the smaller crack widths in PBJ-FP1 compared to PBJ-OP1. The PBJ-CP1 north reinforcement was different from PBJ-FP1 in that the bars extended 10 ft on each side of the center to ensure adequate development in the DLS. The only difference in reinforcement in the north and south half of PBJ-CP1 was that the north girder line had longitudinal bottom reinforcement (proposed detailing), while the south did not (current TxDOT detailing).

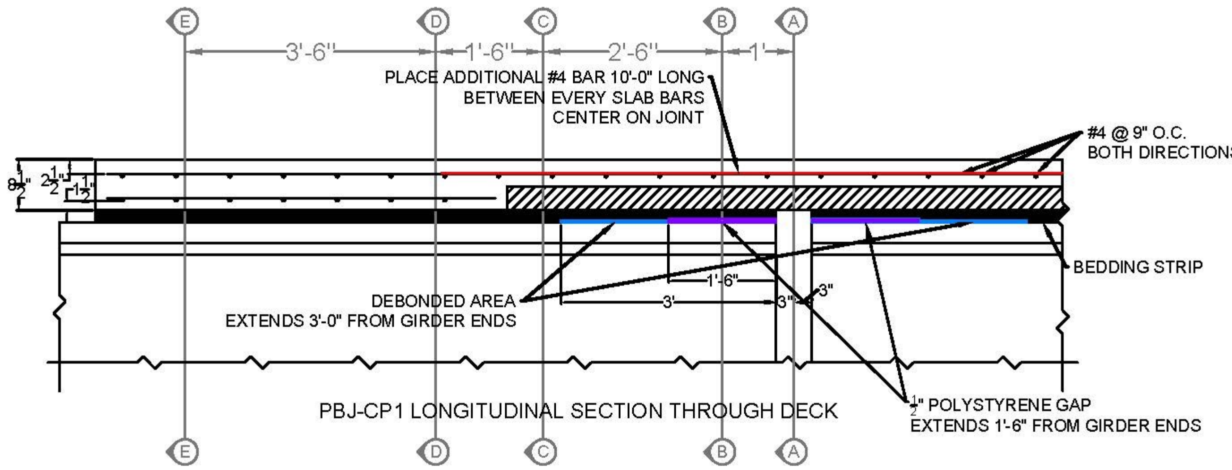

Figure 9.13. PBJ-CP1 details—elevation view.

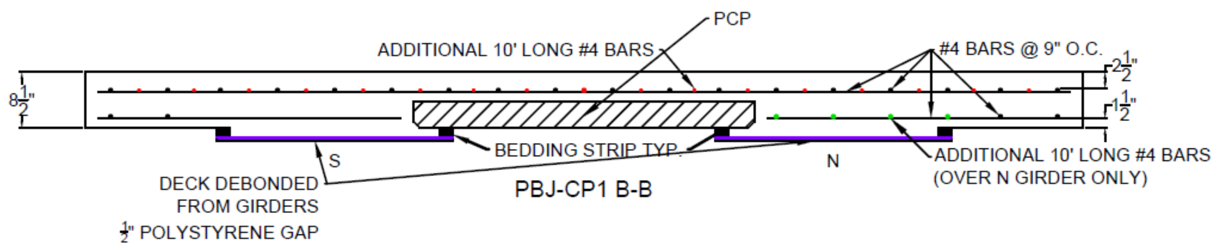

Figure 9.14. PBJ-CP1 details—cross-section (B-B) showing details where gap is present at end of girders.

9.3 CONSTRUCTION

Construction and testing of the link slabs took place at the Texas A&M University Center for Infrastructure Renewal High-Bay Structural and Materials Testing Laboratory. Prestressed girders and panels were fabricated by Bexar Concrete Works in San Antonio, Texas. Bexar Concrete Works provided cylinders for material testing. The following sections provide details on the construction of the bridges in the lab. Sections 9.3.1 and 9.3.2 provide general details for construction of all bridge decks. Sections 9.3.3 through 9.3.8 provide details unique to each design. Section 9.3.9 provides recommendations for best practices of construction for future tests and/or field construction.

9.3.1 Girder and Panel Placement

Girders were placed on steel-laminated elastomeric bearing pads seated on concrete pedestals. Detail of pedestals are provided by Smith (2022). At the exterior ends of each span, a pedestal supported one end of a girder. At the interior ends, each pedestal supported both the east and west spans of a single girder line. The pedestals (design provided by TxDOT Project 0-6982) have pipes near each corner to tie down rods aligning with the 3-ft spacing of holes in the laboratory strong floor. At the exterior pedestals, tie-down rods were provided in two locations.

The bearing pad footprint was 21 in. × 8 in., consistent with that used for non-skewed Tx girders in standard bridge designs. Bearing pad thickness was approximately 3 in. and was selected based on the availability of eight similar pads in the inventory of the lab and through a donation of four pads by Heldenfels Enterprise in San Marcos, Texas. The location of the bearing pads measured from the edge of the pedestals was larger than the distance from the end of bent caps in standard bridge designs. This was governed by the capacity of the pedestals and did not impact the performance of the girders or deck. Figure 9.15(a) shows the placement of bearing pads prior to girder placement.

Eight girders, all with the same design, were used to complete the full test program. The girders were numbered 1–8 by the fabricator. In addition to these numbers, a letter (A or B) was arbitrarily assigned to each end. Table 9.2 provides a summary of which girders were used at which location in each test, as well as which end (A or B) was at the interior and exterior ends. These girder identifications are not critical to the scope of the work in the project. However, any tested bridge components may be valuable to future researchers; thus, girder damage was documented during testing.

After placement of the girders (Figure 9.15[b]), the camber was measured and documented. Additionally, the distance between girder ends was measured and documented since the varying camber and placement tolerances led to slightly different gaps for the two girder lines.

Bedding strips and placement of panels on bedding strips were provided in accordance with TxDOT specifications. ASTM C578 Type VI polystyrene, with a compressive strength of 40 psi, was used. The strips were 2 in. wide and located at the edge of the girder. Notches were placed every 8 in. to provide an outlet for air during placement of concrete. Panels overlapped the bedding strip by 6 in., allowing for 4 in. of concrete beneath the panel. Bedding strips were secured to the girders using a general construction epoxy (Loctite Power Grab). Epoxy was placed on the bedding strip prior to placement of the panel.

The girder camber was used to make final adjustments to the dimensions of bedding strips to allow for the PCPs and overhang formwork to lay flat. TxDOT specifies that the minimum bedding strip thickness should not be less than ½ in. With upward camber in the girders, the minimum thickness would be near midspan. Since there is no deck in this region, the bedding strips in the decked region were adjusted such that the thickness was 2 in. at the end. This was estimated to result in approximately ½-in. thickness at midspan should the deck have extended that far. For consistency between all specimens, 2 in. was used at the end for all decks and decreased along the length as necessary to allow the panel to lay flat.


(a)

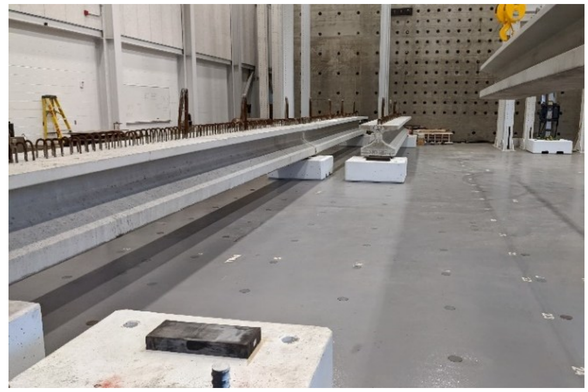
(b)

Figure 9.15. Placement of pedestals, bearing pads, and girders (shown for PBJ-FP1).

Table 9.2. Summary of girder location and orientation.

Specimen Name	G-NW		G-NE		G-SW		G-SE	
	Int	Ext	Int	Ext	Int	Ext	Int	Ext
PBJ-FP1 and PBJ-FP1R	X3-A	X3-B	X2-A	X2-B	X5-A	X5-B	X4-A	X4-B
PBJ-OP1 and PBJ-OP1R	X2-B	X2-A	X3-B	X3-A	X4-B	X4-A	X5-B	X5-A
PBJ-OP2	X1-A	X1-B	X6-A	X6-B	X7-A	X7-B	X8-A	X8-B
PBJ-CP1	X6-A	X6-B	X1-A	X1-B	X8-A	X8-B	X7-A	X7-B

9.3.2 Cast-in-Place Deck Construction

The PCPs served as stay-in-place formwork for most of the deck between the girders. In all decks, the overhang lumber formwork was constructed to support the concrete from below. For offset panel designs, this was also done for the continuous deck region between girders. In the flush panel designs, this formwork between girders was placed at the outer edges of the deck to support that CIP region. For simplicity of construction, this formwork was also placed under a portion of the PCPs; however, this support was not needed. The full set of bottom formwork, including panels, is shown in Figure 9.16 for PBJ-FP1.

(a) (b)

Figure 9.16. Installation of bottom formwork and placement of PCPs (shown for PBJ-FP1).

In the flush and offset designs, formwork was also needed between the ends of the girders. One challenge was fitting formwork in a narrow space with inconsistent dimensions while ensuring that concrete would not leak through a gap. Figure 9.17 shows the approach used in PBJ-FP1. A subassembly of 2×6s supported on a frame of 2×4s was placed between the girder ends. This left only a small gap between the formwork and the ends of the girders, which was filled with a backer rod with caulk above. This approach had been validated with a trial batch in a small mockup prior to casting concrete. However, when implemented in the actual specimen, there was significant difficultly in removing the formwork because the self-weight of the concrete and effects of shrinkage led to a small compressive force acting on the formwork. At the backer rods, the pressure from concrete caused a sag, contributing to the difficulty in removal. In offset panel construction (PBJ-OP1 and PBJ-OP2), the bedding strip foam was used instead (Figure 9.18). While compression was still present after casting and curing the deck, the foam was easier to remove.

Figure 9.19 shows an example of the full preparation prior to casting concrete. Side formwork was installed with intermediate bracing for support. Rebar was supported using a combination of various height chairs and slab bolsters to account for the steel located in overhangs, over girders, and over panels. Form release was applied to all lumber formwork.

Concrete was TxDOT Class S concrete with a specified 28-day strength of 4 ksi and was provided by Smyrna Ready Mix. Concrete was placed in the deck using an overhead bucket. Concrete rakes were used to spread the concrete in the deck. Vibrators were used to consolidate the concrete, with a flexible ¾-in. diameter vibrator used to ensure concrete filled the gap beneath the panel overlap on the girder. A 14-ft magnesium screed was used to level the concrete. Several passes were needed near the center of the deck and near the lifting hooks to ensure the deck surface was flat and there was no doming at the center. A bull float was used to finish the deck, with hand floats used along the edges. The deck was covered with a large piece of black plastic during curing. Once concrete reached sufficient strength, typically several days later, the formwork was removed.

(a) (b)

Figure 9.17. Formwork used between girder ends for PBJ-FP1.

Figure 9.18. Formwork used between girder ends for offset panel tests (PBJ-OP1 shown); post-installed dowel bars not present.

(a) Looking west

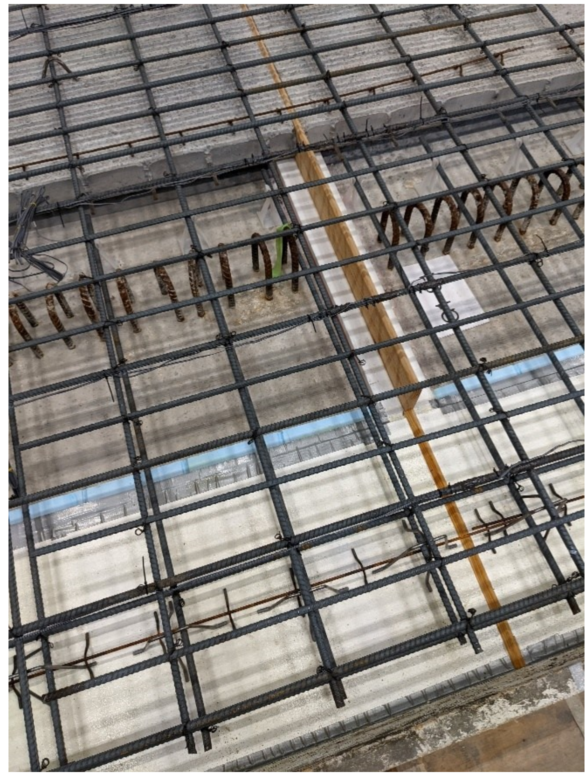

(b) North overhang

Figure 9.19. FP1 prior to casting concrete.

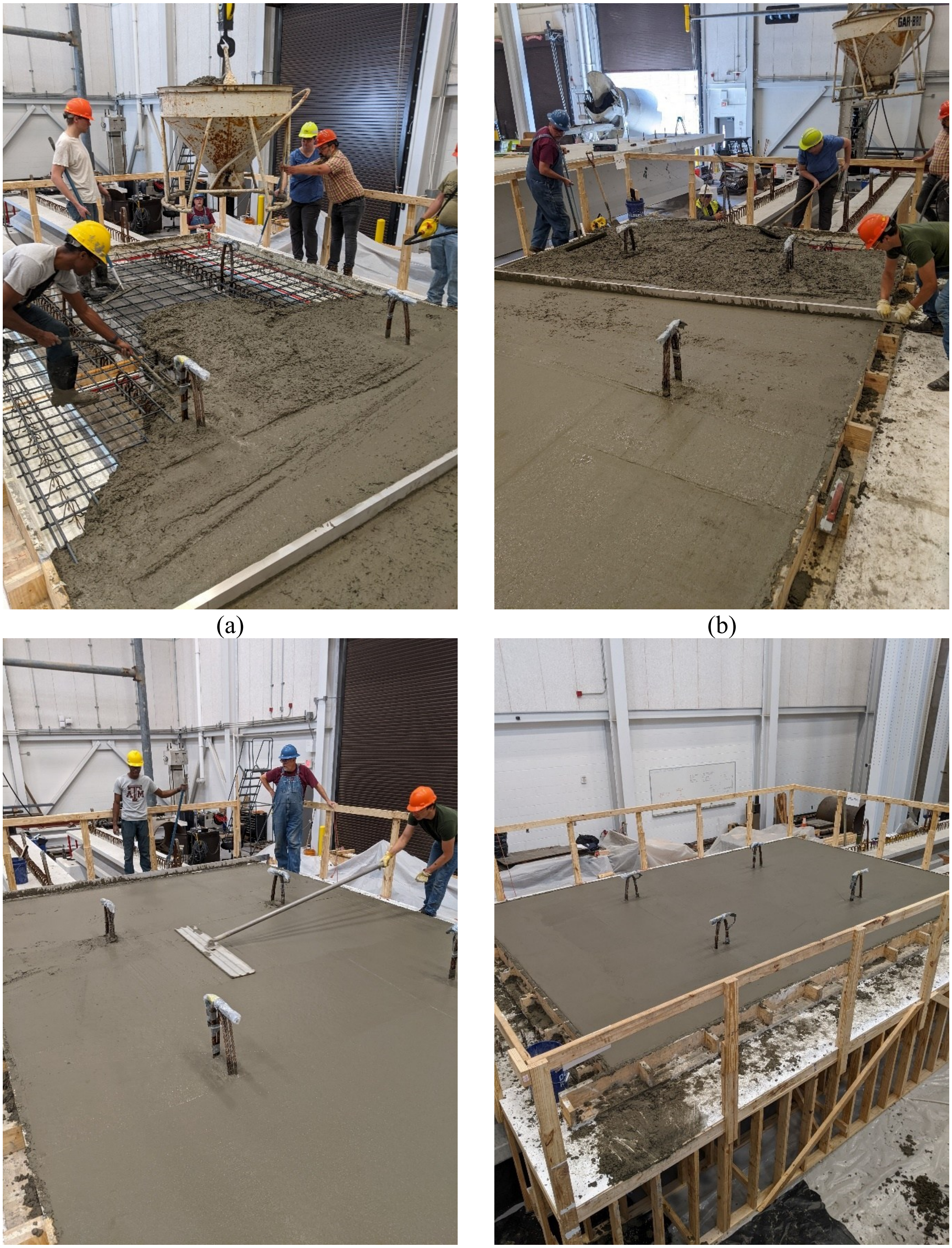

(a) (b)

(c) (d)

Figure 9.20. Placement and finishing of concrete.

9.3.3 PBJ-FP1 Construction Details

After placing the girders and formwork, the researchers observed that the bearing pad under the interior end of the southeast was slightly slanted, likely from damage during use in previous projects. This may have affected the measured camber slightly, as well as the distance of the gap between the ends of the girders.

The ¾-in. thick board between the PCPs was planned to form a notch at the top of the board to match the requirements in the TxDOT standard detail. Location of the board is shown in Figure 9.21. The board was epoxied to the panels. After the initial placement of the panels, the board was significantly off center between the girder ends. The accuracy of placement was limited due to the tolerance of the overhead crane. Following initial placement with the crane, a large crowbar was used to shift the panels slightly so that the board was approximately centered. This was not achieved perfectly in part due to the imperfect gaps between the girder ends in each girder line. During the adjustments, loud cracks were heard, indicating some cracking of the bedding strips or separation of the bedding strip from the girder. An inspection indicated no concerning damage. While the epoxy holding the board to the panel may also have been broken, there were no concerns given that this region would be in compression during the test.

In the north overhang, the notch on the bottom of the deck was created by attaching a ¾-in. triangle-shaped piece of molding to the bottom formwork (visible in Figure 9.19[b]). This did not shift during placement and was successful in forming the notch seen in a typical overhang.

Concrete was placed from west to east. When the pour reached the center region of the deck near the continuous deck portion, the unbalanced concrete led to a shift of the board in the south overhang. Once this was observed, the placement was slowed down and the board adjusted back to its original location. After that, concrete was carefully placed in the region to minimize further shifting of the board.

The concrete was placed on the morning of May 26, 2022. After finishing, the deck was covered with plastic and no observations were made over a four-day holiday weekend during closure of the lab. On May 31, 2022, the plastic was removed, and a small hairline crack was located at the center of the continuous deck region.

(a) Looking east

(b) Looking south

Figure 9.21. FP1 board located between panels.

9.3.4 PBJ-FP1R Construction Details

PBJ-FP1R was constructed as a retrofit of PBJ-FP1. Figure 9.22 shows the removal of existing concrete. The top 4.5 in. of concrete was removed from the retrofit region. Two-inch deep saw cuts were made at the exterior of the retrofit region; existing reinforcement was not cut so as to allow for splicing with the new reinforcement. Two additional 4.5-in. deep cuts were made closer to the center to help with the removal. Most of the concrete was removed using a jackhammer, with work near the final surface completed using a smaller-impact hammer drill. Shoring was placed under overhangs to provide additional support during the demolition process.

During removal of the concrete, some damage occurred to the bottom portion of the deck. In the south overhang, a diagonal crack formed, as shown in Figure 9.23(a). This crack was located 13 in. east (at the bottom) of the center of the link slab. While the crack formed during use of the jackhammer and may simply have been the result of the force applied to the unsupported deck, the location suggests the possibility that preexisting damage played a role. The distance from the center was approximately the same as the distance to where secondary cracks were located. The east secondary crack in the south overhang was not observed to extend to the edge of the deck following testing. It is possible that microcracks had formed and developed to a visible crack during demolition. Figure 9.23(b) shows a 2-in. diameter punch out adjacent to the west face of the board between the north girders. The hole was patched with a DOT-approved repair mix (Figure 9.23[c]). Figure 9.23(d) shows damage to PCPs adjacent to the board; the damage was unable to easily be removed without risk of further damage. Thus, no repair was completed.

All top reinforcement in the retrofit region was removed, except for 1 ft 6 in. of the longitudinal reinforcement extending from the existing deck. The tops of concrete chairs and PCP lifting hooks were cut so that the roofing paper used for debonding could lay flat on the deck.

Formwork was needed only on the sides of the deck, as shown in Figure 9.24(a). A 2×12 board was attached to each side of the deck using 8⅜-in. diameter, 8-in. long expansion anchors. Prior to placing TxDOT Class S concrete, form release was applied to the formwork and the existing concrete in the transition zone was surface-saturated to promote a good bond.

Debonding of the new concrete was achieved using synthetic roofing underlayment (0.392 in. thick), as shown in Figure 9.24(b). Prior to use in the deck, the roofing paper was tested to confirm it was sturdy enough for use during the placement of the concrete and sufficient separation was achieved. The 48-in. wide underlayment was placed transversely. Two sheets were needed, with a 6-in. overlap at the continuous deck region. Since the lifting hooks were located partially in the debonded zone and partially in the bonded transition zone, polystyrene block-outs were used to ensure the lifting hooks did not provide any unintentional bond between new and existing concrete.

The new reinforcement was placed using the same depth slab bolsters previously used over the panels. For the elevated 5-ft bars, taller chairs were used. Most strain gages were provided on the bars at the original depth, with one raised bar instrumented to provide strains for monitoring during testing.

(a)

(b)

Figure 9.22. Removal of concrete from FP1 in preparation for FP1R.

(a) Crack in southeast overhang

(b) Hole adjacent to board between north girders

(c) Patched hole

(d) PCP damage at board

Figure 9.23. Damage to CIP concrete during demolition for FP1R.

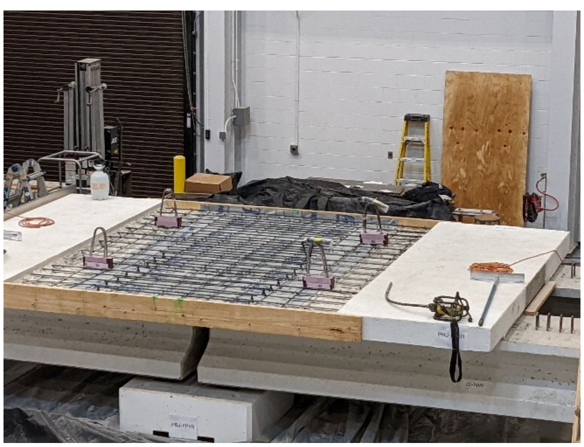

(a)

(b)

Figure 9.24. Preparation for concrete for FP1R.

9.3.5 PBJ-OP1 Construction Details

PBJ-OP1 utilized the far end of the girders from the PBJ-FP1 and PBJ-FP1R tests. After completion of the FP1R test, the two spans were separated at the center of the continuous deck, with the girder lines in each span remaining connected by the slab. A concrete saw with a 4⅝-in. cutting depth was used to make a single full-width cut at the center of the link slab. Since this was located over the board separating the panels, a full separation everywhere except the north overhang occurred. Two relief cuts were made in the north overhang approximately 6 in. each side of the main cut. A jackhammer was used to remove sufficient concrete to cut reinforcement and fully separate the two spans.

The deck on the interior ends of the FP1/FP1R girders provided stability during the move. Several angles were temporarily welded between exposed R-bars on the far ends of the girder to provide stability of those ends. Additionally, compressive bracing was added using lumber between the flanges. Rigging was created using lifting straps and steel header beams.

The spans were swapped so that the northeast and northwest girders became the southeast and southwest girders, and vice versa. The bearing pads were not moved from the previous locations, ensuring that the support locations were equal between each test. As a result of the damage imposed in prior tests, the elevations of the girder ends were slightly different, but not sufficient to be of concern to the performance of the test. For OP1 deck construction, the difference is accounted for in the bedding strips, which are custom fit on each girder edge to ensure a level and consistent depth deck. Figure 9.25 shows the girders in place to begin construction on OP1.

Figure 9.26 shows the panels in place before and after post-installation of the dowel bars. Half-inch diameter holes were drilled in the panel ends. Holes were located slightly below center to avoid drilling into the prestressing strands and were spaced at 9 in. to align with the CIP rebar spacing. Bars were #3, embedded 5 in. in the panels with Red Head C6+ epoxy. The strength was confirmed to provide adequate capacity for the loads applied in the tests. However, the capacity is not sufficient should the specimen be loaded such that the bottom reinforcement is in tension.

The concrete was placed on October 2, 2022. Placement of concrete in PBJ-OP1 was sequenced similar to construction in the field, with the concrete placed first over the girders (Figure 9.27) and then in the link slab. The concrete was covered in plastic for several days prior to removal. No shrinkage cracks were observed.

Figure 9.25. Girders in place for PBJ-OP1 deck construction (far ends of the girders have the deck from the PBJ-FP1R test).

(a) Without PCP dowels (b) With post-installed PCP dowels

Figure 9.26. PBJ-OP1 panel placement.

Figure 9.27. PBJ-OP1 concrete sequence.

9.3.6 PBJ-OP1R Construction Details

PBJ-OP1R was constructed as a retrofit of the north half of PBJ-OP1. The top portion of concrete was removed for a 4-ft length of deck. New longitudinal reinforcement was installed and HPC placed.

A full-depth, longitudinal saw cut was made on all deck regions (tested region and far ends of girders containing deck from PBJ-FP1 and PBJ-FP1R). This enabled retrofit and testing of only the north half without influence from the south half. Following cutting, the deck of the north girder tilted slightly such that the inner side was higher than the overhang. Partial-depth transverse saw cuts were made at the boundary of the retrofit region. The cut was approximately 2 in. deep to avoid cutting the reinforcement. The top 3.75 in. of concrete was removed by jackhammer and chipping hammer. Transverse reinforcement was removed to help accelerate the demolition. At the edges of the deck, minor damage occurred during removal, with the removal depth essentially being slightly larger in isolated locations. This is shown in Figure 9.28(b).

The middle 2 in. of the existing longitudinal reinforcement was removed by cutting with a saw. This provided bars extending from the existing deck into the retrofit, without providing strength to the link slab. New longitudinal bars were spliced to these bars. Transverse reinforcement was not replaced because it was not beneficial to the loading planned for the single-girder line test.

Formwork on the north edge was the same as that used for PBJ-FP1R. The board sat slightly lower than the existing deck on the northeast corner, leading to a slightly thinner deck. On the south edge, roofing paper was used to prevent bonding of the HPC to the deck on the south half of the original PBJ-OP1 specimen. The existing concrete was surface-saturated prior to placing HPC.

Concrete was placed on December 6, 2022. Figure 9.29 shows photos from the mixing and placement. HPC was mixed in a high-shear mixer with a 1.9 ft^3 capacity, led by TxDOT 0-6982 team members. Small batches of approximately 1.25 ft^3 (less than 70 percent of the mixer capacity) were performed to ensure sufficient power to mix HPC. Seven batches were made, with the first 6.5 being used on the deck and the remaining used to make material samples. To reduce construction joints, the first three batches were placed in completely sealed 5-gal buckets until the fourth batch was mixed. While the fourth batch was mixed, the buckets were poured into the deck and allowed to flow to fill the void. The HPC was primarily added in the northeast corner and allowed to flow to fill the rest. Given the slant of the deck, the concrete from initial batches was thicker on the north and thinner on the south. In later batches, concrete was added near the southeast corner. In the first two batches, steel fibers settled near the bottom by the time the fresh HPC was stored temporarily in the buckets due to the high flow spread, leading to clumps of steel fibers. These were mainly located near the northeast corner and along the west edge. After the fourth batch, and following every subsequent batch, the concrete was covered with plastic to avoid surface drying that may cause elephant skin between placements. The formation of elephant skin causes issues of consolidation of concrete. Lumber was used to keep the plastic from sticking after the final batch (Figure 9.30[b]). Material samples were made from the final batch.

Table 9.3 provides flow and temperature values for each batch. Flow was measured immediately after mixing. Temperature was measured when the HPC was placed. The flow values were outside the range recommended (10–10.5 in. desired, 9.5–11.0 in.) by the TxDOT 0-6982 research team for the mix, which was designed for use in prestressing girders. A concrete mix designed for a specific link slab application would likely have lower flow spread that may help reduce segregation of fibers.

(a) (b)

Figure 9.28. (a) Saw cutting and (b) concrete removal from OP1 in preparation for OP1R.

(a) (b)

Figure 9.29. PBJ-OP1R (a) mixing of HPC and (b) formwork with buckets staged for placement.

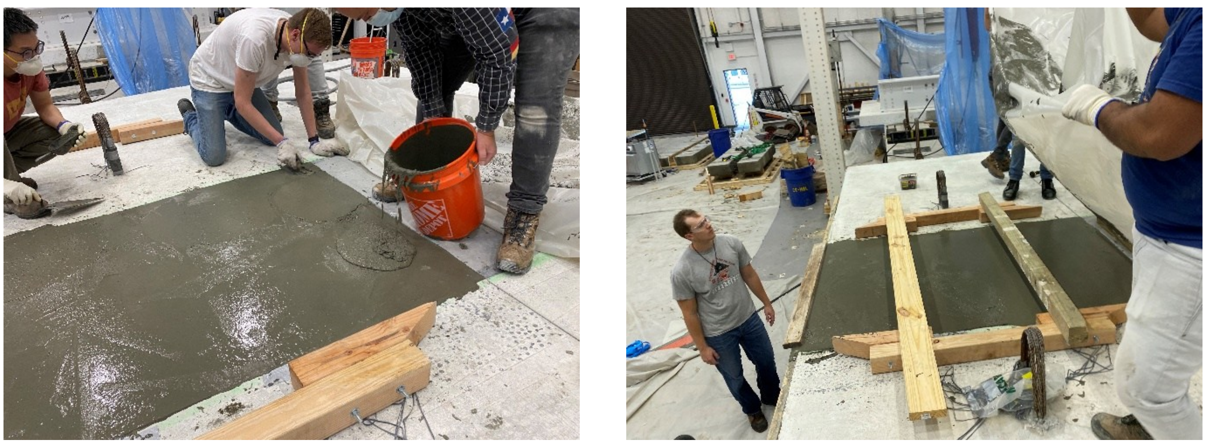

(a) (b)

Figure 9.30. Finishing of PBJ-OP1R.

Table 9.3. HPC batch flow and temperature at placement. A dash indicates no measurement.

Batch	Flow, in. (Reading 1)	Flow, in. (Reading 2)	Temp, °C (Reading 1)	Temp, °C (Reading 2)
1	11	10.75	26.8	26.3
2	11.25	11.5	28.1	28.2
3	10.75	10.75	28.3	29.1
4	11	11.25	29.2	28.7
5	11	11.25	29.5	29.2
6	11	11.25	29.5	27.7
7	10.25	11	N/A	N/A

9.3.7 PBJ-OP2 Construction Details

PBJ-OP2 was the first test constructed on the second set of girders. The same procedure and documentation of camber done for the second set of girders was done for the new set of girders. The construction of the formwork and placement of panels was identical to PBJ-OP1, including post-installed dowel bars in the PCPs.

The R-bars were cut and ground flush with the top of the girders (Figure 9.31[a]) for the first 3 ft of each girder. The final bar cut was one prior to the lifting hook, allowing the lifting hook to be used as a reference point for the debonded region during testing. Roofing paper was placed on top of the girder (Figure 9.31[b]) to prevent bonding of the deck concrete to the girder. Two pieces were used on each girder to ensure the full surface was covered, accounting for the smaller width at the panel due to a bedding strip. A small amount of epoxy was used to keep the roofing paper in place on top of the girder. Figure 9.32 shows the completed formwork with rebar placed.

Concrete was placed on March 8, 2023. Originally, researchers planned to have a placement sequence the same as for PBJ-OP1 (over girders first, with center completed last). Concrete was first placed in the west end. When the placement reached the region where roofing paper was on the southeast girder, the force from the concrete shifted the paper out of place. Placement was halted and the concrete moved by hand to allow adjustment of the roofing paper back to its original position. The paper could not be fully restored to the adjusted position, resulting in some bunching of the paper where two pieces overlapped. While this may affect a flush final surface on the bottom of the CIP deck, it is believed that debonding is still achieved. Due to this incident, placement of the concrete was continued west to east, as opposed to the original plan of center last. When placing the concrete in the debonded region of the other three girders, small amounts of concrete were hand placed at the edges to weigh the paper down, and concrete was placed slowly. Due to the delays in the debonded region, the concrete work ability was low by the time all concrete was placed, resulting in limited ability to float the concrete on the east end.

The concrete was covered in plastic for several days prior to removal. No shrinkage cracks were observed.

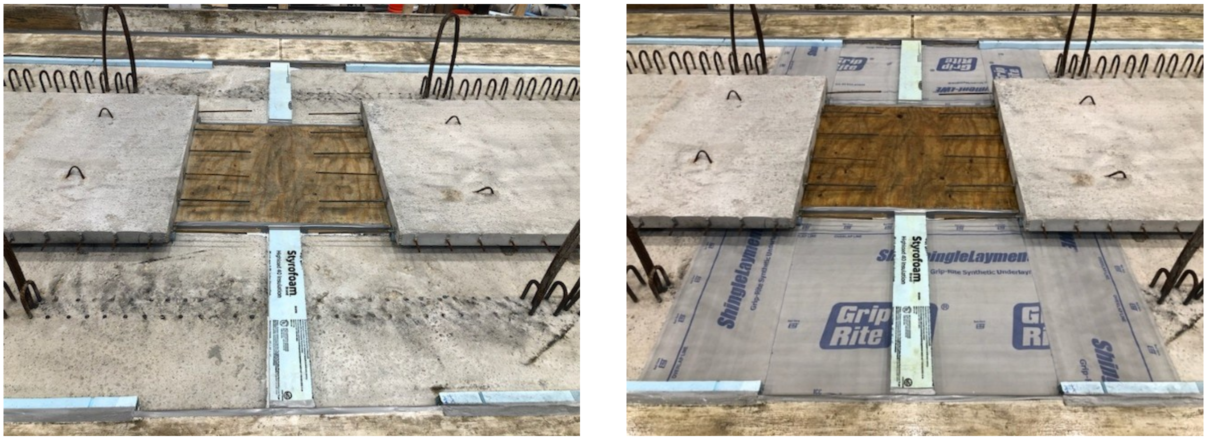

(a) (b)

Figure 9.31. PBJ-OP2 (a) R-bars removed in debonded region and (b) roofing paper to debonded deck concrete from top of girder.

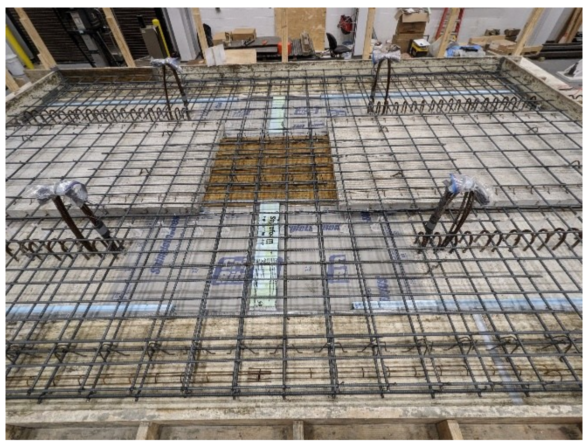

Figure 9.32. PBJ-OP2 formwork with all rebar (the north girder is at bottom and has supplemental top bars).

9.3.8 PBJ-CP1 Construction Details

PBJ-CP1 was the final test and utilized the far end of the girders from the PBJ-OP2 test. After completion of the PBJ-OP2 test, the two spans were separated at the center of the continuous deck similar to that described in Section 9.3.5 for PBJ-OP1 construction. Formwork was generally the same as that for PBJ-FP1, with the only difference being the placement of the panels due to the use of a single continuous panel.

Figure 9.33 shows the panels and reinforcement in place prior to placement of the concrete. In Figure 9.33(a), the configuration of the single PCP panel, centered over the link slab region, is clear. Figure 9.33(b) shows a close-up of the link slab region. The debonded region was prepared the same as that for PBJ-OP2, with roofing paper epoxied to the girder to better prevent slippage that occurred during PBJ-OP2. For PBJ-CP1, the 0.5-in. thick polystyrene (white in the photo) was placed at 1.5 ft at the ends of each girder for the haunch gap.

Concrete was placed on May 3, 2023. Concrete was placed from west to east for simplicity of construction. When formwork was removed, researchers saw that the south overhang at the link slab center was not well vibrated, leading to honeycombing. Figure 9.34 shows the honeycombing prior to repair following the specifications of the TxDOT Concrete Repair Manual (2021). During testing, no adverse effects of the repair were noted.

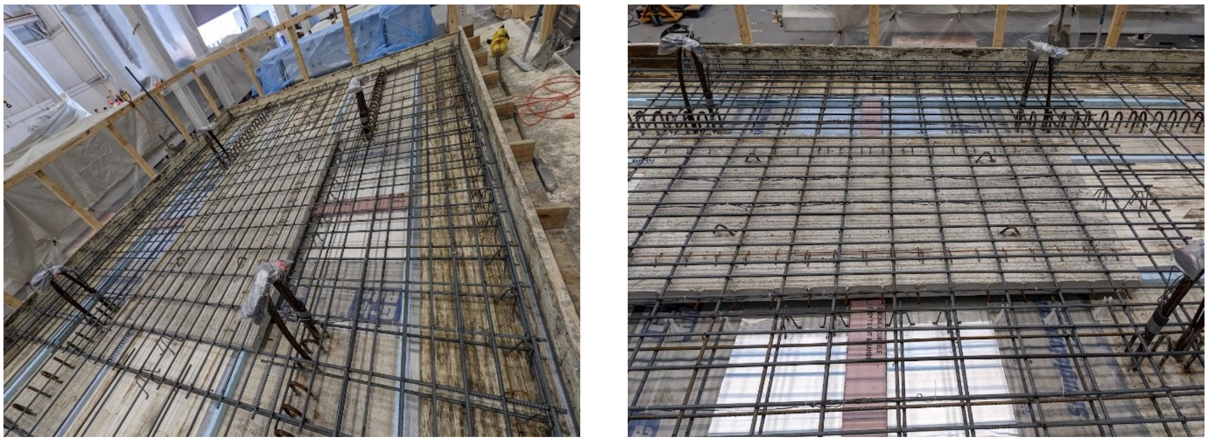

(a) (b)

Figure 9.33. PBJ-CP1 prior to concrete pour: (a) overall view and (b) close-up of link slab region.

(a) (b)

Figure 9.34. PBJ-CP1 honeycombing in south overhang prior to repair.

9.3.9 Recommendations for Future Construction

The following recommendations are made:

- In future experimental tests using a board in the overhang, the board should be attached to the side and/or bottom formwork with a screw. In bridge construction, the board is unlikely to be in the overhang and thus not likely to be an issue. Between panels, the board is secure, and the short extension should be fairly rigid over the girders. If multiple boards are needed to cover the width of the bridge, care should be taken when the boards terminate. It is recommended that this be between the panels where the ends will be secured from movement.

- Concrete should be placed in the link slab region after the rest of the deck to minimize the demands from deadload and to help avoid shifting of the board.
- For the formwork between the girder ends, the slight compression induced by the self-weight of the concrete made it difficult to remove. A more flexible option, such as the polystyrene used for the bedding strips, should be considered to avoid difficulty in removal of formwork.
- If roofing paper is used to prevent bonding of the deck concrete to the top of girders, it should be placed prior to panels and other formwork, which can be used to keep the paper from slipping. If debonding occurs after panels and formwork are placed, a debonding agent should be used instead.

9.4 MATERIALS

Material properties quantified were slump, compressive strength (f'_c), modulus of elasticity (MOE; E_c), modulus of rupture (MOR; f_r), and indirect tensile strength (ST; f_{ct}). Hardened properties were tested at 28 days and on test day, and for some tests, additional increments. Tested properties for the deck concrete are provided in Table 9.4 and Table 9.5 for 28-day and test-day strength, respectively. Limited tests on concrete for precast components were conducted on test day for some of the tests. The results are presented in Table 9.6.

Slump tests were performed on all ready-mix concrete placed at the lab. Slump tests followed the ASTM C143/C143M standard. The cylinders were 4 in. × 8 in. and were made following ASTM C39/C39M. Beams for MOR tests were both 6 in. × 6 in. and 4 in. × 4 in. Compressive tests followed the requirements of ASTM C469/C469M. MOR tests followed ASTM C78/C78M. ST tests followed ASTM C496/C496M. For girders, only cylinders tests were conducted, with the cylinders made by Bexar Concrete Works and picked up the following day.

Table 9.4. 28-day material tests for deck concrete.

Specimen Name	f'_c ksi	E_c ksi	MOR psi	ST psi
PBJ-FP1	5.73	6043	571	–
PBJ-FP1R	7.24	5896	669	983
PBJ-OP1	4.92	5167	640	758
PBJ-OP1R	–	–	–	–
PBJ-OP2	5.37	5804	604	866
PBJ-CP1	5.46	5895	463	886

– No test completed.

Table 9.5. Test-day material tests for deck concrete.

Specimen Name	Age at Test	f'_c ksi	E_c ksi	MOR psi	ST psi
PBJ-FP1	34	6.27	5304	682	934
PBJ-FP1R	7	5.18	5512	581	838
PBJ-OP1	18	4.58	5174	612	776
PBJ-OP1R	7	13.06	5851	1683	–
PBJ-OP2	28	5.37	5804	604	866
PBJ-CP1	19	4.95	5699	604	789

– No test completed.

Table 9.6. Test-day material tests for precast components.

Component	f'_c ksi	E_c ksi
Girders: FP1	10.68	5193
Girders: OP2	10.76	5382
Panels: OP1	10.04	–
Panels: OP2	9.92	4939
Panels: CP1	9.73	–

– No test completed.

EXPECTED STRENGTHS

Figure 9.35 provides a preliminary analysis of the expected response of the link slab. Moment-curvature analysis was conducted using design material properties. Curvature was converted to rotation assuming a 12-in. link slab length. While each design was expected to have a different effective link slab length, the same length was used for simplicity in predicting the response prior to testing.

Offset panel strength used full-depth CIP concrete and the top and bottom layers of steel. The flush panel strength used a linear elastic material to capture the influence of the board between the panels, and thus provided an estimate of the response of the south girder line. For FP1R (flush panel retrofit), two curves were provided, with both using only a 4.5-in. slab and ignoring any contribution of the bottom layer of deck. The first variation, FP1R-S, used the same reinforcement as the flush panel detail. The second variation, FP1R-N, used elevated supplemental bars. The depth of the supplemental bars was the originally intended value and thus slightly lower (farther from surface) than what was constructed.

For each response, cracking was marked with a triangle marker, yield with a circle, and 60 percent of yield with a square. For FP1R-N, a yield point is not shown because the strain was not recorded in the supplemental steel. However, the change in stiffness around 0.007 rad was yield of the supplemental steel. Rotation limits were not the maximum capacity but were rather limited for easy viewing of the difference of responses. All designs were under reinforced and not expected to have deformations approaching anywhere near the crushing limit of the concrete.

The OP1 and FP1 designs had similar cracking rotations, although the cracking moment was larger in OP1. After cracking, FP1 had greater stiffness than OP1, as well as a larger yield moment and rotation. This finding was a result of the supplemental reinforcing bars. In the FP1 responses, the strengths dropped significantly. However, since the design of link slabs is a deformation-controlled design, the strength was not a concern. Compared to OP1 and FP1, the cracking moment and rotation were only slightly larger. However, the post crack stiffness was much lower, resulting in large rotations before the key values for the strain in the steel were reached.

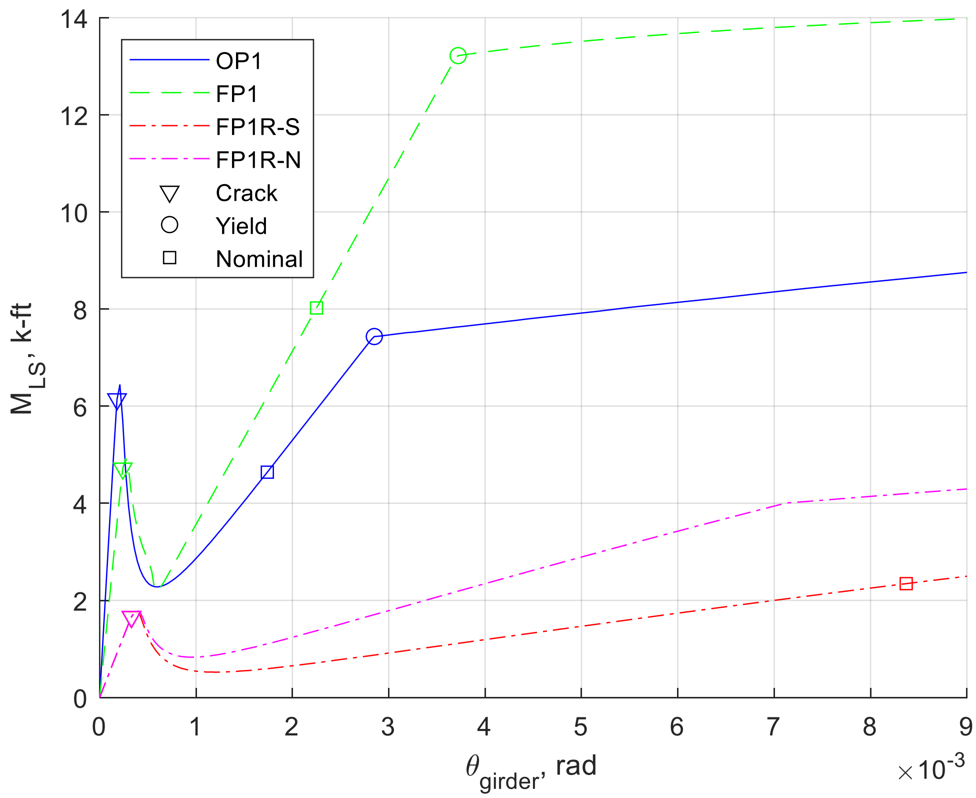

Figure 9.35. Moment-rotation response of link slab for design material properties and assumed link slab length of 12 in.

9.5 DATA COLLECTION

During testing, multiple methods were used to collect data to quantify the response of the link slabs. The configuration, quantity, and locations were determined by balancing the available equipment, the desired responses, and the time available for installation. During this process, the findings of prior experimental test programs and preliminary finite element models were considered. Section 9.5.1 provides a summary of more traditional instrumentation, such as string pots. Section 9.5.2 provides a summary of a motion capture system used to monitor the displacement of a dense grid of points. Section 9.5.3 describes measurements of crack widths taken during the tests. Finally, Section 9.5.4 provides a summary of nondestructive evaluation completed before and after the test.

9.5.1 Traditional Instrumentation

The primary information of interest to the tests was the rotation at the interior ends of the girders. Rotations were calculated using LVDT measurements of the relative displacement between the top flange of each span of a girder line and the same on the bottom flange. This setup was the same as was used in the field monitoring of bridges. Use of these data to calculate end rotation is discussed in Section 10.3.

Despite the rotation being the dominant response of interest, deformation of girders is the typical measure used to report results for link slab tests in previous literature, so this information was collected to provide a comparison to other tests. Girder deformation can also be useful in estimating the distribution of forces in the indeterminate system and can provide an additional estimate of girder end rotation. Figure 9.36 shows the general layout of string pots for a single girder in the setup.

Internal strain gages were placed on the longitudinal steel in the link slab region. General plans for offset and flush panel designs are shown in Figure 9.37. Exact plans varied for each specimen. Strain gages were provided on the top bars in both options, with bars instrumented over the girders, between the girder lines, and in the overhang. All instrumented bars had gages at the center of the continuous deck. Additional gages were located 4 in. and 8 in. from the center (except FP1R overhangs). However, these were not provided on both sides of all bars due to the need to limit strain gage channels. With the exception of one bar in PBJ-FP1R, all bars instrumented were main longitudinal bars; in PBJ-FP1R, one 5-ft long bar was instrumented. In the offset panel tests, reinforcement was also provided on bottom longitudinal reinforcement to provide additional information for developing strain profiles in the link slab.

Figure 9.38 provides generic plans for measuring surface strains. Figure 9.39 shows an example installation of a gage. As best possible, the surface strains were at the same transverse locations as the steel strain gages to allow for assessment of strain profile. Measurements were all at the longitudinal center of the continuous deck. On the top of the deck, strain gages were used accordingly. Strain gages were not practical on the bottom due to the board (flush panels) or notch (overhang and offset panels), so LVDTs were used to measure the relative displacement of either side of the center for use in estimating strain.

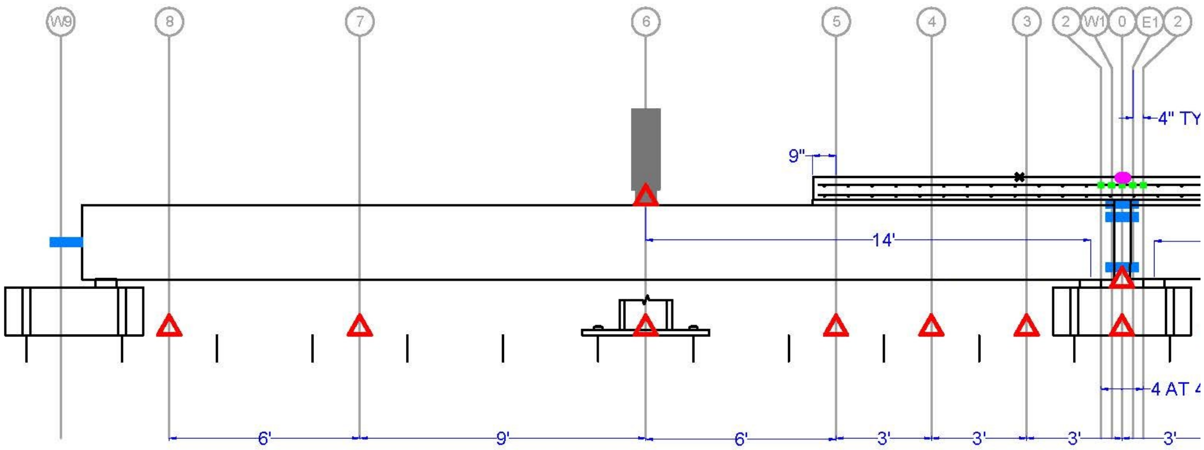

Figure 9.36. Generic elevation for string pots and LVDTs (single full span shown with portion of other span; blue rectangles represent LVDTs, and red triangles represent string pots).

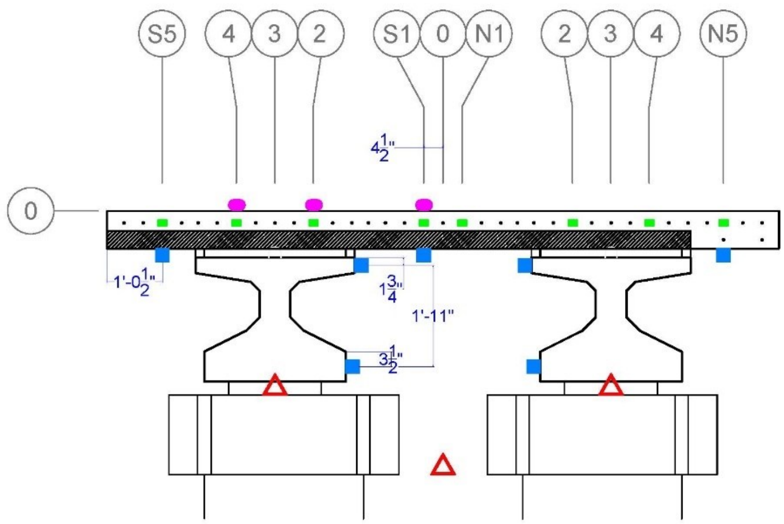

Figure 9.37. Instrumentation on general cross-section (FP1 shown; blue rectangles represent LVDTs, pink ovals represent concrete surface gages, green rectangles represent steel strain gages, and red triangles represent string pots).

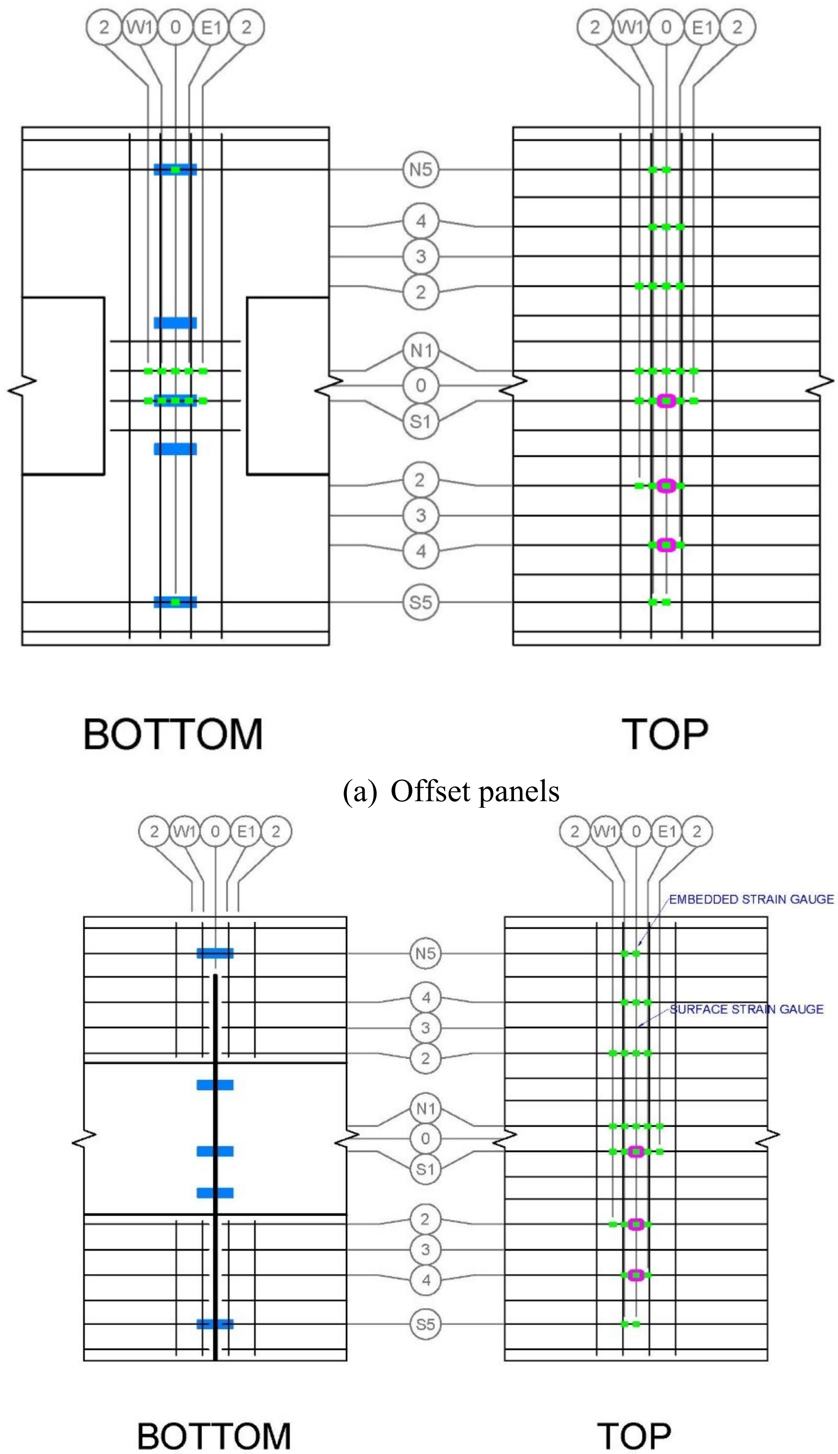

(a) Offset panels

(b) Flush panels

Figure 9.38. Generic plan for concrete strain gages and LVDTs for surface strain and steel strain gages in (a) offset panel designs and (b) flush panel designs (blue rectangles represent LVDTs, pink ovals represent concrete surface gages, and green rectangles represent steel strain gages).

Figure 9.39. Surface strain measurements on bottom of deck using LVDTS.

For PBJ-OP1R, only the north girder line was tested. Thus, only the string pots and LVDTs on the north girder were used. The LVDT on the far end of the south girder was moved to the far end of the northeast girder to provide an additional reading. The bottom steel strain gages from PBJ-OP1 were kept, and new gages were installed on the top longitudinal bars and on the top surface.

9.5.2 Optotrak

Optotrak is a motion capture system that tracks the positions of light-emitting diode (LED) targets. The positions can be used to monitor the deformation at many points in a manner not practical with traditional instrumentation such as string pots. The displacements can also be used to determine strains between the targets. The size of the cameras used in monitoring the target positions is large and thus only practical to use when positioned on the floor. Given this and the fact that the out-of-plane accuracy is lower than the in-plane accuracy, the system was used to monitor displacements on the edge of the deck.

Figure 9.40 shows the general configuration of the cameras and the field of view. Two cameras were used with overlapping volume. When the cameras' fields of vision were registered together, they provided an expanded single field of view. The cameras were generally set up 9 ft apart at a distance 7 ft from the edge of the deck. This provided a coverage of 8.5 ft along the edge of the deck with an error of approximately 0.44 mm (0.017 in) (varied exactly based on each setup). The south overhang of the deck was monitored with the Optotrak.

For each test, the field of view and target configuration were different based on the unique characteristics of the test and findings from the data collected in previous tests. Figure 9.41 shows a generic target configuration. In general, four rows of targets were used. This allowed for evaluation of deformation and strains at multiple depths and for the generation of corresponding strain profiles. Numerous columns of targets were provided at a spacing of approximately 4 in. In the continuous deck region and along the girders to at least the inside of the bearing pads, the columns had targets in each of the row locations. At farther distances from the continuous deck center, the strain profile was of less interest and the number of markers in each column decreased. In planning the termination of the targets, consideration was made for where the field of vision ended and where the inflection point was expected.

In addition to the targets on the side of the deck, two pairs of targets were placed on each of the south girders. These were located at approximately the center of the top and bottom flanges and used to calculate girder rotation. The first pair on each girder was attached at the same locations where LVDTs were attached to the flanges (but opposite face) to allow for a comparison of the data provided by the traditional and Optotrak data. The second pair on each girder was located at the center of the bearing pads and thus corresponded with the girder end rotation used in design. Finally, a set of targets was attached to the pedestal to provide a reference and to allow calculation of the deformations relative to the pedestal rather than relative to the laboratory floor.

In PBJ-FP1, the targets were centered on the continuous deck because researchers anticipated that doing so would capture the inflection point in each span. For PBJ-FP1R, the targets were shifted west to capture the full debonded region and portions of the transition region. Since the markers could not easily be located at the true top of the bottom slab or the true bottom of the top slab, a couple of extra pairs were added on the interface to measure slip. These locations were chosen where they could be attached on the top and bottom decks very close to the interface. During the south load patterns, the cameras were moved farther west to capture a longer portion of the deck; as a result, portions of the east girder were not captured. Since the new locations captured some of the girder with shear cracks, additional targets were placed on the girder to use in estimating shear strains. For PBJ-OP1, the shifted concept was preserved, with additional changes made to change some columns of targets to double columns to provide the ability to calculate a more localized strain than possible in prior tests. Additional targets were added on the girders at the bottom and above the corners of the bearing pads; the objective was to attempt to measure the deformation of the bearing pads.

For PBJ-OP1R, the same concept as PBJ-OP1 was used. The targets were located on the north side, and due to conflicts with the data acquisition (DAQ) system, only one camera could be used. Thus, the region viewed was shorter.

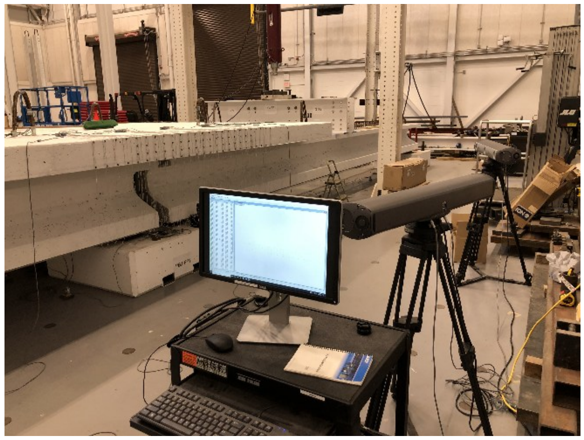

Figure 9.40. Setup of Optotrak cameras (shown for PBJ-FP1).

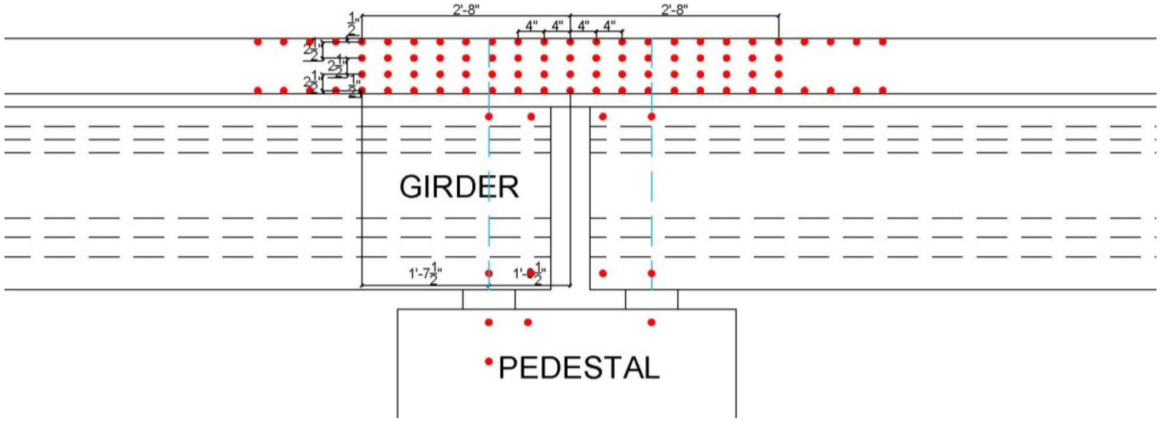

(a) FP1

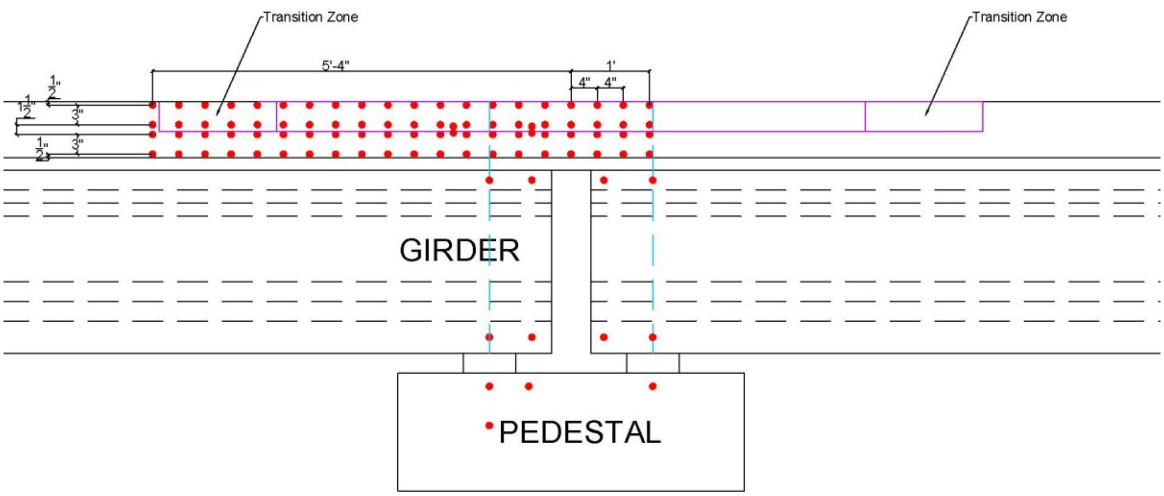

(b) FP1R

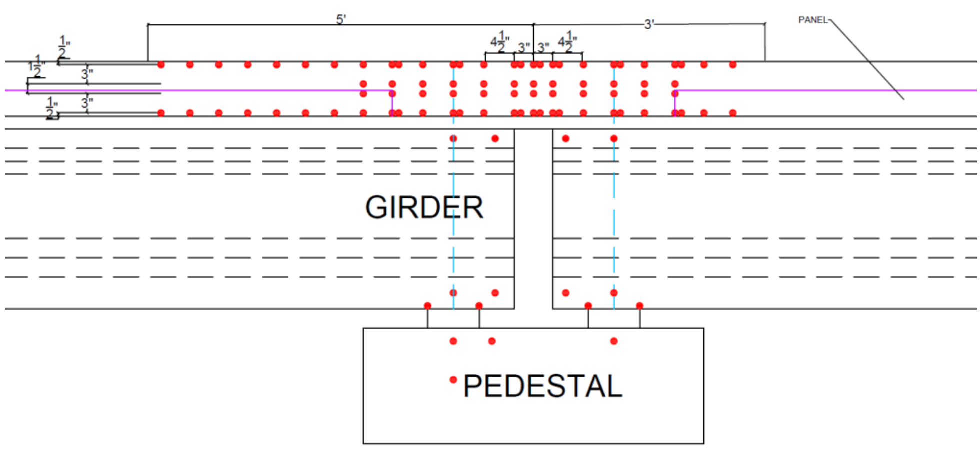

(c) OP1

Figure 9.41. Optotrak grid of targets for each test.

9.5.3 Damage Documentation

During testing, frequent pauses were made to document damage and to measure crack widths. Damage was limited to cracks. Generally, cracks were marked with permanent markers when they first appeared for better visibility in photographs. Exceptions were made for the initial load pattern for each test, where the cracks were only marked once the peak load for that test had been reached. Cracks were not marked in regions for digital image correlation (DIC) to avoid interference with the processing.

Figure 9.42 shows a generic drawing of a link slab with various types of cracks marked. Labels indicate the terminology used to describe each type of crack:

- **Main, or PBJ**—Main cracks are transverse cracks located at approximately the center of the continuous deck. These cracks are also referred to as poor boy joint cracks, or PBJ cracks, at various times in the project report.
- **Offset main**—Offset main cracks form in the continuous deck but are offset from the center, typically over the end of the girders. Often these are found in pairs, but they may be solo. If found in conjunction with a centered main crack, cracks over the ends of girders are considered to be secondary cracks.
- **Branched main**—In the overhangs, the main cracks can be angled slightly and have two branches; these are referred to as branched main cracks. In the discussion of each portion of the branch, the cardinal direction indicating side of the main crack is specified. In the case of the experimental tests, these are east branch or west branch.
- **Secondary**—Cracks that form parallel, or primarily parallel, to the main, offset main, or branched main cracks, are referred to generically as secondary cracks.
- **Bottle-shaped secondary**—These secondary cracks are at varying distances from main cracks and/or have portions that are at an angle relative to the original cracks
- **Longitudinal link slab, or longitudinal PBJ—**Cracks that form perpendicular to, or nearly perpendicular to, the main cracks are referred to as longitudinal link slab, or longitudinal PBJ cracks. In field observations, these are typically associated with skewed bridges. In documenting damage in the tests, these are primarily associated with asymmetric loading of girder lines.
- **Diagonal or torsion—**These cracks run diagonal (transverse and longitudinal components) between the interior edges of the girders. They are outside the main link slab region of interest. Diagonal cracks in the overhangs in or near the continuous deck are referred to more specifically by the prior definitions of cracks (branched main and/or secondary cracks).

On the top surface of the deck, crack widths were measured at specified locations at each pause. This was done to allow for consistent comparison between tests and for a systematic comparison of the performance of the link slab in the overhangs, over the girders and between the girders.

Figure 9.43 shows the locations of these measurements and the name used to describe them in presentation of the results. Primarily, the measurements were taken on the main crack. In overhangs where a branched main crack formed, measurements were taken at both branches. Where secondary, longitudinal, or diagonal cracks formed, more limited crack measurements were taken.

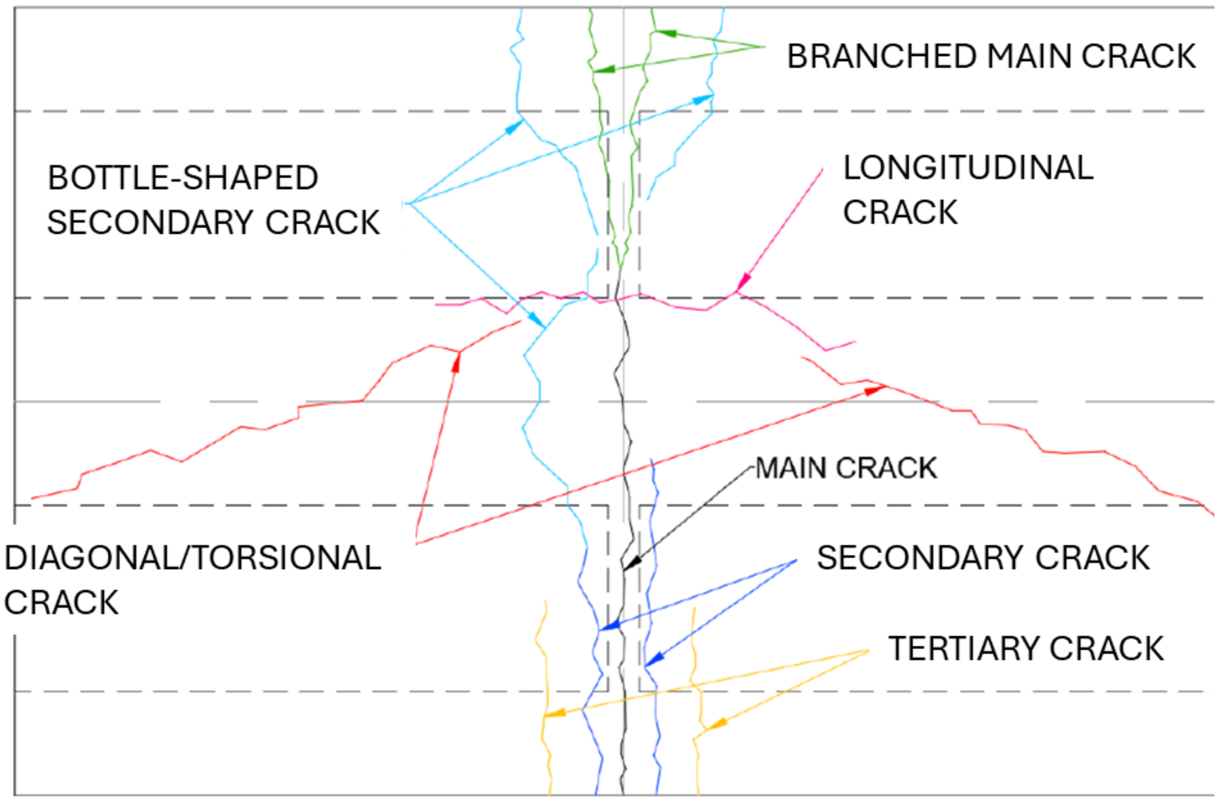

Figure 9.42. Examples of crack types used in describing damage in the link slabs.

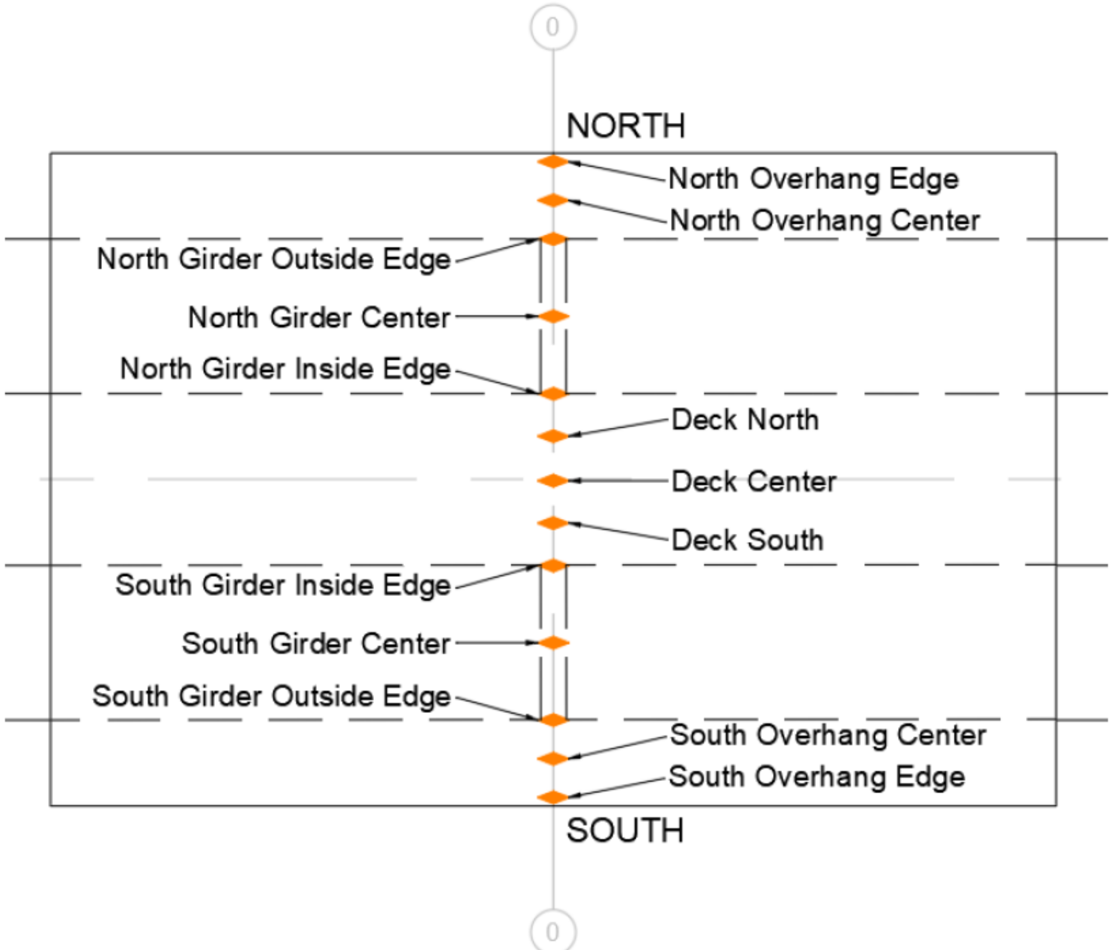

Figure 9.43. Locations of crack width measurements on top of deck.

9.5.4 Nondestructive Evaluation

Prior to and/or after the tests, small regions of the decks were evaluated using nondestructive evaluation methods used in the prior part of the project. NDE methods used were GPR and UST. The goal was to try to capture how well the CIP concrete was bonded to the existing concrete prior to testing, and to see if there were any changes during the test. Figure 9.44 shows the location of NDE on each specimen.

In PBJ-FP1 and FP1R, a 2-ft by 4-ft grid was located over the northwest portion of the link slab. The edge was along the main crack and adjacent to the DIC region so that the grid would not interfere with the DIC processing. NDE data were collected prior to the first test and after the final test in FP1, and after the final test in FP1R.

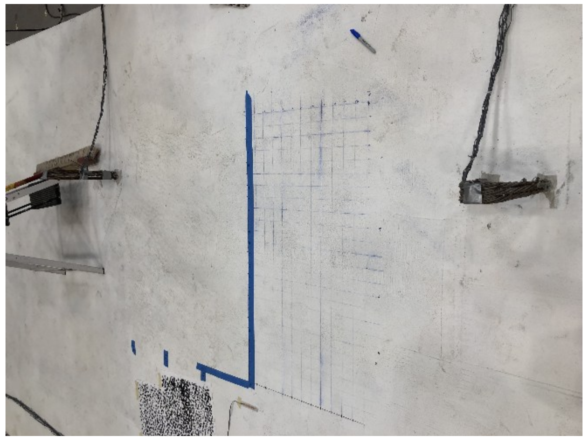

Figure 9.44. Locations of NDE grids.

9.6 LOADING

Application of the loads to the specimens was done by applying forces to each girder to induce positive bending that in turn would result in negative bending in the link slab. One actuator was used in each span. For all tests expect PBJ-OP1R, a spreader beam was used to transfer the loads to each individual girder. The location of the actuators between the girder lines and the relative load in each actuator varied between individual tests on a specimen. This allowed for exploration of multiple loading scenarios that effectively considered that the position of live (truck) loads in the bridge is not consistent or symmetric in an actual bridge. In referring to loads, the girder labels indicated in Figure 9.2 are used. The girders run east-west and are referred to as the north girder line or the south girder line. Spans are referred to as the east spans or west spans. For PBJ-OP1R, the specimen consisted of a single girder line, so the actuator applied load to the girder without the spreader beam.

Table 9.7 provides a summary of the load patterns applied to each test. The pattern **Name** is used in discussions in this report and provides an indication of the girders that have the largest loading in the load pattern. The **ID** is preliminary naming that corresponds with file naming and is included for clarity to future users of data files. The final column shows an **Icon** that is used in presentation of results to help clarify what load pattern is shown. The icons have large arrows that indicate the girder loads that are increasing during the full duration of the test. Smaller arrows indicate locations where the load is held constant or significantly smaller (in the case of south girders for the north [N], northwest [NW], and northeast [NE] loading patterns).

For each test, the order of load patterns applied varied, as well as the maximum load in each actuator. Steel strain gages at the center of the link slab were monitored throughout the test to ensure yielding did not occur until desired. The maximum load applied in each pattern was determined by a combination of (a) avoiding yield (except final pattern), (b) avoiding significant differences in cracked stiffnesses of girders, and (c) considering time constraints on the lab testing schedule. A detailed summary is provided at the beginning of the experimental results for each specimen.

Table 9.7. Load pattern summary.

Name	ID	Description	Actuator Location	West Load	East Load	Icon
All	A	All spans/girders loaded equally	Center	Increasing	Increasing	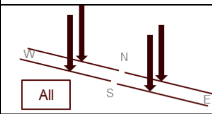
W	BW	Small loads in each span, west span increased thereafter	Center	Increasing	Small, hold	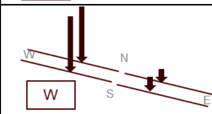
E	BE	Small loads in each span, east span increased thereafter	Center	Small, hold	Increasing	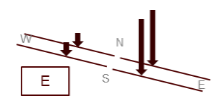
N	C	Actuators positioned over north girders, both spans loaded equally	North girder	Increasing	Increasing	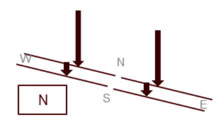
NW	DW	Actuators positioned over north girders, small loads in each span, west span increased thereafter	North girder	Increasing	Small, hold	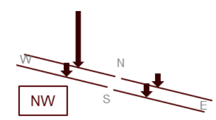
NE	DE	Actuators positioned over north girders, small loads in each span, east span increased thereafter	North girder	Small, hold	Increasing	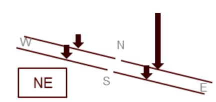
S	N/A	Actuators positioned over south girders, both spans loaded equally	South girder	Increasing	Increasing	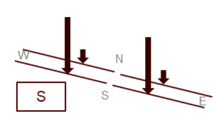
SW	N/A	Actuators positioned over south girders, small loads in each span, west span increased thereafter	South girder	Increasing	Small, hold	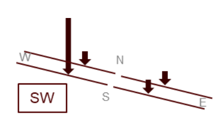
SE	N/A	Actuators positioned over south girders, small loads in each span, east span increased thereafter	South girder	Small, hold	Increasing	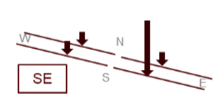

Control of loads during each pattern was based on the forces in the actuators to provide a consistent measure between all tests. However, during the loading, two key readings were monitored: (a) strain gages on the longitudinal bars, and (b) average rotation of girders.

The rotation at the ends of the girders was a calculated value from the LVDTs measuring the relative displacement of the flanges of the two spans. The rotation was calculated as:

$$\theta = \sin^{-1}\left(\frac{0.5\left(L_{top} - L_{bot}\right)}{L_{vg}}\right) \tag{9.1}$$

where θ is the average rotation of the girder ends; L_{top} is the change in length of the LVDT between the girders at the top flange; L_{bot} is the change in length of the LVDT between the girders at the bottom flange; and L_{vg} is the vertical distance between the gages.

The girder end rotations are key values that are used in the design of link slabs. Ideally, the control of loading would be to regular intervals of rotations to allow a direct comparison to design values. However, due to the simplistic loading provided by the actuators, the variability of stiffness throughout the test, and the variability of stiffness of one specimen relative to another specimen, tests were paused at specific load values due to practicality. That said, the rotations monitored during the tests played an important role in decision-making by allowing comparison of test rotations to values expected for typical TxDOT I-girder bridges. For example, the "hold" load in PBJ-FP1 asymmetric loading patterns was chosen because it was not only a reasonable interval but also resulted in an average girder end rotation of approximately the lower-bound rotation from thermal loads. Thus, a simulated scenario of having some thermal load plus a live load in just one span was achieved. Another example was deciding the final load pattern could be terminated once the rotation exceeded any practical design values, even if the link slab had not reached a true capacity in terms of strength of deformation. The rotations for service and strength load combinations are shown in Figure 9.45; details of these calculations are provided in Section 7.1. Design rotations are presented against a normalized girder flexural stiffness, EI/L^2, to efficiently compare values for a large set of girder sizes, spacings, and lengths.

During the testing, decisions were made based on comparing the experimental rotations to the service design values. There is a gap of data points between rotations of about 0.0025 to 0.0035 rad. The larger values are generally associated with the longest practical spans for each girder size. A breakdown of values discussed in Section 7.1 indicates that these are due to large rotations that exceed what many researchers recommend as an upper bound of live load rotations (0.00375 rad). In many cases, the larger service rotations may not be the most realistic demands. Thus, two limits are considered. The first is 0.003 rad, which is referred to as the upper-bound design rotation for most practical bridges. The second is 0.005 rad, which is referred to as the upper bound for the full range of potential I-girder bridges.

In addition to monitoring girder end rotation during each load pattern, several strain gages were monitored in real time to ensure the link slab reinforcement did not yield prior to the final test. The gages selected were typically the gages at the center of the continuous deck and located over the girders; gages between the girder lines and/or 4 in. off the center were monitored in the case of failed gages or questionable data.

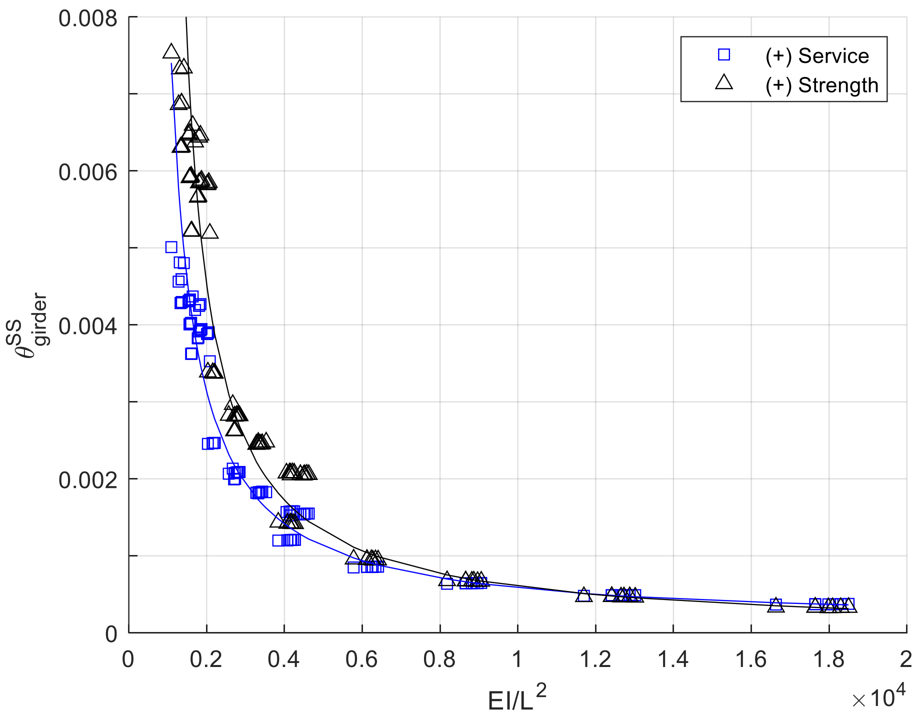

Figure 9.45. Girder end rotations for design of TxDOT standard I-girder bridges (only positive bending shown).

Loads were applied by a single actuator in each span. The west loading frame is shown in Figure 9.46(a). The load was transferred to each girder by a spreader beam, also shown in Figure 9.46(a). The R-bars were cut off in the load zone to provide a flat surface. A 12-in. × 24-in. × ¼-in. 70 durometer pad was placed beneath the beam on each girder to protect the beam from the roughened surface at the top of the girder.

(a) West loading frame

(b) East loading frame with spreader beam

Figure 9.46. Loading frame and spreader beams for application of loads to each girder.

9.7 PBJ-FP1 TEST SUMMARY

A detailed summary of the design of PBJ-FP1, the flush panel reference test, is provided in Section 9.2.1. Key features of the specimen are:

- Flush panels.
- CIP concrete bonded with tops of girders and PCPs.
- Link slab top steel of #4 @ 9 in. (same as deck longitudinal) with additional 5-ft long #4 bars centered between each deck longitudinal bar.
- North overhang detailed as traditional overhang.
- South overhang detailed as effective flange width for interior girder (vertical board present).
- No zip strip or other preformed crack on top surface.

Testing was conducted using a set of eight unique applications of loads. Details of the load pattern configurations are provided in Table 9.7. Table 9.8 provides a summary of the specific order and load magnitudes used for PBJ-FP1.

Initially, Pattern All-1 was applied, which is consistent with most prior experimental testing of link slabs. The actuator loads were specified to be the same in both spans. On the initial pattern, frequent pauses were made to avoid missing critical measurements because the rate at which crack widths would increase was unknown. For subsequent load patterns, larger force increases were used, and for some repeated patterns, measurements were taken only at peak loads.

Next, asymmetric loading was investigated. Both actuators were loaded to 40 kips, after which the east actuator was locked in place and the load increased only in the west (Pattern West [W]). A load of 40 kips was chosen since in Pattern All-1, it had provided a small amount of rotation.

To avoid unsymmetric girder stiffness in future tests, Pattern East (E) was done next with the objective of cracking the east girders a similar amount. In Pattern E, both actuators were loaded to 40 kips, but the west was then decreased to 35 kips so that the average girder rotation was approximately the rotation at the same point of Pattern W. Next, Pattern All-2 was done to quantify the stiffness of the specimen under symmetric loading with minorly cracked girders. Cracks were measured only at the peak loads.

Actuators were moved to be located over the center of the north girder lines. The spreader beams were still in place, so a small amount of load was being applied to the south girders. With this configuration, Pattern N, Pattern NW, and Pattern NE were applied. For simplicity, the non-main actuators were held at 40 kips in Pattern NW and Pattern NE. The maximum load was determined such that the loads did not exceed the maximum load that had been applied to individual girders in prior tests.

Finally, Pattern All-Yield returned the actuator to the center. Loads were applied well past that of prior tests so that the link slab reinforcement would be yielded. While the pattern took the test past reasonable design rotations, researchers desired seeing if additional cracking could be generated. Given the uncertainty of the sounds heard and the loads approaching the estimate yield moment of the girders, as well as the need to preserve the structural integrity of the girders for future tests, it was decided to load no higher. The load was reduced to 440 kips for documentation of girder damage and subsequent unloading.

Table 9.8. PBJ-FP1 load pattern and damage summary.

Pattern ID	Peak Load West, kips	Peak Load East, kips	Summary of New Damage
Pre-test	N/A	N/A	PBJ crack in south overhang and between girder
All-1	270	270	North overhang branched extension of pre-test crack
W	360	40	None
E	360	35	Secondary overhang cracks
All-2	100	100	None
N	160	160	Longitudinal cracks over north girder Diagonal cracks between girders
NE	40	180	Minor extension of diagonal cracks
NW	180	40	Minor extension of diagonal cracks
All-Yield	455	455	No new deck cracks; girder shear cracks

Damage during all load patterns applied to specimen PBJ-FP1 was limited to cracks. Figure 9.47 shows the crack patterns on the top and sides of the deck, with each subfigure showing the cracks at peak load of an individual pattern. Load patterns for which no new cracks formed are not shown. Red cracks are cracks that formed during the specified load pattern. Gray cracks had formed in previous load patterns or prior to testing. Girder cracking, when it occurred, is noted in the written descriptions here, but since damage is not relevant to the behavior and performance of the link slabs, details such as widths and crack maps are not included.

The main PBJ crack formed during curing of the concrete. The concrete was cast on a Thursday before a four-day holiday weekend closure of the lab, so the condition of the deck was not checked for several days. The crack was most pronounced in the south overhang and was barely visible in between the girders. The crack was located over the board where present. At the edge of the south overhang, the depth of the crack could be observed extending to the top of the board; it was not possible to measure the depth of the crack at other locations. In the north overhang, there was no board, but a notch was present in the bottom of the deck. Despite this notch, the main PBJ crack had a slight angle, starting near the north end of the board; this would ultimately be seen as the west branch of a branched main PBJ crack. In the weeks between casting concrete and testing, the crack width visibility was occasionally checked for crack growth. During this time, the crack expanded very slightly, becoming more pronounced on the south girder overhang where the board was present. On the north overhang, the crack remained barely discernible, with the crack angling to the west as it progressed from the outer edge of the north girder to the northern edge of the deck. The north overhang crack did not penetrate the full depth of the slab prior to testing.

Pattern All-1 loaded all girders equally until strain gages indicated the top deck steel was nearing the yield strain. At 15 kips, there was a slight extension of the west branch of the branched main crack in the north overhang. At 90 kips, the east branch formed on the branched main crack. No other new cracks formed. The maximum crack widths were observed in the southern overhang and at the center of the deck. The maximum measured crack width was 0.5 mm (0.0197 in.).

During Pattern W, no new cracks were observed in the deck. Toward the end of Pattern W, flexural cracks were observed in the west girders. The cracks were barely visible during the pause at 320 kips, but researchers suspected that they began to form around 300 kips when the load versus rotation response monitored in real time began to soften slightly.

In Pattern E, secondary cracks were observed in both overhangs, although the characteristics of the cracks in each overhang were distinct from each other. In the north overhang, the secondary cracks were diagonal and parallel to the branched main cracks, approximately 12 in. from the branched main cracks. The cracks intersected the main crack at roughly the center of the north girder line. On the south overhang, the secondary cracks intersected the main crack closer to the south edge of the south girder line. Near the edge of the girder, the secondary crack was diagonal, but for most of the overhang length, the crack was parallel to the main crack, with a spacing of approximately 6 in. This bottle shape of the crack is similar to cracks observed in the field between girders. The east girders developed limited flexure cracks, with G-SE having only small cracks on the inside face.

Researchers found it curious that the secondary cracks seemed to form under Pattern E but not Pattern W despite the patterns being essentially the same other than being mirrored. Future analysis of measured responses such as string pots and strain gages may provide some insight into this behavior. However, it is worth pointing out some subtleties in the documentation of the damage, particularly since the real-time monitoring of data and crack growth in girders during pauses indicated that creep was a factor during the pauses. In Pattern W, girder cracks were marked prior to unloading, at essentially the same time deck damage was documented and crack widths measured. During the Pattern E test, fewer team members were available to document damage, so girder and deck documentation did not occur simultaneously. Given that cracks were expected in the girders but not the deck, the girder damage was marked first, and then the deck cracks were measured. Based on this timeline, the formation was possibly impacted by creep. The secondary cracks in both overhangs that formed during this asymmetric load pattern did not seem to grow in width during subsequent loading patterns with symmetric loads in each span, providing further support that mechanics of asymmetric loading results in a unique stress state in the overhangs.

Three load patterns—Pattern N, Pattern NE, and Pattern NW—were done with loads primarily going to the north girders. Pattern N applied the same loads in the east and west spans. During the pause at 80 kips, cracks were observed that indicated a torsion response of the specimen, with diagonal cracks running between the interior edges of the girders away from the link slab region. This torsional behavior is reasonable given the location and magnitudes of the loads. Just prior to the pause at which the cracks were observed, there was an apparent change in the load-rotation stiffness of the south girders. The diagonal cracks are not of any concern, but notably, the cracks are longitudinal in the link slab near the interior edge of the north girders. These cracks perpendicular to the main crack are similar to cracks observed in link slabs on skewed bridges. To the researchers' knowledge, similar damage has not been seen in other link slab experimental tests. Thus, the data provided by this test provide unique data to the literature. During the asymmetric Pattern NE and Pattern NW, there was minor extension of the diagonal cracks, but otherwise no notable damage.

For the final test, Pattern All-Yield, the actuators were returned to the center. No new deck cracks were observed. The widths of the main and branched main cracks increased with increasing load, but the secondary overhang and torsion-related cracks had minimal, if any, increase in width.

During Pattern All-Yield, additional flexural cracks were observed in the girders, with the length of prior cracks extending and the length of the cracked region expanding. At 360 kips, shear cracks were first observed in the interior ends. Researchers believe that these cracks occurred slightly before 360 kips based on the change in stiffness of the real-time monitored responses and the lack of other new damage. By the end of the load pattern cracks were observed in all but one girder.

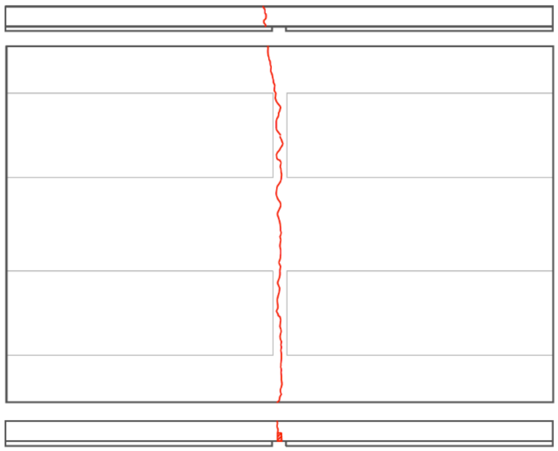

(a) Pre-test

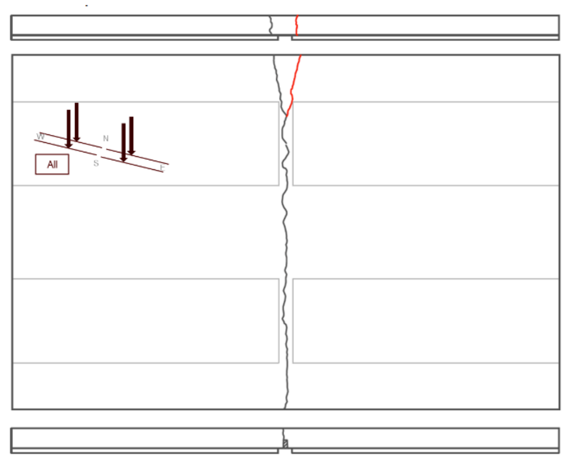

(b) Pattern All-1

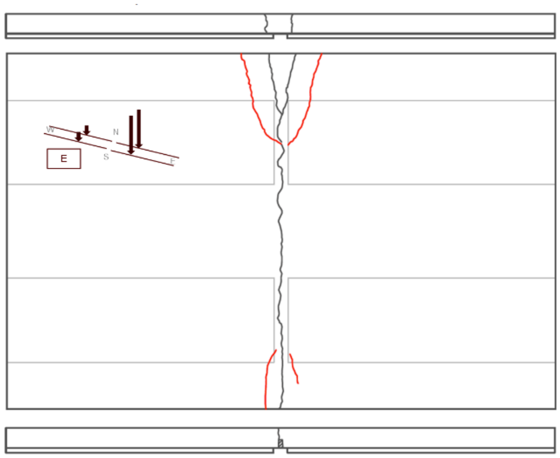

(c) Pattern E

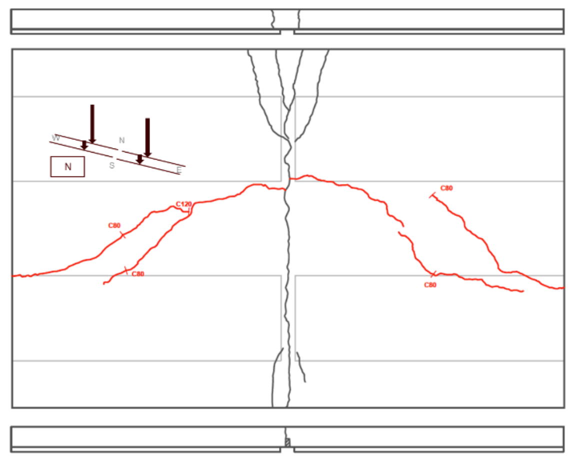

(d) Pattern N

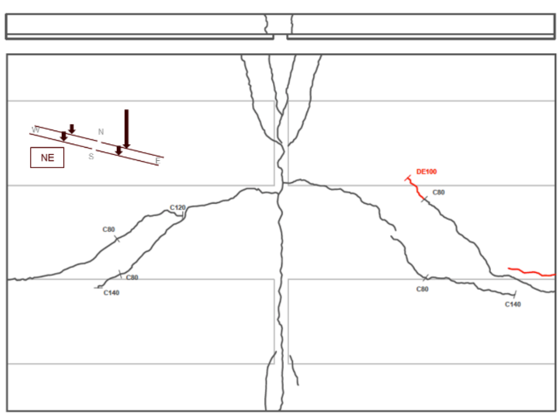

(e) Pattern NE

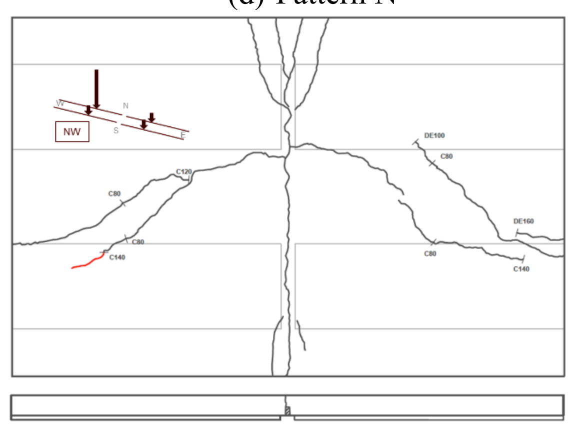

(f) Pattern NW

Figure 9.47. PBJ-FP1: Crack patterns at various stages of testing.

9.8 PBJ-FP1R TEST SUMMARY

Specimen PBJ-FP1R was a retrofit of PBJ-FP1. A detailed summary of the design is provided in Section 9.2.2. Key features of the specimen are:

- Flush panels.
- Top 4.5 in. of concrete removed from center 10 ft 6 in. of specimen.
- New CIP concrete debonded from existing over 3 ft 6 in. at end of girders; remaining new concrete is bonded with existing concrete and contains lap splice to existing reinforcement.
- South half has same reinforcement as PBJ-FP1 (#4 @ 9 in. with additional #4 bars between each longitudinal bar).
- North half has same reinforcement as north half, but the supplemental bars are elevated such that only 1.75-in. cover is provided).
- No zip strip or other preformed crack on top surface.

Testing was conducted using a set of 10 unique applications of load patterns. Details of the load pattern configurations are provided in Table 9.7. Table 9.9 provides a summary of the specific order and load magnitudes used for PBJ-FP1R.

In general, consistency with the prior test (PBJ-FP1R) was considered in determining load sequence and maximum load for each pattern. This includes similar increments of force for pauses. In some sense, a consistent force can be thought of as a proxy for consistent live and thermal loads on a simply supported beam. However, given differences in stiffness of girders between tests (uncracked on FP1 initial patterns and cracked on all FP1R patterns), direct comparisons could not be made. The major difference between loading FP1 and FP1R was that loads for a specific pattern were generally higher in FP1R tests. This is due in part to the greater flexibility of the link slab but was also a result of not being concerned about inducing unsymmetric cracked stiffness of girders (girders were cracked at the beginning of tests).

Pattern All-1 was applied to a peak load of 320 kips in each actuator. Initially, pauses were made every 20 kips to check for damage. Once several cracks had been documented, increments were increased to 40 kips.

In asymmetric loading Pattern W and Pattern E, both actuators were loaded to 40 kips and then the nondominant span was held at 40 kips. This was a slight change from FP1 loading, in which a consistent rotation was achieved to determine the exact load of the nondominant actuator. The maximum loads for each asymmetric pattern were significantly larger in FP1R than in FP1 due to the fact that there were no concerns about the extent of cracking (girders had seen this load in the FP1 Pattern All-Yield test).

Actuators were moved to be located over the center of the north girder lines. The spreader beams were still in place, so a small amount of load was being applied to the south girders. With this configuration, Pattern N, Pattern NW, and Pattern NE were applied. Initially, Pattern N applied a small amount of load to provide a comparison to the FP1 test with the same loading. In applying Pattern NW, care was not taken to avoid loads higher than previously applied, leading to additional cracking in the northwest girder. Thus, Pattern NE was taken to similar loads, and Pattern South (S), Pattern Southwest (SW), and Pattern Southeast (SE) were added to crack girders a similar amount for future tests. Due to logistics of the lab testing schedule, the south pattern suite was applied after Pattern All-2, which was intended to apply loads such that the deck reinforcement yielded. However, Pattern All-2 had not yielded when the maximum load for the loading frame was reached.

Table 9.9. PBJ-FP1R load pattern and damage summary.

Pattern ID	Peak Load West, kips	Peak Load East, kips	Summary of New Damage
Pre-test	N/A	N/A	None
All-1	320	320	Offset cracks on both sides of north girder line and west side of south girder line; additional transverse cracks in north half; north transition zone transverse cracks
W	440	40	Minor extension of shear and flexure cracks in west girders; limited new girder cracks
E	40	440	Minor extension of shear and flexure cracks in east girders; limited new girder cracks
N	180	180	Diagonal and longitudinal cracking
NW	280	40	Diagonal and longitudinal cracking; extension of existing and formation of new girder flexure and shear cracks
NE	40	270	Diagonal and longitudinal cracking; extension of existing and formation of new girder flexure and shear cracks
All-2	440	440	Offset crack at end of southeast girder
S	120	120	Diagonal and longitudinal cracking
SW	255	40	Diagonal and longitudinal cracking; extension of existing and formation of new girder flexure and shear cracks
SE	40	275	Diagonal and longitudinal cracking; extension of existing and formation of new girder flexure and shear cracks

Damage during all load patterns applied to specimen PBJ-FP1R was limited to cracks.

Figure 9.48 shows the crack pattern from all load patterns. Load patterns for which no new cracks formed are not shown. Girder cracking, when it occurred, is noted in the written descriptions here.

Unlike PBJ-FP1, PBJ-FP1R did not have any cracks at the start of testing. Pattern All-1 loaded all girders equally until 320 kips. Cracks were first observed during the pause at 60 kips, with changes in monitored response suggesting the cracking occurred at slightly smaller loads. The cracks were primarily located over the ends of the girders and can be classified as offset cracks.

On the south half of the deck, the initial crack was located over the end of the southwest girder. Throughout Pattern All-1, or subsequent Pattern W and Pattern E, this crack grew in width; a similar crack over the end of the southeast girder did not form until Pattern All-Yield, although it occurred as a similar load as the initial offset crack. In the overhang, an additional crack formed about 1–2 in. west of the original crack (observed at 120 kips in Pattern All-1).

On the north half of the deck, the initial crack was located over the end of the northwest girder. At increasing loads, additional transverse cracks formed at various distances from the longitudinal center of the specimen. None of these additional cracks were located within the continuous deck region but rather were located at over the end of the girder or farther away from the continuous deck. Generally, the cracks were transverse, with some having portions that were diagonal leading to merging with other cracks. At higher loads (240 to 280 kips), transverse cracks formed in or near the transition zone where the new reinforcement was spliced with existing reinforcement. The cracks just outside the transition zone were located at approximately the location of the termination of the longitudinal deck steel in the original deck.

Between the girder lines, the south half had a single crack on the west edge of the continuous deck region (same distance as over the south girder line). In the north half, two cracks were located on the west side of the centerline, with a slight angle that led to them merging with the south half crack at the transverse center of the specimen.

At 280 kips in Pattern All-1, a longitudinal crack formed along the southeast panel edge near the eastern edge of the retrofit concrete. This aligned with the location of a similar crack in the existing deck that had formed under torsional demands in the PBJ-FP1 tests. Researchers expect that the crack in FP1R was due to similar behavior given that the southeast girder was slightly stiffer (less cracked) than rest of the girders, resulting in less deformation.

During Pattern W and Pattern E, no new cracks formed. Crack width measurements were taken at several increments of higher load during Pattern W for comparison to other tests. For Pattern E, cracks were measured only at the peak load. In both asymmetric patterns, there was a minor increase in shear and flexure cracks in girders, with some cracks growing in length. Additional cracks formed, with some located between previous cracks and others extending the range of cracking slightly. Cracks did not exceed hairline width. The crack extensions were marked at peaks loads.

In the suite of off-center loading patterns (N, NW, NE, S, SW, and SE), diagonal and longitudinal cracks formed similar to those in the equivalent tests in PBJ-FP1. In Pattern N, pauses were made to mark and measure cracks at intervals leading up to the peak. For other center loads, the cracks were measured only at the peaks. In NW, NE, SW, and SE patterns, cracks also formed on the bottom of the panels. Researchers believe this is due more to the magnitude of the loads than to any characteristics of the debonded retrofit; a more thorough analysis will be conducted in the future.

Girder damage was primarily new and extended flexure and shear cracks during the off-center loading patterns. The maximum flexure shear crack was 0.15 mm (0.0059 in.) in the northwest girder and 0.1 mm (0.0039 in.) in the other girders. Shear cracks were hairline cracks. During Pattern SW and Pattern SE, there was some minor cover spalling at the top underneath the point of load application. Upon close inspection, it was clear that this was a bearing failure where the spreader beam tilt resulted in load applied to the aggregate sticking up at the edge.

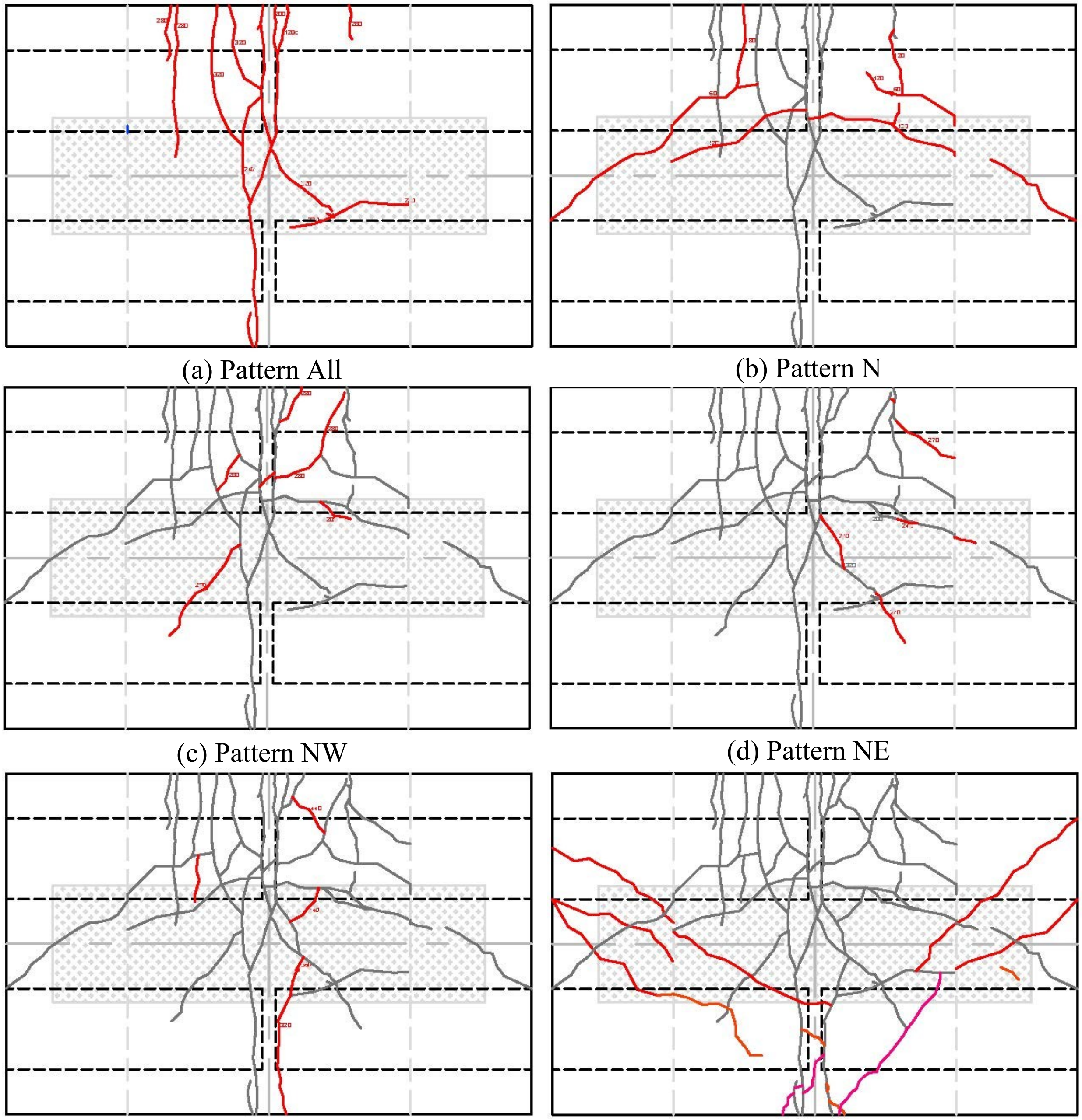

(a) Pattern All (b) Pattern N

(c) Pattern NW (d) Pattern NE

(e) Pattern All-Yield (f) Pattern S, SW, and SE

Figure 9.48. PBJ-FP1R: Cracks for all load patterns.

9.9 PBJ-OP1 TEST SUMMARY

Specimen PBJ-OP1 is the offset panel detailing reference test. A detailed summary of the design is provided in Section 9.2.3. Key features of the specimen are:

- Offset panels (1.5 ft from end of girders).
- CIP concrete bonded with tops of girders and PCPs.
- Link slab top steel is #4 @ 9 in. (same as deck longitudinal); no supplemental top steel.

- Link slab bottom reinforcement is #4 @ 9 in. Between panels, bars are spliced with dowel bar extensions from PCPs.
- Bottom reinforcement is included over the north girder, but not the south girder.
- North and south overhangs are detailed the same.
- Chamfer on bottom of deck runs transverse to the full width of the deck.
- No zip strip or other preformed crack on top surface.

Details of the load pattern configurations are provided in Table 9.7. Table 9.10 provides a summary of the specific order and load magnitudes used for PBJ-OP1.

Pattern All-1 was applied to a peak load of 180 kips in each actuator. A pause was made at 20 kips to check for damage, at which time cracking was observed. Cracks were measured at 40 kips and subsequent 40-kip increments. The final pause was at 180 kips, where the load was stopped because the strain gages neared the yield strain. Patterns W-1 and E-1 loaded the primary span to 280 kips, with the secondary span held to 40 kips. Pauses were made at 40-kip increments for documentation of cracks.

In the asymmetric load suite, Pattern N was paused every 20 kips for documentation. The test was stopped just short of 100 kips (96 kips) due to increasing strains and the goal of avoiding yield prior to final testing. In Pattern NW and Pattern NE, both spans were loaded to 40 kips. Then the secondary span was locked and the primary span was loaded in 40-kip increments up to 160 kips.

For PBJ-OP1, an additional suite of asymmetric load patterns (NW-2, NE-2, W-2, and E-2) were completed that had not been done for PBJ-FP1 or PBJ-FP1R. In these, the primary girders were loaded to the same load as in the similar load patterns (NW-1, NE-1, W-1, and E-1), but the secondary girders did not apply any load. This was done to collect data for comparison to finite element models, which have a simplified loading involving only loading the primary span for the pattern. In the second suite of asymmetric patterns, pauses for documentation were made only at the peak.

During Pattern All-Yield, loading was paused at 40-kip increments to document damage. Loading was terminated at 430 kips because one of the strain gages indicated a significant spike in strain and there was cause for concern for the extent of flexure cracking in one of the girders.

After Pattern All-Yield, an additional east pattern, Pattern E-Yield, was applied. The objective was to collect additional data on the behavior under asymmetric loading of the spans for comparison to models, specifically at higher rotation than achieved in Pattern E-2. The east pattern was selected over the west pattern because of the configuration of the Optotrak target layout. A maximum load of 430 kips in the east girder ensured load in girders did not exceed that applied during Pattern All-Yield.

Table 9.10. PBJ-OP1 load pattern and damage summary.

Pattern ID	Peak Load West, kips	Peak Load East, kips	Summary of New Damage
Pre-test	N/A	N/A	No cracks observed
All-1	180	180	Offset (west) main crack over interior flange of girders and between girder lines; south overhang branched main cracks; north overhang offset crack
W	280	40	None
E	40	280	D-shaped crack on west side between girder lines
N	96	96	Diagonal cracks
NW	160	40	Secondary crack on east side of north overhang
NW-2	160	0	None
NE	40	160	Secondary crack on west side of north overhang
NE-2	0	160	None
W-2	280	0	None
E-2	0	280	None
All-Yield	430	430	East offset crack; cracks over southwest girder
E-Yield	0	430	No new damage

Figure 9.49 shows the cracks for all PBJ-OP1 load patterns. While there were no cracks present before testing, initial cracking occurred very early at a load less than 20 kips during the initial loading, Pattern All-1. The initial crack spanned the full width of the deck over the interior flanges of girders and between the girder lines. The crack angled inward at the center of the girders, crossing over the center of the link slab and continuing on the east side. On the south overhang, the crack presented as a portion of a branched main crack (angled near girder and transverse at edge). On the north overhang, the crack was an offset crack (primarily transverse). Both overhang cracks had a small branch or parallel crack adjacent to them. During the pause at 120 kips, another branched main crack formed on the south overhang, this time on the west side, at a distance farther from the center than the east branch crack.

During the initial asymmetric patterns, only one new crack formed. In Pattern E-1, a D-shaped crack formed on the west side of the link slab center (Figure 9.50). The D was not centered transversely, with the north leg over the girder flange and the south leg slightly north of the south girder edge. The transverse portion of the D was located over the edge of the panel. The crack was hairline at formation and fully closed after unloading. This was the first such damage observed in the experimental test but was similar to damage that was seen on one bridge in field evaluations.

In the suite of patterns with actuators located over the north girders, diagonal cracks formed between the girders along the full length of the deck, with the north end located at the link slab and the south ends located at the exterior ends of the deck. These cracks were first observed during Pattern N, with extensions and new cracks forming throughout the suite. In Pattern NW-1, a secondary crack formed on the east side of the north overhang. In the overhang, the crack was transverse, offset from the northwest overhang offset crack. Over the girder flange, the crack was diagonal and terminated at the offset crack near the center of the girder. The secondary crack was observed during the pause at 160 kips but is suspected to have formed at around 140 kips based on drop in a strain gage in the region. Given this relationship between formation of the secondary crack and the drop in strain, during Pattern NE-1, a similar crack was expected in the west side of the overhang following an observed drop in strain gage reading. However, at the peak load, a crack was not yet visible. Given that cracks had previously appeared during pauses, the peak load was held constant for an additional 15 minutes to see if the crack appeared, which it did. The crack eventually became visible at the edge of the deck, and then by the time documentation was completed, the crack extended to the center of the girder and met up with the offset crack. When viewing the full crack pattern, researchers noted that this secondary crack appeared to be a continuation of one of the diagonal cracks on the east side; the same was not true for the northeast secondary crack. Figure 9.51 shows the secondary overhang cracks.

During Pattern All-Yield, new cracks formed and significant widths were measured for existing cracks. The first new crack to form was an offset crack between the girder lines, located approximately 6 in. east of the center, which was farther back than the west offset crack. The crack angled toward the center near the girders, ending near the center of the girders where it converged with existing cracks. The crack was not visible at the beginning of the pause but had appeared by the time crack widths had been documented. At loads of 360 kips and higher, some additional new cracks formed near the end of the southwest girder; these cracks did not match any of the typical crack damage documented in the field. Loading was terminated at 430 kips because one of the strain gages had a large spike; the gage was located near the location of the offset crack (formed during the initial load pattern), which had grown to 2 mm (0.0787 in.) in width. On the north edge of the deck, the east offset crack branched into a longitudinal crack at the depth of the top reinforcement for approximately 1 in. before continuing as a vertical crack (Figure 9.52). After unloading, the 2 mm (0.0787 in.) wide crack had closed significantly.

Girders were checked for cracks only at the peak load in each pattern and at higher loads during the yield patterns. Some new flexure cracks formed underneath the load points and existing cracks extended. During Pattern W-1, the southwest girders developed horizontal cracks at the top and bottom interfaces of the web with the flanges; this spanned most of the region below the deck on the link slab end. During Pattern All-Yield, shear cracks formed on the interior ends of the girders between 320 and 360 kips; this was consistent with the development of the same cracks on the other ends of the girders during the same pattern for PBJ-FP1.

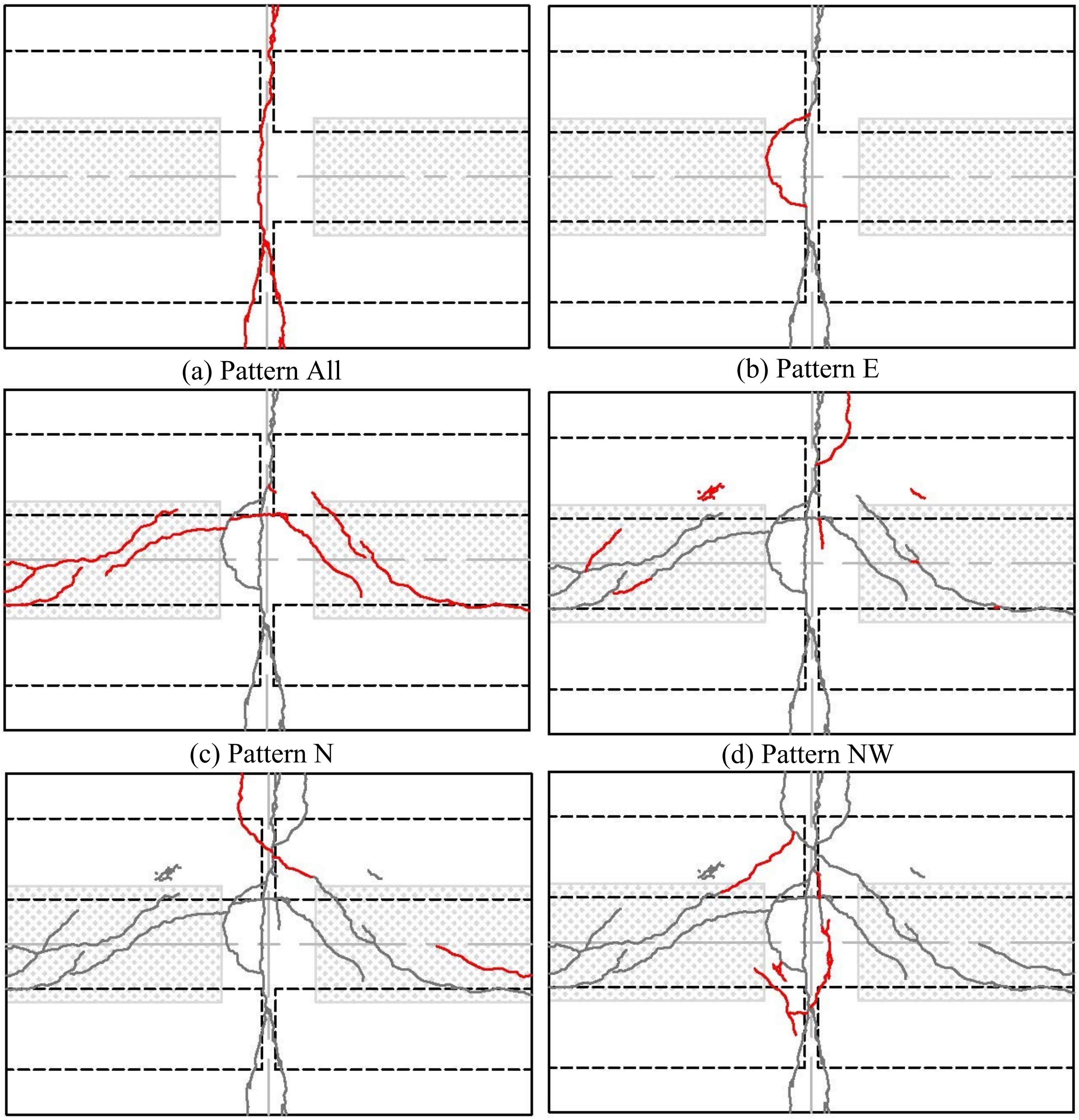

(a) Pattern All
(b) Pattern E
(c) Pattern N
(d) Pattern NW
(e) Pattern NE
(f) Pattern All-Yield

Figure 9.49. PBJ-OP1: Cracks for all load patterns.

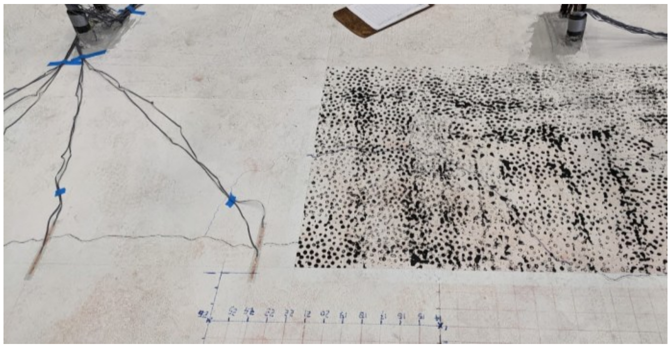

(a)

(b)

Figure 9.50. PBJ-OP1 D-shaped crack: (a) formed during Pattern E-1 and (b) similar damage observed in LUB4.

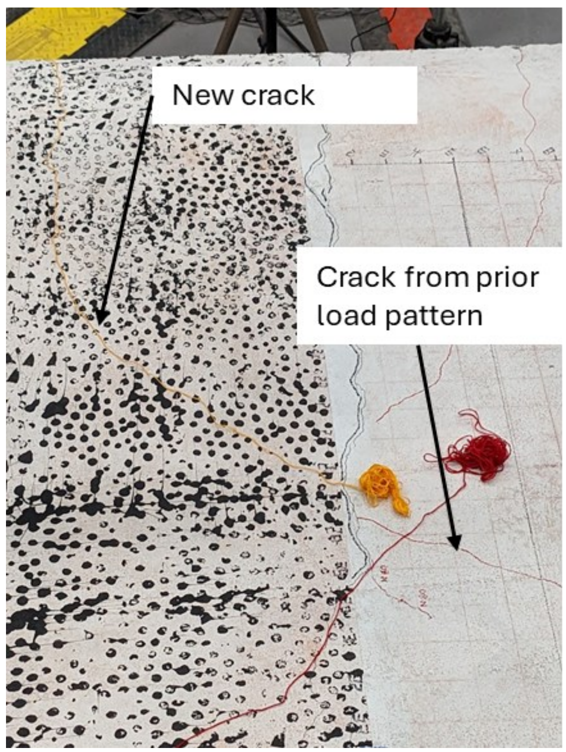

Figure 9.51. PBJ-OP1: North overhang cracks formed during Pattern NW-1 (red sharpie) and Pattern NE-1 (gold string) (right edge of speckled region is center of link slab).

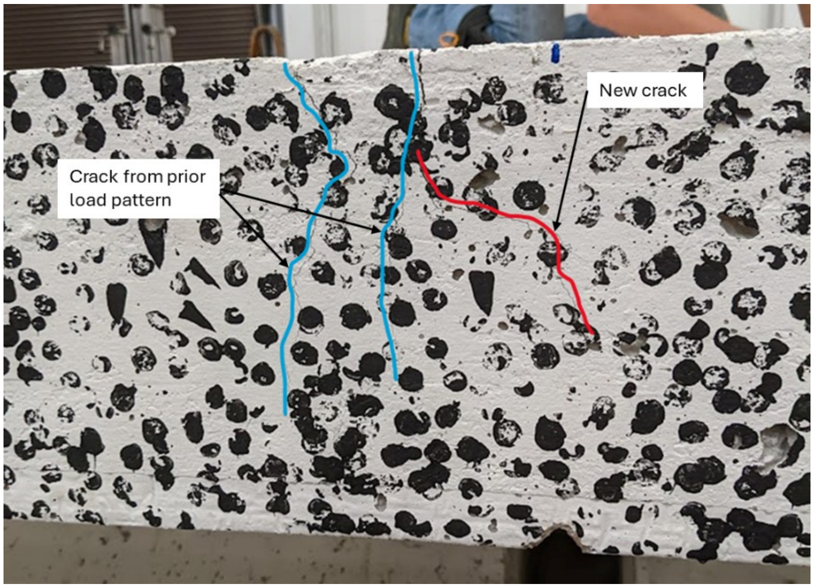

Figure 9.52. PBJ-OP1: East offset crack on north edge of deck at 430 kips in Pattern All-Yield (cracks at prior load steps shown in blue, new crack shown in red).

9.10 PBJ-OP1R TEST SUMMARY

PBJ-OP1R was a retrofit of test PBJ-OP1. A detailed summary of the design is provided in Section 9.2.4. Key features of the specimen are:

- Offset panels.
- North girder line only; separated from south girder line by longitudinal saw cut at the center of the specimen.
- Top 3.75 in. of concrete removed from the center 4 ft of specimens.
- Center 2 in. of longitudinal from OP1 test removed; new longitudinal bars spliced to existing bars.
- Transverse rebar removed and not replaced.
- New concrete is HPC bonded to existing concrete.
- No zip strip or other preformed crack on top surface.

Testing was conducted using a set of six unique applications of three load patterns. This was fewer patterns than other tests since there was only one girder line. Details of the load pattern configurations are provided in Table 9.7. Table 9.11 provides a summary of the specific order and load magnitudes used for PBJ-OP1R. A direct comparison of actuator loads to similar loads in other tests could not be made since the loads went to one girder rather than being spread between two girders, as in other tests.

Pattern All was applied to a load of 140 kips in each actuator, with pauses made every 20 kips to document damage. Patterns W-1 and E-1 loaded the primary span to 140 kips, with the secondary span held to 20 kips. The secondary span loads were one-half of what was used in other tests since a single girder line was used for PBJ-OP1R. Pauses were made at 20-kip increments for documentation of cracks. The two patterns were repeated as Patterns W-2 and E-2, with the secondary span actuator not applying load and a maximum load of 140 kips in the primary span. As with PBJ-OP1, this was done to allow simpler comparison to model results. Crack width measurements were made only at the peak loads.

The final test was Pattern All-Yield. As this was the final test before disposal of girders, the loads girders were pushed to larger rotations than done for prior tests. As a result, after a load of 220 kips (equivalent to 440-kip maximum load in tests on other specimens), target deformations were set because the actuator strokes increased without increase in the load. Pauses for documentation were made starting at loads of 140 kips and pauses made every 20 kips up to a load of 220 kips. After 220 kips, which had a girder rotation of approximately 6000 microradians, pauses were made at girder rotations of approximately 6500 and 6900 microradians.

Table 9.11. PBJ-OP1R load pattern and damage summary.

Pattern ID	Peak Load West, kips	Peak Load East, kips	Summary of New Damage
Pre-test	N/A	N/A	None
All-1	140	140	Cracks run full width of deck, with branched cracks in overhang
W-1	200	40	Minor crack extension over girder center
E-1	40	200	None
W-2	140	0	None
E-2	0	140	None
All-Yield	220*	220*	Offset crack over girder; branches of off overhang cracks

* After 220, loads did not dramatically increase, but test continued to maximize rotation in girders.

Figure 9.53shows the cracks for all load pattens applied to PBJ-OP1R. Existing cracks, including those in the south half of the deck, are shown in gray.

For Pattern All-1, the initial crack occurred in the south overhang, west of the centerline, with a slight angle consistent with cracks seen in overhangs for prior tests. A second crack formed in the south overhang at 40–60 kips and was located at the center over the girder, having a slight angle toward the edge of the deck. A secondary crack was observed in the south overhang, outside of the original crack, during the pause at 120 kips, extending to the girder center at higher loads.

On the north overhang, surface cracks formed later than on the south overhang. North overhang cracks on the deck surface were first observed during the pauses at 80 kips (crack east of centerline) and 100 kips (crack west of centerline). The north overhang cracks were parallel to the centerline, offset approximately the distance to the edge of the girder. The east crack in the north overhang angled to the center at the location of the girder edge, with this extension occurring at slightly higher loads than the initial crack; this was consistent with prior tests having cracks form at the edge and extend toward the girder center as loads increased.

The deck edges were visible only on the north edge because the south girder and deck from PBJ-OP1 blocked the view of the south edge. On the north edge, a diagonal crack was observed on the west end of the HPC region (Figure 9.54[a]). The initial crack was observed at 20 kips in Pattern All-1, with a more dominate adjacent crack appearing in the subsequent 40-kip pause. Further extensions were observed throughout the remainder of the pattern. A similar crack was observed at the east end at loads of 100 kips and 120 kips. Also at 120 kips, a horizontal crack was observed at the interface between the new and existing concrete.

During the east and west loading patterns, new surface cracks were limited to minor extension of existing cracks over the center of the girder. On the north edge of the deck, the diagonal crack on the west end and the horizontal crack extended during Pattern W-1.

During Pattern All-Yield, new surface cracks were observed. Over the girder center, an offset crack formed on the east side leading up to 220 kips. In the north overhangs, new branches formed off the branched main cracks. These were observed on the west and east sides at pauses of 180 kips and 220 kips, respectively. In the south overhang, the west secondary crack that formed in Pattern All-1 extended to the girder at a rotation of 6500 microradians. An additional crack formed on the east side at the same time.

On the edge of the deck, the damage at ends increased in the west end (Figure 9.54[b]). In the east end, cracks formed near the interface widened to a much smaller extent (Figure 9.54[c]). Figure 9.54(d) show the depth of the surface cracks on the north edge extended only a couple of inches toward the bottom of the deck, with many much shallower. This was a noticeable improvement of performance over that of PBJ-OP1, where the depth of the cracks was nearly to the bottom of the deck. New cracks were observed at a depth consistent with the existing deck, but since the concrete was HPC that slipped through the formwork, it was not clear if the crack was in the existing concrete.

Following testing, the girders were separated for removal from the lab. A partial-depth saw cut was made on both sides of the center. The HPC concrete was sufficiently debonded from the bottom of the deck so that the section of HPC between the saw cuts could be removed by prying with a crowbar. The remaining concrete was removed with a jackhammer, which caused sufficient damage. A post-demo autopsy could not provide useful information on the damage in areas not visible during the testing. One area that was useful to examine post-demo was the cross-section of the east girder, shown in Figure 9.55. A horizontal crack was seen mid-depth of the HPC.

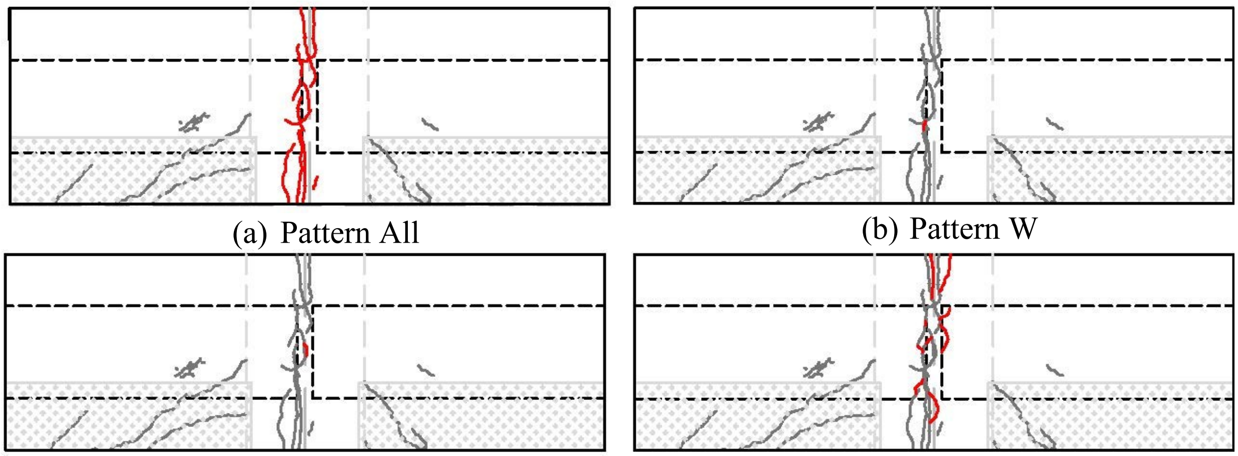

(a) Pattern All

(b) Pattern W

(c) Pattern E

(d) Pattern All-Yield

Figure 9.53. PBJ-OP1R: Cracks for all tests, with hatched region not tested (gray cracks are from prior test [PBJ-OP1]).

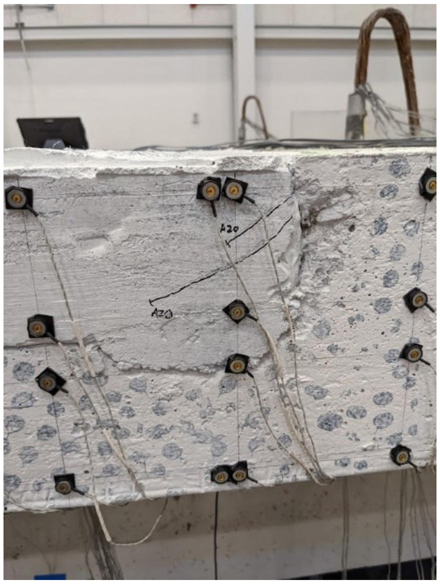

(a)

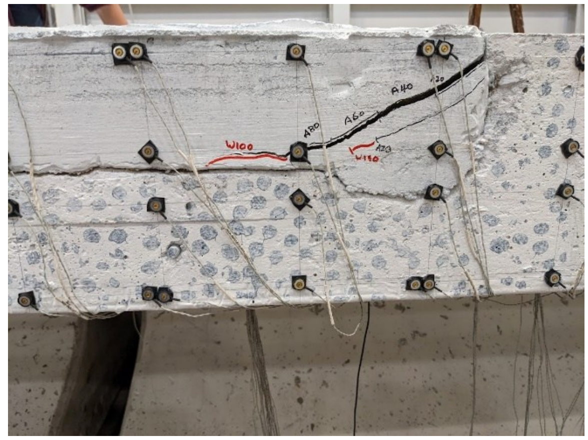

(b)

(c)

(d)

Figure 9.54. PBJ-OP1R—north overhang of HPC retrofit region: (a) diagonal cracks formed at west end during loading to 20 kips of Pattern All-1; (b) west end after all loading; (c) east end after all loading; and (d) shallow vertical cracks at center of slab after all loading.

Figure 9.55. PBJ-OP1R: Post-test demolition view of concrete over east girder showing horizontal crack at mid-depth.

9.11 PBJ-OP2 TEST SUMMARY

Specimen PBJ-OP2 is the offset panel detail modified to include debonding from the girder. A detailed summary of the design is provided in Section 9.2.5. Key features of the specimen are:

- Offset panels (1.5 ft from end of girders).
- CIP concrete debonded from the top of the girders (bonded to the PCPs).
- Debonded length is 3 ft from the ends of the girders.
- Link slab top steel is #4 @ 9 in. (same as deck longitudinal) with 10-ft long supplemental #4 @ 9 in. in the north half of the deck.
- Bottom reinforcement not provided over the girder lines.
- North and south overhangs detailed the same other than the top reinforcement differences.
- No chamfer on the bottom of the deck.
- No zip strip or other preformed crack on top surface.

Testing was conducted using a set of 12 unique applications of loads. Details of the load configurations are provided in Table 9.7. Table 9.12 provides a summary of the order and load magnitudes for PBJ-OP2.

Pattern All-1 was applied to a peak load of 200 kips in each actuator. A pause was made at 20 kips to check for cracks, with none identified. The first cracks were seen during the pause at 40 kips. Additional pauses for marking and measuring cracks were at 60, 80, 120, 160, 180, and 200 kips. Given that no new cracks were forming, the slower growth in strains compared to PBJ-OP1, and having tested beyond the Pattern All-1 peak load in PBJ-OP1, the pattern was concluded and loads removed. Patterns W-1 and E-1 loaded the primary span to 280 kips, with the secondary span held to 40 kips. Pauses were made at 40-kip increments for documentation of cracks. Then Patterns W-2 and E-2 loaded the primary span to 280 kips, with the secondary span without load. No pauses were made. The second suite of west and east loading was done for simplicity of comparison to models.

Patterns N, NW, and NE were conducted to be the same as PBJ-OP1 to provide a direct comparison between the two tests. A second set of NW and NE, with zero load in the secondary span, was skipped because it was not expected to provide meaningful data given the limited damage in the prior tests.

In Pattern All-Yield, the loading was paused every 40 kips from 80 kips to 400 kips, with a final step to 430 kips. Following Pattern All-Yield, a final Pattern E-Yield was completed to see if additional damage would be caused by higher asymmetric loads; pauses were made to look for cracks at 40-kip increments higher than 280 kips, with limited crack width recordings along the way.

Table 9.12. PBJ-OP2 load pattern and damage summary.

Pattern ID	Peak Load West, kips	Peak Load East, kips	Summary of New Damage
Pre-test	N/A	N/A	No cracks observed
All-1	200	200	North half—main crack with two secondary cracks South half—offset main cracks
W-1	280	40	Minor extension of one crack on north edge, east of main crack
E-1	0	280	Minor extension of cracks on top of deck
W-2	280	0	None
E-2	0	280	None
N	100	100	Diagonal cracks
NW	100	0	Minor extensions of diagonal cracks
NE	0	100	Minor extensions of diagonal cracks
All-Yield	430	430	North half—secondary/tertiary cracks
E-Yield	0	430	Minor extensions

No cracks were present before testing PBJ-OP2. The initial cracks were observed at the 40-kip pause during Pattern All-1. This was a slightly larger demand than for PBJ-OP1. However, given the stiffer girders of the PBJ-OP2 specimen, it was necessary to evaluate initial cracking relative to girder rotations. The cracks on the top of the deck after all load patterns are shown in Figure 9.56.

In the north half of the deck (more heavily reinforced), the initial cracks were a main crack at approximately the center of the link slab and a secondary crack over the west girder; these continued to extend at increasing loads. Unlike secondary cracks in previous specimens, this crack was a bit farther back from the end of the girder, spaced approximately 8–11 in. from the main crack. On the east, another crack formed, offset from the main crack by up to 18 in. in the overhang. Initially, this was thought to be another secondary crack, but ultimately during Pattern All-Yield, another crack formed between this crack and the main crack that was more appropriately called a secondary crack, with this crack being a tertiary crack. On the west side, a tertiary crack formed during Pattern All-Yield. The tertiary cracks were located in the overhangs only and had a slight angle, adjoining the secondary cracks near the exterior edge of the girders. Some additional short-length diagonal cracks connected the secondary and main cracks in the overhang.

In the south half of the deck, the initial crack was at an angle east of the centerline, eventually becoming transverse over the girder at higher loads and considered to be an offset main crack. Under increasing loads, the other offset main crack formed. In the overhang, only one main crack (west side) was present until Pattern All-Yield, during which the east offset main crack appeared and a secondary crack occurred at approximately the panel end on the west side. On the east side, the start of a secondary crack appeared but was only present a couple inches from the edge.

For both the north and south surfaces, limited crack extensions occurred during Pattern W and Pattern E.

Cracks on the edges of the deck are shown in Figure 9.57. During the asymmetric patterns, cracks extended slightly toward the bottom on the north edge but did not extend on the south edge, although the overall depth was greater on the south edge following Patterns All-1, W, and E. During Pattern All-Yield, minor increases in depth occurred on the north main crack (to 2 in. from bottom of deck), with larger extensions on the north secondary/tertiary cracks (up to mid-depth). No extensions were seen on the south edge during Pattern All-Yield; however, after Pattern E-Yield, the crack became full depth. The load at which this occurred was not known; however, it provides evidence that full-depth crack occurrence may be caused by asymmetric span loading.

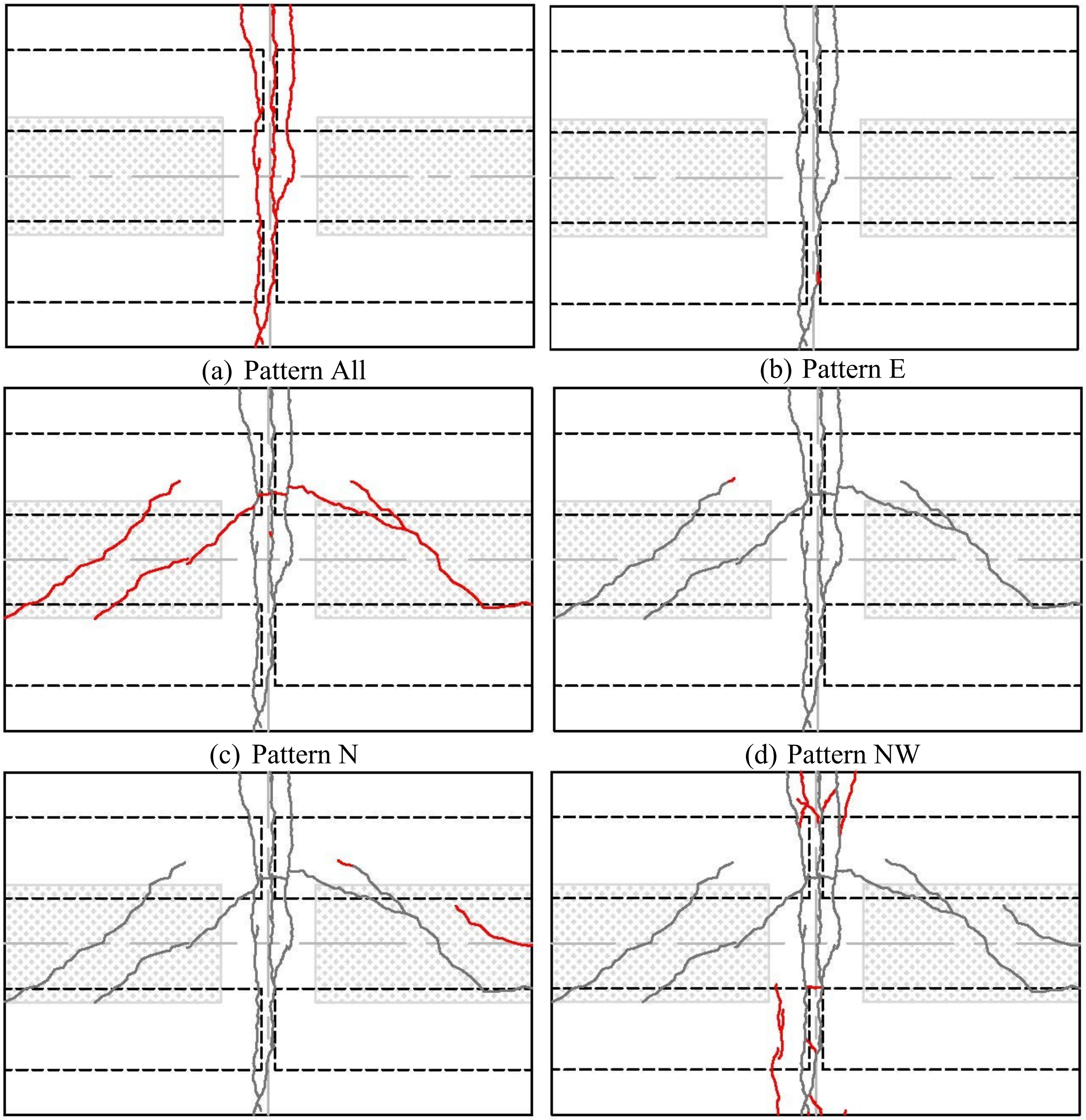

(a) Pattern All

(b) Pattern E

(c) Pattern N

(d) Pattern NW

(e) Pattern NE

(f) Pattern All-Yield

Figure 9.56. PBJ-OP2: Cracks for all load patterns.


(a)


(b)

Figure 9.57. PBJ-OP2: Deck edge cracks following Pattern All-Yield on (a) north half of deck and (b) south half of deck.

9.12 PBJ-CP1 TEST SUMMARY

Specimen PBJ-CP1 introduces the continuous panel detail and includes debonding from the girder. A detailed summary of the design is provided in Section 9.2.6. Key features of the specimen are:

- Panel continuous over ends of girder.
- CIP concrete debonded from the top of the girders (bonded to the PCPs).
- Debonded length is 3 ft from the ends of the girders.
- 1.5-ft long, 0.5-in. thick gap in bottom of haunch at ends of girders.
- Link slab top steel is #4 @ 9 in. (same as deck longitudinal) with 10-ft long supplemental #4 @ 9 in. in the full width of the deck.
- Bottom reinforcement provided over the north girder line.
- North and south overhangs detailed the same.
- No chamfer on the bottom of the deck.
- No zip strip or other preformed crack on top surface.

Testing was conducted using a set of 12 unique applications of loads. Details of the load configurations are provided in Table 9.7. Table 9.13 provides a summary of the order and load magnitudes for PBJ-CP1.

Pattern All-1 was applied to a peak load of 220 kips in each actuator. Pauses were made at 20 and 40 kips to check for cracks. The first cracks were observed during the pause at 60 kips. Additional pauses for marking and measuring cracks were at 80, 120, 160, 180, 200, and 220 kips. Patterns W-1 and E-1 loaded the primary span to 280 kips, with the secondary span held to 40 kips. Pauses were made at 40-kip increments for documentation of cracks. Then Patterns W-2 and E-2 loaded the primary span to 280 kips, with the secondary span without load.

No pauses were made. The second suite of west and east loading was done for simplicity of comparison to models.

In the asymmetric load suite, Pattern N was paused every 20 kips, beginning at 40 kips, for documentation. In Pattern NW and Pattern NE, both spans were loaded to 40 kips. Then the secondary span was locked and the primary span was loaded in 40-kip increments up to 160 kips.

In Pattern All-Yield, the loading was paused every 40 kips from 80 kips to 400 kips, with a final step to 430 kips. Following Pattern All-Yield, Pattern E-Yield was completed to see if additional damage would be caused by higher asymmetric loads. No loads were applied in the secondary span (west). Pauses were made to look for cracks at 40-kip increments higher than 280 kips, with limited crack width recordings along the way.

Testing time permitted additional tests at the completion of the planned loading, so additional load patterns were introduced to provide measured responses under different loading conditions. These patterns were not analyzed extensively, but collected data are available as part of the experimental data. The first additional pattern was Pattern All-AsymmUnload, in which the All pattern was applied to 280 kips in each actuator (no pauses). Typically, Pattern All unloaded approximately symmetrically in each actuator. For Pattern All-AsymmUnload, the unloading was asymmetric and more reflected that of unloading from Pattern E or Pattern W, with one actuator unloaded to zero while the other held at 280 kips. Once the first span was unloaded, the held force was removed. The second additional pattern was Pattern All-SmallCycles, in which Pattern All was applied until target rotations (as estimated from displacements measured in real time) were reached. Two cycles were applied to approximately 1000 microradians, followed by three cycles to approximately 2000 microradians. The goal of these were to see if the additional rotation increased the cracks under repetitive loading. During Pattern All-SmallCycles, no new cracks were observed, likely because the crack pattern had already been well established during the prior loading cycles.

Table 9.13. PBJ-CP1 load pattern and damage summary.

Pattern ID	Peak Load West, kips	Peak Load East, kips	Summary of New Damage
Pre-test	N/A	N/A	No cracks observed
All-1	220	220	Distributed main cracks full width; branch cracks in overhang
W-1	280	40	Minor extensions of prior transverse cracks
E-1	40	280	Minor extensions of prior transverse cracks
W-2	280	0	No new cracks
E-2	0	280	No new cracks
N	100	100	Longitudinal cracks along north girder interior edge; diagonal cracks between girders away from debonded region; new transverse crack on east side of link slab (over girder only); branch main crack on east side of north overhang extended to full depth
NW	160	40	Diagonal cracks
NE	40	160	No new cracks
All-Yield	430	430	Additional transverse cracks throughout link slab; girder cracks first observed at 320 kips (NW) and 360 kips (NE, SE, SW)
E-Yield	0	430	No new deck cracks; some additional girder cracks
All-AsymmUnload	280	280	No new damage
All-SmallCycles	Rotation based	Rotation based	No new damage

No cracks were present before testing PBJ-CP1.

Figure 9.58 shows the cracks from all load patterns.

The initial cracks were observed at the 60-kip pause during Pattern All-1 and continued to develop throughout. Given the extensive number of cracks, it is not practical to discuss the formation order of distinct cracks as was the case for other tests. The main transverse cracks closest to the center of the link slab could be considered offset main cracks because they were primarily located over the ends of the girders, without distinct cracks at the center of the link slab. Between the girders (over the panel), the location of the cracks varied a bit more. Secondary and tertiary cracks developed on both sides of the link slab, with more occurring over the east girders during Pattern All-1. However, once all testing was completed (following Pattern All-Yield), the crack pattern was generally symmetric. In the overhangs, the main cracks were branched main cracks, which had an angle to them. The secondary cracks in the overhangs were transverse cracks. At the conclusion of Pattern All-1, the cracks in the overhang in the center of the link slab had extended to near full depth. At 110 kips during Pattern All-1, noises were heard and were confirmed at the next pause to be some slight uplift in some of the bedding strips.

Given the different stiffnesses of the girders on PBJ-OP2 (uncracked) and PBJ-CP1 (cracked from PBJ-OP2 test), a comparison of the initial cracking could not be made based on the loads alone; however, monitored rotations confirmed that the initial cracking in PBJ-CP1 occurred at a larger rotation than for PBJ-OP2. Since both tests had the same debonded characteristics and the same reinforcement, this finding suggests that the gap in the haunch is beneficial to the performance. The larger number of cracks in PBJ-CP1 were also consistent with finite element models that indicated greater distribution of cracks when the gap is used.

During the asymmetric loading suite of Patterns W-1, E-1 minimal new cracks formed, primarily occurring as extensions of cracks observed in prior patterns. During Patterns W-2 and E-2, no new cracks were observed.

During the single-girder line loading suite of Patterns N, NW, and NE, the new cracks observed were primarily diagonal cracks between the girders; these cracks were consistent with the other specimens during other loading patterns. Longitudinal cracks formed along the south edge of the north girder line from the ends of the girders, extending along the length of the debonded region. These longitudinal cracks extended farther than in other tests, although researchers could not determine conclusively if this finding was directly the result of detailing of the specimen or indirectly influenced by the large quantity of cracks formed during the prior loading patterns of PBJ-CP1. Other crack formations were primarily extensions of preexisting cracks. Notably, new cracks did not form in the north overhang, but the east main branch crack did extend to full depth at a load of 80 kips during Pattern N, though the crack was only hairline and extended only approximately 0.25 in. from the edge of the deck on the bottom of the overhang.

During Pattern All-Yield, additional transverse cracks formed throughout the debonded region of the link slab. No other cracks were full depth at completion of testing, but many, particularly on the south edge, were nearly full depth. No cracks were observed on the bottom of the PCPs, other than those that formed during the north load suite.

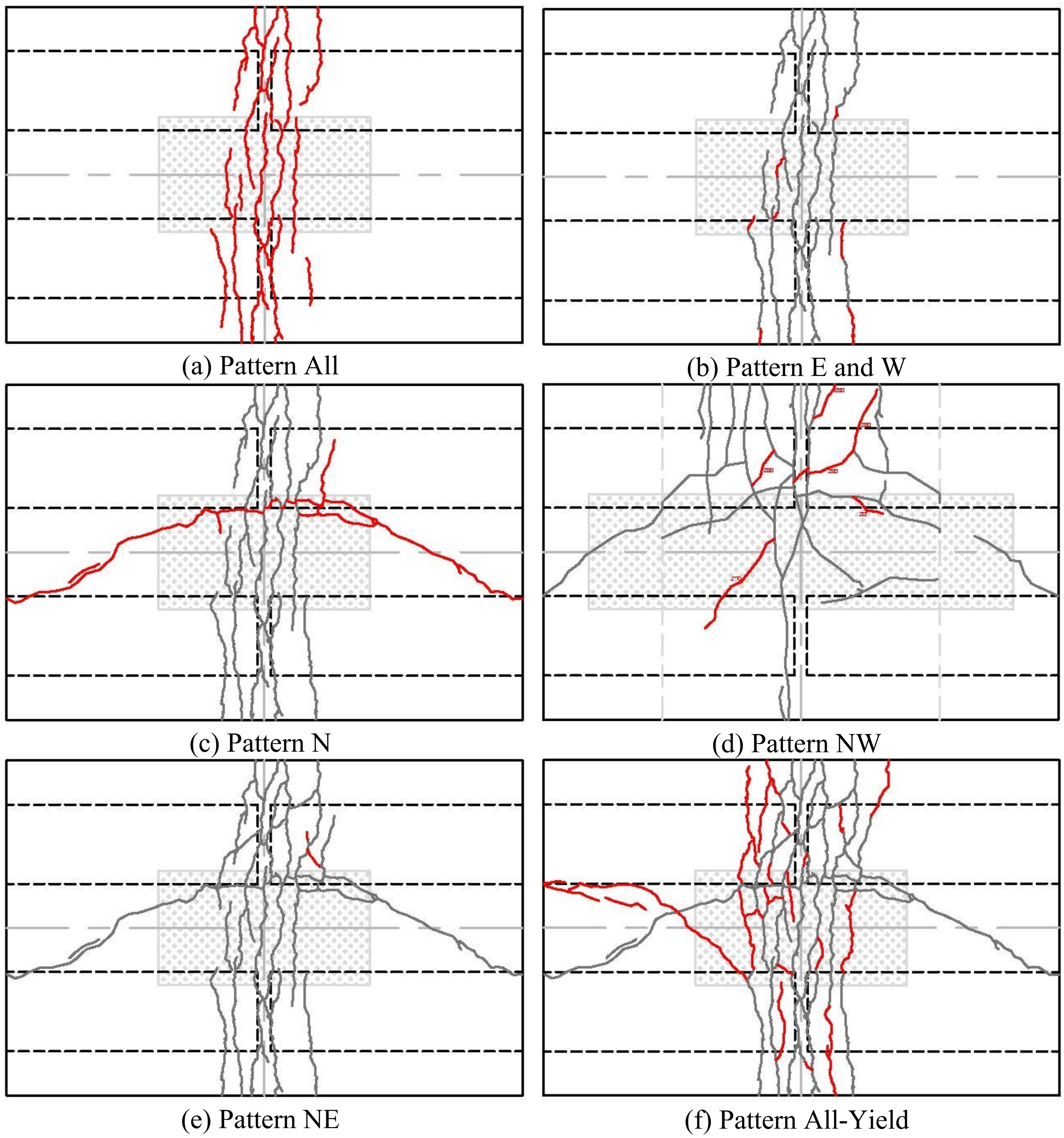

(a) Pattern All (b) Pattern E and W

(c) Pattern N (d) Pattern NW

(e) Pattern NE (f) Pattern All-Yield

Figure 9.58. PBJ-CP1: Cracks for all load patterns.

9.13 SUMMARY

Six full-scale experimental tests were conducted to investigate the performance link slabs constructed using (a) current TxDOT flush panel (PBJ-FP1) and offset panel (PBJ-OP1) details, (b) retrofits (PBJ-FP1R and PBJ-OP1R), and (c) proposed details using debonded link slabs (PBJ-OP2) and continuous panels (PBJ-CP1). The specimens were subjected to a series of load patterns to explore different loading conditions. Primarily, these were for positive bending (top of link slab in tension); however, PBJ-OP2 and PBJ-CP1 did pickup tests in which the ends were lifted with a crane to induce negative bending (bottom in tension). During each test, pauses were made to document the formation of cracks and measure crack widths.

This chapter presented details of each individual specimen design, construction, and loading patterns applied, as well as summaries of observed damage, generally presented in the form of crack maps. Analysis of measured responses from instrumentation installed on the specimens was presented in Chapter 5.

The first test, PBJ-FP1, uses one of two standard details used at the time of this research project. Partial-depth panels are flush at the continuous deck region, with separation provided only by a ¾-in. board. Through application of several load patterns, damage was replicated as what is observed in the field. Crack widths were measured for future comparison to girder end rotations. Key observations from the FP1 test include:

- The main crack formed at the center of the continuous deck during curing of the concrete. The crack was more pronounced in the overhang where a board was present. In the other overhang with full-depth CIP concrete, the main crack formed as one part of a branched crack. However, it was significantly less pronounced than in the south overhang or between the girders.
- Secondary cracks formed in the overhangs during asymmetric loading of the spans. In the north overhang (overhang detailing), the secondary cracks were parallel to the branched main cracks. In the south overhang (board detailing), the secondary cracks were bottle-shaped.
- Longitudinal cracks formed over the tops of the girders under asymmetric loading of the girders.

The second test, PBJ-FP1R, retrofitted the PBJ-FP1 test with a partial-depth DLS. The top 4.5 in. of concrete was removed (to the top of PCPs) and yielded longitudinal reinforcing steel replaced with new steel. The new concrete was debonded from the existing concrete. The DLS was expected to provide more flexibility than the original design. Key observations from the retrofit test include:

- No cracks formed during curing. Potential contributing factors that were different from FP1 include the smaller volume of concrete placed, the notched board being leveled where possible, and the roofing paper preventing absorption of water from concrete by the board.
- Transverse cracking was first observed at a rotation lower than what was estimated by models prior to testing.
- There were notable differences in the damage observed in the north and the south halves of the deck. The north half had some bars elevated, while the south had all bars the same depth as in current TxDOT flush panel details. The south-half damage was very similar to

FP1 damage, except for being over the girder end rather than at the center of the continuous deck. The north-half damage consisted of a greater number of cracks that were smaller width than the south.

- The offset center (secondary) transverse cracks resembled some observed damage seen in field visits during a prior portion of the research project. While those bridges did not have partial-depth DLSs, the findings of this test can provide insight into the potential for occurrence in the field. Further evaluation will be needed in the future.
- The multiple cracks in the north half of FP1R resembled damage seen in DLS tests published in the literature. There is a clear benefit to having a more flexible slab (attracts less force) and a mechanism for the formation of multiple cracks. The best method of achieving multiple cracks is something that will require further exploration.
- Transverse cracking in and near the transition zone indicated the need for detail revisions that can be explored through design and numerical modeling.
- The confirmation of the expected behavior of the partially debonded link slab indicates that there is value in providing a more flexible link slab. Other ways to achieve this include using a more flexible concrete material and/or providing a full-depth debonded link slab. Both designs are considered potential options for future tests.

PBJ-OP1 uses the other standard detail used at the time of this research project. Partial-depth panels are offset from the ends of the girders, resulting in a full-depth CIP region at the link slab. Key observations from the OP1 test include:

- Main cracks formed early on in the loading, suggesting that while the cracks did not occur during curing, shrinkage strains were present. In the south overhang, the crack was a branched main (west only). Elsewhere, the main crack was an offset crack located at the ends of the girders, although occurring only at the end of one span.
- Secondary cracks formed in the overhang under asymmetric loading. Additionally, a D-shaped crack formed between the girders during asymmetric load. The D-shaped crack was similar to a crack observed during field observations of LUB4.
- Crack widths in OP1 were larger than at similar rotations for FP1.

PBJ-OP1R retrofit the PBJ-OP1 test, replacing the top portion of the deck with HPC. Key observations include:

- Like previous tests, there were multiple branched cracks in the overhangs, with those converging to more central locations over the girders.
- There were slightly more cracks than in PBJ-OP1, with crack widths smaller at equivalent rotations within the range of design demands. This finding demonstrates the improved performance of the retrofit design using HPC.
- The north and south overhangs had significantly different responses, with the cracks forming much earlier in the south overhang. The south overhang cracks were angled,

similar to those in overhangs for prior tests. The north overhang cracks had less angle and were most similar to those observed in the PBJ-FP1R test, pointing to the HPC being debonded from the existing concrete in the north overhang.

- Real-time monitoring of select strain gages provided further evidence that the north and south overhangs behaved differently. Given that the cross-section was the same for both, it would be expected that the strains would be similar. However, in the south overhang, greater strains were measured in the top steel, while the north overhang had small strains in the top reinforcement, and the bottom reinforcement had much larger strains, suggesting the load was being transferred only by the bottom portion of the slab, not the HPC. Further analysis, including examination of the Optotrak data from the north edge, will help to further understand the behavior of the slab.
- During demo of the specimens, it was confirmed that the HPC was not well bonded to the existing concrete. The HPC utilized was not designed specifically for application in a deck rehabilitation, and mixing in small batches may have contributed to the poor bond. Link slab construction utilizing HPC should require contractor mockup to demonstrate bond is achieved in the field.

PBJ-OP2 tested the offset panel detail with debonding between the slab and the end 3 ft of the girder, with no bottom chamfer. The south half contained reinforcement from the current detail, and the north half contained twice as much top longitudinal reinforcement. Key observations are:

- The half of the deck with higher reinforcement had a main crack, with secondary cracks spaced at 8–11 in. The half with less reinforcement had offset main cracks at the ends of girders, with no secondary cracks.
- No new damage was observed under asymmetric span loading.
- Magnitude of cracks were larger than in PBJ-OP1 at similar rotations.

The final specimen, PBJ-CP1, used a continuous panel detail to eliminate the potential for cracks to form at discontinuities in the stiffness. The deck was debonded from the girders for the same length as PBJ-OP2, but with a gap in the bottom of the haunch for 1.5 ft at the ends of the girders. Key observations were a significant increase in the quantity of cracks.

10. EXPERIMENTAL TEST PROGRAM: DATA ANALYSIS

This chapter provides an overview of the experimental test program, details of loading for each test, and observed damage. Section 10.1 discusses data processing to clean and organize the data. Section 10.2 provides displacement profiles for the girders, and Section 10.3 discusses girder loads and end rotations. Section 10.4 presents an analysis of the crack widths measured, while Section 10.5 shows preliminary results for examining strains in the steel. Section 10.6 includes an introductory look at the data collected by the Optotrak motion capture system. Section 10.7 discusses effective link slab length, while Section 10.8 provides a chapter summary. A brief discussion of future work is included throughout the sections.

10.1 DATA PROCESSING

The data consist of data collected by a DAQ system and the Optotrak motion capture system. The DAQ consists of dozens of channels of data for strain gages, string pots, and LVDTs. The Optotrak collects three deformations for each of approximately 100 targets on each test. From each specimen, multiple files were used for the testing of different patterns on different days. These files were imported into MatLAB for cleaning, correcting, and calculation of key responses.

The first stage of data processing was to (1) synchronize the data between the DAQ and Optotrak systems to allow for use of the Optotrak data with other data, particularly forces; and (2) remove pauses for clearer presentation of the data. In synching such systems, it is necessary to consider a deformation since this is the only reading directly measured by each system. Typically, this is done with a vertical or horizontal deformation measured by a string pot. However, the unique nature of these tests meant that the string pots in the Optotrak view were producing small deformations. Instead, the rotation was used. For both systems, this was a calculated value. For the DAQ data, the rotation was calculated from LVDTs mounted between the girder flanges on the interior face of the girders. The calculations are described in Section 9.6. For the Optotrak data, LED targets were placed on the exterior face of the girders at the same location as the LVDT ends. The relative displacements between targets were used in the same manner as the LVDTs to calculate rotation. Rotation was calculated for each girder line (north and south). To synchronize the two systems, the rotations were plotted and used to identify the point where deformations initialized relative to the baseline readings. Timestamps were adjusted and Optotrak data were reduced to account for the different data collection frequency. The adjusted data were replotted to confirm the data aligned. After that, the pauses were identified and removed.

Phase 2 of the data processing was to remove data points that provided bad readings due to a sensor falling off or being bumped, or for strain gages that failed to provide readings.

Phase 3 of the data processing was to calculate any remaining basic values for the data that would be used in understanding the response of the link slabs. These calculations included (a) strains from LVDTs mounted on the bottom of the link slab where it was not practical to install strain gages, (b) individual girder rotations from string pots, (c) strains from the Optotrak targets, and (d) estimation of load in each girder.

The final task of data processing was to export the cleaned data and calculated data to new .csv files.

During data processing, data were frequently plotted to confirm tasks conducted correctly. A detailed summary of verification of the cleaning, synchronization, and validation of data is provided by Krajeck (2023) and is not included in this report.

An important clarification of the results is the synchronization of data between individual load patterns. The loading for each specimen was spread over multiple days, without the data collection occurring overnight. At the beginning and end of tests, some baseline data were collected; however, creep of concrete and rebound of the elastomeric bearing pads can result in slight differences in the values from the final data point in a load pattern to the first data point in the subsequent loading pattern. For traditional data, it is practical to consider the residual readings at the start of each test. However, for the Optotrak data, it is not possible to retain residual data between each test. In the context of the objective of this project to consider relative performance of different designs and quantify the way detailing impacts the response, these are trivial matters. However, should the findings or data be used to consider more detailed behavior under loading and unloading cycles, revisiting the raw data might be prudent.

10.2 DISPLACEMENT PROFILES

String pots were placed along the length of each girder to measure the vertical displacements. Displacements of the girders are not a quantity of interest in the understanding of the link slab response. However, an examination of the deformed shapes provides a validation that the system is responding as intended. Figure 10.1 shows the displacement profiles for PBJ-FP1 Pattern All-1 and Pattern E. Each subplot is a girder, with gray background showing the region with deck. Multiple lines are shown for each girder. These are arbitrarily selected at equal load increments throughout the test. After all tests are completed, displacement profiles will be examined to identify any unique behaviors. Finally, the displacements in each girder can be used to more accurately estimate the load in each girder. For Patterns All/E/W, the actuator is centered and should theoretically lead to one-half the load in each girder.

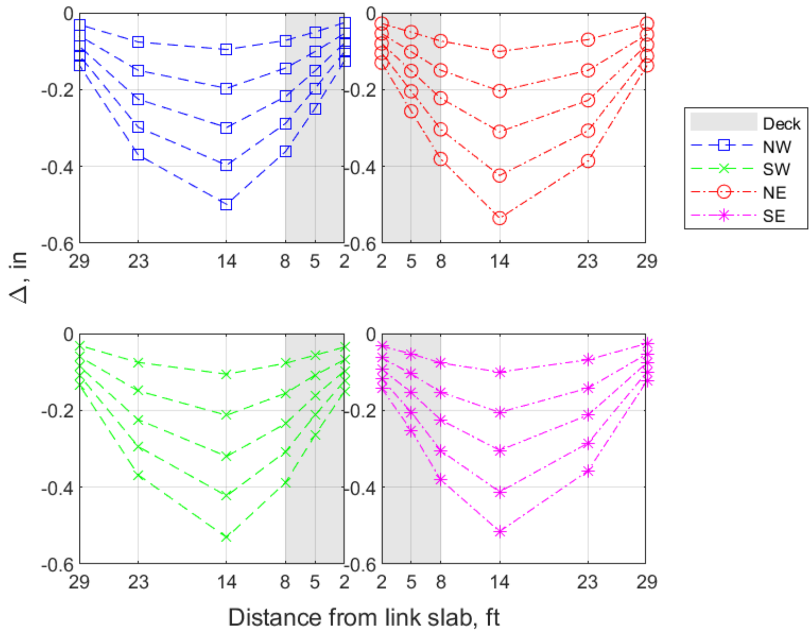

(a) Pattern All

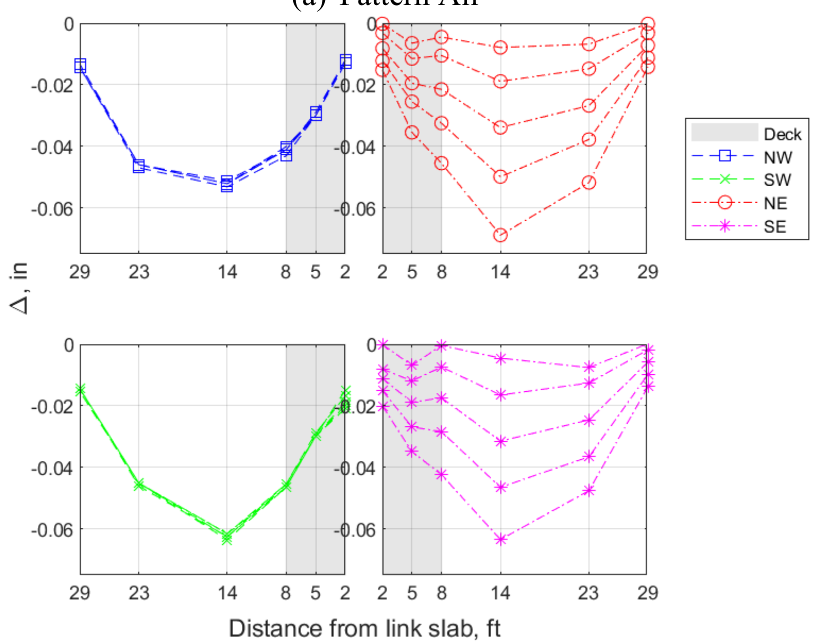

(b) Pattern E

Figure 10.1. PBJ-FP1: Girder displacement profiles at select loads.

10.3 GIRDER LOADS AND END ROTATIONS

The loads referenced in Chapter 4 regarding the control and pauses of loading patterns referred to the load in an actuator. Spreader beams were used to transfer the loads to individual girders. During testing and preliminary data analysis, loads were assumed to be equally distributed to the two girders for patterns with the actuator centered, and fully to the north or south girder lines for the north and south load suites, respectively. However, a more refined look at the individual girder loads is enabled by considering the deformation of the girders. String pots were located under the load point for each girder. A ratio of the girder displacements at each actuator was used to estimate the load in each girder.

During testing, preliminary girder rotations were considered as the average rotation between the girders in a single girder line. The rotation at the ends of the girders was a calculated value from the LVDTs measuring the relative displacement of the flanges of the two spans. The rotation was calculated as:

$$\theta_{girder,avg} = \sin^{-1}\left(\frac{0.5\left(L_{top} - L_{bot}\right)}{L_{vg}}\right) \tag{10.1}$$

where $\theta_{girder,avg}$ is the average rotation of the girder ends; L_{top} is the change in length of the LVDT between the girders at the top flange; L_{bot} is the change in length of the LVDT between the girders at the bottom flange; and L_{vg} is the vertical distance between the gages.

For symmetric load patterns, this is a reasonable assumption; however, with the asymmetric loading of some patterns and often asymmetric damage observed, it is valuable to consider the rotation of each individual girder. Two methods were considered to determine the rotation in individual girders. The first was to use the ratio of the girder displacements, as was done for the load distribution. The second was to use the string pots measuring displacement near the girder ends to determine the end rotation. The results were different from the two methods. To determine which was the more appropriate method, the Optotrak data were used as the targets on the south face of the south girders allowed for direct calculation of individual rotations; the Optotrak data could not be used overall since data were not available for the north girder lines. The first method using the ratio of girder displacement under load application was found to provide results similar to those from the Optotrak data; thus, this information was used to report the rotations for individual girders.

Validation of the method of determining individual girder loads and rotations is documented by Krajeck (2023). Included with this is an evaluation of load versus rotation for each individual girder. The response was found to be approximately linear, and for each specimen/load pattern combination, the stiffness of all girders was found to be similar. Given these findings, further exploration of load versus rotation response of the girders in not presented in this report.

10.4 MEASURED CRACK WIDTHS

Extensive crack widths measurements were taken throughout the tests as described in Section 9.6. The most basic analysis of the crack width data is to look at the maximum crack widths and compare them to acceptable crack widths. The maximum acceptable crack width limit is taken as 0.017 in. (0.043 mm), which is the crack width indicated in the AASHTO LRFD Section 5.6.7 commentary for Class 1 exposure. This is referred to as the AASHTO crack limit in presenting the results. Table 10.1 presents the maximum crack width for key load patterns of each specimen; values are presented in mm because this is the unit the cracks are measured in and the comparison of values in a table is easier with mm units than with inches. In general, the crack presented is the largest of all measured cracks. For PBJ-OP2, an exception is made to exclude values from the south overhang where a single large crack formed; these values are listed separately in the table as OP2 (SO).

For the existing TxDOT details, PBJ-FP1 and PBJ-OP1, both had maximum crack widths at or near the acceptable limit. Crack widths were larger for PBJ-FP1 in which cracking was concentrated to a single main crack for most of the deck width. Comparison of the existing design widths to those of the proposed designs using DLSs (PBJ-OP2 and PBJ-CP1) revealed that the crack widths were smaller and did not exceed the acceptable limit until the All-Yield pattern. The smallest cracks of the non-retrofit designs were observed in PBJ-CP1, which is consistent with the observed crack pattern having more cracks. This finding confirms that the debonded slab with gap demonstrates the desired performance of greater distribution of smaller cracks. Greater distribution of cracks also occurred in the partial-depth DLS used in the PBJ-FP1R retrofit specimen, with smaller maximum crack widths also observed, although generally these were larger crack widths than those for PBJ-CP1. Retrofit PBJ-OP1R utilized fiber-reinforced concrete and had the lowest overall crack widths, providing further support for the use of fiber-reinforced materials.

Table 10.1. Maximum observed crack width (mm) for key load patterns of each specimen.

Pattern	FP1	FP1R	OP1	OP1R	OP2	OP2 (SO)	CP1
All	0.5*	0.4	0.4	0.2	0.35	0.45*	0.25
West	0.4	0.3	0.35	0.2	0.25	0.4	0.25
East	0.4	0.35	0.4	0.2	0.3	0.45*	0.2
North	0.35	0.25	0.5*	–	0.25	0.15	0.25
NW	0.2	0.2	0.4	–	0.3	0.15	0.3
NE	–	0.2	0.5*	–	0.25	0.15	0.3
All-Yield	1.0*	0.55*	2.0*	0.35	0.95*	1.5*	0.45*

* Values that exceed AASHTO acceptable crack width limit.
– No crack for load pattern

For each specimen, it is desired to consider differences in the crack widths for different regions of the deck (overhang, over girders, and between girders) and at different distances from the center of the link slab, as well as the changes over time. Strains are presented as profiles along the width of the deck. Crack widths presented are those of the main cracks, which are the larger cracks measured. Additional crack widths are available in the published data set associated with this report. An example of the profiles is shown in Figure 10.2 for PBJ-FP1. The profiles are shown with the north edge of the deck on the right side of the figure. The horizontal position of each measurement is measured from the center of the deck, with positive values indicating north of center. Gray shaded backgrounds on the graphs indicate the location of the girders to support interpretation of differences in the crack widths in different regions of the deck (overhangs, over girders, and between girders). On each profile, the measurements at select pauses were reported. In general, the aim was to provide values as consistent girder rotations for all tests/patterns (e.g., 1000, 2000, and 3000 microradians); however, since the pauses for cracks were based on loads, there is some deviation from the intended values. The values reported are for the pauses nearest to the target values, as well as the peak load for the pattern presented. Horizontal lines are used to indicate the AASHTO crack width limit; values below the line are acceptable. For each test, crack width profiles are presented for the All, West, and All-Yield patterns; other patterns generally provide similar conclusions. In cases where valuable conclusions can be drawn from the additional patterns, figures are included here.

For PBJ-FP1, which is constructed with the current TxDOT offset panel detail, crack width profiles are shown in Figure 10.3. The shape of the crack width profiles is similar for all rotation demands and patterns. This is a common trend for most tests. For PBJ-FP1, the crack widths are larger between the girders and in the overhang than over the girders. Cracks exceed the AASHTO limit at demands greater than approximately 0.003. This finding suggests that flush panel details should be avoided on bridges with design girder end rotations exceeding 3000 microradians.

Figure 10.3 provides crack widths for PBJ-OP1, the design with the current TxDOT offset panel detail. Crack widths are generally the same shape for all patterns and rotations presented. The crack widths are larger over the girder than between the girders or in the overhangs; this is opposite that of PBJ-FP1. The widths are slightly larger over the north girder. While there are slight differences in the reinforcement (north girder has bottom bars over the girders, while the south does not), it is not believed that this influences the crack widths. Instead, the crack pattern shows that there is a single crack over the north girder line, while on the south side, the main crack in overhang is a branched main crack with the branch staring near the center of the girder line, so there are two locations for deformation to impact the crack width.

Comparison of the crack widths for PBJ-OP1 and PBJ-FP1 at similar rotations shows that the cracks are larger in the offset panel test for similar rotations; however, it is important to recall that the top longitudinal reinforcement is significantly different, with the offset panel having one-half the reinforcement of the flush panel deck.

PBJ-OP2 tested an offset panel detail with a DLS. Crack widths are shown in Figure 10.4. The primary difference of OP2 relative to OP1 was debonding. Comparison of the data for Pattern All for the two tests shows that the crack widths are considerably lower than those for at approximately 0.002 rad girder rotation. While the OP1 cracks exceed the crack width limits for at this demand, the cracks in OP2 do not, with the exception of the single crack in the south overhang (left side of figure). Excluding the single large crack in the overhang, the OP2 design provided significant reduction in the crack width, with the AASHTO limit being exceeded first during Pattern All-Yield at a rotation of approximately 0.005 rad.

PBJ-OP2 used two different reinforcement amounts for the top longitudinal reinforcement. In the south half, the reinforcement is that of the deck (#4 @ 9 in.) and is the same as that in PBJ-OP1. In the north half of the deck, reinforcement also includes supplemental bars between the main deck reinforcement, resulting in twice as much steel. Comparing the south (left) and north (right) half in Figure 10.4 reveals minimal difference in the crack widths, with the north cracks slightly larger for some profiles shown. In interpreting this finding, it is important to consider that the profiles present the crack widths along the main crack only. The crack pattern shows that there are two cracks in the link slab over the south girder and three over the north girder, so the overall distribution of cracks and their widths should be considered. Despite this, there is still limited impact of the additional reinforcement, but it is likely more an artifact of the limited distribution of cracking. On both halves of the deck, the cracks formed at the ends of the girders, suggesting the performance would be improved by including the haunch gap used in PBJ-CP1.

Figure 10.5 provides the crack widths for PBJ-CP1, which was a debonded link slab with continuous panel and a haunch gap. The reinforcement utilized supplemental bars between the main longitudinal reinforcement.

Crack widths for PBJ-FP1R are shown in Figure 10.6. This retrofit design used a partial-depth DLS, in which the top concrete was replaced and debonded from the bottom portion of the deck. As seen in the crack map for the specimen, a greater number of cracks occurs than in the original deck (PBJ-FP1). As seen in the crack width profiles, the crack widths are significantly smaller in the retrofit design. Crack widths are larger over the girders than in the overhang, which is different from PBJ-FP1 but consistent with PBJ-OP1. Two different reinforcement patterns were used in the deck. Both have the same reinforcement as PBJ-FP1, but in the north half (right side of figure), the supplement bars are raised to have lower cover. There are a greater number of cracks in the north half, and as seen in Figure 10.6, the crack widths are significantly smaller, never exceeding the AASHTO crack width limit despite reaching a girder end rotation of nearly 0.0065 rad. In the south half, the cracks were wider, but still significantly smaller than in the PBJ-FP1 test. The south half exceeded the AASHTO crack width limit at a rotation exceeding 0.005 rad.

Crack widths for PBJ-OP1R are shown in Figure 10.7. Crack widths are larger over the girder than in the overhang. The maximum girder end rotation applied to the specimen was approximately 0.0065 rad, at which time the largest crack was smaller than the AASHTO acceptable crack width limit.

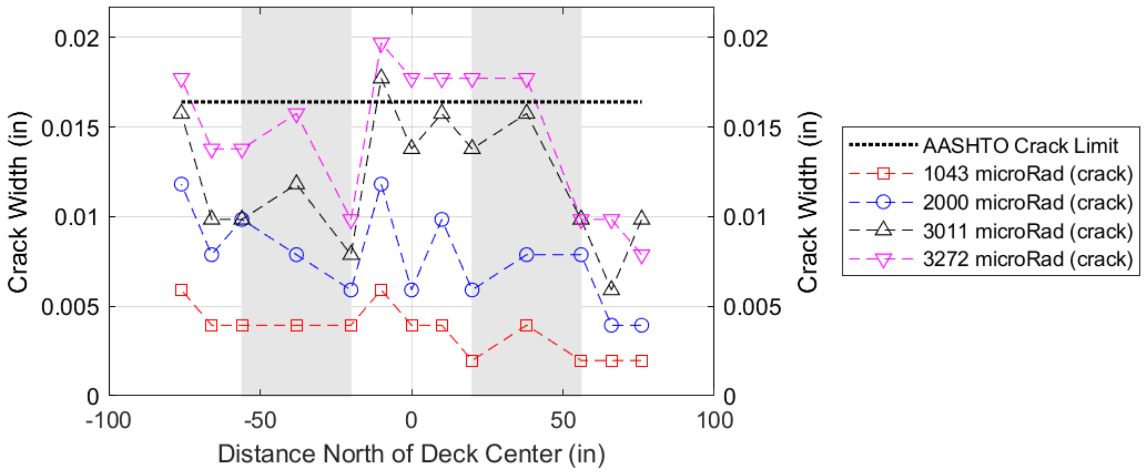

(a) Pattern All

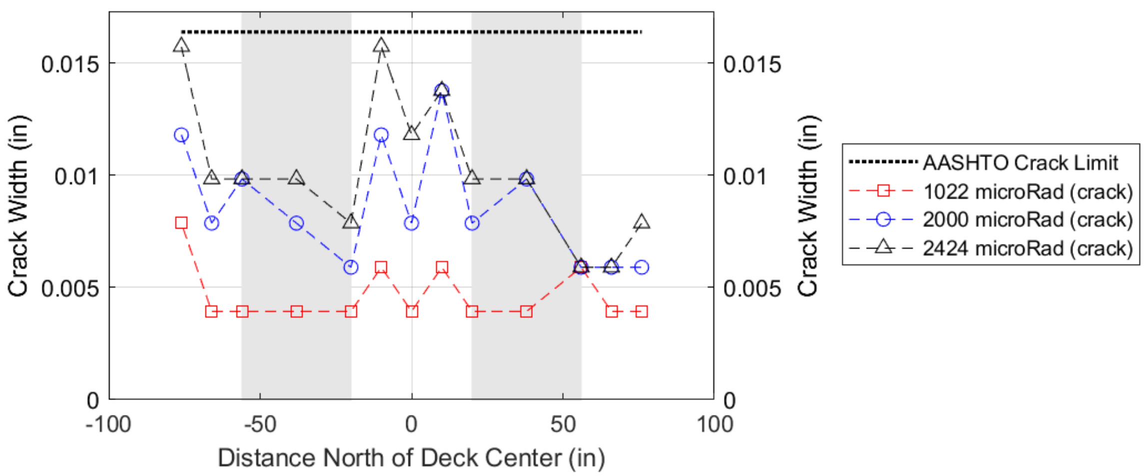

(b) Pattern W

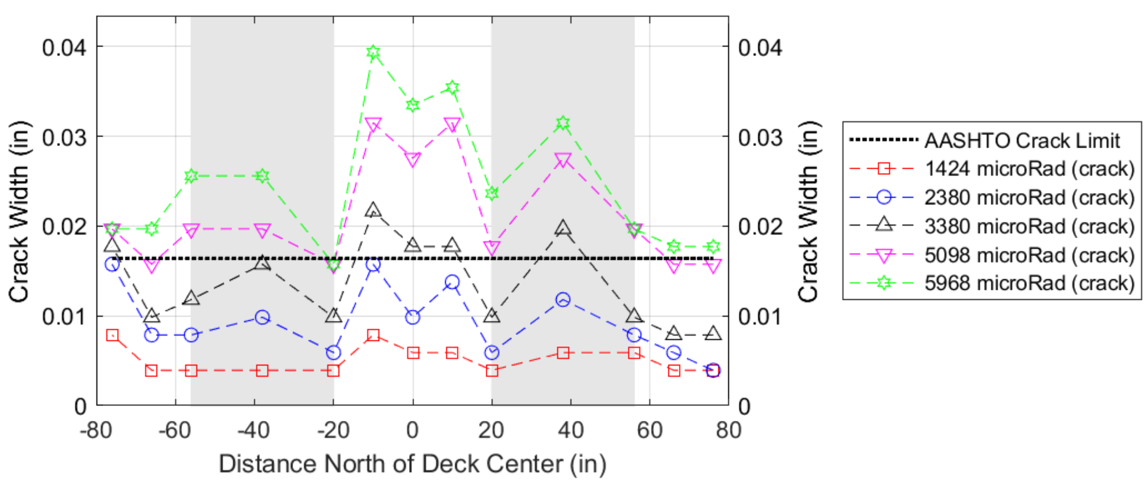

(c) Pattern All-Yield

Figure 10.2. PBJ-FP1: Crack width profiles for select patterns.

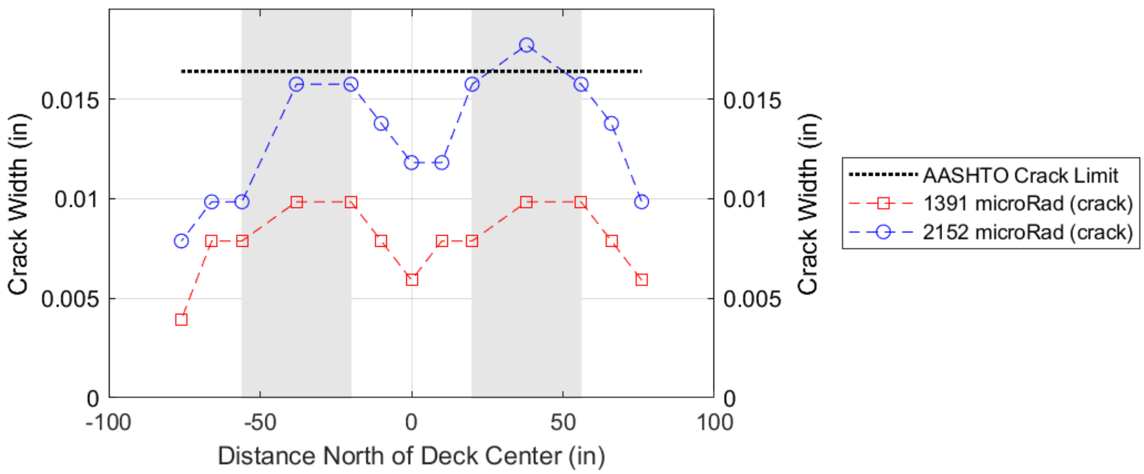

(a) Pattern All

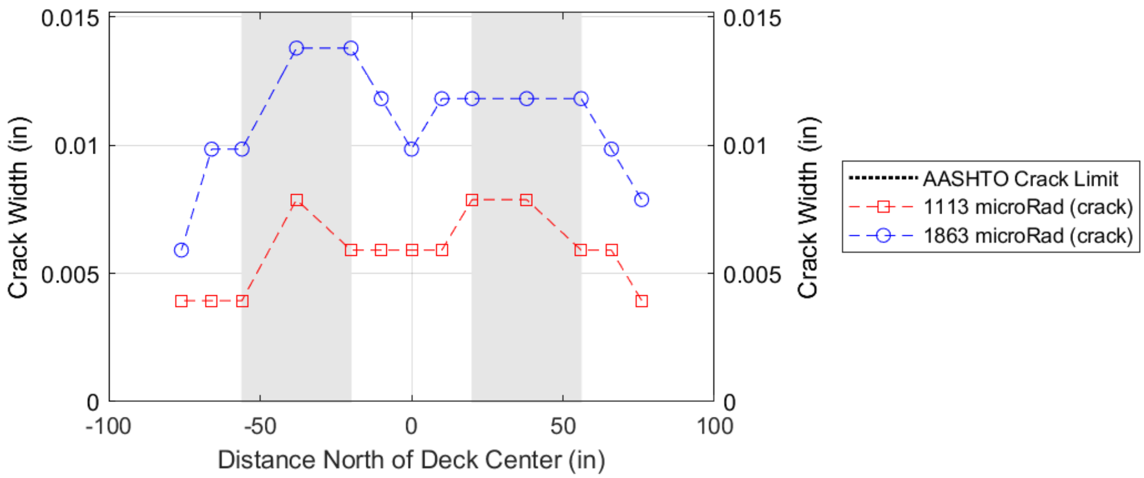

(b) Pattern W

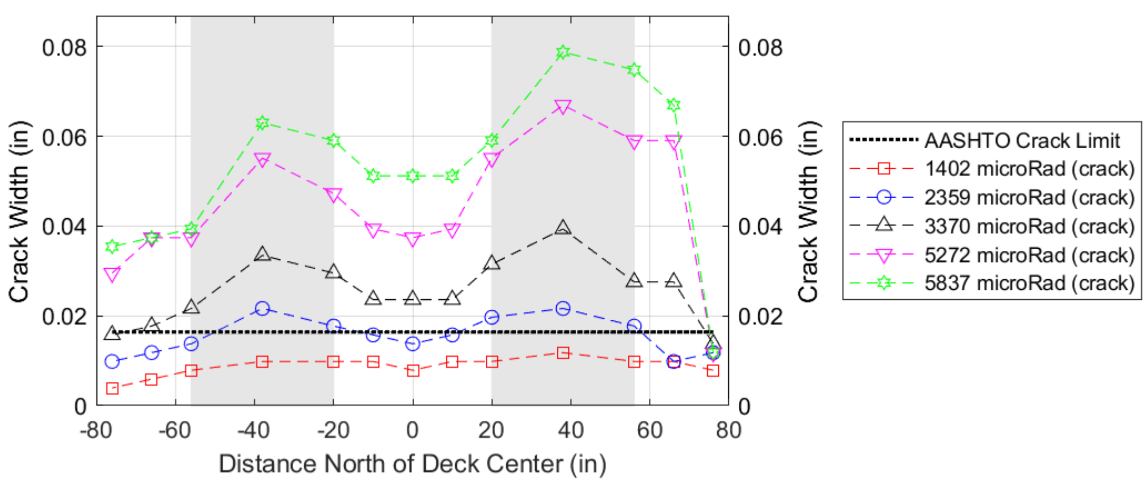

(c) Pattern All-Yield

Figure 10.3. PBJ-OP1: Crack width profiles for select patterns.

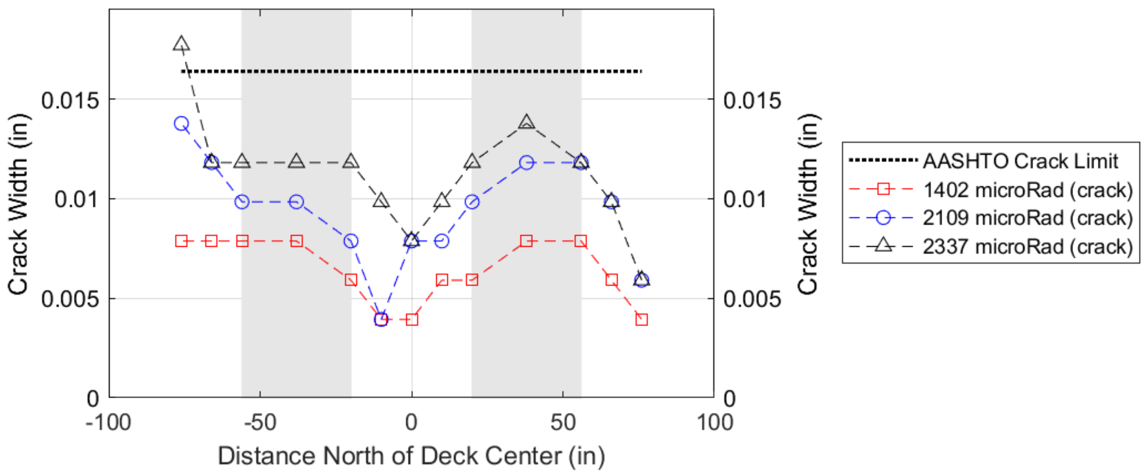

(a) Pattern All

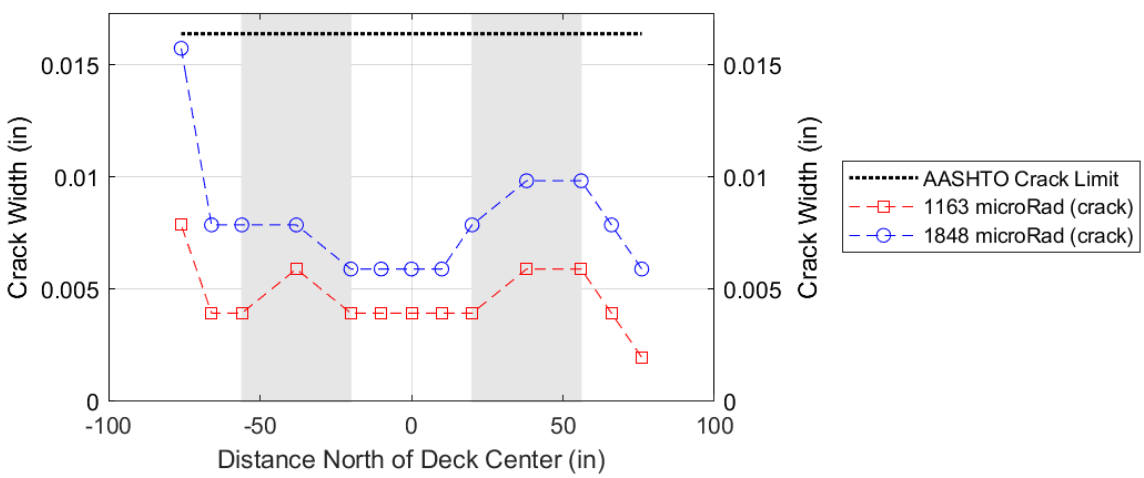

(b) Pattern W

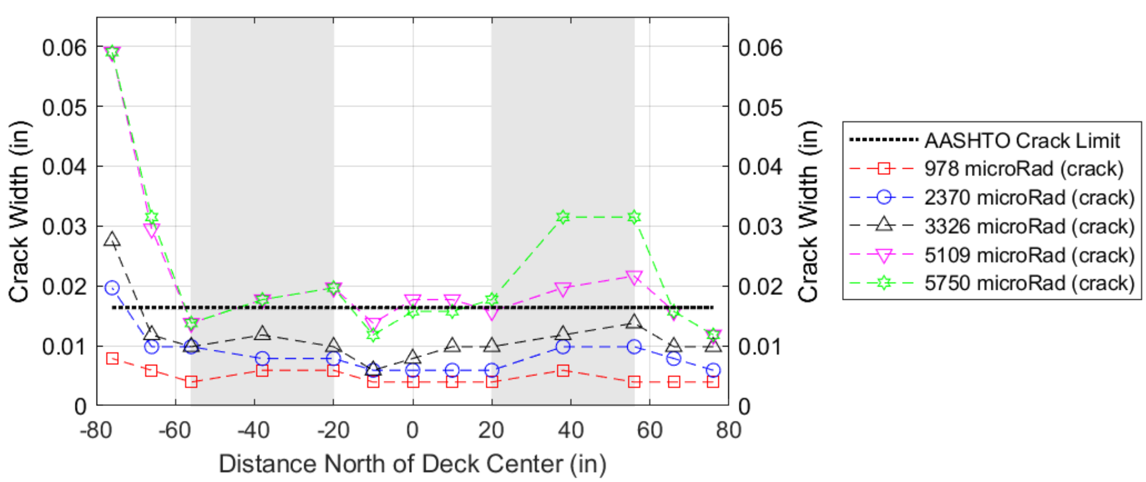

(c) Pattern All-Yield

Figure 10.4. PBJ-OP2: Crack width profiles for select patterns.

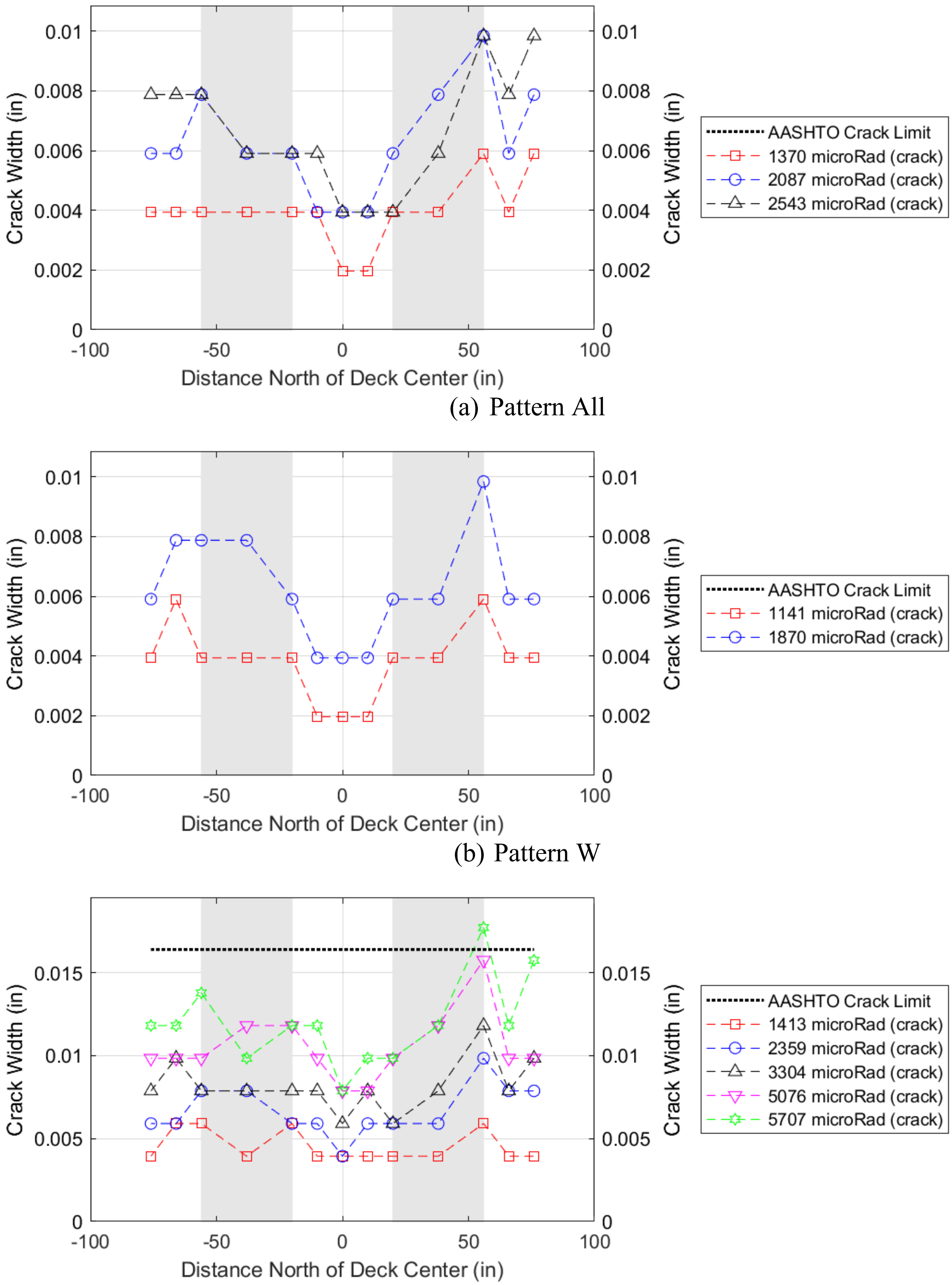

(a) Pattern All

(b) Pattern W

(c) Pattern All-Yield

Figure 10.5. PBJ-CP1: Crack width profiles for select patterns.

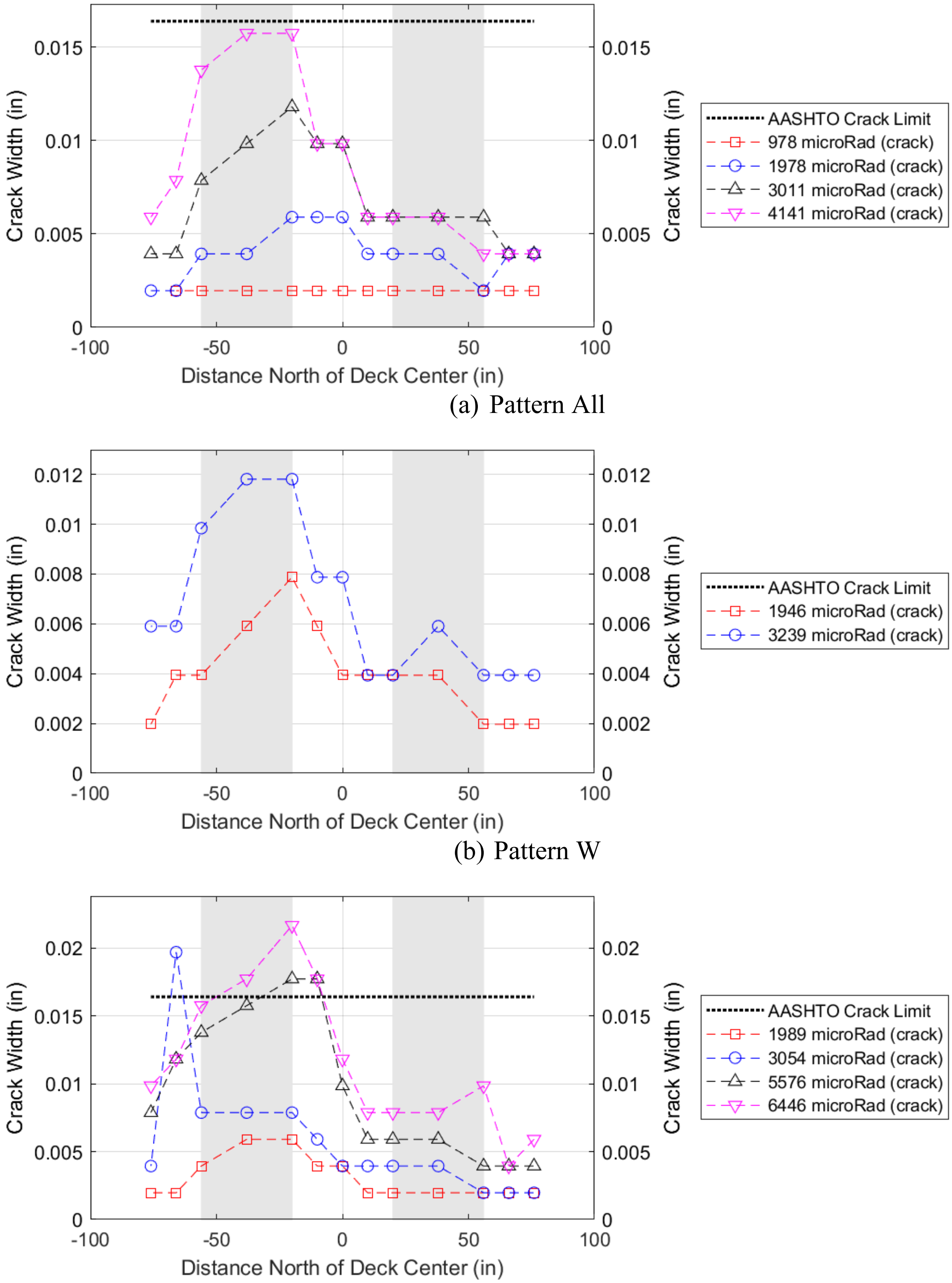

(a) Pattern All

(b) Pattern W

(c) Pattern All-Yield

Figure 10.6. PBJ-FP1R: Crack width profiles for select patterns.

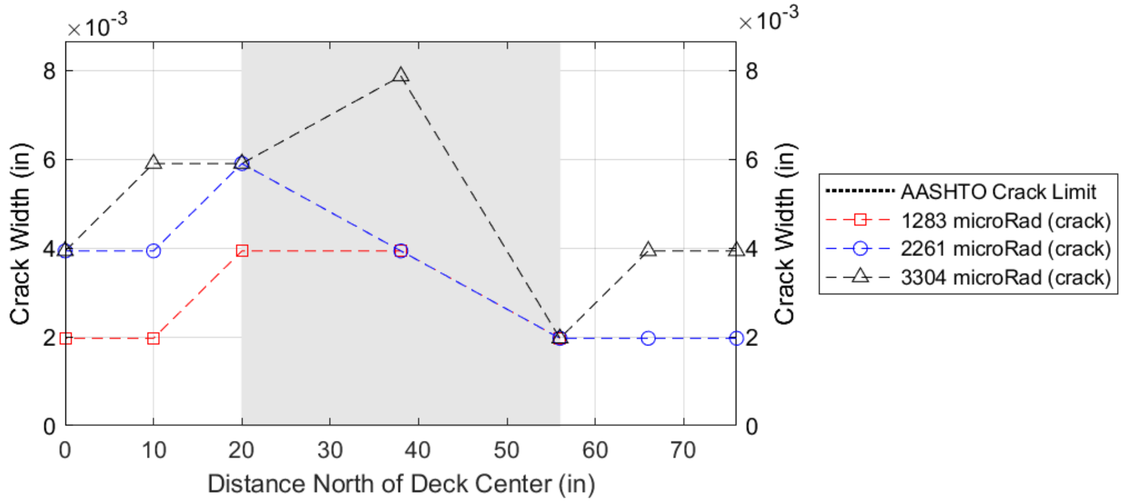

(a) Pattern All

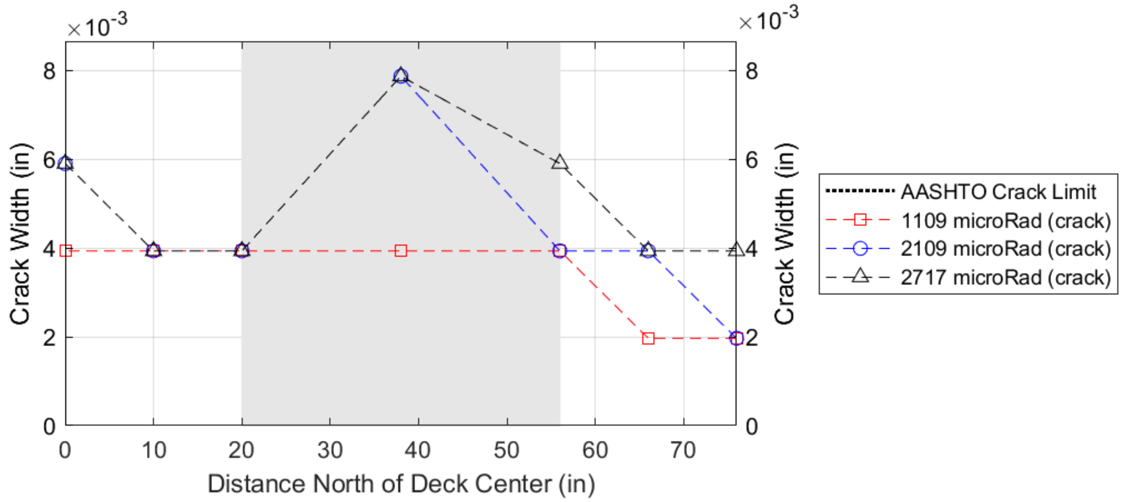

(b) Pattern W

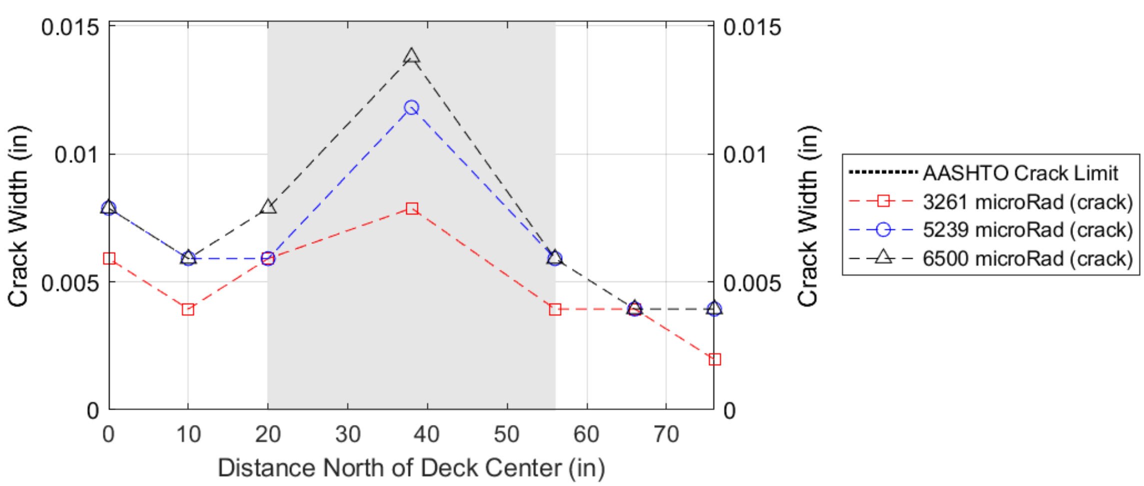

(c) Pattern All-Yield

Figure 10.7. PBJ-OP1R: Crack width profiles for select patterns.

10.5 STEEL STRAINS

Strain gages were installed on longitudinal reinforcing bars over the girders, in the overhangs, and in the deck between the girders. These strains provide additional insight to the response of the link slabs. Spatially, there is interest in the difference in strains (a) along the width of the deck and (b) along the length of an individual bar. Additionally, the changes in strain over the course of a load pattern are of interest. Two methods of presenting strain data are therefore considered. The first is strain profiles, in which a transverse section of the deck is considered, with all strain values plotted at a specific point in the loading history. These are comparable to the crack width profiles presented in the prior section. The second is strain maps, in which, for a single point in the loading history, Figure 10.8 through Figure 10.13 provide for each specimen a comparison of the crack width profiles (presented in previous section) and the strain width profiles for Pattern All. The crack widths and strains are presented at approximately the same rotations, but the strain rotations were determined based on actual measurements rather than being limited to the pauses, as is the case for the crack width measurements. Strain profiles are presented at the center of the link slab and thus are at approximately the same longitudinal location as the crack widths; however, since the cracks may have formed slightly off center, the strains and crack widths may be slightly misaligned, a factor that may contribute to inconsistencies between the two. For the strain profiles, horizontal red dashed lines indicate the expected yield strain of 0.00207 for Grade 60 steel.

In general, the shape of the strain profiles is similar to that of the crack width profiles. For the offset and continuous panel tests without retrofit, the strains are larger over the girder than between the girders, with the overhang strains sometimes being similar or slightly higher than over the girders. For the flush panel test (PBJ-FP1), limited good readings were available over the south girder and between the girders, making it more difficult to conclusively make observations relative to the more detailed crack width readings available. Deviations in the shape of the strain profile occur when strain gages yield, as shown in Figure 10.14 for PBJ-OP1 and PBJ-OP2. There are other instances of yielding occurring that do not produce changes in the shape, indicating that it is only large, localized strains associated with larger cracks that cause deviations in the trends seen.

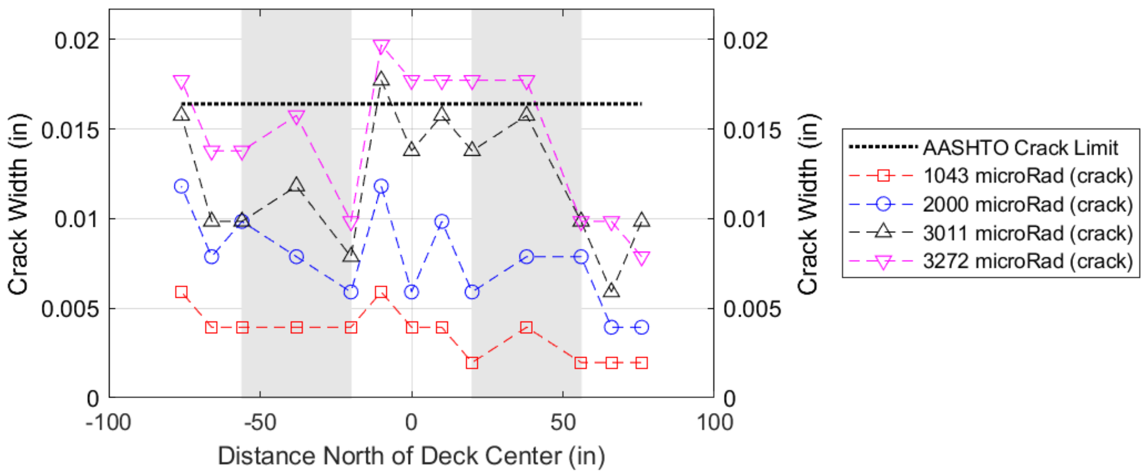

(a)

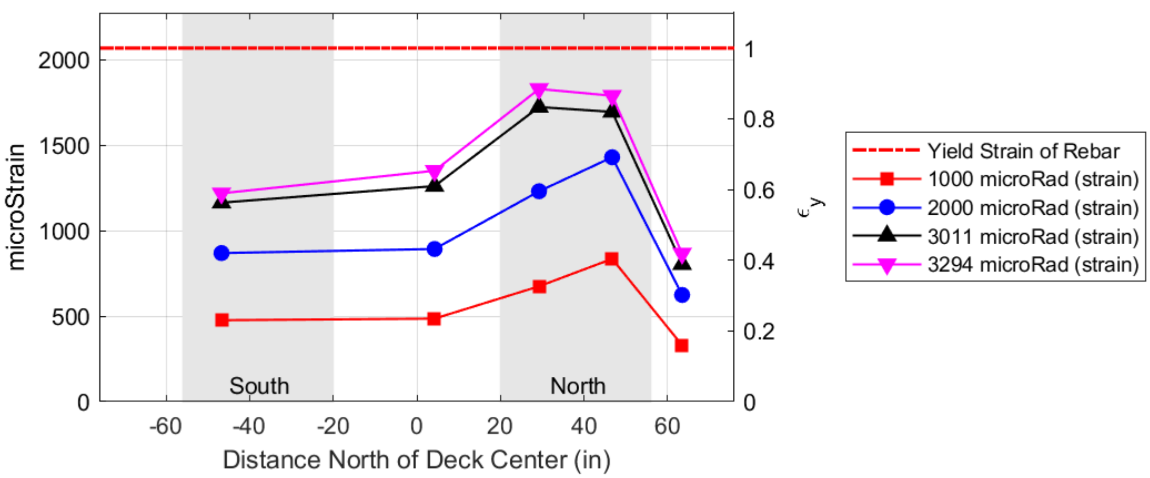

(b)

Figure 10.8. PBJ-FP1: Pattern All comparison of (a) crack width profiles and (b) strain width profiles.

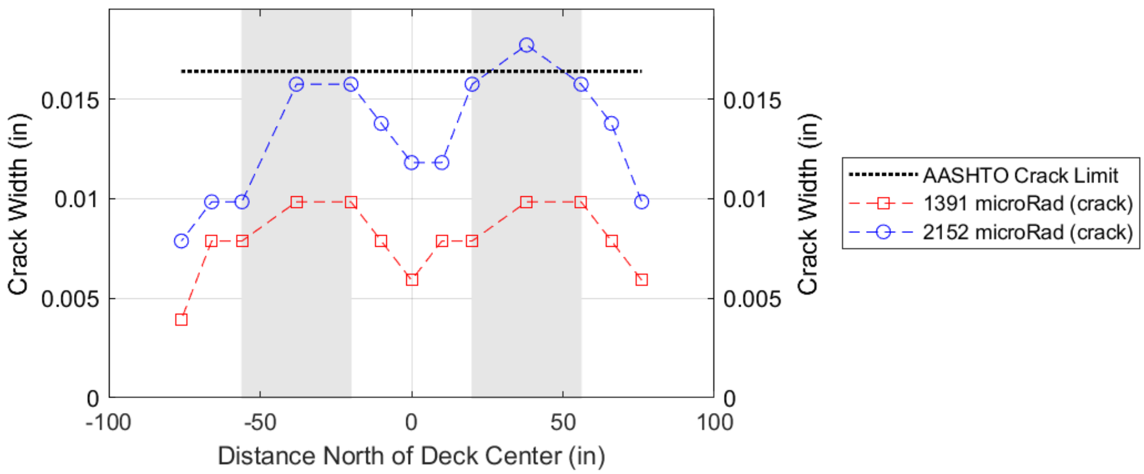

(a)

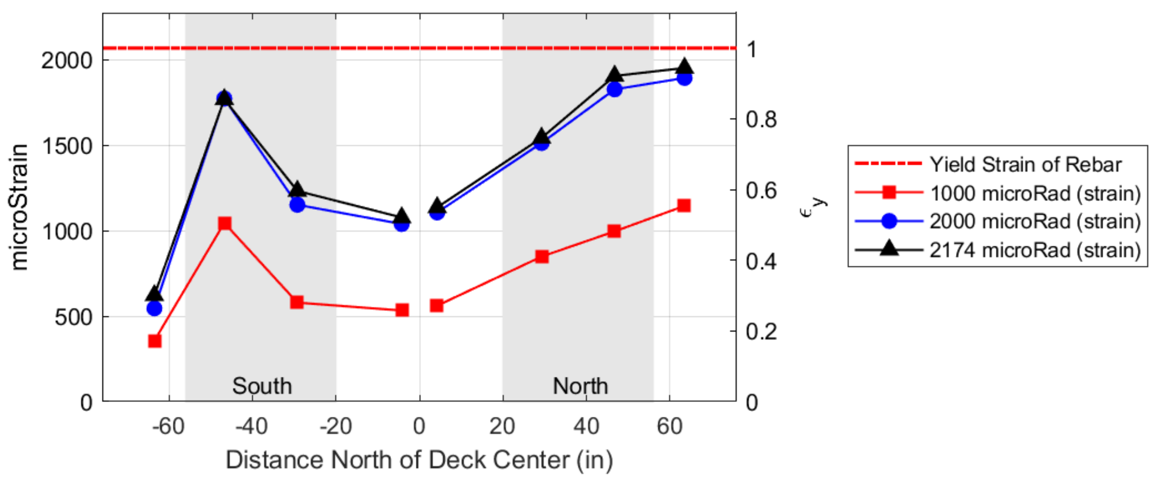

(b)

Figure 10.9. PBJ-OP1: Pattern All comparison of (a) crack width profiles and (b) strain width profiles.

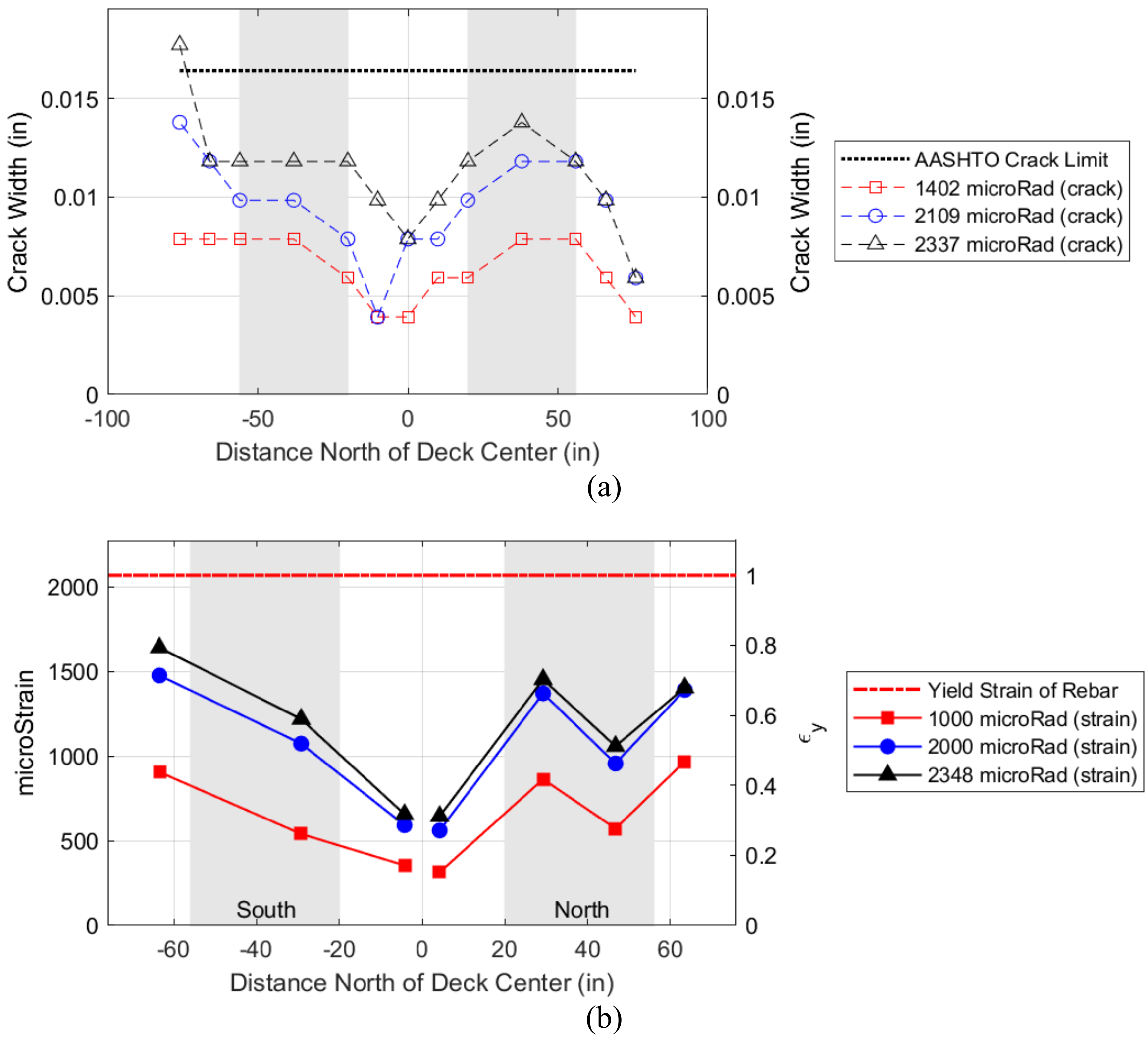

Figure 10.10. PBJ-OP2: Pattern All comparison of (a) crack width profiles and (b) strain width profiles.

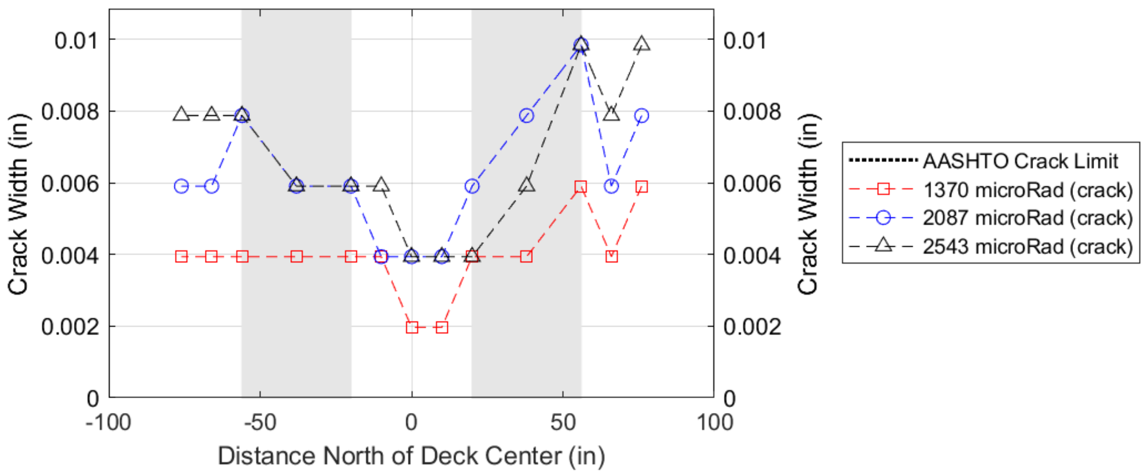

(a)

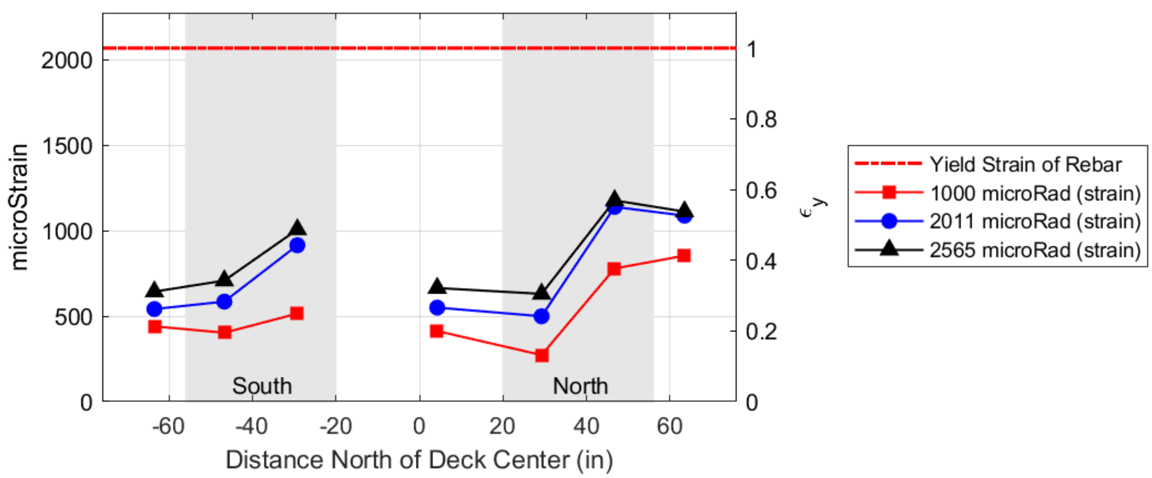

(b)

Figure 10.11. PBJ-CP1: Pattern All comparison of (a) crack width profiles and (b) strain width profiles.

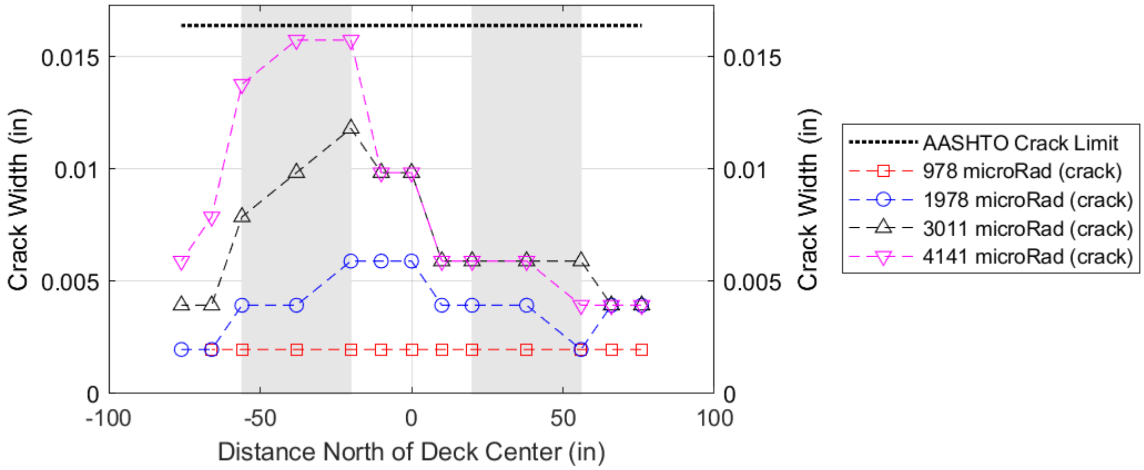

(a)

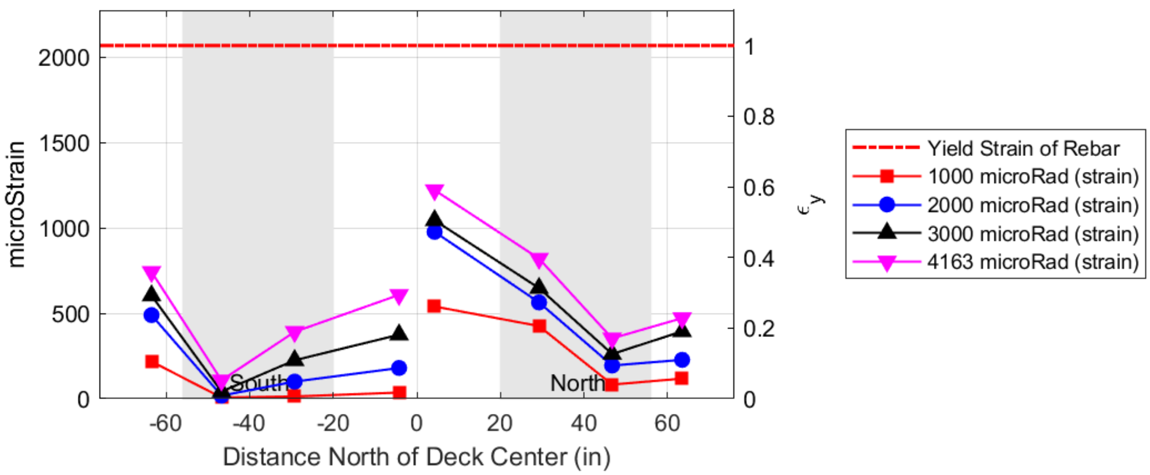

(b)

Figure 10.12. PBJ-FP1R: Pattern All comparison of (a) crack width profiles and (b) strain width profiles.

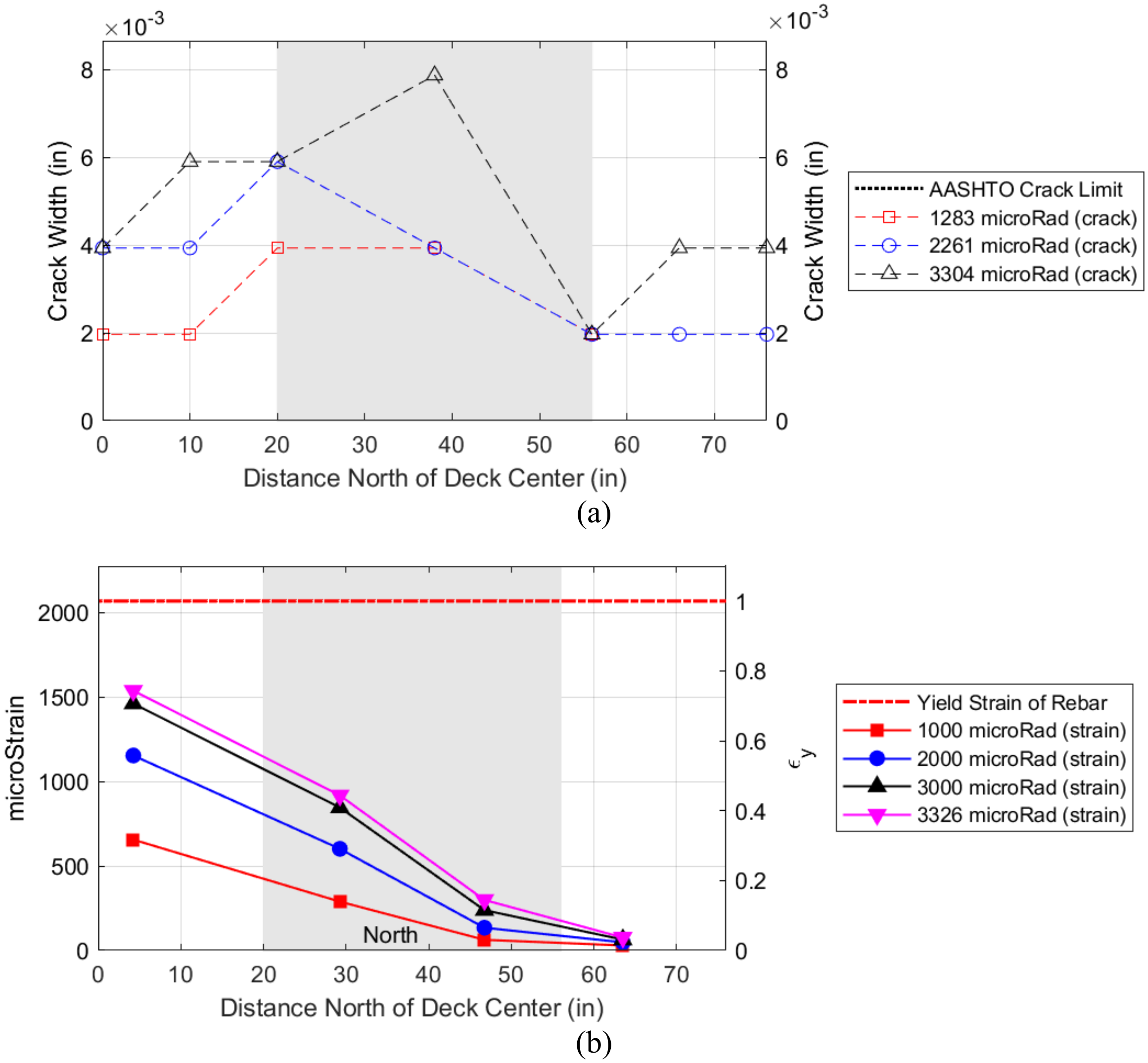

Figure 10.13. PBJ-OP1R: Pattern All comparison of (a) crack width profiles and (b) strain width profiles.

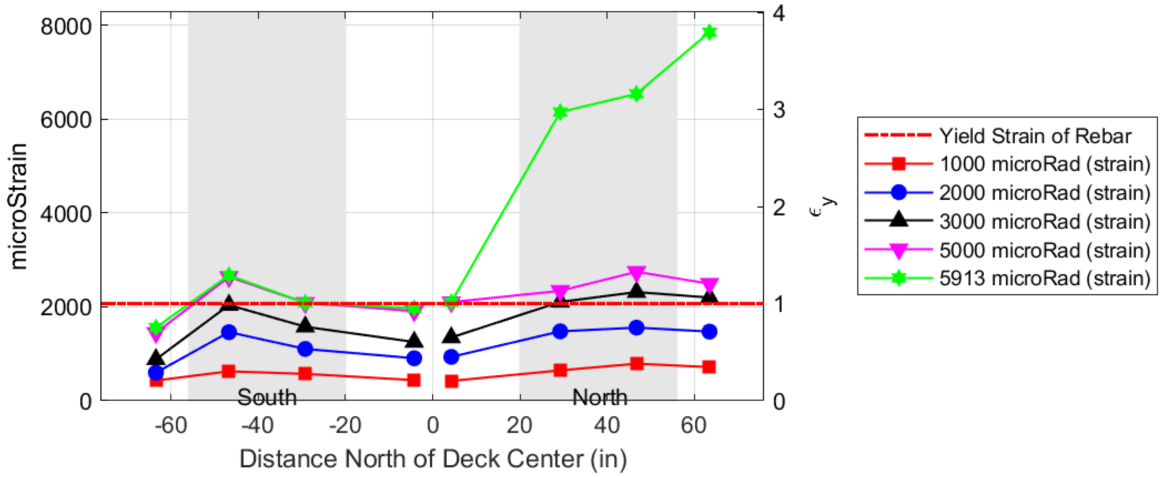

(a) PBJ-OP1 Pattern All-Yield

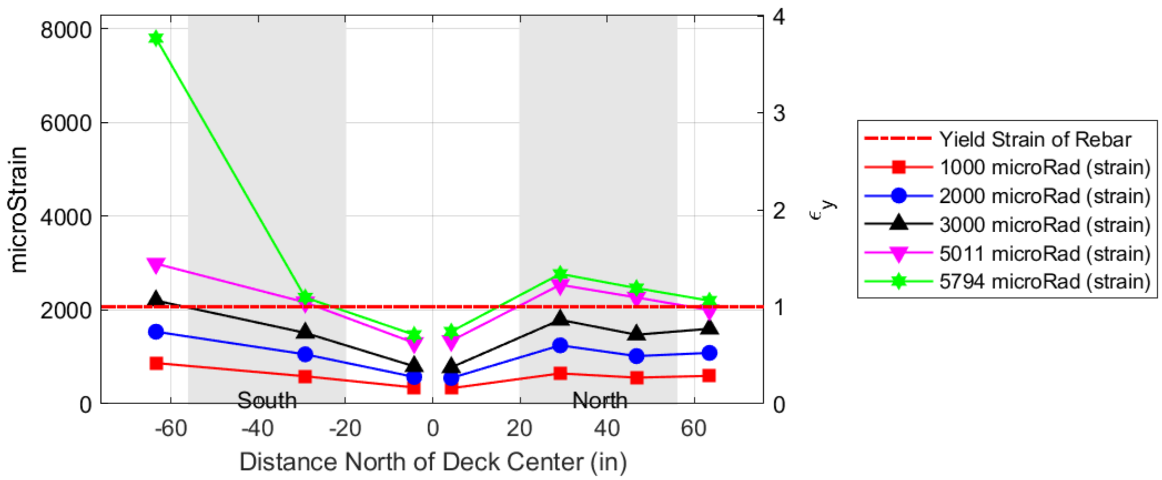

(b) PBJ-OP2 Pattern All-Yield

Figure 10.14. Deviations in shape of strain profile associated with yielding.

Because of the similarities of the strain profile shapes compared to crack widths and the similarities in shape at increasing rotation demands, limited analysis of strain profiles is presented. Instead, an alternative approach that allows for better consideration of the distribution of strains in the slab is taken. In this, the strains for all gages are shown, for a single point in the loading history, on a plan view of the deck. An example of this is shown in Figure 10.15. The top of the plan is north, and gray rectangles indicate the location of the four girders. The horizontal Grid 00 is at the center of the link slab, with other labels indicating the position of the strain gages on the west (W) or east (E) of center. Grid 1 is 4 in. from the center, and Grid 2 is 8 in. from the center. Vertical labels of NX and SX indicate the north or south bar instrumented.

Each box is located at a gage location. The number above the box is the measured strain presented as the strain normalized by the yield strain, with the box colored based on this value and in accordance with the color bar below the strain map. The color bar indicates strains of approximately zero as gray and compressive strains (negative values) as blue. Tension strains (positive values) are colored to indicate the magnitude relative to yield. A service limit of 40 percent of the steel yield strain is considered, with values below this indicated by green and values at approximately this limit indicated by yellow. Values exceeding this limit but less than yield are less desired but still acceptable since yielding has not occurred and thus may be acceptable for strength design. In this range, the boxes are colored orange to red. Values at or slightly over yield are indicated by black. At values well more than yield, the colors are purple to white.

In Figure 10.15, the top row shows the tests based on the current TxDOT details for flush panels (PBJ-FP1 in Figure 10.15[a]) and offset panels (PBJ-OP1 in Figure 10.15[b]). In assessing the relative values, consideration should be made for the differences in rotation at which each specimen is presented; the captions indicate the average girder rotation. When comparing the two current designs, the strains at the center of the link slab (Grid 00) are similar, but for PBJ-OP1, there is greater distribution of the strains at the gages farther from the center of the link slab. While two tests are presented at different rotations (higher for PBJ-FP1) and the amount of reinforcement is different (twice as much in PBJ-FP1), the relative colors on each horizontal grid line indicate the strains can better distribute in the offset panel design. This confirms what is seen in the crack patterns and in finite element models that indicate that deformation and damage is concentrated over the board in flush panel designs. However, in both tests, numerous gages exceed the service limit of $0.4\varepsilon_y$. Both tests also exceed the crack width limit during Pattern All; however, the strain exceeds the limit by a greater amount.

The second row of Figure 10.15 shows the tests based on the proposed designs utilizing DLSs (PBJ-CP1 in Figure 10.15[c] and PBJ-OP2 in Figure 10.15[d]). These are best compared to Figure 10.15(b) showing the offset panel reference test (PBJ-OP1). The debonded tests are presented at slightly larger rotations (around 2300–2500 microradians) than PBJ-OP1 (approximately 2200 microradians) but have lower strains. For PBJ-OP2, the strains have greater distribution of stresses than PBJ-OP1, with the W1 and E1 gages having strains similar in magnitude to those of the 00 gages. Farther away, the strains decrease significantly, similar to the drop off seen in PBJ-OP2. This may be a result of the girder ends bearing into the deck and not allowing full distribution of demands. In PBJ-CP1, the strains are still smaller at the gages farther from the center, but the distribution of the strains is much more uniform.

In the case of PBJ-CP1, the strains are below the desired limit of $0.4\varepsilon_y$ in most locations and only slightly higher where they are exceeded. In PBJ-OP2, there is twice as much longitudinal reinforcement in the north half of the deck. While limited conclusions can be drawn due to missing gage data at the 00 grid, examination of the strains farther from the center of the link slab indicates that the additional reinforcement is helpful in reducing the magnitude of the strains.

Figure 10.16 provides the same comparisons as Figure 10.15, but for Pattern All-Yield; here, the rotation values are similar for the four tests. The relative patterns described above are seen again. The flush panel test (PBJ-FP1) has concentrated strains at Grid 00, with strains the next grid back generally not exceeding the $0.4\varepsilon_y$ limit, while in the offset panel test (PBJ-OP1) higher strains, including strains at yielding and above, being seen at the center at all gages. In the first debonded tests (PBJ-OP2), strains are reduced relative to the reference offset panel test, and strains are lower in the north half with more reinforcement. In the final design using continuous panels and a haunch gap (PBJ-CP1), strains do not exceed the yield strains at any point, although at nearly all gage locations, the $0.4\varepsilon_y$ limit is exceeded (AASHTO crack width limits are not exceeded).

For load patterns that placed the spans under asymmetric loading (Pattern West and Pattern East), new cracks, if any, formed on the side of the span that was the secondary loading. As presented in Section 10.6.1, there was also a noticeable axial horizontal movement of the link slab toward the primary loaded span. From these observations, it was expected that the strain maps might also indicate asymmetric response of the deck. Figure 10.17 and Figure 10.18 present the strain maps for the bonded and debonded link slab specimens, respectively. The Pattern West strains are shown in the left column of the figures, and the Pattern East strains are shown in the right column of the figures. While the strains were not always equal on both sides of the center of the link slab, the strains at individual locations were essentially unchanged regardless of which span was the primary span.

Figure 10.19 and Figure 10.20 present the strain maps for the retrofit specimens (PBJ-FP1R and PBJ-OP1R) for Pattern All and Pattern All-Yield, respectively.

For PBJ-FP1R, the strains should be analyzed separately for the north and south half due to the different reinforcement. While the PBJ-FP1 test had strains larger between the girders, the PBJ-FP1R test had strains larger over the girders like most other specimens. The overhang strains were larger in the south half; however, this observation should consider that not only was the reinforcement different, but also the board between the panels extended into the south overhang. Most notably for PBJ-FP1R, the strains did not exceed yield strains at any point during the tests, including the final pattern that went to rotation demands of nearly 0.0065 rad, higher than any design values for bridges considered in this study.

For PBJ-OP1R, larger strains were observed in the south portion of the deck. In the north portion of the deck, strains were nearly zero. Note that debonding of the interface between new and existing concrete may be a factor, and strain gages were not available on bottom reinforcing bars to see if demand was present in that portion of the deck. However, Section 10.6.2 presents concrete surface strains in the north overhang that support the theory that load transfer is happening more in the bottom portion of the deck. Looking at the strains in the south portion of the deck shows that strains are larger at the center of the link slab.

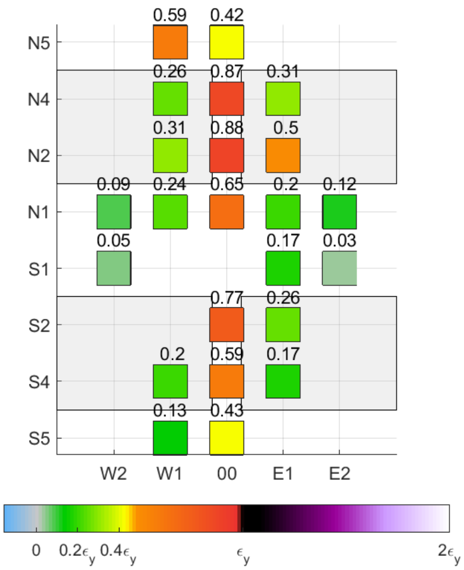

(a) PBJ-FP1 (3294 microradians)

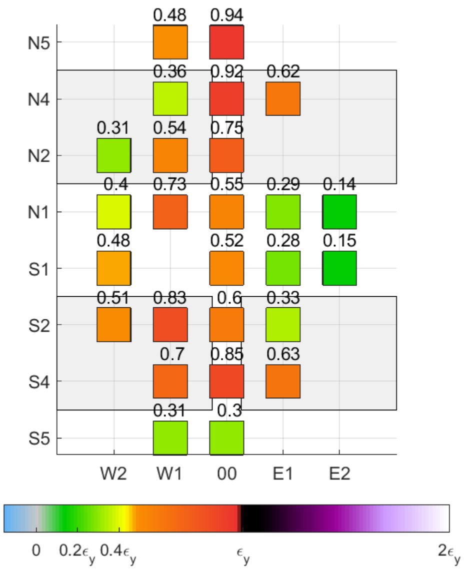

(b) PBJ-OP1 (2174 microradians)

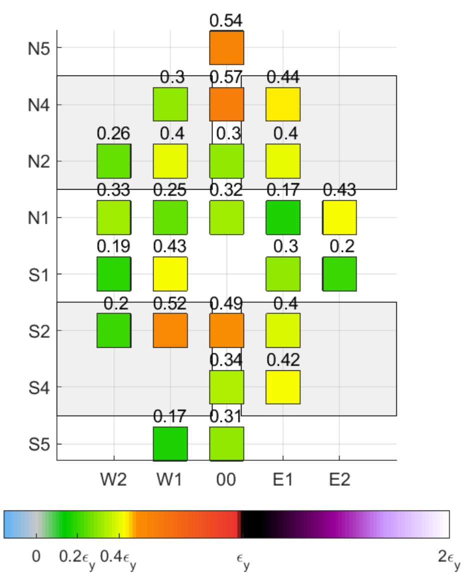

(c) PBJ-CP1 (2565 microradians)

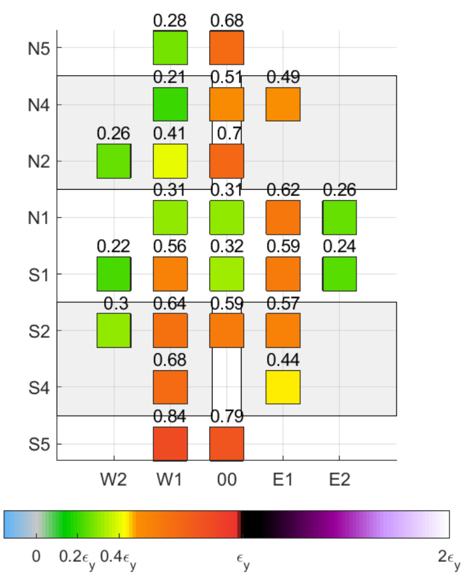

(d) PBJ-OP2 (2348 microradians)

Figure 10.15. Strain maps for non-retrofit designs at the peak load during Pattern All.

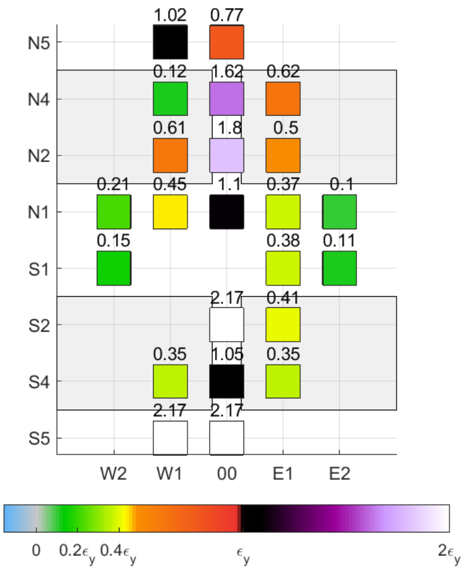

(a) PBJ-FP1 (6446 microradians)

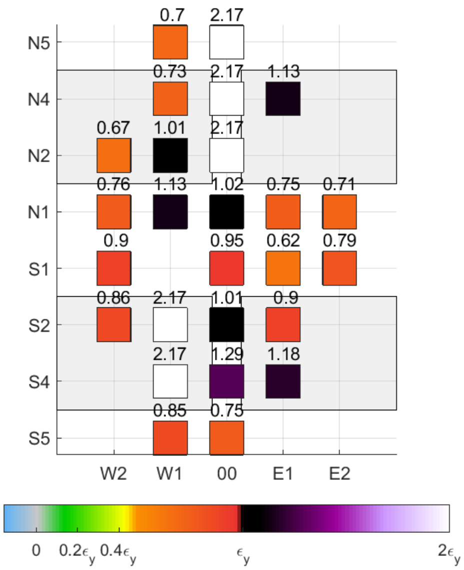

(b) PBJ-OP1 (5913 microradians)

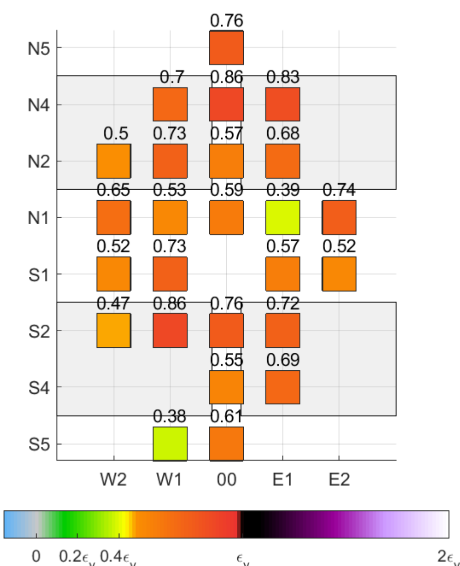

(c) PBJ-CP1 (5820 microradians)

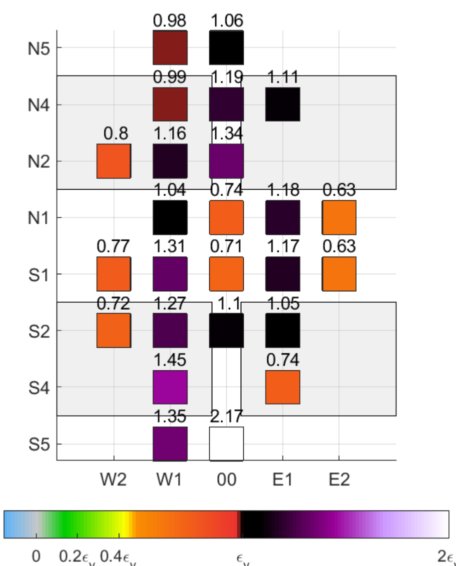

(d) PBJ-OP2 (5794 microradians)

Figure 10.16. Strain maps for non-retrofit designs at the peak load during Pattern All-Yield.

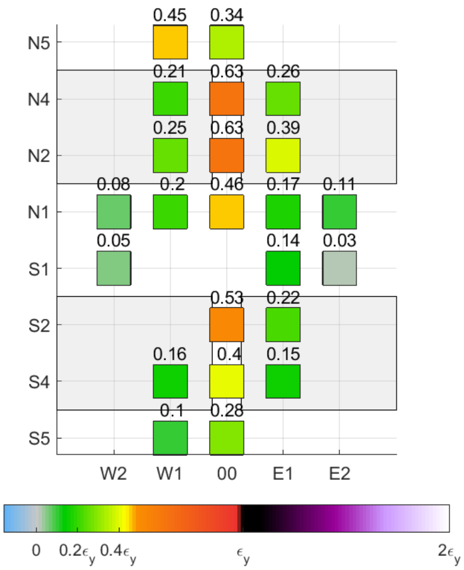

(a) PBJ-FP1 Pattern West

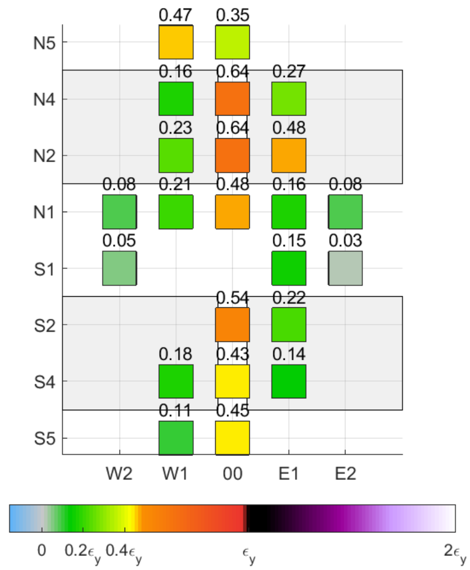

(b) PBJ-FP1 Pattern East

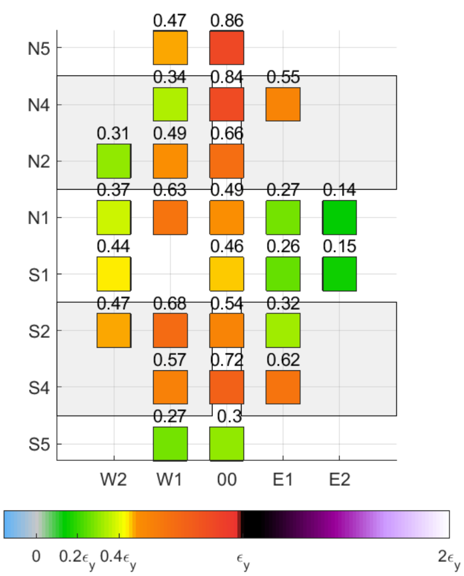

(c) PBJ-OP1 Pattern West

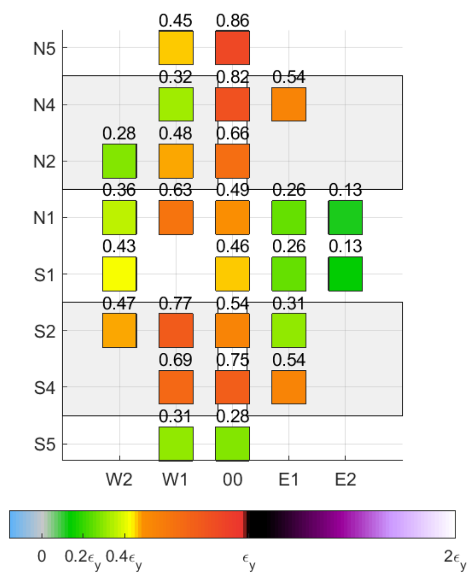

(d) PBJ-OP1 Pattern East

Figure 10.17. Strain maps for PBJ-FP1 and PBJ-OP1 at the peak load during Pattern West and Pattern East.

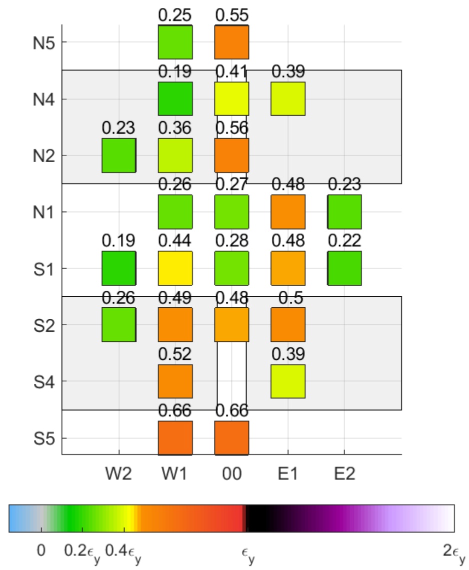

(a) PBJ-OP2 Pattern West

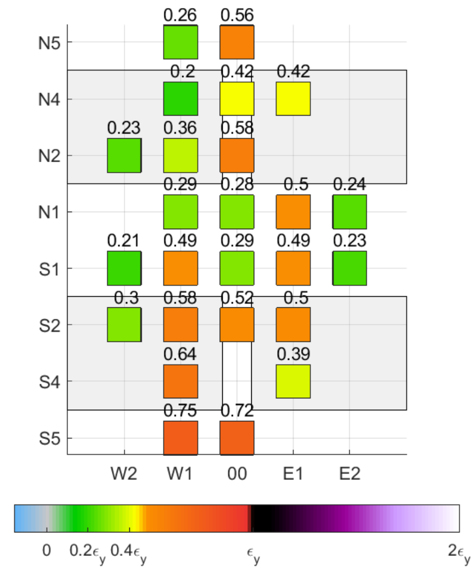

(b) PBJ-OP2 Pattern East

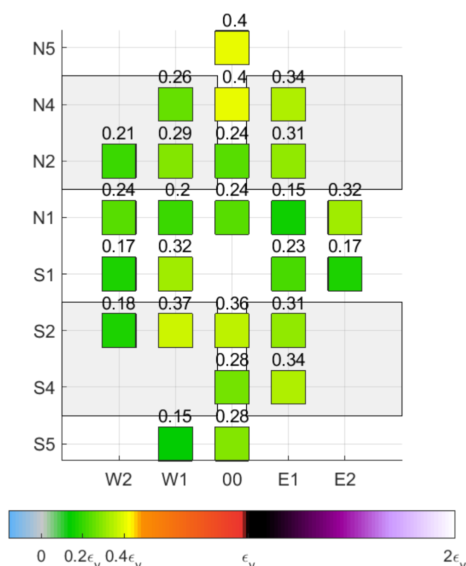

(c) PBJ-CP1 Pattern West

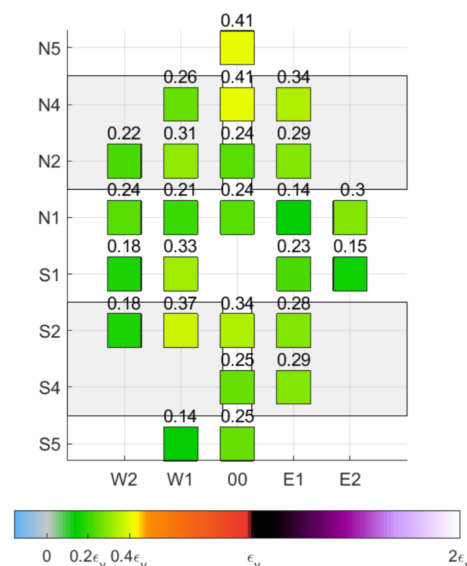

(d) PBJ-CP1 Pattern East

Figure 10.18. Strain maps for PBJ-OP2 and PBJ-CP1 at the peak load during Pattern West and Pattern East.

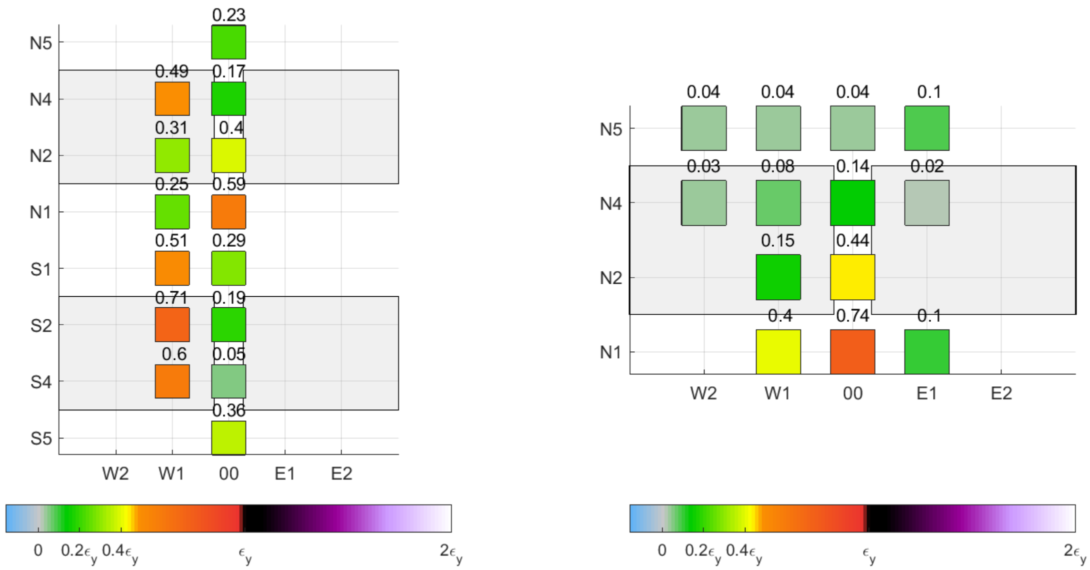

(a) PBJ-FP1R (4163 microradians)　　(b) PBJ-OP1R (1663 microradians)

Figure 10.19. Strain maps for retrofit designs at the peak load during Pattern All.

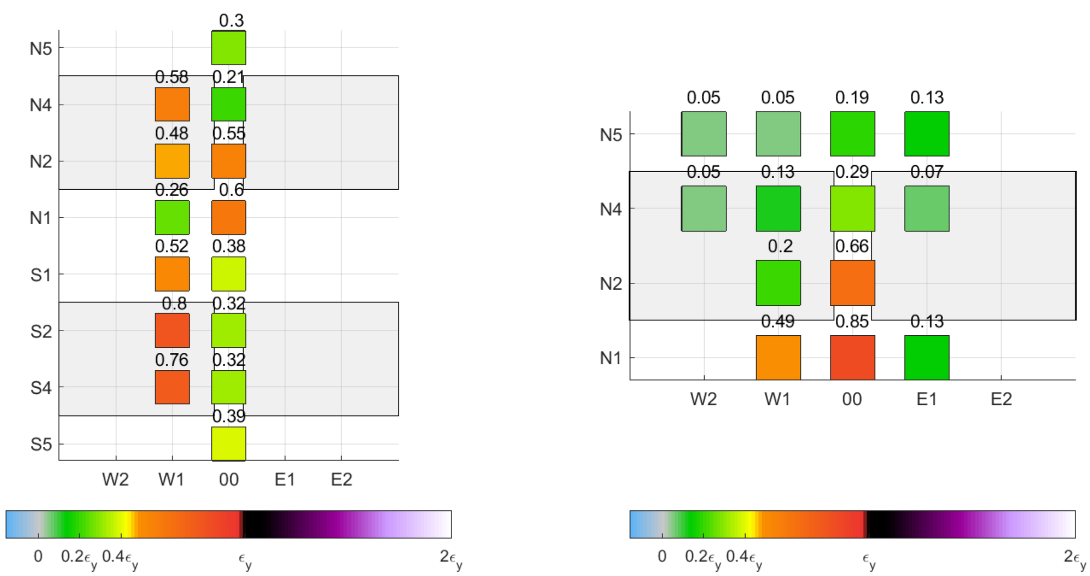

(a) PBJ-FP1R (6478 microradians)　　(b) PBJ-OP1R (3457 microradians)

Figure 10.20. Strain maps for retrofit designs at the peak load during Pattern All-Yield.

10.6 OPTOTRAK DATA

The Optotrak data provide extensive information about displacements along the edge of the deck in the link slab region. These data allow for a refined look at the behavior of the specimen that is not permitted by traditional instrumentation. Targets placed on the girders were used to confirm rotations, as discussed in Section 10.1, and targets on the pedestals were used to confirm minimum deformation of the support blocks during testing. The most insightful information from the Optotrak data comes from the dense array of targets on the edge of the deck. Section 10.6.1 provides a discussion of observed displacement history of individual targets. Section 10.6.2 provides a discussion of calculation of strains from the displacement data and observations for individual tests.

10.6.1 Deformation Under Asymmetric Loading

Figure 10.21 shows the displacement history of each target on PBJ-FP1 during Pattern W. The girder and deck are shown as gray rectangles. Each colored line represents a target and is a series of points showing the position over the course of loading, with displacement magnified 50 times to be easily viewable. On the deck over the west girder (primarily loaded girder), the lines are mostly vertical, with the target starting at the top of the line and moving toward the ground as the test progresses. This is expected given the expected displaced shape confirmed by the displacement profiles presented in Figure 10.1.

The findings are more interesting in the deck over the east girder, where the path history is an L-shape laying on its side. The shorter vertical leg of the path history occurs when the 40-kip load is placed in the secondary girder (east in this case). At higher loads in the primary girder (west), the east load is held constant. During that portion of the load pattern, the east deck targets have the longer horizontal leg of the L response. This observation is referred to as drag or tug of the deck on the secondary girder. It suggests an axial deformation of the deck that may explain the offset and secondary cracks that form during the asymmetric loading and are observed in the field. Such a behavior has not been suggested as a design considered in the literature. Further exploration of this behavior, including for other tests, is needed. It is worth mentioning that these findings have been compared to results from finite element models, and it was shown that the behavior matched.

Figure 10.21. PBJ-FP1: Optotrak target displacement history for Pattern W.

10.6.2 Distribution of Strains

Aside from use to assess the deformation of the link slab region, the Optotrak data can be used to calculate high-fidelity strains along the edge of the deck. Details of the calculations are presented by Krajeck (2023).

In Figure 10.22 through Figure 10.27, the results of Pattern All-1 for each specimen are presented. Select results from other load patterns are provided in Figure 10.28 through Figure 10.31. In each figure, three strain values: (a) the horizonal strain (x-direction), (b) vertical strain (y-direction), and (c) shear strain. The letters (a), (b), and (c) are used in each figure presenting Optotrak strain fields. For all three types of strains, the same colormap is used, with gray indicating strains around zero, warm colors indicating tensile strains, and cool colors indicating compression strains. Except for PBJ-OP1R, the figures show the south edge of the deck, with the right girder being the east girder and the left being the west girder. For PBJ-OP1R, the Optotrak was collected on the north edge of the deck, with the right side of the figure being the west girder and the left side the east girder. Below each set of strain fields, the cracks on the edge of the deck in the Optotrak region are included to allow comparison of the strains to the observed cracks (crack maps are final crack maps). On the strain fields and crack maps, small vertical lines are present to indicate the edge of the girders. When comparing the strain fields between different specimens, this aspect is particularly important to consider since different configurations of targets were used on each test. A discussion of each specimen is presented in the following paragraphs. In general, the observations made for all are consistent with those from other load patterns; thus, not all strain fields are included. Where interesting observations can be made for other load patterns, additional strain fields are presented. The horizonal strains are associated with flexural cracks and present the most useful data to interpret. Vertical and shear strains are generally negligible and thus are only discussed when the data are of value to interpreting the behavior of the specimen.

For PBJ-FP1 (Figure 10.22), tensile strains developed on the top of the deck and concentrated primarily at the center of the link slab above the timber board. Compression strains also developed. Smaller regions of tension are seen approximately over the bearing pads. On the west girder (left), this region is a bit farther out than the observed crack. This suggests that the link slab has a tendency to develop a greater distribution of cracks but is unable to overcome the concentration of the damage over the board. Also noteworthy is that the secondary regions of tensile strain concentration are equally distributed over the depth of the slab, suggesting that axial load and deformation may be a greater factor in flush panel designs since such an observation is not made in other specimens except where full-depth cracks develop. For PBJ, compressive stresses are concentrated in the region around the board. For tests without boards, such a concentration is not seen, with compressive strains provided with a greater distribution, as would be expected when considering the compressive stress block of a slab in flexure.

In PBJ-FP1R, shown in Figure 10.23, compressive stresses are again seen concentrated around the board and a distinct tension region located over the end of the west (left) girder. This is offset from the board slightly but is consistent with the location of observed cracks. Cracks over the east (right) girder occurred during Pattern All-Yield, with the tensile strains becoming significant during that pattern, as seen in Figure 10.29. While shear and vertical strains were minor in PBJ-FP1, significant strains were seen for PBJ-FP1R. For vertical strains, the values confirm that the debonding is effective in allowing the top and bottom portion. Under asymmetric loading, the vertical and shear strain effects are more pronounced, as shown in Figure 10.30 for Pattern East, where vertical strains are larger on the east (right) girder that is loaded and smaller over the secondary west (left) girder. Compressive vertical and shear strains in the region of the board indicate that consideration must be made for how forces are transferred through the top and bottom portions of the deck.

In PBJ-OP1, shown in Figure 10.24, two distinct regions of concentrated tension strains are seen at approximately the same locations of the vertical cracks. The strains were of greater magnitude over the east (left) girder, which is consistent with the development of two cracks in that region. Also seen is a small amount of vertical and shear strains in the area where a horizontal crack formed. While the results for Pattern All-1 do not show compressive strains (cool colors) this is due to the small values calculated. In other load patterns, compressive strains are visible in the strain fields; an example of this is shown in Figure 10.28 for Pattern All-Yield. While full-depth cracks occur, full-depth regions of tension strains were not observed as was the case for PBJ-FP1.

In PBJ-OP1R, shown in Figure 10.25, significant shear strains and vertical strains are present in the repaired region and the interface with the existing concrete. This is consistent with the observed damage at the interface. Horizontal strains are more limited, but a distinct tension region is seen at the top of the existing and new concrete, indicating that the slab is behaving as debonded in the north overhang.

In PBJ-OP2, shown in Figure 10.26, the region of concentrated tensile strains is located where the single crack forms. Regions of light concentration of horizontal and shear strain are seen where the horizontal cracks form during later patterns. In Figure 10.31, the strains are shown for Pattern All-Yield, in which the areas of greater intensity of the strains are located in the region of cracks and where the location of the secondary crack over the west (left) girder has a concentrated region of tension strain.

In PBJ-CP1, shown in Figure 10.27, there is a region of tension strain in the bottom of the deck where a full-depth crack formed in later load patterns. This is in the region where honeycombing occurred and was patched, which was likely the reason for the strain concentration. It is notable that on the opposite girder, there is a region of compression concentration not seen in other tests, indicating a redistribution of demands due to the imperfection and highlighting of the sensitivity of link slab performance to the detailing near the ends of the girders and panels.

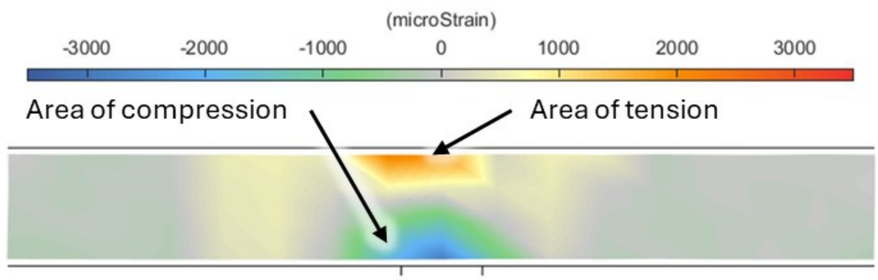

(a)

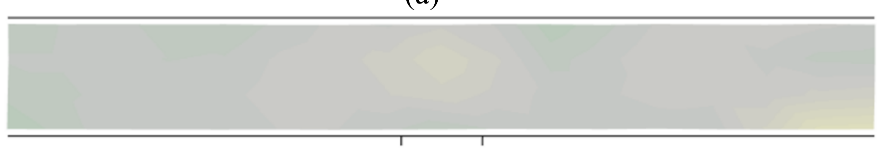

(b)

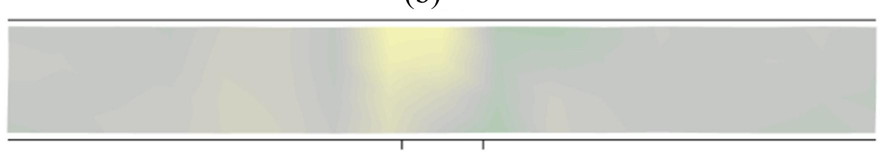

(c)

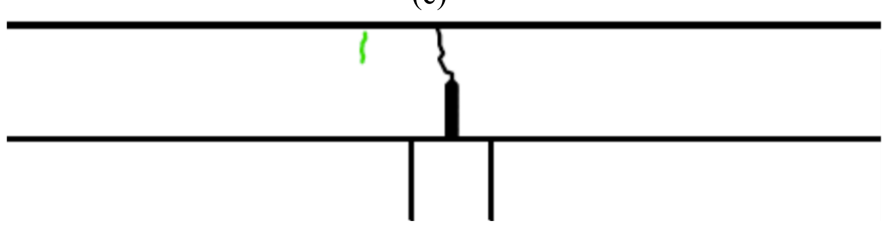

(d)

Figure 10.22. Optotrak strains for PBJ-FP1 Pattern All: (a) horizontal, (b) vertical, (c) shear strain, and (d) crack pattern.

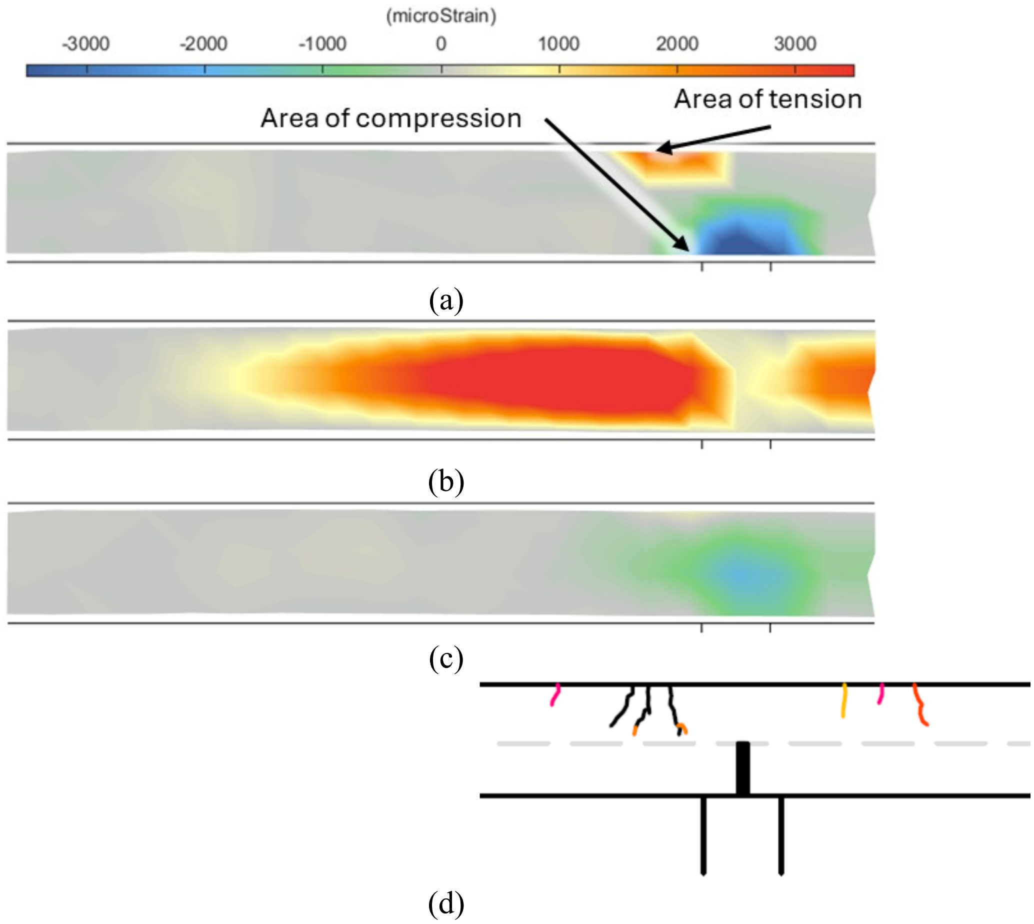

Figure 10.23. Optotrak strains for PBJ-FP1R Pattern All: (a) horizontal, (b) vertical, (c) shear strain, and (d) crack pattern.

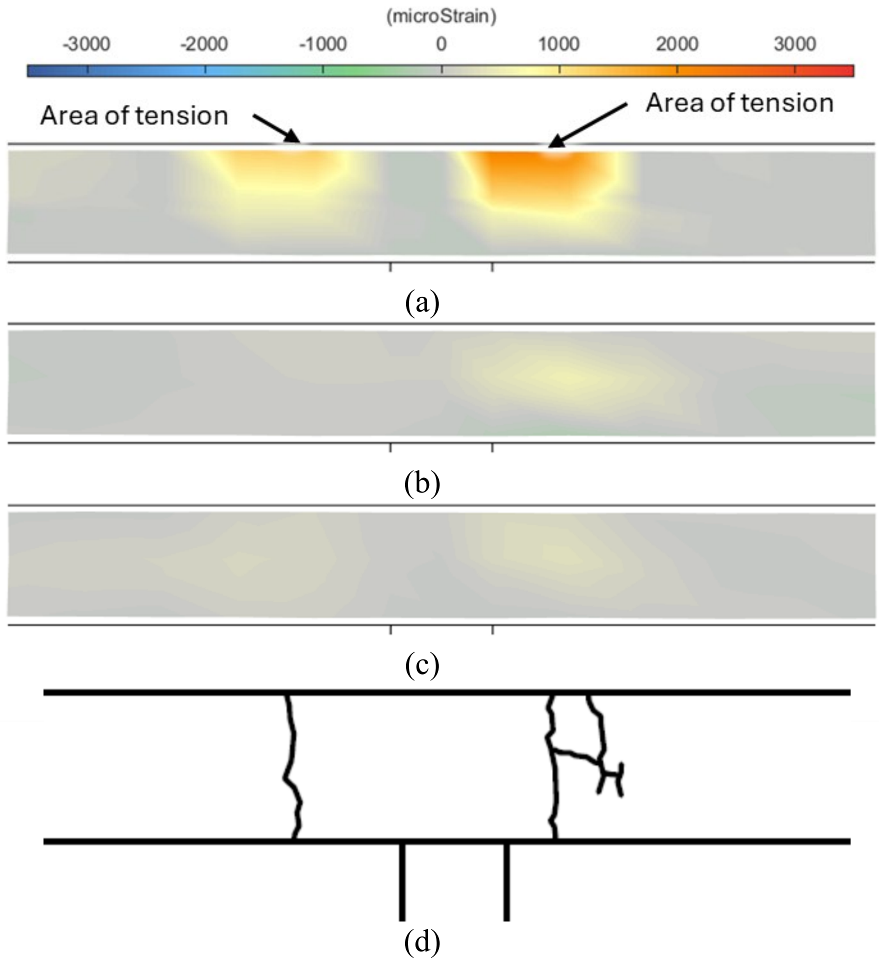

Figure 10.24. Optotrak strains for PBJ-OP1 Pattern All: (a) horizontal, (b) vertical, (c) shear strain, and (d) crack pattern.

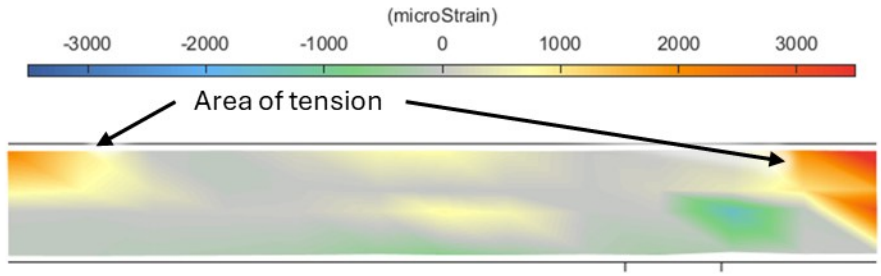

(a)

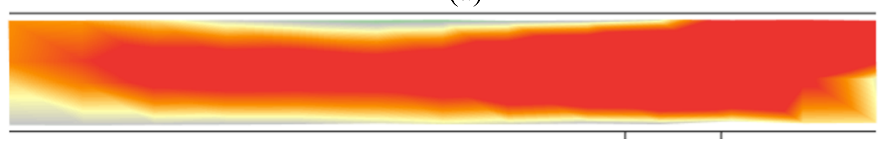

(b)

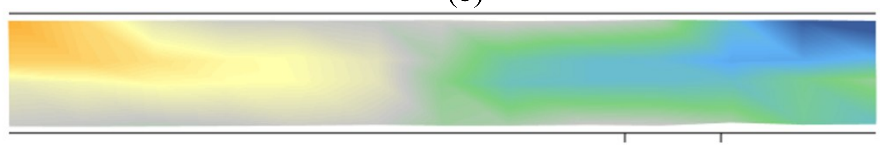

(c)

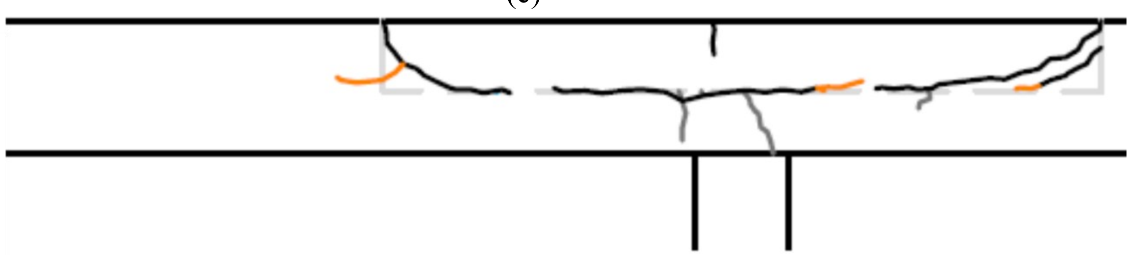

(d)

Figure 10.25. Optotrak strains for PBJ-OP1R Pattern All: (a) horizontal, (b) vertical, (c) shear strain, and (d) crack pattern.

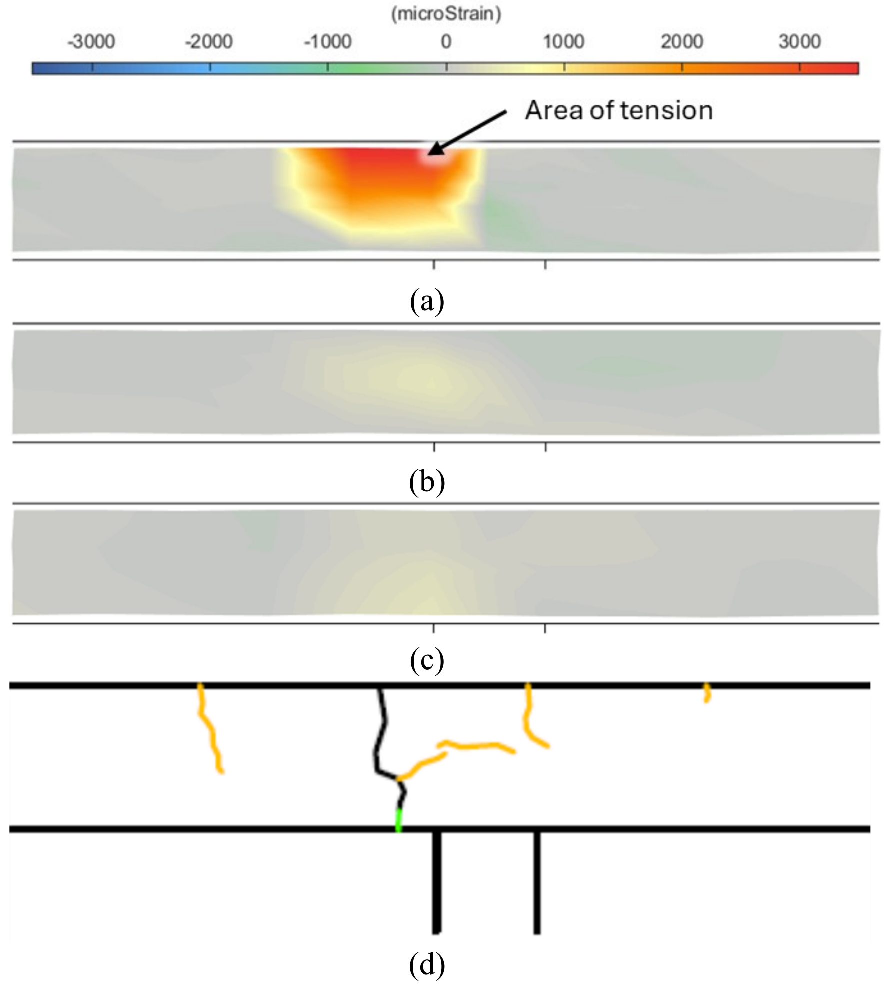

Figure 10.26. Optotrak strains for PBJ-OP2 Pattern All: (a) horizontal, (b) vertical, (c) shear strain, and (d) crack pattern.

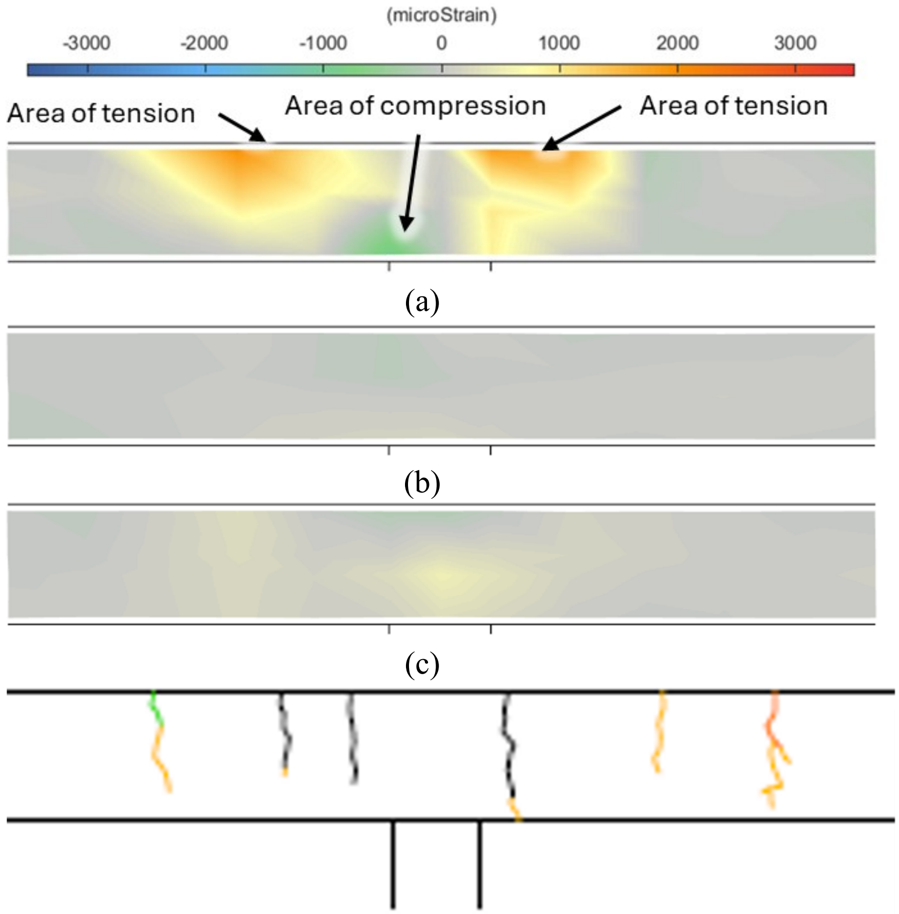

(a)

(b)

(c)

(d)

Figure 10.27. Optotrak strains for PBJ-CP1 Pattern All: (a) horizontal, (b) vertical, (c) shear strain, and (d) crack pattern.

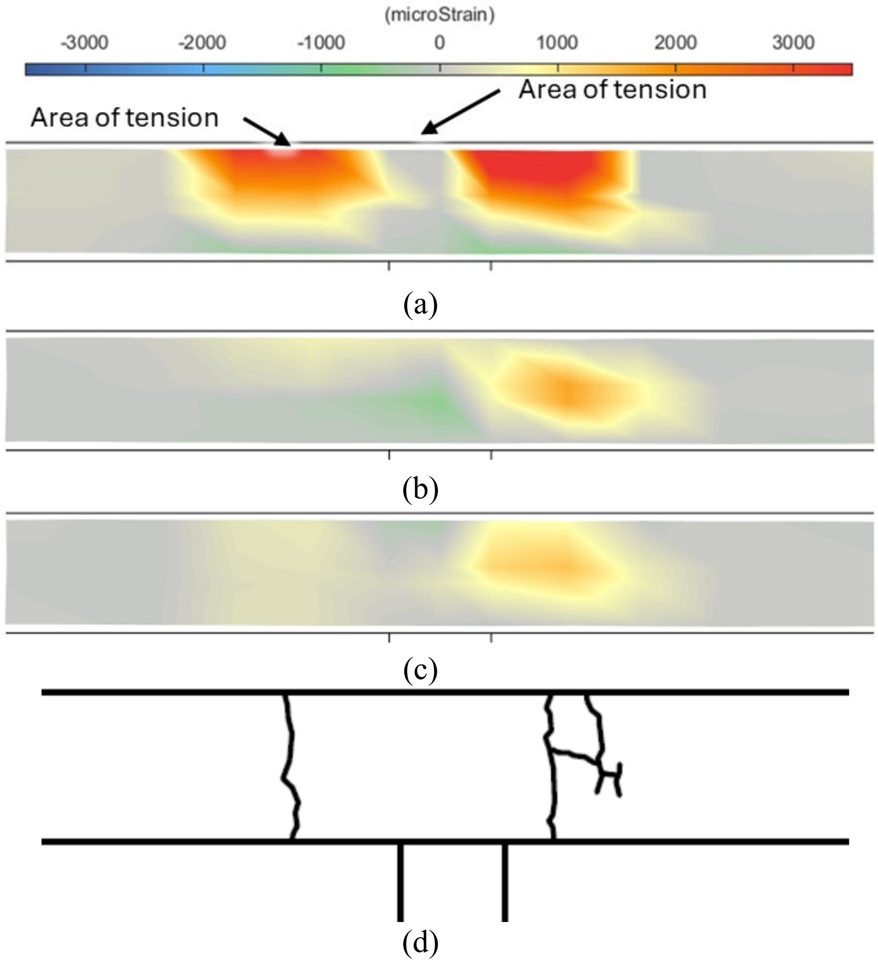

Figure 10.28. Optotrak strains for PBJ-OP1 Pattern All-Yield: (a) horizontal, (b) vertical, (c) shear strain, and (d) crack pattern.

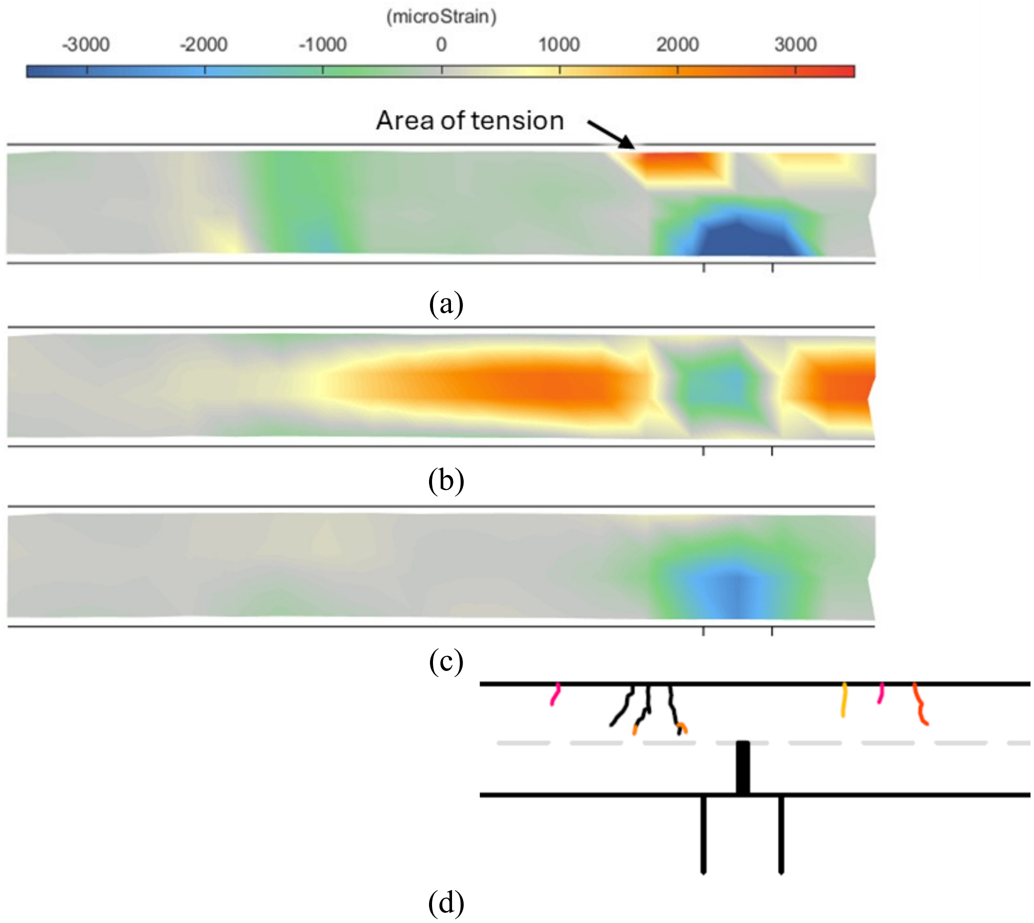

Figure 10.29. Optotrak strains for PBJ-FP1R Pattern All-Yield: (a) horizontal, (b) vertical, (c) shear strain, and (d) crack pattern.

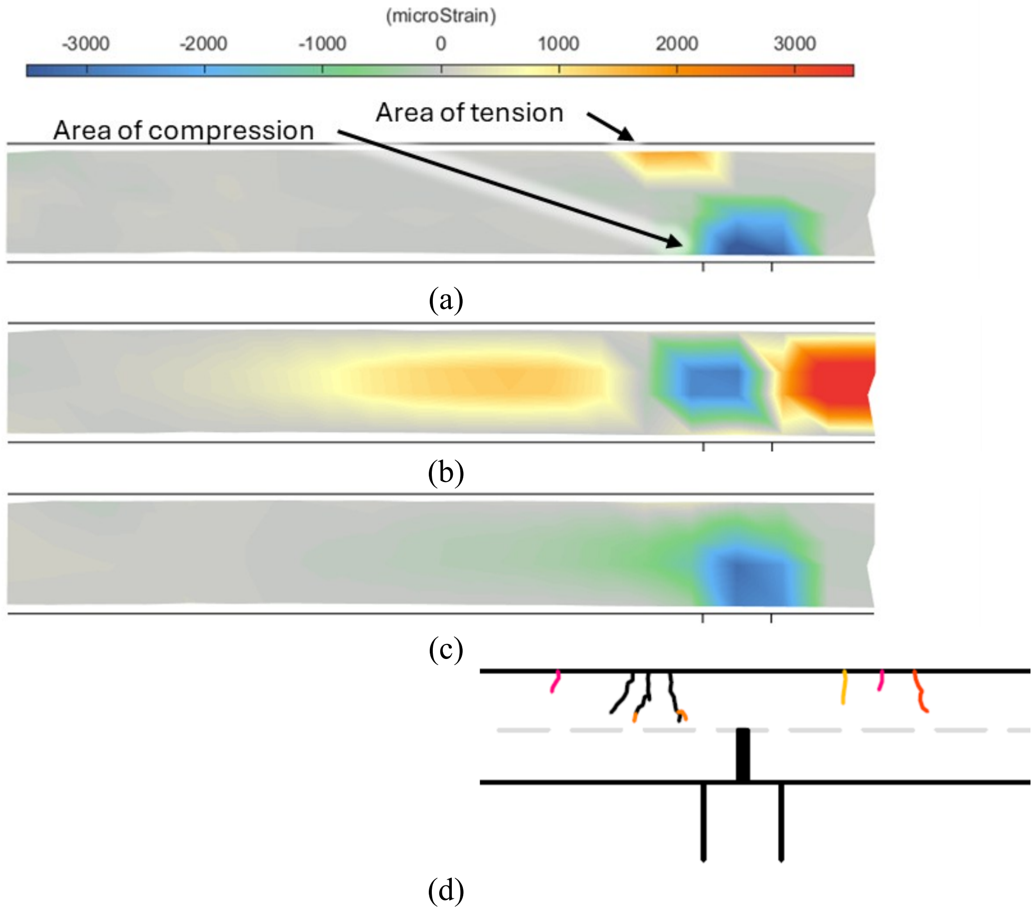

Figure 10.30. Optotrak strains for PBJ-FP1R Pattern East(a) horizontal, (b) vertical, (c) shear strain, and (d) crack pattern.

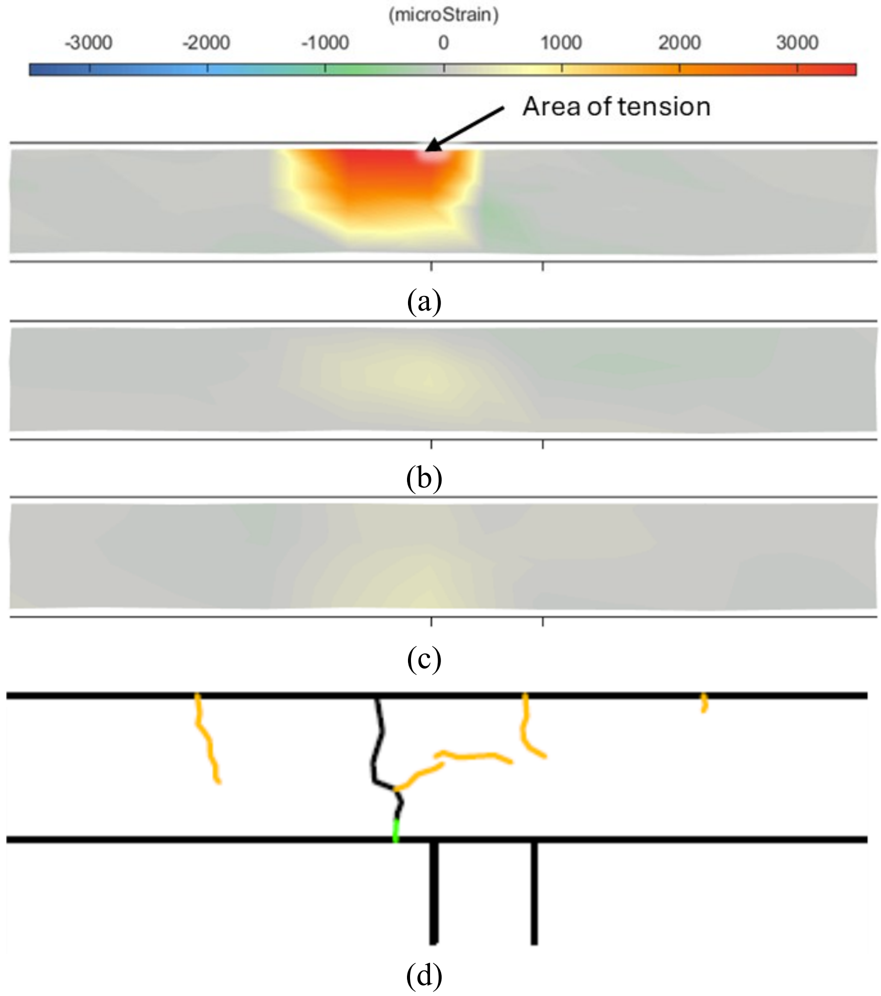

Figure 10.31. Optotrak strains for PBJ-OP2 Pattern All-Yield: (a) horizontal, (b) vertical, (c) shear strain, and (d) crack pattern (cracks formed during the load pattern are shown as yellow lines).

10.7 EFFECTIVE LINK SLAB LENGTH

An important aspect to consider in the design of link slabs is length used. Most design recommendations for link slabs focus on establishing a design moment used to select reinforcement. The equation for doing so is based on girder end rotation, link slab flexural stiffness, and link slab length. Thus, the length used is crucial to understanding the performance of link slabs and making appropriate design recommendations. In the case of debonded link slabs, this length is typically the debonded length. In bonded link slabs, the appropriate length is less clear, and prior studies have used rather simplistic assumptions (simple supports at end of girder) in models that make it difficult to apply to the conditions of typical TxDOT bridges in which the girders are supported on bearing pads set in from the ends of the girders. In this study, the length used for design of bonded link slabs was considered to be the effective length of the link slab, L_{eff}.

Evaluation of the experimental data on non-retrofit tests (PBJ-FP1, PBJ-OP1, PBJ-OP2, and PBJ-CP1) used to identify appropriate effective lengths is valuable to make design recommendations. Several methods were used to evaluate the effective lengths. Table 10.2 summarizes the effective link slabs determined using each method. For simplicity, only Pattern All and Pattern All-Yield are considered. Details of the methods are provided in the following paragraphs. For context of the numbers presented, the distance between the ends of the girders is 6 in. The center of bearing pads are 9 in. from the ends of the girders, so the center-to-center distance of the bearing pads is 24 in. The 6-in. and 24-in. lengths are those that might be considered based on the recommendations of other research studies; thus, findings other than those suggest the need to modify recommended design procedures for bonded link slabs. For debonded specimens (PBJ-OP2 and PBJ-CP1), the debonding is for 3 ft along the length of the girder for a link slab length of 78 in. Findings other than this suggest the need to modify recommended design procedures for debonded link slabs.

Table 10.2. Effective link slab lengths (all units in inches).

Specimen	Method 1			Method 2		Method 3	
	1a—Bottom Strain	1b—All Load Pattern	1b—All-Yield Load Pattern	All Load Pattern	All-Yield Load Pattern	All Load Pattern	All-Yield Load Pattern
FP1	27.0	62.5	71.5	64.5	67.5	57.0	57.0
OP1	54.5	37.5	37.0	37.0	42.0	31.0	44.5
OP2	55.0	50.5	61.0	51.5	52.5	58.5	59.0
CP1	72.5	60.5	90.5	85.0	96.0	64.5	78.5

In the field monitoring studies documented in Chapter 4 of this report, measured deformations between the ends of girders were used to estimate the rotation under live and thermal loads. Together with the measured strains on the bottom of the deck, estimates were made for effective link slab lengths that would be appropriate to use for various details. A single value was provided for the full history of the loading on each bridge. To begin the estimation of effective link slab lengths, the same approach was initially taken with the experimental data. This is referred to as Method 1.

In applying Method 1 to the experimental data, the calculated rotations were used to calculate the theoretical strain at different points in the bridge deck using a series of assumed L_{eff} values. These strains were then compared to the actual strains measured during experimental testing, either with strain gages or LVDTs attached to the surface of the concrete. All points in the load history for an individual pattern were considered, and the errors between the theoretical and measured strains were computed. The effective length with the smallest overall error, determined using the root sum of the squares, was determined to be the effective link slab length presented in Table 10.2.

Two different strains were considered in applying Method 1 to the experimental data. Method 1a refers to the use of strains at the bottom surface of the deck, calculated from LVDTs installed on the bottom of the slab. While these data have low resolution relative to the data from strain gages, they provide for a direct comparison to the strains used in the field evaluations and thus a comparison of the link slabs found. As an alternative, Method 1b was also done using strain gages on the steel-reinforcing bars.

With Method 1a, the two offset panel tests had an effective length of approximately 55 in., about twice that of the flush panel test (27 in.) and shorter than the continuous panel test (72.5 in.). These values are much larger than those from the field evaluations: approximately 6 in. for flush panel designs and approximately 17 in. for offset panel designs. One factor to consider in assessing the flush panels is that the monitoring was done on bridges that had a larger gap (approximately 3 in.) between the panels, while the testing was done using the current detail of having a ¾-in. timber board separating the panels. Thus, it was expected that the field-monitored flush panels decks would be more flexible and thus have a short effective link slab length.

Method 1b showed a larger distinction in the effective link slab lengths between decks. PBJ-FP1 now had the longest effective link slab length, followed closely by PBJ-CP1. Both these decks had the PCPs oriented at or near the center of the link slab. Conversely, PBJ-OP1 was now the shortest effective link slab length, while PBJ-OP2 (the debonded version of PBJ-OP1) had a longer effective link slab length. Method 1b was performed for both the All and All-Yield load patterns, with every deck except PBJ-OP1 exhibiting an increased effective link slab length in Pattern All-Yield.

A couple factors had to be considered in assessing this large discrepancy of the field and experimental numbers. The first was the range of rotations used since the field investigations measured responses under in-situ loads, reaching girder end rotations less than 1000 microradians, while experimental tests reached on the order of 3000 microradians for Pattern All and upwards of 6000 microradians for Pattern All-Yield. Given the vast differences in the number of data points used, a more refined analysis of the appropriate link slab length from field monitoring data was conducted. Resolution of the instrumentation should be considered since the values at small rotation may not be consistent between the different instruments used in the field monitoring and experimental tests. Finally, there is a difference in the cracked conditions of the link slabs. Since the monitoring was done for one week on bridges that have been in service for years, the cracks in the surface of the deck were expected to be unchanged throughout testing. In the experimental tests, the decks developed cracks during testing, so the stiffness of the slab was continuously changing during Pattern All. In Pattern All-Yield, cracks were established at the start of testing, but some tests had additional cracks formed, and yield of the reinforcement affected the stiffness of the slab and thus the effective length. Given these factors, other methods of determining the effective length were considered for the experimental tests.

Method 2 was a slight variation to Method 1 but considered the effective length of the link slab at each individual rotation reading rather than the full rotation history. In other words, instead of finding a single value for the full test, an effective length was found at each time step. This variation was necessary because the deck damage evolved during testing, with the formation and growth of additional cracks in the link slab region. The minimum error and corresponding effective length were found for each rotation value. Method 2 used the higher-resolution steel strain data instead of the lower-resolution bottom strain data, and thus is best compared to Method 1b values.

Figure 10.32 shows the effective link slab length versus rotation for the four experimental tests of non-retrofitted specimens for Pattern All and Pattern All-Yield. For Pattern All, shown by the blue lines, there is a drop in the effective length between 0 and 1000 microradians, indicating the formation of microcracks in most decks. This does not occur on PBJ-FP1 because the initial crack had formed during the curing of the concrete and was not a result of the loading of the deck. As the rotation increases, the effective length also increases due to additional crack formation and strain redistribution. In Pattern All-Yield, shown by the orange lines, the effective length initially climbs sharply until reaching a plateau, often matching the length near the end of the Pattern All test. This plateau continues until the rebar yields, indicated by black stars, after which the length increases again. For PBJ-OP1 (Figure 10.32[b]), a notable drop is present due to a strain gage exceeding its limit at high rotation and strain.

For Method 2, the effective link slab length values presented in Table 10.2 were taken at the peak rotation for Pattern All and at approximately 3000 microradians for Pattern All-Yield. The 3000 microradian value was selected since it fell within the plateau for each test and was prior to yield.

From these values, it is seen that the debonded continuous panel detail (PBJ-CP1) had the longest effective link slab length, with 85 in. and 96 in. for the two patterns, respectively. These lengths are longer than the debonded length of 76 in. The next longest was the bonded flush panel detail (PBJ-FP1) at 64.5 in. and 67.5 in. for both load patterns. For the offset panel designs, the debonded design (PBJ-OP2) had longer lengths than the bonded design (PBJ-OP1) but less than the debonded length and less than that in PBJ-CP1. This finding demonstrates the benefit of having the debonding, and also the need to have a gap in the haunch to fully realize the benefits of debonding. When comparing the PBJ-OP1 and PBJ-OP2 values, it is also important to note that the latter was not only debonded but also lacked chamfer at the bottom, so it is not clear how much of the increase in effective length is attributed to the debonding alone because the chamfer is expected to impact the effective length since it offers a region for the damage to concentrate. In all tests, the effective length was longer for Pattern All-Yield, highlighting the importance of considering the extent of cracking in establishing effective length values to use for design and evaluation.

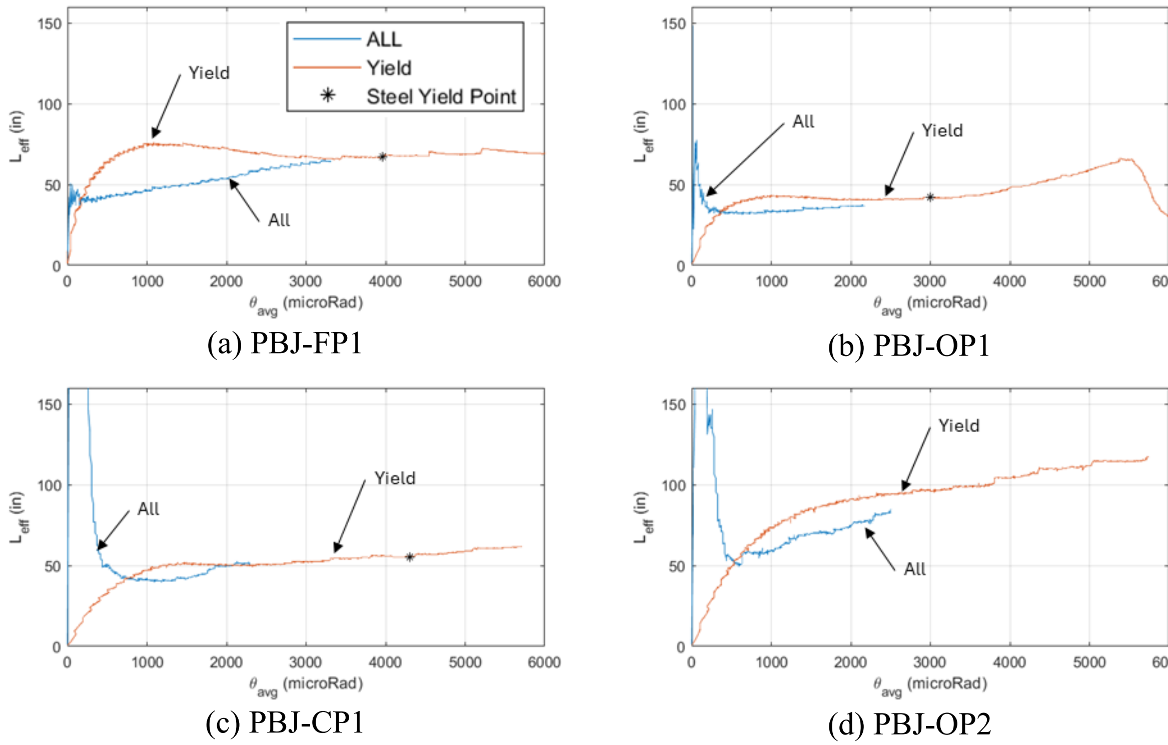

(a) PBJ-FP1 (b) PBJ-OP1

(c) PBJ-CP1 (d) PBJ-OP2

Figure 10.32. Effective link slab lengths calculated with Method 2 for Pattern All and Pattern All-Yield.

The final approach used in establishing the effective link slab length, referred to as Method 3, utilized readings from the Optotrak measurement system. While Method 1 and 2 took an approach based on local data, Method 3 took a more wholistic approach and looks at the overall deformation. The curvature of the deck was determined using the coordinate data from the Optotrak for Pattern All and Pattern All-Yield. A best-fit line was applied to the curve, and the inflection points were identified. The distance between these inflection points was identified and considered the effective length of the link slab.

For Method 3, the findings were similar to those of Method 2, although the lengths were slightly longer except for PBJ-FP1 (flush panels). It was again seen that the debonded continuous panel detail (PBJ-CP1) had the longest effective link slab length, with 78.5 in. for Pattern All-Yield, which is essentially the length of the DLS.

Both Method 2 and Method 3 have pros and cons related to the most appropriate value for the effective length. For the overall deformations, Method 3 is in some ways more beneficial since the entire link slab is expected to take part in the response. In the case of PBJ-CP1, the damage was very well distributed, and the full debonded length was realized. One downside of this is the measurements are limited to the edge of the deck, whereas the deformation profile along the girder centerline would be more appropriate. In Method 2, strains closer to the girder lines are able to be used. In tests with more localized damage, it might be more appropriate to use the localized response in Method 2 to establish the effective length. In future experimental tests, consideration should be made to account for instrumentation to ensure that the global and local responses of the specimen are recorded accurately to estimate effective slab length. In particular, deformation measurements near expected regions of inflection points should be included to ensure the inflection point can be best estimated.

Considering the values from each method and the full history presented in Figure 10.32, recommendations for use in design can be made to provide lengths that err to the shorter potential values, thus producing conservative designs. For debonded designs that include a gap in the haunch at the end of the girder, the debonded length is an appropriate value when considering demands large enough to develop full cracking of the link slab. From the load history, a length of 60 percent of the effective length is the conservative lower bound to use for designs not expected to develop full cracking and would be appropriate for bridge rotation demands found for typical TxDOT bridges. The same 60 percent is a reasonable lower bound for debonded designs without a gap in the haunch. For bonded slabs, consideration for the effective length is less clear because the field and experimental data provide conflicting results. In part, this is complicated by the differences in detailing of the flush panel decks in the field and in the lab. However, damage observed in the lab confirms that damage is more concentrated in the bonded link slabs, so there is a trade-off between the continuity provided by the slab and the potential for concentrated damage. A very conservative approach is to take the effective length as the distance between the center of the bearing pads; however, a more realistic approach would be to determine effective length using a simple continuous beam model with the cracked stiffness of the models.

10.8 SUMMARY

This chapter presented an analysis of data measured during the tests on the six specimens described in Chapter 9. The analysis of data utilized a variety of instrument and crack width measurements to better understand the observed behavior and to support the development of design recommendations described in Chapter 11.

Strain gages were effective in capturing the distribution of strains throughout the link slab region, providing results that are consistent with the crack maps. Strains were most concentrated in the reference tests built with current TxDOT details, with the flush panel design having the greater concentration of strains. The best distribution of strains was significantly improved in the two specimens with debonding, with the best distribution occurring in the specimen with the haunch gap. The deck with the haunch gap was also the only non-retrofit specimen to not have yielding in the longitudinal reinforcement after completion of all tests.

Evaluation of measured crack widths, in conjunction with the crack maps presented in Chapter 9, provide the best assessment of the performance of the individual designs. The flush panel and offset reference tests exceeded crack width limits at girder rotations of 0.003 rad and 0.002 rad, respectively. This finding indicates that unacceptable performance may occur in bridges with higher design demands. Using DLS without a haunch gap significantly reduced the crack widths, providing acceptable performance for bridges with girder end rotations of up to 0.005 rad, which accounts for nearly all bridges in the suite of typical bridges considered in this study. However, increasing the reinforcement in such a slab did not make a noticeable impact on the performance. When debonding included the haunch gap, the effects of the debonding were able to be fully realized, with greater distribution of cracking occurring and significantly smaller crack widths. In PBJ-CP1, the AASHTO crack width limit was not exceeded until a rotation demand of approximately 0.0057 rad, considerably higher than the reference tests of current TxDOT detailing.

A partial-depth debonded slab (PBJ-FP1R) was tested as a potential retrofit option. The design provided acceptable performance up to 0.005 rad when the flush panel reinforcement was used and up to 0.006 rad when the supplemental bars were raised closer to the surface of the concrete. The strain fields from PBJ-FP1R indicate that the partial-depth DLS performed as intended; however, the presence of the board restricted transfer of forces across the bottom portion of the slab to compression only.

In the PBJ-OP1R test, high-performance fiber-reinforced concrete replaced the top portion of the bridge deck. The test was implemented as a retrofit of PBJ-OP1 but can also provide insight into potential new design options utilizing fiber-reinforced concretes. PBJ-OP1R consisted of only the north girder line from the original specimen; thus, the north overhang of PBJ-OP1R was full-depth CIP, while the south overhang was between the girder deck of the original specimen. Due to time and space constraints, the south girder was left in place, so the progression of damage could not be observed during testing. On the north side, debonding of the new concrete from the existing concrete occurred. Strain gages indicated that the top steel had negligible strains in the north overhang and substantial strains in the south overhang. Optotrak data on the north overhang showed significant strains at the interface of the new and existing concrete. It is possible that damage occurred to the bottom of the south overhang during demolition, and thus deformations and forces were forced to transfer through the upper portion of the deck, while on the north overhang, the bottom concrete and steel were intact and provided a better load path. While the specimen itself did not represent ideal construction conditions, sufficient data were gathered, particularly regarding crack width and depth, to demonstrate that the use of fiber-reinforced concrete is effective in improving the performance of concrete, particularly where there are concerns about full-depth cracks developing.

Acceptable performance of the link slabs was assessed for each specimen by considering the AASHTO crack width limit since this crack limit provides a way to assess prevention of water instruction into the deck that can contribute to deterioration of the deck and reduced life span. In the design of concrete, it is often difficult to accurately predict crack width, so limiting steel strains is a viable alternative. In assessing steel strains, a limit of $0.4\varepsilon_y$ was considered. Results showed that when the crack width limits were exceeded, the strain limits were also exceeded, but when the steel strain limits were exceeded, the crack limits were not necessarily exceeded. Thus, limiting steel strains to $0.4\varepsilon_y$ is expected to result in acceptable crack widths for link slabs.

Using the Optotrak measurement system, researchers could make detailed observations about the response of the specimens. This included a dragging effect in the asymmetric loading in Pattern W and Pattern E, which suggests axial loading may be more pronounced in such loading scenarios. Strain fields were used to look at the horizontal, vertical, and shear strains in the overhangs. Comparison of the horizontal strains to the crack maps indicates that tensile stresses were generally concentrated in areas where cracks were observed. For flush panels, the main area of concentration was over the board, with additional regions of concentration offset from the board, suggesting the potential for greater distribution of cracks, but ultimately, the concentration at the board. This finding, along with the measured crack widths, suggests that designs can be improved by eliminating the notch in the board to minimize the effect. A better design option is to eliminate the weak plan at the board altogether by using continuous panels or panels where the edges are angled and sit over one another. For offset and continuous panels, full-depth cracks were associated only with the crack in PBJ-CP1, which appears to be more an anomaly and may be due to the honeycombing that occurred during construction due to lack of proper consolidation.

Finally, the measured data were used to estimate effective link slab lengths that can be used in design procedures.

11. DESIGN RECOMMENDATIONS

In this chapter, the results of the finite element modeling and experimental testing are synthesized to provide recommendations for link slabs in TxDOT bridges. For making rotation limit recommendations for various details, the acceptable crack width limit is taken as 0.017 in., as was used in presenting the experimental test results in Section 10.4. Section 11.1 provides recommendations for (a) limitations to the use of current details, and (b) modifications to improve performance. Section 11.2 provides recommendations for DLS designs for TxDOT bridges. In both recommendations, it is assumed that typical details will apply to most bridges. For bridges where higher performance criteria are needed or design demands have been shown to be higher than those for the typical details, recommendations are made for design procedures to determine the necessary reinforcement and/or material properties. Section 11.3 summarizes the design procedure. Section 11.4 provides a summary of the chapter.

11.1 DETAILING MODIFICATIONS—CURRENT DESIGNS

TxDOT provides two standard details for continuous decks (link slabs) in I-girder bridges: offset panels and flush panels. Both were investigated through experimental testing and finite element modeling. The following subsections provide a summary of recommended limits of use and proposed modifications.

The recommendations are primarily based on positive bending of the girders (top of link slab in tension) and therefore focus on the top longitudinal reinforcement. Under thermal demands, girders can experience negative bending, which places the bottom of the link slab in tension. Simple experimental tests to introduce tension in the bottom of the link slab demonstrated that the location of bottom cracks was typically the same as for top cracks, introducing the potential for full-depth cracks to form. Current TxDOT details do not provide longitudinal reinforcement in the bottom of the deck over the girders. To control width and depth of bottom cracks, sufficient reinforcement should be provided. For decks with partial-depth PCPs, the current details note that bottom reinforcement is provided in the panels, but no bottom longitudinal reinforcement is used over the girders. Since the link slab undergoes negative bending of the girders, only the top reinforcement can restrain cracks for negative bending, leading to nearly full-depth cracks. By including bottom longitudinal bars over the gaps between the girder ends, crack control is significantly improved. The bars over the girders need not extend along the full length of the girder. For consistency with the rest of the deck reinforcement, #4 bars are recommended, with three bars over the girder providing similar spacing to the remainder of the deck. For simplicity, it is recommended that the length of the bars be the same as that of the supplemental reinforcement. In the overhang, it is recommended to increase the number of bottom bars to help control cracks. The addition of two bars in the overhang will provide similar spacing to the recommended increase for top bars.

For both designs, it is recommended to consider modifying the depth of the supplemental reinforcing bars. While this will provide less cover to those bars, the link slabs are deformation controlled, and thus the controlling of crack widths is more critical than the strength provided by the bars. By locating some of the bars closer to the surface, better crack control is provided, and a greater number of small cracks can form. While this was not investigated experimentally for new designs, the concept was validated in the PBJ-FP1R retrofit test.

11.1.1 Offset Panels

The current standard TxDOT detail for offset panels essentially continues the deck top reinforcement through the link slab region, with the continuous deck full-depth CIP for at least 18 in. at the ends of the girders. The minimum length was used in models and experimental tests, and no negative performance was associated with the location of the termination of the panel; thus, no changes are recommended to that aspect of the design. The reinforcement in current details is #4 @ 9 in. This is half what is used in the flush panel details and led to larger crack widths at comparable demands. For the offset panel tests, cracks exceeded the AASHTO crack width limit at girder rotations of approximately 0.002 rad. Thus, it is recommended that the current detail be restricted to bridges with 0.002 rad or smaller. Table 11.1 through Table 11.6 indicate acceptable use for TxDOT standard bridges considered in this report (values provided in Appendix A).

For larger rotation demands, it is recommended to increase the reinforcement by adding supplemental reinforcing bars in between the deck top longitudinal reinforcement; this is the same as is done for the flush panel detail. Finally, it is recommended to eliminate the use of the chamfer on the bottom of the deck and use a haunch gap to eliminate points of potential strain concentrations.

11.1.2 Flush Panels

The current standard TxDOT detail for flush panels utilizes a ¾-in. board between the panels, with a notch at the top of the board to act as a crack former. Reinforcement in the link slab region is #4 @ 4.5 in. (the deck reinforcement of #4 @ 9-in. spacing plus supplemental bars in between the main bars). In finite element modeling and experimental testing, the damage was shown to concentrate over the board. Given the concentration of damage at the center of the link slab, the 10-ft length of the supplemental longitudinal bars is acceptable, and no modifications are recommended. From measured crack widths, the design was found to be acceptable for bridges with girder end rotation design values of 0.003 rad or smaller. Table 11.1 through Table 11.6 indicate acceptable use for TxDOT standard bridges considered in this report (values provided in Appendix A). For bridges with larger demands, other details are recommended, or modifications to reduce the crack widths.

Crack widths can be reduced with additional longitudinal reinforcement or alternative concretes such as fiber-reinforced concrete that can help to reduce the crack widths. Additional longitudinal reinforcement can be provided by increasing the number of supplemental bars such that the total spacing is #4 @ 3 in. To help reduce the tendency for damage to concentrate at the board, it is recommended to remove the notch at the top of the board. In the overhang, it is recommended to avoid the use of the chamfer to allow the strains and damage to be better dispersed.

Field observations of flush panel details indicated some bridges were constructed with a larger than ¾-in. gap between the panels. While such a design was not tested in the lab, finite element models show slight improvement in the behavior of such a construction detail; thus, there are no concerns for adverse effects of bridges constructed in such a manner.

11.1.3 Continuous Panels

As an alternative to flush panels, it is recommended to modify current flush panel details to be continuous panel details, with the flush panels serving as a limited-use alternative if continuous panels are not practical. The continuous panel provides continuity of the bottom of the deck and provides some prestressing to improve the crack resistance of the concrete. While experimental tests were not conducted on bonded continuous panel designs, finite element modeling demonstrated greater distribution of cracks than flush panel designs. For bonded link slabs with continuous panels, it is recommended to use a haunch gap to eliminate a point of potential strain concentrations. A haunch gap is a small void between the top of the girder and the bottom of the haunch. The purpose is to reduce the potential for cracks to form in the top of the deck above the girder ends due to vertical displacement of the girder end. The gap can be formed using polystyrene or compressible gasket and needs to be only 0.5 inch thick.

From a planning perspective, care is needed to ensure panels of the appropriate length are specified for a continuous panel bridge. Typical practice for offset panels is to use 8-ft long panels. The full-depth region specifies only a minimum length, so the need for custom panel lengths is avoided. For flush panels, custom-length panels may be needed depending on the span length, with some construction tolerance available by allowing a wider gap between the flush panels. If continuous panels are used, custom-length panels are also needed, but construction tolerance cannot be accommodated in the link slab. Instead, it can be accommodated by permitting those same tolerances at the ends of the panel that is continuous over the girder ends. While this will simply shift the weak point to a different location, the weak point will be closer to the inflection point where strains are lower and where water leakage through potential cracks will not impact the bents and ends of girders.

Table 11.1. Acceptable use of current TxDOT offset panel and flush panel details for 24-ft wide standard bridges (6.67-ft girder spacing).

Girder Size	Span Length, ft	Offset Panels	Flush Panels
Tx28	40	yes	yes
Tx28	55	no	yes
Tx28	75	no	no
Tx34	40	yes	yes
Tx34	60	no	yes
Tx34	85	no	no
Tx40	40	yes	yes
Tx40	70	no	yes
Tx40	100	no	no
Tx46	40	yes	yes
Tx46	75	yes	yes
Tx46	115	no	no
Tx54	40	yes	yes
Tx54	80	yes	yes
Tx54	125	no	no

Table 11.2. Acceptable use of current TxDOT offset panel and flush panel details for 28- and 44-ft wide standard bridges (8-ft girder spacing).

Girder Size	Span Length, ft	Offset Panels	Flush Panels
Tx28	40	yes	yes
Tx28	55	no	yes
Tx28	70	no	no
Tx34	40	yes	yes
Tx34	60	no	yes
Tx34	85	no	no
Tx40	40	yes	yes
Tx40	65	yes	yes
Tx40	95	no	no
Tx46	40	yes	yes
Tx46	70	yes	yes
Tx46	105	no	no
Tx54	40	yes	yes
Tx54	80	yes	yes
Tx54	125	no	no

Table 11.3. Acceptable use of current TxDOT offset panel and flush panel details for 30-ft wide standard bridges (8.67-ft girder spacing).

Girder Size	Span Length, ft	Offset Panels	Flush Panels
Tx28	40	yes	yes
Tx28	55	no	yes
Tx28	70	no	no
Tx34	40	yes	yes
Tx34	60	no	yes
Tx34	80	no	no
Tx40	40	yes	yes
Tx40	65	yes	yes
Tx40	95	no	no
Tx46	40	yes	yes
Tx46	70	yes	yes
Tx46	105	no	no
Tx54	40	yes	yes
Tx54	80	yes	yes
Tx54	120	no	no

Table 11.4. Acceptable use of current TxDOT offset panel and flush panel details for 32-ft wide standard bridges (9.33-ft girder spacing).

Girder Size	Span Length, ft	Offset Panels	Flush Panels
Tx28	40	yes	yes
Tx28	50	yes	yes
Tx28	65	no	no
Tx34	40	yes	yes
Tx34	60	no	yes
Tx34	80	no	no
Tx40	40	yes	yes
Tx40	65	yes	yes
Tx40	90	no	no
Tx46	40	yes	yes
Tx46	70	yes	yes
Tx46	100	no	no
Tx54	40	yes	yes
Tx54	80	yes	yes
Tx54	120	no	no

Table 11.5. Acceptable use of current TxDOT offset panel and flush panel details for 38-ft wide standard bridges (8.5-ft girder spacing).

Girder Size	Span Length, ft	Offset Panels	Flush Panels
Tx28	40	yes	yes
Tx28	55	no	yes
Tx28	70	no	no
Tx34	40	yes	yes
Tx34	60	no	yes
Tx34	80	no	no
Tx40	40	yes	yes
Tx40	65	yes	yes
Tx40	95	no	no
Tx46	40	yes	yes
Tx46	70	yes	yes
Tx46	105	no	no
Tx54	40	yes	yes
Tx54	80	yes	yes
Tx54	125	no	no

Table 11.6. Acceptable use of current TxDOT offset panel and flush panel details for 40-ft wide standard bridges (9-ft girder spacing).

Girder Size	Span Length, ft	Offset Panels	Flush Panels
Tx28	40	yes	yes
Tx28	50	yes	yes
Tx28	65	no	no
Tx34	40	yes	yes
Tx34	60	no	yes
Tx34	80	no	no
Tx40	40	yes	yes
Tx40	65	yes	yes
Tx40	90	no	no
Tx46	40	yes	yes
Tx46	70	yes	yes
Tx46	105	no	no
Tx54	40	yes	yes
Tx54	80	yes	yes
Tx54	120	no	no

11.2 PROPOSED DESIGNS

DLSs are viable options for offset and continuous panel details. Debonded link slabs with flush panel detail are not recommended because the weak plane at the panel gap leads to concentration of deformation that is not overcome by the debonding, making the additional construction efforts inefficient. Experimental tests demonstrated that debonded link slab designs are acceptable for bridges with girder rotations as large as 0.005 rad or 0.0057 if a haunch gap is used. Given the overall improved performance of the debonded slabs as determined by the crack widths, debonded link slabs can be used for any bridges without concern for durability as related to cracks forming on the top of the deck. However, where it is desired to minimize the labor and materials to debond the slab, or where there is concern for durability related to the interface of the deck and top of the girder, lower-bound girder rotations to trigger the use should be the upper-bound rotations for the existing details, as indicated in the prior section.

For debonded link slabs, the debonding should be limited to a distance not expected to impact the composite response of the girder and deck and to not negatively impact the shear strength of the girder since the deck is considered part of the depth for calculation of shear strength. To ensure this, the length of debonding, L_{db}, should be limited to a distance of d_v from the center of the bearing pad, where d_v is the effective depth of the girder without the deck. The experimental tests confirm this is reasonable since shear cracks were not observed in this region of the girders. The recommended maximum debonded length, L_{db}, along a girder is taken as d_v plus 9 in. from the center of the bearing pad to the end of the girder. The maximum debonded length varies based on the size of the girder. Table 11.7 provides these values for Tx28 through Tx70. Also included is the associated full effective link slab length, L_{eff}, which is calculated as the L_{db} along each girder plus the design 6-in. gap between the ends of the girders.

Table 11.7. Recommended debonded lengths, L_{db}, for girder size.

Girder Size	d_v, in.	L_{db}, in.	L_{eff}, in.
Tx28	26.75	36	78
Tx34	31	40	86
Tx40	36.5	45	96
Tx46	41.75	50	106
Tx54	49	58	122
Tx62	56.25	65	136
Tx70	63.5	72	150

Debonding provides an improved performance over bonded link slabs because the effective length of the link slab is longer, providing a greater range for cracks to disperse. The debonding is best realized when other details are eliminated that can cause strain concentrations that result in cracks forming. In addition to avoiding flush panel details, concentrations to eliminate are the use of zip strips and bottom chamfers because these encourage cracks to form at certain locations. The end of the girder is another potential cause of early cracking that can limit the overall dispersion of cracks. To avoid this, use of a haunch gap at the ends of the girders is recommended. The haunch gap used in the experimental tests was shown to be effective and is recommended for inclusion in any debonded link slab detail. The haunch is formed by placing a 0.5-in. thick piece of compressible material (e.g., polystyrene or rubber gasket) at the top of the girder at the ends.

11.3 DESIGN PROCEDURE

Although the behavior of link slabs is fundamentally a deformation-controlled response since the deformations and thus internal forces of the link slab are determined by the girder end rotations, most design recommendations focus on utilizing the girder end rotation to calculate a design moment. Should a bridge warrant consideration for an individual design, a designer may choose to use such a design procedure due to the simplicity of the process. This section provides a summary of this design procedure and recommendations for values to use.

The link slab moment, M, can be calculated as:

$$M = \frac{2EI_{eff}}{L_{eff}}\theta \qquad (11.1)$$

where M is the link slab moment, k-in; E is the modulus of elasticity of the concrete, ksi; I_{eff} is the effective moment of inertia, in^4; L_{eff} is the effective link slab length, in.; and θ is the average girder end rotation.

The girder end rotation should be determined using the thermal and live load demands for both the service and strength load combinations, as outlined in Chapter 2. For the live load, the average girder end rotation should be found by using the lane load in both spans, with the truck live load acting in the longer of the two spans. Alternatively, the live load girder end rotation can be taken as the lane load and one-half the truck when spans are the same length.

The I_{eff} used should be based on a determination of the cracked condition of the slab and may more generally be considered as the flexural stiffness EI_{eff} and determined from a moment-curvature analysis of the slab. For designs with ordinary concrete, the cracked stiffness should be used; it is recommended to include both layers of steel in such a calculation. For designs where alternative material is used, I_{eff} can be taken as the gross moment of inertia if the objective of the design is to avoid cracking. If cracking is expected to begin but not be fully developed, a more detailed analysis is required to determine an appropriate stiffness for design. Such an analysis will need to consider the effective length, so a nonlinear analysis or iterative elastic analysis is recommended.

The effective link slab length, L_{eff}, is dependent on the type of link slab detail used. For debonded designs that include a gap in the haunch at the end of the girder, the debonded length is an appropriate value for the design when considering demands large enough to develop full cracking of the link slab. For all other debonded link slabs, 60 percent of the effective length is a conservative lower bound to use for design. For bonded slabs, a very conservative approach is to take the effective length as the distance between the center of the bearing pads. A more realistic approach would be to determine effective length using a simple continuous beam model with the cracked stiffness of the deck.

11.4 SUMMARY

Current offset panel designs are acceptable for bridges with girder rotations less than 0.002 rad. For larger demands, it is recommended to include supplemental top longitudinal reinforcing bars similar to those used for current flush panel details. Regardless of girder rotation demands, it is recommended to modify the detail to remove the chamfer on the bottom of the deck; this will eliminate a point where deformation and therefore damage can concentrate.

Flush panel designs are acceptable for bridges with girder rotations less than 0.003 rad. However, due to the weak plane at the panel gap, damage concentrates at a single crack over the board, and crack widths are larger than those for other details. It is recommended to limit flush panel use where continuous panels are a practical alternative.

Debonded link slab designs are acceptable for bridges with girder rotations as large as 0.005 rad or 0.0057 if a haunch gap is used. Supplemental reinforcement bars are recommended to help reduce crack widths, and a gap haunch is strongly recommended to promote distributed cracking and smaller cracks. The length of the debonded zone should be maximized to provide flexibility to the link slab but should not exceed the recommended limits for girder depth. The limits are based on not providing debonding farther than the shear depth from the center of the bearing pad, thereby avoiding reduction in the shear strength of the girder.

Finally, for all designs, it is recommended that bottom longitudinal bars be included over the girder lines and increase the number of bars for bottom longitudinal reinforcement in the overhangs. This is to provide better control of cracks that form due to negative bending of the girders under thermal loads, reducing the potential for full-depth cracks to form.

12. SUMMARY AND CONCLUSIONS

12.1 OVERVIEW

TxDOT Research Project 0-7013 was undertaken to investigate the performance of continuous deck details in I-girder bridges and make recommendations for improved designs. Such details, commonly known as link slabs, are referred to as poor boy joints in Texas because of the design being a continuation of the deck reinforcement through the link slab region. Decks in Texas bridges utilize partial-depth PCPs as stay-in-place formwork and the bottom 4 in. of 8.5-in. thick decks. The remainder of the deck is CIP concrete. The use of the panels requires unique consideration in the continuous deck region. At the time the research project was initiated, two standard details were available. The first uses offset panels, in which the panels terminate prior to the ends of the girders and the link slab is full-depth CIP. The second uses flush panels, in which the panels from each span terminate in the gap between the ends of the girders and are separated only by a ¾-in. board. Despite widespread use of PBJ details, a comprehensive investigation of the performance had not been done, leading to the initiation of Project 0-7013.

The research project consisted of the following tasks:

- Literature Review.
- Inventory Survey.
- Finite Element Modeling.
- Full-Scale Experimental Testing.
- Design Recommendations.

Chapters 2–6 presented the literature review and inventory survey, which consisted of evaluation of nearly as-built drawings and inspection reports for nearly 500 bridges, nondestructive evaluation of eight bridges, and monitoring five bridges for deformations under live and thermal loads. Chapters 7–11 presented the finite element modeling, full-scale experimental testing, and design recommendations. This chapter concludes the final report of the study. Section 12.2 summarizes the findings. Section 12.3 provides recommendations for future research.

12.2 FINDINGS

The demands in link slabs are governed by the rotation of the girder ends. Prior studies on link slabs have primarily used an assumption that live load, with no thermal demands, control the response of the link slab. Consequently, the girder end rotation for design is that associated with the maximum deflection limit allowed for girders. Such an approach does not consider the positioning of trucks and what will cause the rotation, or how the live and thermal deformations interact. In this research project, a more robust investigation of demands was conducted, in which girder end rotations were considered for all truck positions and combined with rotation estimates for thermal loads. This was completed for a suite of typical TxDOT I-girder bridges with various lengths. The result of this task was a relationship between the girder stiffness (including slab) and the design rotation. This allows for bridges to be designed for appropriate demands for the girder size, spacing, and span length, rather than a single value for all bridges. This brings the rotation down to approximately one-third of the demands recommended by others.

The performance of designs was investigated first through detailed finite element models and full-scale experimental tests that were constructed with the same details used in actual bridge construction, including the same girders, bearing pads, PCPs, bedding strips, and deck reinforcement. The first two specimens were reference tests constructed based on the TxDOT standard details for offset and flush panels. Both specimens were subsequently used to explore retrofit options. The performance of link slabs is determined by the extent and size of cracks. Given the complexity of detailing at the girder ends, there are several ways in which cracks can be introduced. The finite element models served as an efficient way to explore these small details. The findings of the models with different characteristics were used to determine the detailing that was expected to best improve the performance. The most influential details were found to be the use of debonding, use of a haunch gap at the end of the girders, and elimination of chamfer on the bottom of the center of the link slab. These details were implemented in the final two specimens of the experimental test program and demonstrated significantly improved behavior.

Flush panel designs were found to be acceptable for bridges with girder rotations less than 0.003 rad. However, due to the weak plane at the panel gap, damage concentrates at a single crack over the board and crack widths were larger than those for other details options. The use of continuous panels is an alternative to flush panels that can eliminate the weak plane that occurs at the gap between panels in the flush panel design. Wherever practical, continuous panels should be used over flush panels. Where flush panel details are used, consideration should be made for additional steel to reduce crack widths.

Offset panel designs with the current details were found to be acceptable to girder end rotations of 0.002 rad. While the finite element models and experimental studies showed a slight increase distribution of damage relative to the flush panels, the acceptable rotation was less due to less reinforcement being used. Thus, for bridges with design demands greater than 0.002 rad, it is recommended to include supplemental reinforcement bars to minimize crack widths. Finally, it is recommended to eliminate the use of the chamfer on the bottom of the deck and to use a haunch gap to eliminate points of potential strain concentrations.

Debonded link slab designs are acceptable for bridges with girder rotations as large as 0.005 rad or 0.0057 if a haunch gap is used. Supplemental reinforcement bars are recommended to help reduce crack widths, and a gap haunch is strongly recommended to promote distributed cracking and smaller cracks. The length of the debonded zone should be maximized to provide flexibility to the link slab but should not exceed the recommended limits for girder depth. The limits are based on not providing debonding further than the shear depth from the center of the bearing pad, thereby avoiding reduction in the shear strength of the girder.

Finally, for all designs, it is recommended that at least three #4 bottom longitudinal bars be included over the girder lines and the number of bars be increased for bottom longitudinal reinforcement in the overhangs (two additional bars). This is to provide better control of cracks that form due to negative bending of the girders under thermal loads, reducing the potential for full-depth cracks to form.

Two retrofit options were considered. In both, only the top portion of the slab was removed and replaced with new material. In the first, a partial-depth debonded slab provided acceptable performance up to 0.005 rad when the flush panel reinforcement was used and up to 0.006 rad when the supplemental bars were raised closer to the surface of the concrete. The raised bars were shown by finite element modeling to provide improved performance due to the depth allowing the bars to carry tension throughout loading history. The retrofit was tested on a deck originally conducted with the flush panel detail. The Optotrak data revealed that transfer of forces in the lower half of the deck was primarily through compression. The behavior of a partial-depth debonded retrofit on a deck originally with full-depth CIP slab was not studied experimentally.

In the second retrofit option, the use of high-performance fiber-reinforced concrete (investigated in specimen PBJ-OP1R), the crack depths were considerably less than those in the new designs and crack widths were smaller. Performance issues were observed in the transition region, and there were apparent differences in the transfer of forces, likely due to the demolition methods performed on the specimen and limited time available to construct a more detailed transition zone. Despite these performance issues in the transition zone, use of fiber-reinforced concrete for new and retrofit designs can be a viable option with improved detailing of the transition zones, which can be achieved using recommendations found in the literature. However, given the costs and construction expertise needed in using various alternative materials, it is recommended to limit the use of such materials to the design of bridges expected to have large girder end rotations or bridges where extended service life is desired.

Experimental tests were subjected to several suites of loading patterns. The main one, Pattern All, applied equal loads to both spans and was consistent with experimental tests found in the literature as well as design procedures. In the next set of load patterns (Pattern W and Pattern E), one span (primary) was loaded while the other span (secondary) was held with a constant small load. The objective was to simulate the behavior of unequal live load in the two spans. In many tests, no new damage was seen beyond that in the Pattern All tests. When new cracks did occur, they were more likely to occur over the ends of the secondary span. Optotrak deformations on the overhangs also indicated behavior suggesting that the cracks were occurring as the result of horizontal deformation of the link slab between the girder ends that was not seen in the symmetric loading pattern. However, data from internal strain gages attached to the reinforcing bars did not indicate any differences in the response from one side to the other, with the magnitude of the strains the same on each side of the link slab regardless of which span was loaded. The final set of load patterns (Pattern N, Pattern NW, and Pattern NE) loaded a single girder line more than the other to simulate live loads present on only a portion of the width of the deck. These produced some damage seen in the field evaluations but not otherwise seen in the literature.

The results from the final suite of load patterns were used for validation of finite element models subjected to complex loading states. The models were in turn used to investigate performance of link slabs for skewed bridges. Findings revealed that skewed girder ends produced more linear and controlled cracking than using non-skewed ends, but differences in the onset of cracking or the crack widths were not excepted. Skewed models with debonding were shown to delay and distribute cracking better than bonded models.

12.3 RECOMMENDATIONS FOR FUTURE RESEARCH

Recommendations for future research include the following:

- Many experimental tests found in the literature are scaled and/or use end conditions that do not reflect the fact that bearing pads are typically located in from the end of the girders. This can influence the types of crack patterns. For future experimental tests, it is recommended to use support locations and conditions that reflect field conditions.
- While recommendations for effective link slab lengths to use in design were made for bonded link slabs, the recommended values are very conservative. A more in-depth study is needed to consider the appropriate value that should be undertaken, particularly considering the relative stiffness of the girders and deck and the potential presence of crack formers/chamfers that concentrate damage.
- AASHTO load combinations, thermal gradients, and live load calculations should be evaluated for appropriateness for use with link slabs. Such an effort would be supported by extensive monitoring of bridges (a) over longer periods of time, in a greater distribution of regions, and with controlled live load tests using design trucks; and (b) with greater range of link slab detailing, slab thicknesses, and girder types. Simplified numerical models would support monitoring efforts and could be used to determine if load combinations are appropriate for link slab design.
- Further experimental testing and/or finite element modeling of partial-depth DLS designs are needed to better consider conditions in which such a retrofit might be applied. This testing includes original depths that have full-depth CIP link slabs so that the manner of transfer of forces, particularly under asymmetric loading, can be understood.

- The performance of retrofit on decks thinner than 8.5” thick should be evaluated prior to widespread implementation.
- Experimental testing of link slabs in skewed bridges would be beneficial.
- Testing and monitoring of bonded and unbonded link slab performance under cyclic loading is needed to better characterize performance over time.
- As part of the field monitoring and experimental tests, effective link slab lengths were estimated using girder end rotations and deck strains. Given the discrepancies in the data collected, a more robust investigation would be beneficial to improving recommendations to use for design procedures. The effective link slab length is not a value that has been considered in prior experimental studies; thus, it is recommended that any future experimental tests consider such measurements whenever practical. In particular, field monitoring of flush panel designs would be of value to better understand the performance. For all designs, better understanding would be achieved by monitoring decks from the time of construction onward with instrumentation including internal strain gages.

REFERENCES

AASHTO. (2012). *LRFD Bridge Design Specifications* (6th ed).

AASHTO. (2017). *LRFD Bridge Design Specifications* (8th ed).

AASHTO. (2018). *LRFD Guide Specifications for Accelerated Bridge Construction*.

Aktan, H., Attanayake, U., and Ulku, E. (2008). *Combining Link Slab, Deck Sliding over Backwall, and Revising Bearings*. Western Michigan University, Michigan Department of Transportation.

Al-Rousan, R. Z., Alhassan, M., and Al-Wadi, R. (2020). Nonlinear finite element analysis of full-scale concrete bridge deck slabs reinforced with FRP bars. *Proc., Structures*, Elsevier, 1820–1831.

Au, A., Lam, C., Au, J., and Tharmabala, B. (2013). Eliminating deck joints using debonded link slabs: research and field tests in Ontario. *Journal of Bridge Engineering*, 18(8), 768–778.

Azizinamini, A., Power, E. H., Myers, G. F., and Ozyildirim, H. C. (2014). *Bridges for Service Life Beyond 100 Years: Innovative Systems, Subsystems, and Components*. Florida International University.

Banks, R. K. (1984). *Inspection and Maintenance of Concrete Bridges.* American Society of Civil Engineers.

Bayrak, O., Chao, S. H., Jirsa, J. O., Klingner, R. E., Azimov, U., Foreman, J., and Foster, S. (2013). *Bridge Deck Reinforcement and PCP Cracking: Final Report*. Center for Transportation Research.

Bazant, Z. P., and Murphy, W. (1995). Creep and shrinkage prediction model for analysis and design of concrete structures-model B3. *Matériaux et Constructions*, 28(180), 357–365.

Burke Jr, M. P. (1989). *Bridge deck joints*. Transportation Research Board, National Research Council.

Butler, H. (1988). *Bridge Slab Construction Using Super Water Reducers: Final Report*. Texas State Department of Highways and Public Transportation, Bridge Division.

Canales Jr., M. T. (2019). *Performance Study of Link Slab Continuity in Prestressed Concrete Bridges*. Doctoral Dissertation, Louisiana State University.

Canales, M., and Okeil, A. (2019). Parametric study of partially continuous bridge spans. Paper presented at the 98th Transportation Research Board Annual Meeting.

Caner, A., and Zia, P. (1998). Behavior and design of link slabs for jointless bridge decks. *PCI Journal*, 43, 68–81.

Charuchaimontri, T., Senjuntichai, T., Ožbolt, J., and Limsuwan, E. (2008). Effect of lap reinforcement in link slabs of highway bridges. *Engineering Structures*, 30(2), 546–560.

Chaudhari, S., and Chakrabarti, M. (2012). Modeling of concrete for nonlinear analysis using finite element code ABAQUS. *International Journal of Computer Applications*, 44(7), 14–18.

Davidson, E., White, D., and Kahn, L. (2012). *Evaluation of Performance and Maximum Length of Continuous Decks in Bridges: Part 2.* Georgia Department of Transportation.

Davis, R. T., Thompson, M., Wood, B., Breen, J., and Kreger, M. (1999). *Measurement-Based Performance Evaluation of a Segmental Concrete Bridge*. Center for Transportation Research.

El-Safty, A. K. (1995). *Behavior of Jointless Bridge Decks*. Doctoral Dissertation, North Carolina State University.

English, B. A., Klinger, R. E., and Yura, J. A. (1994). *Elastomeric Bearings: Background Information and Field Study*. Interim Research Report 1304-1. Center for Transportation Research.

Folliard, K., Smith, C., Sellers, G., Brown, M., and Breen, J. (2003). *Evaluation of Alternative Materials to Control Drying-Shrinkage Cracking in Concrete Bridge Decks*. Center for Transportation Research.

French, C. E., Eppers, L., Le, Q., and Hajjar, J. (1999). *Transverse Cracking in Bridge Decks: Summary Report*. Minnesota Department of Transportation.

Frosch, R. J., Blackman, D. T., and Radabaugh, R. D. (2003). *Investigation of Bridge Deck Cracking in Various Bridge Superstructure Systems*. Joint Transportation Research Program, Indiana Department of Transportation and Purdue University.

Gastal, F. (1986). *Instantaneous and Time-Dependent Response and Strength of Jointless Bridge Beams*. Doctoral Dissertation, North Carolina State University.

Ge, X., Munsterman, K., Deng, X., Reichenbach, M., Park, S., Helwig, T., Engelhardt, M. D., Williamson, E., and Bayrak, O. (2021). *Designing for Deck Stress over Precast Panels in Negative Moment Regions*. Center for Transportation Research. https://library.ctr.utexas.edu/ctr-publications/5-6909-01-1.pdf

Gergely, P., and Lutz, L. A. (1968). Maximum crack width in reinforced concrete flexural members. *American Concrete Institute Journal & Proceedings,* Special Publication, 20, 87–117.

Gergess, A. N. (2019). Analysis of bonded link slabs in precast, prestressed concrete girder bridges. *PCI Journal,* 64(3), 47–65.

Gross, S. P., and Burns, N. H. (2000). *Field Performance of Prestressed High Performance Concrete Highway Bridges in Texas*. Center for Transportation Research.

Hedlund, H. (2000). *Hardening Concrete: Measurements and Evaluation of Non-elastic Deformation and Associated Restraint Stresses*. Luleå Tekniska Universitet.

Holt, E. E. (2001). *Early Age Autogenous Shrinkage of Concrete*. Technical Research Centre of Finland Espoo.

Holt, J., and Smith, A. (2014). Reducing steel in bridge decks. *Concrete Bridge Views*, 78.

Hou, M., Hu, K., Yu, J., Dong, S., and Xu, S. (2018). Experimental study on ultra-high ductility cementitious composites applied to link slabs for jointless bridge decks. *Composite Structures*, 204, 167–177.

Husain, I., and Bagnariol, D. (2000). Design and performance of jointless bridges in Ontario: New technical and material concepts. *Transportation Research Record,* 1696(1), 109–121.

Keoleian, G. A., Kendall, A., Dettling, J. E., Smith, V. M., Chandler, R. F., Lepech, M. D., and Li, V. C. (2005). Life cycle modeling of concrete bridge design: Comparison of engineered cementitious composite link slabs and conventional steel expansion joints. *Journal of Infrastructure Systems*, 11(1), 51–60.

Kim, Y. Y., Fischer, G., and Li, V. C. (2004). Performance of bridge deck link slabs designed with ductile engineered cementitious composite. *Structural Journal*, 101(6), 792–801.

Kowalsky, M. J., and Wing, K. M. (2003). *Analysis of an Instrumented Jointless Bridge: Final Report*. North Carolina State University Department of Civil Engineering.

Krajeck, D. D. (2023). *Experimental Testing and Behavior of TxDOT "Poor-Boy" Link Slab Details for Multi-Span Bridge Decks*. Master's Thesis, Texas A&M University.

Kumar, A. (1998). Deckslab continuity for composite bridges. *The Structural Engineer*, 76(23/24), 447–458.

Lam, C., Lai, D., Au, J., Lim, L., Young, W., and Tharmabala, B. (2008). Development of concrete link slabs to eliminate bridge expansion joints over piers. *Proc., 2008 Annual Conference of the Transportation Association of Canada*.

Lárusson, L. H., Stang, H., and Fischer, G. (2013). *Development of Flexible Link Slabs Using Ductile Fiber Reinforced Concrete*. PhD Thesis, Technical University of Denmark.

Lepech, M., and Li, V. C. (2005). Design and field demonstration of ECC link slabs for jointless bridge decks. *Proc., Proceedings of the 3rd International Conference on Construction Materials: Performance, Innovations and Structural Implications*, 22–24.

Lepech, M. D., and Li, V. C. (2009). Application of ECC for bridge deck link slabs. *Materials and Structures*, 42(9), 1185–1195.

Mothe, R. N. (2006). *Partial Continuity in Prestressed Concrete Girder Bridges with Jointless Decks*. Master's Thesis, Louisiana State University.

Munsterman, K. (2017). *Designing for Deck Stress over Precast Panels in Negative Moment Regions*. Master's Thesis, University of Texas at Austin.

Okeil, A. M., and ElSafty, A. (2005). Partial continuity in bridge girders with jointless decks. *Practice Periodical on Structural Design and Construction*, 10(4), 229–238.

Paraschos, A., and Amde, A. M. (2011). A survey on the status of use, problems, and costs associated with integral abutment bridges. *Better Roads*, 1–20.

Pesek, P., Riding, K., Schindler, A., Folliard, K., Drimalas, T., and Byard, B. (2013). *Development of Predictive Model for Bridge Deck Cracking: Final Report.* Center for Transportation Research.

Peterman, R. J., and Rammirez, J. (1998). Restraint moments in bridges with full-span prestressed concrete form panels. *PCI Journal*, 43(1).

Qian, S., Lepech, M. D., Kim, Y. Y., and Li, V. C. (2009). Introduction of transition zone design for bridge deck link slabs using ductile concrete. *ACI Structural Journal*, 106(1).

Roberts, C. L., Breen, J. E., and Kreger, M. E. (1993). *Measurement Based Revisions for Segmental Bridge Design and Construction Criteria*. Center for Transportation Research.

Romkema, M., Attanayake, U. B., Aktan, H. M., and Ulku, E. (2011). *Incorporating Link Slabs in High Skew Bridges during Repair Activities—Design Recommendations*.

Saber, A., and Aleti, A. R. (2012). Behavior of FRP link slabs in jointless bridge decks. *Advances in Civil Engineering*, 2012, 1–9.

Samani, S. G. (2015). *Structural Performance of Link Slabs Subjected to Monotonic and Fatigue Loading Incorporating Engineered Cementitious Composites*. Master's Thesis, Ryerson University.

Shafei, B., Taylor, P., Phares, B., Dopko, M., Karim, R., Hajilar, S., and Najimi, M. (2018). *Material Design and Structural Configuration of Link Slabs for ABC Applications*. Bridge Engineering Center.

Snedeker, K., White, D., and Kahn, L. (2011). *Evaluation of Performance and Maximum Length of Continuous Decks in Bridges: Part 1*. Georgia Institute of Technology.

Smith, D. M. (2022). *Experimental Testing and Behavior of TxDOT "Poor-Boy" Link Slab Details Using Flush Panels*. Master's Thesis, Texas A&M University.

Stringer, D. J., and Burgueño, R. (2012). *Identification of Causes and Solution Strategies for Deck Cracking in Jointless Bridges.* Michigan Department of Transportation.

Terzioglu, T. (2015). *Behavior and Design of Spread Prestressed Concrete Slab Beam Bridges.* Doctoral Dissertation, Texas A&M University.

Thippeswamy, H. K., and Gangarao, H. V. (1995). Analysis of in-service jointless bridges. *Transportation Research Record*, 1476.

TxDOT. (2021). *Concrete Repair Manual*.

Wassef, W. G., Smith, C., Clancy, C. M., and Smith, M. J. (2003). *Comprehensive Design Example for Prestressed Concrete (PSC) Girder Superstructure Bridge with Commentary (in US Customary Units)*. Federal Highway Administration.

Wang, C., Shen, Y., Zou, Y., Zhuang, Y., and Li, T. (2019). Analysis of mechanical characteristics of steel-concrete composite flat link slab on simply-supported beam bridge. *KSCE Journal of Civil Engineering*, 23, 3571–3580.

Wing, K. M., and Kowalsky, M. J. (2005). Behavior, analysis, and design of an instrumented link slab bridge. *Journal of Bridge Engineering*, 10(3), 331–344.

Yang, E.-H., Li, V. C., and Qiu, J. (2015). Early age cracking in a SHCC bridge deck link slab. In *Forensic Engineering*, pp. 746–755.

Zheng, Y., Zhang, L., and Xia, L. (2018). Investigation of the behaviour of flexible and ductile ECC link slab reinforced with FRP. *Construction and Building Materials*, 166, 694–711.

Zia, P., El-Safty, A. K., and Caner, A. (1995). *Jointless Bridge Decks*. Center for Transportation Engineering Studies, North Carolina State University.

Zuk, W. (1980). *Jointless Bridges: Interim Report*. Virginia Transportation Research Council.

Zuk, W. (1981). *Jointless Bridges*. Virginia Transportation Research Council.

APPENDIX A. DESIGN GIRDER ROTATIONS FOR TYPICAL TXDOT I-GIRDER BRIDGES

Table A.1. Unfactored girder end rotations for live load and thermal gradient for 24-ft wide standard bridges (6.67-ft girder spacing).

Girder Size	Span Length, ft	$\frac{EI}{L^2}$ kips × 10^4	θ_{lane} rad × 10^{-3}	θ_{truck} rad × 10^{-3}	θ_{live} rad × 10^{-3}	θ_{neg} rad × 10^{-3}	θ_{pos} rad × 10^{-3}
Tx28	40	0.38	0.26	1.12	0.82	0.75	−2.51
Tx28	55	0.20	0.68	2.51	1.94	1.04	−3.46
Tx28	75	0.11	1.73	5.15	4.30	1.41	−4.71
Tx34	40	0.58	0.17	0.75	0.55	0.60	−2.01
Tx34	60	0.26	0.59	2.05	1.61	0.91	−3.02
Tx34	85	0.13	1.67	4.50	3.92	1.28	−4.28
Tx40	40	0.82	0.12	0.53	0.39	0.50	−1.67
Tx40	70	0.27	0.66	2.07	1.69	0.88	−2.92
Tx40	100	0.13	1.92	4.53	4.19	1.25	−4.17
Tx46	40	1.17	0.09	0.36	0.27	0.42	−1.42
Tx46	75	0.33	0.57	1.69	1.41	0.80	−2.65
Tx46	115	0.14	2.04	4.30	4.19	1.22	−4.07
Tx54	40	1.66	0.06	0.26	0.19	0.35	−1.17
Tx54	80	0.42	0.48	1.38	1.17	0.70	−2.35
Tx54	125	0.17	1.85	3.59	3.64	1.10	−3.67

Table A.2. Unfactored girder end rotations for live load and thermal gradient for 28-ft and 44-ft wide standard bridges (8-ft girder spacing).

Girder Size	Span Length, ft	$\frac{EI}{L^2}$ kips × 10^4	θ_{lane} rad × 10^{-3}	θ_{truck} rad × 10^{-3}	θ_{live} rad × 10^{-3}	θ_{neg} rad × 10^{-3}	θ_{pos} rad × 10^{-3}
Tx28	40	0.41	0.30	1.03	0.81	0.78	−2.59
Tx28	55	0.22	0.77	2.32	1.93	1.07	−3.56
Tx28	70	0.13	1.59	4.03	3.60	1.36	−4.53
Tx34	40	0.61	0.20	0.69	0.54	0.62	−2.07
Tx34	60	0.27	0.67	1.88	1.61	0.93	−3.11
Tx34	85	0.14	1.89	4.08	3.93	1.32	−4.41
Tx40	40	0.87	0.14	0.49	0.38	0.52	−1.72
Tx40	65	0.33	0.60	1.60	1.40	0.84	−2.80
Tx40	95	0.15	1.87	3.65	3.69	1.23	−4.09
Tx46	40	1.24	0.10	0.34	0.27	0.44	−1.46
Tx46	70	0.41	0.52	1.33	1.19	0.77	−2.56
Tx46	105	0.18	1.76	3.16	3.34	1.15	−3.84
Tx54	40	1.76	0.07	0.24	0.19	0.36	−1.22
Tx54	80	0.44	0.55	1.25	1.17	0.73	−2.43
Tx54	125	0.18	2.09	3.18	3.68	1.14	−3.80

Table A.3. Unfactored girder end rotations for live load and thermal gradient for 30-ft wide standard bridges (8.67-ft girder spacing).

Girder Size	Span Length, ft	$\frac{EI}{L^2}$ kips × 10^4	θ_{lane} rad × 10^{-3}	θ_{truck} rad × 10^{-3}	θ_{live} rad × 10^{-3}	θ_{neg} rad × 10^{-3}	θ_{pos} rad × 10^{-3}
Tx28	40	0.42	0.31	1.00	0.81	0.79	−2.62
Tx28	55	0.22	0.81	2.23	1.93	1.08	−3.60
Tx28	70	0.14	1.68	3.86	3.61	1.38	−4.59
Tx34	40	0.63	0.21	0.66	0.54	0.63	−2.10
Tx34	60	0.28	0.70	1.82	1.61	0.95	−3.15
Tx34	80	0.16	1.67	3.42	3.38	1.26	−4.20
Tx40	40	0.89	0.15	0.47	0.38	0.52	−1.75
Tx40	65	0.34	0.63	1.54	1.40	0.85	−2.84
Tx40	95	0.16	1.98	3.46	3.71	1.24	−4.14
Tx46	40	1.27	0.10	0.33	0.27	0.44	−1.48
Tx46	70	0.42	0.55	1.27	1.19	0.78	−2.59
Tx46	105	0.18	1.86	2.98	3.35	1.17	−3.89
Tx54	40	1.81	0.07	0.23	0.19	0.37	−1.23
Tx54	80	0.45	0.58	1.19	1.17	0.74	−2.47
Tx54	120	0.20	1.95	2.75	3.33	1.11	−3.70

Table A.4. Unfactored girder end rotations for live load and thermal gradient for 32-ft wide standard bridges (9.33-ft girder spacing).

Girder Size	Span Length, ft	$\frac{EI}{L^2}$ kips × 10^4	θ_{lane} rad × 10^{-3}	θ_{truck} rad × 10^{-3}	θ_{live} rad × 10^{-3}	θ_{neg} rad × 10^{-3}	θ_{pos} rad × 10^{-3}
Tx28	40	0.43	0.33	0.96	0.81	0.80	−2.65
Tx28	50	0.27	0.64	1.72	1.50	0.99	−3.32
Tx28	65	0.16	1.41	3.14	2.98	1.29	−4.31
Tx34	40	0.64	0.22	0.64	0.54	0.64	−2.13
Tx34	60	0.28	0.74	1.74	1.61	0.96	−3.19
Tx34	80	0.16	1.76	3.26	3.39	1.28	−4.25
Tx40	40	0.91	0.16	0.45	0.38	0.53	−1.77
Tx40	65	0.34	0.67	1.47	1.40	0.86	−2.87
Tx40	90	0.18	1.77	2.94	3.24	1.19	−3.97
Tx46	40	1.30	0.11	0.31	0.26	0.45	−1.50
Tx46	70	0.43	0.58	1.21	1.18	0.79	−2.62
Tx46	100	0.21	1.69	2.55	2.96	1.12	−3.75
Tx54	40	1.85	0.08	0.22	0.19	0.37	−1.25
Tx54	80	0.46	0.61	1.13	1.17	0.75	−2.50
Tx54	120	0.21	2.05	2.58	3.34	1.12	−3.75

Table A.5. Unfactored girder end rotations for live load and thermal gradient for 38-ft wide standard bridges (8.5-ft girder spacing).

Girder Size	Span Length, ft	$\frac{EI}{L^2}$ kips × 10^4	θ_{lane} rad × 10^{-3}	θ_{truck} rad × 10^{-3}	θ_{live} rad × 10^{-3}	θ_{neg} rad × 10^{-3}	θ_{pos} rad × 10^{-3}
Tx28	40	0.42	0.31	1.01	0.81	0.78	−2.61
Tx28	55	0.22	0.80	2.25	1.93	1.08	−3.59
Tx28	70	0.14	1.65	3.91	3.61	1.37	−4.57
Tx34	40	0.62	0.21	0.67	0.54	0.63	−2.09
Tx34	60	0.28	0.69	1.84	1.61	0.94	−3.14
Tx34	80	0.16	1.65	3.46	3.38	1.26	−4.19
Tx40	40	0.88	0.15	0.47	0.38	0.52	−1.74
Tx40	65	0.33	0.62	1.56	1.40	0.85	−2.83
Tx40	95	0.16	1.95	3.51	3.70	1.24	−4.13
Tx46	40	1.27	0.10	0.33	0.27	0.44	−1.48
Tx46	70	0.41	0.54	1.29	1.19	0.78	−2.58
Tx46	105	0.18	1.83	3.03	3.35	1.16	−3.88
Tx54	40	1.80	0.07	0.23	0.19	0.37	−1.23
Tx54	80	0.45	0.57	1.20	1.17	0.74	−2.46
Tx54	125	0.18	2.18	3.03	3.69	1.15	−3.84

Table A.6. Unfactored girder end rotations for live load and thermal gradient for 40-ft wide standard bridges (9-ft girder spacing).

Girder Size	Span Length, ft	$\frac{EI}{L^2}$ kips × 10^4	θ_{lane} rad × 10^{-3}	θ_{truck} rad × 10^{-3}	θ_{live} rad × 10^{-3}	θ_{neg} rad × 10^{-3}	θ_{pos} rad × 10^{-3}
Tx28	40	0.42	0.32	0.98	0.81	0.79	−2.64
Tx28	50	0.27	0.63	1.74	1.50	0.99	−3.30
Tx28	65	0.16	1.38	3.20	2.98	1.29	−4.29
Tx34	40	0.63	0.21	0.66	0.54	0.63	−2.11
Tx34	60	0.28	0.72	1.78	1.61	0.95	−3.17
Tx34	80	0.16	1.71	3.34	3.38	1.27	−4.23
Tx40	40	0.90	0.15	0.46	0.38	0.53	−1.76
Tx40	65	0.34	0.65	1.50	1.40	0.86	−2.85
Tx40	90	0.18	1.72	3.02	3.23	1.19	−3.95
Tx46	40	1.29	0.11	0.32	0.27	0.45	−1.49
Tx46	70	0.42	0.57	1.24	1.19	0.78	−2.61
Tx46	105	0.19	1.91	2.90	3.36	1.17	−3.91
Tx54	40	1.83	0.07	0.23	0.19	0.37	−1.24
Tx54	80	0.46	0.59	1.17	1.18	0.74	−2.48
Tx54	120	0.20	2.00	2.66	3.33	1.12	−3.72

Table A.7. Service and strength load combo girder end rotations for 24-ft wide standard bridges (6.67-ft girder spacing).

Girder Size	Span Length, ft	$\theta_{service}^{pos}$ rad × 10^{-3}	$\theta_{service}^{neg}$ rad × 10^{-3}	$\theta_{strength}$ rad × 10^{-3}
Tx28	40	1.20	−2.51	1.44
Tx28	55	2.45	−3.46	3.39
Tx28	75	5.01	−4.71	7.53
Tx34	40	0.85	−2.01	0.96
Tx34	60	2.07	−3.02	2.82
Tx34	85	4.56	−4.28	6.86
Tx40	40	0.64	−1.67	0.68
Tx40	70	2.13	−2.92	2.97
Tx40	100	4.81	−4.17	7.32
Tx46	40	0.48	−1.42	0.47
Tx46	75	1.81	−2.65	2.47
Tx46	115	4.80	−4.07	7.34
Tx54	40	0.37	−1.17	0.33
Tx54	80	1.52	−2.35	2.05
Tx54	125	4.19	−3.67	6.37

Table A.8. Service and strength load combo girder end rotations for 28-ft and 44-ft wide standard bridges (8-ft girder spacing).

Girder Size	Span Length, ft	$\theta_{service}^{pos}$ rad × 10^{-3}	$\theta_{service}^{neg}$ rad × 10^{-3}	$\theta_{strength}$ rad × 10^{-3}
Tx28	40	1.20	−2.59	1.42
Tx28	55	2.46	−3.56	3.38
Tx28	70	4.28	−4.53	6.31
Tx34	40	0.85	−2.07	0.95
Tx34	60	2.07	−3.11	2.81
Tx34	85	4.59	−4.41	6.88
Tx40	40	0.64	−1.72	0.67
Tx40	65	1.82	−2.80	2.45
Tx40	95	4.31	−4.09	6.46
Tx46	40	0.49	−1.46	0.47
Tx46	70	1.57	−2.56	2.07
Tx46	105	3.91	−3.84	5.84
Tx54	40	0.37	−1.22	0.33
Tx54	80	1.54	−2.43	2.05
Tx54	125	4.25	−3.80	6.44

Table A.9. Service and strength load combo girder end rotations for 30-ft wide standard bridges (8.67-ft girder spacing).

Girder Size	Span Length, ft	$\theta_{service}^{pos}$ rad × 10^{-3}	$\theta_{service}^{neg}$ rad × 10^{-3}	$\theta_{strength}$ rad × 10^{-3}
Tx28	40	1.20	−2.62	1.42
Tx28	55	2.47	−3.60	3.37
Tx28	70	4.30	−4.59	6.31
Tx34	40	0.85	−2.10	0.94
Tx34	60	2.08	−3.15	2.82
Tx34	80	4.01	−4.20	5.91
Tx40	40	0.65	−1.75	0.67
Tx40	65	1.83	−2.84	2.45
Tx40	95	4.33	−4.14	6.49
Tx46	40	0.49	−1.48	0.47
Tx46	70	1.57	−2.59	2.07
Tx46	105	3.93	−3.89	5.86
Tx54	40	0.37	−1.23	0.33
Tx54	80	1.54	−2.47	2.05
Tx54	120	3.88	−3.70	5.82

Table A.10. Service and strength load combo girder end rotations for 32-ft wide standard bridges (9.33-ft girder spacing).

Girder Size	Span Length, ft	$\theta_{service}^{pos}$ rad × 10^{-3}	$\theta_{service}^{neg}$ rad × 10^{-3}	$\theta_{strength}$ rad × 10^{-3}
Tx28	40	1.21	−2.65	1.42
Tx28	50	2.00	−3.32	2.63
Tx28	65	3.63	−4.31	5.22
Tx34	40	0.86	−2.13	0.94
Tx34	60	2.09	−3.19	2.82
Tx34	80	4.03	−4.25	5.93
Tx40	40	0.65	−1.77	0.67
Tx40	65	1.83	−2.87	2.46
Tx40	90	3.84	−3.97	5.67
Tx46	40	0.49	−1.50	0.46
Tx46	70	1.58	−2.62	2.07
Tx46	100	3.53	−3.75	5.19
Tx54	40	0.38	−1.25	0.33
Tx54	80	1.55	−2.50	2.06
Tx54	120	3.90	−3.75	5.85

Table A.11. Service and strength load combo girder end rotations for 38-ft wide standard bridges (8.5-ft girder spacing).

Girder Size	Span Length, ft	$\theta_{service}^{pos}$ rad × 10^{-3}	$\theta_{service}^{neg}$ rad × 10^{-3}	$\theta_{strength}$ rad × 10^{-3}
Tx28	40	1.21	−2.61	1.43
Tx28	55	2.47	−3.59	3.37
Tx28	70	4.29	−4.57	6.31
Tx34	40	0.86	−2.09	0.95
Tx34	60	2.08	−3.14	2.82
Tx34	80	4.01	−4.19	5.91
Tx40	40	0.64	−1.74	0.67
Tx40	65	1.83	−2.83	2.45
Tx40	95	4.32	−4.13	6.48
Tx46	40	0.49	−1.48	0.46
Tx46	70	1.57	−2.58	2.08
Tx46	105	3.93	−3.88	5.86
Tx54	40	0.37	−1.23	0.32
Tx54	80	1.54	−2.46	2.05
Tx54	125	4.27	−3.84	6.46

Table A.12. Service and strength load combo girder end rotations for 40-ft wide standard bridges (9-ft girder spacing).

Girder Size	Span Length, ft	$\theta_{service}^{pos}$ rad × 10^{-3}	$\theta_{service}^{neg}$ rad × 10^{-3}	$\theta_{strength}$ rad × 10^{-3}
Tx28	40	1.21	−2.64	1.42
Tx28	50	1.99	−3.30	2.62
Tx28	65	3.62	−4.29	5.21
Tx34	40	0.86	−2.11	0.95
Tx34	60	2.09	−3.17	2.82
Tx34	80	4.02	−4.23	5.92
Tx40	40	0.64	−1.76	0.67
Tx40	65	1.83	−2.85	2.45
Tx40	90	3.83	−3.95	5.66
Tx46	40	0.49	−1.49	0.47
Tx46	70	1.58	−2.61	2.08
Tx46	105	3.95	−3.91	5.88
Tx54	40	0.37	−1.24	0.33
Tx54	80	1.55	−2.48	2.06
Tx54	120	3.89	−3.72	5.83

APPENDIX B. CONSTRUCTION DRAWINGS FOR EXPERIMENTAL TESTS

For individual specimens, detailed construction drawings are provided in this appendix. Cross-section views are available at consistent locations. Section A-A is located at the center of the continuous deck and has a consistent 8.5-in. thickness for the full width. The remaining sections are located over the girders and have the additional haunch on top of the girder shown (haunch dimension is generic). Section B-B is located at the center of the bearing pads and thus within the full-depth CIP region for offset panel designs.

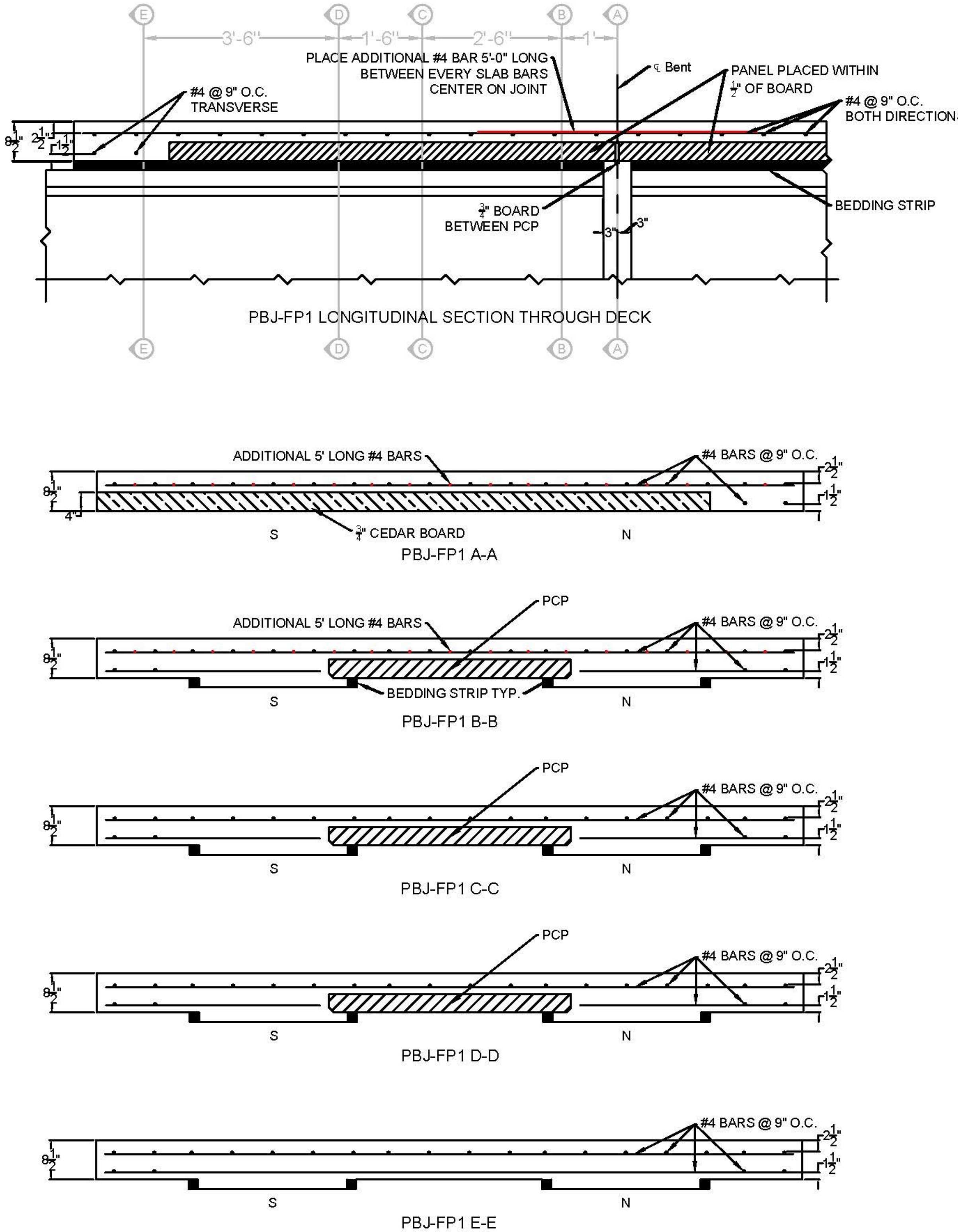

Figure B.1. PBJ-FP1: construction drawings.

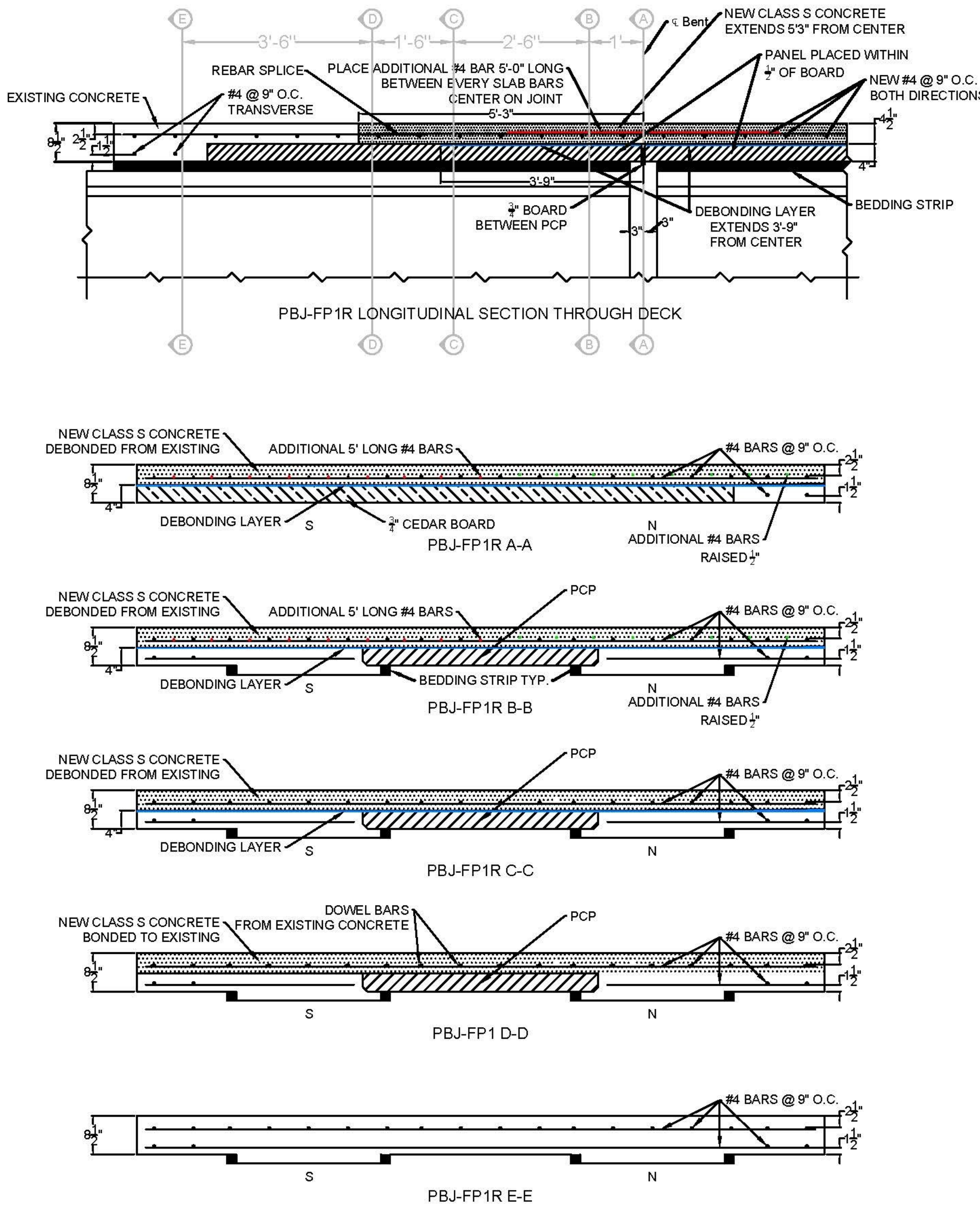

Figure B.2. PBJ-FP1R: construction drawings.

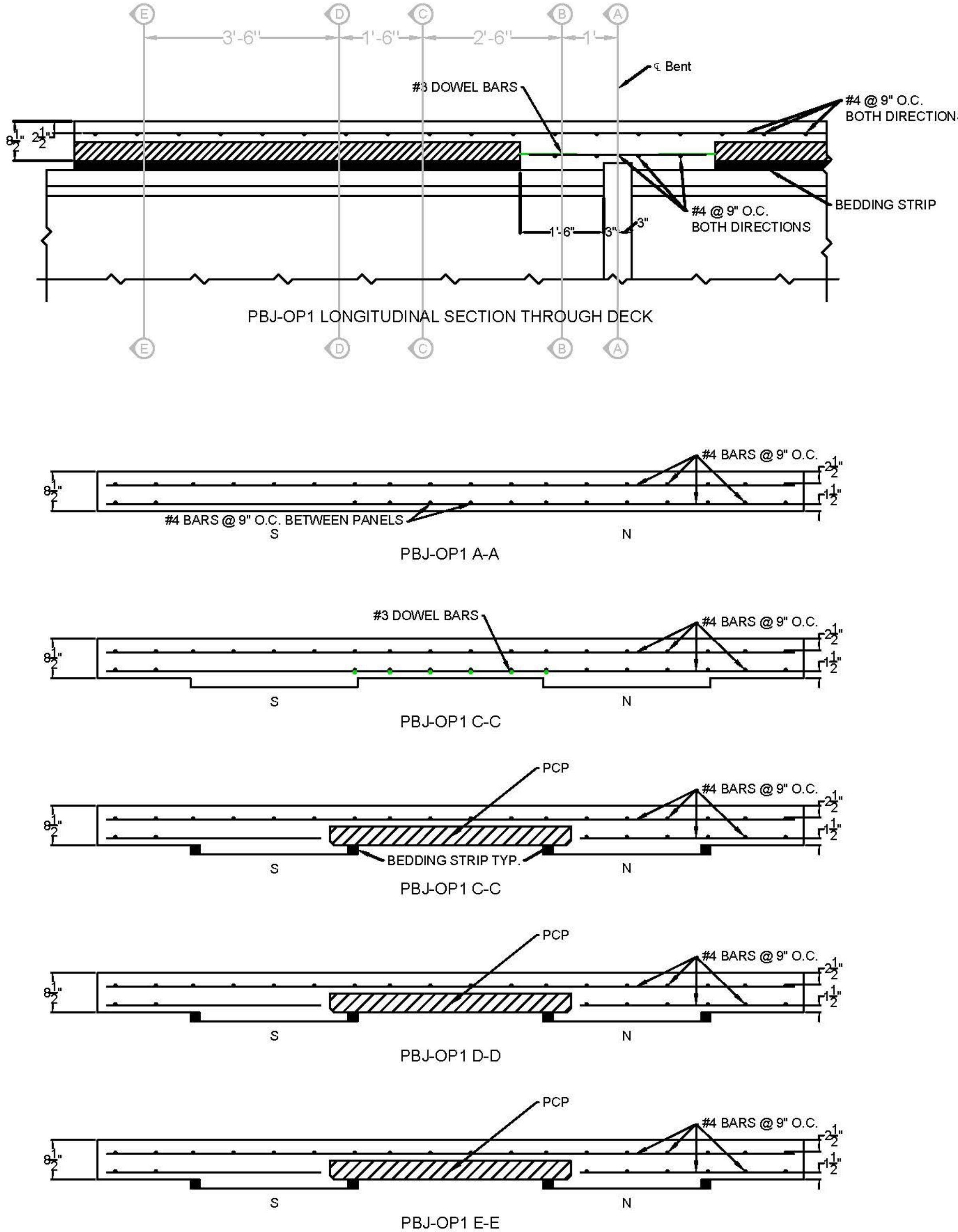

Figure B.3. PBJ-OP1: construction drawings.

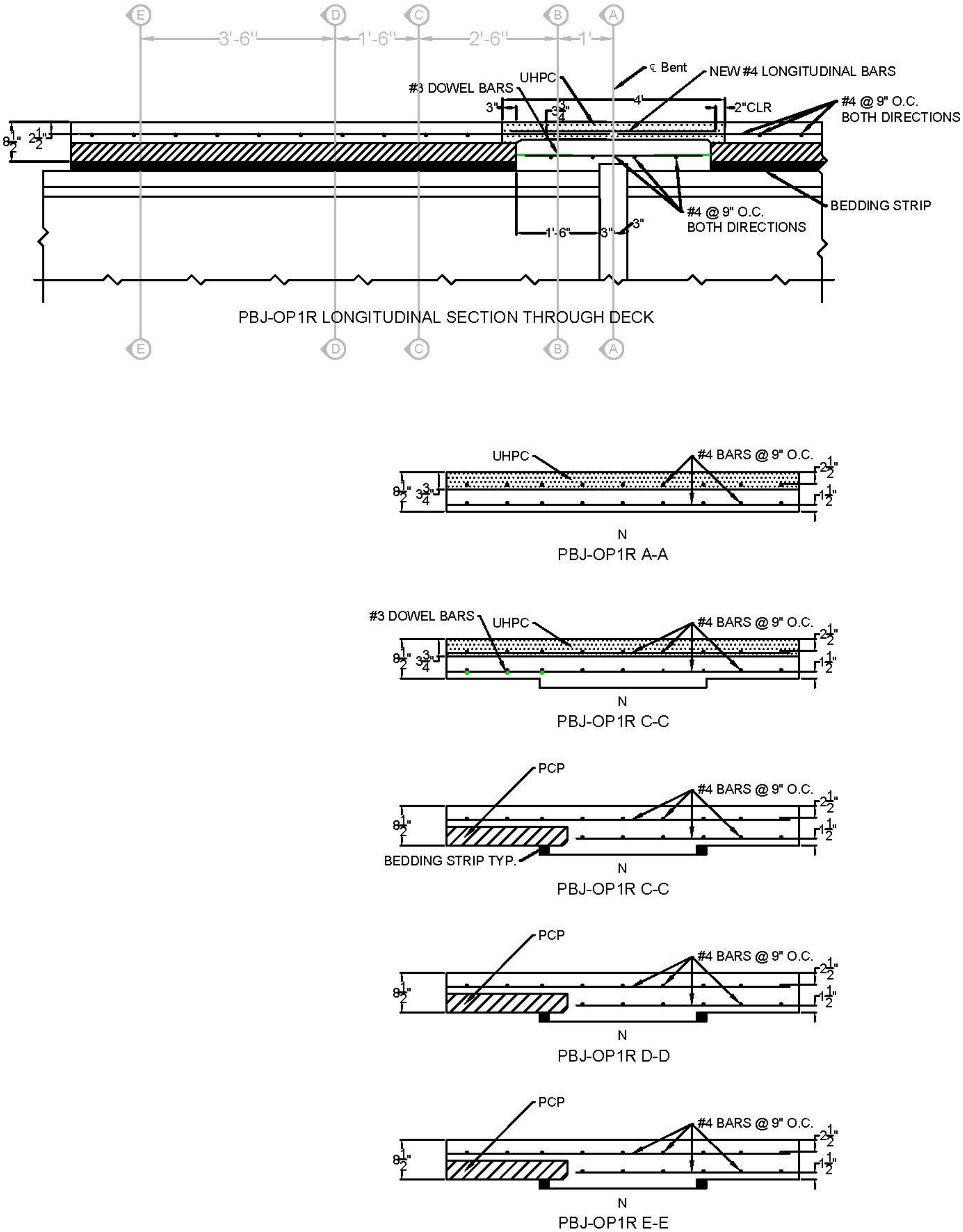

Figure B.4. PBJ-OP1R: construction drawings.

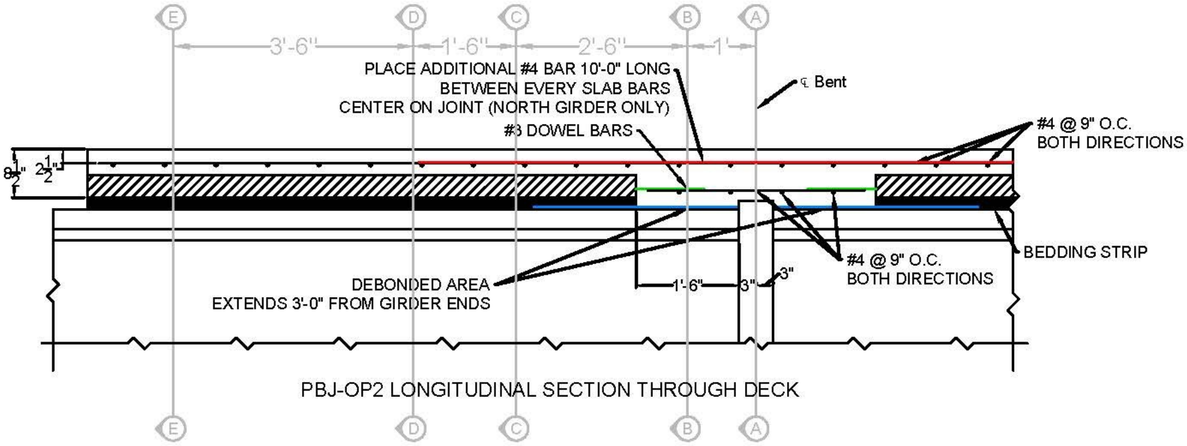

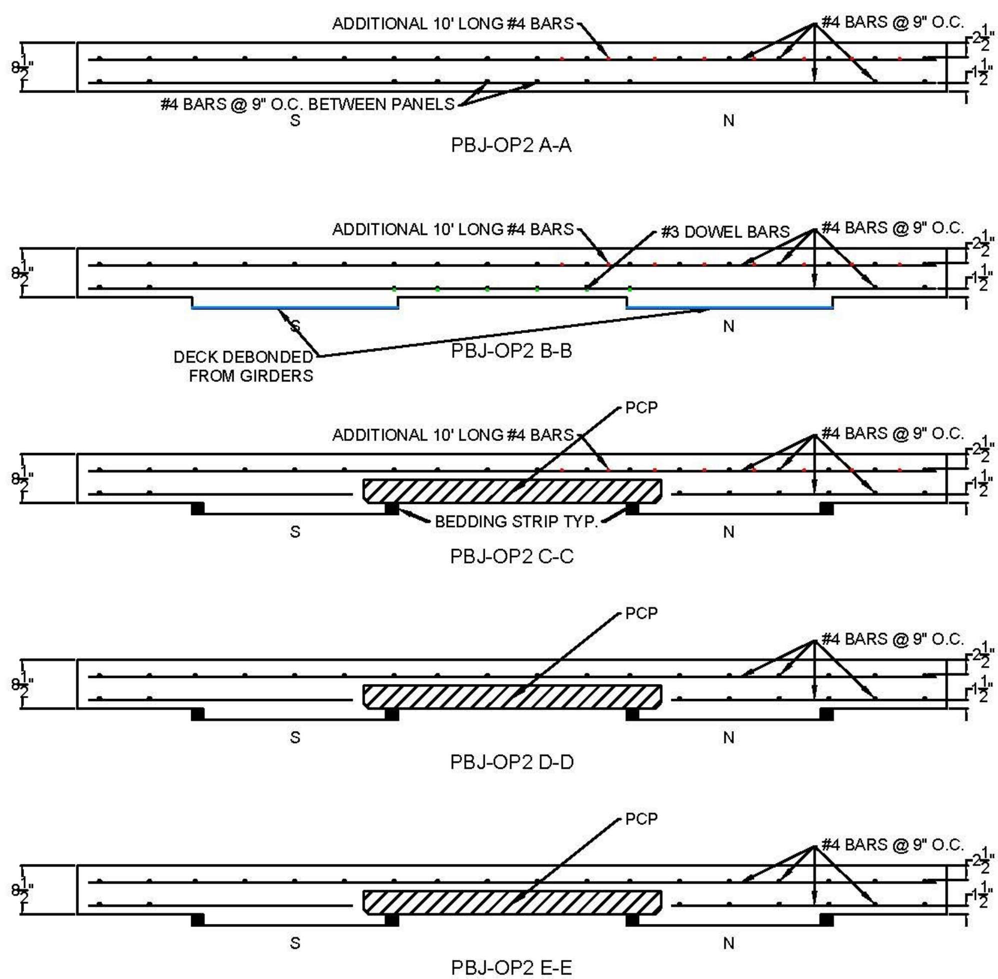

Figure B.5. PBJ-OP2: construction drawings.

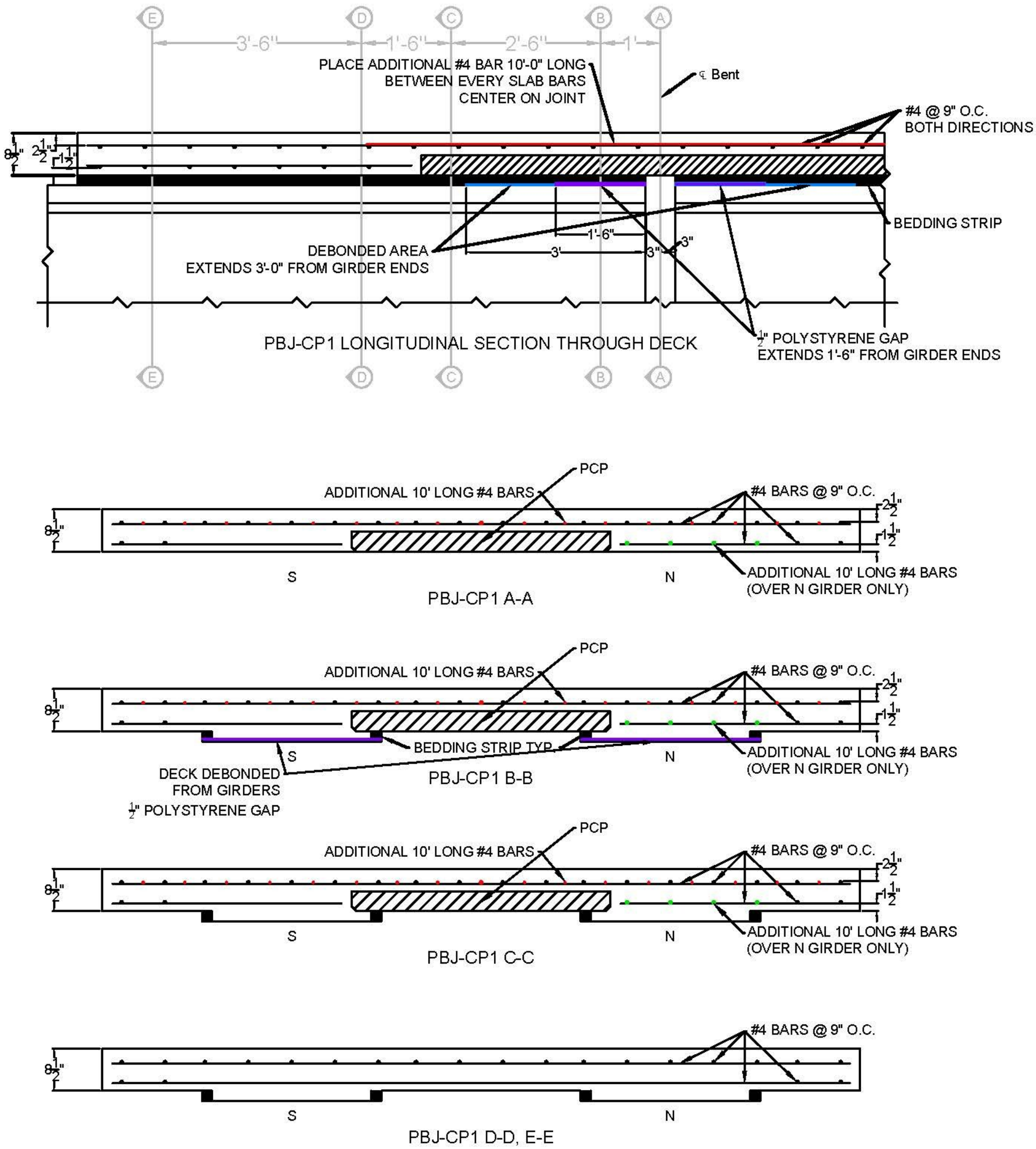

Figure B.6. PBJ-CP1: construction drawings.

APPENDIX C. VALUE OF RESEARCH

C.1 MOTIVATION AND SIGNIFICANCE

The Texas Department of Transportation (TxDOT) maintains over 55,000 bridges and builds over 500 new bridges every year. With such a large inventory to manage, consideration of maintenance and durability issues is critical to providing long-lasting bridges and managing life-cycle costs. A majority of TxDOT bridges have simple-span girders, with a gap between the ends of the girders at the interior supports. At this gap, expansion joints are common sources of maintenance needs and lead to deck durability issues. To reduce the number of expansion joints, link slabs may be used, in which the deck is made continuously between the girder ends.

TxDOT has utilized bonded link slabs for approximately four decades. These are commonly referred to as “poor boy” continuous deck details, or “poor boy” joints (PBJs), on account because of the reinforcement for the link slab region being the same as that used in the remainder of the deck.

Although some prior research studies have touched on the performance of PBJs, a comprehensive study has not been conducted. Thus, there is a need to evaluate the performance of bridges using current details and to make recommendations for design alternatives, particularly the performance of the newer flush panel detail. Design alternatives may be driven by constructability and/or performance and may range from minor detailing changes to the use of alternative materials.

The objective of this project was to conduct a comprehensive review of PBJ details and to provide recommendations for design and detailing methods to improve or alter the continuous deck details presently used by TxDOT. Specific technical objectives were to understand the performance of existing PBJ details and recommend modified details for new and existing decks.

C.2 QUALITATIVE VALUES

Qualitative values are non-monetary intangible subjective benefits. They cannot be measured and may influence business and legislative decisions. Qualitative values are assets such as patents, relationships, and software trained workforce. Therefore, qualitative values can be defined as intellectual capital that can be used to produce fundings and cost savings (TxDOT, 2015).

C.2.1 Level of Knowledge

In Texas, the poor boy continuous deck detail has been used for decades to build continuous reinforced concrete bridge decks. This research will conduct a comprehensive study of the poor boy details that include evaluation of as-built drawings and inspection reports of nearly 500 bridges, non-destructive evaluation of eight bridges, and monitoring five bridges for deformations under live and thermal loads, and implementation of finite element modeling and full-scale experimental testing. Based on comprehensive study, this project will provide recommendations for design and detailing methods to improve or alter the continuous deck details presently used by TxDOT.

With this knowledge, TxDOT can implement specific design improvements, leading to more durable and maintenance-friendly bridges, reducing long-term repair costs, and extending the lifespan of the infrastructure.

C.2.2 Management and Policy

This study provides the limitations to the use of current design and details and modifications to improve performance. In addition, the research team will provide detailed alternative design recommendations for TxDOT bridges. These will be thoroughly documented to ensure that all necessary steps are clear, enabling the integration of these findings into new design standards. Implementing these recommendations will improve the service life of PBJs and influence the design of standard bridge decks as outlined in bridge standards.

C.3 ECONOMIC VALUES

This project aims to deliver economic benefits to TxDOT by suggesting alternative design recommendations that can extend the service life of the link slabs. Calculations such as net present value (NPV) and cost-benefit analysis are described in this section as they are fundamental to economic value. Possible saving areas due to successful implementation of this research project are classified in four main categories: (1) savings due to increased service life, (2) reduced construction, operations, and maintenance cost.

C.3.1 Increased Service Life

The results of this research increase the service life of bridge decks because of load distribution and reducing the intensive stresses at connections. It was assumed that the service life of the improved PBJ detail increases by 25%. The average width of a multilane bridge deck is assumed to be 40 ft (TxDOT, 2023). The area to replace a PBJ is considered 5 ft on each side resulting in 400 ft^2. The cost to replace a PBJ is \$100 per ft^2 that makes it \$40,000 to replace one PBJ. Traffic control is assumed to be about the same as the cost to replace a PBJ. Therefore, a cost saving of 25% of the \$40,000 construction cost was considered for the increase in service life and 25% of the \$40,000 for traffic control per PBJ. The cost of the detour is assumed to be \$1,000 and helps the residents of Texas.

To estimate the number of bridges that include PBJs, the number of bridges either rehabilitated or newly constructed annually was estimated based on Table C.1 and Table C.2. According to Texas Bridge Database (TxDOT, 2023), there are on average 127 bridges rehabilitated and on average 610 bridges newly built every year. Approximately 10% of these bridges have PBJs, which was estimated based on the number of bridges with PBJs in the Panhandle district. In the

Panhandle, 258 out of 2,463 bridges incorporate PBJs, as shown in Table C.3. Therefore, assuming 10% of the either rehabilitated or newly constructed bridges have PBJs across Texas, approximately 74 of the 737 bridges rehabilitated or newly built annually will include PBJs as shown in Table C.4. Assuming each bridge contains 2 PBJs on average, the total number of PBJs constructed annually is estimated to be 147 (Table C.5).

Table C.1. Average Number of Rehabilitated Bridges in Texas

Year	Number of Rehabilitated Bridges
2014	143
2015	152
2016	176
2017	126
2018	170
2019	131
2020	220
2021	32
2022	25
2023	91
Average	127

Table C.2. Number of Newly Built Bridges in Texas

Year	Number of Newly Built Bridges
2014	673
2015	680
2016	640
2017	627
2018	634
2019	534
2020	632
2021	595
2022	655
2023	429
Average	610

Table C.3. Percentage of PBJ bridges in the Panhandle

Total Bridges in the Panhandle	2,463
Number of Bridges with PBJs	258
Percentage of PBJ Bridges	10 %

Table C.4. Number of Bridges with PBJs Built per Year

Number of Rehabilitated Bridges per Year	127
Number of Newly Built Bridges per Year	610
Total Number of Constructed Bridges per Year	737
Percentage of PBJ Bridges	10%
Number of Bridges with PBJs	74

Table C.5. Total Number of PBJs Constructed per Year

Number of PBJs per Bridge	2
Total Number of PBJs per Year	147

The cost benefit associated with extended bridge deck replacement cycles is approximately \$10,000 per PBJ. Similarly, the cost benefit associated with traffic control is approximately \$10,000 per PBJ. Therefore, the combined economic benefit of these engineering design improvements can be estimated at \$20,000 per PBJ. For the 147 joints considered, this results in a total of \$2,940,000.

C.3.2 Reduced Construction, Operation, and Maintenance Cost

The economic benefits of this project derived from the increased service life and reduced construction operation and maintenance cost are closely related. The extended service life of the PBJs directly leads to decreased costs associated with their construction and maintenance. Therefore, the economic benefit associated with the extended bridge deck replacement cycles and traffic control are already accounted for in the area of increased service life. In this section, only the cost associated with detour is included as the cost benefit of reduced construction, operations, and maintenance, which is approximately \$1,000 per PBJ. Consequently, the total economic benefit from reduced construction, operations, and maintenance cost can be estimated at \$1,000 for each of the 147 joints annually. This amounts to a total saving of \$147,000.

C.4 BOTH QUALITATIVE AND ECONOMIC VALUES

This section describes functional areas such as engineering design improvements, which have qualitative and economic values for the state of Texas.

C.4.1 Engineering Design Improvement

Two variables were considered to determine the economic benefit of engineering design improvement on the outcomes of this research. These are the costs associated with construction and detour. The construction cost is assumed to be \$200 higher for the new PBJ design over the conventional PBJ. The cost has a negative effect on the overall economic impact of using PBJ in TxDOT continuous bridges because it counts for implementing the new PBJ detail such as putting paper down between the girder and the deck to unbonded the link slab. The cost associated with detour was assumed to be $1,000, which is like the cost of detour estimated for reduced construction, operations, and maintenance cost. Therefore, the economic benefit of engineering design improvement can be estimated at $117,600 for an average of 147 joints. This includes the negative impact of construction is $29,400, and the benefit of detour is estimated at $147,000.

The yearly expected value is $3,204,600 for the upcoming years. The evaluation of the total savings is a static mathematical technique and can be generated by summing up the expected values per year minus the project budget and the one-time engineering cost. The expected total saving after 10 years is calculated to be $28,114,102. Another relevant number is the payback period which indicates the length of time it requires to recover the budget of the project. The payback period for this project is 0.23 years, thus after a little more than a year after termination of this research project, the project has reached the break-even point and starts to generate profits.

The net present value is a dynamic calculation method to identify the cost because it also regards the discount rate per year. The handbook published by TxDOT (2015) provides the net present value as:

$$NPV = \sum_{t=1}^{T} \frac{C_t}{(1+r)^t} - C_0 \tag{C.1}$$

where

C_t= net cash inflow during the period

C_0= initial investment

r = discount rate

t = number of time periods

The discount rate is typically 5% (TxDOT, 2015) and the number of time periods is 10 years. Figure 1 presents the development of the net present value for the next 10 years and the reader will see that the net present value becomes positive between the first and the second year. After 10 years, NPV = $23,019,404. The benefit-cost ratio (BCR) is given by:

$$BCR = \frac{NPV}{\text{Project Budget}} \tag{C.2}$$

The benefit-cost ratio is 32, which indicates that TxDOT can expect a benefit of $32 with each dollar invested in this research project.

C.5 SUMMARY AND FUTURE WORK

This research project provides benefit to both the state of Texas and TxDOT. This project has qualitative as well as quantitative or economic values and will save TxDOT and the state of Texas more than $28 million in 10 years following the implementation of the project guidelines.

Figure C.1 presents the evaluation of the net present value for the next ten years with the start in year zero after the completion of the project and the one-time engineering cost and with the final savings of $28,114,102. Because of the positive net present value, the research is profitable, and the cost-benefit ratio is 32, which represents the benefit for each dollar invested in this research project. The payback period is 0.23 years which means that after 0.23 years of termination of this research project, TxDOT will start to generate profits, and the total savings are calculated to be $28,114,102 within 10 years.

The net present value and the total savings only include the direct cost, such as inspector or administrative cost, and not the expected indirect cost of $23M per year for the reduction in traffic congestion and the potential additional cost for injuries or fatalities. All indirect costs will be considered as part of a full econometric analysis as part of this project.

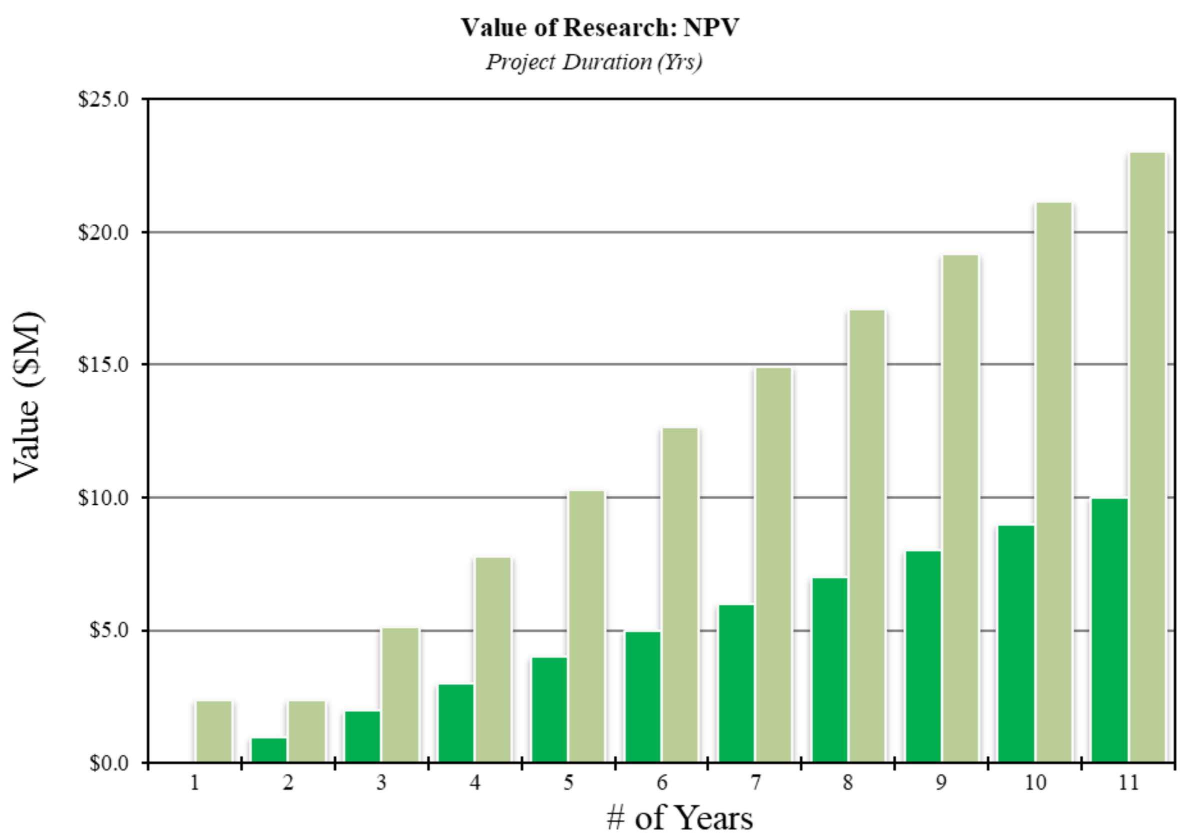

Figure C.1. Net Present Values for the Next 10 Years

REFERENCES

TxDOT. (2015). University Handbook 2016 The Research and Technology Implementation Office: Texas Department of Transportation.

TxDOT. (2023). TxDOT Bridges. TxDOT Open Data Portal. Retrieved from https://gis-txdot.opendata.arcgis.com/datasets/83af0d2957ca4c2eb340e4bd04a1046f/explore